Probing lipidation of membrane active peptides and integral membrane proteins by liquid chromatography-mass spectrometry and ion mobility separation-mass spectrometry

ISMAIL, VIAN,SDIQ,ISMAIL

Durham University
Department of Chemistry

Probing lipidation of membrane active peptides and integral membrane proteins by liquid chromatography-mass spectrometry and ion mobility separation-mass spectrometry

A thesis submitted in partial fulfilment of the requirements for the degree of Doctor of Philosophy

Vian Sdiq Ismail

2017

Abstract

Liquid chromatography coupled with mass spectrometry (LC-MS) and tandem mass spectrometry (LC-MS^2) are shown to have the sensitivity and functionality to detect protein/peptide modifications by fatty acyl chains *in vitro* and *in vivo* studies. Further analysis was also performed by direct infusion ion mobility separation coupled with mass spectrometry (IMS-MS) or tandem mass spectrometry (IMS-MS^2).

Peptide lipidation *in vitro* was investigated using the membrane active peptide, melittin. Non-enzymatic melittin lipidation by lysophospholipids has been observed for the first time. When the effect of lysophospholipids was studied in direct competition with diacylphospholipids, the acyl transfer from the lysophospholipids is seen to be preferential with acylation visible after just 3 hour. The longer the interaction time, the greater the amount and number of modifications with double and triple acylation observed after 96 hour. The locations of the modifications identified through LC-MS^2 were assigned on different sites of the peptide, including N-terminus, K7, S18, K21, K23, R22 and R24 and with the highest reactivity towards N-terminus and K23. Comparing the lipidation of synthetic melittin (SynM) with the lipidation of naturally occurring melittin from venom of honey bee (BVM) highlights the effect of the PLA_2 enzyme that is naturally present in BVM. Here, the action of the enzyme to hydrolyse the diacylphospholipid at the *sn*-2 position to give the corresponding lysophospholipid is reflected in the acyl transfer to the BVM such that the resulting lysophospholipid clearly dominates the acyl transfer to BVM. In contrast, the acyl transfer to SynM clearly demonstrates that acyl transfer is possible in the absence of an enzyme.

In vivo protein lipidation of one of the most abundant integral membrane proteins in mammalian eye lens, AQP0, was also studied. A wide range of acyl groups are shown to modify this protein at the known modification sites, N-terminus and at the amino acid residue K238, many of which are reported here for the first time. These acyl group modifications reflect the biological lipid composition of the membrane leaflet that the acylation sites are proximal to.

In an attempt to further distinguish between different forms of lipidated melittin, whether with the same acyl chain modification to different amino acids or to discriminate between palmitoylation and oleoylation modifications, travelling wave ion mobility spectrometry (TWIMS) coupled with MS or MS^2 was applied. Results suggested that resolving positional isomers of diacylphospholipids and lysophospholipids (*sn*-1 *vs* *sn*-2 positions) is not possible under the conditions described herein. However, the presence of fatty acyl chains covalently bound to melittin change the conformation of acylated melittin in the gas-phase such that for lower charge states it is possible to suggest a small degree of separation between palmitoylated and oleoylated melittin or their isomers including acylation on N-terminus *vs* K23. This small degree of separation is enough so that when combined with tandem mass spectrometry, the time-aligned product ion spectra are clearer and improve characterisation.

To conclude, the research in this thesis has shown that two of the most abundant biomolecules, lipid and peptides/proteins that are known to exist in close proximity to each other, or interact with each other, are not as chemically inert as previously thought. This reactivity has been reflected herein via aminolysis reaction between membrane lipid composition and each of membrane active peptide, melittin and integral membrane protein, AQP0.

Table of contents

List of figures ..... **viii**
List of tables ..... **xiii**
List of abbreviations and units ..... **xvi**
Declaration and Statement of copyright ..... **xix**
Acknowledgment ..... **xx**
Chapter one: Introduction **1**
1.1. Cell membrane 2
1.2. Biomimetic membrane 4
1.3. Membrane lipids 6
1.3.1. Phospholipids 6
1.3.1.1. Glycerophospholipids 6
1.3.1.1.1. Phase behavior of phospholipid bilayer 10
1.3.1.1.2. Action of Phospholipase enzyme on phospholipids 11
1.3.1.1.3. The influence of lysophospholipid and fatty acid partitioning on lipid membrane 13
1.3.1.2. Sphingophospholipid (SPL) 15
1.3.2. Sterols 16
1.4. Analytical methods for lipid analysis 17
1.5. Lipid-protein interaction 20
1.6. Protein lipidation 21
1.7. Melittin 22
1.8. AQP0 in mammalian eye lens 24
1.9. References 27
Chapter two: Instrumentation **44**
2.1. Mass spectrometry 45
2.1.1. Ion sources 46
2.1.1.1. Electrospray ionisation (ESI-MS) 47
2.1.1.2. Matrix-assisted laser desorption/ionisation (MALDI-MS) 49
2.1.2. Mass analysers 50
2.1.2.1. Quadrupole mass analyser (Q-MS) 52
2.1.2.2. Linear ion trap mass analyser (LIT-MS) 55
2.1.2.3. Fourier transform ion cyclotron resonance mass analyser (FTICR-MS) 57
2.1.2.4. Time-of-flight mass analyser (ToF-MS) 61
2.1.3. Tandem mass spectrometry of peptides and proteins 64
2.1.3.1. Collision induced dissociation 66

2.2. Ion mobility separation 68
2.3. Schematic of applied instruments 71
2.3.1. LTQFT 71
2.3.2. Autoflex II ToF/ToF 74
2.3.3. Synapt G2-s 75
2.4. References 77
Chapter three: Understanding the role of lysophosphatidylcholine (LPC) and diacylphosphatidylcholine (PC) in the lipidation of melittin 85
3.1. Phase behavior of the lipid systems studied 86
3.2. Reaction of melittin with lysophospholipids 88
3.2.1. Reaction of synthetic melittin (SynM) with oleoylphosphatidylcholine (OPC) 88
3.2.2. Reaction of synthetic melittin (SynM) with palmitoylphosphatidylcholine (PPC) 96
3.2.3. Reaction of synthetic melittin (SynM) with PPC:OPC mixtures 99
3.2.4. Reaction of bee venom melittin (BVM) with different lysophospholipids 104
3.3. Reaction of SynM with diacylphosphatidylcholine (PC) 105
3.4. Reaction of SynM with PC:LPC mixtures 108
3.4.1. Competitive acyl transfer from PC:LPC system to give SynM single acylation 109
3.4.2. Competitive acyl transfer from PC:LPC system to give SynM double acylation 114
3.4.3. Competitive acyl transfer from PC:LPC system to give SynM triple acylation 116
3.5. LC-MS^2 analysis of SynM double acylation 118
3.5.1. LC-MS^2 analysis of $SynM_{2pal}$ 119
3.5.1.1. Summarised $SynM_{2pal}$ fragmentation 126
3.5.2. LC-MS^2 analysis of $SynM_{2ole}$ 127
3.5.2.1. Summarised $SynM_{2ole}$ fragmentation 133
3.5.3. LC-MS^2 analysis of $SynM_{pal+ole}$ 134
3.5.3.1. Summarised $SynM_{pal+ole}$ fragmentation 142
3.6. BVM *vs* SynM selectivity towards *sn*-1 and *sn*-2 acyl chains 144
3.6.1. Selectivity comparison using POPC and OPPC 145
3.6.2. Reaction with OPC:DPPC 151
3.7. Conclusion 153
3.8. References 154
Chapter four: New insight to integral membrane protein (AQP0) lipidation by membrane lipids 158
4.1. Analysis of the intact AQP0 from four different regions of bovine eye lens (b-AQP0) 159
4.1.1. The identification of b-AQP0 modifications by ESI-LC-MS 159
4.1.2. The identification of truncated proteins by ESI-LC-MS 174

4.1.3. The identification of neutral lipid classes in bovine lens by ESI-LC-MS 176
4.1.4. Analysis of the intact b-AQP0 by MALDI-MS 180
4.2. Exploring the modifications on AQP0 by LC-MS analysis 182
4.2.1. Analytical approach in proteolytic analysis of bovine AQP0 (b-AQP0) 182
4.2.1.1. Method development: improving the LC separation and the proteolytic digestion 187
4.2.1.1.1. Optimising the LC-MS 187
4.2.1.1.2. Optimising the proteolytic digestion 191
4.2.2. Biological approach in proteolytic analysis of b-AQP0 192
4.2.2.1. The localisation of acylation modification on b-AQP0 by LC-MS^2 198
4.2.2.2. The effect of lens aging on the peptide modifications in b-AQP0 205
4.2.2.3. Bovine lens PE/PEpl correlation with acylated b-AQP0 210
4.2.3. Biological approach in proteolytic analysis of h-AQP0 213
4.2.3.1. The effect of lens aging on h-AQP0 modifications 222
4.2.3.2. Human lens lipid correlation with acylated h-AQP0 225
4.3. The lipid-binding amphipathic helix in AQP0 227
4.4. Conclusion 230
4.5. References 232
Chapter five: Application of ion mobility separation-mass spectrometry (IMS-MS) to the analysis of phosphatidylcholine and synthetic lipidated melittin analogues 237
5.1. Analysis of phosphatidylcholine by ion mobility separation-mass spectrometry (IMS-MS) 238
5.1.1. IMS-MS analysis of lysophosphatidylcholine (LPC) 238
5.1.2. IMS-MS analysis of diacylphosphatidylcholine (PC) 241
5.2. Analysis of synthetic lipidated melittin analogous by ion mobility separation-mass spectrometry (IMS-MS) 245
5.3. Ion mobility separation and transfer cell CID fragmentation (IMS-MS^2) for synthetic lipidated melittin 258
5.4. Conclusion 264
5.5. References 265
Chapter six: Conclusion 268
6.1. Conclusion 269
6.2. References 272
Chapter seven: Future work 274
7.1. Future work 275
7.2. References 277

Chapter eight: Materials and methods 279
8.1. Sample preparation and instrument parameters for chapter three: Understanding the role of lysophosphatidylcholine (LPC) and diacylphosphatidylcholine (PC) in the lipidation of melittin 280
8.1.1. Chemicals and sample preparation 280
8.1.1.1. Liposome and lysophospholipid preparation 280
8.1.1.2. Melittin acylation preparation 281
8.1.2. LC-MS and instrument parameters 281
8.1.2.1. LC-MS on LTQFT instrument 281
8.1.2.1.1. LC-FTICR-MS 281
8.1.2.1.2. LC-LTQ-MS^2 282
8.1.2.2. LC-MS on Synapt G2-s 283
8.1.2.2.1. LC-QToF-MS 283
8.2. Sample preparation and instrument parameters for chapter four: New insight to integral membrane protein (AQP0) lipidation by membrane lipids 284
8.2.1. Chemicals and sample preparation 284
8.2.1.1. Chemicals 284
8.2.1.2. Lens membrane extraction 284
8.2.2. LC-MS and instrument parameters 285
8.2.2.1. LC-MS on LTQFT instrument 286
8.2.2.1.1. Analysis of intact protein by LC-FTICR-MS 286
8.2.2.1.2. Analysis of protein digestion by LC-FTICR-MS 286
8.2.2.2. LC-MS on Synapt G2-s instrument 287
8.2.2.2.1. Analysis of protein digestion by LC-QToF-MS 287
8.2.2.2.2. Analysis of protein digestion by LC-QToF-MS^2 and LC-QToF-MS^E 287
8.2.3. Analysis of intact protein by MALDI-ToF-MS (Autoflex II instrument) 288
8.2.4. Prediction of potential lipid binding regions 288
8.3. Sample preparation and instrument parameters for chapter five: Application of ion mobility separation-mass spectrometry (IMS-MS) to the analysis of phosphatidylcholine and synthetic lipidated melittin analogues 289
8.3.1. Chemicals and sample preparation 289
8.3.2. IMS-MS/MS^2 and instrument parameters on Synapt G2-s instrument 289
8.3.2.1. IMS-MS analysis for phosphatidylcholine 289
8.3.2.2. IMS-MS/MS^2 analysis for synthetic lipidated melittin analogous 290
8.4. References 290
Chapter nine: Appendices 292
9.1. Appendix A 293

9.2. Appendix B: Supplementary information for Chapter three - Understanding the role of lysophosphatidylcholine (LPC) and diacylphosphatidylcholine (PC) in the lipidation of melittin.....296
9.3. Appendix C: Supplementary information for Chapter four - New insight to integral membrane protein (AQP0) lipidation by membrane lipids 324
9.4. References.....344

List of figures

Figure 1.1. The fluid-mosaic model for the cell membrane as proposed by Singer-Nicolson 3
Figure 1.2. Peptide-membrane binding mechanism 4
Figure 1.3. Schematic to illustrate different types of liposomes 5
Figure 1.4. Structural representation for GPLs 7
Figure 1.5. Structural representation for the two common ether GPLs of plasmalogen-/plasmenyl GPL and plasmanyl GPL 9
Figure 1.6. The three phase states ($L_{\beta'}$, L_{α} and $P_{\beta'}$) for hydrated PL bilayer 11
Figure 1.7. The cleavage sites of PL by the hydrolysis activity of phospholipase enzymes 12
Figure 1.8. The products LPC and free FA from the hydrolysis of PC by the PLA_2 enzyme and different polymorphic phases for aggregated lipid molecules in water 13
Figure 1.9. Incorporation of LPC, free FA and both LPC and free FA into the lipid bilayer of PC and their impact on lipid bilayer curvature stress 14
Figure 1.10. Sphingomyelin (SM) structure 16
Figure 1.11. Cholesterol structure 17
Figure 1.12. Lipid bilayer representation for annular lipids and non-annular lipids 21
Figure 1.13. *α*-Helix structure from tetramer aggregation of melittin 23
Figure 1.14. The structure of human eye and the illustration of cellular fractions in the eye lens 24
Figure 1.15. The water pore in junctional AQP0 and non-junctional AQP0 26
Figure 2.1. Schematic for mass spectrometer basic components 45
Figure 2.2. The strength scale for the range of ionisation techniques 46
Figure 2.3. Schematic illustration of ESI source in positive ion mode 47
Figure 2.4. The two proposed mechanisms in ESI, charge residue model (CRM) and ion evaporation model (IEM) 49
Figure 2.5. Ionisation principle in MALDI source 50
Figure 2.6. Peak width definition for a single isolated peak 52
Figure 2.7. Diagram of quadrupole 53
Figure 2.8. Stability diagram for different ions in quadrupole 54
Figure 2.9. Linear ion trap (LTQ) as featured in the LTQFT 55
Figure 2.10. Stability diagram for trapped ions in LTQ device 57
Figure 2.11. Diagram of FTICR 58
Figure 2.12. Ions motion within FTICR cell 59
Figure 2.13. Illustration of ion excitation and ion detection steps in FTICR cell 61
Figure 2.14. Schematic illustration of linear ToF-MS and reflectron ToF-MS 63
Figure 2.15. Schematic description of reflectron ToF-MS fitted with an orthogonal acceleration aperture (oa ToF) 64
Figure 2.16. Illustration of common cleavage sites of peptide backbone 65
Figure 2.17. Schematic illustration for drift time ion mobility spectrometry (DTIMS) and travelling wave ion mobility spectrometry (TWIMS). 69
Figure 2.18. The LTQFT (ThermoFinnigan) instrument schematic 71
Figure 2.19. The conversion dynode detector, secondary electron multiplier (SEM) equipped with LTQ analyser 73
Figure 2.20. Schematic of Autoflex II ToF/ToF mass spectrometer (Bruker Daltonik GmbH) 74
Figure 2.21. Schematic of online coupling between UPLC and Synapt G2-s instrument (Waters Corporation) 76
Figure 3.1. Melittin aminolysis reaction with the *sn*-1 glyceryl ester of the LPC 88
Figure 3.2. Total ion chromatogram (TIC) for SynM/OPC incubation for 24 h 90
Figure 3.3. The product ions nomenclature for melittin during amide bond cleavage of the peptide to yield b- and y-ions 90
Figure 3.4. Mass spectra for $SynM_{ole}$ taken from SynM/OPC incubation over 24 h 91
Figure 3.5. TIC for SynM/OPC incubation for 168 h 93

Figure 3.6. Mass spectra for $SynM_{ole}$ taken from SynM/OPC incubation over 168 h 94
Figure 3.7. The relationship between the peak area for non-acylated SynM and acylated SynM with the incubation time in the OPC micelle system 95
Figure 3.8. The relationship between the peak area for non-acylated SynM and acylated SynM with the incubation time in the PPC micelle system 96
Figure 3.9. TIC for SynM/PPC incubation for 168 h 98
Figure 3.10. Mass spectra for $SynM_{pal}$ taken from SynM/PPC incubation over 168 h 99
Figure 3.11. TIC for SynM/50:50 PPC:OPC incubation for 168 h 100
Figure 3.12. LC-MS^2 spectra for product ions correspond to K23 site of palmitoylation or oleoylation, taken from SynM/50:50 PPC:OPC 101
Figure 3.13. LC-MS^2 spectra for product ions correspond to N-terminus site of palmitoylation or oleoylation, taken from SynM/50:50 PPC:OPC 102
Figure 3.14. The relationship between the peak area for single acylated SynM with the incubation time in the SynM/50:50 PPC:OPC 103
Figure 3.15. EIC for $[PPC + H]^+$ and $[OPC + H]^+$, taken from mixture of 50:50 PPC:OPC 104
Figure 3.16. Combined EIC for BVM_{pal} and BVM_{ole} in equimolar mixture of PPC:OPC; PPC:OPS; PPC:OPG; PPC:OPE and incubated over 168 h 105
Figure 3.17. TIC for SynM incubation with DPPC and DOPC over 168 h 106
Figure 3.18. Base peak chromatogram (BPC) for DPPC liposome and DOPC liposome. 108
Figure 3.19. TIC for SynM incubation with a mixture of 50:50 OPC:DPPC and PPC:DOPC over 168 h 109
Figure 3.20. The competitive production of SynM single acylation as a function of time for 75:25 OPC:DPPC; 50:50 OPC:DPPC and 25:75 OPC:DPPC 110
Figure 3.21. The competitive production of SynM single acylation as a function of time for 75:25 PPC:DOPC; 50:50 PPC:DOPC and 25:75 PPC:DOPC 111
Figure 3.22. Mass spectra for SynM single acylation, obtained from the EIC for SynM/50:50 PPC:DOPC and SynM/50:50 OPC:DPPC incubated over 168 h 113
Figure 3.23. EIC for $SynM_{pal}$ and $SynM_{ole}$ for incubations between SynM and DPPC:OPC and incubations between SynM and DOPC:PPC over 48 h and 168 h. 114
Figure 3.24. Mass spectra for SynM double acylation, obtained from the EIC for SynM/50:50 PPC:DOPC and SynM/50:50 OPC:DPPC incubated over 168 h 115
Figure 3.25. Mass spectra for SynM labile triple acylation and triple acylation, obtained from the EIC for SynM/50:50 PPC:DOPC incubated over 168 h 117
Figure 3.26. Mass spectra for SynM labile triple acylation and triple acylation, obtained from the EIC for SynM/50:50 OPC:DPPC incubated over 168 h 118
Figure 3.27. TIC of product ions from the CID of $SynM_{2pal}$ at *m/z* 832 (z=4) for SynM and 50:50 PPC:DOPC incubated over 168 h 119
Figure 3.28. LC-MS^2 spectra for product ions correspond to N-terminus/K23 double palmitoylation, and K7/K21 double palmitoylation 120
Figure 3.29. LC-MS^2 spectra for product ions correspond to S18/K21 double palmitoylation, K21/K23 double palmitoylation and N-terminus/K21 double palmitoylation 124
Figure 3.30. LC-MS^2 spectra for product ions correspond to N-terminus/R22 double palmitoylation, and N-terminus/R24 double palmitoylation 126
Figure 3.31. TIC of product ions from the CID of $SynM_{2ole}$ at *m/z* 845 (z=4) for SynM and 50:50 PPC:DOPC incubated over 168 h 128
Figure 3.32. LC-MS^2 spectra for product ions correspond to S18/K21 double oleoylation, K21/K23 double oleoylation and N-terminus/K21 double oleoylation 129
Figure 3.33. LC-MS^2 spectra for product ions correspond to K7/K21 double oleoylation and N-terminus/K23 double oleoylation 131
Figure 3.34. LC-MS^2 spectra for product ions correspond to N-terminus/R22 double oleoylation, and N-terminus/R24 double oleoylation 132
Figure 3.35. TIC of product ions from the CID of $SynM_{pal+ole}$ at *m/z* 838 (z=4) for SynM and 50:50 PPC:DOPC incubated over 168 h 134

Figure 3.36. LC-MS^2 spectra for product ions correspond to S18 oleoylation and K21 palmitoylation and S18 palmitoylation and K21 oleoylation 136
Figure 3.37. LC-MS^2 spectra for product ions correspond to K21 oleoylation and K23 palmitoylation and K21 palmitoylation and K23 oleoylation 137
Figure 3.38. LC-MS^2 spectra for product ions correspond to N-terminus oleoylation and K21 palmitoylation and N-terminus palmitoylation and K21oleoylation 138
Figure 3.39. LC-MS^2 spectra for product ions correspond to K7 oleoylation and K21 palmitoylation and K7 palmitoylation and K21oleoylation 139
Figure 3.40. LC-MS^2 spectra for product ions correspond to N-terminus oleoylation and K23 palmitoylation and N-terminus palmitoylation and K23 oleoylation 140
Figure 3.41. LC-MS^2 spectra for product ions correspond to N-terminus oleoylation and R22 palmitoylation and N-terminus palmitoylation and R22 oleoylation 141
Figure 3.42. LC-MS^2 spectra for product ions correspond to N-terminus oleoylation and R24 palmitoylation and N-terminus palmitoylation and R24 oleoylation 142
Figure 3.43. The formation of LPC and free FA by the hydrolysis of *sn*-2 position of PC by PLA_2 enzyme 145
Figure 3.44. Base peak chromatogram (BPC) of melittin incubation with each of POPC and OPPC liposomes over 168 h 146
Figure 3.45. Bar chart representation of the abundance for palmitoylated melittin (M_{pal}) and oleoylated melittin (M_{ole}) following SynM and BVM incubation with each of POPC and OPPC over 96 h and 168 h 147
Figure 3.46. Bar chart representation of the abundance for palmitoylated BVM (BVM_{pal}), oleoylated BVM (BVM_{ole}), stearoylated BVM (BVM_{ste}) and linoleoylated BVM (BVM_{lin}) following BVM incubation with each of POPC:SLPS and OPPC:SLPS at a ratio (4:1) over 24 and 72 h. 149
Figure 3.47. Bar chart representation of PPC and OPC abundance following SynM and BVM incubation with each of POPC and OPPC over 96 and 168 h. 151
Figure 3.48. Bar chart representation of the abundance for palmitoylated melittin (M_{pal}) and oleoylated melittin (M_{ole}) following SynM and BVM incubation with 50:50 OPC:DPPC over different incubation times 152
Figure 4.1. Schematic diagram of bovine eye lens fractions 160
Figure 4.2. Total ion chromatogram (TIC) of intact b-AQP0-OC 161
Figure 4.3. Deconvoluted mass spectrum of intact b-AQP0-OC 161
Figure 4.4. Amino acid sequence for b-AQP0 162
Figure 4.5. Magnified regions of b-AQP0-OC single acylation and double acylation (from deconvoluted mass spectrum 164
Figure 4.6. Deconvoluted mass spectrum of intact b-AQP0-IC 166
Figure 4.7. Magnified regions of b-AQP0-IC single acylation and double acylation (from deconvoluted mass spectrum 168
Figure 4.8. Deconvoluted mass spectrum of intact b-AQP0-ON 169
Figure 4.9. Magnified regions of b-AQP0-ON single acylation and double acylation (from deconvoluted mass spectrum 170
Figure 4.10. Deconvoluted mass spectrum of intact b-AQP0-IN 171
Figure 4.11. Magnified regions of b-AQP0-IN single acylation and double acylation (from deconvoluted mass spectrum 172
Figure 4.12. Combined extracted ion chromatogram (EIC) for intact b-AQP0 174
Figure 4.13. Deconvoluted mass spectra of intact b-AQP0, including truncated peptides 175
Figure 4.14. MALDI mass spectra for b-AQP0 181
Figure 4.15. TIC from trypsin digestion of b-AQP0-OC 182
Figure 4.16. Confirmed peptides from b-AQP0-OC tryptic digestion, using digestion protocol Method-A and LC-MS Method-I 184
Figure 4.17. Topology of b-AQP0 with six transmembrane domains spanning the lens lipid-bilayer. 185

Figure 4.18. Combined EIC for acylated peptide [234-259] and acylated peptide [1-5], using digestion protocol Method-A and LC-MS Method-I 186
Figure 4.19. The two LC methods over 20 min and 35 min used for separating tryptic digestion mixture of b-AQP0 on the LTQFT 188
Figure 4.20. Combined EIC for acylated peptide [234-259] and acylated peptide [1-5], using digestion protocol Method-A and LC-MS Method-II 189
Figure 4.21. The abundance of identified lipidated peptides for b-AQP0 for both lipidated sites of peptide [1-5] and peptide [234-259] 190
Figure 4.22. Confirmed peptides from b-AQP0-OC tryptic digestion, using digestion protocol Method-D and LC-MS Method-IIII 193
Figure 4.23. Mass spectra for the range of acylated products for peptide [234-259] from trypsin digestion of b-AQP0-OC, using digestion protocol Method-D and LC-MS Method-IIII 194
Figure 4.24. Mass spectra for the range of acylated products for peptide [1-5] from trypsin digestion of b-AQP0-OC, using digestion protocol Method-D and LC-MS Method-IIII 195
Figure 4.25. The abundance of identified lipidated peptides for b-AQP0 for both lipidated sites of peptide [234-259] and peptide [1-5] 196
Figure 4.26. MS^2 spectra of peptide [1-5] + oleoyl (C18:1) for $[M + H]^+$ and peptide [234-259] + oleoyl (C18:1) for $[M + 3H]^{3+}$ 199
Figure 4.27. MS^2 spectra of peptide [1-5] + stearoyl (C18:0) $[M + H]^+$ and peptide [234-259] + stearoyl (C18:0) $[M + 3H]^{3+}$ 202
Figure 4.28. MS^2 spectra of peptide [1-5] + palmitoyl (C16:0) $[M + H]^+$ and peptide [234-259] + palmitoyl (C16:0) $[M + 3H]^{3+}$ 203
Figure 4.29. MS^2 spectra of peptide [1-5] + palmitoleoyl (C16:1) $[M + H]^+$ and peptide [1-5] + dihomo-γ-linolenoyl (C20:3) $[M + H]^+$ 204
Figure 4.30. MS^2 spectra of peptide [1-5] + eicosadienoyl (C20:2) $[M + H]^+$ and peptide [1-5] + eicosenoyl (C20:1) $[M + H]^+$ 205
Figure 4.31. The relative percentage of each single lipidation and total lipidation modification on N-terminus site of b-AQP0, using digestion protocol Method-D and LC-MS Method-IIII 206
Figure 4.32. The relative percentage of each single lipidation species and total lipidation on K238 AA site, using digestion protocol Method-D and LC-MS Method-IIII 208
Figure 4.33. The relative ratio of K238 lipidation on truncated peptides *vs* the relative ratio of truncation in the four different bovine lens fractions, using digestion protocol Method-D and LC-MS Method-IIII 209
Figure 4.34. Correlations between the amount of ester-linked transferrable fatty acyl content of bovine lens lipids and the peak area for lipidated peptides ($A_{Lipidation}$) of b-AQP0-OC and b-AQP0-IN, using digestion protocol Method-D and LC-MS Method-IIII 212
Figure 4.35. Correlations between the amount of PE ester-linked transferrable fatty acyl content of bovine lens lipids and the peak areas for lipidated peptides of b-AQP0 213
Figure 4.36. Schematic diagram for human eye lens fractions 214
Figure 4.37. Characteristic representation of h-AQP0 amino acid sequence 214
Figure 4.38. Confirmed peptides from h-AQP0-N (M22) tryptic digestion, using digestion protocol Method-D and LC-MS Method-IIII 215
Figure 4.39. Mass spectra for the range of acylated products for peptide [227-263] and peptide [229-263], from trypsin digestion of h-AQP0-N (M22), using digestion protocol Method-D and LC-MS Method-IIII 216
Figure 4.40. Mass spectra for the range of acylated products for peptide [1-5] from trypsin digestion of h-AQP0-N (M22), using digestion protocol Method-D and LC-MS Method-IIII 217
Figure 4.41. MS^E spectra of peptide $[1-5]_{ole}$ (C18:1) and peptide $[229-263]_{ole}$ (C18:1), using digestion protocol Method-D and LC-MS Method-IIII 218
Figure 4.42. The abundance of each identified lipidation modification on K238 and N-terminus site of h-AQP0-N (M22), using digestion protocol Method-D and LC-MS Method-IIII 221
Figure 4.43. The relative ratio of total lipidation modification on N-terminus and K238 sites of h-AQP0 in 5 different human candidates 223

Figure 4.44. The relative ratio of K238 lipidation on truncated peptides *vs* the relative ratio of truncation for five different human lens candidates (nucleus fraction), using digestion protocol Method-D and LC-MS Method-IIII 224
Figure 4.45. Correlations between the amount of ester-linked transferrable fatty acyl content of human lens lipids and the peak areas for lipidated peptides of h-AQP0-C (M22) and h-AQP0-N (M22) 227
Figure 4.46. X-ray structure for cattle AQP0 monomer. 228
Figure 4.47. Variation in discrimination factor (D) according to human and bovine helix number 229
Figure 4.48. Application of 18-AA analysis window from HELIQUEST to examine [214-263] region of b-AQP0 and h-AQP0 230
Figure 5.1. Mobilogram display and Arrival time distribution (ATD) for individual PPC 239
Figure 5.2. Mobilogram display and Arrival time distribution (ATD) for individual OPC 240
Figure 5.3. ATD display from comparison EIMs for PPC and OPC taken from 50:50 OPC:PPC mixture 241
Figure 5.4. ATD display from EIM for six individual PCs including, DMPC, DPPC, POPC, OPPC, SLPC and DOPC 243
Figure 5.5. ATD display from EIM for equimolar mixture of six PCs including, DMPC: DPPC:POPC:OPPC:SLPC:DOPC 243
Figure 5.6. Mobilogram display for N-M_{pal} and K23-M_{pal} 246
Figure 5.7. Mobilogram display for N-M_{ole} and K23-M_{ole} 247
Figure 5.8. ATD display from EIM for N-M_{pal} at different charge states 249
Figure 5.9. ATD display from EIM for K23-M_{pal} at different charge states 250
Figure 5.10. ATD display from EIM for N-M_{ole} at different charge states 251
Figure 5.11. ATD display from EIM for K23-M_{ole} at different charge states 252
Figure 5.12. ATD display from EIM for non-acylated melittin (M) at different charge states 255
Figure 5.13. ATD display from comparison of EIMs for N-M_{ole}/K23-M_{ole} and N-M_{pal}/K23-M_{pal} 257
Figure 5.14. Mobilogram display for product ions obtained through collision fragmentation of precursor ion $[M_{pal} + 4H]^{4+}$ for each individual species of K23-M_{pal} and N-M_{pal} 259
Figure 5.15. Mobilogram display for product ions obtained through collision fragmentation of precursor ion $[M_{ole} + 4H]^{4+}$ for each individual species of K23-M_{ole} and N-M_{ole} 260
Figure 5.16. ATD for $[M_{pal} + 4H]^{4+}$ upon CID in the transfer cell and the corresponding product ion spectra, taken from a mixture of N-M_{pal} and K23-M_{pal} 262
Figure 5.17. ATD for $[M_{ole}+ 4H]^{4+}$ upon CID in the transfer cell and the corresponding product ion spectra, taken from a mixture of N-M_{ole} and K23-M_{ole} 263
Figure 9.1. The relative percentage of each single lipidation species and total lipidation on K238 AA site, using digestion protocol Method-D and LC-MS Method-IIII 333
Figure 9.2. Correlations between the amount of ester-linked transferrable fatty acyl content of bovine lens lipids and the peak areas for lipidated peptidesof b-AQP0-OC and b-AQP0-IN 334
Figure 9.3. Correlations between the amount of ester-linked transferrable fatty acyl content of human lens lipids and the peak areas for lipidated peptides h-AQP0-C (M56) and h-AQP0-N (M56) 338
Figure 9.4. Correlations between the amount of ester-linked transferrable fatty acyl content of human lens lipids and the peak areas for lipidated peptides of h-AQP0-C and h-AQP0-N (M80) 339
Figure 9.5. Correlations between the amount of ester-linked transferrable fatty acyl content of human lens lipids and the peak areas for lipidated peptides of h-AQP0-C (F56) and h-AQP0-N (F56) 340
Figure 9.6. Correlations between the amount of ester-linked transferrable fatty acyl content of human lens lipids and the peak areas for lipidated peptides of h-AQP0-C (F76) and h-AQP0-N (F76) 341

List of tables

Table 1.1. Common head-groups with GPL lipid classes 7
Table 1.2. The common fatty acid chains present with GPLs 8
Table 1.3. Mole% of different GPL compositions in bovine and rabbit eye lens membrane 8
Table 1.4. The reported values for LPLs CMC 15
Table 3.1. Lipids phase behaviour in different lipid systems created with data obtained by NMR 87
Table 3.2. The mole ratio for phospholipids mixed with melittin in the reaction medium. 87
Table 3.3. The percentage of total conversion for each of DPPC to PPC and DOPC to OPC 108
Table 3.4. Ions produced by fragmenting $SynM_{2pal}$ at *m/z* 832 (*z*=4) correspond to N-terminus/K23 double palmitoylation, obtained from incubation SynM/50:50 PPC:DOPC 121
Table 3.5. Ions produced by fragmenting $SynM_{2pal}$ at *m/z* 832 (*z*=4) correspond to K7/K21 double palmitoylation, obtained from incubation SynM/50:50 PPC:DOPC 122
Table 3.6. The sequence ladder of y-type and b-type ions for $SynM_{2pal}$ at different RT 127
Table 3.7. The sequence ladder of y-type and b-type ions for $SynM_{2ole}$ at different RT 133
Table 3.8. The sequence ladder of y-type and b-type ions for $SynM_{pal+ole}$ at different RT 143
Table 3.9. The percentage of total conversion of unmodified melittin to total lipidated melittin following SynM and BVM incubation with each of POPC and OPPC 148
Table 3.10. The percentage of total conversion of unmodified BVM to lipidated BVM followed BVM incubated with each of POPC:SLPS and OPPC:SLPS (4:1) 150
Table 4.1. The identified modified proteins in deconvolved spectra of b-AQP0-OC 163
Table 4.2. The identified modified proteins in deconvolved spectra of b-AQP0-IC 167
Table 4.3. The identified modified proteins in deconvolved spectra of b-AQP0-ON 169
Table 4.4. The identified modified proteins in deconvolved spectra of b-AQP0-IN 172
Table 4.5. The identified truncated proteins in deconvolved spectra of b-AQP0-IN 175
Table 4.6. Free neutral PLs and LPLs identified in the four fractions of bovine lens extracts 177
Table 4.7. Weight% of fatty acyl groups in bovine lens PE and PC lipids 179
Table 4.8. The identified acylated peptides followed trypsin digestion of b-AQP0-OC 187
Table 4.9. Results obtained from different digestion protocols/LC-MS methods used for b-AQP0-OC 191
Table 4.10. The deconvoluted truncated peptides identified from b-AQP0-OC tryptic digestion 197
Table 4.11. Product ions identified following the isolation and fragmentation of the $[M + H]^+$ precursor ion N-oleoylated peptide [1-5] at *m/z* 998.61 200
Table 4.12. Product ions identified following the isolation and fragmentation of the $[M + 3H]^{3+}$ precursor ion K238-oleoylated peptide [234-259] at *m/z* 1006.23 200
Table 4.13. The proportion of oxidation level in the four different lens age fractions 210
Table 4.14. Bovine lens transferrable fatty acid composition by lipid type 211
Table 4.15. The deconvoluted truncated peptides identified from h-AQP0-N (M22) tryptic digestion 219
Table 4.16. The level of h-AQP0 oxidation in the five different human eye lens candidates 225
Table 4.17. Human lens transferrable fatty acid composition by lipid type 226
Table 5.1. ATDs obtained from the mobilogram for each of PPC and OPC individually and from a mixture of 50:50 PPC:OPC 241
Table 5.2. Different diacylphosphatidylcholine lipids with their chemical formula, fatty acyl chains and theoretical masses 242
Table 5.3. ATDs obtained from the mobilogram for each of individual PC lipids including, DMPC, DPPC, POPC, OPPC, SLPC and DOPC and a mixture of all the PCs at equal mole ratio 244
Table 5.4. ATDs obtained from the mobilogram for each individual species of non-acylated melittin (M), N-M_{pal}, K23-M_{pal}, N-M_{ole} and K23-M_{ole} and equimolar mixture of (M:N-M_{pal}:K23-M_{pal} :N-M_{ole}:K23-M_{ole}) 254
Table 8.1. Different digestion protocols and LC-MS methods used in AQP0 analysis 286

Table 9.1. Amino acid residues with their abbreviation and molecular mass 293
Table 9.2. The structure and nomenclature for common phospholipids 294
Table 9.3. The range of single and multiple acylation ions observed from SynM/50:50 PPC:DOPC incubation at 37 °C for 168 h 296
Table 9.4. The range of single and multiple acylation ions observed from SynM/50:50 OPC:DPPC incubation at 37 °C for 168 h 297
Table 9.5. Ions produced by fragmenting $SynM_{2pal}$ at *m/z* 832 (*z*=4) correspond to S18/K21 double palmitoylation, obtained from incubation SynM/50:50 PPC:DOPC 298
Table 9.6. Ions produced by fragmenting $SynM_{2pal}$ at *m/z* 832 (*z*=4) correspond to K21/K23 double palmitoylation, obtained from incubation SynM/50:50 PPC:DOPC 299
Table 9.7. Ions produced by fragmenting $SynM_{2pal}$ at *m/z* 832 (*z*=4) correspond to N-terminus/K21 double palmitoylation, obtained from incubation SynM/50:50 PPC:DOPC 300
Table 9.8. Ions produced by fragmenting $SynM_{2pal}$ at *m/z* 832 (*z*=4) correspond to N-terminus/R22 double palmitoylation, obtained from incubation SynM/50:50 PPC:DOPC 301
Table 9.9. Ions produced by fragmenting $SynM_{2pal}$ at *m/z* 832 (*z*=4) correspond to N-terminus/R24 double palmitoylation, obtained from incubation SynM/50:50 PPC:DOPC 302
Table 9.10. Ions produced by fragmenting $SynM_{2ole}$ at *m/z* 845 (*z*=4) correspond to S18/K21 double oleoylation, obtained from incubation SynM/50:50 PPC:DOPC 303
Table 9.11. Ions produced by fragmenting $SynM_{2ole}$ at *m/z* 845 (*z*=4) correspond to K21/K23 double oleoylation, obtained from incubation SynM/50:50 PPC:DOPC 304
Table 9.12. Ions produced by fragmenting $SynM_{2ole}$ at *m/z* 845 (*z*=4) correspond to N-terminus/K21 double oleoylation, obtained from incubation SynM/50:50 PPC:DOPC 305
Table 9.13. Ions produced by fragmenting $SynM_{2ole}$ at *m/z* 845 (*z*=4) correspond to K7/K21 double oleoylation, obtained from incubation SynM/50:50 PPC:DOPC 306
Table 9.14. Ions produced by fragmenting $SynM_{2ole}$ at *m/z* 845 (*z*=4) correspond to N-terminus/K23 double oleoylation, obtained from incubation SynM/50:50 PPC:DOPC 307
Table 9.15. Ions produced by fragmenting $SynM_{2ole}$ at *m/z* 845 (*z*=4) correspond to N-terminus/R22 double oleoylation, obtained from incubation SynM/50:50 PPC:DOPC 308
Table 9.16. Ions produced by fragmenting $SynM_{2ole}$ at *m/z* 845 (*z*=4) correspond to N-terminus/R24 double oleoylation, obtained from incubation SynM/50:50 PPC:DOPC 309
Table 9.17. Ions produced by fragmenting $SynM_{pal+ole}$ at *m/z* 838 (*z*=4) correspond to S18 oleoylation and K21 palmitoylation, obtained from incubation SynM/50:50 PPC:DOPC 310
Table 9.18. Ions produced by fragmenting $SynM_{pal+ole}$ at *m/z* 838 (*z*=4) correspond to S18 palmitoylation and K21 oleoylation, obtained from incubation SynM/50:50 PPC:DOPC 311
Table 9.19. Ions produced by fragmenting $SynM_{pal+ole}$ at *m/z* 838 (*z*=4) correspond to K21 oleoylation and K23 palmitoylation, obtained from incubation SynM/50:50 PPC:DOPC 312
Table 9.20. Ions produced by fragmenting $SynM_{pal+ole}$ at *m/z* 838 (*z*=4) correspond to K21 palmitoylation and K23 oleoylation, obtained from incubation SynM/50:50 PPC:DOPC 313
Table 9.21. Ions produced by fragmenting $SynM_{pal+ole}$ at *m/z* 838 (*z*=4) correspond to N-terminus oleoylation and K21 palmitoylation, obtained from incubation SynM/50:50 PPC:DOPC 314
Table 9.22. Ions produced by fragmenting $SynM_{pal+ole}$ at *m/z* 838 (*z*=4) correspond to N-terminus palmitoylation and K21 oleoylation, obtained from incubation SynM/50:50 PPC:DOPC 315
Table 9.23. Ions produced by fragmenting $SynM_{pal+ole}$ at *m/z* 838 (*z*=4) correspond to K7 oleoylation and K21 palmitoylation, obtained from incubation SynM/50:50 PPC:DOPC 316
Table 9.24. Ions produced by fragmenting $SynM_{pal+ole}$ at *m/z* 838 (*z*=4) correspond to K7 palmitoylation and K21 oleoylation, obtained from incubation SynM/50:50 PPC:DOPC 317
Table 9.25. Ions produced by fragmenting $SynM_{pal+ole}$ at *m/z* 838 (*z*=4) correspond to N-terminus oleoylation and K23 palmitoylation, obtained from incubation SynM/50:50 PPC:DOPC 318
Table 9.26. Ions produced by fragmenting $SynM_{pal+ole}$ at *m/z* 838 (*z*=4) correspond to N-terminus palmitoylation and K23 oleoylation, obtained from incubation SynM/50:50 PPC:DOPC 319
Table 9.27. Ions produced by fragmenting $SynM_{pal+ole}$ at *m/z* 838 (*z*=4) correspond to N-terminus oleoylation and R22 palmitoylation, obtained from incubation SynM/50:50 PPC:DOPC 320

Table 9.28. Ions produced by fragmenting $SynM_{pal+ole}$ at *m/z* 838 (*z*=4) correspond to N-terminus palmitoylation and R22 oleoylation, obtained from incubation SynM/50:50 PPC:DOPC 321
Table 9.29. Ions produced by fragmenting $SynM_{pal+ole}$ at *m/z* 838 (*z*=4) correspond to N-terminus oleoylation and R24 palmitoylation, obtained from incubation SynM/50:50 PPC:DOPC 322
Table 9.30. Ions produced by fragmenting $SynM_{pal+ole}$ at *m/z* 838 (*z*=4) correspond to N-terminus palmitoylation and R24 oleoylation, obtained from incubation SynM/50:50 PPC:DOPC 323
Table 9.31. The deconvoluted *m/z* for non-acylated peptides identified from b-AQP0-OC tryptic digestion 324
Table 9.32. The deconvoluted *m/z* for identified acylated peptides followed trypsin digestion of b-AQP0-OC 325
Table 9.33. The deconvoluted *m/z* for non-acylated peptides identified from b-AQP0-OC tryptic digestion 326
Table 9.34. The deconvoluted *m/z* for identified acylated peptides followed trypsin digestion of b-AQP0-OC 327
Table 9.35. Product ions identified following the isolation and fragmentation of the $[M + H]^+$ precursor ion N-stearoylated peptide [1-5] at *m/z* 1000.63 328
Table 9.36. Product ions identified following the isolation and fragmentation of the $[M + 3H]^{3+}$ precursor ion K238-stearoylated peptide [234-259] at *m/z* 1006.91 328
Table 9.37. Product ions identified following the isolation and fragmentation of the $[M + H]^+$ precursor ion N-palmitoylated peptide [1-5] at *m/z* 972.59 329
Table 9.38. Product ions identified following the isolation and fragmentation of the $[M + 3H]^{3+}$ precursor ion K238-palmitoylated peptide [234-259] at *m/z* 997.56 330
Table 9.39. Product ions identified following the isolation and fragmentation of the $[M + H]^+$ precursor ion N-palmitoleoylated peptide [1-5] at *m/z* 970.58 331
Table 9.40. Product ions identified following the isolation and fragmentation of the $[M + H]^+$ precursor ion N-dihomo-γ-linolenoylated peptide [1-5] at *m/z* 1022.61 331
Table 9.41. Product ions identified following the isolation and fragmentation of the $[M + H]^+$ precursor ion N-eicosadienoylated peptide [1-5] at *m/z* 1024.63 332
Table 9.42. Product ions identified following the isolation and fragmentation of the $[M + H]^+$ precursor ion N-eicosenoylated peptide [1-5] at *m/z* 1026.64 332
Table 9.43. The deconvoluted *m/z* for non-acylated peptides identified from h-AQP0-N (M22) tryptic digestion, using Method-D and LC-MS Method-IIII 335
Table 9.44. The deconvoluted *m/z* for identified acylated peptides followed trypsin digestion of h-AQP0-N (M22). 336
Table 9.45. Product ions identified for N-oleoyl h-AQP0-N (M22) peptide [1-5] from MS^E experiment 337
Table 9.46. Product ions identified for K238-oleoyl h-AQP0-N (M22) peptide [229-263] from MS^E experiment 337
Table 9.47. HELIQUEST analysis of the [214-263] region of b-AQP0 342
Table 9.48. HELIQUEST analysis of the [214-263] region of h-AQP0 343

List of abbreviations and units

AA	Amino acid
AMP	Antimicrobial peptide
ATB	Arrival time distribution
AC	Alternating current
AQP0	Aquaporine-0
BVM	Bee venom melittin
b-AQP0	Bovine aquaporine-0
CMC	Critical micelle concentration
C	Cortex
CID	Collision induced dissociation
CCS	Collision cross-section
DOPC	1,2-Dioleoyl-*sn*-glycero-3-phosphatidylcholine
DPPC	1,2-Dipalmitoyl-*sn*-glycero-3-phosphatidylcholine
DMPC	1,2-Dimyristoyl-*sn*-glycero-3-phosphatidylcholine
PL	Diacylphospholipid
DC	Direct current
t_d	Drift time
DTIMS	Drift time ion mobility spectrometry
DTT	Dithiothreitol
EIC	Extracted ion chromatogram
EIM	Extracted ion mobilogram
ECD	Electron capture dissociation
ETD	Electron transfer dissociation
ESI	Electrospray ionisation
FA	Fatty acid
FWHM	Full width at half maximum
FT	Fourier transform
FTICR	Fourier transform ion cyclotron resonance
FAIMS	Field-asymmetric ion mobility spectrometry
GPL	Glycerophospholipid
HPLC	High performance liquid chromatography
h-AQP0	Human aquaporine-0
IC	Inner cortex
IN	Inner nucleus
IM	Ion mobility
IMS	Ion mobility separation
lin	Linoleoyl/Linoleoylation
LPL	Lysophospholipid

LC	Liquid chromatography
LIT	Linear ion trap
MCL	Missed cleavage
Meas	Measured
m/z	Mass-to-charge ratio
MALDI	Matrix-assisted laser desorption/ionisation
MS	Mass spectrometry
N	Nucleus
O	Oxidation
ole	Oleoyl/Oleoylation
OPC	1-Oleoyl-2-hydroxy-*sn*-glycero-3-phosphatidylcholine
OPE	1-Oleoyl-2-hydroxy-*sn*-glycero-3-phosphatidylethanolamine
OPS	1-Oleoyl-2-hydroxy-*sn*-glycero-3-phosphatidylserine
OPG	1-Oleoyl-2-hydroxy-*sn*-glycero-3-phosphatidylglycerol
OPPC	1-Oleoyl-2-palmitoyl-*sn*-glycero-3- phosphatidylcholine
OC	Outer cortex
ON	Outer nucleus
oaToF	Orthogonal acceleration time-of-flight
M_{ole}	Oleoylated melittin
pal	Palmitoyl/Palmitoylation
POPC	1-Palmitoyl-2-oleoyl-*sn*-glycero-3-phosphatidylcholine
PPC	1-Palmitoyl-2-hydroxy-*sn*-glycero-3-phosphatidylcholine
PC	Phosphatidylcholine
PA	Phosphatidic acid
PE	Phosphatidylethanolamine
PG	Phosphatidylglycerol
PI	Phosphatidylinositol
PS	Phosphatidylserine
PLA_2	Phospholipase A_2
P	Phosphorylation
A	Peak area
PFOA	Pentafluorooctanoic acid
PTM	Post-translational modification
M_{pal}	Palmitoylated melittin
Q	Quadrupole
QIT	Quadrupole ion trap
RT	Retention time
RF	Radio frequency
sn	Stereospecifically numbered
SLPS	1-Stearoyl-2-linoleoyl-*sn*-glycero-3- phosphatidylserine

SLPC	1-Stearoyl-2-linoleoyl-*sn*-glycero-3-phosphatidylcholine
ste	Stearoyl/Stearoylation
SDS	Sodium dodecyl sulfate
SynM	Synthetic melittin
SEM	Standard error of the mean
SM	Sphingomyelin
Theor	Theoretical
TIC	Total ion chromatogram
TWIMS	Travelling wave ion mobility spectrometry
MS^n/MS^2	Tandem mass spectrometry
UPLC	Ultra performance liquid chromatography
a.u.	Arbitrary units
Da	Daltons
°C	Degrees Celsius
eV	Electron volt
g	Grams
h	Hours
kDa	Kilo Daltons (10^3 Daltons)
keV	Kilo-electron volts (10^3 electron volts)
L	Litres
mm	Millimetres (10^{-3} metres)
M	Molarity in moles per litre (= mol/dm^3)
mM	Molarity in millimoles (10^{-3} moles) per litre
µM	Molarity in micromoles (10^{-6} moles) per litre
pM	Molarity in picomoles (10^{-12} moles) per litre
mL	Millilitres (10^{-3} litres)
µL	Microlitres (10^{-6} litres)
mg	Milligrams (10^{-3} grams)
µg	Micrograms (10^{-6} grams)
ms	Milliseconds (10^{-3} seconds)
min	Minutes
nm	Nanometres (10^{-9} metres)
ppm	Parts-per-million
V	Volts
v/v	Volume to volume
w/v	Weight to volume
λ	Wavelength

Declaration

The work presented herein was carried out in the Department of Chemistry at Durham University between April 2013 and July 2016. Unless otherwise stated all work is my own and has not been submitted for a qualification at this or any other university.

Statement of copyright

Acknowledgements

Foremost, I would like to express my special appreciation and thanks to my supervisor Dr. Jackie Mosely for her continues support, motivation and immense knowledge over the last four years of my PhD research. Beside my supervisor, I would especially like to thank my co-supervisor Dr. John Sanderson, for his guidance. My sincere thank also goes to Prof. Roy Quinlan, for offering me different protein samples in order to complete my project.

A special grateful to my beloved father who has passed away before witnessing my achievements but I owe it all to you. Words cannot express how I am grateful to my family for your continuous support along the way. Your prayers for me were what sustained me thus far. Also a very special gratitude to my husband Saman, who incented me to strive towards my goal. Appreciation goes for all of the sacrifices that he has made on my behalf and for being a wonderful father for our lovely kids, Zhin and Nawdar. I could not have imagined to complete my PhD study without all of you being apart in my life journey.

My sincere thanks also goes to members of Durham University Mass Spectrometry group, past and present; in particular Dr. Dave Parker, Peter Stokes, Andy, Lottie, Chris and Hannah, for their assistance and advice. I would also like to thank my colleagues (past and present) of office 217 for supplying cakes and entertainment on a regular basis.

Last but not least, I am grateful to Ministry of Higher Education and Scientific Research from Kurdistan Regional Government (KRG) for funding PhD research. Also I thank my friends and colleagues in Kurdistan and around the UK, for the encouragement and friendship. At the end I would like to thank Faculty of Science/Soran University for their support.

Chapter one: Introduction

1.1. Cell membrane

All living organisms are composed of cells, with either a single cell such as microscopic organism or multicellular such as large organism. The external boundary of the cell is the plasma membrane which is called the cell membrane, which surrounds the inner compartment of the cell containing nucleus and other organelles such as featured in eukaryote cell of animals and plants or without nucleus such that found in prokaryote cell or bacteria. Membranes are the basic unit for all living cells and have a specialised structure that favours their gate keeping function.[1] These are dynamic structures that are made mainly of lipid, protein and carbohydrate[2]. Lipid molecules are the essential component of the cell, with protein molecules acting as a transport system of pumps and channels. These two main biomolecules facilitate the permeability of the membrane and control the movement of substances in and out of the cell to maintain the equilibrium.[3-5]

The first structure of the cell membrane was described by Gorter *et al.* in 1925 as a simple lipid-bilayer.[6,7] This was followed by a number of researchers to further characterise membrane structure.[7-9] Singer-Nicolson proposed the fluid-mosaic model in 1972.[10,11] This is still the most popular model of the lipid membrane and includes amphiphilic lipid molecules arranged as two opposite sheets (leaflet, lamellae), together with protein molecules that can be present as integral or peripheral membrane proteins[5] as shown in Figure 1.1. A new insight of this fluid-mosaic model[8,9,12] was obtained by Simons *et al.* and Brown *et al.* in 1997. They have extended the model to show lipid membrane domains or called lipid rafts[13-17].

The exoplasmic surface of the cell membrane is interacting with other cells and the existing components within the extracellular fluid, while the cytoplasmic surface contains the cell organelles, and the inclusions. Organelles in eukaryote cell include; nucleus, endoplasmic reticulum, Golgi apparatus, mitochondria, ribosomes, transport vesicles, cytoskeleton and lysosome.[1,4]

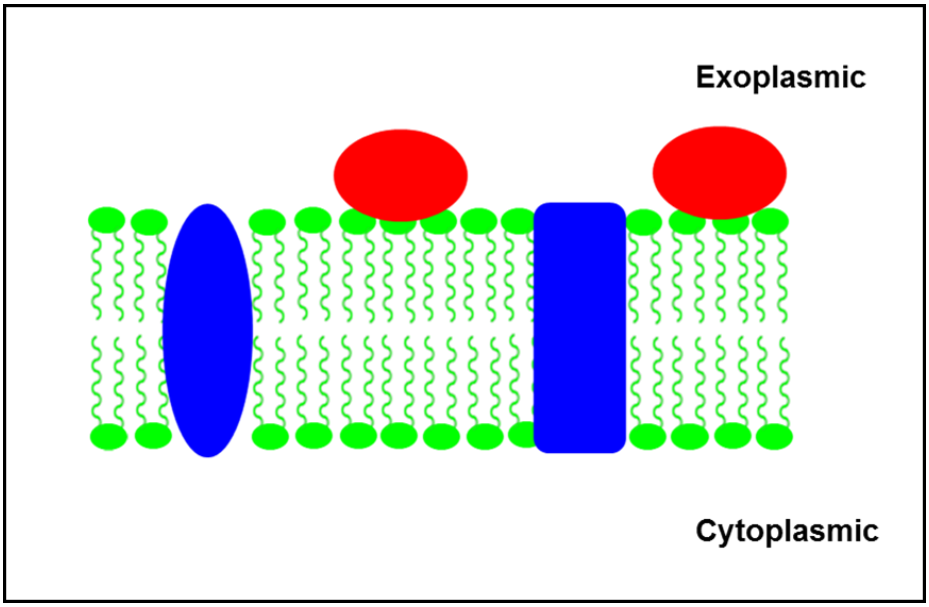

Figure 1.1. **The fluid-mosaic model for a typical cell membrane as proposed by Singer-Nicolson. Tail-to-tail phospholipid bilayer is shown in green; integral membrane proteins traversing the cell membrane are shown in blue; peripheral proteins on the surface of the cell membrane are shown in red.**

Further, peptide molecules also exist in the cell and they perform different interactions with the cell membrane through electrostatic interactions and/or hydrophobic interactions[18]. Such interactions depend on the amino acid (AA) composition of bound peptides, charge, structure and as well as the composition of bound lipid. An example for that is antimicrobial peptides (AMP), which are also known as membrane active peptides because of their amphiphilic behaviour that results from the presence of both hydrophobic and hydrophilic domains within the peptide.[19] Lipid-peptide interactions were described by different mechanisms[18-22] such as carpet mechanism, toroidal pore mechanism and barrel stave mechanism, as shown in Figure 1.2. Interestingly, all of these mechanisms are concentration dependent of bound peptide to lipid ratio (**peptide:lipid**). They cause membrane permeability (Figure 1.2 B) or pores in the membrane (Figure 1.2 C and D) only when **peptide:lipid** reaches a critical ratio that is known as critical amount or **peptide:lipid***.[18]

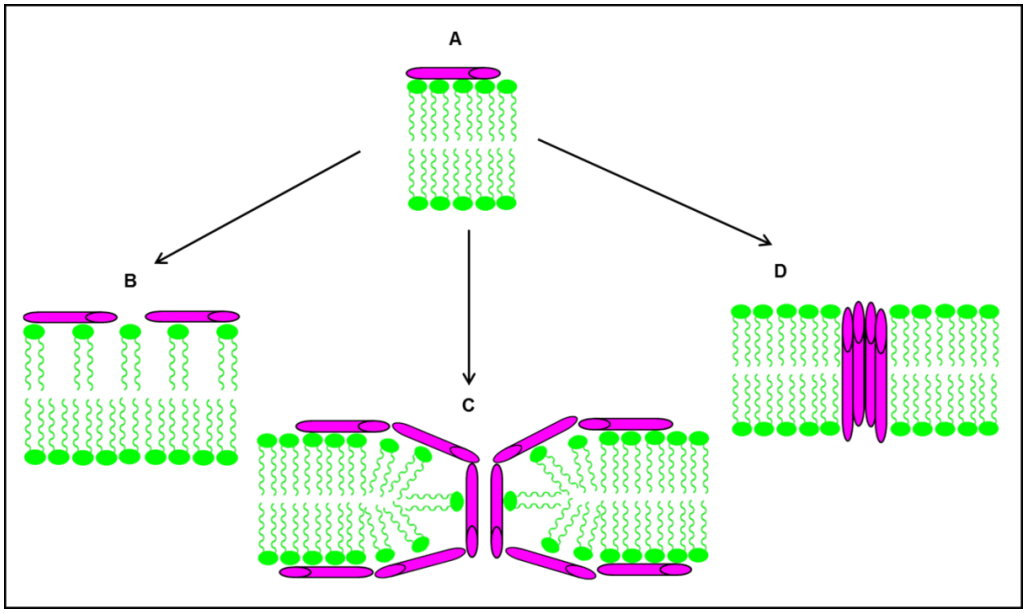

Figure 1.2. **Peptide-membrane binding mechanism. (A) Electrostatic interaction between peptide (pink) and membrane (green) below peptide:lipid*; (B) Carpet mechanism, disrupting ordered orientation of membrane lipids; (C) Toroidal pore mechanism, disrupting lipid-lipid interactions and curving the membrane by interacting aggregated peptides with polar head-groups then eventually pore formation in the membrane; (D) Barrel stave mechanism, disrupting lipid-lipid interaction by spanning aggregated peptides through the hydrophobic tail-groups of membrane bilayer and thus pore formation.**

1.2. Biomimetic membrane

The complexity of natural membranes can be simplified by making artificial membranes or so called biomimetic membranes in order to perform different experimental analysis to explore the membrane's phase behaviour, functions, properties and activity towards different species such as peptides/proteins, surfactants and pharmaceutical drugs. Common biomimetic membranes include: lipid monolayers, lipid vesicles or liposomes and supported lipid-bilayers.[8] The most popular biomimetic membranes that best reflect the composition and structural design of natural membranes are liposomes,[8,23-25] with a wide range of application in different fields such as in food industry[26], cosmetic formulation[27] and most importantly as pharmaceutical products for drug delivery[24,28-30]. Liposomes were first described by Bangham and Horne in 1962[31], and are formed spontaneously by dispersing dry lipids in aqueous phase. This results in formation of

spherical fluid membrane with onion structure called multilamellar vesicle (MLV) with a micron size (> 0.1 μm). MLV can be downsized with a single lipid-bilayer using different methods, commonly using sonic energy in forms of sonication or mechanical energy in form of extrusion,[23,28] as shown in Figure 1.3. Generally, liposomes with small diameter size, in range of 25-40 nm,[7] are generated by sonication[23] and are called small unilamellar vesicle (SUV) but with less application because of their small sizes.[7] While larger liposomes with a range of sizes depending on the pore size of the membrane filter, typically in range of 50-500 nm,[7] are generated by extrusion[23,32] and are called large unilamellar vesicle (LUV). LUVs have a broad application as biomimetic membranes because of their convenient size and symmetric distribution of lipids between inner and outer monolayers (≈ 1:1).[7]

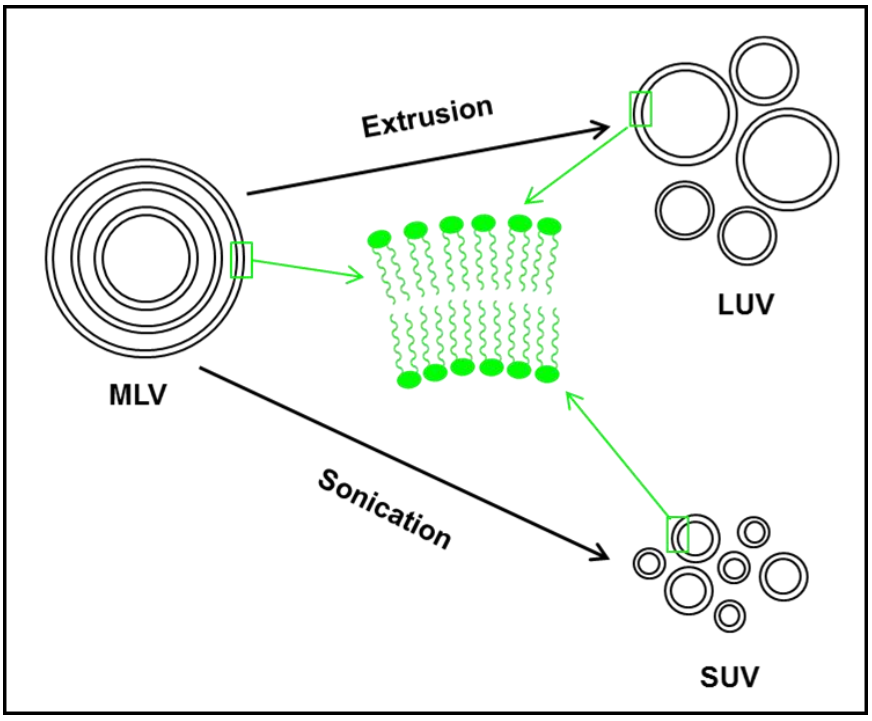

Figure 1.3. **Schematic to illustrate different types of liposomes; multilamellar vesicle (MLV), large unilamellar vesicle (LUV) and small unilamellar vesicle (SUV). The enlarged fractions show the lipid-bilayer composition (green) in each layer.**

1.3. Membrane lipids

Lipids in the membrane can be classified to phospholipids, sterols and glycolipids.[7,8,33] Each lipid class can be further classified to a range of different sub-classes and this shows lipids diversity in the biological system with serving different functions. Their main three functions[33] can be summarised to: **first**, energy storage; **second**, first and second messengers in signal transduction and molecular recognition processes; **third**, as a barrier between exoplasmic and cytoplasmic surfaces of the cell, a function that is driven by the amphiphilic principle of lipids with hydrophilic head-groups interacting with aqueous phase and hydrophobic tail-groups interacting with each other. The amount and composition of lipids are different in various organisms and also in different cell functions within one organism. Because glycerophospholipids (GPL) are the most abundant lipid class in eukaryote membrane, mammals,[7,8,33] and are broadly applied in this study, this will be discussed in more detail in this chapter.

1.3.1. Phospholipids

1.3.1.1. Glycerophospholipid (GPL)

The basic unit for all glycerophosholipids (GPLs) is *sn*-glycero-3-phosphate, Figure 1.4, either esterified at both *sn*-1 and *sn*-2 positions of the glycerol with a range of different fatty acids (X and Y) to form diacylphospholipids (PL) or esterified at just one position (*sn*-1 or *sn*-2) to give lysophospholipids (LPL). Different PL and LPL classes are classified depending on the different groups attached to the phosphate polar head-group (Table 1.1). Generally, in nature the fatty acid in position *sn*-1 of the PLs is saturated preferentially, while in *sn*-2 position it is commonly unsaturated (≥ 1 double bond) and longer acyl chains[7,34] with the *cis* conformation[34]. A number of common fatty acids[35] esterified with PLs/LPLs are listed in Table 1.2. Interestingly, the major GPL class in natural cell are PLs[7,8] and found to build up 40-60 mole%[8] of the total lipid composition relative to < 5 mole%[36,37] of the minor LPL class. An example, relevant to the

nature of this research for the proportion of different lipid classes is given for bovine and rabbit lenses[38] (Table 1.3).

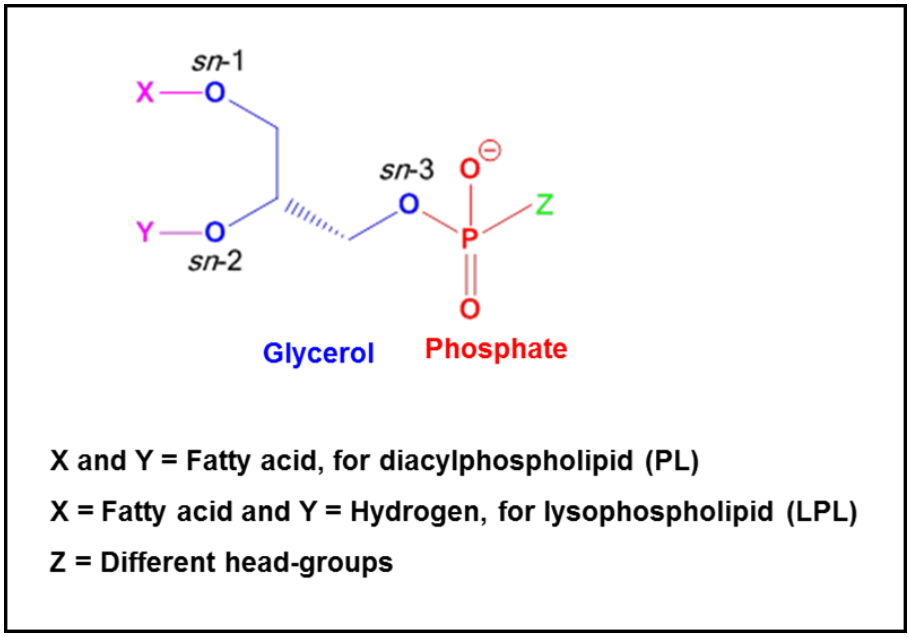

Figure 1.4. **Structural representation for GPLs.**

Table 1.1. **Common head- groups (Z) with GPL lipid classes (see Figure 1.4).**

Molecular Structure of Z groups	Name	Net Charge at pH 7
—OH	Phosphatidic acid (PA)	-1
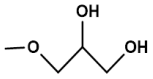	Phosphatidylglycerol (PG)	-1
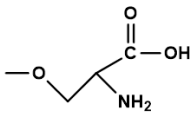	Phosphatidylserine (PS)	-1
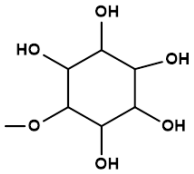	Phosphatidylinositol (PI)	-1
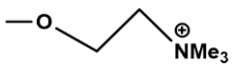	Phosphatidylcholine (PC)	Neutral (zwitterionic)
	Phosphatidylethanolamine (PE)	Neutral (zwitterionic)

Table 1.2. **The common fatty acid chains (X and Y) present with GPLs (see Figure 1.4).**

Fatty Acid Structure	Common Name	Systematic Name	Shorthand Name
$CH_3(CH_2)_8COOH$	Capric	*n*-Decanoic	C10:0
$CH_3(CH_2)_{10}COOH$	Lauric	*n*-Dodecanoic	C12:0
$CH_3(CH_2)_{12}COOH$	Myristic	*n*-Tetradecanoic	C14:0
$CH_3(CH_2)_{14}COOH$	Palmitic	*n*-Hexadecanoic	C16:0
$CH_3(CH_2)_{16}COOH$	Stearic	*n*-Octadecanoic	C18:0
$CH_3(CH_2)_{18}COOH$	Arachidic	Eicosanoic	C20:0
$CH_3(CH_2)_5CH=CH(CH_2)_7COOH$	Palmitoleic	9-Hexadecenoic	C16:1 (9)
$CH_3(CH_2)_7CH=CH(CH_2)_7COOH$	Oleic	*Cis*-9-Octadecenoic	C18:1 (9)
$CH_3(CH_2)_4CH=CHCH_2CH=CH(CH_2)_7COOH$	Linoleic	*Cis,Cis*-9,12-Octadecadienoic	C18:2 (9,12)
$CH_3CH_2CH=CHCH_2CH=CHCH_2CH=CH(CH_2)_7COOH$	α-Linolenic	9,12,15-Octadecatrienoic	C18:3 (9,12,15)
$CH_3(CH_2)_4CH=CHCH_2CH=CHCH_2CH=CH(CH_2)_4COOH$	γ-Linolenic	6,9,12-Octadecatrienoic	C18:3 (6,9,12)

Table 1.3. **Mole% of different GPL compositions in bovine and rabbit eye lens membrane, created with data obtained by chromatography methods (Anderson *et al.*)[38]. Errors were reported as the standard error of the mean (SEM), when n=2.**

GPL Composition	Mole%	
	Bovine	Rabbit
PC	26.0 ± 0.7	22.6 ± 1.4
PE	33.6 ± 1.6	27.9 ± 0.7
PI	1.6 ± 0.3	1.5 ± 0.2
PS	8.2 ± 1.0	12.3 ± 1.4
LPC	0.9 ± 0.3	-
LPE	3.1 ± 0.8	3.1 ± 0.6
SM	22.3 ± 0.6	32.2 ± 0.9

One of the most important features that cell membranes have is the asymmetric distribution of lipid composition on both inner and outer leaflets.[7,8,39-43] This was first proposed by Bretscher in 1972 for mammalian erythrocytes membrane,[39] but then proposed for different cell functions in

one organism and as well as in different organisms[7,41,42]. The reported data suggested that the inner leaflet of the lipid-bilayer (cytoplasmic) is rich with amino-based PLs such as PE and PS, while the outer leaflet of the lipid-bilayer (exoplasmic) is rich with choline-based PLs such as PC and sphingomyelin (SM).[39-43] Consequently, lipid asymmetry is not absolute because each PL is present on both membrane leaflets but in different amount.[41] This asymmetry is shown to be preserved with asymmetric distribution of proteins within the membrane[7,41,42] and this has a consequence on different functions provided by both membrane leaflets[42]. A recent study showed that lipid asymmetry regulates mechanical stability of the cell membrane and this is proven by interaction of skeletal proteins with PS constituent in the inner leaflet of red cell membrane.[44]

Further, a good review by Braverman-Moser[45] describes the importance and the relevant ratio for different plasmalogen lipids in various mammalian tissues. Plasmalogen lipids are a class of ether GPL[45] that has a vinyl ether (1-O-(1-*cis*-alkenyl)) linkage at *sn*-1 position of the glycerol backbone instead of fatty acid (Figure 1.5 A), which is also known as plasmenyl. The other less abundant class of ether GPL is plasmanyl GPL with alkyl ether (1-O-alkyl) linkage at *sn*-1 position (Figure 1.5 B). Interestingly, it is found that the majority of PE lipid in eye lens of mammals is present in the form of plasmalogen PE[38,46-48].

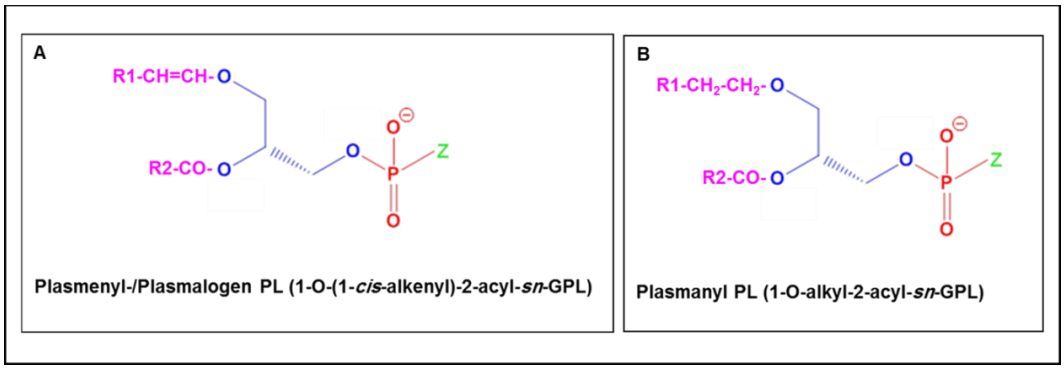

Figure 1.5. **Structural representation for the two common ether GPLs. (A) plasmalogen-/plasmenyl GPL and (B) plasmanyl GPL. Z is usually ethanolamine group (most common) or choline group (less common). See Table 1.1 and 1.2 for the molecular structure for different polar head-groups (Z) and hydrophobic acyl chains respectively.**

1.3.1.1.1. Phase behavior of phospholipid bilayer

Hydrated PL bilayers can exist in different phase states. This depends on PLs chemical structure, degree of hydration, temperature, pressure, ionic strength and pH[8,49]. Most PL bilayers exist as liquid-crystalline or fluid phase (L_α) under physiological conditions but sometimes in the gel phase or solid phase ($L_{\beta'}$).[49] The fluid phase (L_α) of lipid-bilayer has a characteristic behavior when hydrophobic acyl chains are unsaturated. In the presence of cholesterol it can be liquid ordered (L_o) or in the absence of cholesterol liquid disordered (L_d)[8,43]. PLs with saturated hydrophobic acyl chains are highly ordered, all are in *trans* conformation, and exhibit gel phase ($L_{\beta'}$) behavior. The intermediate phase between L_α and $L_{\beta'}$ is called rippled gel phase ($P_{\beta'}$)[8,18,35]. Biological membranes with the characteristic of lipid diversity and different chemical identity for each lipid class in respect of their hydrophilic head-groups and hydrophobic fatty acyl chains are experiencing both fluid phase and gel phase behavior (Figure 1.6).[8]

Although the phase transition of PLs is influenced by several factors, thermally phase transition is the most common factor that has been studied and more biological relevance,[49] as there is a direct relation between thermally phase transition and membrane structure[18]. At a certain temperature the bilayer can exhibit phase changes or phase transition. At the pre-transition temperature (Tp) the lipid phase changes from $L_{\beta'}$ to $P_{\beta'}$, and at the main transition temperature (Tm) from $P_{\beta'}$ to L_α.[8,18,35] Interestingly, PCs can exhibit both Tp and Tm, while PEs just exhibit Tm.[8,50] PLs with unsaturated fatty acyl chain have very low Tm (< 0 ˚C)[18,50] compared to saturated counter parts; for example Tm is -16.5 ˚C for 1,2-dioleoyl-PC (DOPC)[52,53] *vs* 41.3 ˚C for 1,2-dipalmitoyl-PC (DPPC)[54-6]. Further, PLs with longer acyl chains have higher Tm than shorter PLs. This is because of increasing van der Waals forces between longer acyl chains. High Tm is also found with fewer degrees of unsaturation due to the lower disruption in the ordered chain packing than higher degree of unsaturation.[18,57] In addition, the polarity of PLs head-groups and their affinity to bind with water molecules has also a great impact on both Tm and Tp.[35]

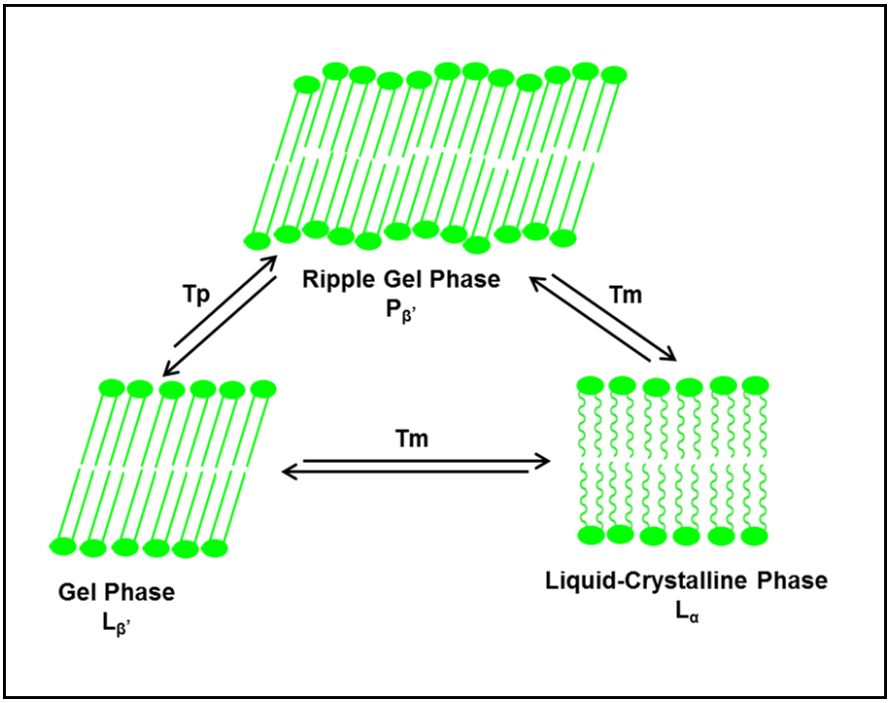

Figure 1.6. **The three phase states ($L_{\beta'}$, L_{α} and $P_{\beta'}$) for hydrated PL bilayer with the illustration of transition temperatures (Tm and Tp) between each two phases in a reversible pathway.**

1.3.1.1.2. Action of Phospholipase enzyme on phospholipids

The two low abundant water soluble amphiphilic monoacyl lipids in most biological membranes, LPL and free fatty acid (free FA),[36,37,58,59] are principally formed by phospholipase enzyme on PL substrates[58,60,61]. The phospholipase enzyme family can be classified into four main classes (Figure 1.7) including: **first**, PLA enzymes with PLA_1 and PLA_2 sub-classes, hydrolysis *sn*-1 and *sn*-2 positions of the PLs respectively; **second**, PLB enzymes, hydrolysis both *sn*-1 and *sn*-2 positions; **third**, PLC enzymes, hydrolysis the linkage between the phosphate head-group and glycerol backbone; **fourth**, PLD enzymes, forms phosphatidic acid by removing phosphate head-group from the PL.[35,60-62] Interestingly, PLA_2 enzyme with the mass of 13-15 kDa[35,60,62] is the common component of many animal venoms and pancreatic juices[60,62] and is one of the phospholipase enzymes that has been broadly studied[61,62]. Their major roles recorded to be inflammation regulation, immune function and smooth muscle contraction[60].

In this chapter the focus will be on PLA_2 enzyme due to the nature of the research has concentrated on venom of the bee.

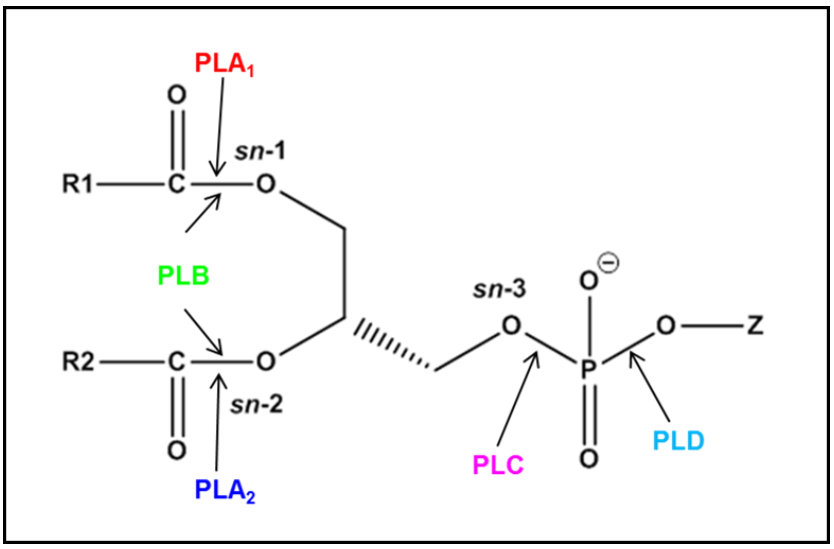

Figure 1.7. **The cleavage sites of PL by the hydrolysis activity of phospholipase enzymes. Different polar head-groups and fatty acyl chains are provided in Tables 1.1 and 1.2.**

Formation of an equimolar amount of LPC and free FA by PLA_2 activity[63-65] is shown in Figure 1.8. Interestingly, it has been reported that the activity of this enzyme towards single lipid molecules is very low, while during lipid aggregation in the forms of micelle, liposome, or lipid-bilayer the activity of PLA_2 is extensively enhanced.[37,58,62,64-68] In addition, in the aggregated lipid system this activity is also influenced by lipid composition,[69] membrane phase in terms of gel phase and fluid phase,[64,70,71] liposome curvature,[72] surface charge,[73] monolayer surface pressure[74] and interfacial water activity[75].[65] It is interesting to see that (Figure 1.8, bottom) the balanced size between head-group and tail-group sections in PC lipids provides cylindrical shape that favours their lipid-bilayer phase with low intrinsic curvature; LPCs with larger head-group size relative to their smaller tail-group prefer highly curved structure with inverted cone shape and micelle phase (non-bilayer phase); free FAs with much smaller head-group than LPCs form cone shape with inverted micelle phase (non-bilayer hexagonal H_{II} phase).[2,7,18,64,76,77]

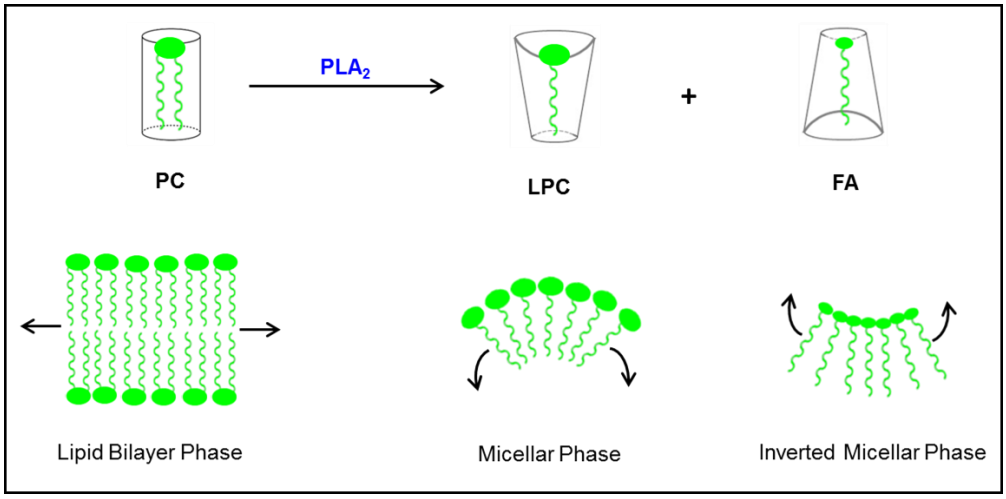

Figure 1.8. **The products LPC and free FA from the hydrolysis of PC by the PLA_2 enzyme (top route) and different polymorphic phases for aggregated lipid molecules in water for each of PC, LPC and free FA (bottom).**

1.3.1.1.3. The influence of lysophospholipid and fatty acid partitioning on lipid membrane

The partitioning ability of LPCs and free FAs in both lipid phase and aqueous phase is shown to have a great impact on both membrane-membrane[2,59,76,78-85] and membrane-protein[86-89] interactions. This is shown to be strongly related with LPC/free FA geometrical shape (see Figure1.8) and a consequent impact on morphological changes in the membrane.[90,91] Consequently, LPCs induce a positive curvature of the membrane upon their addition (Figure 1.9, route (a)), but a negative curvature is induced upon addition of free FA[2,59] (Figure 1.9, route (b)). On the other hand, equimolar amounts of both LPC and free FA are reported to keep membrane bilayer structure with no curvature[68,92-94] (Figure 1.9, route (c)). Consequently, the recorded disruption/destabilisation influence on the membrane by the individual addition of LPL and free FA such as morphology,[79] permeability,[59,80,81] fusion process,[82] and a consequent lysis[84,85] will be reduced.[2,76,92]

In addition, there are several factors that control the extent of LPL and/or free FA activity or incorporation into the membrane such as PLs phase behaviour whether they are in fluid phase or gel phase[76,90,93,95-99]. Also LPL/free FA chemical nature such as their acyl chain length and degree of

unsaturation[37,90,85,92,94] plus head-group size and polarity[37,58,77,100] have a great influence. Consequently, LPLs concentration above which they form micelles, the critical micelle concentration (CMC)[37,56,101] is also highly affected (Table 1.4). CMC decreases by increasing the length of the acyl chain and increases by decreasing the size of the polar head-group. Below CMC just monomers exist, while above CMC the monomer concentration remains constant and is equal to CMC[35].

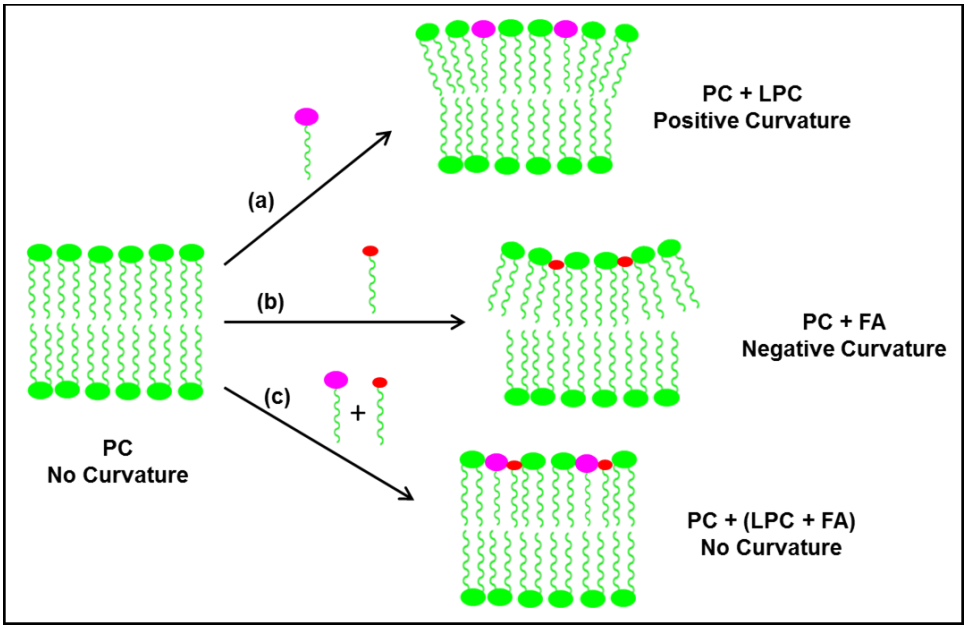

Figure 1.9. **Incorporation of LPC, free FA and both LPC and free FA into the lipid-bilayer of PC and their impact on lipid-bilayer curvature stress.**

Table 1.4. **The reported values for LPLs CMC[37,56] at 25 °C in the following solutions: X, pure water and Y, buffer solution composed of 0.14 M NaCl + 0.02 M Tris-HCl (pH 7.2)[37]. The comparative CMC value in different studies[101-103] is also provided.**

Lysohospholipid (LPL)	**Head-Groups Size (nm^3)[77]**	**CMC (mM) for Specific LPLs in X**		**CMC (mM) for Specific LPLs in Y**
Lysophosphatidylcholine (LPC)	0.101	(C14:0)	0.07,[37] 0.063,[101] 0.043[102]	0.07,[37] 0.063,[101] 0.043[102]
		(C16:0)	0.007,[37,103] 0.0083,[101] 0.0043[102]	0.007,[37,103] 0.0083,[101] 0.0043[102]
		(C18:1)	0.004[37]	0.004[37]
Lysophosphatidylserine (LPS)	0.087	(C14:0)	-	-
		(C16:0)	-	-
		(C18:1)	-	-
Lysophosphatidylethanolamine (LPE)	0.063	(C14:0)	-	-
		(C16:0)	-	-
		(C18:1)	-	-
Lysophosphatidylglycerol (LPG)	-	(C14:0)	3.0[37]	0.16[37]
		(C16:0)	0.6[37]	0.018[37]
		(C18:1)	-	-

1.3.1.2. Sphingophospholipid (SPL)

Sphingophospholipids (SPLs) are the second most abundant PL class with sphingosine backbone.[1,5,7,8] Amide linked acyl chain sphingosine forms ceramide, while sphingomyelins (SM) formed by the attachment of choline or ethanolamine polar groups to the hydroxyl group of ceramide (Figure 1.10). SM is the major class of SPLs in animal cell membrane[33,94] and they constitute 2-15%[104] of total PLs. This ratio is even higher in some tissues such as brain, nervous tissue and ocular lens, for example in human eye lens they have found to build up > 25% of the total lens PLs.[48] Their main features are their extensive ability to form hydrogen bonds and are asymmetric molecules because of the presence of very long fatty acyl chain of the amide linkage (longer than C20) and high degree of saturation relative to short paraffin residues on the sphingosine backbone.[8,94,104,105] Consequently, they serve vital functions in the natural cell such as their participating with GPLs

as building blocks for cell membrane formation, signalling molecules and their involvement in formation of lipid rafts.[8,104-106] Lipid rafts are localised regions in the membrane and known for their liquid ordered domain, characteristic resistance to solubilise by detergents and less fluidity than the rest of the cell membrane.[8,13-17,107] It is also reported that there is a strong relation between the amount of lens SM and cataract eye lens. It is found that the amount of SM increases with increasing age and cataract.[108-111]

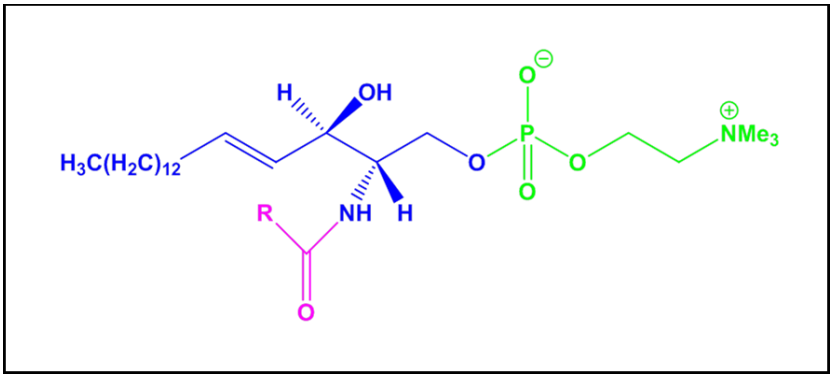

Figure 1.10. **Sphingomyelin (SM) structure, illustrating phosphatidylcholine head-group (green) and fatty acid tail-group (pink) attached to the sphingosine backbone (blue).**

1.3.2. Sterols

The other important lipid class in eukaryote membranes are sterols but they are rarely found in prokaryote membranes.[1,5,7] Cholesterol is the major class of sterol in mammals[1,5,7,8,108] and found at 30-50 mole% of total lipids[8]. It is composed of four cyclic rings with the polar hydroxyl group and hydrocarbon chain attached to it (Figure 1.11). Their excessive amount is found in lenses[112,113] with the highest recorded amount in human lenses relative to other animal lenses.[48,108] For example the concentration of cholesterol is 4-8 mg/g[48,113] of whole lens weight in human lenses, while it is 1-2 mg/g in rat and bovine lenses.[113] The amount of cholesterol has also shown to be related with lens age and cataract.[108-113] Interestingly, cholesterol increases membrane rigidity by introducing ordering distribution of the membrane to produce liquid ordered phase behaviour (L_o) and also shares the formation of lipid rafts with SM lipids.[8,105,106,111,114-117]

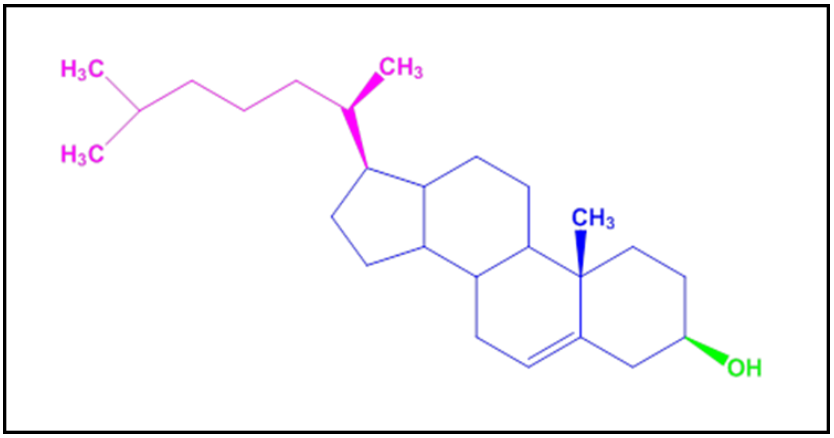

Figure 1.11. **Cholesterol structure, illustrating hydroxyl head-group (green) and hydrocarbon tail-group (pink) attached to the steroid backbone (blue).**

1.4. Analytical methods for lipid analysis

The lipidome represents the complete profile of lipid species present in a cell, organelle or tissue, while lipidomics represents the study of lipid profiles within biological systems.[118,119] Performing lipidomics research is quite challenging because of the diversity and complexity in the cell membrane, while performing lipid analysis for synthetic standard samples is less challenging. Consequently, relying on multiple tools for lipid analysis is very much needed and each single analytical tool will offer some pros and cons during their application.

Extraction techniques involving liquid-liquid extraction (LLE) and solid-phase extraction (SPE) have been widely used in lipid analysis to clean-up the sample mixture by carefully selecting the best extraction solvent to disrupt lipid and non-lipid species interactions and subsequently removing non-lipid species to get efficient extraction. Chromatographic method is another separation tool with a broad application in this field. This includes gas phase chromatography (GC) which is not so common because the majority of cell membrane lipids are non-polar and non-volatile so they require an extra step of chemical modification in order to enable this type of analysis. Thin-layer chromatography (TLC) is another chromatographic technique which is widely used because of their versatility, quick and high efficiency. High-performance liquid chromatography (HPLC) is the most popular method through normal phase HPLC and reverse phase HPLC to

separate and target a wide range of lipid species in one analysis with no need for lipid modification prior their HPLC analysis and also with high sensitivity.[119] In addition, nuclear magnetic resonance (NMR) spectroscopy is another applicable tool in lipid analysis. This involves ^{1}H and ^{13}C NMR for single PLs because of their complexity, while ^{31}P NMR is more common in both individual and a mixture of lipids because of the ability of ^{31}P NMR to provide separate signal for each PL class.[120] However, NMR method is very insensitive and requires a large amount of sample solution to perform the analysis and is more challenging for crude lipid sample than individual sample analysis.

Further, lipids can be analysed directly by mass spectrometry (MS)[118,119,121] using the two common ionisation techniques, electrospray ionisation (ESI)[122] and matrix-assisted laser desorption/ionisation (MALDI)[123]. This can be done without prior LC separation to produce intact lipid ions with the necessary level of sensitivity and high sample throughput. This is referred as shotgun lipidomics,[119,124] but the main disadvantage of this method is ion suppression by ionisation competition between different available ionised specie and thus limiting sensitivity. On the other hand, coupling LC with MS (LC-MS) offers a solution to ion suppression and increasing the sensitivity,[119,125] although LC slows down the sample throughput performance. Direct lipid identification based on their *m/z* in high resolution MS instruments refereed as top-down lipidomics, whereas using fragmentation (tandem) MS referred as bottom-up lipidomics.[119,121] In addition, combining the advantages from MALDI-MS with imaging principle provides a powerful tool to map tissue and investigate lipids spatial distribution,[126-130] while the anatomical integrity of the tissue is maintained.[131,132]

Additional improvements and information in the field of lipid analysis has been gained by coupling ion mobility separation (IMS) with MS (IMS-MS) to provide not just accurate *m/z* information for the analyte but also structural (ion conformation) by measuring their collision cross-section (CCS) or drift time.[133-135] The improvements in the analysis by using IMS-MS is found to be in the detection limit, speed of analysis, and selectivity.[135,136] The three common IMS-MS techniques include; drift time ion mobility spectrometry

(DTIMS), travelling wave ion mobility spectrometry (TWIMS) and field-asymmetric ion mobility spectrometry (FAIMS) or differential ion mobility spectrometry (DMS). IMS-MS has been widely applied in the field of peptide/protein gas phase study[136] but just recently has shown its application in lipidomics analysis[131,132,134,135].

Separation by IMS-MS can be performed for both neutral lipids such as PC, PE and SM, which are readily ionised in positive ion mode, and negative/acidic lipids such as PS, PG, PA and PI, which are efficiently ionised in negative ion mode.[121,132] Reported data showed that a sample composed of a mixture of lipids can be separated and classified based on their different head-group sizes with equivalent fatty acyl chains by measuring their structural changes in the gas phase and correlate it with the difference in their drift time.[132,135,137-139] Faster mobility/smaller drift time were recorded for lipids with smaller head-group sizes such as PA, while slower mobility/larger drift time for lipids with larger head-group size such as PC. In addition, lipids with longer acyl chains have higher drift time than shorter acyl chains, while increasing the number of double bonds causes a decrease in drift time,[132,140,141] but this has shown to have less impact on drift time than acyl chain length.[140] On the other hand, separating lipid isomers such as *cis*-isomer from *trans*-isomer,[140] PLs from plasmalogen PLs and hydroxylated from non-hydroxylated lipids[132] is more challenging due to little or no change in the drift time. Separating lipid isomers in terms of positioning fatty acyl substituents such as POPC from OPPC was only achieved under special IMS-MS conditions, for example by coupling dual stage collision induced dissociation (CID) fragmentation with TWIMS[142] or by using DMS for cation adduct formation (Ag^+) with the lipid of interest[143]. DMS was also shown its ability to quantify the amount of LPLs in biological samples through direct infusion (shotgun lipidomics) by using multiple reaction monitoring (MRM) mode and/or precursor ion scan (PIS).[139] Further, it is also possible to localise the position of the double bond on PC lipids by using CID with TWIMS and it is not just applicable for synthetic standard lipid samples, but also in biological samples.[142]

1.5. Lipid-protein interaction

The two most abundant biomolecules, lipids and proteins, serve a range of vital functions in the fluid system of the membrane. Their interactions can result in formations that possess new functions which differ from the individual function of the independent lipid or protein. This interaction depends on the type of available proteins and lipids. Soluble proteins in the membrane, extrinsic or peripheral membrane proteins, interact with the surface of the lipid membrane through electrostatic interactions, while proteins with hydrophobic domains, intrinsic or integral membrane proteins, interact with lipids by spanning through membrane lipid-bilayer.[7] On the other hand, lipids either have no contact with proteins (bulk lipids) or they have a contact with proteins[144,145] (Figure 1.12). Lipids with contact with proteins can be classified to two classes[144,145]; annular lipids (Figure 1.12A), they are known to have lower affinity to proteins with non-specific interactions; non-annular lipids (Figure 1.12B), this class of lipid have higher affinity and specific interactions with membrane proteins to form lipid-protein complexes.

Studying this lipid-protein interactions is very challenging,[18,145,146] mainly due to the diversity of lipid/protein compositions in the cell, different phase behaviour/physical properties of lipids and how the presence and absence of proteins/peptides influence membrane lipids phase behaviour. In order to understand lipid-protein interactions, different analytical tools have applied with different outcomes. Electron spin resonance (ESR), often called electron paramagnetic resonance (EPR) and 2DIR are very useful techniques to follow dynamic/time scale of lipid-protein interactions.[145-148] Both methods are known for their sensitivity and speed,[145] but they are difficult to apply for biological samples[148]. EPR is also a useful technique to evaluate the number of lipid molecules which surrounds the membrane protein.[146] Time-resolved fluorescence is another spectroscopy method to study lipid-protein interaction and shown its compatibility for biological samples.[148] In addition, structural study of lipid-protein complex is also very useful to understand and characterise lipid-protein interactions. This has been done by using X-ray crystallography,[149,150] 2D electron crystallography,[149,151] and solid-state NMR[152].[145,146,148]

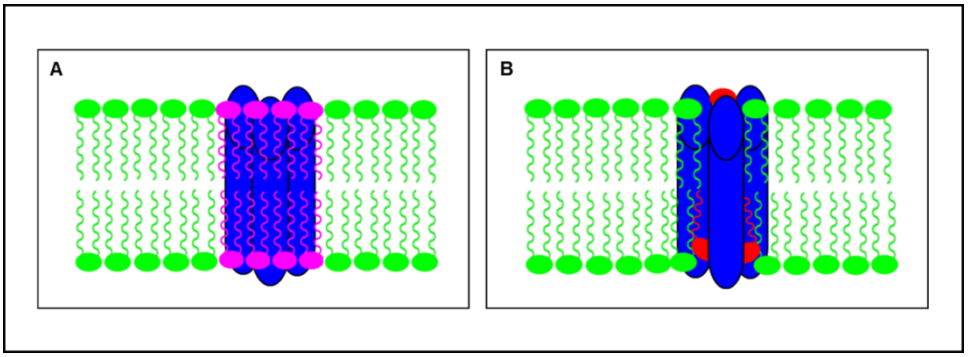

Figure 1.12. **(A) Lipid-bilayer representation of regions where PLs are solvating membrane proteins by forming a shell around protein complex (annular lipids, pink), and (B) PLs buried within protein complex subunits (non-annular lipids, red).**

1.6. Protein lipidation

The addition of an acyl group from a lipid molecule to a peptide or protein i.e. lipidation or fatty acylation produces a modified peptide/protein with higher molecular mass and hydrophobicity, and as a result a higher affinity to membrane. These include, cytoplasmically oriented modifications of post-translational modifications (PTM) such as S-acylation (palmitoylation) and S-prenylation, via thioester linkage, or co-translational modifications such as N-myristoylation, via amide linkage, and also extracellularly oriented modifications such as cholesteroylation and glycosylphosphatidylinositol (GPI) anchoring.[153-158] In addition of S-palmitoylation, N-palmitoylation via amide linkage also reported.[157-159] Usually these processes of modification are done by enzyme catalysis *in vivo*,[160] but non-enzymatic auto acylation has also been described.[156] Modified proteins with modified physical properties[153,154] have a great impact on protein localisation and different physiological functions, such as intracellular targeting, signalling pathways, protein-protein and protein-lipid interactions in different living organisms.[156-161] Protein lipidation is also reported to implicate in some human diseases such as cancer, diabetes and neurological disorders.[157,162] In addition, Sachon *et al.* showed that chemically modified human growth hormone with palmitoylation towards ε-amino group of lysine is stable under extreme pH conditions with desired pharmacological properties, and palmitoylation also increases plasma half-life.[158]

Interestingly, the advantages of high sensitivity, accuracy and resolving power of some MS tools enabled the detection and/or quantification of a range of PTMs.[158,161-172] A typical example for lipidated peptide/protein and their involvement in this study is melittin[168-170] and AQP0[154,165,167,171]. Non-enzymatic acyl transfer was recorded through aminolysis reaction of ester-linked fatty acyl from PLs forming liposome to the N-terminus, side chains of internal lysine and serine residues of melittin within a short timescale of 3-4 h.[169,170] This non-enzymatic acyl transfer was also suggested *in vivo* in a recent publication for AQP0 by reporting a range of lipidation products that mirrors the PL composition of the membrane leaflet that AQP0 acylation sites are located in.[172] However, earlier studies[154,165,167,171] recorded AQP0 lipidation but with only two acyl chains (palmitoyl and oleoyl) and with the lack to provide supporting evidence for acyl transfer from lens membrane to the protein.

1.7. Melittin

Melittin with two special properties; high basicity and surface activity[173] is one of the most extensively utilized model peptides for studying. It is a highly positively charged peptide, +6 at physiological conditions, due to the presence of several basic amino acid (AA) residues in the total of 26 AA residues (Figure 1.13). It is principally a hydrophobic peptide because of the predominantly hydrophobic character at N-terminal portion (1-20 AA residue), while the C-terminal portion is predominantly hydrophilic (21-26 AA residues). Consequently, melittin is amphiphilic peptide and is readily soluble in water. In aqueous solution, within physiological pH, and low melittin concentration it is present as a monomer with a random coil disordered conformation. However, the absence of electrostatic repulsion between the stretch of positive charges under the conditions of increasing ion strength, concentration, pH and temperature[174,175] causes four monomers to aggregate[175] and form α-helical tetramer conformation with a kink at proline AA (P14) in each α-helix monomer (Figure 1.13).[174,175] This structural conformation has been studied by different analytical tools[175] including; circular dichroism (CD),[176] fluorescence spectroscopy,[177,178] NMR

spectroscopy[179,180] and X-ray crystallography[181]. Interestingly, melittin also exists as α-helical structure during its binding with lipid membranes or liposome and micelles.[174,182-185]

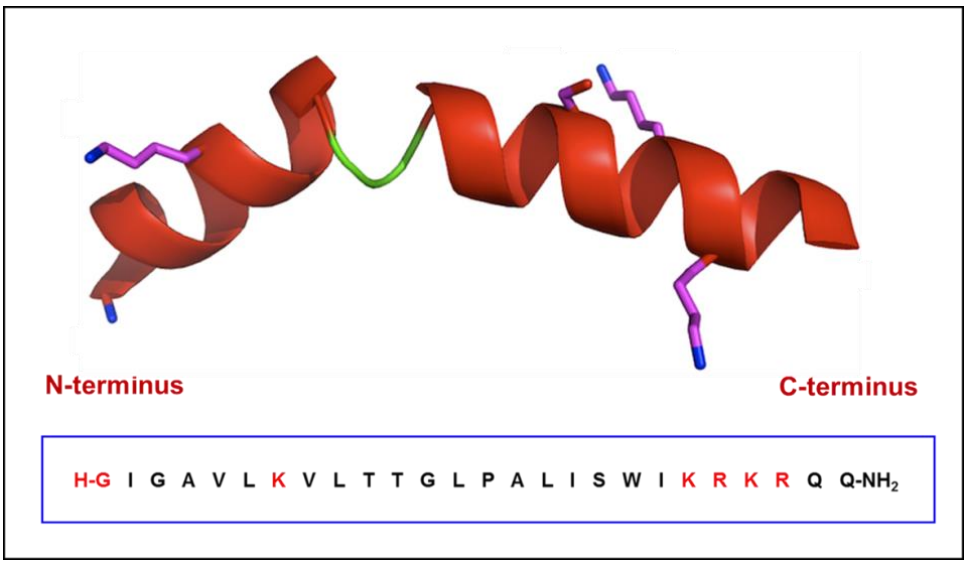

***Figure 1.13.* α-Helix structure from tetramer aggregation of melittin, obtained from (PDB code: 2MLT). 26 AA residues of melittin is obtained from (https://pubchem.ncbi.nlm.nih.gov/compound/16133648); molecular formula, $C_{131}H_{229}N_{39}O_{31}$; average neutral mass, 2846.4694 Da. Highlighted AA residues in red represent positive sites of melittin at physiological condition.**

Melittin, a membrane active peptide, has a range of activities such as moderate antibacterial and antifungal activity at concentration ranges between 0.05-0.2%[173] and it has a powerful hemolytic (membrane perturbation) activity[173,174,186]. This induces a leakage in the erythrocytes membrane and the release of hemoglobin and thus membrane permeability will be increased. This mainly depends on melittin concentration, in which above 1 µg/mL this hemolytic activity will be enhanced.[174,186] This peptide is a major component in the venom of European honey bee (*Apis mellifera*) and present at a ratio 50% (w/w) of dry venom.[173,174,187,188] The second most abundant biomolecule in the venom of honey bee is PLA_2 at concentration 10-12% (w/w) of the dry weight.[187] The hydrolysis activity of this enzyme (see Figure 1.7) in the presence of (Ca^{2+})[62,67] has reported to be enhanced by

melittin.[182,189-191] Synergistic activity for both melittin and PLA_2 on membrane lipids has also been suggested.[182]

1.8. AQP0 in mammalian eye lens

A clear vision is a vital physiological function of the eye. This function is provided by an avascular and transparent organ called lens. Both lens and cornea in the front of the eye are focusing images/light on the retina in the back of the eye (Figure 1.14). Eye lens is surrounded by lens capsule and underneath it there is a single layer of cuboidal epithelial cells in the front/anterior surface. These epithelial cells elongate, lose their light scattering intracellular organelles, synthesize particular crystallin proteins, replace their membrane transport proteins and consequently differentiate into fibre cells at the equator.[192,193] Fibre cells are concentric layers and they constituent the bulk of the lens. They are continuously added to the lens throughout the life and thus an increase in the lens weight[115] as there is no cell turnover in the lens.[192-194] The younger fibre cells at the cortex are always renewed throughout the life by adding new cells to it in periphery, while the core fibre cells have the same original cell constituents that were present since birth.[111,115,194-196] Interestingly, one of the public eye health problems is a cataract where the lens lose its transparency and consequently vision[197,198]. Cataract usually starts after the age of 40 years in human.[198]

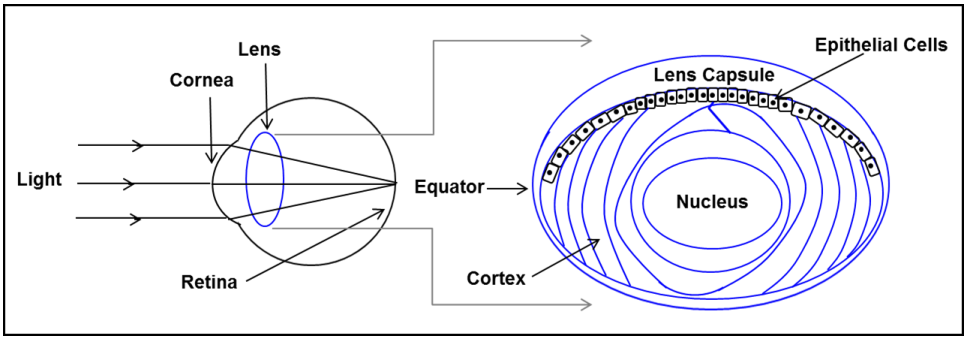

Figure 1.14. **The structure of human eye (left) and the illustration of cellular fractions in the eye lens (right).**

One of the most abundant integral membrane proteins in mammals which is produced by lens fibre cell is AQP0, also called aquaporin-0, major (membrane) intrinsic protein, MIP, MIP26, and MP26.[199,200] Generally, Integral membrane proteins are of great importance in cellular processing in eukaryotes and they make-up one-third of the total proteins encoded by genome and large amount of drug targets.[201] They serve as signalling molecules, transporters, cell-cell interaction, energy generation, vesicle trafficking and intracellular communication.[201-203] The C-terminus and N-terminus of all integral membrane proteins are located at the cytoplasmic surface and they all share tetraspanin properties, because they are composed of four membrane-spanning domains.[204,203]

AQP0 is a member of aquaporin family with 28 kDa mass that comprises nearly 50% of protein in the lens membrane[206-209]. It has a number of different functions in the lens, the major functions being a water channel,[149,210-214] formation of thin junctions in the lens membrane[149,213,214] and facilitating cell-to-cell adhesion[207,215]. Mutation in AQP0 gene leads to cataract formation in the eye,[200,216] which indicates the importance of this protein and the need to understand its behaviour in relation to disease. The significance of this protein has meant it has attracted a lot of attention over the years. During this time a range of different modifications were recorded on AQP0 such as truncation,[217-219] phosphorylation,[201,206,218,220] deamidation,[165,201,218,221] and as well as lipidation[154,165,171,172]. However, recent publication[172] with recording a broad range of novel lipidation products showed that whole range of lipidated AQP0 were not covered in previous works.

Structural studies of this protein showed that it exhibits a tetramer complex in the membrane with six transmembrane α-helices.[220,222,223] Different conformations of junctional and non-junctional AQP0 is shown in Figure 1.15. It has been reported that formation of thin junction in the core of lens membrane is related with proteolytic digestion of AQP0 with a cleavage at intracellular C-terminus,[149,213] while non-junctional AQP0 is specific for intact protein and both C-terminal and N-terminal regions have ordered conformation[149]. Junctional and non-junctional AQP0 also exhibit different water pores and hydrogen bonding pattern. Further, lipid ratio in lens

membrane is low and their overall content is reported to be 4%,[115] these lipid membranes are generally very rigid and this is suggested to be related to their high cholesterol content.[114,115,195] They also have a restricted movement and this is because of their interaction with proteins (see Table 1.3 and chapter four, section 4.1.3 for details about lipid composition in the eye lens).[108,111] AQP0 and membrane lipids are regarded as age related components in mature fibre cells of the lens because there is no or little cellular turnover in the lens,[167,194,224-226] thus these two species are of high interest to study as they regarded as old as the lens itself. Lynnerup *et al.*[225] and Stewart *et al.*[226] have used ^{14}C bomb pulse to reveal proteins without turnover in the human eye lens.

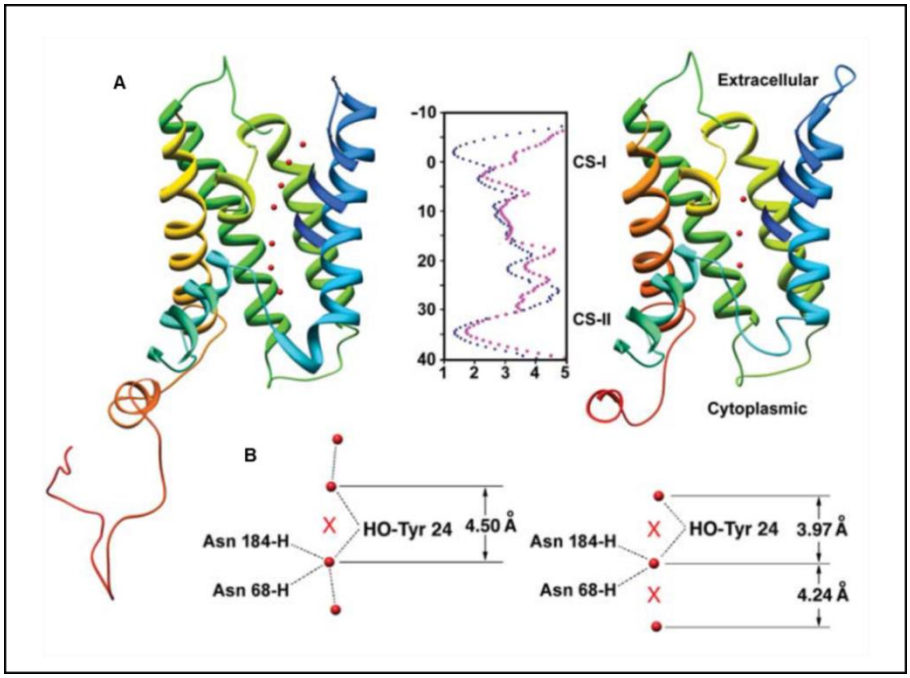

Figure 1.15. **(A) The water pore in junctional AQP0 (right) and non-junctional AQP0 (left). Red spheres represent water molecules in both junctional (3 water molecules) and non-junctional (7 water molecules). The middle data represents the calculated water pore profiles for both junctional AQP0 (purple, more constricted) and non-junctional AQP0 (pink, less constricted). (B) Hydrogen bonding pattern of water molecules (dotted lines) in the pore of junctional AQP0 (right) and non-junctional AQP0 (left). Tyrosine AA residue (Tyr24) of AQP0 introduces a phenolic barrier and disrupt the hydrogen-bonding network. In junctional AQP0 all three water molecules are too far apart to form hydrogen bonds. Reprinted by permission from Macmillan Publishers Ltd: [Nature],[149] copyright (2005).**

1.9. References

1 Nelson, David L., and Micheal M. Cox. "*Principles of Biochemistry*." Worth Publishers, New York, **2000**.

2 Arouri, Ahmad, and Ole G. Mouritsen. "Membrane-perturbing effect of fatty acids and lysolipids." *Progress in Lipid Research,* 52 (**2013**): 130-140.

3 Marrink, Siewert-Jan, and Herman JC Berendsen. "Simulation of water transport through a lipid membrane." *The Journal of Physical Chemistry,* 98 (**1994**): 4155-4168.

4 Lipowski, R., and E. Sackmann. "*Structure and Dynamics of Membranes, volume 1A, Handbook of Biological Physics.*" Elsevier Science B.V., **1995**.

5 Berg, Jeremy M., John L. Tymoczko, Gregory J. Gatto, Jr., and Lubert Stryer. "*Biochemistry*." W. H. Freeman and Company, New York, **2015**.

6 Gorter, Evert, and F. J. E. M. Grendel. "On bimolecular layers of lipoids on the chromocytes of the blood." *Journal of Experimental Medicine,* 41 (**1925**): 439-443.

7 Vance, Dennis E., and Jean E. Vance. "*Biochemistry of Lipids and Membranes.*" The Benajamin/Cummings publishing company, INC, California, **1985**.

8 Eeman, Marc, and Magali Deleu. "From biological membranes to biomimetic model membranes." *Biotechnology, Agronomy, Society and Environment,* 14 (**2010**): 719-736.

9 Bagatolli, Luis A., John H. Ipsen, Adam C. Simonsen, and Ole G. Mouritsen. "An outlook on organization of lipids in membranes: searching for a realistic connection with the organization of biological membranes." *Progress in Lipid Research,* 49 (**2010**): 378-389.

10 Singer, S. Jonathan, and Garth L. Nicolson. "The fluid mosaic model of the structure of cell membranes." *Science,* 175 (**1972**): 720-731.

11 Israelachvili, Jacob N. "Refinement of the fluid-mosaic model of membrane structure." *Biochimica et Biophysica Acta (BBA)-Biomembranes,* 469 (**1977**): 221-225.

12 Simons, Kai, and Gerrit Van Meer. "Lipid sorting in epithelial cells." *Biochemistry,* 27 (**1988**): 6197-6202.

13 Simons, Kai, and Elina Ikonen. "Functional rafts in cell membranes." *Nature,* 387 (**1997**): 569-572.

14 Pike, Linda J. "Lipid rafts bringing order to chaos." *Journal of Lipid Research,* 44 (**2003**): 655-667.

15 Veatch, S. L., I. V. Polozov, K. Gawrisch, and S. L. Keller. "Liquid domains in vesicles investigated by NMR and fluorescence microscopy." *Biophysical Journal,* 86 (**2004**): 2910-2922.

16 Kusumi, Akihiro, and Kenichi Suzuki. "Toward understanding the dynamics of membrane-raft-based molecular interactions." *Biochimica et Biophysica Acta (BBA)-Molecular Cell Research,* 1746 (**2005**): 234-251.

17 Jensen, Mikkel Herholdt, Eliza J. Morris, and Adam Cohen Simonsen. "Domain shapes, coarsening, and random patterns in ternary membranes." *Langmuir,* 23 (**2007**): 8135-8141.

18 Sanderson, John M. "Peptide–lipid interactions: insights and perspectives." *Organic & Biomolecular Chemistry,* 3 (**2005**): 201-212.

19 Galdiero, Stefania, Annarita Falanga, Marco Cantisani, Mariateresa Vitiello, Giancarlo Morelli, and Massimiliano Galdiero. "Peptide-lipid interactions: experiments and applications." *International Journal of Molecular Sciences,* 14 (**2013**): 18758-18789.

20 Shai, Yechiel. "Mechanism of the binding, insertion and destabilization of phospholipid bilayer membranes by α-helical antimicrobial and cell non-selective membrane-lytic peptides." *Biochimica et Biophysica Acta (BBA)-Biomembranes,* 1462 (**1999**): 55-70.

21 Yeaman, Michael R., and Nannette Y. Yount. "Mechanisms of antimicrobial peptide action and resistance." *Pharmacological Reviews,* 55 (**2003**): 27-55.

22 Giuliani, A., G. Pirri, A. Bozzi, A. Di Giulio, M. Aschi, and A. C. Rinaldi. "Antimicrobial peptides: natural templates for synthetic membrane-active compounds." *Cellular and Molecular Life Sciences,* 65 (**2008**): 2450-2460.

23 New, R. R. C. "*Liposomes: a Practical Approach*." Oxford University Press, **1990**.

24 Mouritsen, Ole G. "Lipids, curvature, and nano-medicine." *European Journal of Lipid Science and Technology,* 113 (**2011**): 1174-1187.

25 Akbarzadeh, Abolfazl, Rogaie Rezaei-Sadabady, Soodabeh Davaran, Sang Woo Joo, Nosratollah Zarghami, Younes Hanifehpour, Mohammad Samiei, Mohammad Kouhi, and Kazem Nejati-Koshki. "Liposome: classification, preparation, and applications." *Nanoscale Research Letters,* 8 (**2013**): 1-9.

26 Reza Mozafari, M., Chad Johnson, Sophia Hatziantoniou, and Costas Demetzos. "Nanoliposomes and their applications in food nanotechnology." *Journal of Liposome Research,* 18 (**2008**): 309-327.

27 Memoli, Adriana, Luisa G. Palermiti, Valter Travagli, and Franco Alhaique. "Liposomes in cosmetics. II: entrapment of a hydrophilic probe." *Journal of the Society of Cosmetic Chemists,* 45 (**1994**): 167-172.

28 Sharma, Amarnath, and Uma S. Sharma. "Liposomes in drug delivery: progress and limitations." *International Journal of Pharmaceutics,* 154 (**1997**): 123-140.

29 Agrawal, Ajay K., and C. M. Gupta. "Tuftsin-bearing liposomes in treatment of macrophage-based infections." *Advanced Drug Delivery Reviews,* 41 (**2000**): 135-146.

30 Kelly, Ciara, Caroline Jefferies, and Sally-Ann Cryan. "Targeted liposomal drug delivery to monocytes and macrophages." *Journal of Drug Delivery,* 2011 (**2010**): 1-11.

31 Bangham, A. D., and R. W. Horne. "Action of saponin on biological cell membranes." *Nature,* 196 (**1962**): 952-953.

32 Hope, M. J., M. B. Bally, G. Webb, and P. R. Cullis. "Production of large unilamellar vesicles by a rapid extrusion procedure. Characterization of size distribution, trapped volume and ability to maintain a membrane potential." *Biochimica et Biophysica Acta (BBA)-Biomembranes,* 812 (**1985**): 55-65.

33 Van Meer, Gerrit, Dennis R. Voelker, and Gerald W. Feigenson. "Membrane Lipids: Where they are and how they behave." *Nature Reviews. Molecular Cell Biology,* 9 (**2008**): 112-124.

34 Mcelhaney, Ronald N., and Mark E. Tourtellotte. "The relationship between fatty acid structure and the positional distribution of esterified fatty acids in phosphatidyl glycerol from Mycoplasma laidlawii B." *Biochimica et Biophysica Acta (BBA)-Lipids and Lipid Metabolism,* 202 (**1970**): 120-128.

35 Cevc, Gregor, and Derek Marsh. "*Phospholipid Bilayers: Physical Principal and Models*." A Wiley-Interscience Publication, John and Sons, New York, **1987**.

36 Ansell, G. B., J. M. Hawthorne, and R. M. C. Dawson. "*In Form and Function of Phospholipids*." Elsevier, Amsterdam, **1973**.

37 Stafford, Richard E., Tahsin Fanni, and Edward A. Dennis. "Interfacial properties and critical micelle concentration of lysophospholipids." *Biochemistry,* 28 (**1989**): 5113-5120.

38 Anderson, Robert E., Maureen B. Maude, and Gerald L. Feldman. "Lipids of ocular tissues: I. The phospholipids of mature rabbit and bovine lens." *Biochimica et Biophysica Acta (BBA)-Lipids and Lipid Metabolism,* 187 (**1969**): 345-353.

39 Bretscher, Mark S. "Asymmetrical lipid bilayer structure for biological membranes." *Nature,* 236 (**1972**): 11-12.

40 Verkleij, A. J., R. F. A. Zwaal, B. Roelofsen, P. Comfurius, D. Kastelijn, and L. L. M. Van Deenen. "The asymmetric distribution of phospholipids in the human red cell membrane. A combined study using phospholipases and freeze-etch electron microscopy." *Biochimica et Biophysica Acta (BBA)-Biomembranes,* 323 (**1973**): 178-193.

41 Rothman, James E., and John Lenard. "Membrane asymmetry." *Science,* 195 (**1977**): 743-753.

42 Op den Kamp, J. A. F. "Lipid asymmetry in membranes." *Annual Review of Biochemistry,* 48 (**1979**): 47-71.

43 Ingólfsson, Helgi I., Manuel N. Melo, Floris J. van Eerden, Clément Arnarez, Cesar A. Lopez, Tsjerk A. Wassenaar, Xavier Periole, Alex H. de Vries, D. Peter Tieleman, and Siewert J. Marrink. "Lipid organization of the plasma membrane." *Journal of the American Chemical Society,* 136 (**2014**): 14554-14559.

44 Manno, Sumie, Yuichi Takakuwa, and Narla Mohandas. "Identification of a functional role for lipid asymmetry in biological membranes: phosphatidylserine-skeletal protein interactions modulate membrane stability." *Proceedings of the National Academy of Sciences,* 99 (**2002**): 1943-1948.

45 Braverman, Nancy E., and Ann B. Moser. "Functions of plasmalogen lipids in health and disease." *Biochimica et Biophysica Acta (BBA)-Molecular Basis of Disease,* 1822 (**2012**): 1442-1452.

46 Bartley, W., Ruth Van Heyningen, Brenda M. Notton, and A. Renshaw. "Fatty acid composition of lipids present in different parts of the ox eye." *Biochemical Journal,* 85 (**1962**): 332-335.

47 Broekhuyse, RaM. "Phospholipids in tissues of the eye I. Isolation, characterization and quantitative analysis by two-dimensional thin-layer chromatography of diacyl and vinyl-ether phospholipids." *Biochimica et Biophysica Acta (BBA)-Lipids and Lipid Metabolism,* 152 (**1968**): 307-315.

48 Deeley, Jane M., Todd W. Mitchell, Xiaojia Wei, John Korth, Jessica R. Nealon, Stephen J. Blanksby, and Roger JW Truscott. "Human lens lipids differ markedly from those of commonly used experimental animals." *Biochimica et Biophysica Acta (BBA)-Molecular and Cell Biology of Lipids,* 1781 (**2008**): 288-298.

49 Yeagle, Philip L. "*The Structure of Biological Membranes*." CRC Press, **2004**.

50 McIntosh, T. J. "Differences in hydrocarbon chain tilt between hydrated phosphatidylethanolamine and phosphatidylcholine bilayers. A molecular packing model." *Biophysical Journal,* 29 (**1980**): 237-245.

51 Koynova, Rumiana, and Martin Caffrey. "Phases and phase transitions of the phosphatidylcholines." *Biochimica et Biophysica Acta (BBA)-Reviews on Biomembranes,* 1376 (**1998**): 91-145.

52 Lynch, Daniel V., and Peter L. Steponkus. "Lyotropic phase behavior of unsaturated phosphatidylcholine species: relevance to the mechanism of plasma membrane destabilization and freezing injury." *Biochimica et Biophysica Acta (BBA)-Biomembranes,* 984 (**1989**): 267-272.

53 Ulrich, Anne S., Malkit Sami, and Anthony Watts. "Hydration of DOPC bilayers by differential scanning calorimetry." *Biochimica et Biophysica Acta (BBA)-Biomembranes,* 1191 (**1994**): 225-230.

54 Ladbrooke, B. D., and D. Chapman. "Thermal analysis of lipids, proteins and biological membranes a review and summary of some recent studies." *Chemistry and Physics of Lipids,* 3 (**1969**): 304-356.

55 Biltonen, Rodney L., and Dov Lichtenberg. "The use of differential scanning calorimetry as a tool to characterize liposome preparations." *Chemistry and Physics of Lipids,* 64 (**1993**): 129-142.

56 Marsh, Derek. "*Hand Book of Lipid Bilayers*." CRC Press, **2013**.

57 Cevc, Gregor. "How membrane chain-melting phase-transition temperature is affected by the lipid chain asymmetry and degree of unsaturation: an effective chain-length model." *Biochemistry,* 30 (**1991**): 7186-7193.

58 Stafford, Richard E., and Edward A. Dennis. "Lysophospholipids as biosurfactants." *Colloids and Surfaces,* 30 (**1987**): 47-64.

59 Davidsen, Jesper, Ole G. Mouritsen, and Kent Jørgensen. "Synergistic permeability enhancing effect of lysophospholipids and fatty acids on lipid membranes." *Biochimica et Biophysica Acta (BBA)-Biomembranes,* 1564 (**2002**): 256-262.

60 Brown, William J., Kimberly Chambers, and Anne Doody. "Phospholipase A_2 (PLA_2) enzymes in membrane trafficking: mediators of membrane shape and function." *Traffic,* 4 (**2003**): 214-221.

61 Dennis, Edward A. "Introduction to thematic review series: phospholipases: central role in lipid signaling and disease." *Journal of Lipid Research,* 56 (**2015**): 1245-1247.

62 Burke, John E., and Edward A. Dennis. "Phospholipase A_2 structure/function, mechanism, and signaling." *Journal of Lipid Research,* 50 (**2009**): S237-S242.

63 Wang, Aijun, and Edward A. Dennis. "Mammalian lysophospholipases." *Biochimica et Biophysica Acta (BBA)-Molecular and Cell Biology of Lipids,* 1439 (**1999**): 1-16.

64 Høyrup, P., Kent Jørgensen, and O. G. Mouritsen. "Phospholipase A_2—An enzyme that is sensitive to the physics of its substrate." *Europhysics Letters,* 57 (**2002**): 464-470.

65 Huang, Wei-Ning, Yu-He Chen, Chia-Lu Chen, and Wenguey Wu. "Surface pressure-dependent interactions of secretory phospholipase A_2 with zwitterionic phospholipid membranes." *Langmuir,* 27 (**2011**): 7034-7041.

66 van Dam-Mieras, M. C. E., A. J. Slotboom, W. A. Pieterson, and G. H. De Haas. "Interaction of phospholipase A_2 with micellar interfaces. Role of the N-terminal region." *Biochemistry,* 14 (**1975**): 5387-5394.

67 Dennis, Edward A. " Phospholipases." *The Enzymes,* 16 (**1983**): 307-353.

68 Jain, Mahendra Kumar, Mark Streb, Joe Rogers, and Gerard H. Dehaas. "Action of phospholipase A_2 on bilayers containing lysophosphatidylcholine analogs and the effect of inhibitors." *Biochemical Pharmacology,* 33 (**1984**): 2541-2551.

69 Bell, John D., and R. L. Biltonen. "Molecular details of the activation of soluble phospholipase A_2 on lipid bilayers. Comparison of computer simulations with experimental results." *Journal of Biological Chemistry,* 267, (**1992**): 11046-11056.

70 Kensil, Charlotte Read, and E. A. Dennis. "Action of cobra venom phospholipase A_2 on the gel and liquid crystalline states of dimyristoyl and dipalmitoyl phosphatidylcholine vesicles." *Journal of Biological Chemistry,* 254 (**1979**): 5843-5848.

71 Hønger, Thomas, Kent Jørgensen, R. L. Biltonen, and Ole G. Mouritsen. "Systematic relationship between phospholipase A_2 activity and dynamic lipid bilayer microheterogeneity." *Biochemistry,* 35 (**1996**): 9003-9006.

72 Kensil, Charlotte Read, and Edward A. Dennis. "Action of cobra venom phospholipase A_2 on large unilamellar vesicles: Comparison with small unilamellar vesicles and multibilayers." *Lipids,* 20 (**1985**): 80-83.

73 Leidy, Chad, Lars Linderoth, Thomas L. Andresen, Ole G. Mouritsen, Kent Jørgensen, and Günther H. Peters. "Domain-induced activation of human phospholipase A_2 type IIA: local versus global lipid composition." *Biophysical Journal,* 90 (**2006**): 3165-3175.

74 Yokoyama, S., and F. J. Kézdy. "Monolayers of long chain lecithins at the air/water interface and their hydrolysis by phospholipase A_2." *Journal of Biological Chemistry,* 266 (**1991**): 4303-4308.

75 Peters, Günther H., Martin S. Møller, Kent Jørgensen, Petra Rönnholm, Mette Mikkelsen, and Thomas L. Andresen. "Secretory phospholipase A_2 hydrolysis of phospholipid analogues is dependent on water accessibility to the active site." *Journal of the American Chemical Society,* 129 (**2007**): 5451-5461.

76 Van Echteld, C. J. A., B. De Kruijff, J. G. Mandersloot, and J. De Gier. "Effects of lysophosphatidylcholines on phosphatidylcholine and phosphatidylcholine/cholesterol liposome systems as revealed by ^{31}P-NMR, electron microscopy and permeability studies." *Biochimica et Biophysica Acta (BBA)-Biomembranes,* 649 (**1981**): 211-220.

77 Lundbaek, Jens A., and Olaf S. Andersen. "Lysophospholipids modulate channel function by altering the mechanical properties of lipid bilayers." *The Journal of General Physiology,* 104 (**1994**): 645-673.

78 Henriksen, Jonas R., Thomas L. Andresen, Lise N. Feldborg, Lars Duelund, and John H. Ipsen. "Understanding detergent effects on lipid membranes: a model study of lysolipids." *Biophysical Journal,* 98 (**2010**): 2199-2205.

79 Klibansky, Chaja, and Andre De Vries. "Quantitative study of erythrocyte-lysolecithin interaction." *Biochimica et Biophysica Acta (BBA)-Specialized Section on Lipids and Related Subjects,* 70 (**1963**): 176-187.

80 Weltzien, Hans Ulrich. "Cytolytic and membrane-perturbing properties of lysophosphatidylcholine." *Biochimica et Biophysica Acta (BBA)-Reviews on Biomembranes,* 559 (**1979**): 259-287.

81 Grit, Mustafa, and Daan JA Crommelin. "The effect of aging on the physical stability of liposome dispersions." *Chemistry and Physics of Lipids,* 62 (**1992**): 113-122.

82 Martin, Isabelle, M-C. Dubois, T. Saermark, R. M. Epand, and J-M. Ruysschaert. "Lysophosphatidylcholine mediates the mode of insertion of the NH_2-terminal SIV fusion peptide into the lipid bilayer." *FEBS Letters,* 333 (**1993**): 325-330.

83 Choi, Ji Woong, Deron R. Herr, Kyoko Noguchi, Yun C. Yung, Chang-Wook Lee, Tetsuji Mutoh, Mu-En Lin et al. "LPA receptors: subtypes and biological actions." *Annual Review of Pharmacology and Toxicology,* 50 (**2010**): 157-186.

84 Hsieh, Chien-Cheng, Mao-Hsiung Yen, Hwan-Wun Liu, and Ying-Tung Lau. "Lysophosphatidylcholine induces apoptotic and non-apoptotic death in vascular smooth muscle cells: in comparison with oxidized LDL." *Atherosclerosis,* 151 (**2000**): 481-491.

85 Reman, F. C., R. A. Demel, J. De Gier, L. L. M. Van Deenen, H. Eibl, and O. Westphal. "Studies on the lysis of red cells and bimolecular lipid leaflets by synthetic lysolecithins, lecithins and structural analogs." *Chemistry and Physics of Lipids,* 3 (**1969**): 221-233.

86 Anbazhagan, V., and Musti J. Swamy. "Thermodynamics of phosphorylcholine and lysophosphatidylcholine binding to the major protein of bovine seminal plasma, PDC-109." *FEBS Letters,* 579 (**2005**): 2933-2938.

87 Phillips, Rob, Tristan Ursell, Paul Wiggins, and Pierre Sens. "Emerging roles for lipids in shaping membrane-protein function." *Nature,* 459 (**2009**): 379-385.

88 Nomura, Takeshi, Charles G. Cranfield, Evelyne Deplazes, Dylan M. Owen, Alex Macmillan, Andrew R. Battle, Maryrose Constantine, Masahiro Sokabe, and Boris Martinac. "Differential effects of lipids and lyso-lipids on the mechanosensitivity of the mechanosensitive channels MscL and MscS." *Proceedings of the National Academy of Sciences,* 109 (**2012**): 8770-8775.

89 Stangl, Michael, Anbazhagan Veerappan, Anja Kroeger, Peter Vogel, and Dirk Schneider. "Detergent properties influence the stability of the glycophorin A transmembrane helix dimer in lysophosphatidylcholine micelles." *Biophysical Journal,* 103 (**2012**): 2455-2464.

90 Høyrup, Pernille, Jesper Davidsen, and Kent Jørgensen. "Lipid membrane partitioning of lysolipids and fatty acids: effects of membrane phase structure and detergent chain length." *The Journal of Physical Chemistry B,* 105 (**2001**): 2649-2657.

91 Fuller, N., and R. P. Rand. "The influence of lysolipids on the spontaneous curvature and bending elasticity of phospholipid membranes." *Biophysical Journal,* 81 (**2001**): 243-254.

92 Jain, Mahendra Kumar, and Gerard H. De Haas. "Structure of 1-acyl lysophosphatidylcholine and fatty acid complex in bilayers." *Biochimica et Biophysica Acta (BBA)-Biomembranes,* 642 (**1981**): 203-211.

93 Allegrini, Peter R., Guus van Scharrenburg, Gerard H. De Haas, and Joachim Seelig. "^{2}H-and ^{31}P-NMR studies of bilayers composed of 1-acyllysophosphatidylcholine and fatty acids." *Biochimica et Biophysica Acta (BBA)-Biomembranes,* 731 (**1983**): 448-455.

94 Li, Jing, Xuling Wang, Ting Zhang, Chunling Wang, Zhenjun Huang, Xiang Luo, and Yihui Deng. "A review on phospholipids and their main applications in drug delivery systems." *Asian Journal of Pharmaceutical Sciences,* 10 (**2015**): 81-98.

95 Van Echteld, C. J. A., B. De Kruijff, and J. De Gier. "Differential miscibility properties of various phosphatidylcholine/lysophosphatidylcholine mixtures." *Biochimica et Biophysica Acta (BBA)-Biomembranes,* 595 (**1980**): 71-81.

96 Needham, David, and Doncho V. Zhelev. "Lysolipid exchange with lipid vesicle membranes." *Annals of Biomedical Engineering*, 23 (**1995**): 287-298.

97 Bhamidipati, Shastri P., and James A. Hamilton. "Interactions of lyso 1-palmitoylphosphatidylcholine with phospholipids: a ^{13}C and ^{31}P NMR study." *Biochemistry,* 34 (**1995**): 5666-5677.

98 Gawrisch, Klaus, and Laura L. Holte. "NMR investigations of non-lamellar phase promoters in the lamellar phase state." *Chemistry and Physics of Lipids,* 81 (**1996**): 105-116.

99 Singh, Jasmeet, Amy Jo Lai, Yasmin Alaee, and Radha Ranganathan. "Partitioning of lysolipids, fatty acids and their mixtures in aqueous lipid bilayers: Solute concentration/composition effects." *Biochimica et Biophysica Acta (BBA)-Biomembranes,* 1838 (**2014**): 348-354.

100 Hauser, H., W. Guyer, B. Levine, P. Skrabal, and R. J. P. Williams. "The conformation of the polar group of lysophosphatidylcholine in H_2O; conformational changes induced by polyvalent cations." *Biochimica et Biophysica Acta (BBA)-Biomembranes,* 508 (**1978**): 450-463.

101 Nakagaki, Masayuki, Hiroaki Komatsu, and Tetsurou Handa. "Estimation of critical micelle concentrations of lysolecithins with fluorescent probes." *Chemical and Pharmaceutical Bulletin,* 34 (**1986**): 4479-4485.

102 Kramp, W., G. Pieroni, R. N. Pinckard, and D. J. Hanahan. "Observations on the critical micellar concentration of 1-O-alkyl-2-acetyl-sn-glycero-3-phosphocholine and a series of its homologs and analogs." *Chemistry and Physics of Lipids,* 35 (**1984**): 49-62.

103 Haberland, Margaret E., and Jacqueline A. Reynolds. "Interaction of L-alpha-palmitoyl lysophosphatidylcholine with the AI polypeptide of high density lipoprotein." *Journal of Biological Chemistry,* 250 (**1975**): 6636-6639.

104 Slotte, J. Peter, and Bodil Ramstedt. "The functional role of sphingomyelin in cell membranes." *European Journal of Lipid Science and Technology,* 109 (**2007**): 977-981.

105 Breslow, David K., and Jonathan S. Weissman. "Membranes in balance: mechanisms of sphingolipid homeostasis." *Molecular Cell,* 40 (**2010**): 267-279.

106 Guan, Xue Li, Cleiton M. Souza, Harald Pichler, Gisele Dewhurst, Olivier Schaad, Kentaro Kajiwara, Hirotomo Wakabayashi et al. "Functional interactions between sphingolipids and sterols in biological membranes regulating cell physiology." *Molecular Biology of the Cell,* 20 (**2009**): 2083-2095.

107 Nickels, Jonathan D., Xiaolin Cheng, Barmak Mostofian, Christopher Stanley, Benjamin Lindner, Frederick A. Heberle, Stefania Perticaroli et al. "Mechanical properties of nanoscopic lipid domains." *Journal of the American Chemical Society,* 137 (**2015**): 15772-15780.

108 Zelenka, Peggy S. "Lens lipids." *Current Eye Research,* 3 (**1984**): 1337-1359.

109 Borchman, Douglas, Marta C. Yappert, and Muhammad Afzal. "Lens lipids and maximum lifespan." *Experimental Eye Research,* 79 (**2004**): 761-768.

110 Huang, Li, Vahid Grami, Yernan Marrero, Daxin Tang, Marta C. Yappert, Vittorio Rasi, and Douglas Borchman. "Human lens phospholipid changes with age and cataract." *Investigative Ophthalmology & Visual Science,* 46 (**2005**): 1682-1689.

111 Borchman, Douglas, and Marta C. Yappert. "Lipids and the ocular lens." *Journal of Lipid Research,* 51 (**2010**): 2473-2488.

112 Cotlier, E., Y. Obara, and B. Toftness. "Cholesterol and phospholipids in protein fractions of human lens and senile cataract." *Biochimica et Biophysica Acta (BBA)-Lipids and Lipid Metabolism,* 530 (**1978**): 267-278.

113 Cenedella, Richard J. "Cholesterol and cataracts." *Survey of Ophthalmology,* 40 (**1996**): 320-337.

114 Crilly, J. F., and J. C. Earnshaw. "Cholesterol-induced effects on the viscoelasticity of monoglyceride bilayers." *Biophysical Journal,* 41 (**1983**): 211-216.

115 Li, Lu-Ku, Lydia So, and Abraham Spector. "Membrane cholesterol and phospholipid in consecutive concentric sections of human lenses." *Journal of Lipid Research,* 26 (**1985**): 600-609.

116 Gater, Deborah L., John M. Seddon, and Robert V. Law. "Formation of the liquid-ordered phase in fully hydrated mixtures of cholesterol and lysopalmitoylphosphatidylcholine." *Soft Matter,* 4 (**2008**): 263-267.

117 Mouritsen, Ole G. "The liquid-ordered state comes of age." *Biochimica et Biophysica Acta (BBA)-Biomembranes,* 1798 (**2010**): 1286-1288.

118 Gross, Richard W., and Xianlin Han. "Lipidomics at the interface of structure and function in systems biology." *Chemistry & Biology,* 18 (**2011**): 284-291.

119 Pati, Sumitra, Ben Nie, Robert D. Arnold, and Brian S. Cummings. "Extraction, chromatographic and mass spectrometric methods for lipid analysis." *Biomedical Chromatography,* 30 (**2016**): 695-709.

120 Sotirhos, Nikolaos, B. Herslöf, and Lennart Kenne. "Quantitative analysis of phospholipids by ^{31}P-NMR." *Journal of Lipid Research,* 27 (**1986**): 386-392.

121 Murphy, Robert C., and Simon J. Gaskell. "New applications of mass spectrometry in lipid analysis." *Journal of Biological Chemistry,* 286 (**2011**): 25427-25433.

122 Whitehouse, CRAIG M., R. N. Dreyer, M. Yamashita, and J. B. Fenn. "Electrospray ionization for mass-spectrometry of large biomolecules." *Science,* 246 (**1989**): 64-71.

123 Karas, Michael, and Franz Hillenkamp. "Laser desorption ionization of proteins with molecular masses exceeding 10,000 daltons." *Analytical Chemistry,* 60 (**1988**): 2299-2301.

124 Han, Xianlin, Jingyue Yang, Hua Cheng, Kui Yang, Dana R. Abendschein, and Richard W. Gross. "Shotgun lipidomics identifies cardiolipin depletion in diabetic myocardium linking altered substrate utilization with mitochondrial dysfunction." *Biochemistry,* 44 (**2005**): 16684-16694.

125 Wolf, Claude, and Peter J. Quinn. "Lipidomics: Practical aspects and applications." *Progress in Lipid Research,* 47 (**2008**): 15-36.

126 Pacholski, M. L., and N. Winograd. "Imaging with mass spectrometry." *Chemical Reviews,* 99 (**1999**): 2977-3006.

127 Reyzer, Michelle L., and Richard M. Caprioli. "MALDI mass spectrometry for direct tissue analysis: a new tool for biomarker discovery." *Journal of Proteome Research,* 4 (**2005**): 1138-1142.

128 McDonnell, Liam A., and Ron Heeren. "Imaging mass spectrometry." *Mass Spectrometry Reviews,* 26 (**2007**): 606-643.

129 Boxer, Steven G., Mary L. Kraft, and Peter K. Weber. "Advances in imaging secondary ion mass spectrometry for biological samples." *Annual Review of Biophysics,* 38 (**2009**): 53-74.

130 Jones, Elizabeth Ellen, Thomas W. Powers, Benjamin A. Neely, Lisa H. Cazares, Dean A. Troyer, Alexander S. Parker, and Richard R. Drake. "MALDI imaging mass spectrometry profiling of proteins and lipids in clear cell renal cell carcinoma." *Proteomics,* 14 (**2014**): 924-935.

131 Jackson, Shelley N., Michael Ugarov, Thomas Egan, Jeremy D. Post, Denis Langlais, J. Albert Schultz, and Amina S. Woods. "MALDI-ion mobility-TOFMS imaging of lipids in rat brain tissue." *Journal of Mass Spectrometry,* 42 (**2007**): 1093-1098.

132 Jackson, Shelley N., Damon Barbacci, Thomas Egan, Ernest K. Lewis, J. Albert Schultz, and Amina S. Woods. "MALDI-ion mobility mass spectrometry of lipids in negative ion mode." *Analytical Methods,* 6 (**2014**): 5001-5007.

133 Creaser, Colin S., John R. Griffiths, Claire J. Bramwell, Sadaf Noreen, Carol A. Hill, and CL Paul Thomas. "Ion mobility spectrometry: a review. Part 1. Structural analysis by mobility measurement." *Analyst,* 129 (**2004**): 984-994.

134 Paglia, Giuseppe, Michal Kliman, Emmanuelle Claude, Scott Geromanos, and Giuseppe Astarita. "Applications of ion-mobility mass spectrometry for lipid analysis." *Analytical and Bioanalytical Chemistry,* 407 (**2015**): 4995-5007.

135 Kliman, Michal, Jody C. May, and John A. McLean. "Lipid analysis and lipidomics by structurally selective ion mobility-mass spectrometry." *Biochimica et Biophysica Acta (BBA)-Molecular and Cell Biology of Lipids,* 1811 (**2011**): 935-945.

136 Uetrecht, Charlotte, Rebecca J. Rose, Esther van Duijn, Kristina Lorenzen, and Albert JR Heck. "Ion mobility mass spectrometry of proteins and protein assemblies." *Chemical Society Reviews,* 39 (**2010**): 1633-1655.

137 Jackson, Shelley N., Michael Ugarov, Jeremy D. Post, Thomas Egan, Denis Langlais, J. Albert Schultz, and Amina S. Woods. "A study of phospholipids by ion mobility TOFMS." *Journal of the American Society for Mass Spectrometry,* 19 (**2008**): 1655-1662.

138 Trimpin, Sarah, Bo Tan, Brian C. Bohrer, David K. O'Dell, Samuel I. Merenbloom, Mauricio X. Pazos, David E. Clemmer, and J. Michael Walker. "Profiling of phospholipids and related lipid structures using multidimensional ion mobility spectrometry-mass spectrometry." *International Journal of Mass Spectrometry,* 287 (**2009**): 58-69.

139 Lintonen, Tuulia PI, Paul RS Baker, Matti Suoniemi, Baljit K. Ubhi, Kaisa M. Koistinen, Eva Duchoslav, J. Larry Campbell, and Kim Ekroos. "Differential mobility spectrometry-driven shotgun lipidomics." *Analytical Chemistry,* 86 (**2014**): 9662-9669.

140 Zhang, Fang, Su Guo, Manyu Zhang, Zhixu Zhang, and Yinlong Guo. "Characterizing ion mobility and collision cross section of fatty acids using electrospray ion mobility mass spectrometry." *Journal of Mass Spectrometry,* 50 (**2015**): 906-913.

141 Kim, Hugh I., Hyungjun Kim, Eric S. Pang, Ernest K. Ryu, Luther W. Beegle, Joseph A. Loo, William A. Goddard, and Isik Kanik. "Structural characterization of unsaturated

phosphatidylcholines using traveling wave ion mobility spectrometry." *Analytical Chemistry,* 81 (**2009**): 8289-8297.

142 Castro-Perez, Jose, Thomas P. Roddy, Nico MM Nibbering, Vinit Shah, David G. McLaren, Stephen Previs, Athula B. Attygalle et al. "Localization of fatty acyl and double bond positions in phosphatidylcholines using a dual stage CID fragmentation coupled with ion mobility mass spectrometry." *Journal of the American Society for Mass Spectrometry,* 22 (**2011**): 1552-1567.

143 Maccarone, Alan T., Jackson Duldig, Todd W. Mitchell, Stephen J. Blanksby, Eva Duchoslav, and J. Larry Campbell. "Characterization of acyl chain position in unsaturated phosphatidylcholines using differential mobility-mass spectrometry." *Journal of Lipid Research,* 55 (**2014**): 1668-1677.

144 Lee, Anthony G. "How lipids affect the activities of integral membrane proteins." *Biochimica et Biophysica Acta (BBA)-Biomembranes,* 1666 (**2004**): 62-87.

145 Hsia, Chih-Yun, Mark J. Richards, and Susan Daniel. "A review of traditional and emerging methods to characterize lipid–protein interactions in biological membranes." *Analytical Methods,* 7 (**2015**): 7076-7094.

146 Lee, A. G. "Lipid–protein interactions in biological membranes: a structural perspective." *Biochimica et Biophysica Acta (BBA)-Biomembranes,* 1612 (**2003**): 1-40.

147 East, J. M., D. Melville, and A. G. Lee. "Exchange rates and numbers of annular lipids for the calcium and magnesium ion dependent adenosine triphosphatase." *Biochemistry,* 24 (**1985**): 2615-2623.

148 Smith, Adam W. "Lipid–protein interactions in biological membranes: a dynamic perspective." *Biochimica et Biophysica Acta (BBA)-Biomembranes,* 1818 (**2012**): 172-177.

149 Gonen, Tamir, Yifan Cheng, Piotr Sliz, Yoko Hiroaki, Yoshinori Fujiyoshi, Stephen C. Harrison, and Thomas Walz. "Lipid-protein interactions in double-layered two-dimensional AQP0 crystals." *Nature,* 438 (**2005**): 633-638.

150 Cherezov, Vadim, Daniel M. Rosenbaum, Michael A. Hanson, Søren GF Rasmussen, Foon Sun Thian, Tong Sun Kobilka, Hee-Jung Choi et al. "High-resolution crystal structure of an engineered human β2-adrenergic G protein–coupled receptor." *Science,* 318 (**2007**): 1258-1265.

151 Caffrey, Martin, Dianfan Li, and Abhiram Dukkipati. "Membrane protein structure determination using crystallography and lipidic mesophases: recent advances and successes." *Biochemistry,* 51 (**2012**): 6266-6288.

152 Tycko, Robert. "Solid-state NMR studies of amyloid fibril structure." *Annual Review of Physical Chemistry,* 62 (**2011**): 279-299.

153 Schmidt, Michael FG. "Fatty acylation of proteins." *Biochimica et Biophysica Acta (BBA)-Reviews on Biomembranes,* 988 (**1989**): 411-426.

154 Manenti, Stéphane, Irène Dunia, and E. Lucio Benedetti. "Fatty acid acylation of lens fiber plasma membrane proteins." *FEBS Letters,* 262 (**1990**): 356-358.

155 BAÑÓ, M. Carmen, S. Caroline JACKSON, and I. Anthony MAGEE. "Pseudo-enzymatic S-acylation of a myristoylated yes protein tyrosine kinase peptide in vitro may reflect non-enzymatic S-acylation in vivo." *Biochemical Journal,* 330 (**1998**): 723-731.

156 Magee, Tony, and Miguel C. Seabra. "Fatty acylation and prenylation of proteins: what's hot in fat." *Current Opinion in Cell Biology,* 17 (**2005**): 190-196.

157 Triola, G. "The protein lipidation and its analysis." *Journal of Glycomics & Lipidomics*, S2:001 (**2011**): 1-14.

158 Sachon, Emmanuelle, Per Franklin Nielsen, and Ole Nørregaard Jensen. "Characterization of N-palmitoylated human growth hormone by in situ liquid–liquid extraction and MALDI tandem mass spectrometry." *Journal of Mass Spectrometry,* 42 (**2007**): 724-734.

159 Liddy, Kiersten A., Melanie Y. White, and Stuart J. Cordwell. "Functional decorations: post-translational modifications and heart disease delineated by targeted proteomics." *Genome Medicine*, 5 (**2013**): 1-12.

160 Triola, Gemma, Herbert Waldmann, and Christian Hedberg. "Chemical biology of lipidated proteins." *ACS Chemical Biology,* 7 (**2012**): 87-99.

161 Jagannadham, M. V., and R. Nagaraj. "Detection of peptides covalently modified with multiple fatty acids by MALDI-TOF mass spectrometry." *Chemical Biology & Drug Design,* 66 (**2005**): 94-100.

162 Jensen, Ole Nørregaard. "Modification-specific proteomics: characterization of post-translational modifications by mass spectrometry." *Current Opinion in Chemical Biology,* 8 (**2004**): 33-41.

163 Yoder, Jennifer D., Tsefang Chen, and Dennis E. Hruby. "Sequence-independent acylation of the vaccinia virus A-type inclusion protein." *Biochemistry,* 43 (**2004**): 8297-8302.

164 Larsen, Martin R., Morten B. Trelle, Tine E. Thingholm, and Ole N. Jensen. "Analysis of posttranslational modifications of proteins by tandem mass spectrometry." *Biotechniques,* 40 (**2006**): 790-798.

165 Schey, Kevin L., Danielle B. Gutierrez, Zhen Wang, Junhua Wei, and Angus C. Grey. "Novel fatty acid acylation of lens integral membrane protein aquaporin-0." *Biochemistry,* 49 (**2010**): 9858-9865.

166 Li, Lun, Linjie Dong, Lisha Xia, Tingting Li, and Hongying Zhong. "Chemical and genetic probes for analysis of protein palmitoylation." *Journal of Chromatography B,* 879 (**2011**): 1316-1324.

167 Gutierrez, Danielle B., Donita Garland, and Kevin L. Schey. "Spatial analysis of human lens aquaporin-0 post-translational modifications by MALDI mass spectrometry tissue profiling." *Experimental Eye Research,* 93 (**2011**): 912-920.

168 Pridmore, Catherine J., Jackie A. Mosely, Alison Rodger, and John M. Sanderson. "Acyl transfer from phosphocholine lipids to melittin." *Chemical Communications,* 47 (**2011**): 1422-1424.

169 Dods, Robert H., Jackie A. Mosely, and John M. Sanderson. "The innate reactivity of a membrane associated peptide towards lipids: acyl transfer to melittin without enzyme catalysis." *Organic & Biomolecular Chemistry,* 10 (**2012**): 5371-5378.

170 Dods, Robert H., Burkhard Bechinger, Jackie A. Mosely, and John M. Sanderson. "Acyl transfer from membrane lipids to peptides is a generic process." *Journal of Molecular Biology,* 425 (**2013**): 4379-4387.

171 Wenke, Jamie L., Kristie L. Rose, Jeffrey M. Spraggins, and Kevin L. Schey. "MALDI imaging mass spectrometry spatially maps age-related deamidation and truncation of human lens aquaporin-0 MALDI imaging mass spectrometry." *Investigative Ophthalmology & Visual Science,* 56 **(2015**): 7398-7405.

172 Ismail, Vian S., Jackie A. Mosely, Antal Tapodi, Roy A. Quinlan, and John M. Sanderson. "The lipidation profile of aquaporin-0 correlates with the acyl composition of phosphoethanolamine lipids in lens membranes." *Biochimica et Biophysica Acta (BBA)-Biomembranes,* 1858 (**2016**): 2763-2768.

173 Habermann, E. "Bee and wasp venoms." *Science,* 177 (**1972**): 314-322.

174 Raghuraman, H., and Amitabha Chattopadhyay. "Melittin: a membrane-active peptide with diverse functions." *Bioscience Reports,* 27 (**2007**): 189-223.

175 Liao, Chenyi, Myvizhi Esai Selvan, Jun Zhao, Jonathan L. Slimovitch, Severin T. Schneebeli, Mee Shelley, John C. Shelley, and Jianing Li. "Melittin aggregation in aqueous solutions: insight from molecular dynamics simulations." *The Journal of Physical Chemistry B,* 119 (**2015**): 10390-10398.

176 Wilcox, William, and David Eisenberg. "Thermodynamics of melittin tetramerization determined by circular dichroism and implications for protein folding." *Protein Science,* 1 (**1992**): 641-653.

177 Talbot, J. C., J. Dufourcq, J. De Bony, J. F. Faucon, and C. Lussan. "Conformational change and self association of monomeric melittin." *FEBS Letters,* 102 (**1979**): 191-193.

178 Othon, Christina M., Oh-Hoon Kwon, Milo M. Lin, and Ahmed H. Zewail. "Solvation in protein (un) folding of melittin tetramer–monomer transition." *Proceedings of the National Academy of Sciences,* 106 (**2009**): 12593-12598.

179 Brown, Larry R., Jürgen Lauterwein, and Kurt Wüthrich. "High-resolution ^{1}H-NMR studies of self-aggregation of melittin in aqueous solution." *Biochimica et Biophysica Acta (BBA)-Protein Structure,* 622 (**1980**): 231-244.

180 Iwadate, Mitsuo, Tetsuo Asakura, and Michael P. Williamson. "The structure of the melittin tetramer at different temperatures." *The FEBS Journal,* 257 (**1998**): 479-487.

181 Terwilliger, Thomas C., and David Eisenberg. "The structure of melittin. II. Interpretation of the structure." *Journal of Biological Chemistry,* 257, (**1982**): 6016-6022.

182 Yunes, Rosendo, A. R. Goldhammer, William K. Garner, and E. H. Cordes. "Phospholipases: melittin facilitation of bee venom phospholipase A_2-catalyzed hydrolysis of unsonicated lecithin liposomes." *Archives of Biochemistry and Biophysics,* 183 (**1977**): 105-112.

183 Kleinschmidt, Jörg H., James E. Mahaney, David D. Thomas, and Derek Marsh. "Interaction of bee venom melittin with zwitterionic and negatively charged phospholipid bilayers: a spin-label electron spin resonance study." *Biophysical Journal,* 72 (**1997**): 767-778.

184 Lundquist, Anna, Per Wessman, Adrian R. Rennie, and Katarina Edwards. "Melittin–Lipid interaction: A comparative study using liposomes, micelles and bilayerdisks." *Biochimica et Biophysica Acta (BBA)-Biomembranes,* 1778 (**2008**): 2210-2216.

185 Takahashi, Tomoyoshi, Fumimasa Nomura, Yasunori Yokoyama, Yohko Tanaka-Takiguchi, Michio Homma, and Kingo Takiguchi. "Multiple membrane interactions and versatile vesicle deformations elicited by melittin." *Toxins,* 5 (**2013**): 637-664.

186 Dempsey, Christopher E. "The actions of melittin on membranes." *Biochimica et Biophysica Acta (BBA)-Reviews on Biomembranes,* 1031 (**1990**): 143-161.

187 Dotimas, E. M., and R. C. Hider. "Honeybee venom." *Bee World,* 68 (**1987**): 51-70.

188 Chen, Jun, Su-Min Guan, Wei Sun, and Han Fu. "Melittin, the major pain-producing substance of bee venom." *Neuroscience Bulletin,* 32 (**2016**): 265-272.

189 Fletcher, Jeffrey E., Kirsten Michaux, and Ming-Shi Jiang. "Contribution of bee venom phospholipase A_2 contamination in melittin fractions to presumed activation of tissue phospholipase A_2." *Toxicon,* 28 (**1990**): 647-656.

190 Mingarro, Ismael, Enrique Pérez-Payá, Clemencia Pinilla, Jon R. Appel, Richard A. Houghten, and Sylvie E. Blondelle. "Activation of bee venom phospholipase A_2 through a peptide-enzyme complex." *FEBS Letters,* 372 (**1995**): 131-134.

191 Cajal, Yolanda, and Mahendra Kumar Jain. "Synergism between mellitin and phospholipase A_2 from bee venom: apparent activation by intervesicle exchange of phospholipids." *Biochemistry,* 36 (**1997**): 3882-3893.

192 Mathias, R. T., J. L. Rae, and G. J. Baldo. "Physiological properties of the normal lens." *Physiological Reviews,* 77 (**1997**): 21-50.

193 Bassnett, Steven, and Danijela Mataic. "Chromatin degradation in differentiating fiber cells of the eye lens." *The Journal of Cell Biology,* 137 (**1997**): 37-49.

194 Hughes, Jessica R., Vladimir A. Levchenko, Stephen J. Blanksby, Todd W. Mitchell, Alan Williams, and Roger JW Truscott. "No turnover in lens lipids for the entire human lifespan." *Elife,* 4 (**2015**): 1-7.

195 Taylor, Virginia L., Kristin J. Al-Ghoul, C. Wesley Lane, V. Andrew Davis, Jerome R. Kuszak, and M. Joseph Costello. "Morphology of the normal human lens." *Investigative Ophthalmology & Visual Science,* 37 (**1996**): 1396-1410.

196 Bassnett, Steven. "Lens organelle degradation." *Experimental Eye Research,* 74 (**2002**): 1-6.

197 Hodge, William G., John P. Whitcher, and William Satariano. "Risk factors for age-related cataracts." *Epidemiologic Reviews,* 17 (**1995**): 336-346.

198 Floyd, Kyle A., David R. Stella, Chao-Cheng Wang, Sara Laurentz, George P. McCabe, Om P. Srivastava, and Stephen Barnes. "Genistein and genistein-containing dietary supplements accelerate the early stages of cataractogenesis in the male ICR/f rat." *Experimental Eye Research,* 92 (**2011**): 120-127.

199 Gonen, Tamir, and Thomas Walz. "The structure of aquaporins." *Quarterly Reviews of Biophysics,* 39 (**2006**): 361-396.

200 Hall, James E., and Richard T. Mathias. "The aquaporin zero puzzle." *Biophysical Journal,* 107 (**2014**): 10-15.

201 Han, Jun, and Kevin L. Schey. "Proteolysis and mass spectrometric analysis of an integral membrane: aquaporin 0." *Journal of Proteome Research,* 3 (**2004**): 807-812.

202 Wu, Christine C., and John R. Yates. "The application of mass spectrometry to membrane proteomics." *Nature Biotechnology,* 21 (**2003**): 262-267.

203 Schey, Kevin L., Angus C. Grey, and Joshua J. Nicklay. "Mass spectrometry of membrane proteins: a focus on aquaporins." *Biochemistry,* 52 (**2013**): 3807-3817.

204 Maecker, Holden T., Scotf C. Todd, and Shoshana Levy. "The tetraspanin superfamily: molecular facilitators." *The FASEB Journal,* 11 (**1997**): 428-442.

205 Gonen, Tamir, Angus C. Grey, Marc D. Jacobs, Paul J. Donaldson, and Joerg Kistler. "MP20, the second most abundant lens membrane protein and member of the tetraspanin superfamily, joins the list of ligands of galectin-3." *BMC Cell Biology,* 2 (**2001**): 1-17.

206 LAMPE, Paul D., and Ross G. JOHNSON. "Amino acid sequence of in vivo phosphorylation sites in the main intrinsic protein (MIP) of lens membranes." *The FEBS Journal,* 194 (**1990**): 541-547.

207 Johnson, Keith R., Daryl F. Sas, and Ross G. Johnson. "MP26, a protein of intercellular junctions in the bovine lens: electrophoretic and chromatographic characterization." *Experimental Eye Research,* 52 (**1991**): 629-639.

208 Palanivelu, Dinesh V., David E. Kozono, Andreas Engel, Kitaru Suda, Ariel Lustig, Peter Agre, and Tilman Schirmer. "Co-axial association of recombinant eye lens aquaporin-0 observed in loosely packed 3D crystals." *Journal of Molecular Biology,* 355 (**2006**): 605-611.

209 Bassnett, Steven, Phillip A. Wilmarth, and Larry L. David. "The membrane proteome of the mouse lens fiber cell." *Molecular Vision,* 15 (**2009**): 2448-2463.

210 Jung, Jin Sup, Gregory M. Preston, Barbara L. Smith, William B. Guggino, and Peter Agre. "Molecular structure of the water channel through aquaporin CHIP. The hourglass model." *Journal of Biological Chemistry,* 269 (**1994**): 14648-14654.

211 Mulders, Sabine M., Gregory M. Preston, Peter MT Deen, William B. Guggino, Carel H. van Os, and Peter Agre. "Water channel properties of major intrinsic protein of lens." *Journal of Biological Chemistry,* 270 (**1995**): 9010-9016.

212 Harries, William EC, David Akhavan, Larry JW Miercke, Shahram Khademi, and Robert M. Stroud. "The channel architecture of aquaporin 0 at a 2.2-Å resolution." *Proceedings of the National Academy of Sciences of the United States of America,* 101 (**2004**): 14045-14050.

213 Gonen, Tamir, Yifan Cheng, Joerg Kistler, and Thomas Walz. "Aquaporin-0 membrane junctions form upon proteolytic cleavage." *Journal of Molecular Biology,* 342 (**2004**): 1337-1345.

214 Gonen, Tamir, Piotr Sliz, Joerg Kistler, Yifan Cheng, and Thomas Walz. "Aquaporin-0 membrane junctions reveal the structure of a closed water pore." *Nature,* 429 (**2004**): 193-197.

215 Kumari, S. Sindhu, and Kulandaiappan Varadaraj. "Intact AQP0 performs cell-to-cell adhesion." *Biochemical and Biophysical Research Communications,* 390 (**2009**): 1034-1039.

216 Bateman, J. Bronwyn, Meriam Johannes, Pamela Flodman, David D. Geyer, Kevin P. Clancy, Camilla Heinzmann, Tracy Kojis, Rebecca Berry, Robert S. Sparkes, and M. Anne Spence. "A new locus for autosomal dominant cataract on chromosome 12q13." *Investigative Ophthalmology & Visual Science,* 41 (**2000**): 2665-2670.

217 Ball, Lauren E., Mark Little, Mark W. Nowak, Donita L. Garland, Rosalie K. Crouch, and Kevin L. Schey. "Water permeability of C-terminally truncated aquaporin 0 (AQP0 1-243) observed in the aging human lens." *Investigative Ophthalmology & Visual Science,* 44 (**2003**): 4820-4828.

218 Wang, Zhen, Jun Han, and Kevin L. Schey. "Spatial differences in an integral membrane proteome detected in laser capture microdissected samples." *Journal of Proteome Research,* 7 (**2008**): 2696-2702.

219 Grey, Angus C., Pierre Chaurand, Richard M. Caprioli, and Kevin L. Schey. "MALDI imaging mass spectrometry of integral membrane proteins from ocular lens and retinal tissue." *Journal of Proteome Research,* 8 (**2009**): 3278-3283.

220 Schey, Kevin L., John G. Fowler, Jae C. Schwartz, Mark Busman, James Dillon, and Rosalie K. Crouch. "Complete map and identification of the phosphorylation site of bovine lens major intrinsic protein." *Investigative Ophthalmology & Visual Science,* 38 (**1997**): 2508-2515.

221 Schey, Kevin L., Mark Little, John G. Fowler, and Rosalie K. Crouch. "Characterization of human lens major intrinsic protein structure." *Investigative Ophthalmology & Visual Science,* 41 (**2000**): 175-182.

222 Gorin, Michael B., S. Barbara Yancey, Janice Cline, Jean-Paul Revel, and Joseph Horwitz. "The major intrinsic protein (MIP) of the bovine lens fiber membrane: characterization and structure based on cDNA cloning." *Cell,* 39 (**1984**): 49-59.

223 König, Nicola, Guido A. Zampighi, and P. Jonathan G. Butler. "Characterisation of the major intrinsic protein (MIP) from bovine lens fibre membranes by electron microscopy and hydrodynamics." *Journal of Molecular Biology,* 265 (**1997**): 590-602.

224 Ball, Lauren E., Donita L. Garland, Rosalie K. Crouch, and Kevin L. Schey. "Post-translational modifications of aquaporin 0 (AQP0) in the normal human lens: spatial and temporal occurrence." *Biochemistry*, 43 (**2004**): 9856-9865.

225 Lynnerup, Niels, Henrik Kjeldsen, Steffen Heegaard, Christina Jacobsen, and Jan Heinemeier. "Radiocarbon dating of the human eye lens crystallines reveal proteins without carbon turnover throughout life." *Public Library of Science One,* 3 (**2008**): e1529.

226 Stewart, Daniel N., Jozsef Lango, Krishnan P. Nambiar, Miranda JS Falso, Paul G. FitzGerald, David M. Rocke, Bruce D. Hammock, and Bruce A. Buchholz. "Carbon turnover in the water-soluble protein of the adult human lens." *Molecular Vision,* 19 (**2013**): 463-475.

Chapter two: Instrumentation

2.1. Mass spectrometry (MS)

A schematic of a generic mass spectrometer is given in Figure 2.1. Mass spectrometer workflow starts by ionising the analyte to generate gas phase ions in the ionisation source and a subsequent separation of ions in the mass analyser based on their mass to charge (*m/z*) ratio. This has enabled a substantial MS application in various branches of science and technology for qualitative and/or quantitative purposes. The *m/z* ratio as a function of ion abundance or so called mass spectrum for gas phase ionised atoms or groups of atoms was first measured by the first mass spectrometer invented by J. J. Thomson in 1912.[1-3]

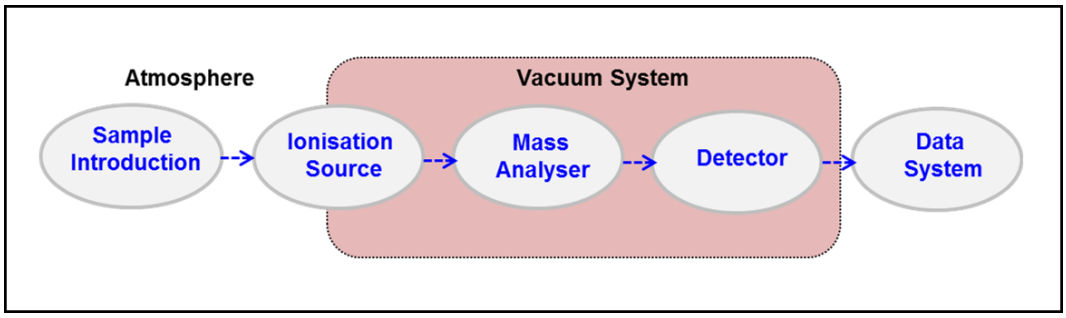

Figure 2.1. **Schematic for mass spectrometer basic components.**

The application of mass spectrometers has been expanded to not just include analysis of small species but also larger species (macro molecules) such as peptides and proteins with the MS benefit in sensitivity, speed and resolution[4-7]. This has been more common since 1990 after two soft ionisation methods were invented, electrospray ionisation (ESI-MS) by Fenn *et al.*[8-12] and matrix-assisted laser desorption/ionisation (MALDI-MS) by Tanaka *et al.*[13,14]. Once these larger molecules could be ionised in a manner that gave stable and intact precursor ions, it was possible to subject them to tandem mass spectrometry (tandem MS or MS^n), primarily collision induced dissociation (CID). This tandem MS enabled detailed structural characterisation, as with small molecules, but for large biopolymers this meant sequence information or the order of building blocks. Consequently,

localising of any modifications such as post-translational modifications (PTM) or otherwise that these building blocks have.[15-21]

In addition, the hyphenation ability between chromatography separation methods and ESI-MS,[4,7,9,22] more commonly, or MALDI-MS,[23-25] less commonly, such as liquid chromatography (LC-MS) added an extra level of improvement in sample analysis by both MS and tandem MS. The main advantage is found in separating mixture components in a sample prior ionisation process and thus reducing ion suppression, increasing sensitivity, improving signal to noise ratio and a consequence improvement in quantification analysis.[22-26]

2.1.1. Ion sources

Different ion sources have different bearing on the ionisation of molecules because of the amount of energy, and the manner in which it is transferred to the sample, from the hardest, electron ionisation (EI) to the softest, nano-electrospray ionisation (nESI), as shown in Figure 2.2. The advantage of this is that a particular ionisation technique can target compounds with a characteristic chemical nature. Among this range of ion sources, detailed principles for ESI-MS and MALDI-MS have been discussed in this chapter because of their application to experimental analysis discussed in chapters three, four and five.

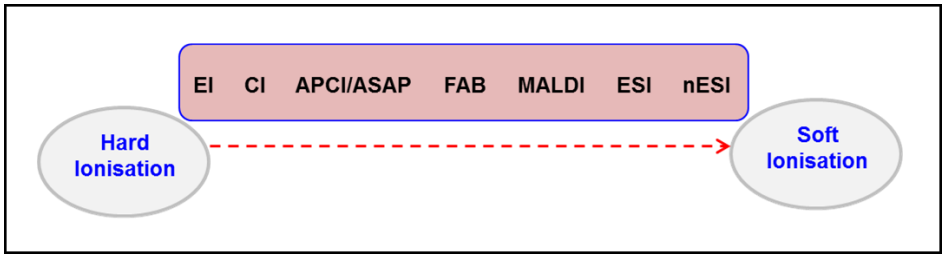

Figure 2.2. **The strength scale for the range of ionisation techniques. The acronyms for the ionisation sources from left to right include: electron ionisation (EI); chemical ionisation (CI); atmospheric pressure chemical ionisation (APCI); atmospheric pressure solids analysis probe (APCI); fast atom bombardment (FAB); matrix-assisted laser desorption/ionisation (MALDI); electrospray ionisation (ESI); nano-electrospray ionisation (nESI).**

2.1.1.1. Electrospray ionisation (ESI-MS)

Electrospray ionisation (ESI) is one of a range of atmospheric pressure ionisation (API) techniques.[7,12,27] This method is suited to ionise small polar or ionic molecules and as well as larger biomolecules. A continuous flow of intact gas phase molecular ions will be introduced to the system and this is perfectly suited to be coupled with LC. ESI is based on dissolving an analyte in a polar solvent and subsequent change from condensed form in the solution to gas phase analyte ions (Figure 2.3).

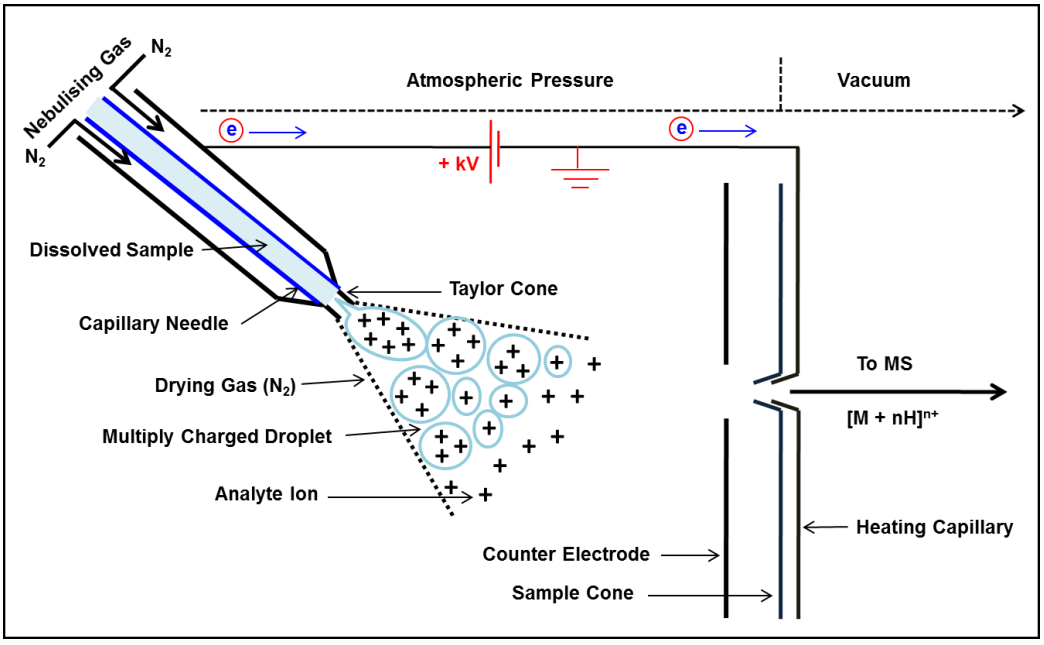

Figure 2.3. **Schematic illustration of ESI source in positive ion mode.**

The ionisation process starts by passing the analyte solution through a stainless steel capillary needle under high voltage (±3 - ±4 kV). This high voltage in combination with the nebulising gas/sheath gas (typically dry nitrogen) around the capillary needle helps solvent evaporation and brings the sample into an aerosol of charged droplets.[27,28] These charged droplets continuously undergo solvent evaporation and shrink in size with the aid of drying gas (nitrogen desolvation gas) and eventually form either positive gaseous ions in the positive ion mode ESI+ with the production of protonated species, $[M + nH]^{n+}$ and/or adduct cation $[M + nCation]^{n+}$ or negative gaseous

ions in the negative ion mode ESI- with the formation of deprotonated species $[M - nH]^{n-}$ and/or adduct anion $[M + nAnion]^{n-}$. The ions will be drawn to the entrance of the mass analyser by the influence of a high vacuum from the mass analyser and a voltage gradient between the capillary needle and counter electrode of the source.

The formation of gas phase ions or desolvation process in ESI is basically described by two proposed mechanisms; the charge residue model (CRM) and ion evaporation model (IEM).[7,12,27,28] In both mechanisms there is the formation of smaller droplet sizes as a consequence of solvent evaporation (Figure 2.4). Consequently, increasing droplets surface charge density until they reach a limit when Coulomb repulsion exceeds surface tension and eventually Coulomb fission. This limit is known as Rayleigh limit. In CRM mechanism (Figure 2.4 (a)), the repeating process of solvent evaporation and Coulomb fission continues until a very small droplet with a single analyte ion is formed and eventually droplet desolvation to leave gas phase analyte ions, while in IEM mechanism (Figure 2.4 (b)) following the continues solvent evaporation and Coulomb fission and subsequent formation of smaller charged droplet, the surface electric field desorbs/emits the analyte ion from the droplet to leave gas phase analyte ions. It is proposed that CRM is more convenient for larger molecules such as peptides and proteins, whereas IEM is more applicable for small molecules.[7] In addition, chain ejection model (CEM) is another ESI mechanism that has recently proposed by Konermann *et al.*[29] to describe unfolded proteins.[29,30]

Further, ESI is the most popular ionisation method for high molecular mass of peptides and proteins because of the presence of more than one ionisation site (multiple protonation sites) on the molecule. Therefore *z* increases so *m/z* falls to a lower mass range that is perfectly suited to the most mass analysers particularly significant for mass analysers with narrow *m/z* range.[4-6,31]

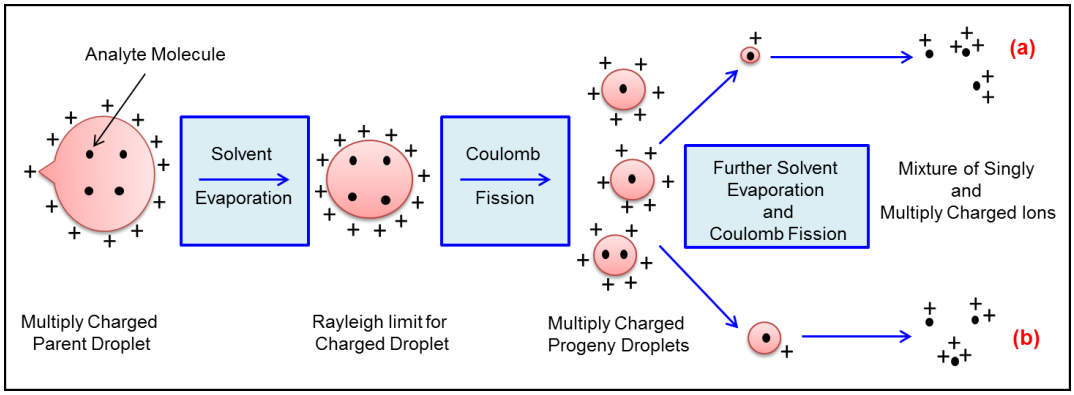

Figure 2.4. **The two proposed mechanisms; (a) charge residue model (CRM) and (b) ion evaporation model (IEM), for describing desolvation process and a consequent gas phase analyte ion formation in ESI+.**

2.1.1.2. Matrix-assisted laser desorption/ionisation (MALDI-MS)

The basic principle in MALDI-MS[2,32,33] starts first by mixing analyte molecule in the form of solid or liquid with a solution of small organic molecules called a matrix solution. The amount of an analyte is usually very little compared to the excessive amount of a matrix, this is shown to be in the range of 1:4000 and 1:40,000 of analyte:matrix molar ratio for peptides/proteins[34,35]. A spotted droplet of analyte:matrix mixture on a conductive target plate is then left for air dry and a subsequent formation of co-crystallised layer. After insertion of the target plate into the MS system under vacuum, a pulsed laser beam is used to irradiate analyte:matrix layer (Figure 2.5). This is often a pulsed nitrogen laser in UV-MALDI at 337 nm wavelength. A strong absorbance of matrix at the wavelength of the laser beam is suited to absorb energy readily and to become excited. Consequently, both matrix and analyte will be desorbed into the gas phase through sublimation/ablation. This followed by ionisation reaction, and this is reported to perform in different pathways such as gas phase photoionisation, excited-state proton transfer, ion-molecule reactions, desorption of preformed ions and energy pooling. Among these suggested mechanisms, proton transfer in the solid phase before desorption or gas phase proton transfer in the expanding plume from photo-ionised matrix molecules, are the two common ionisation pathways described in MADLI-MS with the subsequent formation of pulsed ions.[2,32]

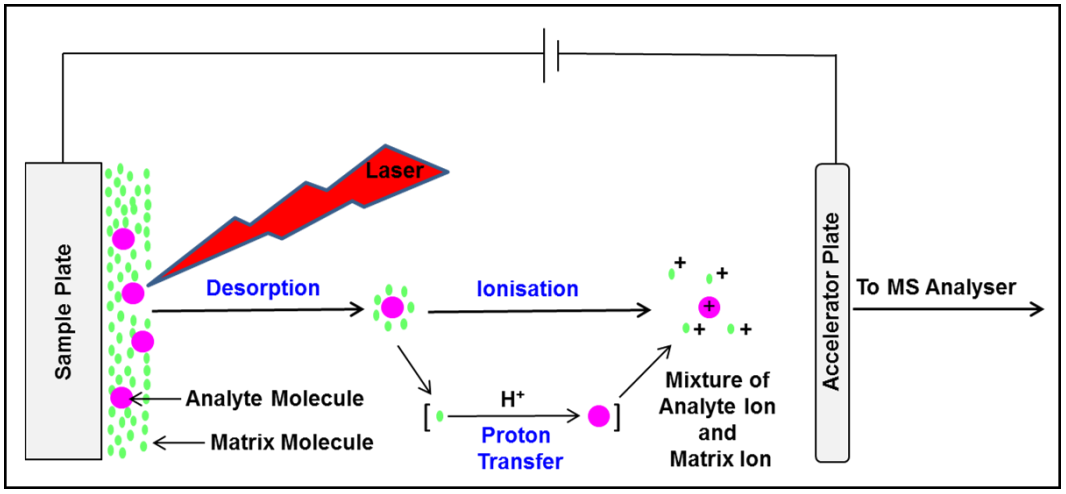

Figure 2.5. **Ionisation principle in MALDI source.**

MADLI ionisation method is very popular for non-volatile biomolecules of peptides and proteins,[4,5,32,35,36] which is especially described and developed by Karas *et al.*[37] and thereafter by Tanaka *et al.*[13,14] Depending on the nature of the analyte and the selected matrix molecule, this technique produces predominantly either $[M + H]^+$ in positive mode or $[M - H]^-$ in negative ion mode. The most common matrix in the field of protein analysis is sinapinic acid (SA), while peptide molecules can generally be best analysed from α-cyano-4-hydroxcinnamic acid (CHCA) or 2,5-dihdroxybenzoic acid (DHB).[20,32,35] The discrete packet of ions is then drawn towards the mass analyser by negative accelerator plate.

2.1.2. Mass analysers

Ions formed in the ion source are focused and transmitted towards a mass analyser where they are separated based on their *m/z* ratio. There are many different types of mass analyser so focus will be given to describing linear ion traps (LIT-MS), quadrupoles (Q-MS), time-of-flight (ToF-MS) and Fourier transform ion cyclotron resonance (FTICR-MS) mass analysers as used within this project. No one mass analyser has the ideal functionality and performance, however by combining different mass analysers the advantages of each can be cumulative. For example, Q-MS has no functionality and poor performance during its individual application, however,

it is known for its relatively small, cheap, robustness and rapid scan rates at sampling frequency of > 10 Hz,[38] while combining three quadrupoles (triple Q-MS or qQq-MS) performs different functionalities. On the other hand, FTICR-MS is the mass analyser with the extreme performance and functionality, although its disadvantage is relatively slow scan rates at sampling frequency of ≥ 1 Hz[39,40]. FTICR-MS is also known as the highest mass accuracy (< 1 ppm)[39-41] and highest resolving power mass analyser (> 10^6 FWHM at *m/z* 400)[39-42].

In order to obtain certainty in the identity of investigated analytes and determining their elemental composition, the accurate mass measurement is required and can be achieved with some mass analysers such as ToF-MS and FTICR-MS. This can be calculated by using equation 2.1, which is usually quoted in parts per million (ppm).

$$\textbf{Accuracy in ppm} = \frac{(m/z)_{\textbf{theortical}} - (m/z)_{\textbf{measured}}}{(m/z)_{\textbf{theoretical}}} \times 10^6 \quad \textbf{Equation 2.1}$$

Accurate mass is largely depending on the stability and the resolving power (R) of the mass analyser. R represents the ability of a mass analyser to resolve two ion peaks with a small difference in their *m/z* value. This can be calculated using equation 2.2. All MS analysers described in this chapter use peak width definition. This definition is applicable for an isolated (single) peak, when ∆m is the full width at half maximum (FWHM) of the peak which is usually 50% (Figure 2.6).[2,43]

$$\mathbf{R} = \frac{\mathbf{m1}}{\Delta \mathbf{m}} \qquad \textbf{Equation 2.2}$$

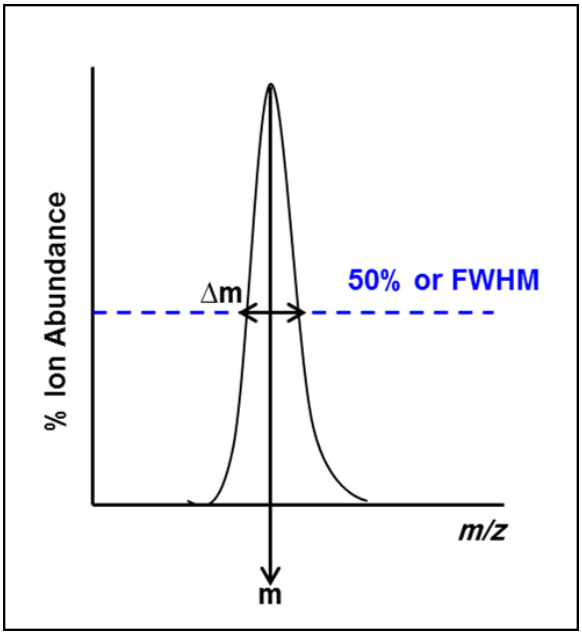

Figure 2.6. **Peak width definition for a single isolated peak.**

2.1.2.1. Quadrupole mass analyser (Q-MS)

Multipole devices with an even number of poles form a quadrupolar field within the space between the poles, typically four (quadrupole), six (hexapole), or eight (octapole). Figure 2.7 gives an example with four poles, quadrupole MS (Q-MS),[2,38,44-46] and demonstrates that the pairs of poles are acting as opposite pairs with applied positive potential for one pair +(U - Vcos ωt) and the negative potential -(U - Vcos ωt) for the other pair. They can be used as a mass analyser but with low resolution (peak width of 1 Da), and also as a focusing device (ion guide), or as a collision cell to perform tandem MS analysis.

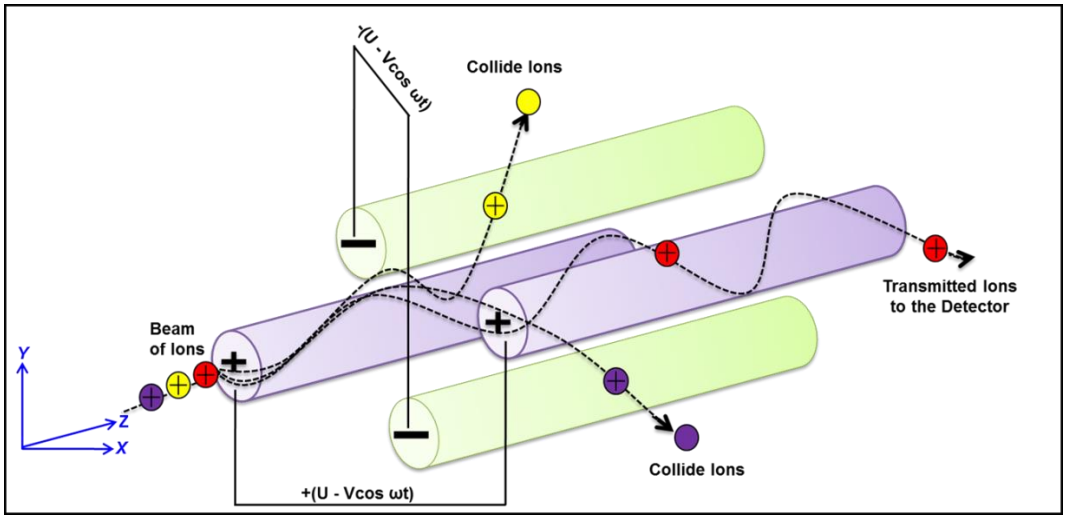

Figure 2.7. **Ions entrance in *Z-axis* direction and oscillation in *X-Y* plane in the quadrupole device, illustrate ions with a successive transmission (red sphere) and no transmission (yellow and purple spheres). Positive potential +(U - Vcos ωt) in *X-Z* plane and negative potential -(U - Vcos ωt) in *Y-Z* plane on each pair of the rod is also shown, where U/-U is the direct voltage or the magnitude of direct current (DC) potential, ω is the angular frequency (Hz) for radio frequency (RF), t is the time (s) and V is the amplitude of RF potential.**

Once the positive ions enter the device they will be attracted towards negative rods and if allowed to strike the rod, the ion will be discharged and the resulting neutral species lost. This would be the case at constant voltage but if the applied voltage on the rods rapidly changes polarity before the hitting process occurs then ions will change their direction. This creates a very high alternating field at the radio frequency (RF) and thus causes the ions to oscillate through the space between the Q rods. In the case of a fixed DC potential (U = 0) and applied RF (V) then all ions (all *m/z*) will be transmitted through Q at the same time making a convenient way to guide ions from one region to the next in a mass spectrometer. In such a case there will be no ion isolation or no MS spectrum and this is known as ion guide performance (Figure 2.8 A), while using both DC and RF together at a specific (DC/RF) ratio creates two regions for ions, a so called stable region for ions transmitting the device and reaching the detector (Figure 2.8 B and C) and an unstable region for non-transmitted ions and do not reach the detector (Figure 2.8 D). Scanning DC/RF at a constant ratio provides mass

separation for ions having a stable path (trajectory) in the Q space one at a time at a specific DC/RF ratio.

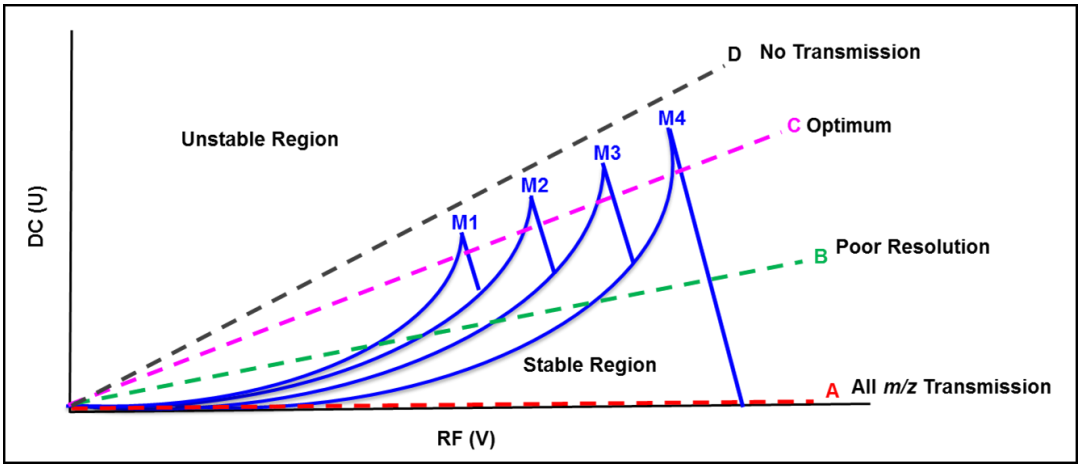

Figure 2.8. **Stability diagram for different ions with different masses (M1 < M2 < M3 < M4). Line A, represents transmission of all ions and no *m/z* separation this creates a quadrupole with ion guide performance; line B, poor resolution below optimum DC/RF ratio; line C, optimum resolution at optimum DC/RF ratio; line D, represents ions with unstable trajectory above optimum DC/RF ratio and no ion transmission.**

The mathematical equations which describe the motion of ions in the Q are given by a physicist Mathieu, as shown in Equation 2.3 and 2.4.

$$\mathbf{a_u} = \frac{\mathbf{8\,zeU}}{\mathbf{m\omega^2 r_\circ^{\,2}}} \qquad \textbf{Equation 2.3}$$

$$\mathbf{q_u} = \frac{\mathbf{4\,zeV}}{\mathbf{m\omega^2 r_\circ^{\,2}}} \qquad \textbf{Equation 2.4}$$

In both equations, trapping parameters a_u and q_u that are related to *X-axis* and *Y-axis* are generated by application of both of DC voltage (U) and RF amplitude (V) on ions with mass (m) and charge (z) along the Q pathway. These ions travel along the Q without neutralize their charges when a_u and q_u are less than the radius of the Q ($r_\circ$), ω represents angular frequency and its value is constant by changing DC/RF ratio and *e* is the charge of an electron (1.6×10^{-19} C).

2.1.2.2. Linear ion trap mass analyser (LIT-MS)

The two main types of ion trap are the linear ion trap (2D, LIT) and the Paul trap, also called a quadrupole ion trap (3D, QIT). They have similar principles of ion motion as described for Q devices.[2,38,45-50] The LIT that is featured in LTQFT (ThermoFinnigan) and that is relevant to this project is called LTQ. It is composed of three sections; front and back sections (electrodes) are end-cap electrodes and the middle section is called the ring electrode, as shown in Figure 2.9. Each section has four rods (2 pairs) with opposite potential for each pair (see Figure 2.7). Ions enter the cavity of the LTQ through front section (*Z-axis*), and are spatially trapped by higher DC axial trapping voltage on end-cap electrodes relative to low DC voltage on the ring electrode.

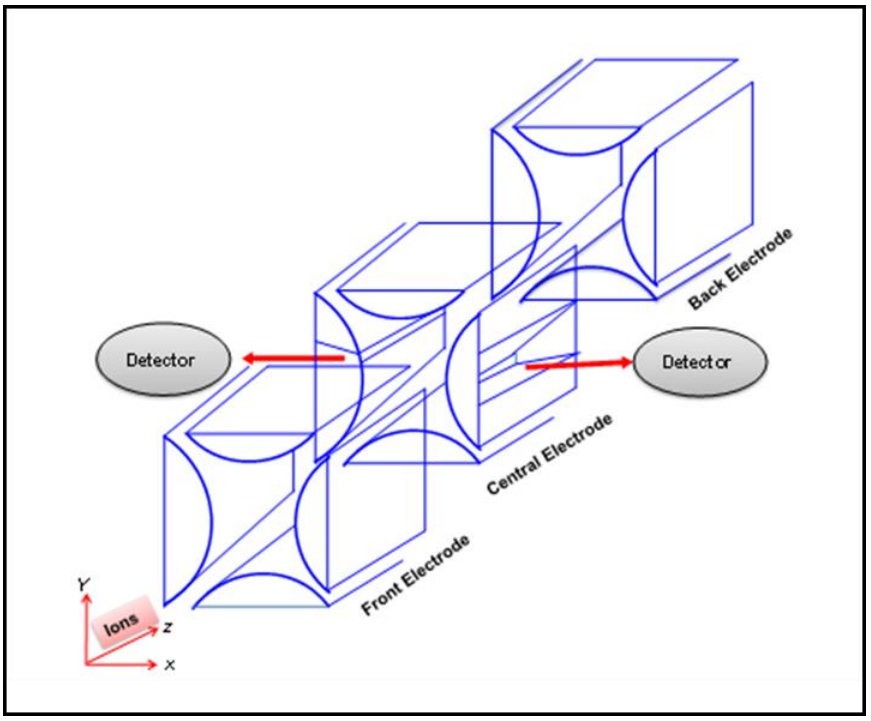

Figure 2.9. **Linear ion trap (LTQ) as featured in the LTQFT (ThermoFinnigan). The three sections are described as front-, central- and back electrodes. Ions are delivered into the LTQ cavity on *Z-axis* and ejected through slits (exit electrodes) on *X-axis* towards detection system.**

All trapped ions are stable and oscillate radially (*X-Y* plain) at low RF voltage, also known as main RF voltage or storage voltage. By applying a high alternating current (AC) voltage equal to the resonance frequency of trapped ions on exit rods (ramping main RF voltage) together with 0 DC voltage on end cap electrodes, the ions gain kinetic energy (E_{kin}) and their radial motion will be unstable. Consequently, ions are sequentially ejected in order of increasing mass towards the detector (*X-axis*) because higher mass ions have lower q_x value (Equation 2.5), where k is the Boltzmann constant (1.38×10^{-23} m^2 kg s^{-1} K^{-1}), V is the RF voltage, e is the charge of an electron, and z and m are the number of charges and mass of the ion respectively. Separating ions in LTQ is directly related with the resonance frequency of the ions which is directly proportion to the ions *m/z*.

$$\mathbf{q_x = k\frac{V}{(\frac{m}{ze})}} \qquad \textbf{Equation 2.5}$$

The presence of helium gas within LTQ has a great advantage in improving LTQ performance in terms of mass resolution with peak width of 0.1 Da and sensitivity and also its functionality in terms of performing tandem MS analysis. This gas acts as a damping gas to reduce E_{kin} of oscillated trapped ions through inelastic collision, and thus more ions can be accumulated. On the other hand, multiple collisions between isolated trapped ions with sufficient E_{kin} and helium atoms causes the ion to gain enough internal energy (E_{int}) to become collisionally activated. Such ions can then undergo unimolecular dissociation to give product ions. This is the basis of tandem MS by CID in an ion trap. Because the ions are spatially trapped, this stage can be repeated and thus achieve MS^n ($n \geq 2$, where n refers to the number of generations of ions being analysed). Both full scan MS and MS^n in LTQ is recorded by ejecting trapped ions through slits on *X-axis* in the middle section or called exit rods to the ion detection system, which is commonly a conversion dynode detection system.

In order to perform MS^n analysis, an ion of interest will be isolated by increasing both DC and RF voltages to eject all trapped ions except the precursor ion. This is then excited by applying resonance excitation AC voltage on exit rods and followed by ejecting product ions by applying

resonance ejection AC voltage on exit rods. The limitation of LTQ during MS^n analysis is due to the phenomenon that is known as low-mass-cut-off (LMCO) or one-third-cut-off, because product ions with q_x less than 0.908 or product ions whose *m/z* are less than 1/3 of precursor ions are unstable (Figure 2.10) and cannot be detected by LTQ. The value of LMCO can be determined by activation q of precursor ion (Equation 2.6).

$$\textbf{Lowest } m/z = \left(\frac{\textbf{activation q}}{0.908}\right) \times \textbf{precursor ion mass} \qquad \textbf{Equation 2.6}$$

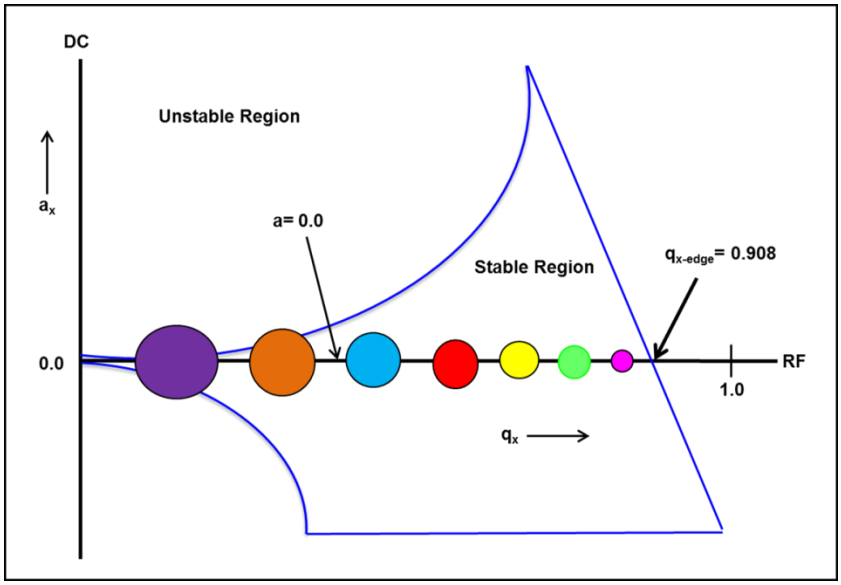

Figure 2.10. **Stability diagram for trapped ions in LTQ device and illustrate ions with LMCO (beyond 0.908 q_x).**

2.1.2.3. Fourier transform ion cyclotron resonance mass analyser (FTICR-MS)

Fourier transform ion cyclotron resonance (FTICR) is another trapping device with the highest recorded resolving power and accurate mass measurement analyser (see section 2.1.2). This mass analyser can have a number of different shapes but the most common shape is segmented open end cylindrical shape, also called Penning trap, as shown in Figure 2.11.[2,39-42,51-59] The body of this analyser (ICR cell) is composed of a number of electrodes including; trapping electrodes are front and rear plates, excitation

electrodes and detection electrodes are around the centre of the cell. These electrodes work sequentially to provide a signal current (image/transient).

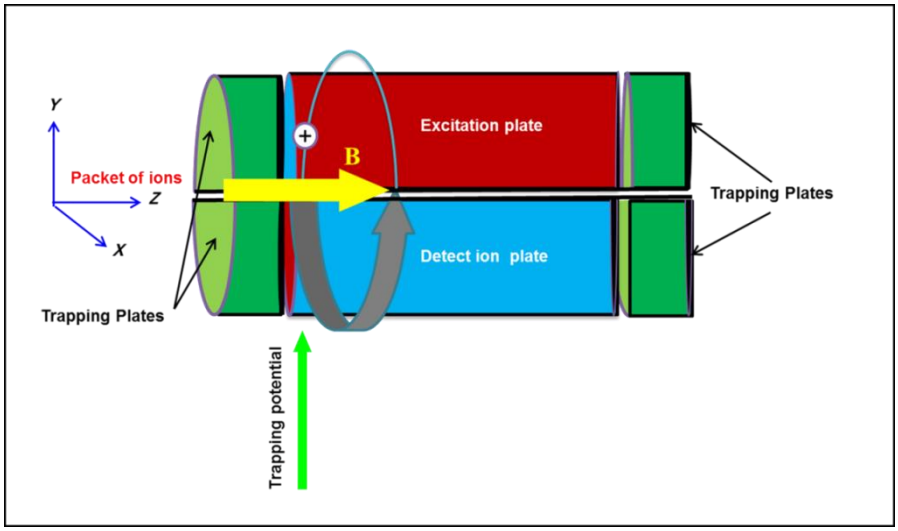

Figure 2.11. **FTICR segmented open ended cylindrical shape with the illustration of confined ions under the influence of magnetic field (B) and trapping potential.**

The cell is housed at the center of a strong and uniform (static) magnetic field (B), which is provided by a superconducting magnet. The strength of B varied between 3 Tesla to 21 Tesla[59].[39,42,53,54,56,58] Once a packet of ions has been injected to the ICR cell on *Z-axis* and parallel to B, they will be trapped by applying a trapping potential perpendicular to B. Consequently, spatially confined ions circulate (or precess) in the direction perpendicular on B by a motion known as cyclotron motion (ω_c) on *X-Y* plane with small orbits and high frequency at 5 kHz-5 MHz. This is the dominant motion of trapped ions in ICR cell, however, the two other less desirable ions' motion can occur including; magnetron motion (ω_m) on *X-Y* plane but with an orbit centered around circular orbit of cyclotron motion and smaller frequency at 1-100 Hz and as well as a trapping motion/axial oscillation (ω_z) on *Z-axis* between trapping electrodes, as shown in Figure 2.12. These three motions of the packet of ions are generated by a combination of electric and magnetic fields to provide a complex three dimensional movement of ions.

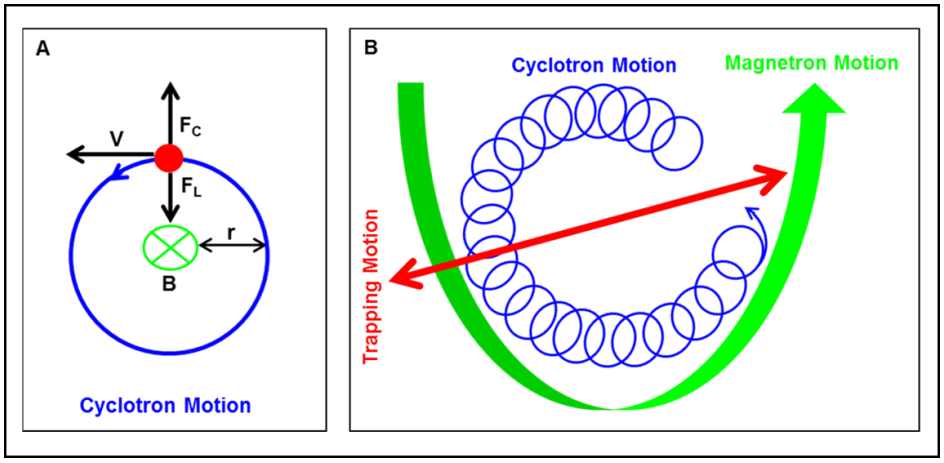

Figure 2.12. **Modes of ion motion within FTICR cell. (A) Cyclotron motion under the influence of magnetic field and free from electric field with the illustration of forces describing this ion motion; (B) A combination of cyclotron motion (blue), magnetron motion (green) and trapping motion (red) under the influence of both electric and magnetic fields.**

The overriding motion of ions (cyclotron motion) in the strong magnetic field can be described by balancing between two forces; Lorentz force (F_L) which exerted on ions moving perpendicular to the magnetic field (Equation 2.7) and centrifugal force (F_C) which is exerted by ions motion (Equation 2.8), as shown in Equation 2.9.

$$\mathbf{F_L = qVB} \qquad \textbf{Equation 2.7}$$

$$\mathbf{F_C = \frac{mV^2}{r}} \qquad \textbf{Equation 2.8}$$

Balancing forces and equation rearrangement:

$$\mathbf{qVB = \frac{mV^2}{r} \longrightarrow \quad \omega_c = \frac{V}{r} = \frac{qB}{m}} \qquad \textbf{Equation 2.9}$$

Where, q is the ion's total charge (q = ze), z and m are the number of charges and ions mass respectively, ω_c is the angular frequency of ions cyclotron motion, e is the charge of an electron, V is the velocity, B is the strength of the magnetic field and r is the radius of the ions orbit. The cyclotron frequency of ions (f_c) is obtained by addition of an angular measurement (Equation 2.10).

$$f_c = \frac{\omega_c}{2\pi} = \frac{qB}{2\pi m}$$ **Equation 2.10**

It is clear from Equation 2.10 that at constant B, f_c is just dependent on the inverse *m/z,* and because the frequency of ions can be measured precisely, this offers unparalleled mass accuracy measurement by this analyser[56]. Further, ions f_c has also the influence on providing the highest mass resolution performance. This is because f_c value is independent on ions velocity and thus their kinetic enrgy.[54-56] Equation 2.10 also shows that by increasing the strength of the magnetic field, ions f_c also increases and thus increasing the mass accuracy and resolving power[39,42,53-56] (Equation 2.11), where R is the resolving power, f_c is the cyclotron frequency and T is the duration of a transient[54]. In addition to the strength of the magnetic field and its homogeneity to achieve high performance FTICR mass analyser, high vacuum is also required. High vacuum in the range of 10^{-10}-10^{-11} mbar in FTICR is essential in order to prevent collisions between trapped ions and neutral gas molecules and a subsequent effect on f_c.[54,55]

$$R = \frac{f_c T}{2}$$ **Equation 2.11**

Trapped ions have a very small orbit or radius of motion that must be enlarged in order to detect them. Applying an RF voltage on excitation plates causes increasing ions E_{kin} and a subsequent incur of ions radial motion away from the central axis in a circular path. This is evident when the frequency of RF field comes into resonance with the cyclotron frequency of the precessing ion packet. Ions of different *m/z* can be excited by applying a burst of RF voltage covering a range of frequencies. Following this excitation step, each packet of ions (a packet with the same *m/z*) pass close to the two opposite detection plates in turn and positive ions will draw electron to the plate (Figure 2.13). In this way packets of all ions with different *m/z* will be measured in one go. This produces a complex time domain spectrum which shows intensity as a function of time, which is then converted to frequency domain spectrum by using Fourier transform algorithm (FT) and by relating intensity as a function of frequency, and this followed by mass correction, gives the intensity as a function of *m/z* and the mass spectrum. It is

interesting to know that ion detection in FTICR is a non-destructive process and consequently the same packet of ion can also perform tandem MS experiments.

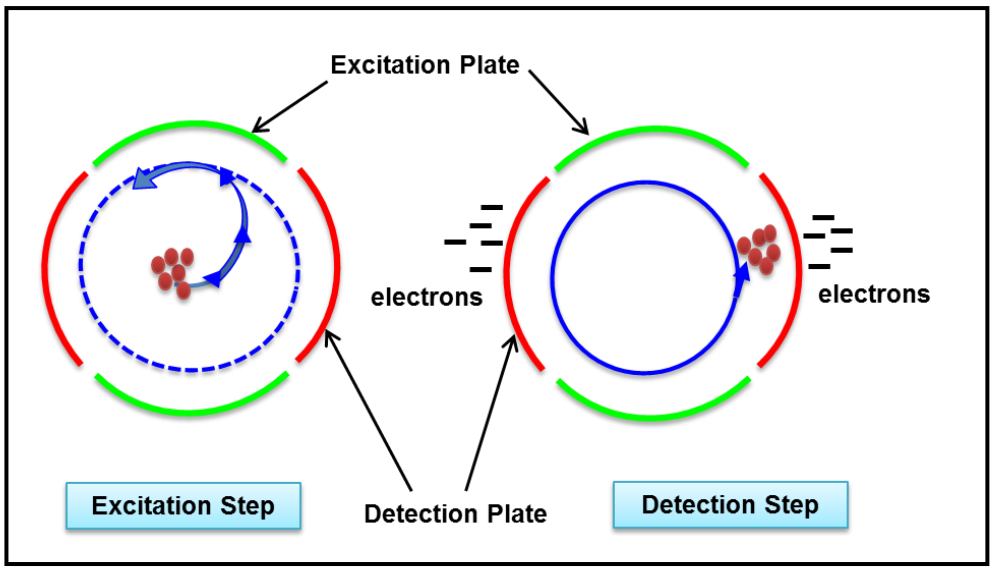

Figure 2.13. **Illustration of ion excitation (left) and ion detection (right) steps in FTICR cell.**

2.1.2.4. Time-of-flight mass analyser (ToF-MS)

Time-of-flight (ToF) mass analyser[2,60-64] is known for its very fast duty cycle, capable of collecting thousands of spectra per second, and relatively simple design. Basically, ToF requires a discrete packet of ions to enter a field free region and also called drift tube or flight tube. Ions will be accelerated from the ion source into a drift tube by applying potential difference (V_{acc}) between the accelerator plates (Figure 2.14). Consequently, ions in flight tube with mass (m) and velocity (V) will gain a E_{kin}, which is defined by Equation 2.12.

$$\mathbf{E_{kin} = \frac{1}{2}mV^2 = zeV_{acc}} \qquad \textbf{Equation 2.12}$$

Where, ze represents total ion charge (q). The velocity of ions can be defined by the distance travelled (d) in time (t), Equation 2.13.

$$\mathbf{V} = \frac{\mathbf{d}}{\mathbf{t}}$$ **Equation 2.13**

Substituting Equation 2.13 in Equation 2.12 generates Equation 2.14.

$$\frac{\mathbf{1}}{\mathbf{2}}\mathbf{m}(\mathbf{d}/\mathbf{t})^{\mathbf{2}} = \mathbf{zeV_{acc}}$$ **Equation 2.14**

Where, both d and V_{acc} are constant, this defines a direct proportion between *m/z* and time of flight (t), Equation 2.15.

$$\boldsymbol{m/z}\,\boldsymbol{\alpha}\,\mathbf{t^2}$$ **Equation 2.15**

This illustrates the detection of smaller ions first then followed by heavier ions carrying the same charge. The common detection device for ToF analyser is microchannel plate (MCP) with secondary electron multipliers (SEM). This basic principle of ToF analyser is applicable in both linear mode [61-64] and reflectron mode [60]. In linear mode ToF analyser, ions are detected at the end of a linear flight path (Figure 2.14 A) and this is more useful for larger ions (> 10 kDa) and with better sensitivity, while for smaller ions (< 10 kDa) and by using the same flight tube path with no change in its physical size, ions can be reflected by a series of electrodes (ion mirror) of increasing voltage (Figure 2.14 B). Consequently, in reflectron ToF ions will travel a further distance and a subsequent spectrum provide peaks that are spaced further apart along the *m/z* axis and consequently better mass resolution. In addition, the focusing effect of the reflectron ToF enhances the sensitivity of this MS analyser.

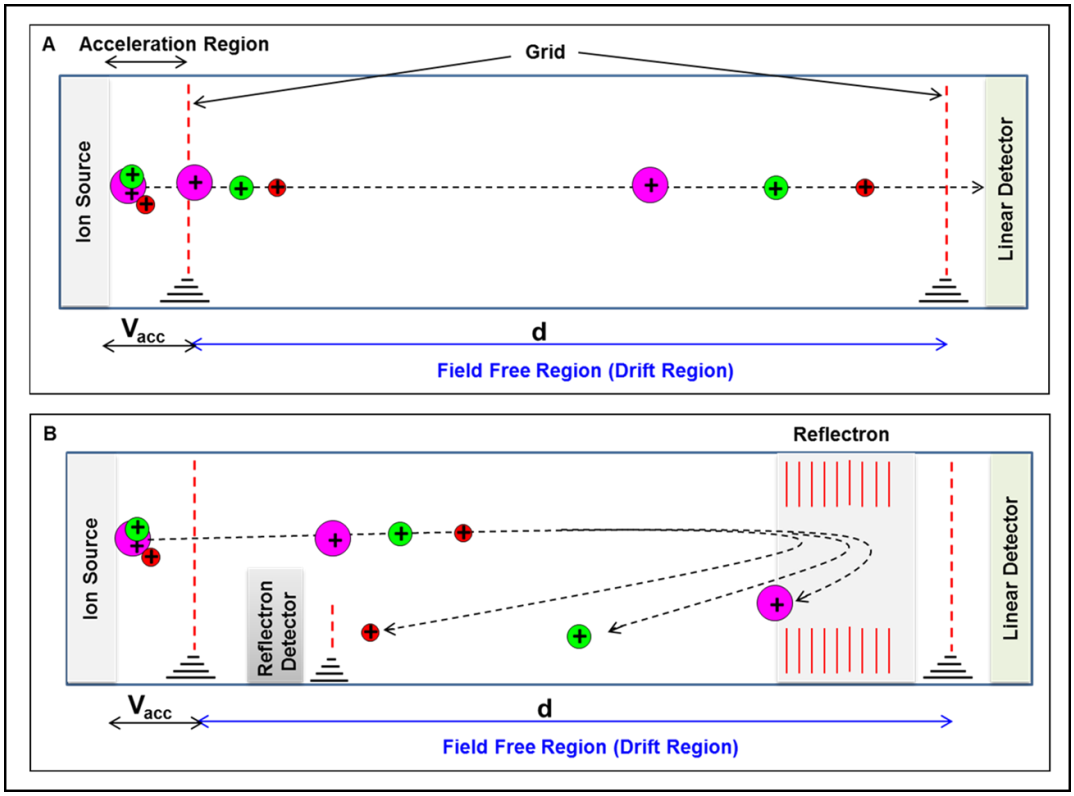

Figure 2.14. **Schematic illustration of (A) linear ToF-MS and (B) reflectron ToF-MS.**

The characteristic feature of the formation of discrete packet of ions in MALDI-MS and the frequency at which the ion packets are produced by the laser beam makes this source fit perfectly with ToF analysers in both linear and reflectron modes to produce ions axially to the flight tube, while ESI features the formation of a continuous flow of ions. This problem has been resolved by introducing the ion beam perpendicular to the axis of ToF by using an electric gate and the concept of orthogonal acceleration (oa), in which ions are orthogonally entering the flight tube,[2,62-64] as shown in Figure 2.15. Consequently, ions are kicked 90˚ angle sideways and a subsequent formation of nice packet of ions. This is applicable in linear ToF and as well as reflectron ToF.

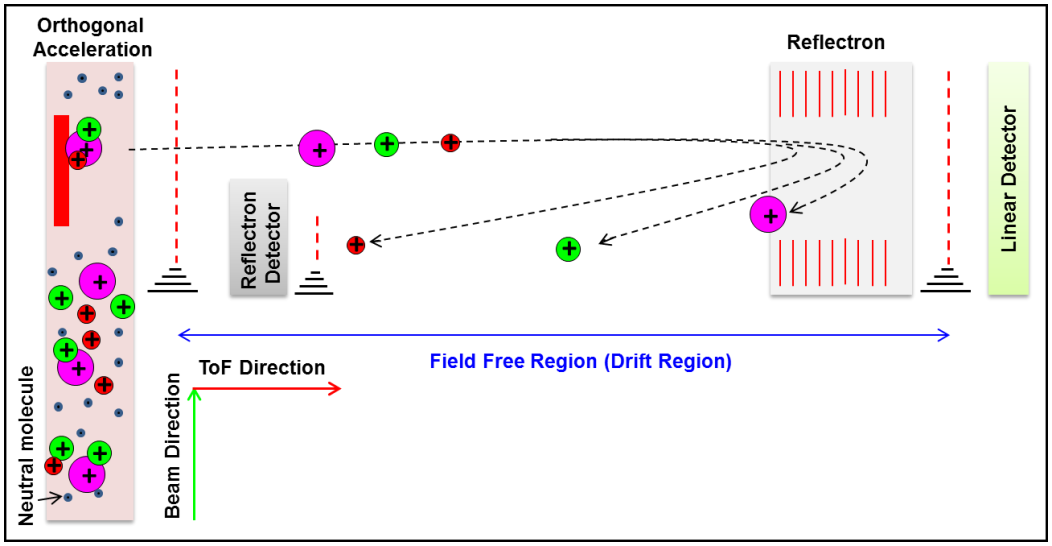

Figure 2.15. **Schematic description of reflectron ToF-MS fitted with an orthogonal acceleration aperture (oa ToF).**

2.1.3. Tandem mass spectrometry of peptides and proteins

Fragmentation in mass spectrometry starts by isolating specific ions and a subsequent bond dissociation by increasing ions internal energy. This is evident in formation of product ions which are charged and MS detected, as well as neutral fragments which are uncharged products and therefore not detected. Protein/peptide backbone cleavage by tandem MS enables the peptide or protein amino acid sequence to be determined. This can be done in two ways: the common "bottom up" approach and the less common "top down" approach.[65-68] The bottom up approach for proteins includes the formation of a set of daughter peptides through proteolytic digestion. The mass of these product peptides is used as a 'fingerprint' to define the identity of original protein through database searches or comparison with an *in silico* digest.[66,67,69] In addition, performing tandem MS experiment on one or more digested peptides confirms a high degree of the amino acid sequence and as well as its advantage in localising peptide modifications. This can also be achieved by top down approach, which involves protein sequencing through tandem MS experiment directly from the intact protein under investigation.[65,66,68,69] However, top down method is a more rapid method of protein sequencing because there is no need to do a time consuming digestion process and/or protein purification.

In the field of proteomics, the cleavage of peptide/protein backbone creates product ions labelled as x, y, and z for charge retain on the C-terminal of the peptide, while a, b, and c labels represent charge retain on the N-terminal of the peptide (Figure 2.16).[2,18-21,70,71] The mass difference between consecutive product ions for the same series of ions such as b_n and b_{n-1} provide amino acid sequence calculation for the peptide precursor ion. The product ions nomenclature of peptides was first described by Roepstorff and Fohlmann in 1984[70,72] and later developed by Biemann in 1988[71,72].

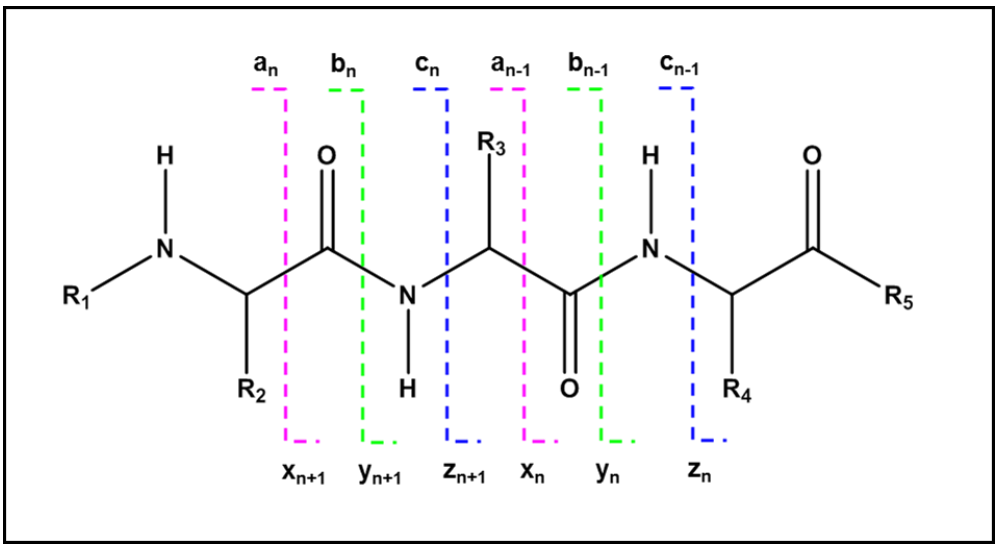

Figure 2.16. **Illustration of common cleavage sites of peptide backbone. The corresponding fragmentation products are highlighted in pink, green and blue for a/x-, b/y- and c/z-ions respectively.**

Fragmentation process is influenced by several factors such as amino acid composition, peptide size, excitation method, time scale of the used instrument and charge state of the ion.[69,72] The common fragmentation techniques in the field of proteomics involve; collision induced dissociation (CID), electron capture dissociation (ECD) and electron transfer dissociation (ETD).[65-69,72-77] For peptides, the weakest bond is the peptide linkage (CO-NH) which when broken generates a series of b- and y-ions through CID mechanism, while ECD and ETD generates c- and z-ions through (N-Cα) bond dissociation.[72,73,76]

Different fragmentation techniques have different dissociation mechanisms and so provide complementary product ions and consequently different MS spectra and structural information. In ECD,[65-68,73-77] low energy electrons (< 1 eV)[67,68,76] interact with multiply protonated peptides/proteins and subsequently capture an electron through a very rapid process (< 10^{-12} s)[65] to form a reduced intermediate of cation radical $[M + nH]^{(n-1)+\bullet}$. This intermediate is electronically excited and thus unstable; ultimately undergoing bond dissociation through (N-Cα) bond. The similar mechanism is described for ETD,[68,73,75-77] but here the electron is supplied by radical anion rather than using free electrons.[68,72,75-77] ECD is mainly implemented on FTICR-MS,[66-68,73-76] while ETD is more applicable in ion trap mass spectrometers[68,72,73,75] and further developed to be used in QToF-MS[75]. Both fragmentation techniques (ECD/ETD) are more powerful for larger proteins with high degree of charges (z > 2)[67,72] and thus valuable in top down approach.[65] They also provide higher sequence coverage[68,72,73] and also localise and identify PTMs that can be missed by CID such as phosphorylation and glycosylation.[67,68,72,73,74,76] This is because a covalent bond between these modified groups and the peptide side chains are sufficiently weak and cleaved by CID, while these weak bonds are preserved by ECD/ETD.[68,73] ECD has also the ability to cleave protein disulphide bonds.[67] However, CID is the more common and robust fragmentation technique in the proteomics which can be associated with most mass spectrometers and to provide up to 100%[65] sequence coverage.[72,75-77] In this chapter the focus will be on describing the basic principle of CID technique, because of its relevance to the research carried out in this project.

2.1.3.1. Collision induced dissociation (CID)

Collision induced dissociation (CID),[67,72-79] also called collision activation dissociation (CAD) can be performed through two energy pathways: low energy CID (1-100 eV), which is commonly found in Q-MS and LIT-MS and high energy CID of several keV, which is seen in ToF-MS and sector instruments[79].[2,16,17,72,78-80] High energy CID has contribution from electronic processes as well as vibrational process to produce a-, x- and

immonium ions.[2,72,78-80] It does not permit peptide rearrangement after the loss of a fragment because it is a very fast process and thus less than 10 collisions will occur in this process. This type of CID is very useful in distinguishing between isobaric amino acid residues such as leucine and isoleucine and as well as reproducible fragmentation pattern.[72] The ability of high energy CID to differentiate between leucine and isoleucine is due to side chain cleavage and the formation of additional product ions that termed as d- and w-ions. On the other hand, low energy CID is a vibrational excitation process with the predominant formation of b- and y-ions.[2,72,78-80] This will be discussed in detail because of its relevance to the research carried out in this project.

In low energy CID the dissociation process is performed in a slower time scale (around ms) that permits peptide rearrangement and multiple collisions (up to 100).[72] The basic principle of low energy CID can be explained in two major steps. **First**, the targeted precursor ion (M_p) with high translational energy collides with a neutral gas (N) through inelastic collisions, typically argon or nitrogen, and energy transfer results in increasing the internal energy of the ion (Equations 2.16). **Second** (Equations 2.17), the internal energy of this vibrational excited state (M_p^{+*}**,** intermediate state) is distributed over all available covalent bonds. Such step leads the cleavage of the more labile bond (CO-NH), and unimolecular dissociation results to give a product ion (m_b^+). Generally, first step is faster than the second step for fast moving ions. Dissociation process in CID can be explained mathematically by Equation 2.18.

$$M_p^+ + N \longrightarrow M_p^{+*} + N \qquad \textbf{Equation 2.16}$$

$$M_p^{+*} \longrightarrow m_b^+ + m_c \qquad \textbf{Equation 2.17}$$

$$E = \left(\frac{N}{N+M_p}\right)E_{kin} \qquad \textbf{Equation 2.18}$$

Where E is the total available energy for the transfer of kinetic energy (E_{kin}) of the precursor ion to internal energy (E_{int}), M_p and N are the masses of precursor ion and collision neutral gas respectively.[78,79] Interestingly, the quasi-equilibrium theory (QET) is commonly used to describe unimolecular

dissociation of gas phase ions under high vacuum. There are several factors affecting the efficiency of CID, some are related with the nature and size of the neutral gas[78,79] and the others related with the nature (number of charges)[81] and size[82] of the precursor ion. In addition, the high pressure of the neutral collision gas has also influence on increasing multiple collisions for a single ion with the neutral gas and also the number of ions that are performing collisions.[78,79]

2.2. Ion mobility separation (IMS)

Ion mobility (IM) is an analytical tool that separates ions in the gas phase depending on their shape and size. Consequently, it can be possible to separate ions of the same *m/z* such as isomers, isobars and conformers. This technique was originally known as plasma chromatography and ion chromatography.[83-85] It was first used to analyse volatile organic compounds and also to investigate the electronic structure of ions, and found wide application in the fields of military for monitoring chemical and biological weapons and explosives; security for the detection of explosives and more recently illegal drugs.[85-87] A profound advantage of IMS in the field of biomolecules to analyse peptides/proteins[87-90] and more recently in lipidomics[91-93] is introduced from coupling IMS with MS to provide both structural (ion conformation) and *m/z* characteristics for an analyte. This has been commercially available in one instrument in the last 10 years.

The simplest and oldest IMS technique is called drift time ion mobility spectrometry (DTIMS),[85,87,94] Figure 2.17 A, which allows the calculation of ions collision cross-section (CCS or Ω) based on the recorded drift time (t_d) in the drift tube under static uniform electric field (5-100 V). Ions with extended structure have stronger interaction/collision with the buffer gas (high CCS) thus slow down them in the drift tube, while compact structures are travelling faster and with smaller CCS.[94] Travelling wave ion mobility spectrometry (TWIMS)[85,87,94] is another type of drift time IMS, Figure 2.17 B, which is featured in Synapt G2-s instrument and the relevant one for this project. This type of IMS is similar to DTIMS in measuring CCS for ions as a function of t_d but by applying an electrodynamic voltage instead of static electric field. This

is composed of a stacked ring ion guide (SRIG) to which a travelling voltage wave is applied. Ions are confined radially by the application of opposite RF voltage to adjacent electrodes. On the other hand, the application of pulsed DC voltage to each electrode in succession from one end to the other causes axial propel of the ions. The voltage will be stepped through the device and this creates travelling wave by which ions will be travelled. Field-asymmetric ion mobility spectrometry (FAIMS)[85,87,94] or differential ion mobility spectrometry (DMS) is another type of IMS but with different separation principle from time based IMS devices (DTIMS and TWIMS). This device cannot be used to calculate CCS and is preferentially performing an ion filter process similar to quadruple mass filter.[94]

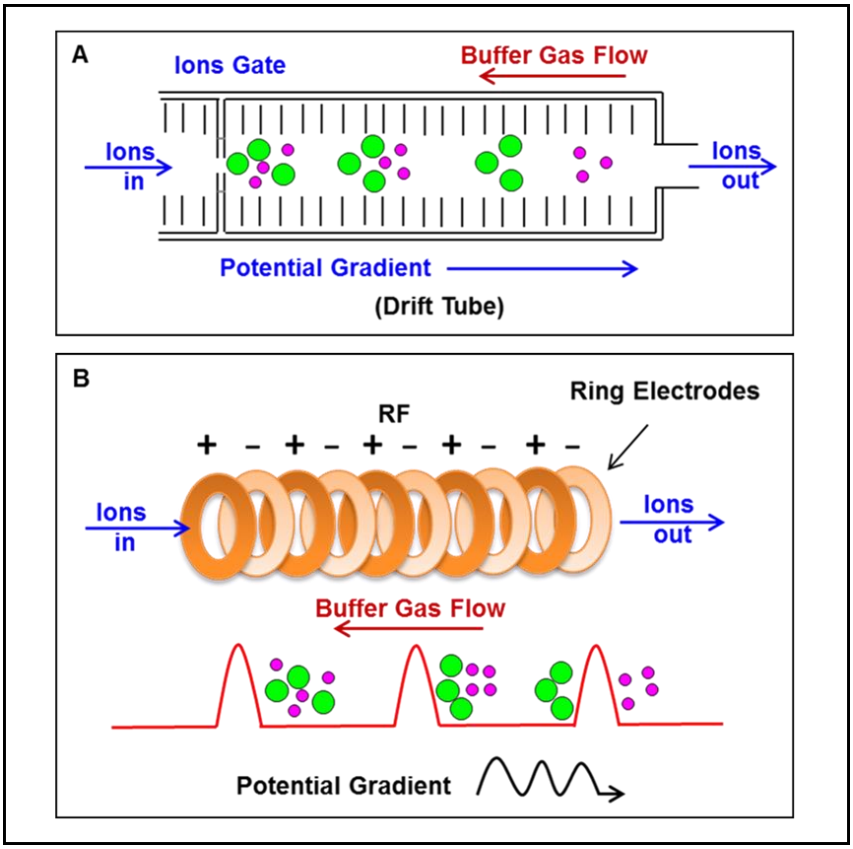

Figure 2.17. **Schematic illustration for comparison between (A) drift time ion mobility spectrometry (DTIMS) and (B) travelling wave ion mobility spectrometry (TWIMS).**

The basic principle of separation in IMS technique starts by injecting pre-formed gas phase ions from the ionisation source into a separation cell or

called drift tube that is filled with neutral buffer gas (usually helium) and operated under weak electric field (gradient). Consequently, ions under this condition will have a drift velocity (V_d, $cm^2\ s^{-1}$) which is directly proportion with the ion mobility (K, $cm^2\ s^{-1}\ v^{-1}$) and the applied electric field (E, $v\ cm^{-1}$),[83-85,87] as shown in Equation 2.19.

$$\boldsymbol{V_d = KE} \qquad \textbf{Equation 2.19}$$

Drift velocity (V_d) can be calculated by the time (t_d, s) taken for the ion to travel through the drift tube at distance (d, cm), as shown in Equation 2.20.

$$\mathbf{V_d = KE = \frac{d}{t_d}} \qquad \textbf{Equation 2.20}$$

The drift time (t_d) of ions is related to the effective area for the interaction between a single ion and the buffer gas, which is known as averaged cross-section area or collision cross-section (CCS or Ω, A^2). This is calculated by Mason-Schamp equation (Equation 2.21).

$$\mathbf{\Omega = \frac{3}{16}\frac{ze}{N}\left(\frac{2\pi}{\mu K_B T}\right)^{\frac{1}{2}}\frac{1}{K}} \qquad \textbf{Equation 2.21}$$

This equation illustrates the dependent of CCS on ions charge (q = ze), the number density of buffer gas (N), the reduced mass of the complex product ion-buffer gas ($\boldsymbol{\mu}$), the absolute gas temperature (T) and the ion mobility (K). For macro molecules the value of $\boldsymbol{\mu}$ can be regarded as a constant parameter because it approaches the mass of buffer gas,[84] as $\boldsymbol{\mu}$ = mM/(m+M), m and M are the masses of the buffer gas and the ion respectively. Consequently, the mobility constant (K) of the ions inversely proportion with CCS, Equation 2.22. The prediction of ions structure can be explained by comparing practical CCS to the theoretical CCS values for computer provided structure.

$$\mathbf{K\ \alpha\ \frac{1}{\Omega}} \qquad \textbf{Equation 2.22}$$

Mobility separation of ions can be achieved by changing the speed and magnitude of the travelling wave voltage. Less collisions between smaller size ions and the buffer gas speed them to travel by the wave (small

CCS) relative to slower mobility of larger ions by experiencing greater collision (high CCS). Consequently, travelling wave voltage separates ions with different size through the device. On the other hand, separation of complex mixture can also be performed by using several travelling waves through the IMS cell in quick succession.[94]

2.3. Schematic for applied instruments

2.3.1. LTQFT

All the results described in chapter three and some in chapter four were carried out on LTQFT (ThermoFinnigan Corporation) mass spectrometer equipped with Surveyor HPLC (ThermoFisher Scientific Inc.) as shown in Figure 2.18. Surveyor HPLC has quaternary pumps.

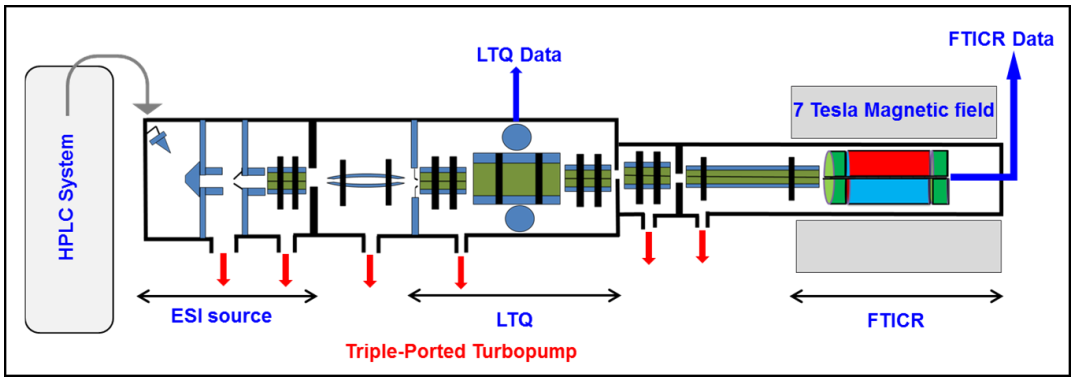

Figure 2.18. **The LTQFT (ThermoFinnigan) instrument schematic.**

The analyte mixture is first separated by HPLC as a function of hydrophobic affinity with an alkylsilica-based sorbent stationary phase. These separated species were passed through an Ion-Max ion source fitted with an ESI probe[95]. Ions were then guided through the instrument by an octapole and into the LIT. The LIT can operate as a stand-alone tandem mass spectrometer (and give the name LTQ by the manufacturers, ThermoFinnigan) to produce product ions through collision with helium gas by using CID principle, which are then detected either by using ICR cell or by using a conversion dynode[58].

It is possible to pass the ion beam out the back of the LTQ and using quadrupole ion guides to move the ions into an FTICR cell. Accurate (1-2 ppm) and high resolution (100,000 FWHM at *m/z* 400) data were processed on FTICR for precursor ion analysis in full MS mode and with acquiring mass range of 200-2000 *m/z*. The cylindrical ICR cell (Penning trap) is built in the center of an actively shielded superconducting magnet with field strength of 7 Tesla, where ions are trapped, excited, ejected and detected sequentially to yield a transient current and a subsequent conversion to MS spectrum by FT system. Generally, the gradient vacuum system in LTQFT can be separated into three main regions: forevacuum (3.5×10^{-3} mbar); transfer area (3.0×10^{-7} mbar); ICR area (2.0×10^{-9} mbar).

The detection process by using a conversion dynode device is happening by striking an ion to the surface of a concave metal which has an opposite potential from the striking ions, as shown in Figure 2.19. This yields more than one secondary particles, which are negative ions and electrons for positively charged striking ions. Subsequently, they are focused and accelerated towards electron multiplier by a voltage gradient. Striking the secondary particles to the inner walls of the electron multiplier cathode with sufficient energy will eject electrons. Ejected electrons in the funnel shape cathode lead to multiple collisions and emit more electrons before they are collected by anode. This formation of a cascade of electrons enables a measurable current at the end of cathode. This current then collected by anode which is proportional to the number of secondary particles striking the cathode.[50]

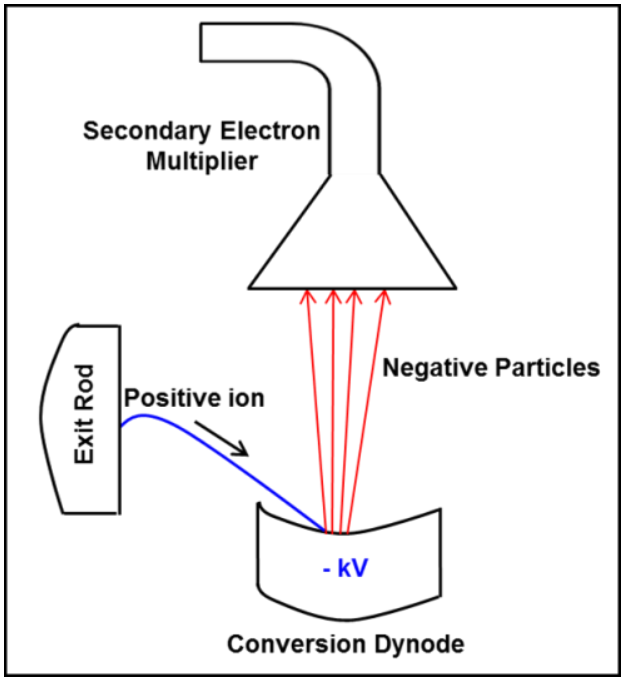

Figure 2.19. **The conversion dynode detector, secondary electron multiplier (SEM) equipped with LTQ analyser.**

2.3.2. Autoflex II ToF/ToF

Autoflex II is a MALDI-ToF mass spectrometer (Bruker Daltonik GmbH) that performs at high vacuum pressure of about 8 x 10^{-7} mbar[96] (Figure 2.20).

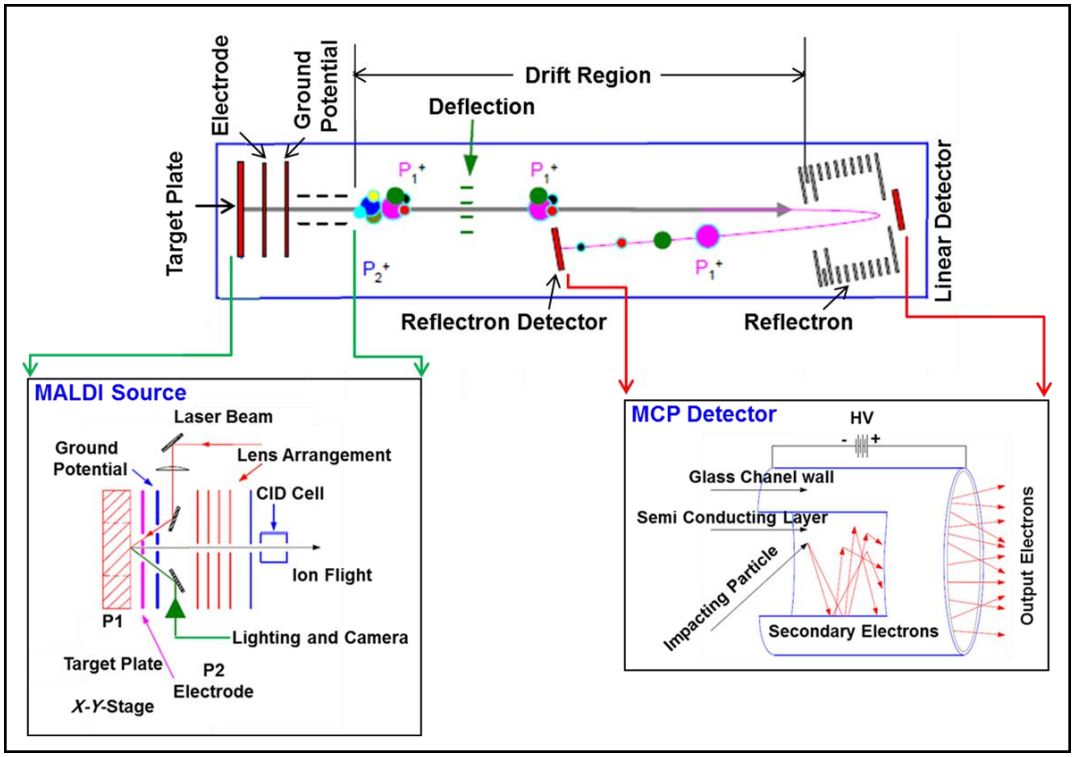

Figure 2.20. **Schematic of Autoflex II ToF/ToF mass spectrometer (Bruker Daltonik GmbH). MALDI source and microchannel plate (MCP) detector are also enlarged and included.**[96]

MALDI ion source has a target plate on *X-Y* coordinates where analyte:matrix mixture is dried out. Following plate insertion, a positive or negative potential will be applied to the target (P1) at equal amount to the applied potential on the electrode (P2) at the beginning. Analyte:matrix mixture is then irradiated by a pulsed nitrogen laser at 337 nm to create ionised analyte with a typical initial velocity of 700 m/s from P1 o P2 (both are at equal potential). Consequently, ions with the same *m/z* have different velocity and kinetic energy (E_{kin}). This velocity distribution would act to decrease ToF-MS resolution and so Wiley-McClaren focusing in the ion

source, otherwise known as pulsed ion extraction (PIE), is used to correct this aberration and enhances both resolution and sensitivity on ToF analyser.

PIE technique based on slopping the potential on P2 electrode from initial 20 kV to 18 kV, which creates a potential difference between P1 and P2. Ions with the same *m/z* and different velocity and E_{kin} in this region influenced differently by this potential difference depending on their position, whether they are close to P1 (slower ions) or closer to P2 (faster ions). Generally, slower ions start on a greater potential difference than the fast ones and so have greater acceleration into the field free region (drift tube) relative to the initial faster ions in the source. Consequently, the arrival time at the detector is identical for ions with the same *m/z* and independent on their initial E_{kin}. Ions enter the ToF analyser in pulses where they are separated, and subsequently detected by a microchannel plate (MCP) detector containing secondary electron multiplier (SEM) in either linear mode or reflectron mode. This detector uses the same basic principle of amplifying the signal from the single particle (ion current) by generating a cascade of electrons (electrical current) as described for LTQ detector (See section 2.3.1) but instead of using a concave metal surface it uses MCP with millions of tiny channel, which are coated inside with a semi-conductive layer.[96]

2.3.3. Synapt G2-s

Synapt G2-s mass spectrometer (Waters Corporation) is equipped with ACQUITY ultra performance liquid chromatography (UPLC^{TM}) I class (Figure 2.21). UPLC system involves a binary solvent manager, sample manager and the detector. The separation system has better efficiency, resolution, sensitivity and speed of analysis than HPLC counterpart. This is because of the solid stationary phase specification of uses very small particles at sub 2 micron, which can operate at very high pressures, up to 15,000 psi. However, UPLC does not have quaternary pumps as featured in Surveyor HPLC (ThermoFisher).

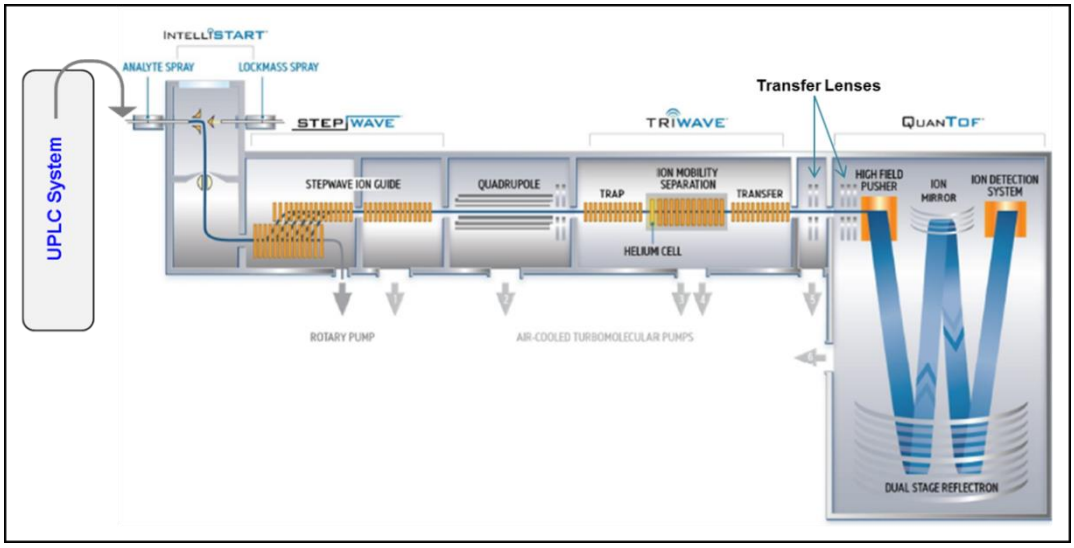

Figure 2.21. **Schematic of online coupling between UPLC and Synapt G2-s instrument (Waters Corporation). Reproduced with the permission from Waters Corporation.**

Following chromatographic separation, the analyte is delivered to the ionisation source, which can be different interchangeable sources such as ESI, MALDI, ASAP, and ESCI. ESI source has been used for all work described herein. ESI probe has nebuliser gas, desolvation gas flow and the desolvation temperature. In addition, LockSpray was employed to provide mass correction by systematically introducing a reference compound with known mass. Subsequently, gas phase ions reach a StepWave transfer optics which is a form of a travelling wave ion guide and called StepWave ion guide, where all ions are focused and transferred to the next stage of a narrow bore ion guide. The off-axis design of the StepWave ion guide removes any neutral species entering the system. The focused ions then enter the quadrupole device (Q-MS), where they are separated (filtered) according to their *m/z* and then delivering ions into TriWave region.[97]

TriWave region consists of three T-Wave ion guides with different distinct functions. The first and third T-Wave guides are called trap and transfer regions respectively. Their function is either delivering ions from earlier stage towards the next stage for full MS scan or they can be used as a collision cells to perform tandem MS analysis (via CID or ETD). The middle T-Wave ion guide is where the ion mobility separation (IMS) takes place. Subsequently, ions transferred to orthogonal acceleration ToF (oa ToF) with

dual-stage reflectron geometry, where the ions orthogonally accelerated down the flight tube by a high voltage pulse. The dual-stage reflectron reflects ions towards the mirror and this in turn reflects them back to the dual-stage reflectron, where they will be finally reflected to the detector. Ions of different *m/z* arrives the detector (MCP, described in section 2.3.2) at different times, where they are amplified and digitized to create a mass spectrum. Three modes can be operated in oaToF-MS including; sensitivity, resolution and high resolution.[97]

2.4. References

1 Thomson, Joseph John. "*Rays of Positive Electricity and their Application to Chemical Analyses*." volume 1, Longmans, Green and Company, London, **1913**.

2 De Hoffmann, Edmond, and Vincent Stroobant. "*Mass Spectrometry: Principles and Applications*." John Wiley & Sons, **2007**.

3 McLafferty, Fred W. "A century of progress in molecular mass spectrometry." *Annual Review of Analytical Chemistry*, 4 (**2011**): 1-22.

4 Biemann, K. "Mass spectrometry of peptides and proteins." *Annual Review of Biochemistry*, 61 (**1992**): 977-1010.

5 Trauger, Sunia A., William Webb, and Gary Siuzdak. "Peptide and protein analysis with mass spectrometry." *Journal of Spectroscopy*, 16 (**2002**): 15-28.

6 Chang, Huan-Cheng. "Ultrahigh-mass mass spectrometry of single biomolecules and bioparticles." *Annual Review of Analytical Chemistry*, 2 (**2009**): 169-185.

7 Banerjee, Shibdas, and Shyamalava Mazumdar. "Electrospray ionization mass spectrometry: a technique to access the information beyond the molecular weight of the analyte." *International Journal of Analytical Chemistry* 2012 (**2012**): 1-40.

8 Yamashita, Masamichi, and John B. Fenn. "Electrospray ion source. Another variation on the free-jet theme." *The Journal of Physical Chemistry*, 88 (**1984**): 4451-4459.

9 Whitehouse, Craig M., Robert N. Dreyer, Masamichi Yamashita, and John B. Fenn. "Electrospray interface for liquid chromatographs and mass spectrometers." *Analytical Chemistry*, 57 (**1985**): 675-679.

10 Whitehouse, CRAIG M., R. N. Dreyer, M. Yamashita, and J. B. Fenn. "Electrospray ionization for mass-spectrometry of large biomolecules." *Science*, 246 (**1989**): 64-71.

11 Fenn, John B. "Ion formation from charged droplets: roles of geometry, energy, and time." *Journal of the American Society for Mass Spectrometry*, 4 (**1993**): 524-535.

12 Fenn, J. "Electrospray ionization mass spectrometry: how it all began." *Journal of Biomolecular Techniques*, 13 (**2002**): 101-118.

13 Tanaka, Koichi, Hiroaki Waki, Yutaka Ido, Satoshi Akita, Yoshikazu Yoshida, Tamio Yoshida, and T. Matsuo. "Protein and polymer analyses up to m/z 100 000 by laser ionization time-of-flight mass spectrometry." *Rapid Communications in Mass Spectrometry*, 2 (**1988**): 151-153.

14 Abate, R., A. Ballistreri, G. Montaudo, D. Garozzo, G. Impallomeni, G. Critchley, and K. Tanaka. "Quantitative applications of matrix-assisted laser desorption/ionization with time-of-flight mass spectrometry: Determination of copolymer composition in bacterial copolyesters." *Rapid Communications in Mass Spectrometry*, 7 (**1993**): 1033-1036.

15 McLafferty, Fred W. "Tandem mass spectrometry." *Science*, 214 (**1981**): 280-287.

16 Deterding, Leesa J., Kenneth B. Tomer, and Arno F. Spatola. "Tandem mass spectrometry for the structural determination of backbone-modified peptides." *Journal of the American Society for Mass Spectrometry*, 1 (**1990**): 174-182.

17 Eng, Jimmy K., Ashley L. McCormack, and John R. Yates. "An approach to correlate tandem mass spectral data of peptides with amino acid sequences in a protein database." *Journal of the American Society for Mass Spectrometry*, 5 (**1994**): 976-989.

18 Jensen, Ole Nørregaard. "Modification-specific proteomics: characterization of post-translational modifications by mass spectrometry." *Current Opinion in Chemical Biology*, 8 (**2004**): 33-41.

19 Steen, Hanno, and Matthias Mann. "The ABC's (and XYZ's) of peptide sequencing." *Nature Reviews. Molecular Cell Biology*, 5 (**2004**): 699-711.

20 Wysocki, Vicki H., Katheryn A. Resing, Qingfen Zhang, and Guilong Cheng. "Mass spectrometry of peptides and proteins." *Methods*, 35 (**2005**): 211-222.

21 Larsen, Martin R., Morten B. Trelle, Tine E. Thingholm, and Ole N. Jensen. "Analysis of posttranslational modifications of proteins by tandem mass spectrometry." *Biotechniques*, 40 (**2006**): 790-798.

22 Pati, Sumitra, Ben Nie, Robert D. Arnold, and Brian S. Cummings. "Extraction, chromatographic and mass spectrometric methods for lipid analysis." *Biomedical Chromatography*, 30 (**2016**): 695-709.

23 Zhang, Zichuan, Jun Kuang, and Lingjun Li. "Liquid chromatography-matrix-assisted laser desorption/ionization mass spectrometric imaging with sprayed matrix for improved sensitivity, reproducibility and quantitation." *Analyst*, 138 (**2013**): 6600-6606.

24 Hattan, Stephen J., Jason Marchese, Nikita Khainovski, Steve Martin, and Peter Juhasz. "Comparative study of [Three] LC−MALDI workflows for the analysis of complex proteomic samples." *Journal of Proteome Research*, 4 (**2005**): 1931-1941.

25 Malmström, Johan, Kristoffer Larsen, Lars Malmström, Ellen Tufvesson, Ken Parker, Jason Marchese, Brian Williamson et al. "Nanocapillary liquid chromatography interfaced to tandem matrix-assisted laser desorption/ionization and electrospray ionization-mass

spectrometry: Mapping the nuclear proteome of human fibroblasts." *Electrophoresis*, 24 (**2003**): 3806-3814.

26 Wolf, Claude, and Peter J. Quinn. "Lipidomics: Practical aspects and applications." *Progress in Lipid Research*, 47 (**2008**): 15-36.

27 Gaskell, Simon J. "Electrospray: Principles and Practice" *Journal of Mass Spectrometry*, 32 (**1997**): 677-688.

28 Kebarle, Paul, and Liang Tang. "From ions in solution to ions in the gas phase-the mechanism of electrospray mass spectrometry." *Analytical Chemistry*, 65 (**1993**): 972A-986A.

29 Konermann, Lars, Elias Ahadi, Antony D. Rodriguez, and Siavash Vahidi. "Unraveling the mechanism of electrospray ionization." *Analytical Chemistry*, 85 (**2013**): 2-9.

30 Yue, Xuanfeng, Siavash Vahidi, and Lars Konermann. "Insights into the mechanism of protein electrospray ionization from salt adduction measurements." *Journal of the American Society for Mass Spectrometry,* 25 (**2014**): 1322-1331.

31 Hendrickson, Christopher L., and Mark R. Emmett. "Electrospray ionization Fourier transform ion cyclotron resonance mass spectrometry." *Annual Review of Physical Chemistry*, 50 (**1999**): 517-536.

32 Zenobi, Renato, and Richard Knochenmuss. "Ion formation in MALDI mass spectrometry." *Mass Spectrometry Reviews*, 17 (**1998**): 337-366.

33 Itina, Tatiana E., Leonid V. Zhigilei, and Barbara J. Garrison. "Microscopic mechanisms of matrix assisted laser desorption of analyte molecules: insights from molecular dynamics simulation." *The Journal of Physical Chemistry B*, 106 (**2002**): 303-310.

34 Yao, Jie, Jill R. Scott, Mary K. Young, and Charles L. Wilkins. "Importance of matrix: analyte ratio for buffer tolerance using 2,5-dihydroxybenzoic acid as a matrix in matrix-assisted laser desorption/ionization-fourier transform mass spectrometry and matrix-assisted laser desorption/ionization-time of flight." *Journal of the American Society for Mass Spectrometry*, 9 (**1998**): 805-813.

35 Lewis, J. Kathleen, Jing Wei, and Gary Siuzdak. "Matrix-assisted laser desorption/ionization mass spectrometry in peptide and protein analysis." *Encyclopedia of Analytical Chemistry***,** Robert A. Meyers (Ed.) (**2000**): 1-14.

36 Jagannadham, M. V., and R. Nagaraj. "Detection of peptides covalently modified with multiple fatty acids by MALDI-TOF mass spectrometry." *Chemical Biology & Drug Design*, 66 (**2005**): 94-100.

37 Karas, Michael, and Franz Hillenkamp. "Laser desorption ionization of proteins with molecular masses exceeding 10,000 daltons." *Analytical Chemistry*, 60 (**1988**): 2299-2301.

38 March, Raymond E. "Quadrupole ion traps." *Mass Spectrometry Reviews*, 28 (**2009**): 961-989.

39 Schaub, Tanner M., Christopher L. Hendrickson, Stevan Horning, John P. Quinn, Michael W. Senko, and Alan G. Marshall. "High-performance mass spectrometry: Fourier transform ion cyclotron resonance at 14.5 Tesla." *Analytical Chemistry*, 80 (**2008**): 3985-3990.

40 Ghaste, Manoj, Robert Mistrik, and Vladimir Shulaev. "Applications of Fourier transform ion cyclotron resonance (FT-ICR) and orbitrap based high resolution mass spectrometry in metabolomics and lipidomics." *International Journal of Molecular Sciences*, 17 (**2016**): 1-22.

41 Smith, Donald F., Andras Kiss, Franklin E. Leach, Errol W. Robinson, Ljiljana Paša-Tolić, and Ron MA Heeren. "High mass accuracy and high mass resolving power FT-ICR secondary ion mass spectrometry for biological tissue imaging." *Analytical and Bioanalytical Chemistry*, 405 (**2013**): 6069-6076.

42 Nikolaev, Eugene N., Yury I. Kostyukevich, and Gleb N. Vladimirov. "Fourier transform ion cyclotron resonance (FT ICR) mass spectrometry: Theory and simulations." *Mass Spectrometry Reviews*, 35 (**2016**): 219-258.

43 Bristow, Anthony WT. "Accurate mass measurement for the determination of elemental formula—a tutorial." *Mass Spectrometry Reviews*, 25 (**2006**): 99-111.

44 Mathieson, E., and T. J. Harris. "The quadrupole mass spectrometer." *American Journal of Physics*, 37 (**1969**): 1054-1059.

45 Jonscher, Karen R., and John R. Yates. "The quadrupole ion trap mass spectrometer—a small solution to a big challenge." *Analytical Biochemistry*, 244 (**1997**): 1-15.

46 March, Raymond E. "An introduction to quadrupole ion trap mass spectrometry." *Journal of Mass Spectrometry*, 32 (**1997**): 351-369.

47 Guan, Shenheng, and Alan G. Marshall. "Ion traps for Fourier transform ion cyclotron resonance mass spectrometry: principles and design of geometric and electric configurations." *International Journal of Mass Spectrometry and Ion Processes*, 146 (**1995**): 261-296.

48 Stafford, George. "Ion trap mass spectrometry: a personal perspective." *Journal of the American Society for Mass spectrometry*, 13 (**2002**): 589-596.

49 Douglas, Donald J., Aaron J. Frank, and Dunmin Mao. "Linear ion traps in mass spectrometry." *Mass Spectrometry Reviews*, 24 (**2005**): 1-29.

50 *LTQ XL Hardware Manual Thermo Electron Corporation* (**2006**).

51 Grosshans, Peter B., and Alan G. Marshall. "General theory of excitation in ion cyclotron resonance mass spectrometry." *Analytical Chemistry*, 63 (**1991**): 2057-2061.

52 Marshal, Alan G., and Peter B. Grosshans. "Fourier transform ion cyclotron resonance mass spectrometry: the teenage years." *Analytical Chemistry*, 63 (**1991**): 215A-229A.

53 Buchanan, Michelle V., and Robert L. Hettich. "Fourier transform mass spectrometry of high-mass biomolecules." *Analytical Chemistry*, 65 (**1993**): 245A-259A.

54 Amster, I. Jonathan. "Fourier transform mass spectrometry." *Journal of Mass Spectrometry*, 31 (**1996**): 1325-1337.

55 Marshall, Alan G., Christopher L. Hendrickson, and George S. Jackson. "Fourier transform ion cyclotron resonance mass spectrometry: a primer." *Mass Spectrometry Reviews*, 17 (**1998**): 1-35.

56 Hendrickson, Christopher L., and Mark R. Emmett. "Electrospray ionization Fourier transform ion cyclotron resonance mass spectrometry." *Annual Review of Physical Chemistry*, 50 (**1999**): 517-536.

57 Marshall, Alan G. "Milestones in Fourier transform ion cyclotron resonance mass spectrometry technique development." *International Journal of Mass Spectrometry*, 200 (**2000**): 331-356.

58 *Finnigan LTQ FT Hardware Manual Thermo Electron Corporation* (**2004**).

59 Shaw, Jared B., Tzu-Yung Lin, Franklin E. Leach, Aleksey V. Tolmachev, Nikola Tolić, Errol W. Robinson, David W. Koppenaal, and Ljiljana Paša-Tolić. "21 Tesla Fourier transform ion cyclotron resonance mass spectrometer greatly expands mass spectrometry toolbox." *Journal of the American Society for Mass Spectrometry*, 27 (**2016**): 1929-1936.

60 Wiley, W. C., and Ii H. McLaren. "Time-of-flight mass spectrometer with improved resolution." *Review of Scientific Instruments*, 26 (**1955**): 1150-1157.

61 Guilhaus, Michael. "Special feature: Tutorial. Principles and instrumentation in time-of-flight mass spectrometry. Physical and instrumental concepts." *Journal of Mass Spectrometry*, 30 (**1995**): 1519-1532.

62 Cotter, Robert J. "Peer Reviewed: The New Time-of-Flight Mass Spectrometry." *Analytical Chemistry*, 71 (**1999**): 445A-451A.

63 Guilhaus, M., D. Selby, and V. Mlynski. "Orthogonal acceleration time-of-flight mass spectrometry." *Mass Spectrometry Reviews*, 19 (**2000**): 65-107.

64 Mamyrin, B. A. "Time-of-flight mass spectrometry (concepts, achievements, and prospects)." *International Journal of Mass Spectrometry*, 206 (**2001**): 251-266.

65 Ge, Ying, Brian G. Lawhorn, Mariam ElNaggar, Erick Strauss, Joo-Heon Park, Tadhg P. Begley, and Fred W. McLafferty. "Top down characterization of larger proteins (45 kDa) by electron capture dissociation mass spectrometry." *Journal of the American Chemical Society*, 124 (**2002**): 672-678.

66 Yates, John R. "Mass spectral analysis in proteomics." *Annual review of biophysics and biomolecular structure,* 33 (**2004**): 297-316.

67 Bogdanov, Bogdan, and Richard D. Smith. "Proteomics by FTICR mass spectrometry: top down and bottom up." *Mass Spectrometry Reviews*, 24 (**2005**): 168-200.

68 Breuker, Kathrin, Mi Jin, Xuemei Han, Honghai Jiang, and Fred W. McLafferty. "Top-down identification and characterization of biomolecules by mass spectrometry." *Journal of the American Society for Mass Spectrometry*, 19 (**2008**): 1045-1053.

69 Paizs, Béla, and Sándor Suhai. "Fragmentation pathways of protonated peptides." *Mass Spectrometry Reviews*, 24 (**2005**): 508-548.

70 Roepstorff, P., and J. Fohlman. "Letter to the editors." *Biological Mass Spectrometry*, 11 (**1984**): 601-601.

71 Biemann, Klaus. "Contributions of mass spectrometry to peptide and protein structure." *Biological Mass Spectrometry*, 16 (**1988**): 99-111.

72 Soares, Renata, Elisabete Pires, André M. Almeida, Romana Santos, Ricardo Gomes, Kamila Koči, Catarina Ferraz Franco, and Ana Varela Coelho. "Tandem mass spectrometry of peptides." *Tandem Mass Spectrometry-Applications and Principles*, Jeevan K. Prasain (Ed.), InTech (**2012**): 35-56.

73 Srikanth, R., Jonathan Wilson, Juma D. Bridgewater, Jason R. Numbers, Jihyeon Lim, Mark R. Olbris, Ali Kettani, and Richard W. Vachet. "Improved sequencing of oxidized cysteine and methionine containing peptides using electron transfer dissociation." *Journal of the American Society for Mass Spectrometry*, 18 (**2007**): 1499-1506.

74 Creese, Andrew J., and Helen J. Cooper. "Liquid chromatography electron capture dissociation tandem mass spectrometry (LC-ECD-MS/MS) versus liquid chromatography collision-induced dissociation tandem mass spectrometry (LC-CID-MS/MS) for the identification of proteins." *Journal of the American Society for Mass Spectrometry*, 18 (**2007**): 891-897.

75 Kim, Min-Sik, and Akhilesh Pandey. "Electron transfer dissociation mass spectrometry in proteomics." *Proteomics*, 12 (**2012**): 530-542.

76 Elviri, Lisa. "ETD and ECD mass spectrometry fragmentation for the characterization of protein post translational modifications." *Tandem Mass Spectrometry-Applications and Principles,* Jeevan K. Prasain (Ed.), InTech (**2012**): 161-178.

77 Quan, Lingdong, and Miao Liu. "CID, ETD and HCD fragmentation to study protein post-translational modifications." *Modern Chemistry & Applications*, 1:e102 (**2012**): 1-2.

78 Shukla, Anil K., and Jean H. Futrell. "Tandem mass spectrometry: dissociation of ions by collisional activation." *Journal of Mass Spectrometry*, 35 (**2000**): 1069-1090.

79 Sleno, Lekha, and Dietrich A. Volmer. "Ion activation methods for tandem mass spectrometry." *Journal of Mass Spectrometry*, 39 (**2004**): 1091-1112.

80 Smith, Richard D., Joseph A. Loo, Charles J. Barinaga, Charles G. Edmonds, and Harold R. Udseth. "Collisional activation and collision-activated dissociation of large multiply charged polypeptides and proteins produced by electrospray ionization." *Journal of the American Society for Mass Spectrometry*, 1 (**1990**): 53-65.

81 Downard, Kevin M., and Klaus Biemann. "The effect of charge state and the localization of charge on the collision-induced dissociation of peptide ions." *Journal of the American Society for Mass Spectrometry*, 5 (**1994**): 966-975.

82 Memboeuf, Antony, Andreas Nasioudis, Sergio Indelicato, Ferenc Pollreisz, Akos Kuki, Sándor Kéki, Oscar F. Van den Brink, Károly Vékey, and László Drahos. "Size effect on

fragmentation in tandem mass spectrometry." *Analytical Chemistry*, 82 (**2010**): 2294-2302.

83 Revercomb, H. E., and Edward A. Mason. "Theory of plasma chromatography/gaseous electrophoresis. Review." *Analytical Chemistry*, 47 (**1975**): 970-983.

84 Verbeck, G. F., B. Ruotolo, H. Sawyer, K. Gillig, and D. Russell. "A fundamental introduction to ion mobility mass spectrometry applied to the analysis of biomolecules." *Journal of Biomolecular Techniques*, 13 (**2002**): 56-61.

85 Cumeras, Raquel, Eduard Figueras, C. E. Davis, Jörg Ingo Baumbach, and Isabel Gracia. "Review on ion mobility spectrometry. Part 1: current instrumentation." *Analyst*, 140 (**2015**): 1376-1390.

86 Creaser, Colin S., John R. Griffiths, Claire J. Bramwell, Sadaf Noreen, Carol A. Hill, and CL Paul Thomas. "Ion mobility spectrometry: a review. Part 1. Structural analysis by mobility measurement." *Analyst*, 129 (**2004**): 984-994.

87 Uetrecht, Charlotte, Rebecca J. Rose, Esther van Duijn, Kristina Lorenzen, and Albert JR Heck. "Ion mobility mass spectrometry of proteins and protein assemblies." *Chemical Society Reviews*, 39 (**2010**): 1633-1655.

88 Kohtani, Motoya, Thaddeus C. Jones, Jean E. Schneider, and Martin F. Jarrold. "Extreme stability of an unsolvated α-helix." *Journal of the American Chemical Society*, 126 (**2004**): 7420-7421.

89 Barran, Perdita E., Nick C. Polfer, Dominic J. Campopiano, David J. Clarke, Patrick RR Langridge-Smith, Ross J. Langley, John RW Govan et al. "Is it biologically relevant to measure the structures of small peptides in the gas-phase?." *International Journal of Mass Spectrometry*, 240 (**2005**): 273-284.

90 McLean, John A., Brandon T. Ruotolo, Kent J. Gillig, and David H. Russell. "Ion mobility–mass spectrometry: a new paradigm for proteomics." *International Journal of Mass Spectrometry*, 240 (**2005**): 301-315.

91 Jackson, Shelley N., Michael Ugarov, Thomas Egan, Jeremy D. Post, Denis Langlais, J. Albert Schultz, and Amina S. Woods. "MALDI-ion mobility-TOFMS imaging of lipids in rat brain tissue." *Journal of Mass Spectrometry*, 42 (**2007**): 1093-1098.

92 Lintonen, Tuulia PI, Paul RS Baker, Matti Suoniemi, Baljit K. Ubhi, Kaisa M. Koistinen, Eva Duchoslav, J. Larry Campbell, and Kim Ekroos. "Differential mobility spectrometry-driven shotgun lipidomics." *Analytical Chemistry*, 86 (**2014**): 9662-9669.

93 Paglia, Giuseppe, Michal Kliman, Emmanuelle Claude, Scott Geromanos, and Giuseppe Astarita. "Applications of ion-mobility mass spectrometry for lipid analysis." *Analytical and Bioanalytical Chemistry*, 407 (**2015**): 4995-5007.

94 Lanucara, Francesco, Stephen W. Holman, Christopher J. Gray, and Claire E. Eyers. "The power of ion mobility-mass spectrometry for structural characterization and the study of conformational dynamics." *Nature Chemistry*, 6 (**2014**): 281-294.

95 *Ion Max and Ion Max-S API Source Hardware Manual Revision B* (**2006**).

96 *Bruker Daltonik GmbH Autoflex II Operator Manual* (**2004**).

97 *Waters Synapt G2-s Mass Spectrometer Operator's Overview and Maintenance Guide Revision C* (**2013**).

Chapter three: Understanding the role of lysophosphatidylcholine (LPC) and diacylphosphatidylcholine (PC) in the lipidation of melittin

Mimicking natural membranes provides a feasible way to study protein/peptide-membrane interactions. This *in vitro* interaction has been well documented by monitoring non-enzymatic fatty acyl transfer from liposomal diacylphospholipids to the N-terminus and the side chains of internal lysine of the membrane active peptide melittin.[1-3] Lysophospholipid, however, is a by-product in melittin lipidation and this study seeks to understand whether melittin could undergo fatty acylation from these monoacylphospholipids. Since both diacyl- and monoacylphospholipids (lysophospholipids) share ester-linked fatty acyl chains, it is hypothesised that both lipid classes could follow identical lipidation mechanisms. LC-MS has been used to study the reactions between melittin and diacylphospholipid and/or lysophospholipid. The results of this reaction has shown that (i) single and multiple acyl chains transfer in a non-enzymatic process; (ii) single acyl transfer is much faster than the second and third acyl transfer; (iii) transfer from lysophospholipid is relatively faster than diacylphospholipid; (iv) there is a competition between N-terminus *vs* K23 site of acylation and palmitoylation *vs* oleoylation modification.

3.1. Phase behaviour of the lipid systems studied

Different phase behavior and the molecular shape of the lipids will have an effect upon their dispersion in the aqueous phase, this depends on several factors such as their molecular geometry and the way that multiple lipid molecules organize themselves (see chapter one, section 1.3.1.1.1 for more details). Lysophosphatidylcholines (LPC) self-assemble into micelles above the critical micelle concentration (CMC),[4-8] while diacylphosphatidylcholines (PC) adopt lipid-bilayer phase[5,7] (see Table 1.4, for the calculated CMC for each lysophospholipid (LPL)).

Results reported by Van Echteld *et al.* from NMR studies[5,9] suggest three distinct types of phase behavior occur for lipids upon the addition of PPC and/or OPC to each of DPPC and DOPC. This includes bilayer, micelle and mixed micelle-bilayer (Table 3.1). Similar results were also presented by Pantusa *et al.* from electron spin resonance (ESR) and spectrophotometric measurements.[10] It is interesting to see that the influence of LPC incorporation into the membrane on the phase behavior lipid is mainly related to the type and amount added as well as the type of PC and the phase state.[11-15] To follow acyl transfer from free LPCs, and upon their mixing with PCs to melittin, different lipid systems at different ratios were applied, as shown in Table 3.2. Based on the results provided in Table 3.1, the expected phase behavior of the different lipid systems applied in this study (Table 3.2) will be described as follows at 25 °C: micelle system (red); liposomal lipid-bilayer (membrane) phase (green); a new system of mixed micelle-bilayer (blue).

Table 3.1. **The phase behaviours in different lipid systems created with data obtained by NMR spectroscopy (Van Echteld *et al.*)[5].**

Lipid System Composition	Lipid System Phase Behaviour	Temperature* (°C)
PPC + DOPC	100% bilayer (0% micelle) at up to 35 mole% PPC	Independent on temperature change
	≈ 50% bilayer (mixed micelle-bilayer) at 50 mole% PPC	
	0% bilayer (100% micelle) above 50 mole% PPC	
OPC + DOPC	100% bilayer (0% micelle) at 0 mole% OPC	
	≈ 65-80% bilayer up to 40 mole% OPC	
	≈ 100% bilayer at 50 mole% OPC	
	0% bilayer (100% micelle) at or above 75 mole% OPC	
PPC + DPPC	100% bilayer (0% micelle) at up to 60 mole% PPC	25 (< Tm)
	≈ (75% bilayer -0% bilayer) above 60 mole% PPC	
	0% bilayer (100% micelle) at 100 mole% PPC	
	100% bilayer (0% micelle) at up to 25 mole% PPC	45 (> Tm)
	≈ (70% bilayer-10% bilayer) from 35- 50 mole% PPC	
	0% bilayer (100% micelle) above 50 mole% PPC	
OPC + DPPC	100% bilayer (0% micelle) at 0 mole% OPC	25 (< Tm)
	≈ (70% -10% bilayer) at up to 20 mole% OPC	
	0% bilayer (100% micelle) above 25 mole% OPC	
	100% bilayer (0% micelle) at 0 mole% OPC	45 (> Tm)
	≈ 50% bilayer (mixed micelle-bilayer) at 25-30 mole% OPC	
	100% bilayer at 50 mole% OPC	
	0% bilayer (100% micelle) above 50 mole% OPC	

*Phase transition temperature (Tm) is -16.5 °C and 41.3 °C for DOPC16,17 and DPPC18-20 respectively.

Table 3.2. **The mole ratio for each lipid mixed with melittin in the reaction medium. The lipid abbreviations include 1,2-dioleoyl-phosphatidylcholine (DOPC), 1,2-dipalmitoyl-phosphatidylcholine (DPPC), 1-oleoyl-2-hydroxy-phosphatidylcholine (OPC) and 1-palmitoyl-2-hydroxyl-phosphatidylcholine (PPC). Highlighted columns in red indicate micelle system; green for membrane phase; blue for mixed micelle-bilayer system.**

Lipid System	PPC:OPC	DOPC	DPPC	DOPC:PPC	DPPC:OPC
%Lipid	50:50	100	100	25:75	25:75
	100:0 or 0:100			50:50	50:50
				75:25	75:25

3.2. Reaction of melittin with lysophospholipids

The proposed mechanism for the aminolysis of ester-linked fatty acyl is shown in Figure 3.1. The reaction shows the formation of acyl-melittin as a main product, leaving the phosphatidylcholine moiety (glycerol-PC) as a by-product. The incubated reaction mixture was separated by reverse phase LC and followed by MS analysis.

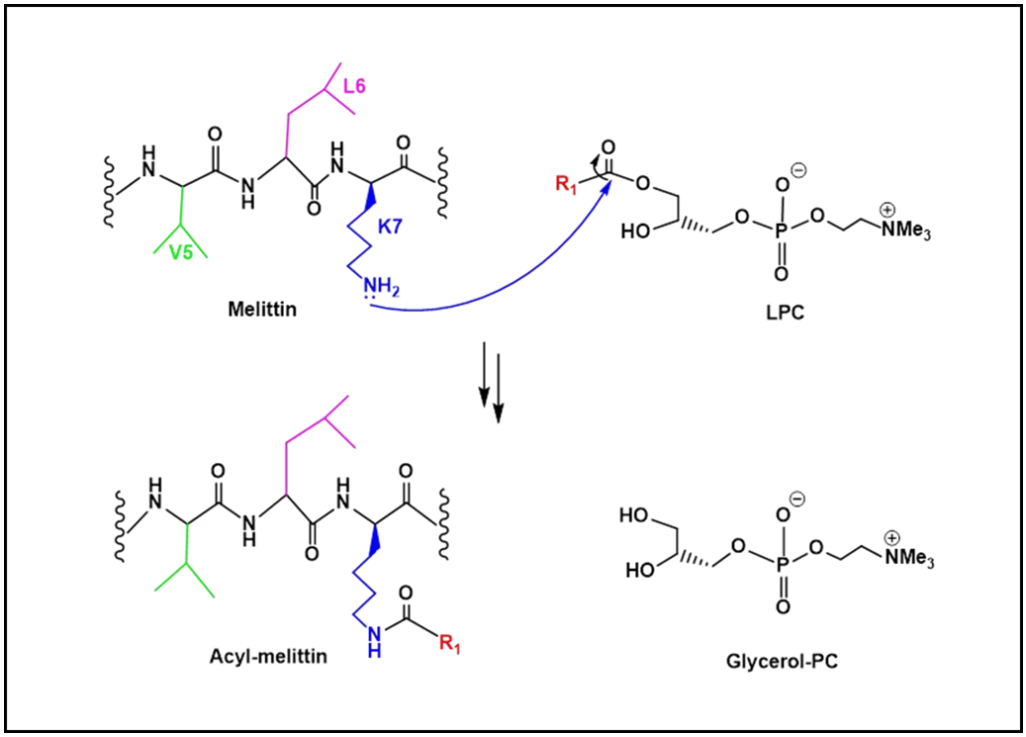

Figure 3.1. **Melittin aminolysis reaction with the *sn*-1 glyceryl ester of the LPC.**

3.2.1. Reaction of synthetic melittin (SynM) with oleoylphosphatidylcholine (OPC)

The analysis of lipidation products following the incubation of SynM with 100% OPC for 24 h is shown in Figure 3.2. The incubations were done at a concentration of 0.65 mM for OPC, which is well above critical micelle concentration (CMC) (see Table 1.4 for LPLs CMC values). SynM with single oleoylation ($SynM_{ole}$) is clearly visible within the RT range 8.0-10.0 min. The longer retention of $SynM_{ole}$ compared to un-reacted SynM highlights their increasing hydrophobicity. The extracted ion chromatogram for [$SynM_{ole}$ +

$4H]^{4+}$ at *m/z* 778.51 shows there are multiple co-eluting peaks around this RT (Figure 3.2 A), resulting from oleoyl modification of different amino acid (AA) residues: N-terminal amine and the three lysine with different reactivities.[1-3] The two most reactive sites were recorded as N-terminus and K23.[2,3] This is also proposed herein indirectly through LC-MS by observing some diagnostic in-source product ions around this RT, and instantly informative without the need for MS^2 analysis. Although, the instrument source conditions has been optimized in order to minimize in-source fragmentation.

The first eluted peak around 8.7 min (Figure 3.2 A, peak (i)) suggests K23 oleoylation due to the presence of some y-ion dissociations that still reside oleoyl modification in the C-terminal portion of the peptide at *m/z* 735.73 $[y24_{ole} + 4H]^{4+}$ and 944.12 $[y13_{ole} + 2H]^{2}$. These labile sites of the peptide backbone are the key points to assess which half of the peptide that resides the modification. The cleavage sites of melittin that correspond to b- and y-ions are shown in Figure 3.3. In addition, the in-source dissociation of $SynM_{ole}$ with the same cleavage sites were also observed around 8.9 min (Figure 3.2 A, peak (ii)), but at *m/z* 669.66 $[y24 + 4H]^{4+}$ and 812.00 $[y13 + 2H]^{2+}$, correspond to the unmodified C-terminal portion and thus N-terminus oleoylation. It is interesting to know that the exact elution time for the in-source product ions and the intact ions of $SynM_{ole}$ excludes the possibility of the presence of in-solution dissociated peptides. In addition, there are two peaks at RT 11.3 and 11.5 min respectively, both corresponding to $[M + H]^{+}$ of OPC and reflect the acyl group mobility between *sn*-1 and *sn*-2 positions of the LPC in a solution.[2]

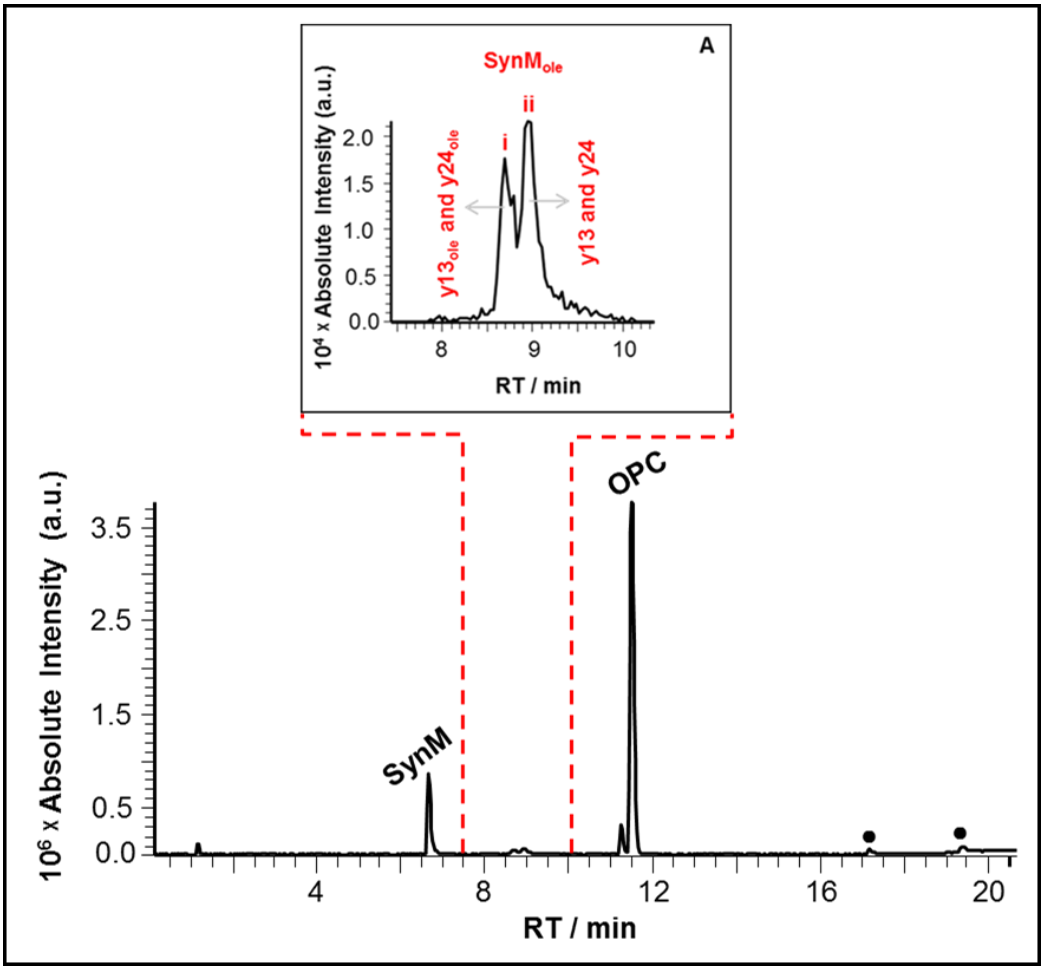

Figure 3.2. **Total ion chromatogram (TIC) for SynM/OPC incubated for 24 h at 37 °C, analysed on the LTQFT using LC-MS Method-II (see section 8.1.2.1.1). The inserted panel (A), is the extracted ion chromatogram (EIC) of *m/z* 778.51 (*z*=4) for single oleoylation (C18:1) product SynM$_{ole}$, different acylation sites were labelled as A(i) and A(ii). The organic impurities are indicated (black dots)**

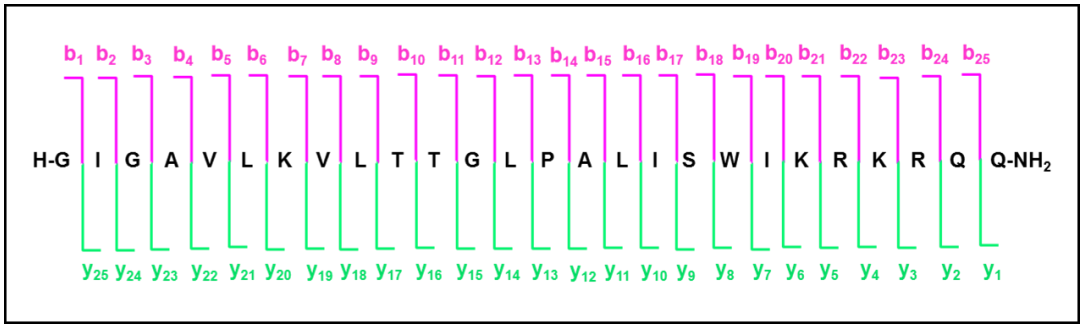

Figure 3.3. **The product ions nomenclature for melittin during amide bond cleavage of the peptide to yield b- and y-ions.**

The mass spectra showing the different charge states (*z*=3-5) for $SynM_{ole}$, and the deconvoluted spectrum are given in Figure 3.4.

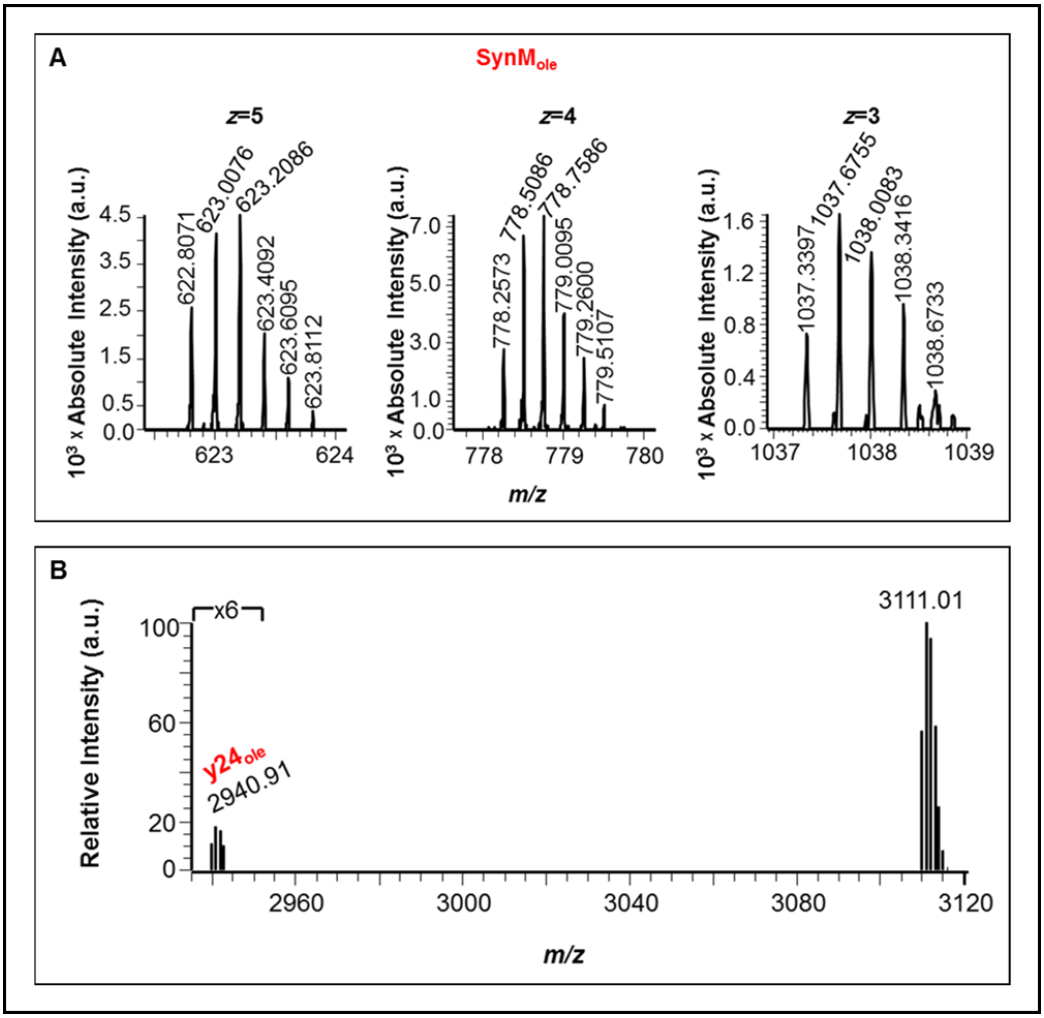

Figure 3.4. **(A) Mass spectra showing the different charge states (*z*=3-5) for $SynM_{ole}$; (B) deconvoluted mass spectrum showing $[M + H]^+$.**

The sample incubation was performed for a range of different periods of time and each followed by LC-MS analysis. Interestingly, $SynM_{ole}$ was not the only observed acylation product, but over longer incubation times the transfer of the second oleoyl ($SynM_{2ole}$) and third oleoyl ($SynM_{3ole}$) products were also detected. This is evident in SynM/OPC incubation over 168 h, as shown in Figure 3.5. This clearly shows the formation of $SynM_{ole}$ first, followed by $SynM_{2ole}$ and then $SynM_{3ole}$ modifications. Moreover, at RT 9.5-11.5 min, albeit eluting very close to the LPC, there is clear evidence for

double oleoylation (Figure 3.5 B, EIC of $[M + 4H]^{4+}$ at *m/z* 844.82) and RT 17.8-19.0 min illustrates the transfer of a third oleoyl group to SynM (Figure 3.5 C, EIC of $[M + 4H]^{4+}$ at *m/z* 910.88). It is interesting to see that even greater hydrophobicity by adding the second and third acyl chains is consistent with increasing the RT for $SynM_{2ole}$ and $SynM_{3ole}$ over 11 min and 18 min respectively. In addition, a peak at RT 17.0-18.5 min (Figure 3.5 B, EIC of $[M + 4H]^{4+}$ at *m/z* 844.82) corresponds to $SynM_{2ole}$. While retention time is consistent with the elution of $SynM_{3ole}$, the observed *m/z* value indicates in-source dissociation of the triple oleoylation species is occurring. The third oleoyl modification is clearly very labile and therefore lost, and this is most likely related to the location of the modification or the tertiary structure of the triple modified peptide. Further, the multiple co-eluting peaks are still indicative of different nucleophilic reactivity on SynM towards ester-linked fatty acyl, as reported in previous study[1-3].

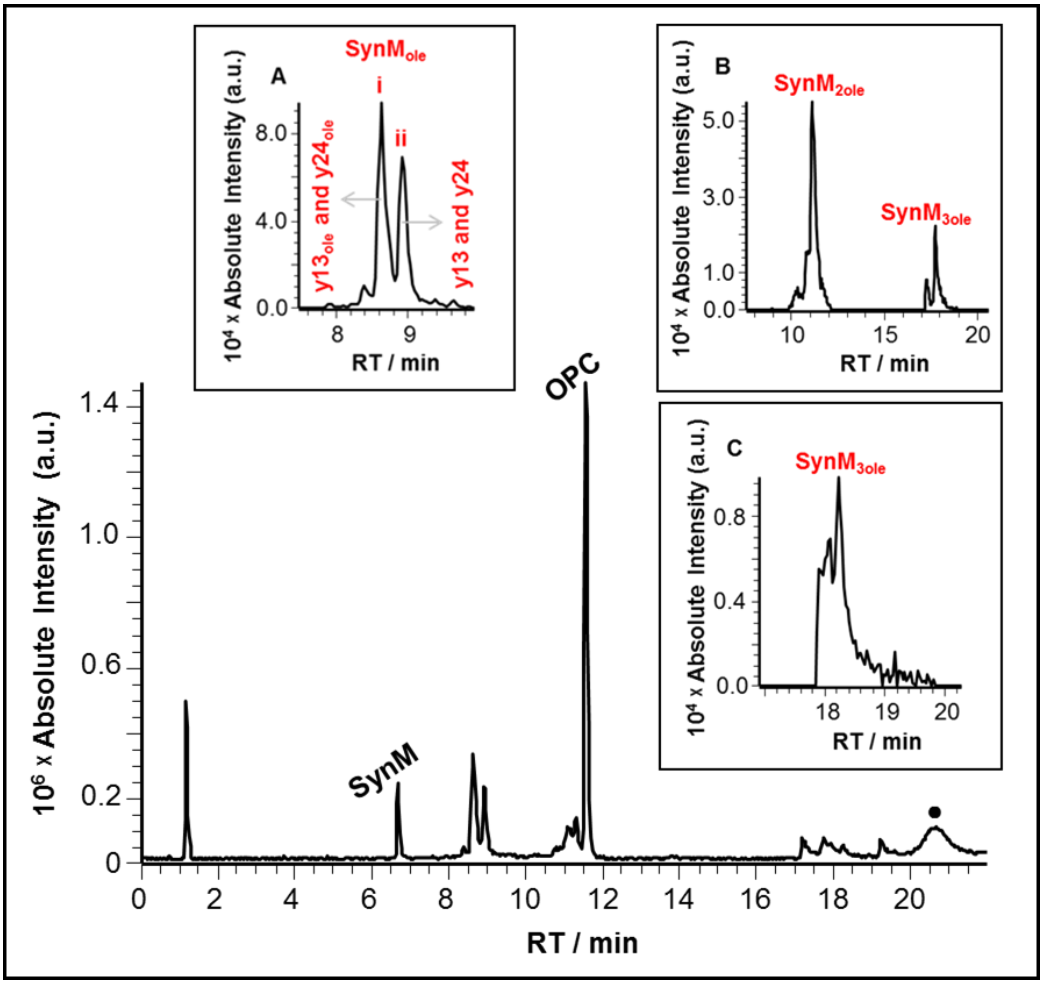

Figure 3.5. **The main chromatogram represents TIC for SynM/OPC incubated for 168 h at 37 °C, analysed on the LTQFT using LC-MS Method-II (see section 8.1.2.1.1). The insert panels are the EIC of (A) *m/z* 778.51 (*z*=4) for SynM$_{ole}$; (B) *m/z* 844.82 (*z*=4) for SynM$_{2ole}$ and labile SynM$_{3ole}$; (C) *m/z* 910.88 (*z*=4) for SynM$_{3ole}$. Single acylation sites labelled as A(i) for K23 site of oleoylation and A(ii) for N-terminus oleoylation. The organic impurities are indicated (black dots).**

All the modifications on SynM, single-, double-, and triple oleoylation, were observed as different charge states. The strongest abundant charge state for all species is for *z*=4, Figure 3.6 top (A-D); the corresponding deconvoluted spectra, deconvoluted to the protonated species are shown in Figure 3.6 bottom (A-D). The labile site of the peptide backbone is again recorded by observing y13$_{ole}$ and y24$_{ole}$ in-source product ions (see Figure 3.3), indicative of K23 oleoylation (Figure 3.6 top A). These product ions were significantly found over 8.6 min for peak (i), Figure 3.5 A(i), which is the most abundant peak for SynM$_{ole}$. However, y13 and y24 in-source product ions

that show N-terminus oleoylation were confirmed as abundant ions over 8.9 min for peak (ii), Figure 3.5 A(ii).

Calculating the area under the peak for each of proposed oleoylated sites K23 and N-terminus showed that the order of reactivity is K23 > N-terminus by the ratio of 1.5:1, for contributing OPC in the acylation process. While this reactivity was shown to be in the order of N-terminus > K23, for the contribution of liposomal PC lipids.[2,3] This suggests OP's greater reactivity towards K23. However, the effect of co-eluting chromatographic peaks for melittin oleoylation on different sites and the peak tailing make the precise quantification analysis hard to follow. Further, the presence of $SynM_{ole}$ in sufficient abundance that when it fragments along the peptide backbone there are enough product ions to detect, while for $SynM_{2ole}$ and $SynM_{3ole}$ it is suspected that there are not enough product ions to detect.

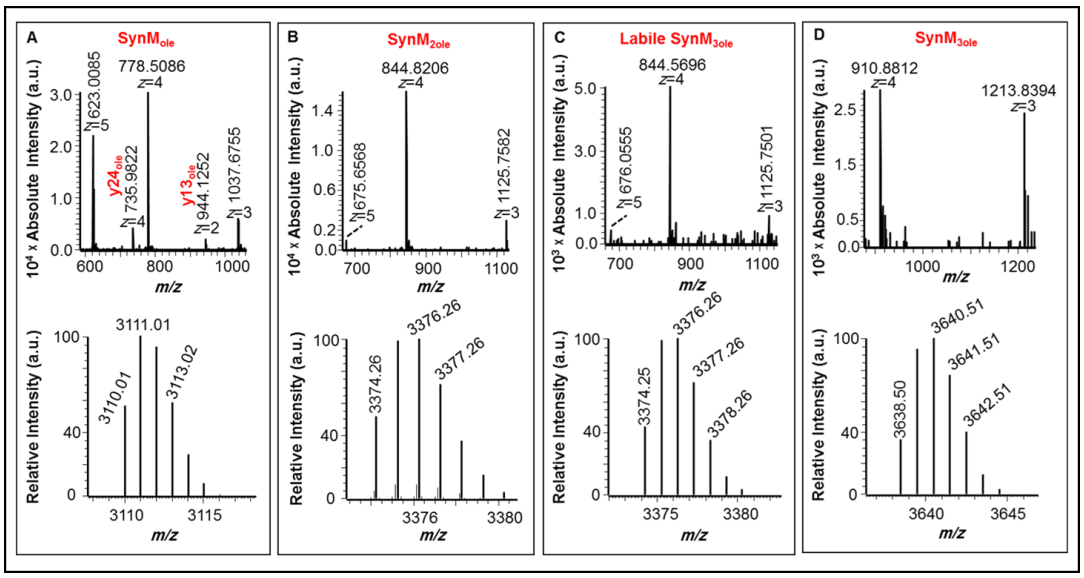

Figure 3.6. **Analysis of SynM/OPC incubation over 168 h at 37 °C. (A) Results for $SynM_{ole}$ around RT 8.6 min, (top) mass spectrum and (bottom) deconvoluted to $[M + H]^+$. (B) Results for $SynM_{2ole}$ around RT 11.1 min, (top) mass spectrum and (bottom) deconvoluted to $[M + H]^+$. (C) Results for labile $SynM_{3ole}$ around RT 17.8 min, (top) mass spectrum and (bottom) deconvoluted to $[M + H]^+$. (D) Results for $SynM_{3ole}$ around RT 18.2 min, (top) mass spectrum and (bottom) deconvoluted to $[M + H]^+$.**

The time dependence of acyl transfer is shown in Figure 3.7. The results show a continuous decrease in the amount of SynM throughout the

acylation process, while a rapid increase in the rate of single acylation is evident up to 48 h incubation then slows down and starts to decrease afterwards. This decrease in oleoylation is consistent with the addition of the second and third oleoyl fatty acyl chains to the peptide at the later incubation time. Overall, these data provide the first reported evidence of melittin lipidation (single and multiple) by LPC via non-enzymatic acyl transfer mechanism.

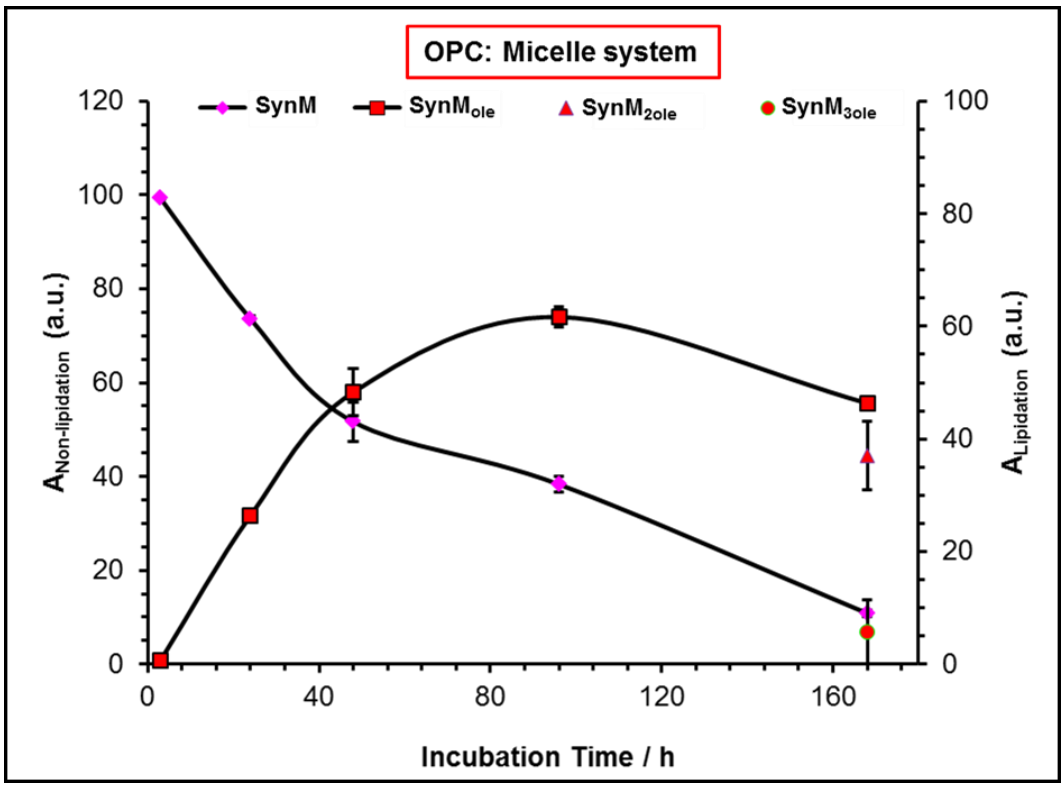

Figure 3.7. **The relationship between the peak area (A) for non-acylated SynM and acylated SynM with the incubation time in the OPC micelle system. Errors are plotted as the standard error of mean (SEM) of normalised peak area (n=2). The normalisation of $SynM_{ole}$ peak area was performed as follows: $\%SynM_{ole}$ = peak area $SynM_{ole}$/total peak area of (SynM + $SynM_{ole}$ + $SynM_{2ole}$ + $SynM_{3ole}$) × 100, the same calculation was also applied for the other species. Peak areas were measured from EIC over all observed charge states at each point of the incubation.**

3.2.2. Reaction of SynM with palmitoylphosphatidylcholine (PPC)

The transfer of palmitoyl fatty acyl from PPC to SynM was also examined over different incubation times (Figure 3.8). It is interesting to see that by using PPC the addition of the second and third acyl chains are very slow even over 168 h. Consequently, the amount of $SynM_{pal}$ is steadily increasing over time rather than decreasing as was evident for SynM/OPC system (see Figure 3.7).

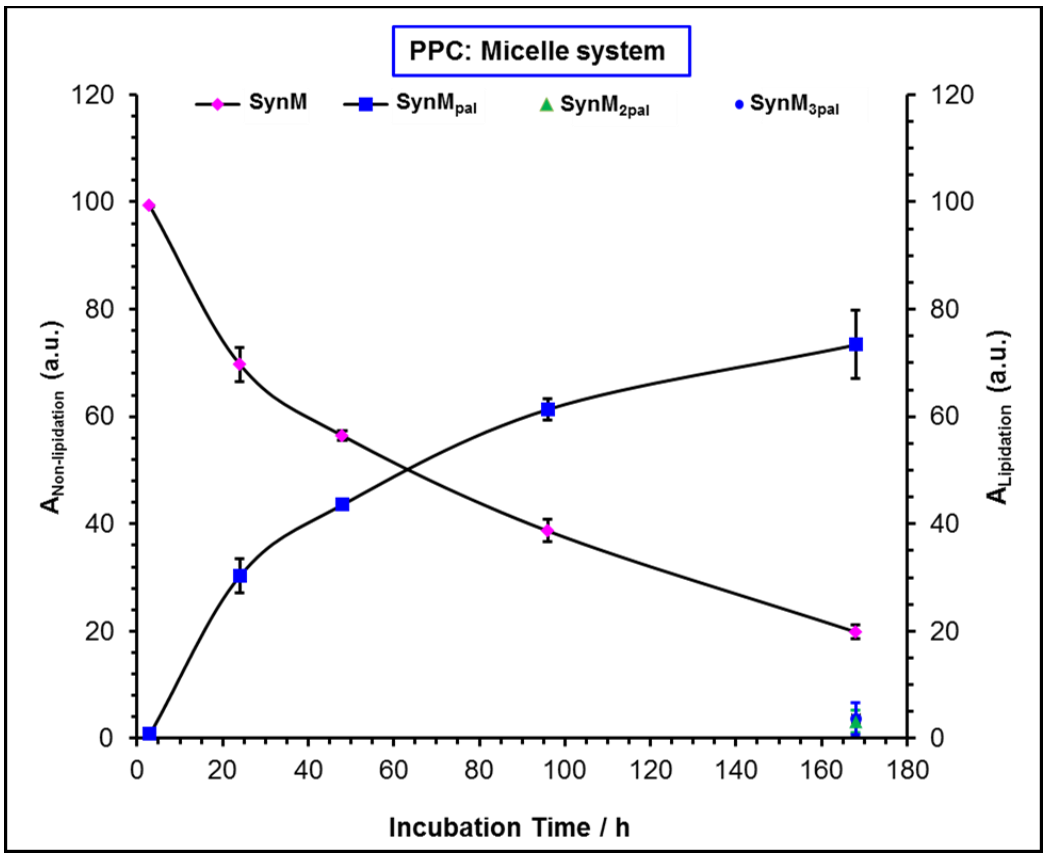

Figure 3.8. **The relationship between the peak area (A) for non-acylated SynM and acylated SynM with the incubation time in the PPC micelle system. Errors are plotted as the standard error of mean (SEM) of normalised peak area (n=2). Peak areas were measured from EIC over all observed charge states at each point of the incubation. The normalisation of peak areas were performed in the same way as described in Figure 3.7.**

The observation of significant palmitoyl transfer following SynM/PPC incubation for 168 h the LC-MS analyses focused on samples obtained under these conditions. As with SynM/OPC, there are multiple co-eluting peaks observed for $SynM_{pal}$ (Figure 3.9 A, EIC for $[M + 4H]^{4+}$ at *m/z* 772.00), and have the same retention time as $SynM_{ole}$. The in-source product ions of y-ion dissociation (see Figure 3.3) for $SynM_{pal}$ at G3 ($y24/y24_{pal}$) and P14 ($y13/y13_{pal}$) suggest K23 palmitoylation for the peak eluted at 8.6 min (Figure 3.9 A(i), *m/z* 729.23 $[y24_{pal} + 4H]^{4+}$ and 931.12 $[y13_{pal} + 2H]^{2+}$) and N-terminus palmitoylation for the peak eluted at 8.9 min (Figure 3.9 A(ii), *m/z* 669.67 $[y24 + 4H]^{4+}$ and 812.00 $[y13 + 2H]^{2+}$). The relative reactivity for both lipidated sites of N-terminus and K23 were shown to be in the ratio of 1:1 by PPC. Likewise, $SynM_{2pal}$ was also observed (Figure 3.9 B, EIC for $[M + 4H]^{4+}$ at *m/z* 831.56). There is only indirect evidence for $SynM_{3pal}$ at retention time 17-19 min (Figure 3.9 B, EIC of $[M + 4H]^{4+}$ at *m/z* 831.56). This is because the *m/z* at this RT indicates $SynM_{2pal}$, but it is known from SynM/OPC that at this RT both intact $SynM_{3ole}$ and $SynM_{2ole}$ with the labile nature of $SynM_{3ole}$ were also observed (see Figure 3.5). It is reasonable to extrapolate those findings here and propose that for SynM/PPC at RT 17-19 min $SynM_{3pal}$ is produced but could not be observed herein as the intact species ($SynM_{3pal}$) but undergoes in-source dissociation to lose one palmitoyl acyl chain and thus leaves $SynM_{2pal}$.

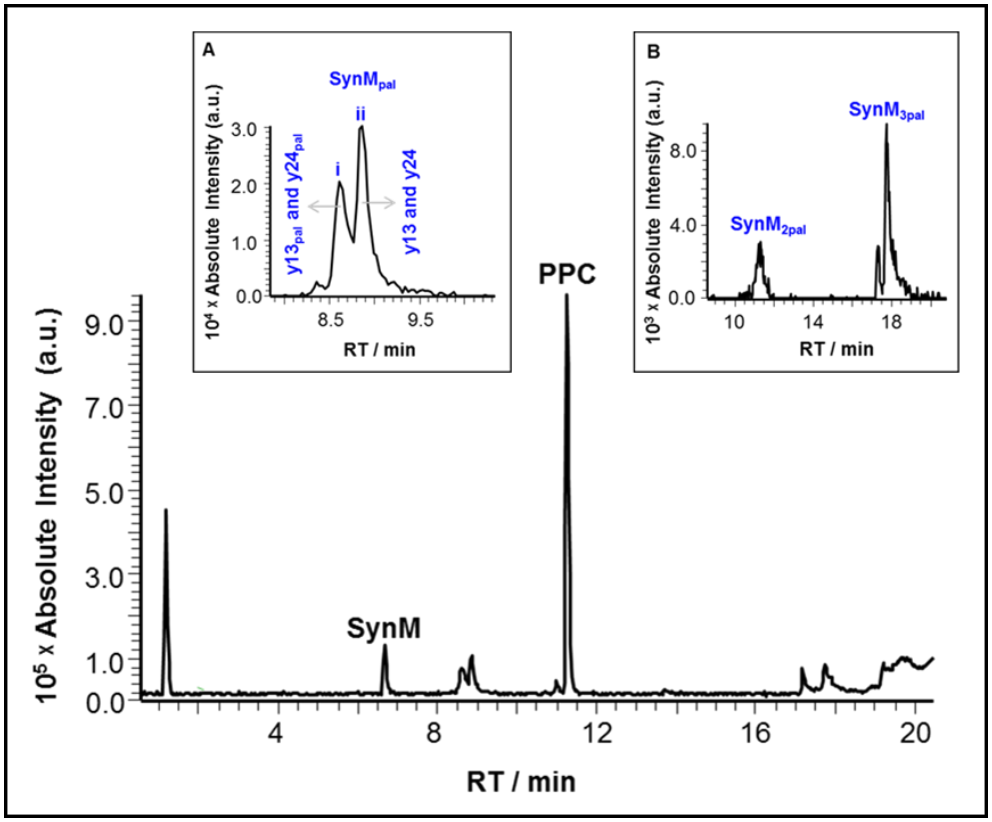

Figure 3.9. **The main chromatogram represents TIC for SynM/PPC incubated over 168 h at 37 °C, analysed on the LTQFT using LC-MS Method-II (see section 8.1.2.1.1). The insert panels are the EIC of (A) *m/z* 772.00 (*z*=4) for SynM$_{pal}$; (B) *m/z* 831.56 (*z*=4) for SynM$_{2pal}$ and labile SynM$_{3pal}$. Single acylation sites labelled as A(i) for K23 palmitoylation and A(ii) for N-terminus palmitoylation.**

The mass spectra for all palmitoyl additions show the expected range of charge states, Figure 3.10 top (A-C); the corresponding deconvoluted spectra, deconvoluted to the protonated species are shown in Figure 3.10 bottom (A-C). Ions with four protonation sites are still favored over other charge state distributions. In summary, the results strongly confirm the contribution of LPC in non-enzymatic peptide lipidation and the formation of single acylation first then followed by multiple acylation.

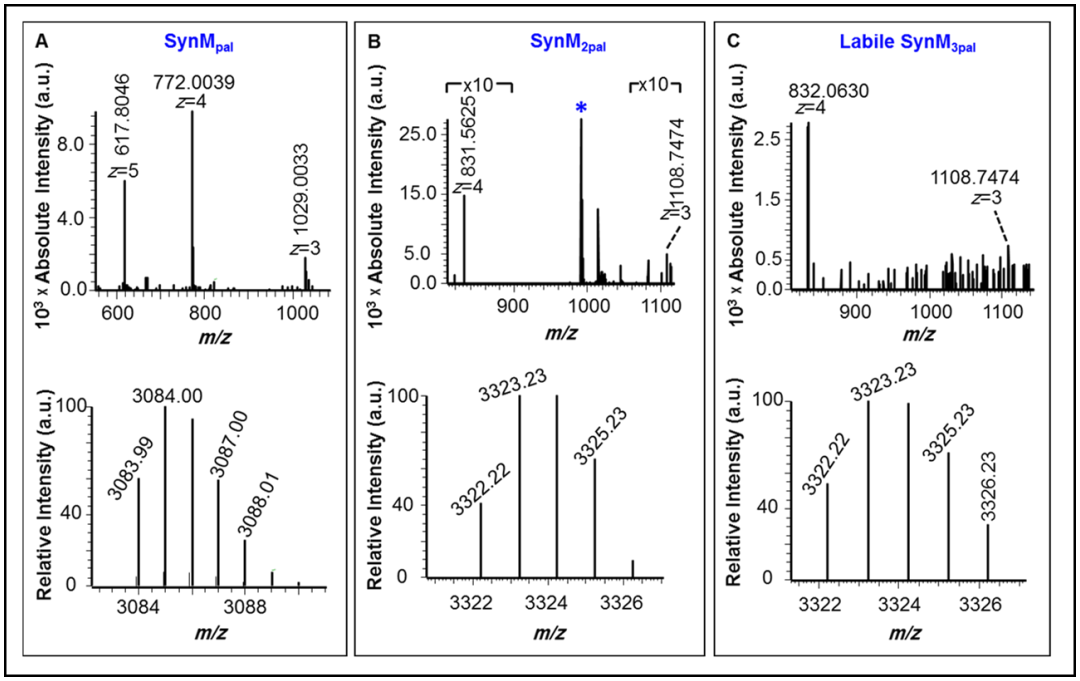

Figure 3.10. **Analysis for SynM/PPC incubated for 168 h at 37 °C. (A) Results for SynM$_{pal}$ around RT 8.9 min, (top) mass spectrum and (bottom) deconvoluted to [M + H]$^+$. (B) Results for SynM$_{2pal}$ around RT 11.2 min, (top) mass spectrum and (bottom) deconvoluted to [M + H]$^+$. The labelled peak with the asterisk represents [PPC + H]$^+$ overlapping with SynM$_{2pal}$. (C) Results for SynM$_{3pal}$ around RT 17.7 min, (top) mass spectrum and (bottom) deconvoluted to [M + H]$^+$.**

3.2.3. Reaction of SynM with PPC:OPC mixtures

The direct competition between LPCs was examined by incubating SynM with 50:50 OPC:PPC for 168 h (Figure 3.11). The two most abundant acylated peaks at 8.6 min and 8.9 min are labelled as K23 and N-terminus respectively. This has been confirmed by performing MS^2 on *m/z* 772.0 and 778.5, for [SynM$_{pal}$ + 4H]$^{4+}$ and [SynM$_{ole}$ + 4H]$^{4+}$ respectively, as shown in Figures 3.12 and 3.13. Knowing that SynM$_{pal}$ *vs* SynM$_{ole}$ and acylation on N-terminus *vs* K23 are not completely separated chromatographically (Figure 3.11 A), peak areas were measured for each species separately. Results show that in a mixture of PPC:OPC the N-terminus of SynM is acylated preferentially by the ratio of 2:1 (N-terminus:K23) for both palmitoyl and oleoyl acyl chains. This is by assuming that both N-terminal and K23 acylated species ionise the same.

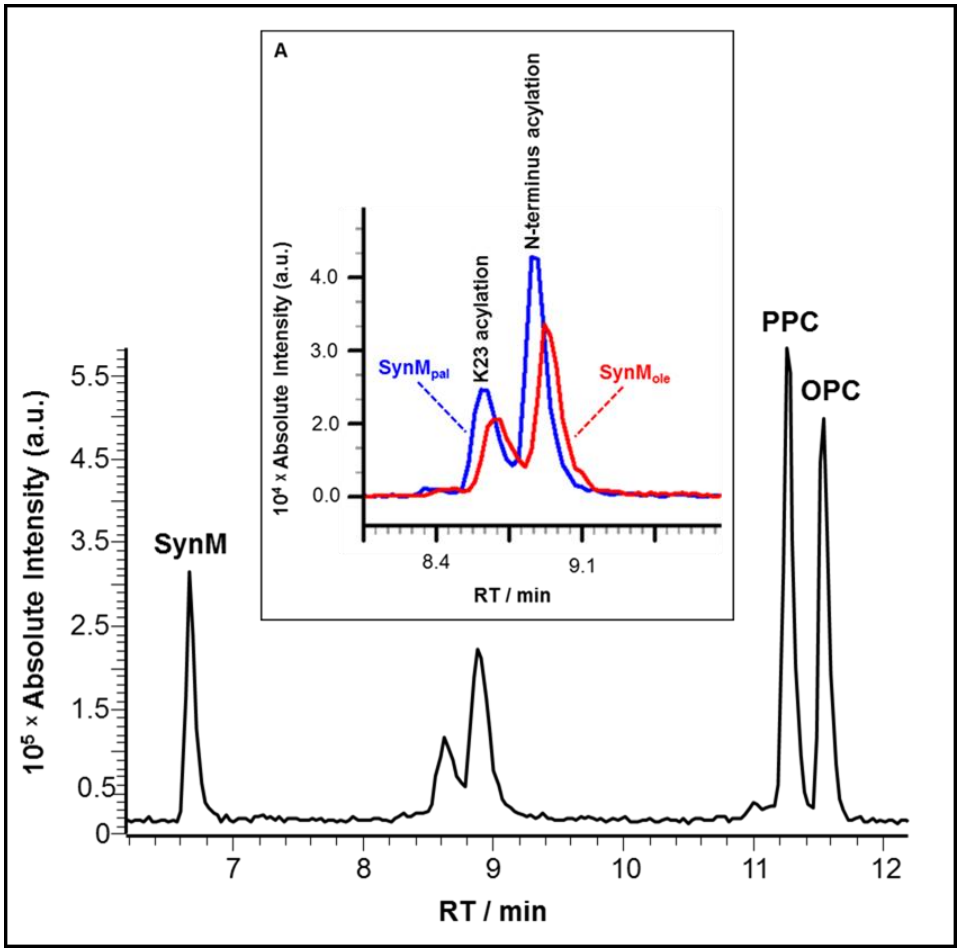

Figure 3.11. **The main chromatogram shows the TIC for SynM/50:50 PPC:OPC incubated for 168 h at 37 °C, analysed on the LTQFT using LC-MS Method-II (see section 8.1.2.1.1). The insert panel (A), is the EIC for SynM$_{pal}$ and SynM$_{ole}$.**

The product ions generated at 8.6 min of the chromatogram (Figure 3.12) for precursor ions SynM$_{pal}$ (Figure 3.12 A) and SynM$_{ole}$ (Figure 3.12 B) indicate acylation has taken place on K23. The most abundant product ions of y13$_{pal}$/y13$_{ole}$ at *m/z* 931.4/944.4 for $[M + 2H]^{2+}$ and y24$_{pal}$/y24$_{ole}$ at *m/z* 972.5/981.1 for $[M + 3H]^{3+}$ still indicate these sites of the peptide backbone as the most labile sites and thus efficiently produced during LC-MS^2.

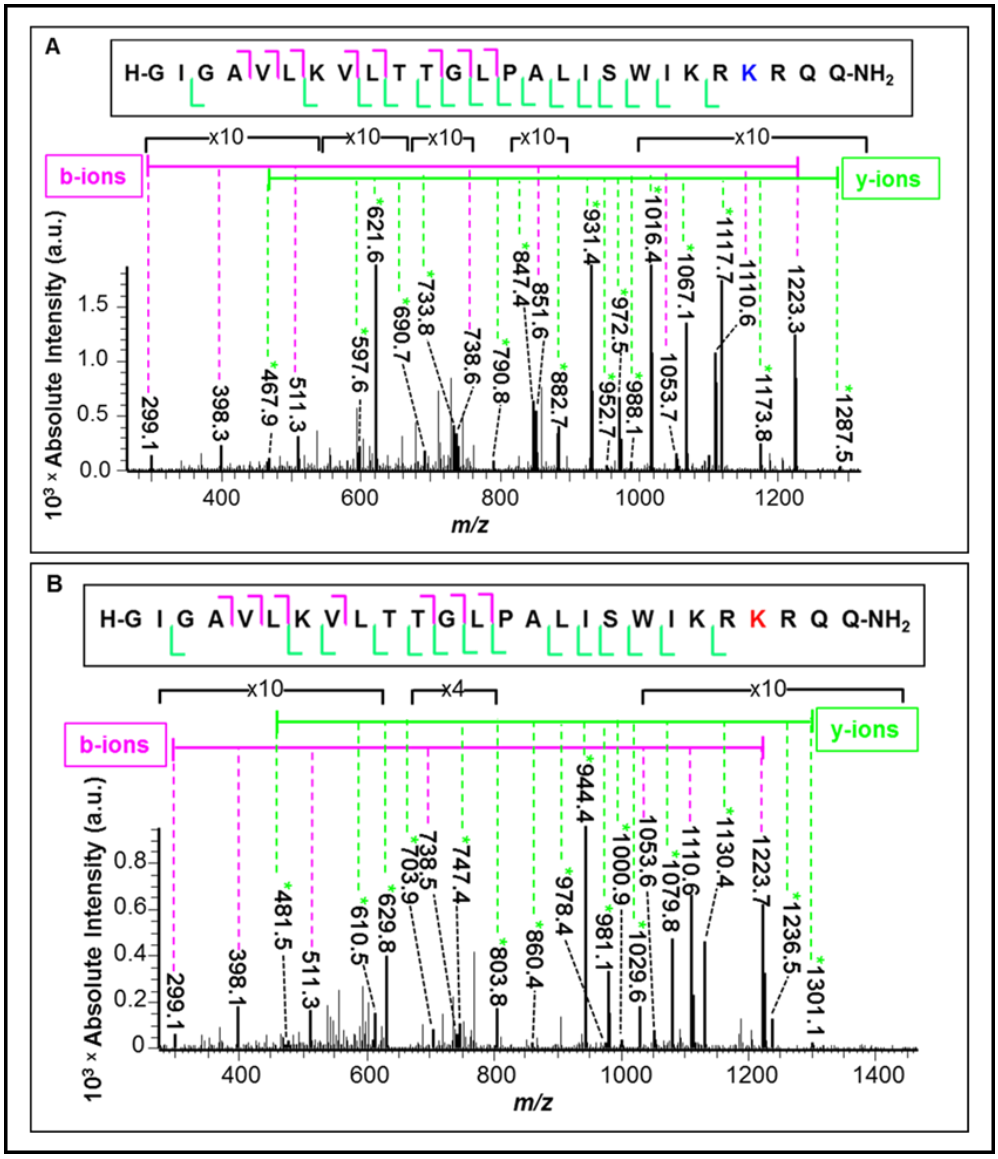

Figure 3.12. **LC-MS^2 spectra for SynM/50:50 PPC:OPC for the precursor ions at (A) *m/z* 772.00 for [SynM$_{pal}$ + 4H]$^{4+}$ and (B) *m/z* 778.51 for [SynM$_{ole}$ + 4H]$^{4+}$, which correspond in each case to single acylation observed at RT 8.6 min (see Figure 3.11 A). The sequence ladder of y-type and b-type ions is illustrated on each spectrum. The highlighted amino acid residues in blue and red indicate the K23 site of palmitoylation and oleoylation respectively. All b-ions are *z*=1, while y-ions are *z*=2 and/ or 3. Peptide fragments containing palmitoyl/oleoyl are marked with an asterisk.**

In addition, LC-MS^2 for precursor ions SynM$_{pal}$ (Figure 3.13 A) and SynM$_{ole}$ (Figure 3.13 B) at 8.9 min generate product ions that confirm N-terminus acylation. The most abundant product ion around this peak is still at *m/z* 812.2 $[M + 2H]^{2+}$ for y13 ion.

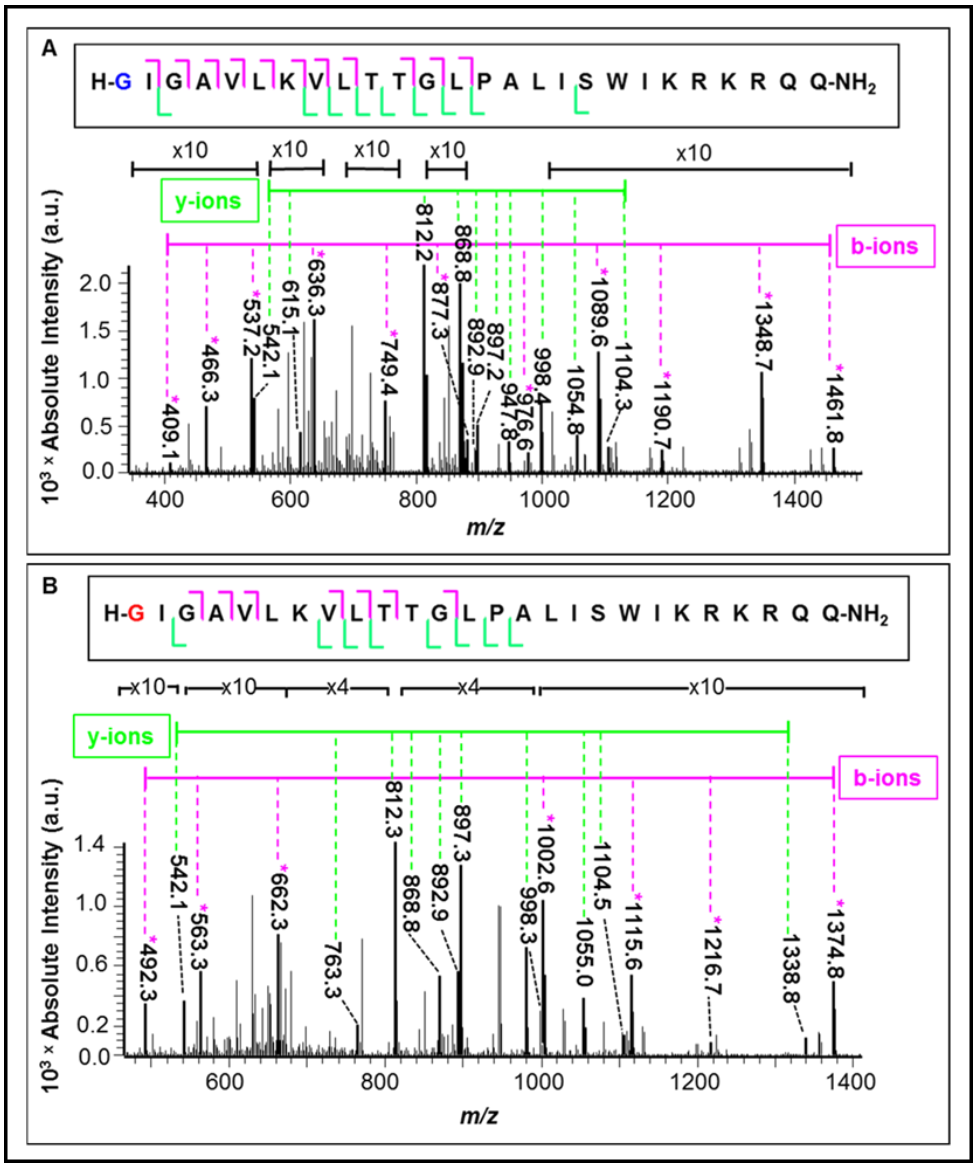

Figure 3.13. **LC-MS^2 spectra for SynM/50:50 PPC:OPC for the precursor ions at (A) *m/z* 772.00 for [SynM$_{pal}$ + 4H]$^{4+}$ and (B) *m/z* 778.51 for [SynM$_{ole}$ + 4H]$^{4+}$, which correspond in each case to single acylation observed at RT 8.9 min (see Figure 3.11 A). The sequence ladder of y-type and b-type ions is illustrated on each spectrum. The highlighted amino acid residues in blue and red indicate the N-terminus site of palmitoylation and oleoylation respectively. All b-ions are *z*=1, while y-ions are *z*=2 and/ or 3. Peptide fragments containing palmitoyl/oleoyl are marked with an asterisk.**

Moreover, monitoring the production of single acylation over different times clearly shows $SynM_{pal}$ is favoured over $SynM_{ole}$ through all incubation times and becomes particularly significant at longer incubation times (Figure 3.14). This indicates SynM has a greater reactivity with PPC than OPC. To conclude, the chemical identity of LPCs fatty acyl chain could play a role in easier palmitoyl transfer than oleoyl fatty acyl chain. Hence, PPC with shorter and saturated fatty acyl chain favors transfer to SynM over OPC with longer and unsaturated fatty acyl chain.

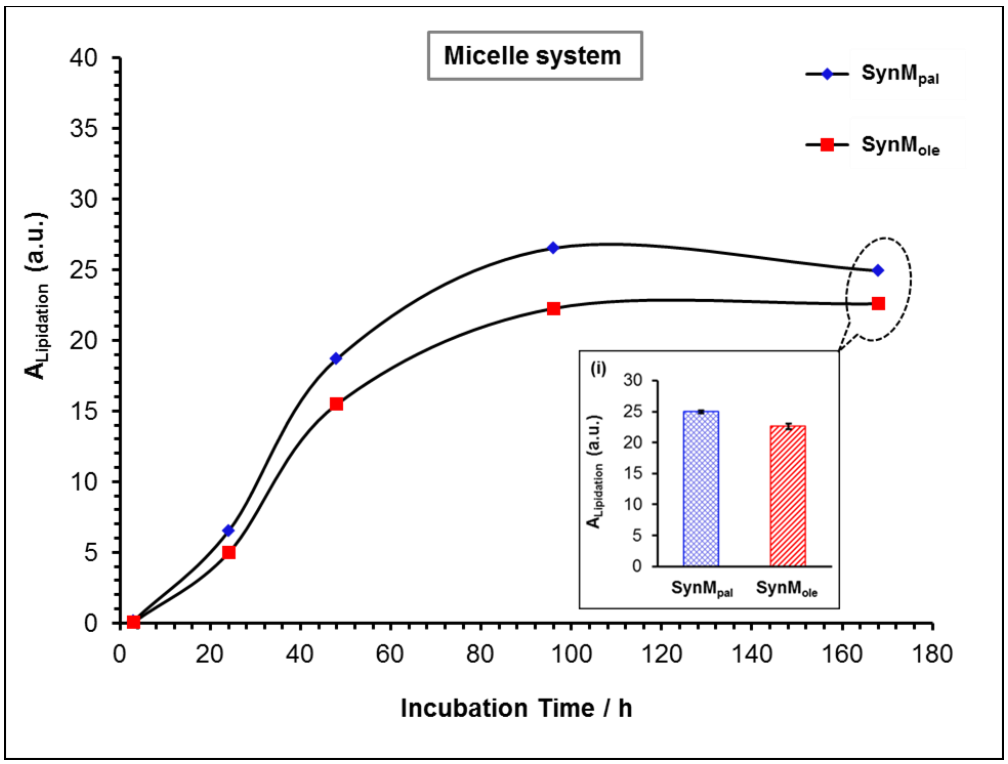

Figure 3.14. **The relationship between the peak area (A) for single acylation ($SynM_{pal}$, blue diamonds and $SynM_{ole}$, red square) and the incubation time for SynM/50:50 PPC:OPC at 37 °C. Peak areas were measured from EIC over all observed charge states at each point of the incubation. The normalisation of peak areas were performed in the same way as described in Figure 3.7. The insert panel (i) represents SynM acylation over 168 h of incubation; errors plotted as SEM of normalised peak area from 6 independent experimental repeats.**

A control experiment was conducted by using a mixture of 50:50 PPC:OPC, but in the absence of SynM (Figure 3.15). The results suggest comparable ionisation efficiencies with ESI for both PPC and OPC. In

addition, both species were eluted as two peaks, consistent with the results reported by Dods *et al*[2]. The most abundant peak at a longer RT is for 1-acyl-LPC, while the minor peak is for 2-acyl-LPC, as reported earlier[2]. The two positional isomers of LPC (1-acyl-LPC and 2-acyl-LPC) are formed by in-solution migration of the acyl chain between both *sn-1* and *sn-2* positions of the lysophospholipid and were resolved and detected herein by LC-MS.

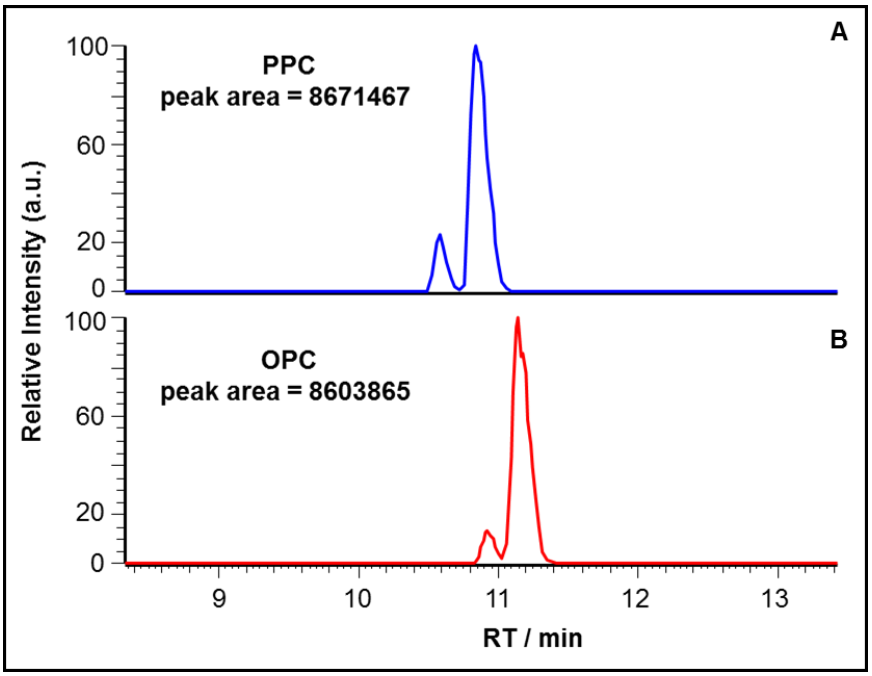

Figure 3.15. **EIC of (A) *m/z* 496.34 for $[PPC + H]^+$ and (B) *m/z* 522.36 for $[OPC + H]^+$ for a mixture of 50:50 PPC:OPC, analysed on the LTQFT using LC-MS Method-II (see section 8.1.2.1.1).**

3.2.4. Reaction of bee venom melittin (BVM) with different lysophospholipids

For further investigation, a number of lysophospholipids (LPLs) with different head groups have been incubated with BVM. The analysis was expanded by including; LPG (lysophosphatidylglycerol), LPE (lysophosphatidylethanolamine) and LPS (lysophosphatidylserine) in addition to LPCs to react with BVM at a ratio of 13:1 lipid:peptide. A pair of LPLs (each with different acyl group) was used at equal mole ratio. The results

(Figure 3.16) show that BVM can be acylated by all the LPLs investigated in this study, regardless of the differences in their polar head groups.

Performing all the experiments under the same instrument conditions, the amount of single palmitoylation and oleoylation products over 168 h for each of SynM (see Figure 3.11) and BVM (Figure 3.16 A) incubation with 50:50 PPC:OPC were compared. The results showed that SynM is more reactive to perform acylation process than BVM. This is evident in the formation of 39% and 33% for $SynM_{pal}$ and $SynM_{ole}$ respectively relative to 28% and 17% for BVM_{pal} and BVM_{ole} respectively.

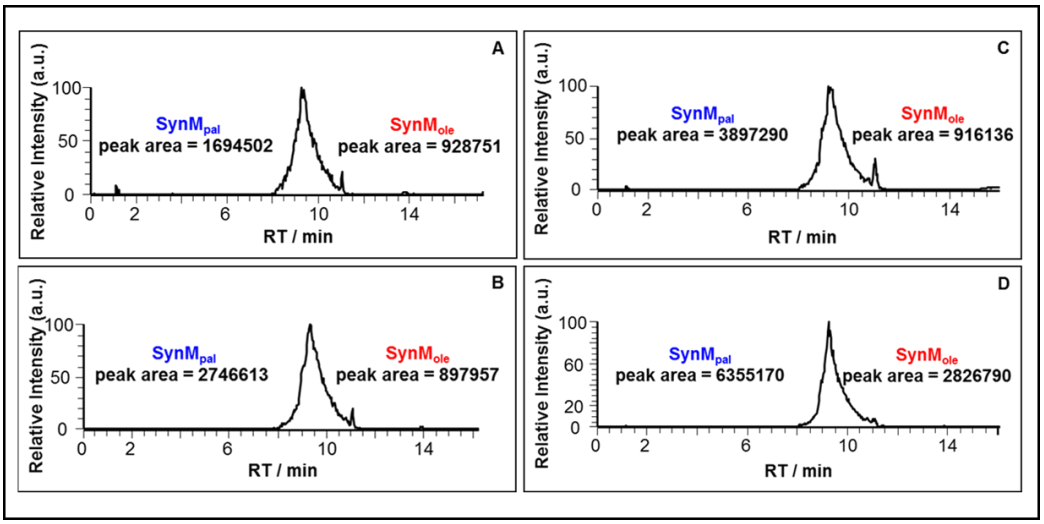

Figure 3.16. **Combined EIC for BVM_{pal} and BVM_{ole} in equimolar mixture of (A) PPC:OPC; (B) PPC:OPS; (C) PPC:OPG; (D) PPC:OPE incubated at 37 °C over 168 h. Peak area for each species was measured individually from EIC (all charge states). The samples were analysed on the LTQFT using LC-MS Method-II (see section 8.1.2.1.1). Note: the final concentration for each LPL is 0.65 mM in lipid:peptide mixture, thus they are well above CMC (see Table 1.4 for LPLs CMC values).**

3.3. Reaction of SynM with diacylphosphatidylcholine (PC)

The two common model lipid systems, DPPC and DOPC,[21] were made as unilamellar liposomes and incubated with SynM at physiological conditions. These two lipid systems represent the two main lipids' phase behavior (liquid crystalline phase (DOPC at 37 °C, > Tm) and gel phase (DPPC at 37 °C, < Tm)) and each with different acyl chain, which are known

to modify SynM. The reactivity of SynM acylation was followed over 168 h, Figure 3.17. All the modifications on SynM, single-, double-, and triple acylation, were observed in both liposomal systems. The in-source product ions of $y13_{pal}/y24_{pal}$ (Figure 3.17 A(i)) and $y13_{ole}/y24_{ole}$ (Figure 3.17 B(i)) for peak (i) and y13/y24 (Figure 3.17 A(ii) and B(ii)) for peak (ii) still show K23 and N-terminus acylation respectively. N-terminus site of the peptide was shown to be acylated preferentially by each PC, supporting earlier results[2,3].

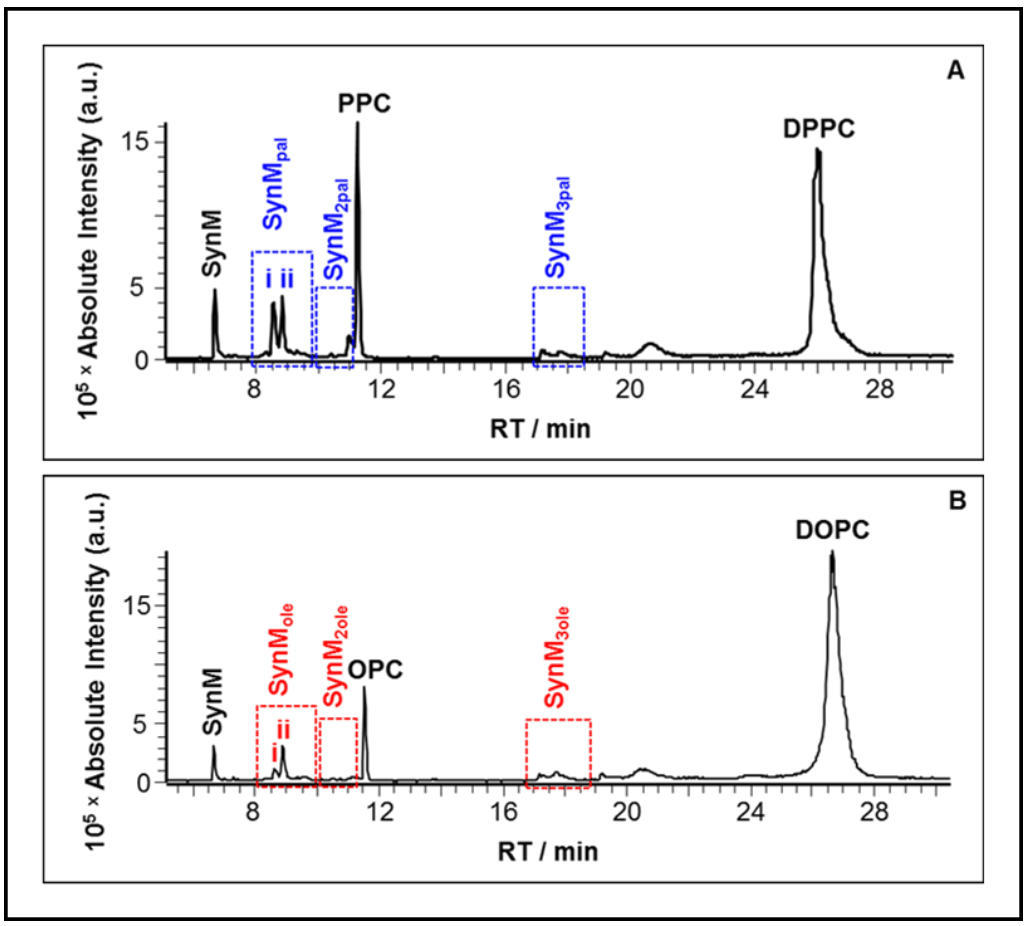

Figure 3.17. **TIC for SynM incubation with (A) DPPC and (B) DOPC at 37 °C over 168 h, analysed by the LTQFT using LC-MS Method-II (see section 8.1.2.1.1). Single and multiple acylation on SynM are highlighted.**

It is interesting to see that the acylation by-products PPC from SynM/DPPC (Figure 3.17 A) and OPC from SynM/DOPC (Figure 3.17 B) exist at a significant abundance relative to their low abundance in the solution of individual liposomes DPPC (Figure 3.18 A) and DOPC (Figure 3.18 B) but in the absence of SynM. This is further supported by measuring the amount of PC conversion to LPC in both experiments and for each species, as shown in Table 3.3. Results show that in the absence of SynM the naturally hydrolysis reaction of PC to produce LPC is very slow, while this process is faster during SynM reaction with PCs (Table 3.3). The amount of PC conversion into LPC in the presence of SynM is shown to be much faster for DPPC than DOPC. This shows faster acyl transfer from DPPC to SynM to leave greater amount of free PPC in the reaction medium than the slower reaction of DOPC to produce less OPC, however, both of PPC and OPC by-products are also reacting with SynM in each peptide:lipid mixture and thus will be consumed by time. While at the same time both LPC by-products cause an increase in the rate of SynM acylation. This also supports preferential palmitoylation reaction over oleoylation reaction, as was described for PPC:OPC mixture (see Figure 3.14).

In addition, based on the results provided in Table 3.1 for lipids phase behavior, it is reasonable to extrapolate that each of DPPC and DOPC lipid systems still keep their bilayer properties over 168 h even though there is 30.4% of PPC and 11.2% of OPC in each system respectively.

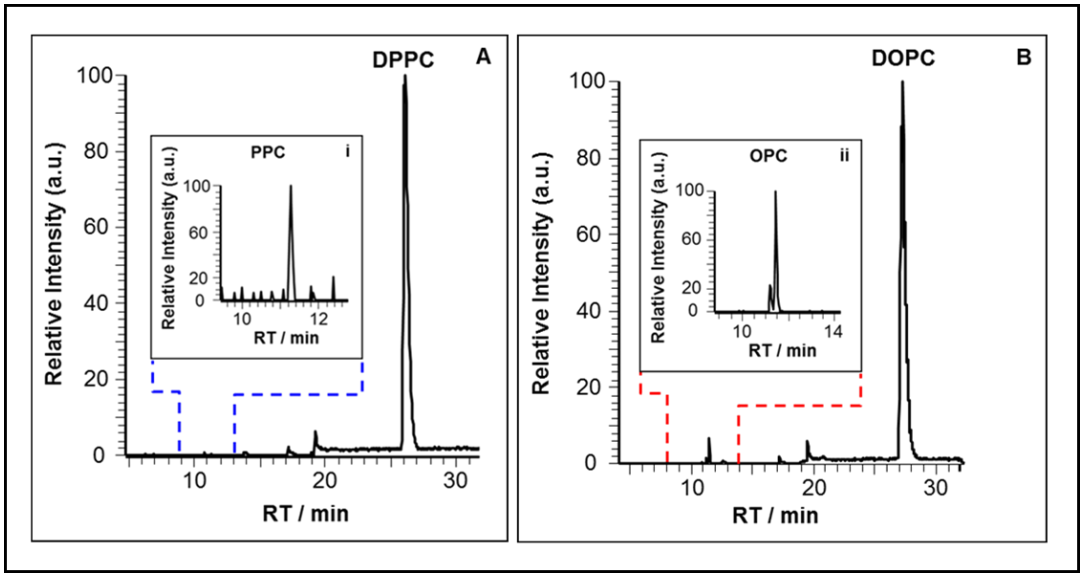

Figure 3.18. **Base peak chromatogram (BPC) for (A) DPPC liposome and (B) DOPC liposome, each incubated individually at 37 °C over 168 and analysed by the LTQFT using LC-MS Method-II (see section 8.1.2.1.1). The inserted panel (i), is the EIC of *m/z* 496.34 for $[PPC + H]^+$; (ii), is the EIC of *m/z* 522.36 for $[OPC + H]^+$.**

Table 3.3. **The percentage of total conversion for each of DPPC to PPC and DOPC to OPC. Subjected experiment represents SynM/DPPC and SynM/DOPC incubation over 168 h at 37 °C (see Figure 3.17); control experiment represents individual incubation for each of DPPC and DOPC liposomes over 168 h at 37 °C (see Figure 3.18) but in the absence of SynM. The percentage of conversion was calculated from measuring the peak area for the EIC of each species as follows: %PPC = peak area PPC/total peak area (PPC + DPPC) × 100; %OPC = peak area OPC/total peak area (OPC + DOPC) × 100.**

Experiment	%PC and LPC			
	%DPPC	%PPC	%DOPC	%OPC
Control experiment	99.9	0.1	98.9	1.0
Subjected experiment	69.6	30.4	88.8	11.2

3.4. Reaction of SynM with PC:LPC mixtures

The effect of different PCs on SynM acylation is well characterised,[1-3] however, the competition between LPCs and PCs is not understood, so 50:50 OPC:DPPC (Figure 3.19 A) and 50:50 PPC:DOPC (Figure 3.19 B)

were chosen as appropriate systems to present all the observed acylation products. It is clearly visible that over 168 h of sample incubation single, double and triple acyl groups were transferred to SynM. Interestingly, the results revealed the existence of SynM with palmitoylation and oleoylation modifications, indicating non-enzymatic acyl transfer from both LPC and PC.

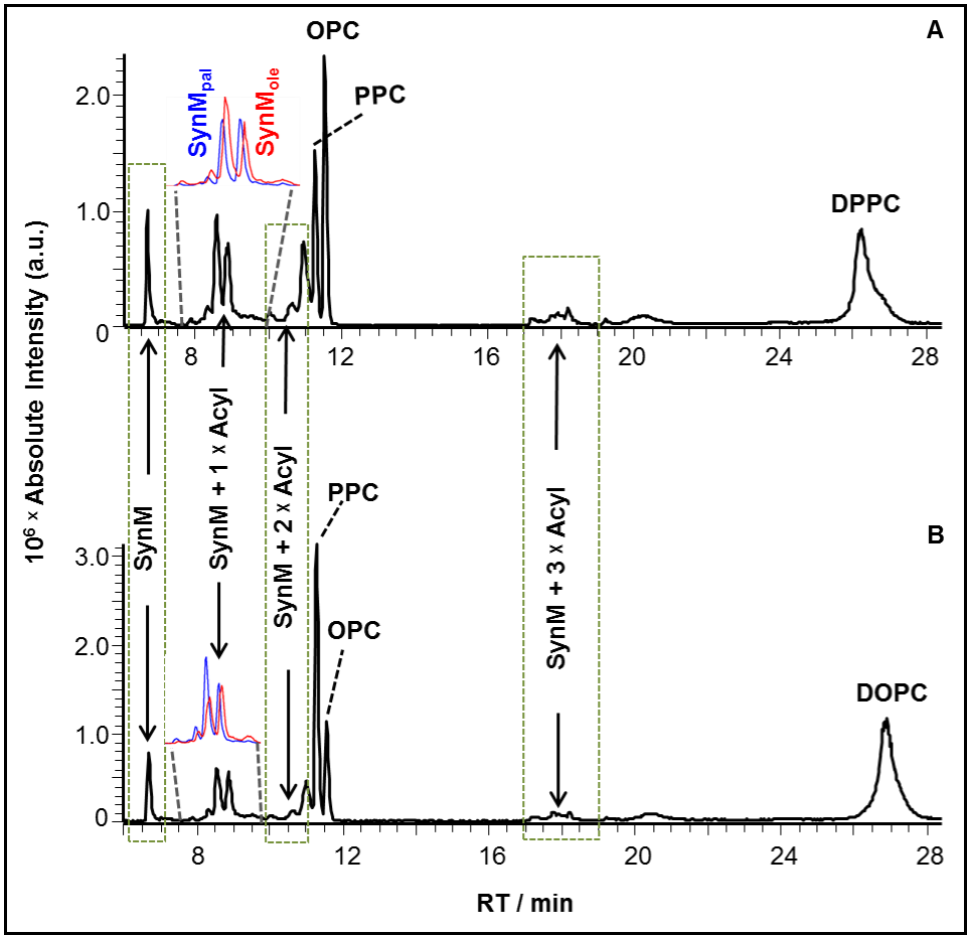

Figure 3.19. **TIC for SynM incubation with a mixture of 50:50 LPC:PC, (A) OPC:DPPC and (B) PPC:DOPC at 37 °C over 168 h, analysed by the LTQFT using LC-MS Method-II (see section 8.1.2.1.1). Single and multiple acylation on SynM are highlighted. For details, see Appendix B Tables 9.3 and 9.4.**

3.4.1. Competitive acyl transfer from PC:LPC system to give SynM single acylation

The lipid system consisting of PC and LPC was incubated with SynM over different times to monitor the amount of acyl transfer by time. Also examined was the possible competition between PC and LPC for acyl

transfer which was followed by incubating SynM with 75:25, 50:50 and 25:75 of LPC:PC (Figures 3.20 and 3.21).

Based on the results provided in Table 3.1 the expected phase behavior for all the lipid systems of OPC:DPPC (Figure 3.20 A-C) is a micelle phase. A lipid system 75:25 OPC:DPPC (Figure 3.20 A) evident faster oleoylation and this would be expected due to more OPC than DPPC. However, even with equimolar amount of OPC:DPPC (Figure 3.20 B) the acylation by OPC is still faster than by DPPC throughout the reaction despite there being twice as many acyl chains available from DPPC as from OPC. Greater reactivity of OPC over DPPC is still visible in 25:75 OPC:DPPC (Figure 3.20 C) up to 48 h despite there being far less OPC. As the reaction proceeds, DPPC will produce PPC that will also react with SynM and hence the palmitoylation reaction overtakes oleoylation. It is interesting to see that in all OPC:DPPC studied systems there is a rapid transfer of palmitoyl and oleoyl acyl chains initially (up to 48 h), which then slows down and/or decreases. This is what would be expected as there is the addition of the second and third acyl chains by proceeding the reaction further.

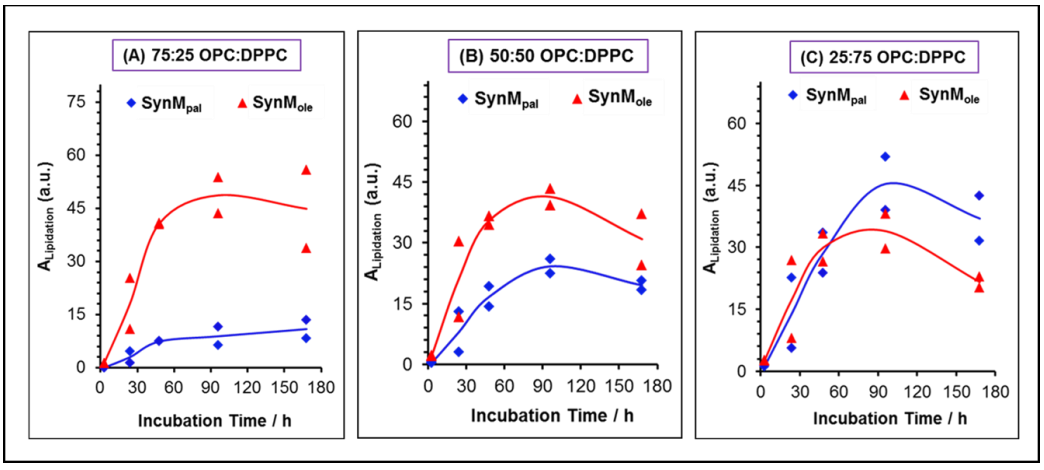

Figure 3.20. **The competitive production of SynM single acylation as a function of time for (A) 75:25 OPC:DPPC; (B) 50:50 OPC:DPPC and (C) 25:75 OPC:DPPC. The EIC peak area (all charge states) for single acylation was normalised relative to the summation of EIC peak area (all charge states) for (non-acylated SynM + single acylated SynM + double acylated SynM + triple acylated SynM). Average data for two experimental repeats are shown as red and blue plots for SynM$_{ole}$ and SynM$_{pal}$ respectively.**

Further, a micelle phase of lipid system 75:25 PPC:DOPC (Figure 3.21 A) is shown to follow the same trend as described earlier for 75:25 OPC:DPPC (see Figure 3.20 A). Greater reactivity of LPC over PC is also confirmed in 50:50 PPC:DOPC (Figure 3.21 B). Interestingly, this lipid system is suggested to form a mixed micelle-bilayer phase however there being the addition of reactive OPC from DOPC throughout proceeding the reaction. Faster oleoylation in 25:75 PPC:DOPC is as expected due to the excess amount of DOPC present and the production of reactive OPC by time. This system is proposed to exhibit a membrane bilayer phase initially, while this might change to mixed micelle-bilayer as the reaction proceeds due to the formation of the reactive OPC by-product. Once more the addition of the second and third acyl chains in PPC:DOPC (Figure 3.21 A-C) is what causes a decrease or a small change in the rate of single acylation over 90 h and thereafter.

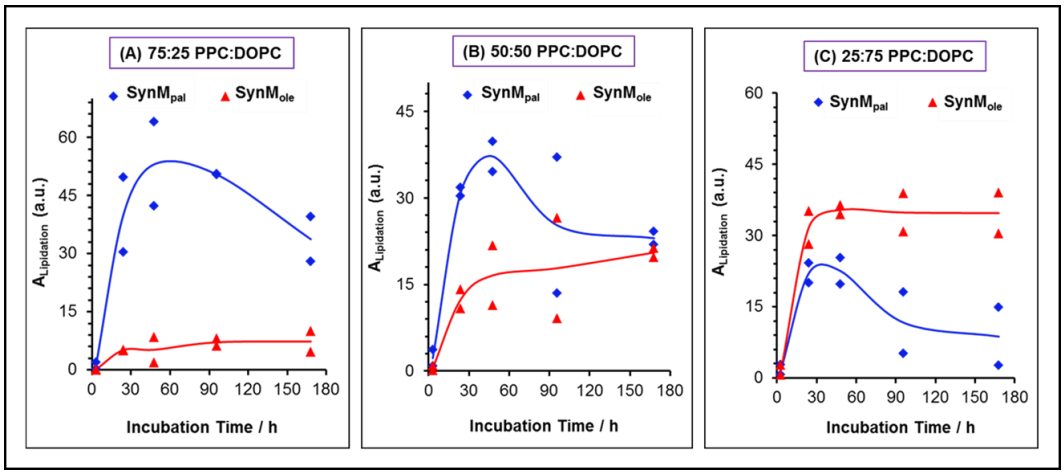

Figure 3.21. **The competitive production of SynM single acylation as a function of time for (A) 75:25 PPC:DOPC; (B) 50:50 PPC:DOPC and (C) 25:75 PPC:DOPC. The EIC peak area (all charge states) for single acylation was normalised relative to the summation of EIC peak area (all charge states) for (non-acylated SynM + single acylated SynM + double acylated SynM + triple acylated SynM). Average data for two experimental repeats are shown as red and blue plots for SynM$_{ole}$ and SynM$_{pal}$ respectively.**

The mass spectrum for single acylation (RT 7.9-9.8 min) is given in Figure 3.22 A and B (PPC:DOPC) and 3.22 C and D (OPC:DPPC). Interestingly, the charge state distributions (*z*=3-5) are different in both systems. Higher abundance of $SynM_{pal}$ is evident when LPC present is PPC, Figure 3.22 A. Consequently, the peak at *m/z* 3085.00 for $SynM_{pal}$ is more intense than *m/z* 3111.01 for $SynM_{ole}$, in the deconvoluted spectra (Figure 3.22 B). The analogous observation is made when the LPC is OPC; here the abundance of $SynM_{ole}$ is greater than $SynM_{pal}$, Figure 3.22 C and D.

Greater reactivity of LPC over PC for SynM acylation is further supported by the in-source product ions in the deconvolved spectra, Figure 3.22 B and D. For PPC:DOPC (Figure 3.22 B) the peptide cleavage at AA G3, *m/z* 2914.89 for $y24_{pal}$, and AA P14, *m/z* 1861.23 for $y13_{pal}$, which represent the C-terminus portion of SynM that carry palmitoyl chain, are more abundant than when the C-terminus portion carry oleoyl chain (*m/z* 2940.90 for $y24_{ole}$ and *m/z* 1888.25 for $y13_{ole}$ respectively), see Figures 3.3 for details about melittin cleavage sites. The analogous observation is made when the LPC is OPC; here the abundance of $y24_{ole}/y13_{ole}$ is greater than $y24_{pal}/y13_{pal}$, Figure 3.22 D. In addition of these representative y-ions for acylation towards C-terminal portion, a number of y-ions correspond to the free peptide dissociation (non-acylated) at AA sites P14, T10, and G3 for y13, y17 and y24 ions respectively, illustrate the probability of the peptide acylation on the N-terminal of the peptide but proposed to be lost during peptide backbone cleavage. Further, product ions correspond to acylated peptide cleavage at AA R24 ($b24_{pal} + H_2O$) and ($b24_{ole} + H_2O$) indicate SynM acylation either on N-terminus or K23; both are reported as the most reactive sites of acylation.[2,3]

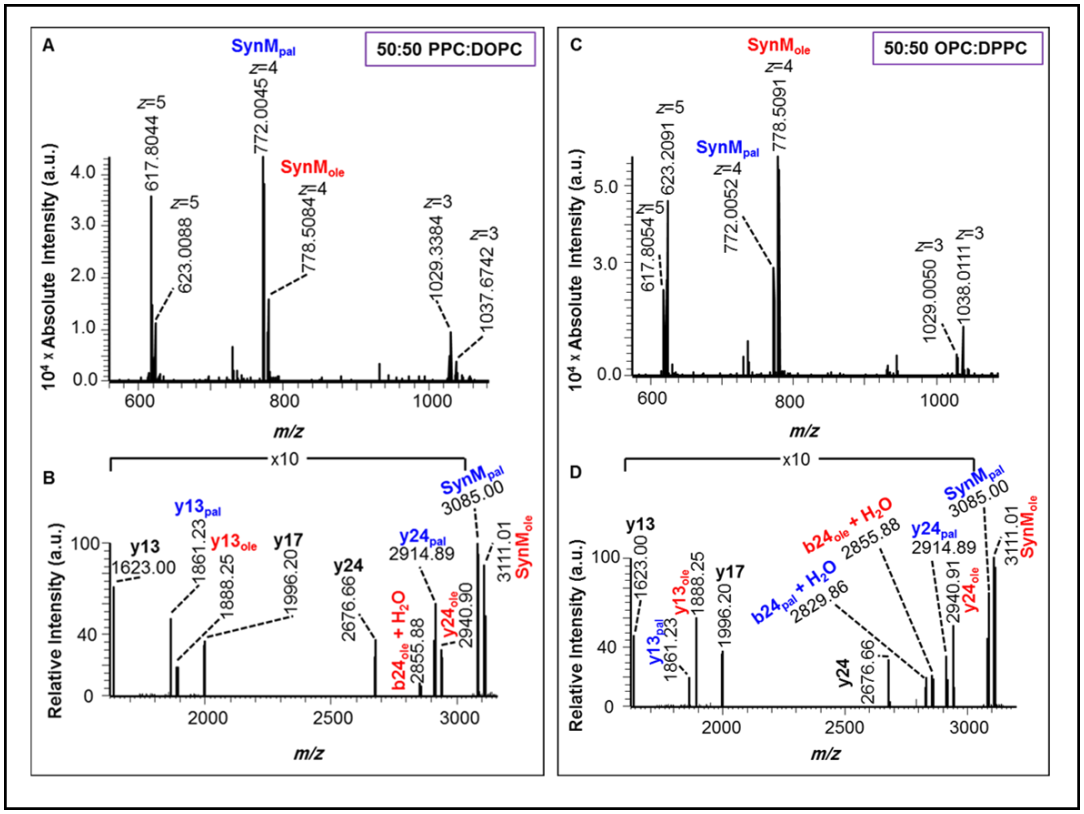

Figure 3.22. **(A) Mass spectrum for SynM single acylation; (B) the deconvolution spectrum to $[M + H]^+$. The spectra were obtained from the EIC (RT 7.9-9.8 min) for SynM/50:50 PPC:DOPC incubation at 37 °C over 168 h. (C) Mass spectrum for SynM single acylation; (D) the deconvolution spectrum to $[M + H]^+$. The spectra were obtained from EIC (RT 7.9-9.8 min) for SynM/50:50 OPC:DPPC incubation at 37 °C over 168 h.**

Following the observation of LPCs' strong contribution towards acyl transfer, selectivity of lipidation for the two most active sites on SynM (N-terminus *vs* K23) was monitored. This is examined by monitoring the proportion of single acylation for different molar ratios of PC:LPC (100:0, 75:25, 50:50, 25:75 and 0:100) at 48 and 168 h, as shown in Figure 3.23. It is interesting to see that both DPPC and DOPC phospholipids favour N-terminus acylation, as reported earlier,[1-3] or competing with K23 (slightly favours N-terminus), around 8.9 min, see also Figure 3.17, as shown in Figure 3.23 A-D (i-iv). While, LPCs have stronger selectivity towards K23 or competing with N-terminus (slightly favours K23), as shown in Figure 3.23 A-D (ii-v). This illustrates different PC *vs* LPC selectivity towards N-terminus and K23 of SynM.

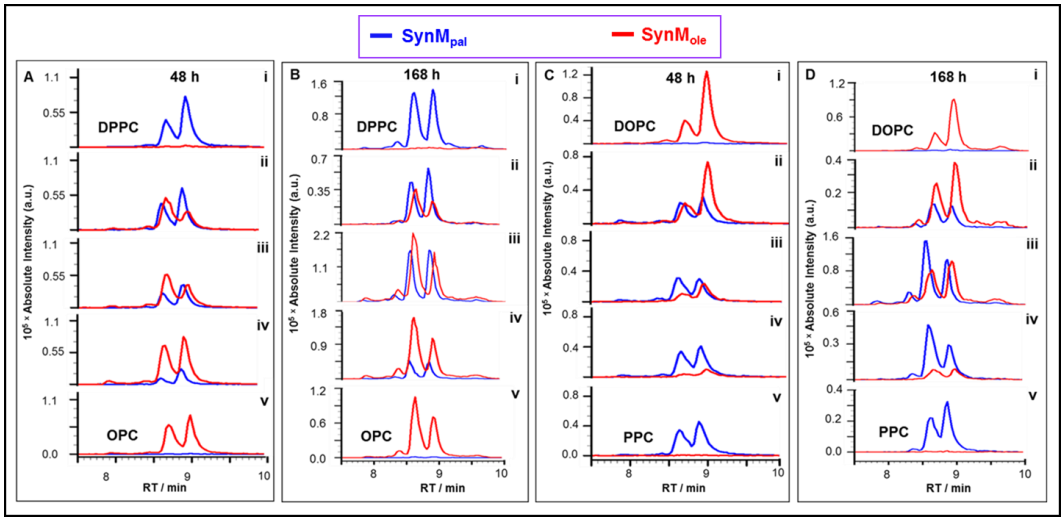

Figure 3.23. **EIC for SynM$_{pal}$ (blue) and SynM$_{ole}$ (red) for incubations between SynM and DPPC:OPC (A and B) and incubations between SynM and DOPC:PPC (C and D) at 37 °C over 48 h and 168 h. (i) SynM incubation with 100% PC; (ii) SynM incubation with 75:25 PC:LPC; (iii) SynM incubation with 50:50 PC:LPC (iv) SynM incubation with 25:75 PC:LPC; (v) SynM incubation with 100% LPCs. A modification of K23 is at 8.6 min and N-terminus is at 8.9 min, as shown previously in Figures 3.11 and 3.17.**

3.4.2. Competitive acyl transfer from PC:LPC system to give SynM double acylation

Moving to the later retention times, the more hydrophobic double acylation products are eluting. At RT 9.5-11.9 min of the chromatogram (see Figure 3.19) a very complicated mixture of double acyl SynM was observed and is shown to consist of a combination of SynM$_{2pal}$, SynM$_{2ole}$ and SynM$_{pal+ole}$ (Figure 3.24). Each of these combinations could further result from the modification of any one of 5 different active sites on the peptide (N-terminus, K23, K21, K7 and S18),[1-3] resulting in a total of 40 possible double acyl SynM species.

As examined earlier (see section 3.4.1), the transfer of the first acyl group from LPC:PC mixture (equal mole ratio) is favoured by LPC. Interestingly, this is still evident in transfer of the second fatty acyl when both transition groups are from LPC. This can be seen in SynM$_{2pal}$ (*m/z* 3323.23) > SynM$_{2ole}$ (*m/z* 3376.26) for PPC:DOPC (Figure 3.24 A and B) and SynM$_{2ole}$ (*m/z* 3376.26) > SynM$_{2pal}$ (*m/z* 3323.23) for OPC:DPPC (Figure 3.24 C and D). Although there is a continuous introduction of LPC into the system from

the dissociation of PC during its reaction with SynM which can then go on to react with SynM, this process can be explained by the comparatively slow transfer from diacylphospholipids (see section 3.3) in conjunction with the high amount of free LPC that is already present in the system. However, participation by both lipids (LPC and PC) in the second acyl transfer shows $SynM_{pal+ole}$ (*m/z* 3350.25) as the most abundant species of the trio of double acylation products. This is because there are 2 isomer products ($SynM_{pal+ole}$ *vs* $SynM_{ole+pal}$) for each double acyl transfer on two different positions of the peptide.

In addition, the two in-source product ions for the peptide dissociation at AA R22, *m/z* 2544.66 for ($b22_{pal}$ + H_2O) and 2571.86 for ($b22_{ole}$ + H_2O), indicate one modification, proposed to be on AA K23, and is lost, leaving the N-terminal portion of the peptide acylated (Figure 3.24 D).

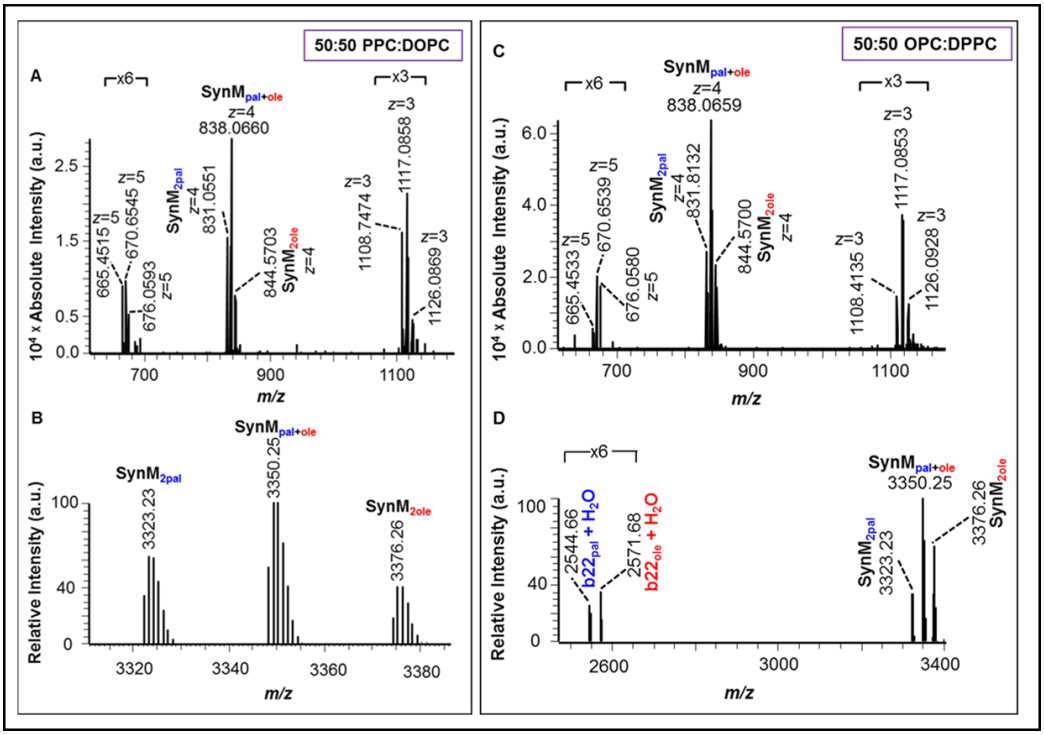

Figure 3.24. **(A) Mass spectrum for SynM double acylation; (B) deconvolution spectrum to $[M + H]^+$. The spectra (A and B) were obtained from the EIC (RT 9.5-11.8 min) for SynM/50:50 PPC:DOPC incubation at 37 °C over 168 h. (C) Mass spectrum for SynM double acylation; (D) deconvolution spectrum to $[M + H]^+$. The spectra (C and D) were obtained from the EIC (RT 9.6-11.9 min) for SynM/50:50 OPC:DPPC incubation at 37 °C over 168 h.**

3.4.3. Competitive acyl transfer from PC:LPC system to give SynM triple acylation

The triple acylation of SynM provides an even more complicated picture than double acylation, because in such case, a total of 80 possible triple acylation products for 5 possible active sites (N-terminus, K23, K21, K7 and S18)[1-3] could result. A distribution of triple acylation products for SynM/50:50 PPC:DOPC incubation was observed at RT 17-19 min, as shown in Figure 3.25. This retention time window was deconvoluted and the mass spectra can be seen in Figure 3.25 B and shows the full extent of the triple acylated SynM species produced. As with double acylation (see section 3.4.2), the two most abundant precursor ions with the contribution of both PC and LPC are $SynM_{2pal+ole}$ and $SynM_{2ole+pal}$ (*m/z* 3588.47 and *m/z* 3614.49 respectively), while $SynM_{3pal}$ and $SynM_{3ole}$ (*m/z* 3562.46 and *m/z* 3640.51 respectively) are less abundant. Once more the greater abundance of $SynM_{3pal}$ over $SynM_{3ole}$ and $SynM_{2pal+ole}$ over $SynM_{2ole+pal}$ for PPC:DOPC (Figure 3.25) indicates that there is greater contribution from the LPC than PC. Interestingly, the observation of intact $SynM_{3pal}$ (Figure 3.25 B) is suggesting enhanced reactivity towards SynM, but only when it is accompanied with DOPC, as intact triple palmitoylation was not observed in SynM reaction with PPC alone (see Figure 3.9).

Closer examination of the RT window where the triple acylated SynM eluted reveals a distribution of ions with the same *m/z* as observed for double acylation (Figure 3.25). This suggests the presence of triple acylation in the analyte, but during ESI ionisation, one of the acyl groups on the peptide has been lost. The in-source dissociation ion ($b24_{pal+ole}$ + H_2O) at *m/z* 3094.11 corresponds to double acylated SynM cleavage at AA R24, this further suggests that the dissociation of triple acylated SynM is loosing one labile modification, leaving two acyl groups proposed to be on the N-terminus and K23 amino acid residue.

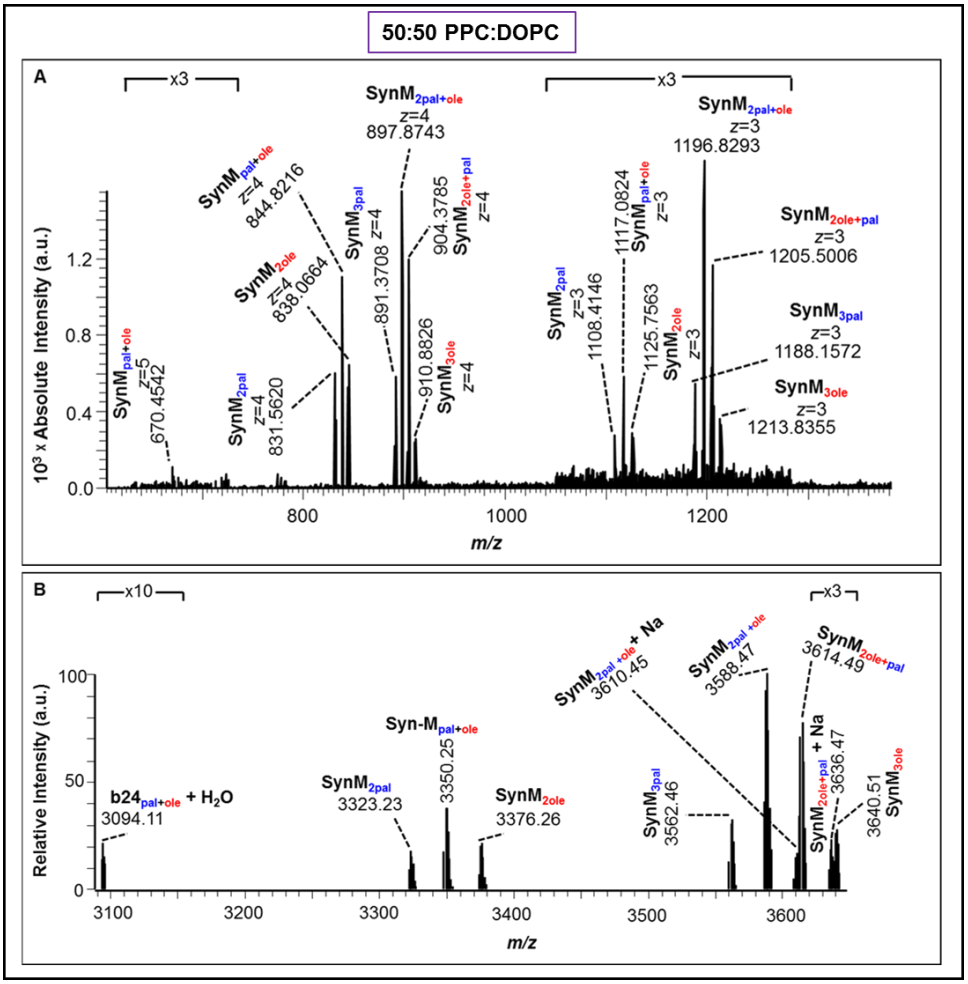

Figure 3.25. **Incubation of SynM with 50:50 PPC:DOPC at 37 °C over 168 h. (A) Mass spectrum for SynM labile triple acylation and triple acylation averaged over RT 17-19 min of the EIC; (B) the deconvolution spectrum to $[M + H]^+$.**

The analogous observation was made for the system of SynM/50:50 OPC:DPPC (Figure 3.26). The intact and labile triple acylation modifications in this system are again indicating that the LPC has a more significant effect than PC. This is further supported by greater abundance of SynM multiple acylation from the LPC over PC as follows: $SynM_{2ole+pal}$ > $SynM_{2pal+ole}$ >> $SynM_{3ole}$ > $SynM_{3pal}$ (Figure 3.26 B).

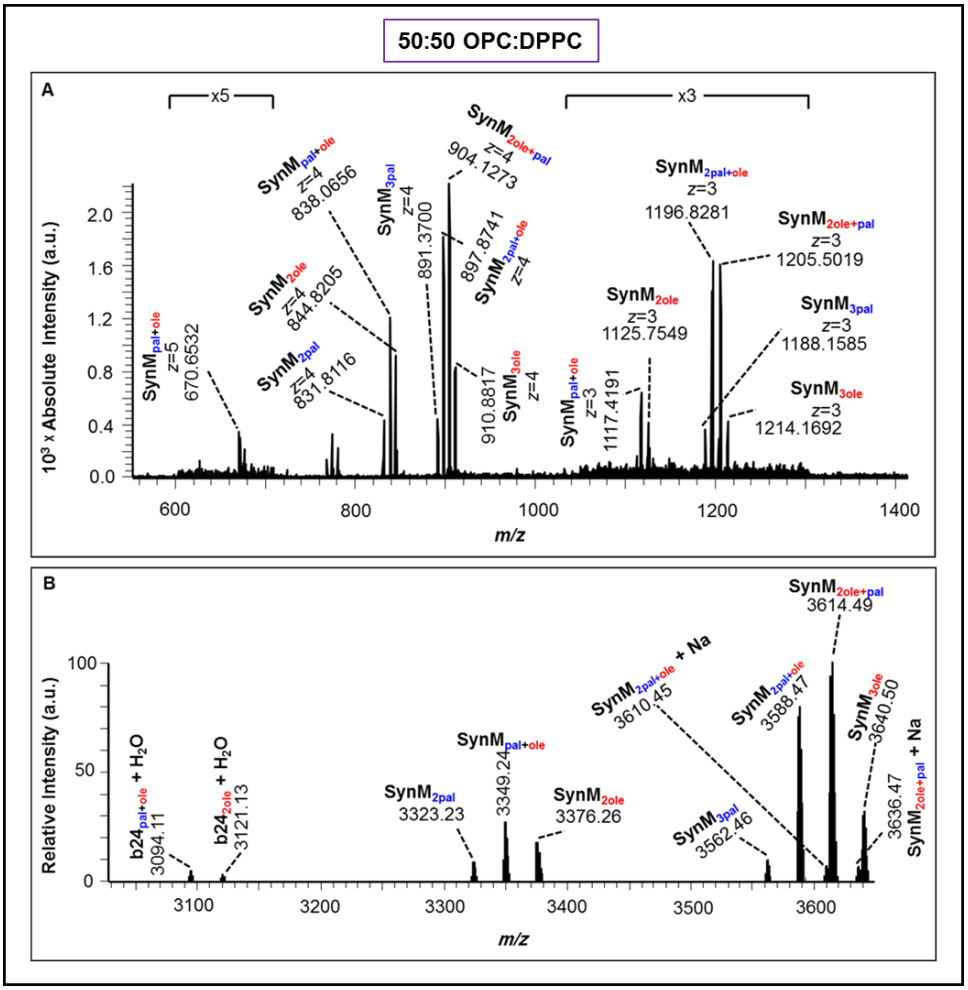

Figure 3.26. **Incubation of SynM with 50:50 OPC:DPPC incubation at 37 °C over 168 h. (A) Mass spectrum for SynM labile triple acylation and triple acylation averaged over RT = 17-19 min of the EIC; (B) the deconvolution spectrum to $[M + H]^+$.**

3.5. LC-MS^2 analysis of SynM double acylation

The evidence of a second and third acyl transfer from the artificial membrane to SynM inspired further molecular characterisation to identify the modification sites of these multiple acylation products; this being known already for monoacylated SynM.[2,3] Here, CID was performed on double acylated SynM precursor ions at *m/z* 832, 838 and 845 for $[M + 4H]^{4+}$, which correspond to $SynM_{2pal}$, $SynM_{pal+ole}$ and $SynM_{2ole}$ respectively. This provided benchmark information about the position of the second acyl group on SynM, however the number of co-eluting species with the same molecular formulae for the triple acylation was deemed too complicated and set aside for experiments into further separation.

3.5.1. LC-MS^2 analysis of SynM$_{2pal}$

Isolating the precursor ion for SynM$_{2pal}$ at *m/z* 832 for $[M + 4H]^{4+}$ in the collision cell (MS^2) gives multiple peaks between 9-11.5 min (Figure 3.27), which reflects the different locations that these two palmitoyl groups can modify on the peptide. There are clearly 6 peaks but tailing suggest others.

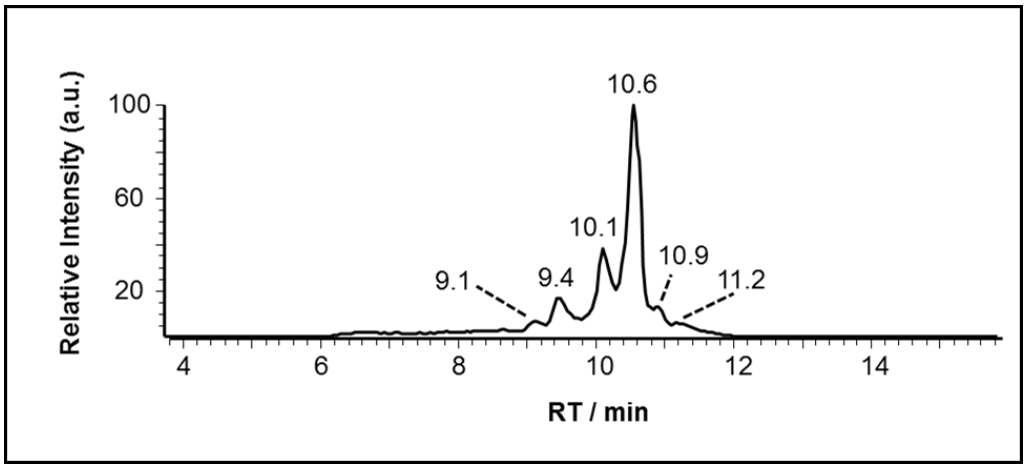

***Figure 3.27*. TIC of product ions from the CID of SynM$_{2pal}$ at *m/z* 832 (*z*=4) for SynM and 50:50 PPC:DOPC incubated over 168 h at 37 °C. Analysis was performed on the LTQFT using LC-MS Method-II (see section 8.1.2.1.1).**

The resulting b- and y-ions from the strongest peak of the chromatogram at 10.6 min (see Figure 3.27) gives a clear evidence of one palmitoyl on the N-terminus (G1) and the other palmitoyl towards C-terminus (K23), as shown in Figure 3.28 A and Table 3.4. Single palmitoylated product ions b3$_{pal}$ (GIG), b4$_{pal}$ (GIGA) and y5$_{pal}$ (RKRQQ) at *m/z* 466.2 (*z*=1), 537.2 (*z*=1) and 477.3 (*z*=2) respectively, are the key ions that confirm this assignment. This is consistent with the understanding that the two most abundant sites of single acylation are K23 and N-terminus (see section 3.2.3, Figures 3.12 and 3.13). The second strongest peak at 10.1 min of the chromatogram (see Figure 3.27) showed SynM acylation on K7 and K21 (Figure 3.28 B and Table 3.5). This is confirmed by observing non-palmitoylated b4 (GIGA), b5 (GIGAV), b6 (GIGAVL) and y4-NH_3 (KRQQ) ions at *m/z* 299.1, 398.2, 511.3 and 271.2 respectively. Moreover, each

terminus of the peptide with one palmitoyl modification could be further confirmed by the strong abundance $y13_{pal}$ at *m/z* 931 (Figure 3.28 A and B) for the peptide cleavage at AA P14.

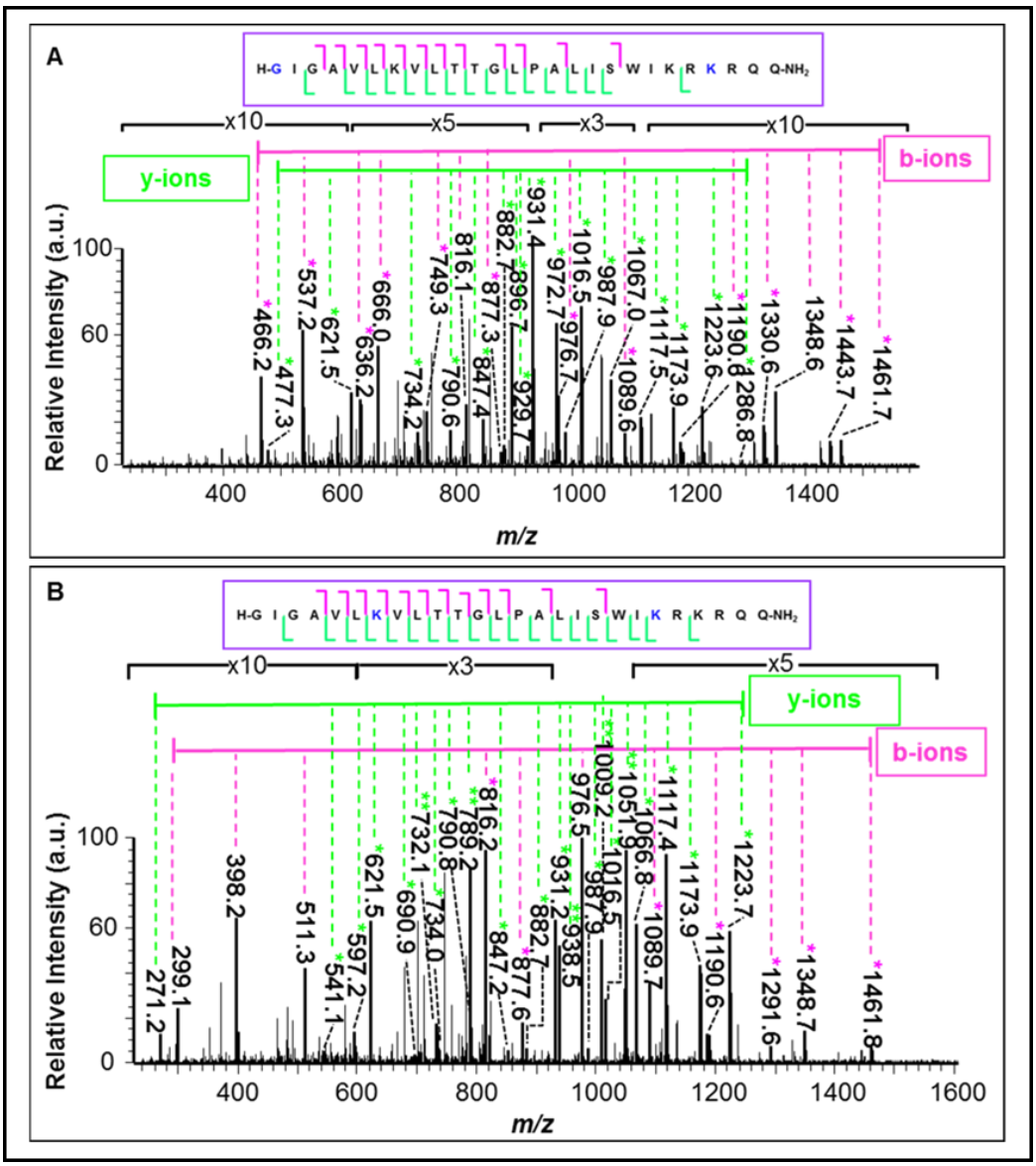

Figure 3.28. **LC-MS^2 spectra for precursor ion SynM$_{2pal}$ at *m/z* 832 for [M + 4H]$^{4+}$ at (A) 10.6 min, corresponds to N-terminus/K23 double palmitoylation, and (B) 10.1 min, corresponds to K7/K21 double palmitoylation, of the EIC (see Figure 3.27, SynM/50:50 PPC:DOPC). Peptide fragments containing single or double palmitoylation are marked with one asterisk and two asterisks respectively. Details provided in Tables 3.4 and 3.5.**

Table 3.4. **Ions produced by fragmenting $SynM_{2pal}$ at *m/z* 832 (*z*=4) over 10.6 min of the EIC (see Figure 3.27, SynM/50:50 PPC:DOPC). Product ions correspond to N-terminus/K23 double palmitoylation (see Figure 3.28 A).**

b-Ions	*m/z*	*z*	Sequence Ladder*	y-Ions	*m/z*	*z*	Sequence Ladder*
b3	466.2	1	H-**G**IG	y24	972.7	3	GAVLKVLTTGLPALISWIKR **K**RQQ-NH_2
b4	537.2	1	H-**G**IGA	y22	929.7	3	VLKVLTTGLPALISWIKR**K**RQQ-NH_2
b5	636.2	1	H-**G**IGAV	y21	896.7	3	LKVLTTGLPALISWIKR**K**RQQ-NH_2
b6	749.3	1	H-**G**IGAVL	y20	1286.8	2	KVLTTGLPALISWIKR**K**RQQ-NH_2
b7	877.3	1	H-**G**IGAVLK	y19	1223.6	2	VLTTGLPALISWIKR**K**RQQ-NH_2
b8	976.7	1	H-**G**IGAVLKV	y18	1173.9	2	LTTGLPALISWIKR**K**RQQ-NH_2
b9	1089.6	1	H-**G**IGAVLKVL	y17	1117.5	2	TTGLPALISWIKR**K**RQQ-NH_2
b10	1190.6	1	H-**G**IGAVLKVLT	y16	1067.0	2	TGLPALISWIKR**K**RQQ-NH_2
b12	1348.6	1	H-**G**IGAVLKVLTTG	y15	1016.5	2	GLPALISWIKR**K**RQQ-NH_2
b12 - H_2O	1330.6	1	H-**G**IGAVLKVLTTG	y14	987.9	2	LPALISWIKR**K**RQQ-NH_2
b12 - H_2O	666.0	2	H-**G**IGAVLKVLTTG	y13	931.4	2	PALISWIKR**K**RQQ-NH_2
b13	1461.4	1	H-**G**IGAVLKVLTTGL	y13	621.5	3	PALISWIKR**K**RQQ-NH_2
b13 - H_2O	1443.7	1	H-**G**IGAVLKVLTTGL	y12	882.7	2	ALISWIKR**K**RQQ-NH_2
b15	816.1	2	H-**G**IGAVLKVLTTGLPA	y11	847.4	2	LISWIKR**K**RQQ-NH_2
				y10	790.6	2	ISWIKR**K**RQQ-NH_2
				y9	734.2	2	SWIKR**K**RQQ-NH_2
				y5	477.3	2	R**K**RQQ-NH_2

*Palmitoylation sites are highlighted in blue within the amino acid sequence of the peptide.

Table 3.5. **Ions produced by fragmenting $SynM_{2pal}$ at *m/z* 832 (*z*=4) over 10.1 min of the EIC (see Figure 3.27, SynM/50:50 PPC:DOPC). Product ions correspond to K7/K21 double palmitoylation (see Figure 3.28 B).**

b-Ions	*m/z*	*z*	Sequence Ladder*	y-Ions	*m/z*	*z*	Sequence Ladder*
b4	299.1	1	H-GIGA	y24	1051.9	3	GAVL**K**VLTTGLPALISWI**K** RKRQQ-NH_2
b5	398.2	1	H-GIGAV	y24	789.2	4	GAVL**K**VLTTGLPALISWI**K** RKRQQ-NH_2
b6	511.3	1	H-GIGAVL	y22	1009.2	3	VL**K**VLTTGLPALISWI**K**RK RQQ-NH_2
b7	877.6	1	H-GIGAVL**K**	y21	732.1	4	L**K**VLTTGLPALISWI**K**RKR QQ-NH_2
b8	976.5	1	H-GIGAVL**K**V	y20	938.5	3	**K**VLTTGLPALISWI**K**RKRQ Q-NH_2
b9	1089.7	1	H-GIGAVL**K**VL	y19	1223.7	2	VLTTGLPALISWI**K**RKRQQ -NH_2
b10	1190.6	1	H-GIGAVL**K**VLT	y18	1173.9	2	LTTGLPALISWI**K**RKRQQ-NH_2
b11	1291.6	1	H-GIGAVL**K**VLTT	y17	1117.4	2	TTGLPALISWI**K**RKRQQ-NH_2
b12	1348.7	1	H-GIGAVL**K**VLTTG	y16	1066.8	2	TGLPALISWI**K**RKRQQ-NH_2
b12 – H_2O	1330.7	1	H-GIGAVL**K**VLTT G	y15	1016.5	2	GLPALISWI**K**RKRQQ-NH_2
b12 – H_2O	666.0	2	H-GIGAVL**K**VLTT G	y14	987.9	2	LPALISWI**K**RKRQQ-NH_2
b13	1461.8	1	H-GIGAVL**K**VLTTGL	y13	931.2	2	PALISWI**K**RKRQQ-NH_2
b13 – H_2O	1443.7	1	H-GIGAVL**K**VLTTGL	y13	621.5	3	PALISWI**K**RKRQQ-NH_2
b15	816.2	2	H-GIGAVL**K**VLTTGLPA	y12	882.7	2	ALISWI**K**RKRQQ-NH_2
				y11	847.2	2	LISWI**K**RKRQQ-NH_2
				y10	790.8	2	ISWI**K**RKRQQ-NH_2
				y9	734.0	2	SWI**K**RKRQQ-NH_2
				y8	734.0	2	WI**K**RKRQQ-NH_2
				y7	597.2	2	I**K**RKRQQ-NH_2
				y6	541.1	2	**K**RKRQQ-NH_2
				y4 - NH_3	271.2	2	KRQQ-NH_2

*Palmitoylation sites are highlighted in blue within the amino acid sequence of the peptide.

The minor peak at 9.1 min of the chromatogram (see Figure 3.27) yielded ions with weak intensity to suggest no palmitoylation on N-terminus but rather located on S18 and K21 of the peptide sequence, as shown in Figure 3.29 A and Appendix B Table 9.5. This is consistent with low reactivity of these sites of the peptide in previous works.[2,3] This is assigned from the most significant $y13_{2pal}$ at *m/z* 1050.5 (*z*=2) for $SynM_{2pal}$ dissociation at AA P14 (PALISWIKRKRQQ), with two palmitoylation modification on the C-terminus cleaved sequence. The following peak at 9.4 min (see Figure 3.27) showed two possibilities. Figure 3.29 B, once more, illustrates double palmitoylation on C-terminus portion of AAs K21 and K23, as shown in Appendix B Table 9.6, though at the same time there are other b- and y-ions represent the indication of one palmitoyl on N-terminus and the second palmitoyl on K21 (Figure 3.29 C and Appendix B Table 9.7). Hence, there is the suggestion of co-eluting species. The difference between the two assigned possibilities at 9.4 min can be quickly judged from P14 cleavage of the peptide for $y13_{2pal}$ at *m/z* 1050.5 corresponds to K21/K23 double palmitoylation (*z*=2) and for $y13_{pal}$ at *m/z* 931.1 corresponds to N-terminus/K21 double palmitoylation (*z*=2).

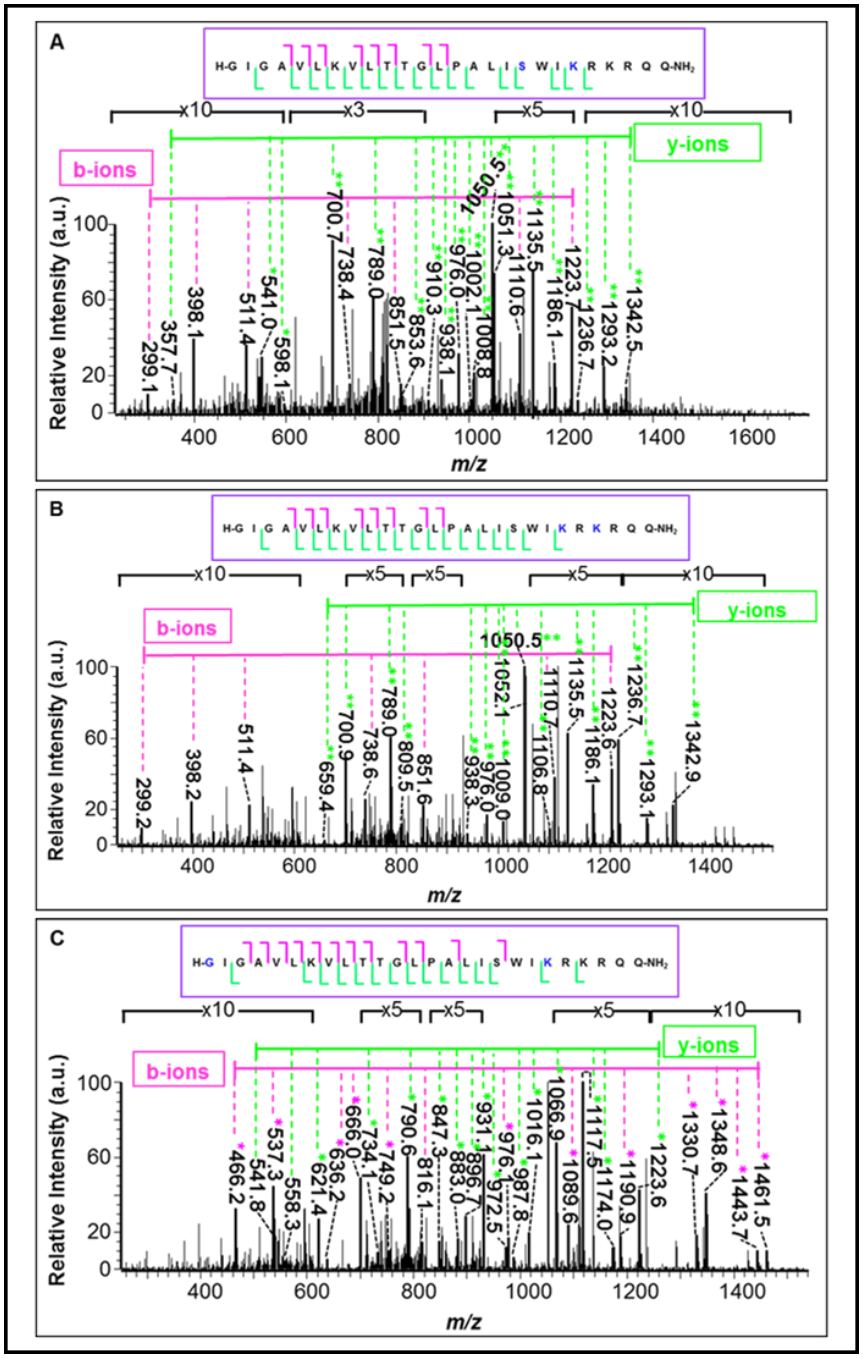

Figure 3.29. **LC-MS^2 spectra for precursor ion SynM$_{2pal}$ at *m/z* 832 for [M + 4H]$^{4+}$ at (A) 9.1 min, corresponds to S18/K21 double palmitoylation, and (B and C) 9.4 min, corresponds to K21/K23 and N-terminus/K21 double palmitoylation respectively, of the EIC (see Figure 3.27, SynM/50:50 PPC:DOPC). Peptide fragments containing single or double palmitoylation are marked with one asterisk and two asterisks respectively. Details provided in Appendix B Tables 9.5-9.7.**

Two minor peaks at 10.9 min and 11.2 min (see Figure 3.27), albeit overlapping with the strongly abundant peaks of LPCs (see Figure 3.19 B) which is likely to effect their ionisation efficiency, suggest one palmitoyl on N-terminus (G1) and the second palmitoyl towards the C-terminal portion. This interpretation can be quickly assessed by the observation of the most abundant peak at *m/z* 931.5 (*z*=2) for the peptide cleavage at AA P14 that corresponds to $y13_{pal}$ (Figure 3.30). Further, the presence of $y5_{pal}$ at *m/z* 477.1 (*z*=2) represents $SynM_{2pal}$ dissociation at AA R22 where one palmitoyl acyl chain resides on the cleaved C-terminus sequence (RKRQQ). This suggests R22, K23 or R24 palmitoylation, however N-terminus and K23 double acylation is already confirmed as eluting at 10.6 min (see Figure 3.28 A and Table 3.4). Interestingly, $SynM_{2pal}$ dissociation at K23 for $y4_{pal}$-NH_3 (*z*=2) at *m/z* 390.5 showed palmitoylated C-terminus sequence (KRQQ) at 11.2 min, which is absent at 10.9 min. Consequently, The peak at 10.9 min is therefore assigned as N-terminus and R22 double palmitoylation (Figure 3.30 A and Appendix B Table 9.8) and the peak at 11.2 min matches N-terminus and R24 double palmitoylation (Figure 3.30 B and Appendix B Table 9.9). These two newly proposed sites of acylation (R22 and R24) suggest that guanidinum groups undergo slow aminolysis reaction with the lipid acyl chains.

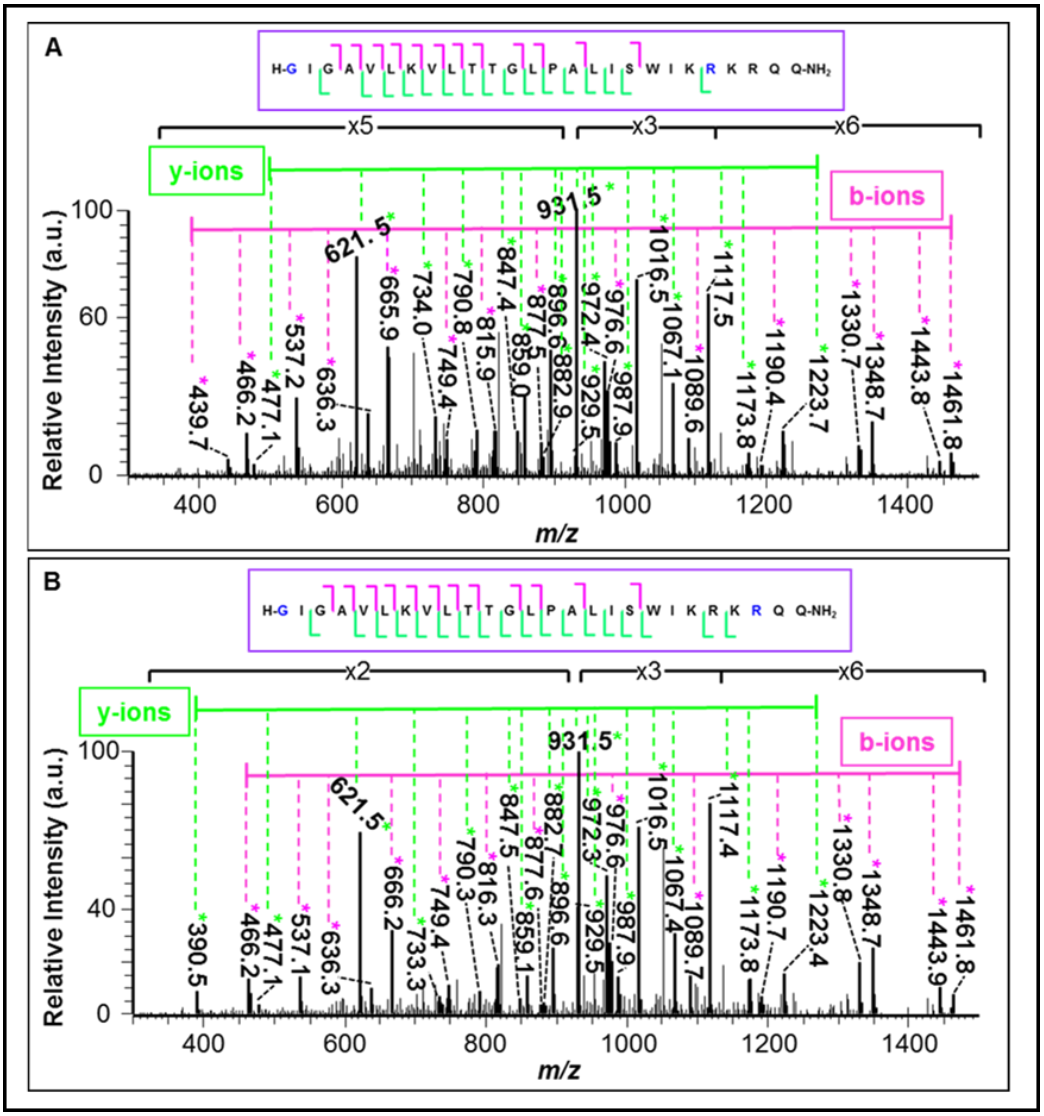

Figure 3.30. **LC-MS^2 spectra for precursor ion SynM$_{2pal}$ at *m/z* 832 for [M + 4H]$^{4+}$ at (A) 10.9 min, corresponds to N-terminus/R22 double palmitoylation, and (B) 11.2 min, corresponds to N-terminus/R24 double palmitoylation, of the EIC (see Figure 3.27, SynM/50:50 PPC:DOPC). Peptide fragments containing single palmitoylation are marked with one asterisk. Details provided in Appendix B Tables 9.8 and 9.9.**

3.5.1.1. Summarised SynM$_{2pal}$ fragmentation

A set of six co-eluting peaks (see Figure 3.27) for SynM$_{2pal}$, when studied by CID, suggest seven possible SynM amino acid residues can be acylated, as shown in Table 3.6. Five residues had already been confirmed in previous work,[2,3] while the two later new modification sites on SynM can be assigned.

Table 3.6. **The sequence ladder of y-type and b-type ions for $SynM_{2pal}$ at different RTs (see Figure 3.27, SynM/50:50 PPC:DOPC). Product ions were produced by fragmenting the precursor ion of double palmitoylation at *m/z* 832 (*z*=4). Full details are provided in Tables 3.4, 3.5 and Appendix B Tables 9.5-9.9.**

RT (min)	Acylated SynM Cleavage Sites‡
9.1	
9.4	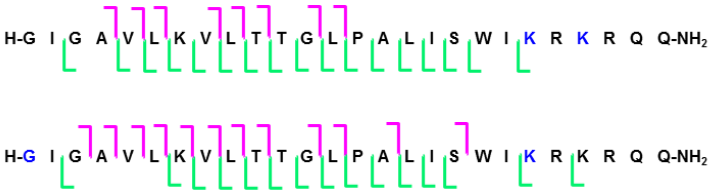
10.1	
10.6	
10.9	
11.2	

‡The sequence site of palmitoylation is highlighted in blue. The cleavage site of b-ions indicated by pink arrow and y-ions by green arrows.

3.5.2. LC-MS^2 analysis of $SynM_{2ole}$

Multiple peaks between 8.5-12 min for $SynM_{2ole}$ at *m/z* 845 for $[M + 4H]^{4+}$ were examined by MS^2 (Figure 3.31). The first peak at 8.8 min to elute is very hard to assign as it is low in abundance and overlaps with single acylation modification (see Figure 3.19 B) and hence there is the likelihood of ion suppression. The following peak at 9.2 min still suggests double acylation towards C-terminal (S18/K21 double oleoylation). This is assigned by the most significant $y13_{2ole}$ at *m/z* 1076.1 (*z*=2) for $SynM_{2ole}$ cleavage at AA P14 (Figure 3.32 A and Appendix B Table 9.10). Two possible assignments for double oleoylation are also confirmed at 9.6 min. Firstly, double oleoylation towards C-terminal (K21/K23 double oleoylation), Figure 3.32 B and

Appendix B Table 9.11, and secondly N-terminus/K21 double oleoylation, Figure 3.32 C and Appendix B Table 9.12. Once more, the differentiation between these two assignments can be assessed from $y13_{2ole}$ at *m/z* 1076.6 for K21/K23 double oleoylation (*z*=2) and $y13_{ole}$ at *m/z* 944.4 for N-terminus/K21 double oleoylation (*z*=2) for the P14 cleavage site.

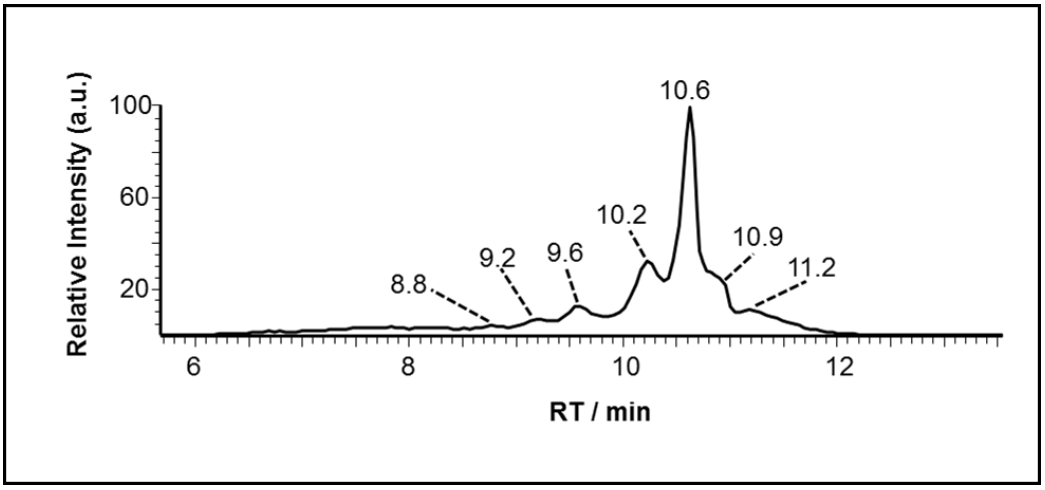

Figure 3.31. **TIC of product ions from the CID of $SynM_{2ole}$ at *m/z* 845 (*z*=4) for SynM and 50:50 PPC:DOPC incubated over 168 h at 37 °C. Analysis was performed on the LTQFT using LC-MS Method-II (see section 8.1.2.1.1).**

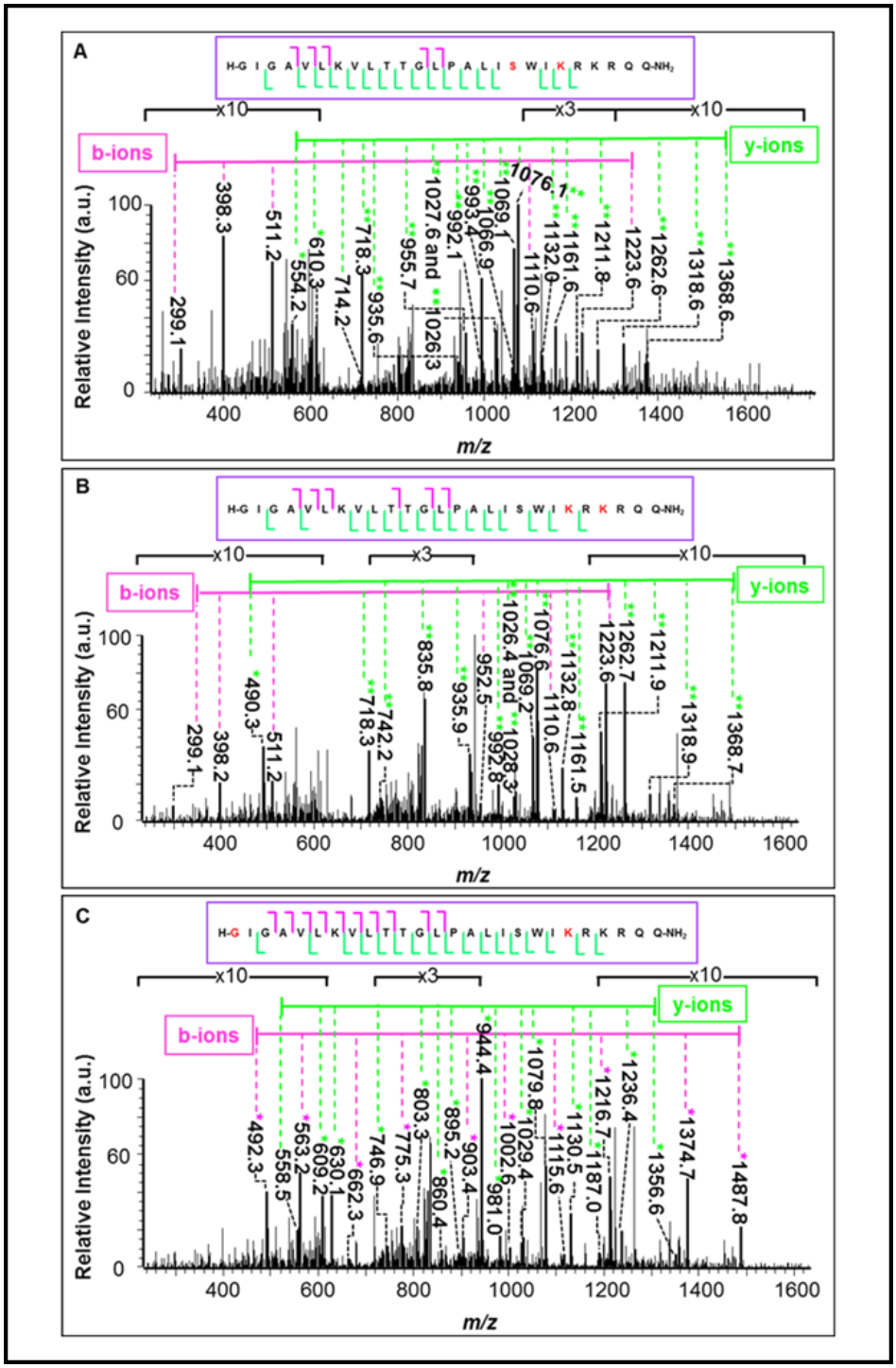

Figure 3.32. **LC-MS^2 spectra for precursor ion SynM$_{2ole}$ at *m/z* 845 for [M + 4H]$^{4+}$ at (A) 9.2 min, corresponds to S18/K21 double oleoylation, and (B and C) 9.6 min, corresponds to K21/K23 and N-terminus/K21 double oleoylation respectively, of the EIC (see Figure 3.31, SynM/50:50 PPC:DOPC). Peptide fragments containing single or double oleoylation are marked with one asterisk and two asterisks respectively. Details provided in Appendix B Tables 9.10-9.12.**

The second most intense peak at 10.2 min corresponds to double oleoylation on K7 and K21 (Figure 3.33 A), and is followed by the most abundant ions for double oleoylation at 10.6 min correspond to AAs G1 (N-terminus) and K23 (Figure 3.33 B). The product ions arise by K7/K21 double oleoylation are tabulated and shown in Appendix B Table 9.13, while G1/K23 double oleoylation are shown in Appendix B Table 9.14. The presence of one oleoylation on C-terminus portion is assigned from $y13_{ole}$ at *m/z* 944 (Figure 3.33 A and B) for $SynM_{2ole}$ cleavage at AA P14, leaving the other oleoyl towards N-terminus.

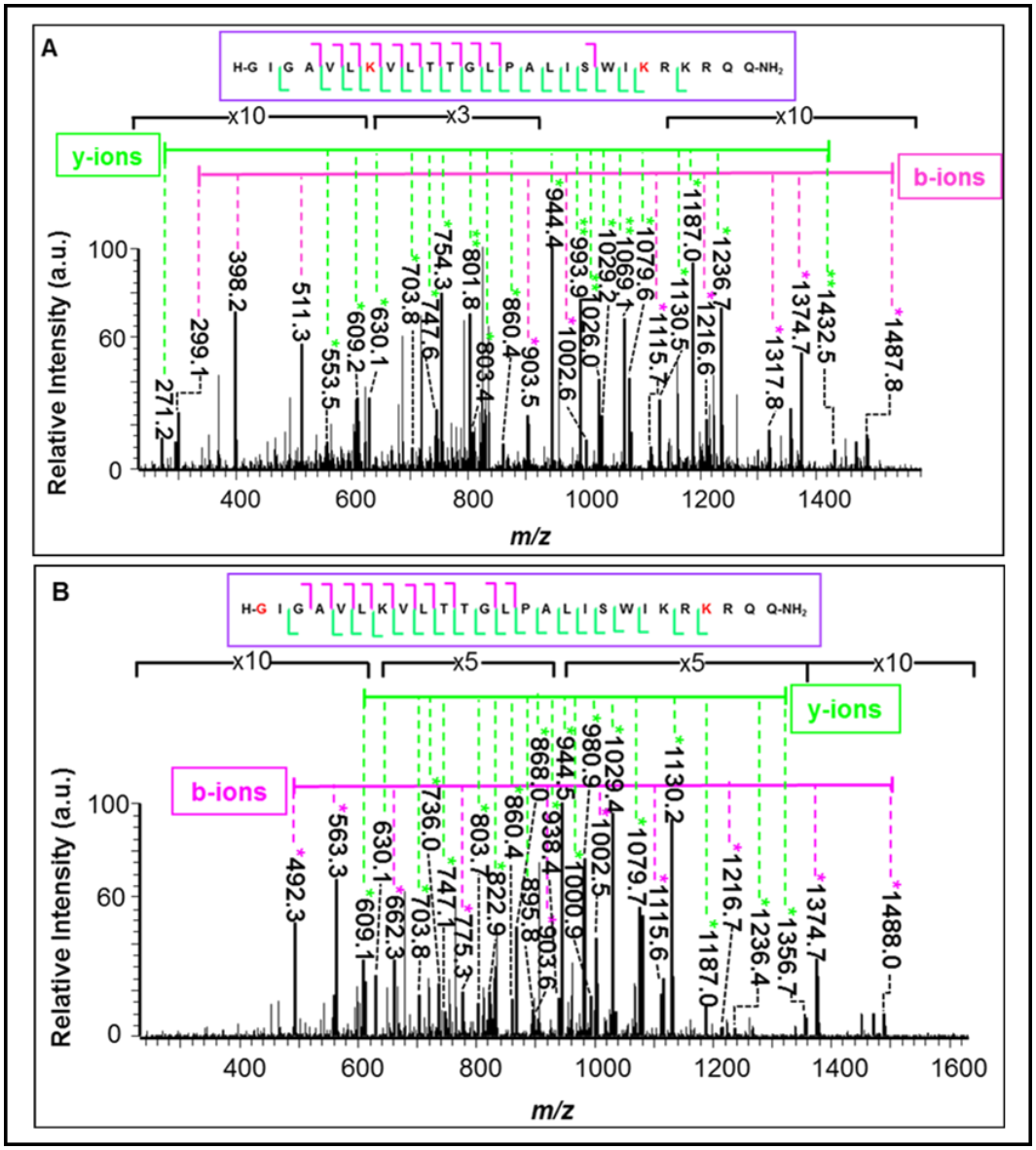

Figure 3.33. **LC-MS^2 spectra for precursor ion SynM$_{2ole}$ at *m/z* 845 for [M + 4H]$^{4+}$ at (A) 10.2 min, corresponds to K7/K21 double oleoylation, and (B) 10.6 min, corresponds to N-terminus/K23 double oleoylation, of the EIC (see Figure 3.31, SynM/50:50 PPC:DOPC). Peptide fragments containing single or double oleoylation are marked with one asterisk and two asterisks respectively. Details provided in Appendix B Tables 9.13 and 9.14.**

The product ions arising from the two later co-eluting peaks at 10.9 and 11.2 min (see Figure 3.31) suggest N-terminus/R22 double oleoylation (Figure 3.34 A and Appendix B Table 9.15) and N-terminus/R24 double oleoylation (Figure 3.34 B and Appendix B Table 9.16) respectively.

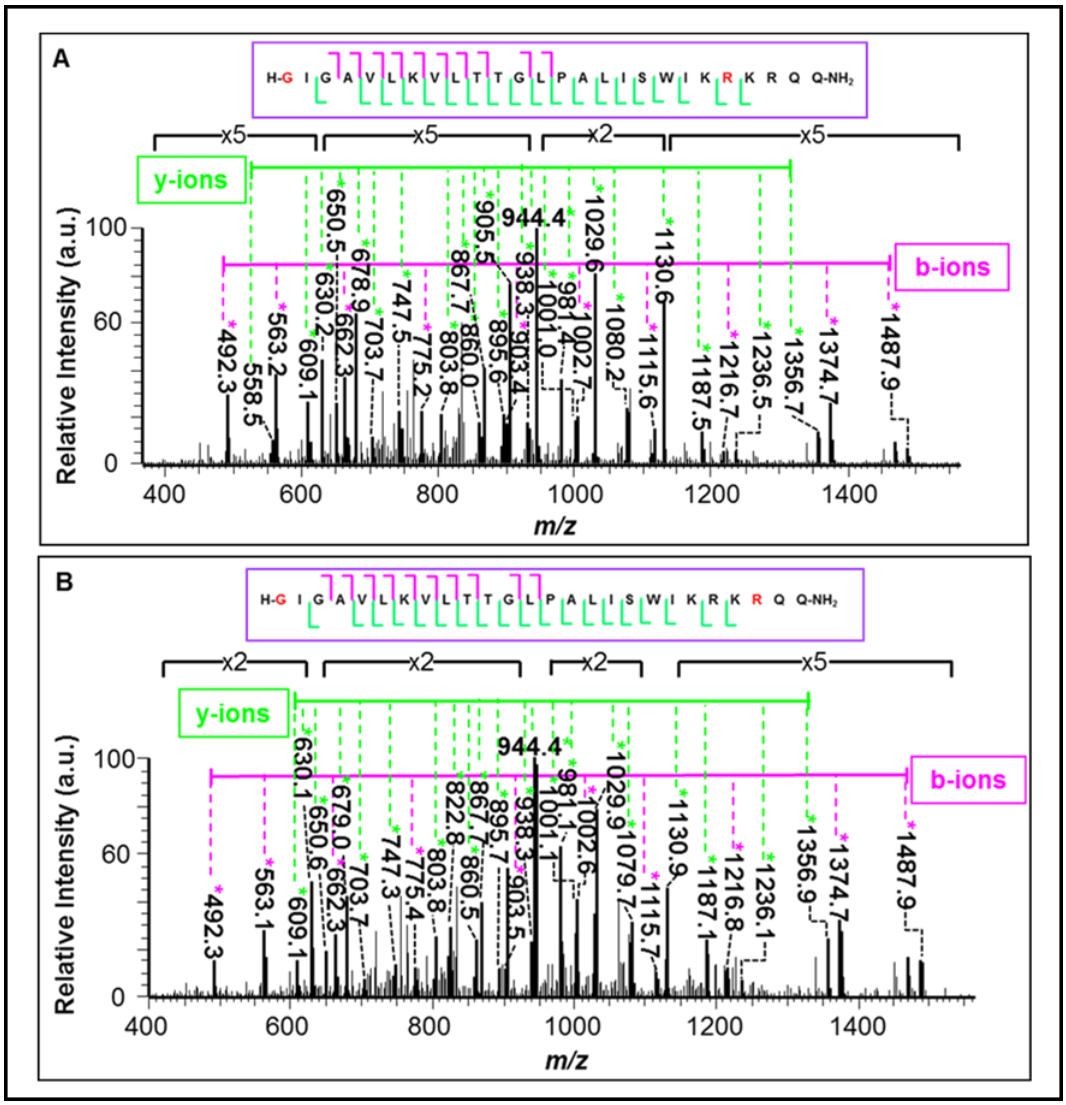

Figure 3.34. **LC-MS^2 spectra for precursor ion SynM$_{2ole}$ at *m/z* 845 for [M + 4H]$^{4+}$ at (A) 10.9 min, corresponds to N-terminus/R22 double oleoylation, and (B) 11.2 min, corresponds to N-terminus/R24 double oleoylation, of the EIC (see Figure 3.31, SynM/50:50 PPC:DOPC). Peptide fragments containing single oleoylation are marked with one asterisk. Details provided in Appendix B Tables 9.15 and 9.16.**

3.5.2.1. Summarised $SynM_{2ole}$ fragmentation

The seven possible assignments for $SynM_{2ole}$ modification are shown in Table 3.7. Overall, the results are analogous to the MS^2 of the $SynM_{2pal}$ and have the same elution order.

Table 3.7. **The sequence ladder of y-type and b-type ions for $SynM_{2ole}$ at different RTs of the EIC (see Figure 3.31, SynM/50:50 PPC:DOPC). Ions produced by fragmenting the precursor ion of double oleoylation at *m/z* 845 (*z*=4). Full details are provided in Appendix B Tables 9.10-9.16.**

RT (min)	Acylated SynM Cleavage Sites‡
9.2	
9.6	
10.2	
10.6	
10.9	
11.2	

‡The sequence site of oleoylation is highlighted in red. The cleavage site of b-ions indicated by pink arrow and y-ions by green arrows.

3.5.3. LC-MS^2 analysis of SynM$_{pal+ole}$

Fragmenting SynM$_{pal+ole}$ precursor ion at *m/z* 838 for $[M + 4H]^{4+}$ again gives multiple co-eluting peaks around 9-12 min of the chromatogram, as shown in Figure 3.35.

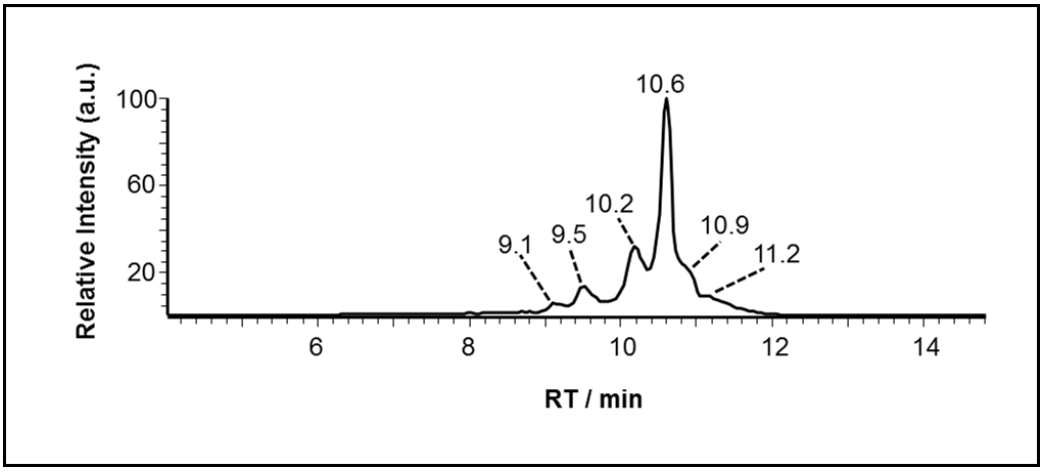

Figure 3.35. **TIC of product ions from the CID of SynM$_{pal+ole}$ at *m/z* 838 (*z*=4) for SynM and 50:50 PPC:DOPC incubated over 168 h at 37 °C. Analysis was performed on the LTQFT using LC-MS Method-II (see section 8.1.2.1.1).**

It is interesting to see that more complication arises during the examination of the ion at *m/z* 838 because there are two different acyl chains, palmitoyl and oleoyl, for each of the two modification sites of SynM. Hence, for each single chromatographic peak there will be two possibilities because when the modification is at a specific location RT is the same regardless of whether it is palmitoyl or oleoyl (see Figures 3.27 and 3.31). The first peak eluting at 9.1 min for example, gives evidence of two co-eluting species: S18 oleoyl and K21 palmitoyl (Figure 3.36 A and Appendix B Table 9.17) and S18 palmitoyl and K21 oleoyl (Figure 3.36 B and Appendix B Table 9.18). The presence of both palmitoyl and oleoyl modification towards the C-terminus portion is confirmed from the most abundant peak for SynM cleavage at AA P14 for y13$_{pal+ole}$ at *m/z* 1063.5 (*z*=2). This ion is also evident at 9.5 min for both possibilities of K21 oleoyl and K23 palmitoyl (Figure 3.37

A and Appendix B Table 9.19) and also K21 palmitoyl and K23 oleoyl (Figure 3.37 B and Appendix B Table 9.20)

When both palmitoyl and oleoyl acyl chains are located towards C-terminus of the peptide such as for S18/K21 or K21/K23 then most product ions were shown to be the same whether it is palmitoyl/oleoyl or changing the positions to oleoyl/palmitoyl (Figures 3.36 and 3.37). The key ions to differentiate between the two products were seen to be $b18_{ole}$ corresponding to S18 oleoyl and K21 palmitoyl, while it is $b18_{pal}$ for S18 palmitoyl and K21 oleoyl (Figure 3.36). For K21 oleoyl and K23 palmitoyl the presence of $y5_{pal}$ is an indication of this product, while the presence of $y4_{ole}$ and $y5_{ole}$ ions show K21 palmitoyl and K23 oleoyl (Figure 3.37). In addition to K21/K23 palmitoylation plus oleoylation at 9.5 min, N-terminus/K21 palmitoylation plus oleoylation is also confirmed at this RT (Figure 3.38 and Appendix B Tables 9.21 and 9.22).

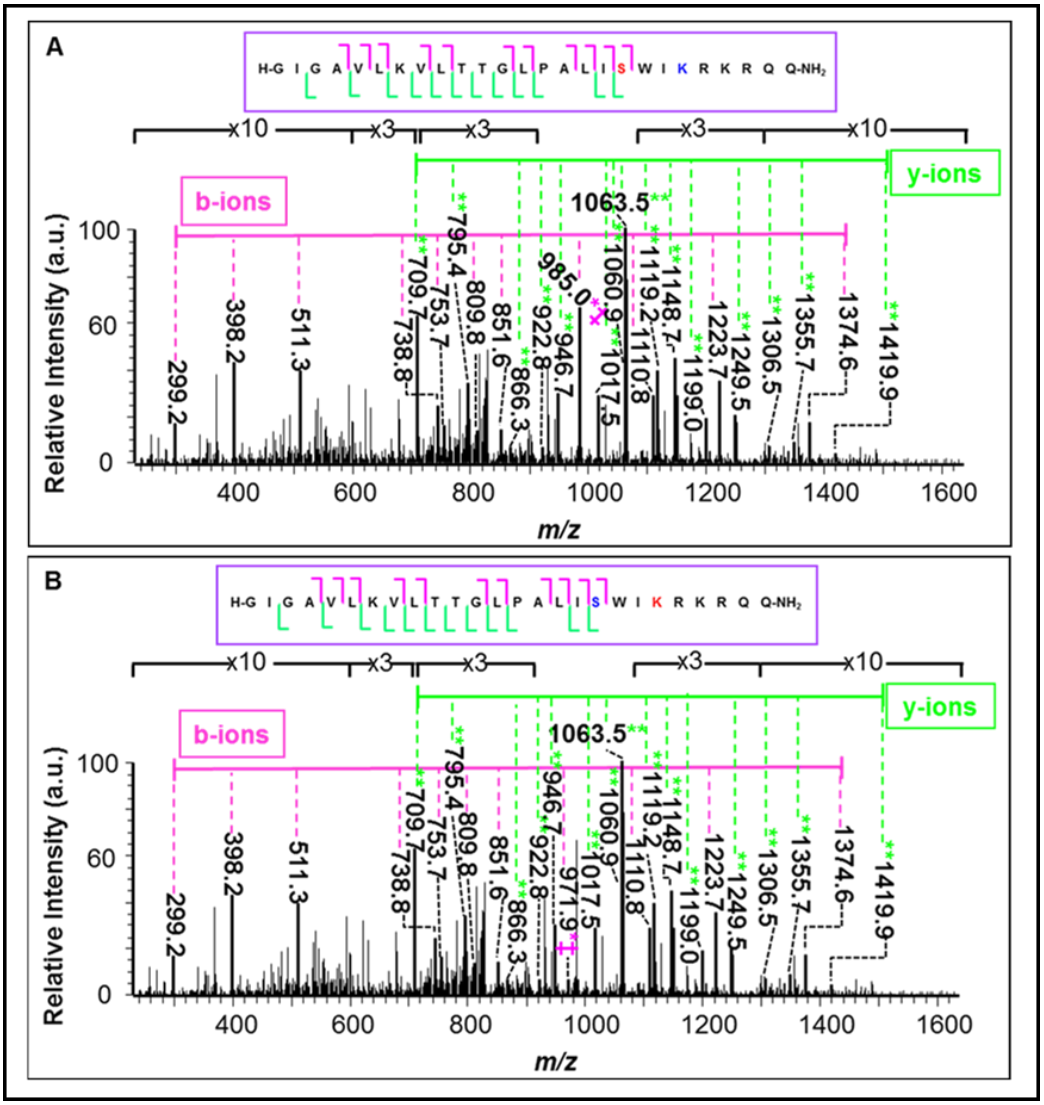

Figure 3.36. **LC-MS^2 spectrum for precursor ion SynM$_{pal+ole}$ at *m/z* 838 for [M + 4H]$^{4+}$ at 9.1 min of the EIC (see Figure 3.35, SynM/50:50 PPC:DOPC). (A) S18 oleoylation and K21 palmitoylation; (B) S18 palmitoylation and K21 oleoylation. Peptide fragments containing single or double acylation are marked with one asterisk and two asterisks respectively. The peaks labelled with double dagger shows b18$_{ole}$ (A); b18$_{pal}$ (B). Details provided in Appendix B Tables 9.17 and 9.18.**

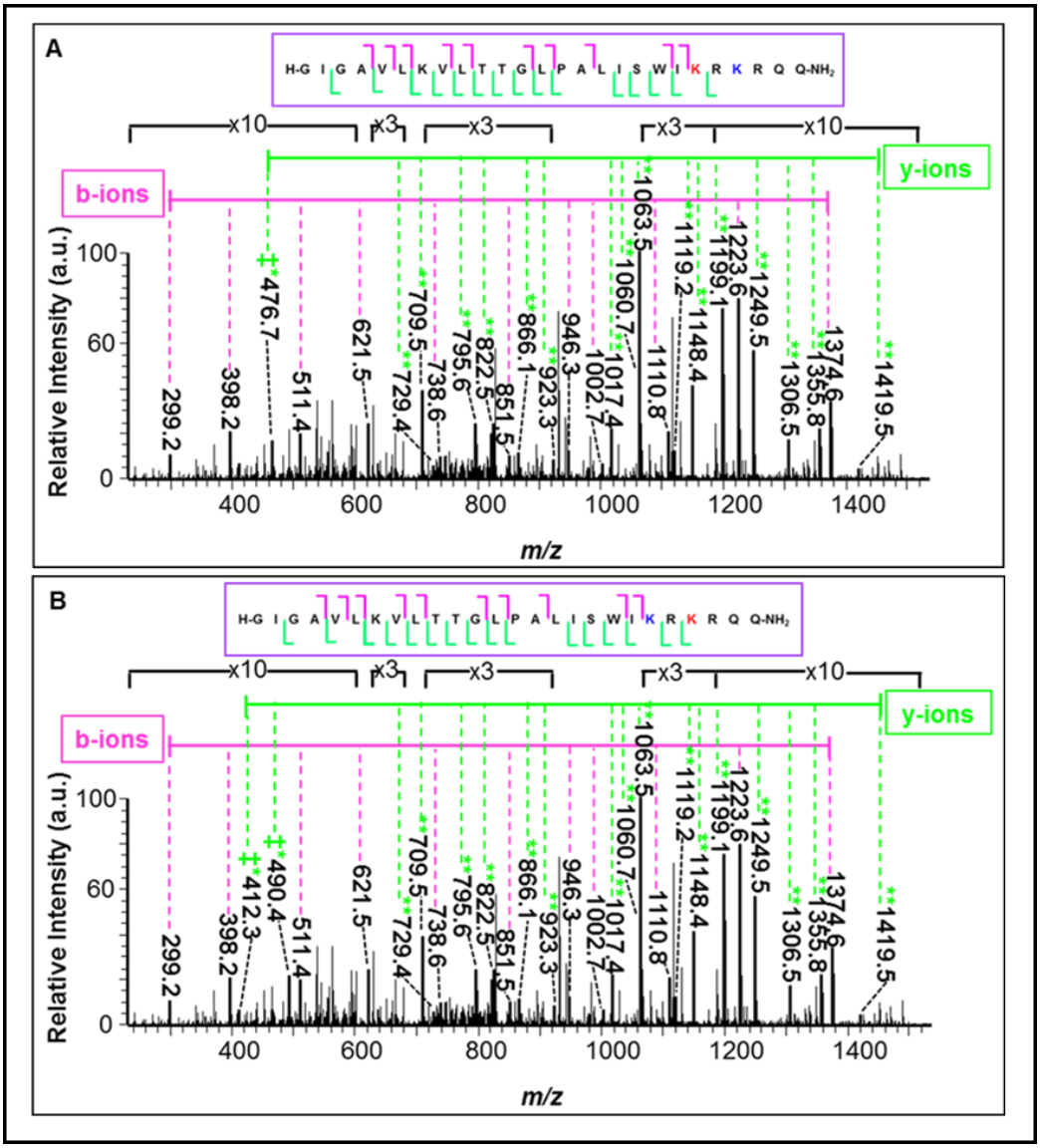

Figure 3.37. **LC-MS^2 spectrum for precursor ion SynM$_{pal+ole}$ at *m/z* 838 for [M + 4H]$^{4+}$ at 9.5 min of the EIC (see Figure 3.35, SynM/50:50 PPC:DOPC). (A) K21 oleoylation and K23 palmitoylation; (B) K21 palmitoylation and K23 oleoylation. Peptide fragments containing single or double acylation are marked with one asterisk and two asterisks respectively. The peaks labelled with double dagger shows y5$_{pal}$ (A); y5$_{ole}$ and y4$_{ole}$ (B). Details provided in Appendix B Tables 9.19 and 9.20.**

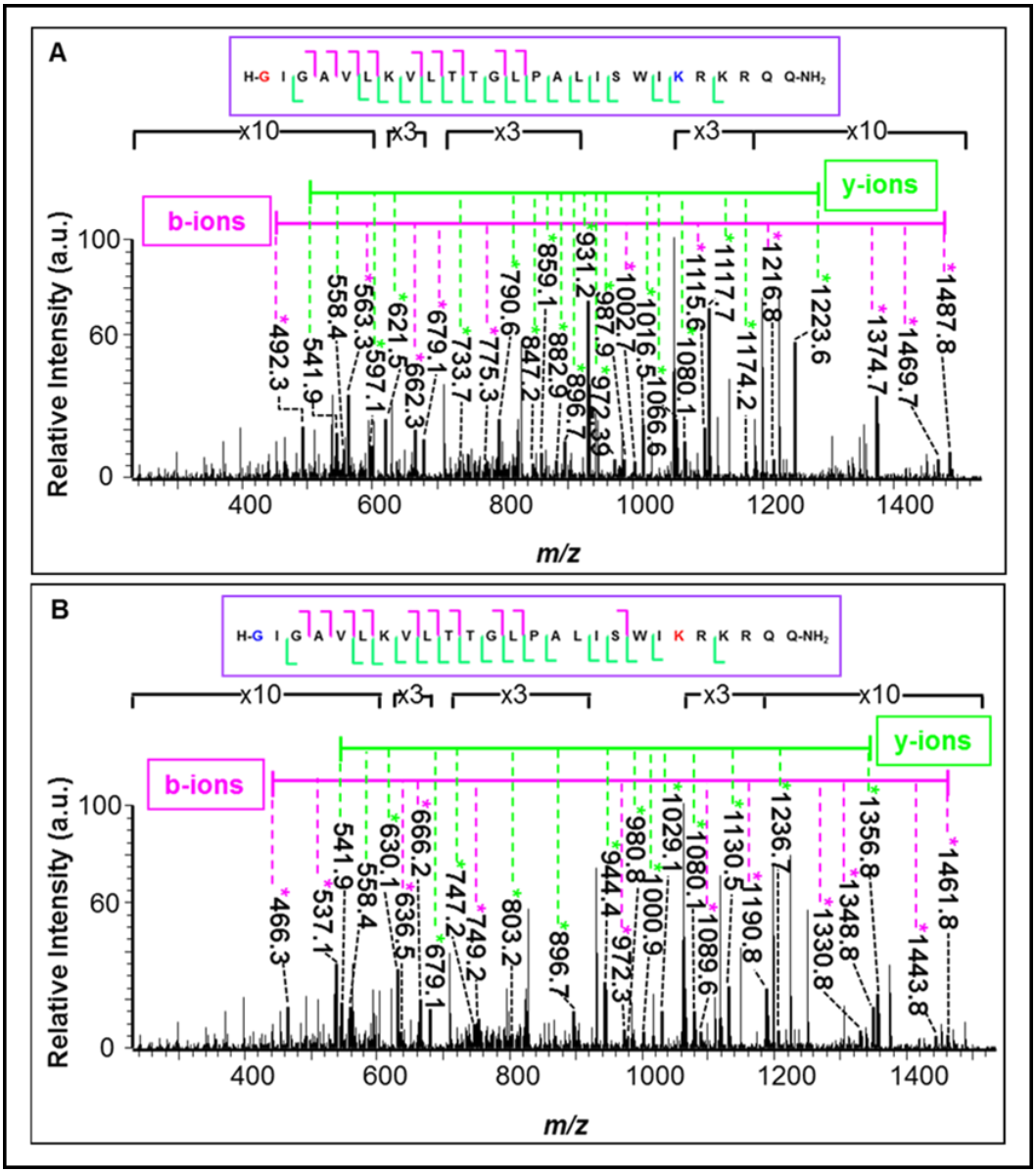

Figure 3.38. **LC-MS^2 spectrum for precursor ion SynM$_{pal+ole}$ at *m/z* 838 for $[M + 4H]^{4+}$ at 9.5 min of the EIC (see Figure 3.35, SynM/50:50 PPC:DOPC). (A) N-terminus oleoylation and K21 palmitoylation; (B) N-terminus palmitoylation and K21 oleoylation. Peptide fragments containing single acylation are marked with one asterisk. Details provided in Appendix B Tables 9.21 and 9.22.**

Product ions arising from the dissociation of SynM$_{pal+ole}$ acylation at 10.2 min is confirmed as two possibilities: K7 oleoyl and K21 palmitoyl (Figure 3.39 A and Appendix B Table 9.23) and K7 palmitoyl and K21 oleoyl (Figure 3.39 B and Appendix B Table 9.24). There are also the two possibilities of N-terminus oleoyl and K23 palmitoyl (Figure 3.40 A and Appendix B Table 9.25) and N-terminus palmitoyl and K23 oleoyl (Figure

3.40 B and Appendix B Table 9.26) at 10.6 min. At both 10.2 min and 10.6 min, $SynM_{pal+ole}$ dissociation at AA P14 clearly shows the C-terminus half resides one acylation modification, *m/z* 931 for $y13_{pal}$ or 944 for $y13_{ole}$ (*z*=2), and leaving the second acyl chain (palmitoyl or oleoyl) towards N-terminus.

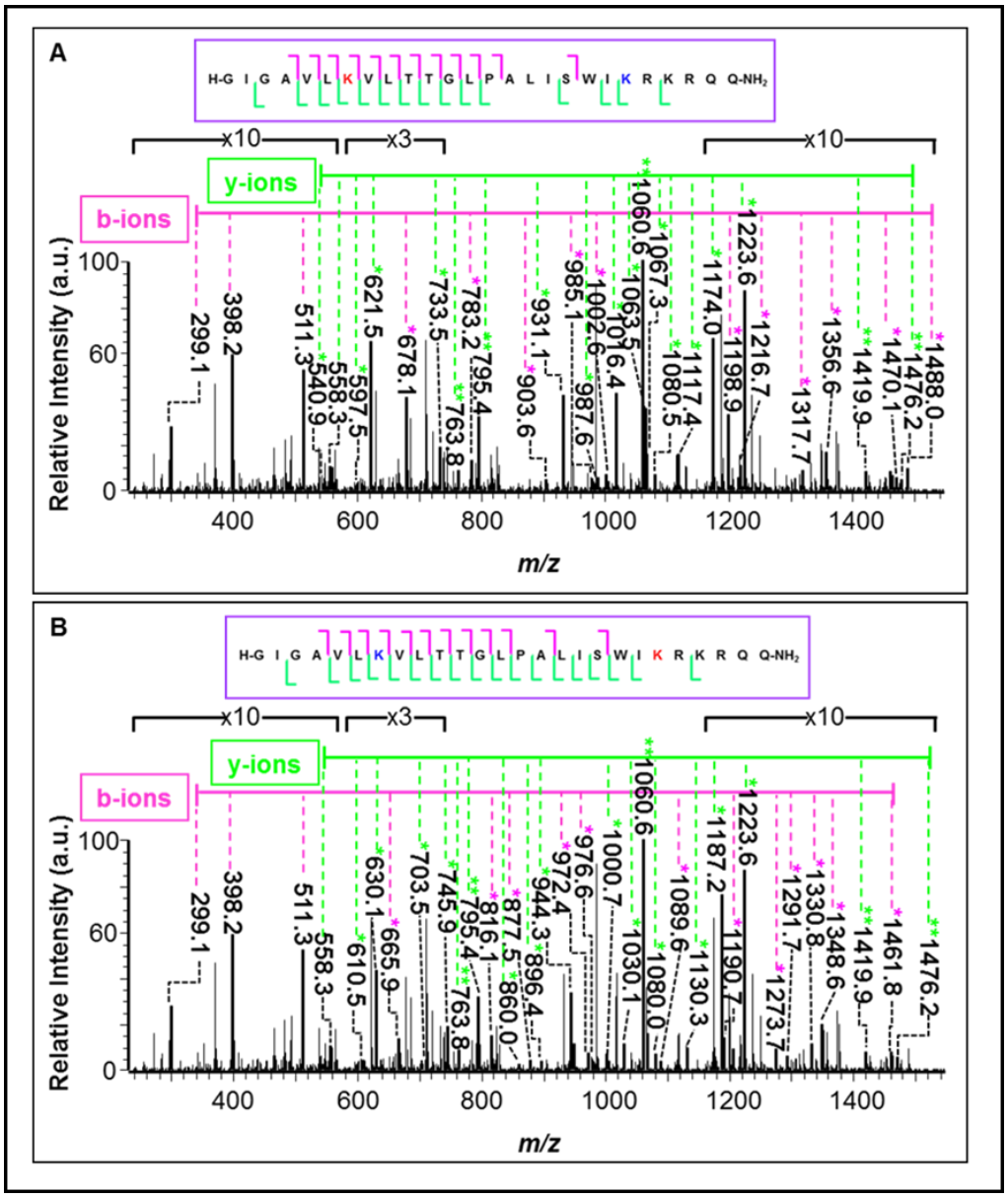

Figure 3.39. **LC-MS^2 spectrum for precursor ion $SynM_{pal+ole}$ at *m/z* 838 for $[M + 4H]^{4+}$ at 10.2 min of the EIC (see Figure 3.35, SynM/50:50 PPC:DOPC). (A) K7 oleoylation and K21 palmitoylation; (B) K7 palmitoylation and K21 oleoylation. Peptide fragments containing single or double acylation are marked with one asterisk and two asterisks respectively. Details provided in Appendix B Tables 9.23 and 9.24.**

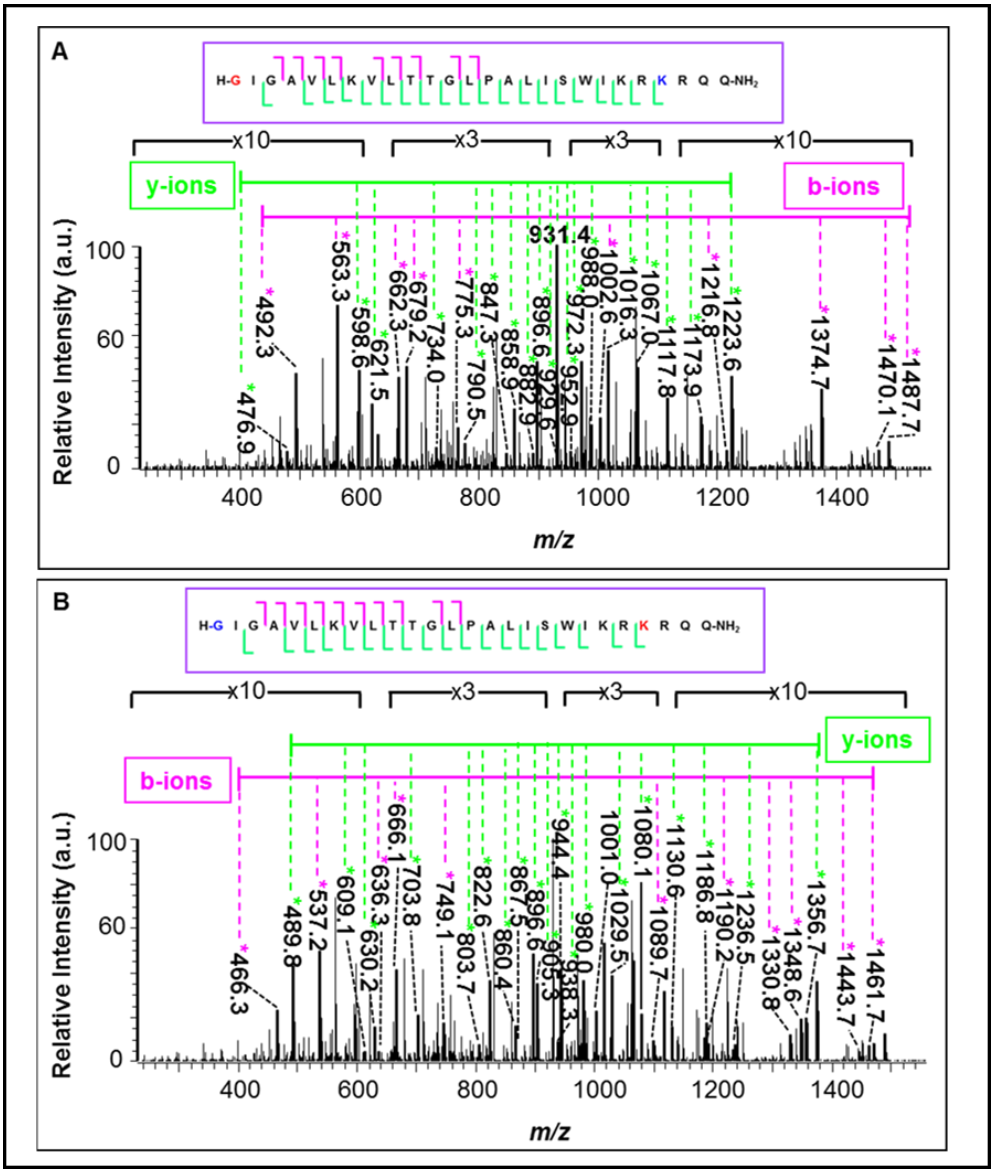

Figure 3.40. **LC-MS^2 spectrum for precursor ion SynM$_{pal+ole}$ at *m/z* 838 for [M + 4H]$^{4+}$ at 10.6 min of the EIC (see Figure 3.35, SynM/50:50 PPC:DOPC). (A) N-terminus oleoylation and K23 palmitoylation; (B) N-terminus palmitoylation and K23 oleoylation. Peptide fragments containing single acylation are marked with one asterisk. Details provided in Appendix B Tables 9.25 and 9.26.**

Figure 3.41 shows N-terminus/R22 palmitoyl plus oleoyl, the product ions are tabulated and shown in Appendix B Tables 9.27 and 9.28. In addition, palmitoylation plus oleoylation on N-terminus and R24 is shown in Figure 3.42 and Appendix B Tables 9.29 and 9.30. The presence of one acyl chain towards C-terminus portion is still evident from the spectra at *m/z* 931

for $y13_{pal}$ or 944 for $y13_{ole}$ (z=2) for $SynM_{pal+ole}$ cleavage at AA P14, and is therefore indicates the second acyl group towards N-terminus of the peptide.

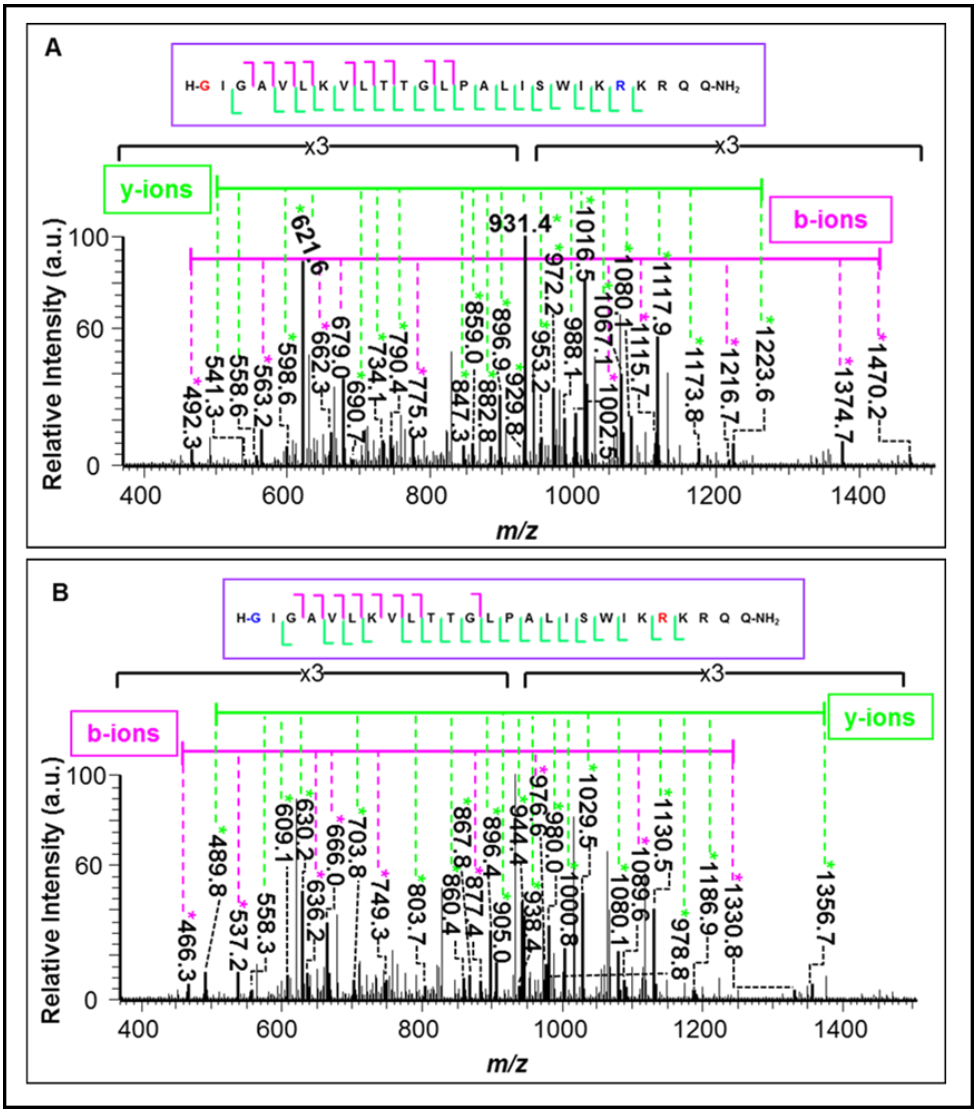

Figure 3.41. **LC-MS^2 spectrum for precursor ion $SynM_{pal+ole}$ at *m/z* 838 for $[M + 4H]^{4+}$ at 10.9 min of the EIC (see Figure 3.35, SynM/50:50 PPC:DOPC). (A) N-terminus oleoylation and R22 palmitoylation; (B) N-terminus palmitoylation and R22 oleoylation. Peptide fragments containing single acylation are marked with one asterisk. Details provided in Appendix B Tables 9.27 and 9.28.**

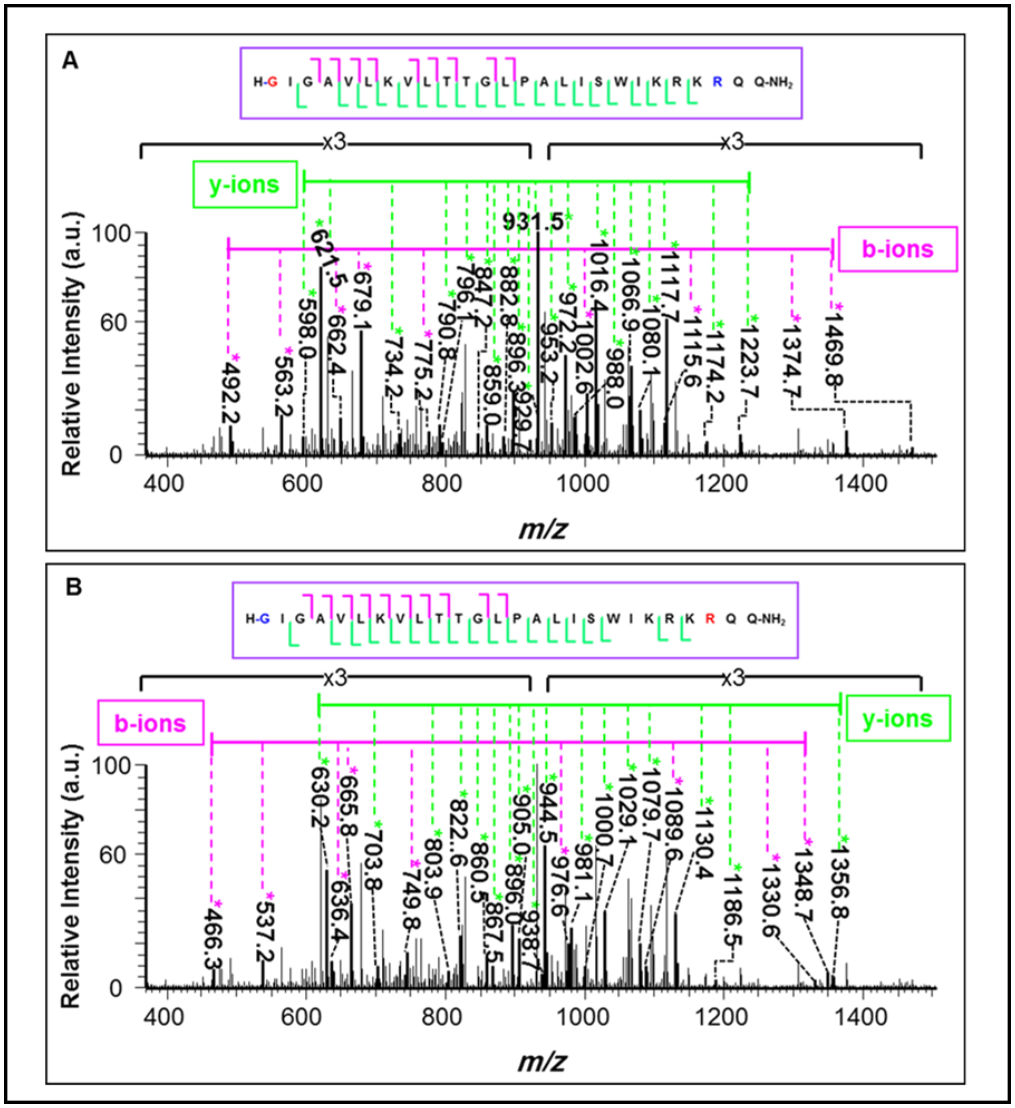

Figure 3.42. **LC-MS^2 spectrum for precursor ion SynM$_{pal+ole}$ at *m/z* 838 for [M + 4H]$^{4+}$ at 11.2 min of the EIC (see Figure 3.35, SynM/50:50 PPC:DOPC). (A) N-terminus oleoylation and R24 palmitoylation; (B) N-terminus palmitoylation and R24 oleoylation. Peptide fragments containing single acylation are marked with one asterisk. Details provided in Appendix B Tables 9.29 and 9.30.**

3.5.3.1. Summarised SynM$_{pal+ole}$ fragmentation

The increase in the number of assigned double acylation products from 7 to 14 (Table 3.8) is clearly related to the presence of two different acyl chains on two different sites of SynM. The results show how complexity is introduced into the system by increasing the number of acyl chain transfers to SynM or how will be the outcomes by moving towards real world systems where lipid content is very heterogeneous.

Table 3.8. **The sequence ladder of y-type and b-type ions for $SynM_{pal+ole}$ at different RTs (see Figure 3.35, SynM/50:50 PPC:DOPC). Product ions were produced by fragmenting the precursor ion of $SynM_{pal+ole}$ at *m/z* 838 (*z*=4). Full details are provided in Appendix B Tables 9.17-9.30.**

RT* (min)	Acylated SynM Cleavage Sites‡
9.1	
9.5	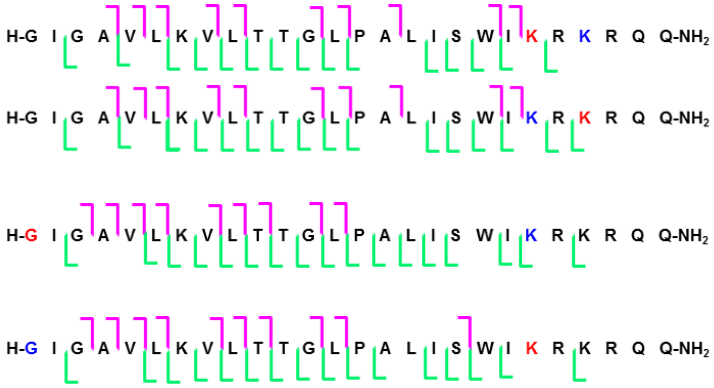
10.2	
10.6	
10.9	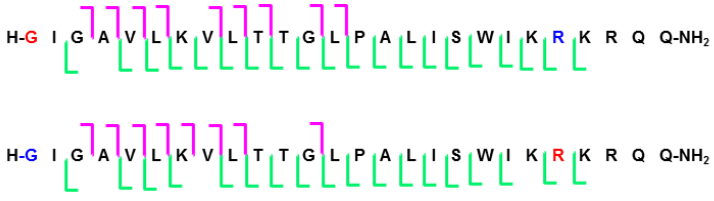

11.2	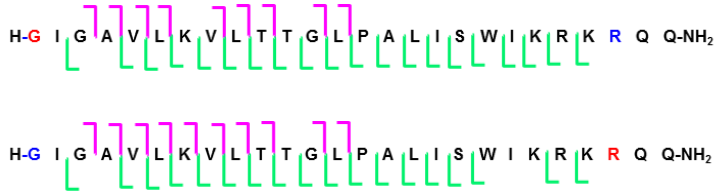

‡The sequence site of palmitoylation is highlighted in blue and oleoylation in red. The cleavage site of b-ions indicated by pink arrow and y-ions by green arrows.

3.6. BVM *vs* SynM selectivity towards *sn*-1 and *sn*-2 acyl chains

The reactivity difference in the lipidation process by each of SynM and naturally occurring melittin purified from bee venom (BVM) were further examined, see also section 3.2.4. The only difference between them is the presence of phospholipase A_2 (PLA_2) co-purified enzyme with BVM. This enzyme is known to hydrolyse the acyl group at the *sn*-2 position of the PC to give the LPC (1-acyl-LPC) and free fatty acid (free FA),[22-26] as shown in Figure 3.43. These two released components therefore change membrane architecture and are also known to effect membrane structure and phase behaviour[5,8-10] (see section 1.3.1.1). This effect is shown to be larger when free FA and LPC are added to pre-formed membranes.[8,13] In our case for example, the unilamellar liposomes were made first then mixed with BVM, which in turn was expected to release LPC and free FA by the action of PLA_2. In addition, cone shape LPC and nearly cylindrical shape FA at equimolar ratio form bilayers as for PCs.[27] Consequently, their role in the lipidation process needs to be considered. A greater role of LPC over PC in the lipidation process is already apparent from the work discussed earlier when PC:LPC were mixed (see section 3.4), while the role of FA in lipidation is not known exactly. A covalent link between peptide/protein and fatty acyl chain is shown in several studies but does not provide a clear evidence for the source of the acyl chain, whether it comes from PC, LPC or free FA. LC-MS analysis of human red cells has confirmed protein post-translational modification (PTM) by nitrated FA *in vivo*.[28] Further, it is also important to consider the amount and the activity of PLA_2 enzyme in the purchased

sample of BVM. The major component of bee venom is shown to be 40-50% (w/w) melittin by dry weight and the second most abundant component is 10-12% (w/w) of PLA_2.[29] However melittin is known to enhance PLA_2 activity[30,31]; the activity of PLA_2 was indicated as ≤ 0.5% according to the supplier (Sigma Aldrich).

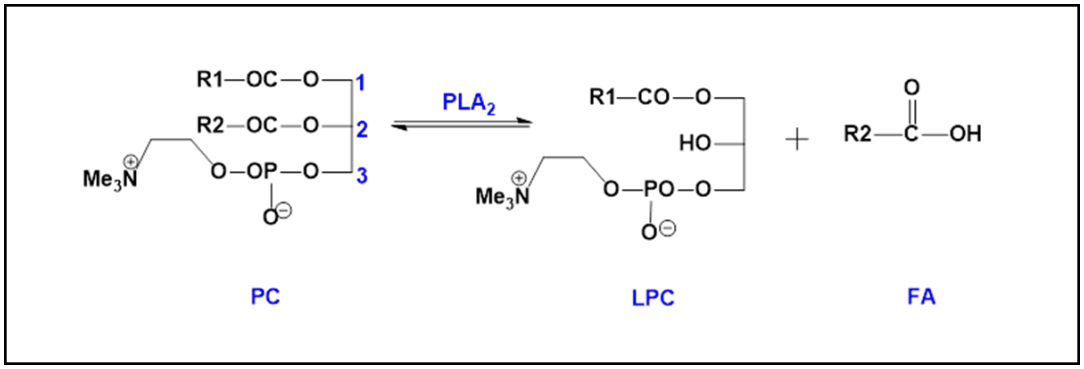

Figure 3.43. **The formation of LPC and free FA by the hydrolysis of *sn*-2 position of PC by PLA_2 enzyme.**

3.6.1. Selectivity comparison using POPC and OPPC

Acylation selectivity of melittin towards the *sn*-1 and *sn*-2 position of the PC was probed using the PC regioisomers POPC and OPPC, Figure 3.44, each isomer being a mixed-chain PC (palmitoyl (C16:0) and oleoyl (C18:1)) reversed positions on the glycerol core.

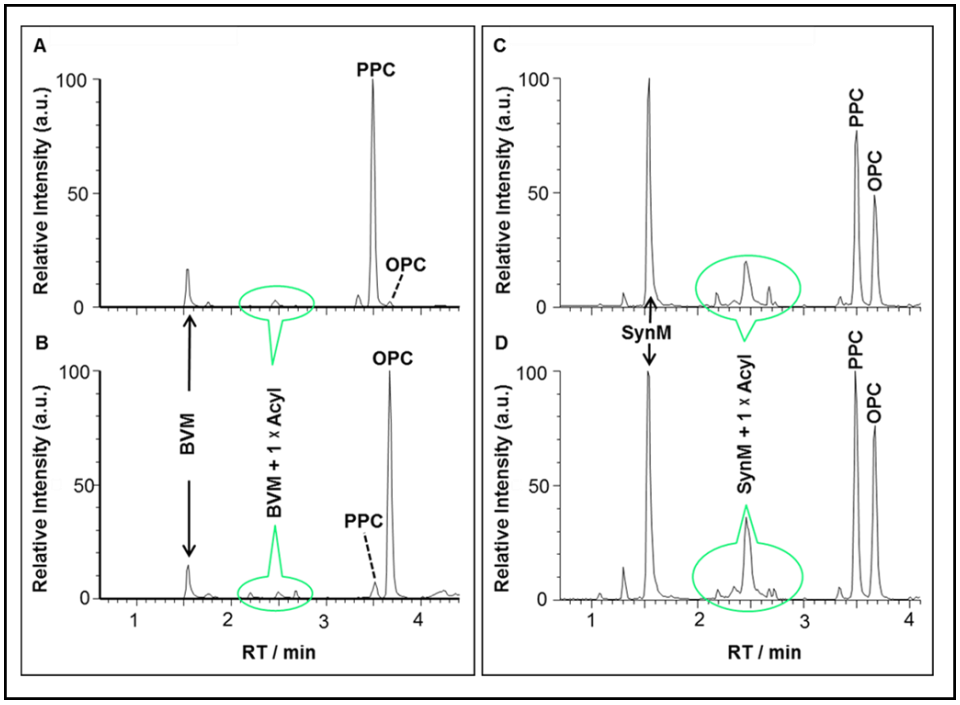

Figure 3.44. **Base peak chromatogram (BPC) of melittin incubation with each of POPC and OPPC liposomes at 37 °C over 168 h, analysed on the Synapt G2-s using LC-MS Method-III (see section 8.1.2.2.1). Single acylation products are highlighted. (A) BVM incubation with POPC; (B) BVM incubation with OPPC; (C) SynM incubation with POPC; (D) SynM incubation with OPPC.**

Incubating SynM with each of POPC and OPPC unilamellar liposomes at physiological conditions showed a slight preference towards the acyl group at *sn*-1 position of the glycerol (Figure 3.45), which is in a good agreement with a previous study[2]. The same reaction with BVM showed a significant difference in acyl transfer between acyl groups at the *sn*-1 and *sn*-2 positions, as shown in Figure 3.45. There is faster formation of BVM_{pal} over BVM_{ole} when using POPC. This indicates faster palmitoyl transfer than oleoyl, while this was the opposite in OPPC membranes. Owing to PLA_2 activity on PCs (see Figure 3.43), PPC (1-palmitoyl-LPC) plus oleoyl FA are released by PLA_2 hydrolysis of POPC at *sn*-2, while OPC (1-oleoyl-LPC) plus palmitoyl FA are released by PLA_2 hydrolysis of OPPC at *sn*-2 position. Consequently, both POPC and the enzymatically released PPC react with BVM and produce the major product from palmitoyl transfer. Similarly, both OPPC and released OPC participate in advanced oleoyl transfer to BVM. Interestingly, there is also evidence of a negligible role of released free FA over a predominant

released LPC role in lipidation process. These results confirm the activity of PLA_2 in spite of its low abundance in the commercial sample. In addition, both LPCs (PPC and OPC) are also added to the system by incubating the peptide (B-VM and SynM) with the PC liposomes through lipidation reaction (see section 3.3), however both BVM and SynM share this later reaction and cannot account for the dramatic difference in lipidation reactivity for both peptides.

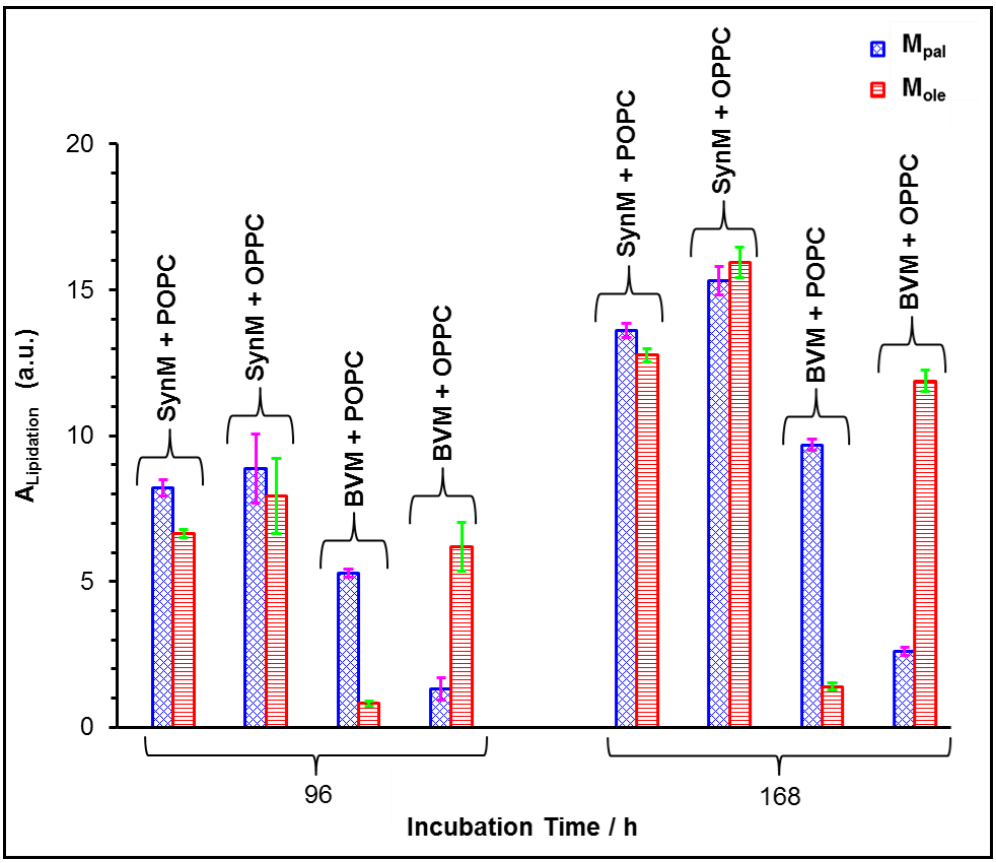

Figure 3.45. **Bar chart representation of the abundance for palmitoylated melittin (M_{pal}) and oleoylated melittin (M_{ole}) following SynM and BVM incubation with each of POPC and OPPC at 37 °C over 96 h and 168 h. Errors plotted as SEM of normalised peak area (n=3). The normalisation of M_{pal} or M_{ole} was performed relative to the summation of peak area for (non-acylated melittin + M_{pal} + M_{ole}) in the reaction medium. Peak areas were measured from EIC of all observed charge states for each species.**

Increasing melittin acylation with time is visible in these lipidation systems (Table 3.9 and see also Figure 3.45). The results also evident are that the melittin reaction with OPPC is marginally faster than that for POPC membranes (Table 3.9 and Figure 3.45). Interestingly, comparison between total acylated melittin in SynM and BVM indicates faster acylation by SynM over BVM for both POPC and OPPC membranes (Table 3.9 and Figure 3.45).

Table 3.9. **The percentage of total conversion of unmodified melittin to total lipidated melittin following SynM and BVM incubation with each of POPC and OPPC at 37 °C over 96 and 168 h, see Figure 3.45.**

Incubation Time (h)	%Total Lipidation*			
	SynM + POPC	SynM + OPPC	BVM + POPC	BVM + OPPC
96	15 ± 0.9	17 ± 2.2	6 ± 0.7	7.5 ± 1.6
168	26 ± 1.0	31 ± 1.4	11 ± 0.8	14.5 ± 1.0

*Total lipidation product includes palmitoylated melittin plus oleoylated melittin (M_{pal} + M_{ole}). Errors represent SEM of normalised peak area (n=3).

To more closely mimic natural membranes in their lipid composition, a binary lipid system of biological relevance for PC:PS (4:1) was included in this study. This binary lipid system is also important to study the effect of lipid classes, PC (neutral) and PS (negative), on the lipidation of BVM. This is because earlier reports showed that melittin has a greater binding affinity for the membrane in the presence of negatively charged lipids.[2,32-36] In addition, to differentiate between the effect of PS and PC post acyl transfer, different acyl chains on the PS have been used. The presence of stearoylated and linoleoylated BVM (BVM_{ste} and BVM_{lin}) is an evident for PS participating in non-enzymatic acyl transfer (Figure 3.46) but at a lower level than that for PC (Table 3.10). This is consistent with the lower ratio of PS relative to PC in accordance with the composition of lipid membrane, and also supporting earlier results[3].

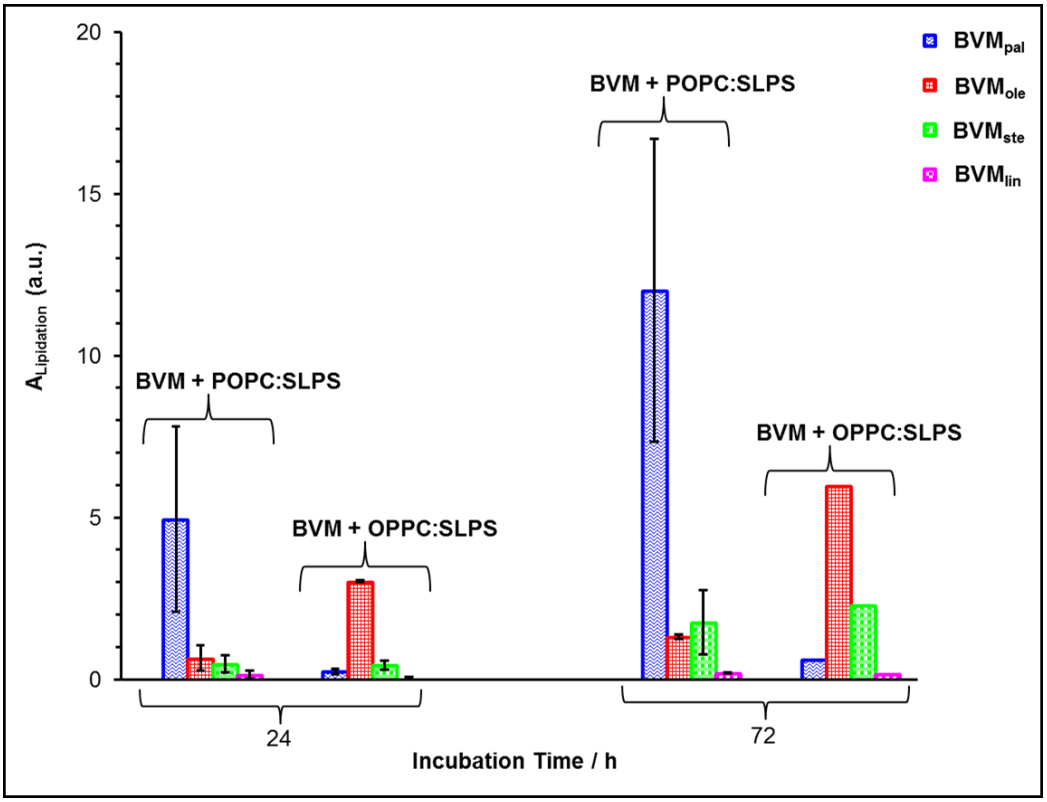

Figure 3.46. **Bar chart representation of the abundance for palmitoylated BVM (BVM_{pal}), oleoylated BVM (BVM_{ole}), stearoylated BVM (BVM_{ste}) and linoleoylated BVM (BVM_{lin}) following BVM incubation with each of POPC:SLPS and OPPC:SLPS at a ratio (4:1) at 37 °C over 24 and 72 h. The samples were analysed on the LQFT using LC-MS Method-I (see section 8.1.2.1.1). Errors plotted as SEM of normalised peak area (n=2). The normalisation for each single acylation were performed relative to summation of peak area for (non-acylated BVM + BVM_{pal} + BVM_{ole} + BVM_{ste} + BVM_{lin}) in the reaction medium. Peak areas were measured from EIC of all observed charge states.**

Table 3.10. **The percentage of total conversion of unmodified BVM to lipidated BVM followed BVM incubated with each of POPC:SLPS and OPPC:SLPS (4:1) at 37 °C over 24 and 72 h, see Figure 3.46.**

Incubation Time (h)	% Total Lipidation*					
	%Lipidation by PC + PS		%Lipidation by PC		%Lipidation by PS	
	BVM + POPC:SLPS	BVM + OPPC:SLPS	BVM + POPC:SLPS	BVM + OPPC:SLPS	BVM + POPC:SLPS	BVM + OPPC:SLPS
24	6 ± 2.7	4 ± 0.7	5.5 ± 2.5	3 ± 0.5	0.6 ± 0.9	0.5 ± 0.6
72	15 ± 3.4	9	13 ± 3.1	6.5	2 ± 1.4	2.5

*Total lipidation product include: BVM_{pal} + BVM_{ole} + BVM_{ste} + BVM_{lin}, for lipidation by PC + PS; BVM_{pal} + BVM_{ole}, for lipidation by PC; BVM_{ste} + BVM_{lin}, for lipidation by PS. Errors represent SEM of normalised peak area (n=2).

In addition, comparing the relative ratio of acyl transfer from PC to BVM in the absence and presence of PS (see Tables 3.9 and 3.10 respectively) shows that PS lipid enhances acyl transfer from PC to BVM, predominantly noticed in POPC system over OPPC. This is visible in the formation of 13% lipidated BVM over 72 h by neutral PC for BVM/POPC:SLPS system (see Table 3.10) relative to 6% conversion over 96 h for BVM/POPC system (see Table 3.9), in agreement with the previous studies[2.3]. Moreover, faster stearoylation over linoleoylation (see Figure 3.46), particularly clear over 72 h, is additionally supporting PLA_2 activity in BVM to hydrolyse SLPS at its *sn*-2 position[25,37-39] to release SPS as lysophospholipid, and this is in turn reacts with BVM in addition of its reaction with SLPS lipid.

For further investigation into PLA_2 activity, LPC generation in the reaction medium was followed. A significant difference between PPC and OPC peak intensities was shown following incubation BVM with each of POPC and OPPC, while this difference is less significant for SynM (see Figure 3.44). This is very evident from Figure 3.47, which shows the peak area for each LPC during SynM and BVM reaction with each of POPC and OPPC liposomes. Much greater abundance of 1-acyl-LPC (PPC in POPC and OPC in OPPC) than 2-acyl-LPC in BVM reaction with artificial membrane

confirms PLA_2 activity on *sn*-2 position, while both LPC by-products have a comparable abundance in SynM reaction with artificial membranes.

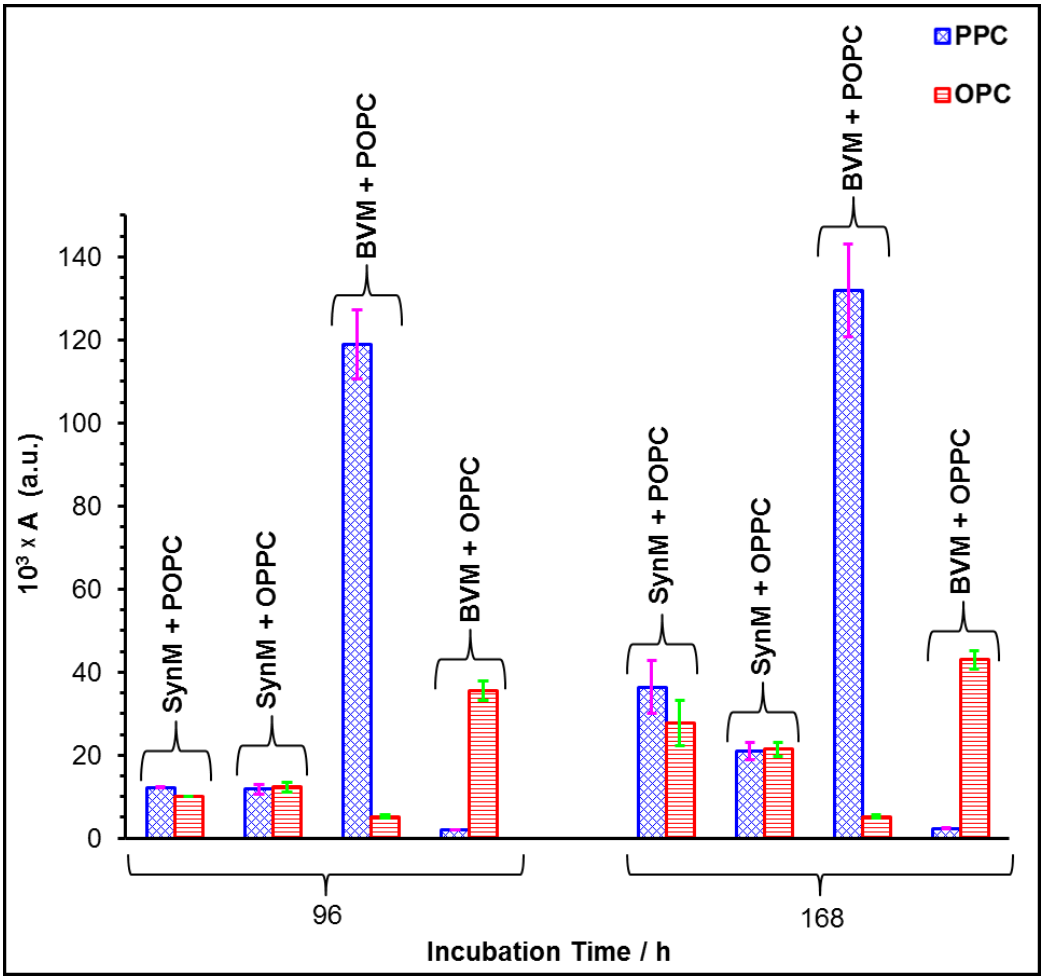

Figure 3.47. **Bar chart representation of PPC and OPC abundance following SynM and BVM incubation with each of POPC and OPPC at 37 °C over 96 and 168 h. Errors plotted as y-axis SEM of the peak area (A), when n=3. Peak areas were measured from EIC.**

3.6.2. Reaction with OPC:DPPC

The role of PLA_2 activity on PCs was extended in a parallel experiment comparing SynM and BVM reactions with 50:50 OPC:DPPC, Figure 3.48. SynM shows greater reactivity towards LPC over PC, yet again demonstrating faster formation of $SynM_{ole}$ from the LPC over $SynM_{pal}$ from the PC throughout the different incubation times. On the other hand, BVM shows a competition between palmitoylation and oleoylation products. This is

because the presence of PLA_2 naturally within BVM solution will hydrolyse DPPC first to release PPC in addition of its formation during aminolysis reaction between BVM and DPPC. This reflects in increasing the amount of PPC in the reaction medium over time and thus increasing the amount of palmitoyl transfer. Comparing SynM and BVM reactivity towards lipidation in this experiment, once more, shows SynM to have faster reactivity than that for BVM. This is calculated from the extent of melittin conversion to acylated melittin (Figure 3.48). The total conversion of non-acylated SynM to acylated SynM increased from ≈ 3% to 75% by increasing incubation time from 3h to 168 h, while during this time the extent of BVM conversion is ≈ 1% to 50%. This is consistent with the earlier results described for SynM *vs* BVM reactivity in 50:50 PPC:OPC (see section 3.2.4).

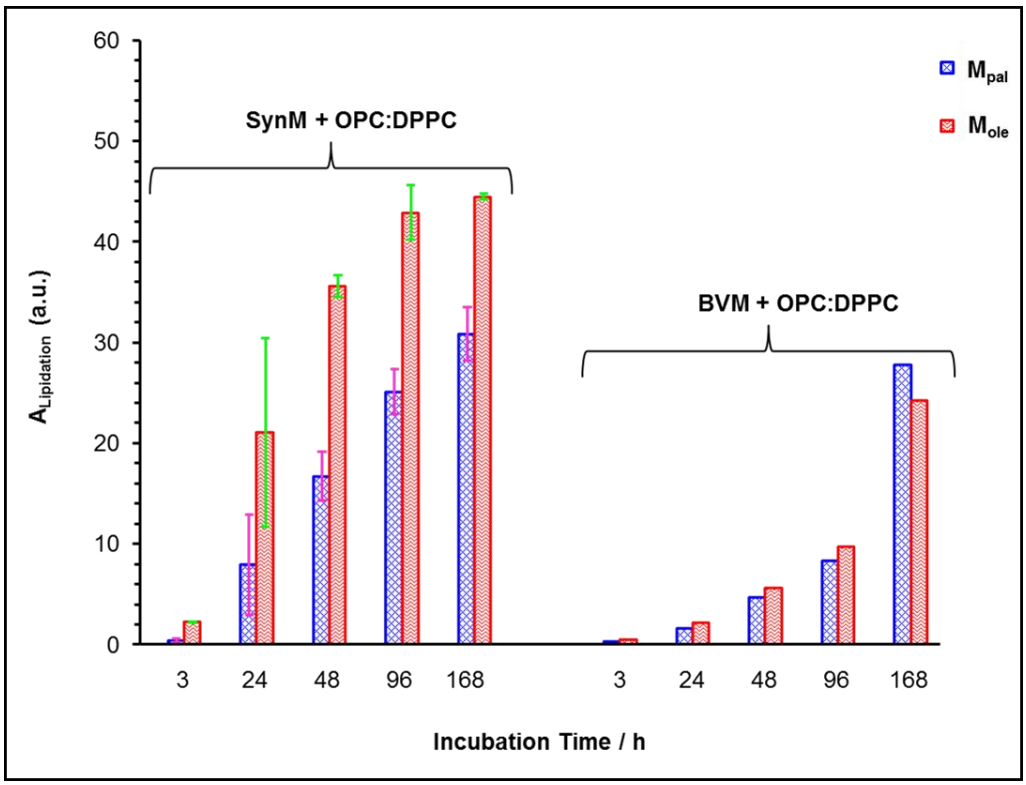

Figure 3.48. **Bar chart representation of the abundance for palmitoylated melittin (M_{pal}) and oleoylated melittin (M_{ole}) following SynM and BVM incubation with 50:50 OPC:DPPC at 37 °C over different incubation times. The samples were analysed on the LTQFT using LC-MS Method-I (see section 8.1.2.1.1). Errors plotted as SEM of normalised peak area (n=2). Peak areas were measured from EIC of all observed charge states. The normalisation of melittin single acylation was performed as described in Figure 3.45.**

3.7. Conclusion

The diversity and complexity of biological membranes was simplified to include the most abundant lipid membrane, PC, and/or the less abundant lipid species, LPC, in the mimicked membrane to explore non-enzymatic fatty acyl transfer to melittin. The orientation of melittin helix in the plane of PC membrane and the penetration to approximately the depth of the glycerol groups of the lipid[2,40] is consistent with the acyl transfer from PC membrane to the nucleophilic groups of melittin. Acyl transfer from LPCs herein also indicates a close proximity between melittin reactive groups and LPC carbonyl group of the acyl chain. The structure of monomeric melittin as α-helical conformation within PC membranes[40,41] or LPC micelles[42] has been confirmed by different methods of analysis, including NMR,[41,42] oriented circular dichroism (OCD) and X-ray diffraction[40]. Interestingly, for the first time, analysis for LPCs involved in the lipidation process is shown to behave differently than PCs counterpart. LPCs have greater reactivity than PCs, evident from melittin aminolysis reaction. This suggests a change in melittin orientation within LPC through a deeper penetration into the hydrophobic core of LPC micelle. This is also shown to have an effect in altering the proportion of selectivity on N-terminus > K23 by PC membrane bilayer phase to K23 > N-terminus by LPC micelle phase. The most reactive sites for acylation was found to be on N-terminal and K23 amino groups, while K7 and K21 amino groups together with hydroxyl group of S18 and guanidinium group of R22 and R24 are the less reactive sites. This is in agreement with the results described by Dods *et al.* for the contribution of amine basicity and the location of lipidated sites on the rate of melittin acylation. In addition, higher selectivity towards palmitoylation *vs* oleoylation is also confirmed herein via a competition of acyl transfer from PPC:OPC at equal mole ratio. This is clearly not related with the difference in the position of acyl chain and/or difference in ionisation efficiency of palmitoyl and oleoyl acyl chains, as both PPC and OPC are involved in acyl transfer from *sn*-1 position and with having similar ionisation efficiency. Consequently, melittin favours aminolysis reaction with saturated fatty acyl chain, palmitoyl, over

unsaturated fatty acyl chain, oleoyl, coming from the same *sn*-position of the lipid.

The lipidation reaction is also found to be independent of PCs phase behaviour, as both DPPC gel phase and DOPC liquid crystalline phase membranes have shown similar results. This illustrates that changing the physical state of lipid-bilayer does not have an influence on changing melittin orientation in the PC membrane and therefore the extent of aminolysis reaction in melittin:DPPC *vs* melittin:DOPC is not affected. Consequently, the reactivity between lipid membrane and bound peptides/proteins can be expected in all membrane phases. The two sources of melittin peptide, SynM (PLA_2-free) and BVM (containing PLA_2), have shown to be acylated non-enzymatically by artificial membranes under physiological conditions but at different reactivity. It is interesting to see that lipidated melittin can be used as a probe to follow PLA_2 activity towards PLs, and this can be applied in different PL systems to follow this activity. Overall, there is a broad relationship between lipid membrane and peptides/proteins, and this relation is further complicated by the peptide:membrane remaining attached together for longer durations. This was found by confirming the transfer of the second and third acyl chain in addition of single acylation. However, LC-MS can still deal with this complexity and provide basics for better understanding the insight of the biological membrane process. Consequently, melittin lipidation opens a gate to deal with unknown peptide/protein modifications occur in nature via non-enzymatic process and particularly important for long-lived proteins.

3.8. References

1. Pridmore, Catherine J., Jackie A. Mosely, Alison Rodger, and John M. Sanderson. "Acyl transfer from phosphocholine lipids to melittin." *Chemical Communications,* 47 (**2011**): 1422-1424.

2. Dods, Robert H., Jackie A. Mosely, and John M. Sanderson. "The innate reactivity of a membrane associated peptide towards lipids: acyl transfer to melittin without enzyme catalysis." *Organic & Biomolecular Chemistry,* 10 (**2012**): 5371-5378.

3. Dods, Robert H., Burkhard Bechinger, Jackie A. Mosely, and John M. Sanderson. "Acyl transfer from membrane lipids to peptides is a generic process." *Journal of Molecular Biology,* 425 (**2013**): 4379-4387.

4. Hauser, H., W. Guyer, B. Levine, P. Skrabal, and R. J. P. Williams. "The conformation of the polar group of lysophosphatidylcholine in H_2O; conformational changes induced by polyvalent cations." *Biochimica et Biophysica Acta (BBA)-Biomembranes,* 508 (**1978**): 450-463.

5. Van Echteld, C. J. A., B. De Kruijff, J. G. Mandersloot, and J. De Gier. "Effects of lysophosphatidylcholines on phosphatidylcholine and phosphatidylcholine/cholesterol liposome systems as revealed by ^{31}P-NMR, electron microscopy and permeability studies." *Biochimica et Biophysica Acta (BBA)-Biomembranes,* 649 (**1981**): 211-220.

6. Grit, Mustafa, and Daan JA Crommelin. "The effect of aging on the physical stability of liposome dispersions." *Chemistry and Physics of Lipids,* 62 (**1992**): 113-122.

7. Mouritsen, Ole G. "Lipids, curvature, and nano-medicine." *European Journal of Lipid Science and Technology,* 113 (**2011**): 1174-1187.

8. Arouri, Ahmad, and Ole G. Mouritsen. "Membrane-perturbing effect of fatty acids and lysolipids." *Progress in Lipid Research,* 52 (**2013**): 130-140.

9. Van Echteld, C. J. A., B. De Kruijff, and J. De Gier. "Differential miscibility properties of various phosphatidylcholine/lysophosphatidylcholine mixtures." *Biochimica et Biophysica Acta (BBA)-Biomembranes,* 595 (**1980**): 71-81.

10. Pantusa, Manuela, Luigi Sportelli, and Rosa Bartucci. "Phase behaviour of DPPC/Lyso-PPC mixtures by spin-label ESR and spectrophotometry." *Journal of Spectroscopy,* 22 (**2008**): 153-163.

11. Allegrini, Peter R., Guus van Scharrenburg, Gerard H. De Haas, and Joachim Seelig. "^{2}H-and ^{31}P-NMR studies of bilayers composed of 1-acyllysophosphatidylcholine and fatty acids." *Biochimica et Biophysica Acta (BBA)-Biomembranes,* 731 (**1983**): 448-455.

12. Needham, David, and Doncho V. Zhelev. "Lysolipid exchange with lipid vesicle membranes." *Annals of Biomedical Eengineering,* 23 (**1995**): 287-298.

13. Bhamidipati, Shastri P., and James A. Hamilton. "Interactions of lyso 1-palmitoylphosphatidylcholine with phospholipids: a ^{13}C and ^{31}P NMR study." *Biochemistry,* 34 (**1995**): 5666-5677.

14. Gawrisch, Klaus, and Laura L. Holte. "NMR investigations of non-lamellar phase promoters in the lamellar phase state." *Chemistry and Physics of Lipids,* 81 (**1996**): 105-116.

15. Høyrup, Pernille, Jesper Davidsen, and Kent Jørgensen. "Lipid membrane partitioning of lysolipids and fatty acids: effects of membrane phase structure and detergent chain length." *The Journal of Physical Chemistry B,* 105 (**2001**): 2649-2657.

16. Lynch, Daniel V., and Peter L. Steponkus. "Lyotropic phase behavior of unsaturated phosphatidylcholine species: relevance to the mechanism of plasma membrane

destabilization and freezing injury." *Biochimica et Biophysica Acta (BBA)-Biomembranes,* 984 (**1989**): 267-272.

17. Ulrich, Anne S., Malkit Sami, and Anthony Watts. "Hydration of DOPC bilayers by differential scanning calorimetry." *Biochimica et Biophysica Acta (BBA)-Biomembranes,* 1191 (**1994**): 225-230.

18. Ladbrooke, B. D., and D. Chapman. "Thermal analysis of lipids, proteins and biological membranes a review and summary of some recent studies." *Chemistry and Physics of Lipids,* 3 (**1969**): 304-356.

19. Biltonen, Rodney L., and Dov Lichtenberg. "The use of differential scanning calorimetry as a tool to characterize liposome preparations." *Chemistry and Physics of Lipids,* 64 (**1993**): 129-142.

20. Marsh, Derek. "*Handbook of Lipid Bilayers*." CRC Press, **2013**.

21. Attwood, Simon J., Youngjik Choi, and Zoya Leonenko. "Preparation of DOPC and DPPC supported planar lipid bilayers for atomic force microscopy and atomic force spectroscopy." *International Journal of Molecular Sciences,* 14 (**2013**): 3514-3539.

22. Wang, Aijun, and Edward A. Dennis. "Mammalian lysophospholipases." *Biochimica et Biophysica Acta (BBA)-Molecular and Cell Biology of Lipids,* 1439 (**1999**): 1-16.

23. Six, David A., and Edward A. Dennis. "The expanding superfamily of phospholipase A_2 enzymes: classification and characterization." *Biochimica et Biophysica Acta (BBA)-Molecular and Cell Biology of Lipids,* 1488 (**2000**): 1-19.

24. Høyrup, P., Kent Jørgensen, and O. G. Mouritsen. "Phospholipase A_2—An enzyme that is sensitive to the physics of its substrate." *Europhysics Letters,* 57 (**2002**): 464-470.

25. Brown, William J., Kimberly Chambers, and Anne Doody. "Phospholipase A_2 (PLA_2) enzymes in membrane trafficking: mediators of membrane shape and function." *Traffic,* 4 (**2003**): 214-221.

26. Burke, John E., and Edward A. Dennis. "Phospholipase A_2 structure/function, mechanism, and signaling." *Journal of Lipid Research,* 50 (**2009**): S237-S242.

27. Jain, Mahendra Kumar, and Gerard H. De Haas. "Structure of 1-acyl lysophosphatidylcholine and fatty acid complex in bilayers." *Biochimica et Biophysica Acta (BBA)-Biomembranes,* 642 (**1981**): 203-211.

28. Batthyany, Carlos, Francisco J. Schopfer, Paul RS Baker, Rosario Durán, Laura MS Baker, Yingying Huang, Carlos Cerveñansky, Bruce P. Branchaud, and Bruce A. Freeman. "Reversible post-translational modification of proteins by nitrated fatty acids in vivo." *Journal of Biological Chemistry,* 281 (**2006**): 20450-20463.

29. Dotimas, E. M., and R. C. Hider. "Honeybee venom." *Bee World,* 68 (**1987**): 51-70.

30. Fletcher, Jeffrey E., Kirsten Michaux, and Ming-Shi Jiang. "Contribution of bee venom phospholipase A_2 contamination in melittin fractions to presumed activation of tissue phospholipase A_2." *Toxicon,* 28 (**1990**): 647-656.

31. Mingarro, Ismael, Enrique Pérez-Payá, Clemencia Pinilla, Jon R. Appel, Richard A. Houghten, and Sylvie E. Blondelle. "Activation of bee venom phospholipase A_2 through a peptide-enzyme complex." *FEBS Letters,* 372 (**1995**): 131-134.

32. Dempsey, Christopher E., and Georgina S. Butler. "Helical structure and orientation of melittin in dispersed phospholipid membranes from amide exchange analysis in situ." *Biochemistry,* 31 (**1992**): 11973-11977.

33. Ohki, Shinpei, Emil Marcus, Dinesh K. Sukumaran, and Klaus Arnold. "Interaction of melittin with lipid membranes." *Biochimica et Biophysica Acta (BBA)-Biomembranes,* 1194 (**1994**): 223-232.

34. Monette, Martine, and Michel Lafleur. "Modulation of melittin-induced lysis by surface charge density of membranes." *Biophysical Journal,* 68 (**1995**): 187-195.

35. Ladokhin, Alexey S., and Stephen H. White. "'Detergent-like' permeabilization of anionic lipid vesicles by melittin." *Biochimica et Biophysica Acta (BBA)-Biomembranes,* 1514 (**2001**): 253-260.

36. McIntosh, Thomas J. "The 2004 Biophysical Society-Avanti Award in Lipids address: roles of bilayer structure and elastic properties in peptide localization in membranes." *Chemistry and Physics of Lipids,* 130 (**2004**): 83-98.

37. Vance, Dennis E., and Jean Eaton Vance. "*Biochemistry of Lipids and Membranes*." Benjamin/Cummings Publishing Company, **1985**.

38. Choi, Ji Woong, Deron R. Herr, Kyoko Noguchi, Yun C. Yung, Chang-Wook Lee, Tetsuji Mutoh, Mu-En Lin et al. "LPA receptors: subtypes and biological actions." *Annual Review of Pharmacology and Toxicology,* 50 (**2010**): 157-186.

39. Dennis, Edward A. "Introduction to thematic review series: phospholipases: central role in lipid signaling and disease." *Journal of Lipid Research,* 56 (**2015**): 1245-1247.

40. Hristova, Kalina, Christopher E. Dempsey, and Stephen H. White. "Structure, location, and lipid perturbations of melittin at the membrane interface." *Biophysical Journal,* 80 (**2001**): 801-811.

41. Lam, Y. H., S. R. Wassall, C. J. Morton, R. Smith, and F. Separovic. "Solid-state NMR structure determination of melittin in a lipid environment." *Biophysical Journal,* 81 (**2001**): 2752-2761

42. Yuan, Peng, Phyllis J. Fisher, Franklyn G. Prendergast, and Marvin D. Kemple. "Structure and dynamics of melittin in lysomyristoyl phosphatidylcholine micelles determined by nuclear magnetic resonance." *Biophysical Journal,* 70 (**1996**): 2223-2238.

Chapter four: New insight to integral membrane protein (AQP0) lipidation by membrane lipids

---

One of the most abundant integral membrane protein in mammals which is produced by lens fibre cells is AQP0, also called aquaporin-0, major (membrane) intrinsic protein, MIP, MIP26, and MP26. This protein was shown to undergo a range of post-translational modifications (PTM) with age, that effect cellular processing and disease. It was hypothesised that AQP0 was lipidated by transfer from membrane through documenting oleoylated and palmitoylated AQP0.[1] Therefore if this is true then there should be more than oleoyl and palmitoyl fatty acyl chains. The application of improved liquid chromatography coupled to mass spectrometry (LC-MS) herein reported for the first time a broad lipidation profile at both positions of N-terminus (M1) and K238 sites of AQP0 in both bovine and human eye lenses. Interestingly, the lipidation profile at both sites is shown to reflect the fatty acid composition of the cytoplasmic membrane leaflet proximal to the site of lipidaion.*[2]

*****Some of the results described in this chapter have also been reported in the following publication: Ismail, Vian S., Jackie A. Mosely, Antal Tapodi, Roy A. Quinlan, and John M. Sanderson. "The lipidation profile of aquaporin-0 correlates with the acyl composition of phosphoethanolamine lipids in lens membranes." *Biochimica et Biophysica Acta (BBA)-Biomembranes,* 1858 (**2016**): 2763-2768.

4.1. Analysis of the intact AQP0 from four different regions of bovine eye lens (b-AQP0)

4.1.1. The identification of b-AQP0 modifications by ESI-LC-MS

Integral membrane proteins have two distinct properties that introduce some challenges for their analysis by MS; they are hydrophobic in nature and are low in abundance.[3,4] Despite AQP0's hydrophobicity[5] and increasing its hydrophobicity by lipidation modification,[1,6,7] the protein was analysed and characterised herein as its intact form by using an MS friendly surfactant of pentafluorooctanoic acid (PFOA). PFOA is a volatile surfactant and it has been successfully used here for the first time to solubilise b-AQP0 membrane protein. The novel advantage of this surfactant is already described to solublise membrane protein pellet as well as its compatibility with MS because of its low boiling point and volatility.[8] The four different age fractions of bovine AQP0 (b-AQP0) are b-AQP0-outer cortex, b-AQP0-inner cortex, b-AQP0-outer nucleus, and b-AQP0-inner nucleus, Figure 4.1. All protein age fractions were solubilised with PFOA surfactant and analysed directly as the intact form by LC-MS (see section 8.2.2.1.1, for experimental details).

It is interesting to know that, although the lens diameter decreases by moving from OC to the IN of the lens and thus expecting higher density of AQP0 in OC and decreases by moving towards IN, but a comparable amount of AQP0 is proposed in all of the four fractions. This is because graded refractive index in squid lenses has shown that proteins are densely packed in the nucleus fraction, while low protein density is found in the cortex fraction.[9]

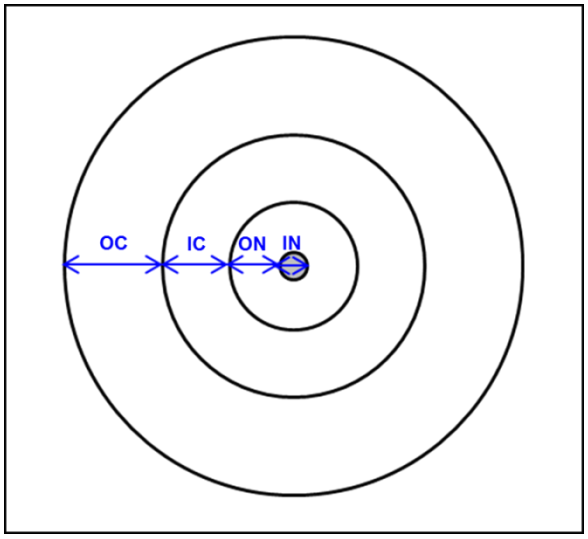

Figure 4.1. **Schematic diagram of bovine eye lens fractions according to the diameter of the membrane pellet. Different lens age fractions include OC = outer cortex (15 mm); IC = inner cortex (10 mm); ON = outer nucleus (8 mm); IN = inner nucleus (4 mm).**

The total ion chromatogram with a number of peaks eluting between 6-14 min of the chromatogram was produced from LC-MS analysis of b-AQP0-OC, as shown in Figure 4.2. The mass deconvolution spectrum was generated from the averaged MS spectrum over 9.7-10.9 min of the chromatogram, which contains several isotopomer envelopes (Figure 4.3).

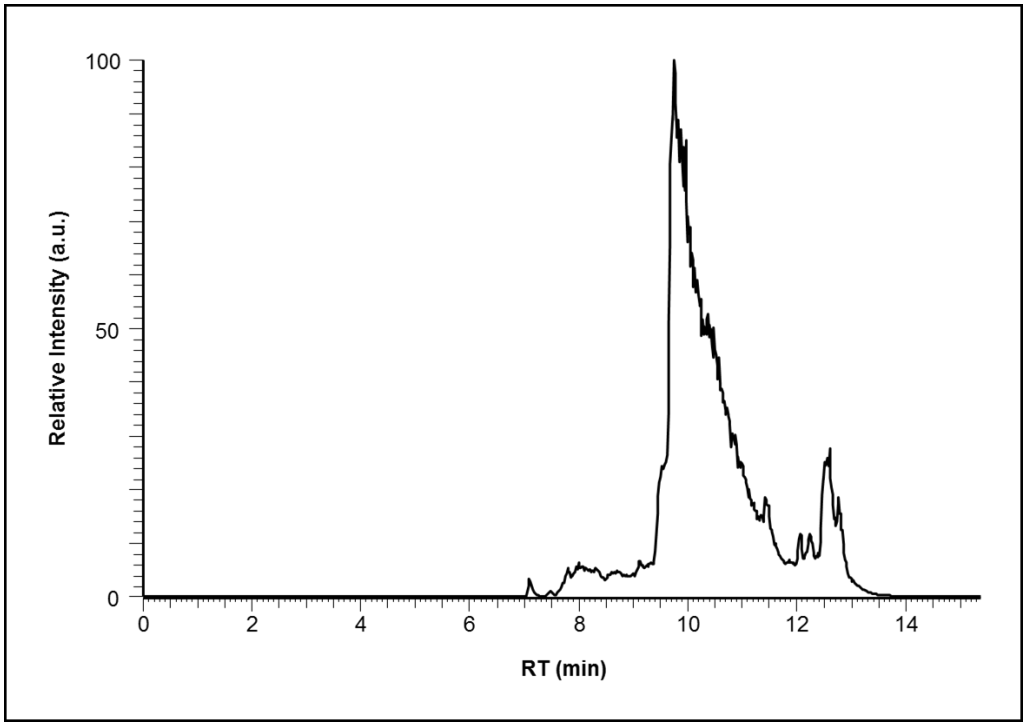

Figure 4.2. **Total ion chromatogram (TIC) of intact b-AQP0-OC analysis on the LTQFT using LC-MS Method-I (see section 8.1.2.1.1). The main peak in the chromatogram represents b-AQP0, the deconvolution mass spectrum $[M + H]^+$ over 9.7-10.9 min is shown in Figures 4.3 and 4.5. Lysophospholipids (LPL) and diacylphospholipids (PL) eluted around 6-10 min and 11-14 min of the chromatogram respectively.**

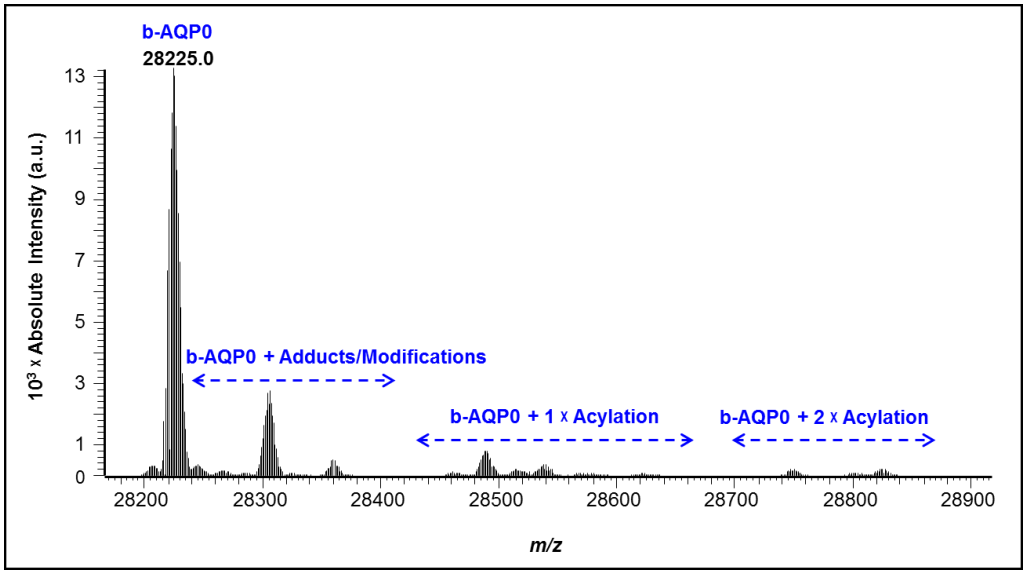

Figure 4.3. **Deconvoluted mass spectrum at 9.7-10.9 min of the LC gradient from the provided chromatogram (see Figure 4.2) for the protonated species $[M + H]^+$, modeled as a Gaussian distribution. Details provided in Table 4.1.**

The most intense peak at *m/z* 28225.0 corresponds to the most abundant isotope for $[M + H]^+$. Comparing this measured mass with the theoretical most abundant isotope $[M + H]^+$ at *m/z* 28222.95, calculated from amino acid sequence of unmodified b-AQP0 (Figure 4.4), indicates a mass shift of 2.05 Da relative to unmodified b-AQP0. This suggests the presence of two asparagine (N) or glutamine (Q) deamidation sites on the analysed b-AQP0, in agreement with the protein deamidation in previous reports[1,5]. Looking to the higher mass range, a number of low abundance species were observed and are assigned for b-AQP0 modification with phosphorylation, acylation, and some adduct ions added to the protein during sample preparation and storage process, details tabulated in Table 4.1. Lysophospholipids (LPL) and diacylphosholipids (PL) were also observed within this sample and eluted around 6-10 and 11-14 min respectively.

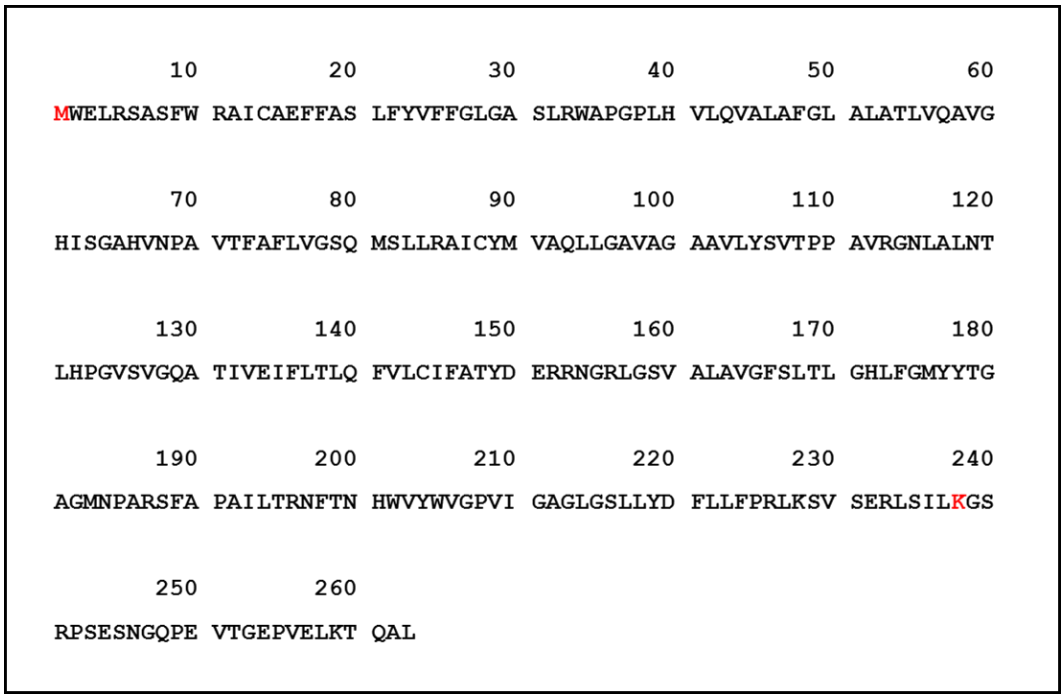

Figure 4.4. **Amino acid sequence for b-AQP0 obtained from (Uniprot entry P06624, http://www.uniprot.org/uniprot/P06624), with an average neutral mass of 28222.7 Da. The two reported sites of acylation, N-terminus (M1) and K238,[1] highlighted in red.**

Table 4.1. **The identified modified proteins in deconvolved spectra of b-AQP0-OC.**

Entry	*m/z* Meas‡	Mass Shift*	Assignment of Identified Modifications
1	28246.9	21.9	Na
2	28266.9	41.9	Acetyl or Azide
3	28304.9	79.9	P (Phosphorylation)
4	28327.0	102.0	Na + P
5	28358.9	133.9	Na + P + 2 × O (Oxidation)
6	28463.2	238.2	Palmitoyl (C16:0)
7	28489.1	264.1	Oleoyl (C18:1)
8	28491.1	266.1	Stearoyl (C18:0)
9	28513.1	288.1	Dihomo-γ-linolenoyl (C20:3)
10	28515.0	290.0	Eicosadienoyl (C20:2)
11	28535.1	310.1	Docosahexaenoyl (C22:6)
12	28537.1	312.1	Docosapentaenoyl (C22:5)
13	28543.5	318.5	Docosadienoyl (C22:2)
14	28569.1	344.1	Oleoyl (C18:1) + P
15	28571.1	346.1	Tetracosadienoyl (C24:2) or Stearoyl (C18:0) + P
16	28623.4	398.4	Palmitoyl (C16:0) + 2 × P
17	28627.2	402.2	Eicosadienoyl (C20:2) + P + 2 × O
18	28749.1	524.1	Oleoyl (C18:1) + Linolenoyl (C18:3)
19	28807.1	582.1	Palmitoyl (C16:0) + Oleoyl (C18:1) + P
20	28823.3	598.3	Palmitoyl (C16:0) + Oleoyl (C18:1) + P + O
21	28825.3	600.3	Palmitoyl (C16:0) + Stearoyl (C18:0) + P + O

‡Meas: measured most abundant isotope, obtained from deconvolution spectrum [M + H]+ (see Figures 4.3 and 4.5).

*Mass shifts calculated from the most abundant b-AQP0 at *m/z* 28225.0 (see Figure 4.3) and thus all modifications matches contain double deamidation.

The use of sodium azide during storing membrane pellets to prevent bacterial growth (see section 8.2.1.2) accounts for some of the adduct ions observed for the intact b-AQP0 (Table 4.1, entries 1 and 2). Both adducts azide (N_3^-) and acetyl (C_2H_3O) are proposed for the protein modification with the mass shift of 41.9 Da, however protein acetylation is more likely herein. This is because azide is unstable and anion organic molecule and more likely to form anionic adducts in the negative ion mode (ESI-). In addition, Gutierrez *et al.* also reported acetylation on AQP0 through direct tissue profiling.[6] The

second most abundance envelope (Figure 4.3) at *m/z* 28304.9 is shown to be for phosphorylated b-AQP0 as there is 79.9 Da mass shift (Table 4.1, entry 3). This phosphorylation modification is already documented for b-AQP0.[5,10-13] Protein modification with double oxidation is also observed (Table 4.1, entry 5), supporting previous studies.[5] The oxidation process in lens can take place by photo and/or chemical oxidation which in turn has influence on lens constituents of lipids and proteins.[14] These modifications followed by a series of species between 28450-28850 Da, suggested for b-AQP0 single acylation (Figure 4.5 A and panel B) and double acylation (Figure 4.5 C).

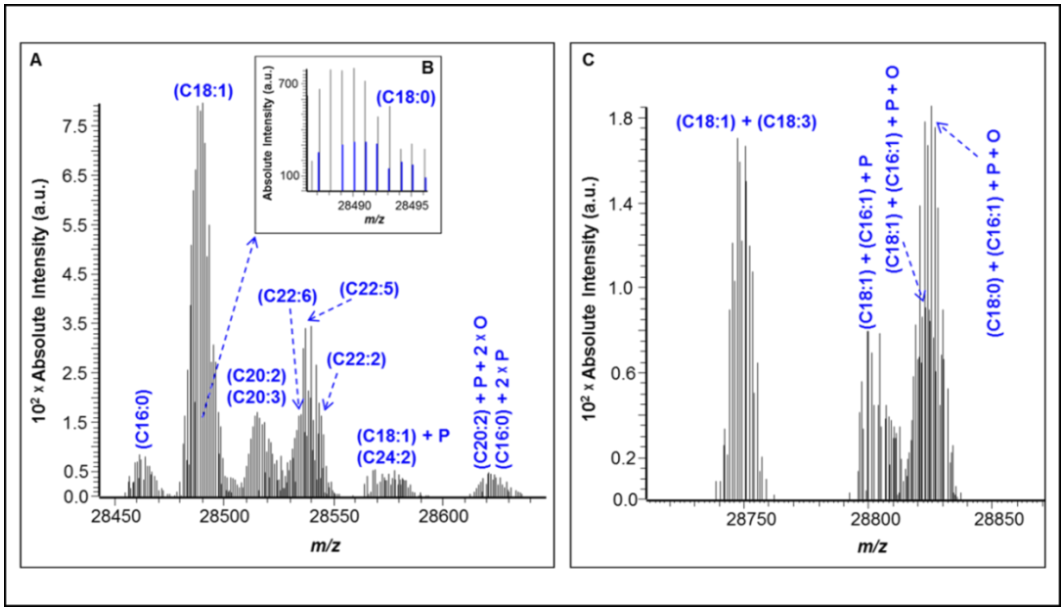

Figure 4.5. **Magnified regions of b-AQP0-OC single acylation and double acylation (see Figure 4.3) from deconvoluted mass spectrum for $[M + H]^+$. (A) b-AQP0-OC single acylation at *m/z* 28450-28650, the insert spectrum (B) represents overlapping envelops of stearoyl (C18:0) with the most abundant oleoyl (C18:1), stearoyl peaks highlighted in blue; (C) b-AQP0-OC double acylation at *m/z* 28700-28850. Details provided in Table 4.1.**

The most abundance species among this series is proposed to be for b-AQP0 oleoylation (C18:1) with 264.1 Da mass shift (Table 4.1, entry 7). In addition, a mass shift of 238.2 Da is also visible (Table 4.1, entry 6), which is consistent with the addition of palmitoylation modification (C16:0). These two PTMs in mammalian lenses have been documented in numerous

studies.[1,6,7,15] Interestingly, the mass resolution is sufficient to resolve protein stearoylation (C18:0) from oleoylation (C18:1), Figure 4.5 panel B and Table 4.1 entry 8. This novel acylation with other longer polyunsaturated acyl chains (C20, C22 and C24) were also observed here for the first time, Table 4.1, entries 9-13. Most of the observed acylation modifications were also found together with phosphorylation (Table 4.1, entries 14-16) and/or oxidation (Table 4.1, entries 17, 20 and 21). It is difficult to assign the peak with *m/z* 28571.1 whether it represents modified b-AQP0 by tetracosadienoyl (C24:2) or stearoyl (C18:0) plus phosphorylation (Table 4.1, entry 15), because each of which provide 346.3 Da and 346.2 Da of theoretical monoisotopic mass respectively. Further, the possibility of b-AQP0 acylation with two acyl groups is also observed in this fraction but at low abundance (Figure 4.5 C and Table 4.1, entries 18-21). Coupling of two acyl chains with b-AQP0 had not been reported previously *in vivo* and shows the possibility of transfer of more than one acyl chain to the protein.

Moving from the outer part of the lens cortex fraction (OC) to the older fraction of the cortex (IC) is still evident the presence of intact b-AQP0 together with a number of modification envelopes, as shown in Figure 4.6 and Table 4.2.

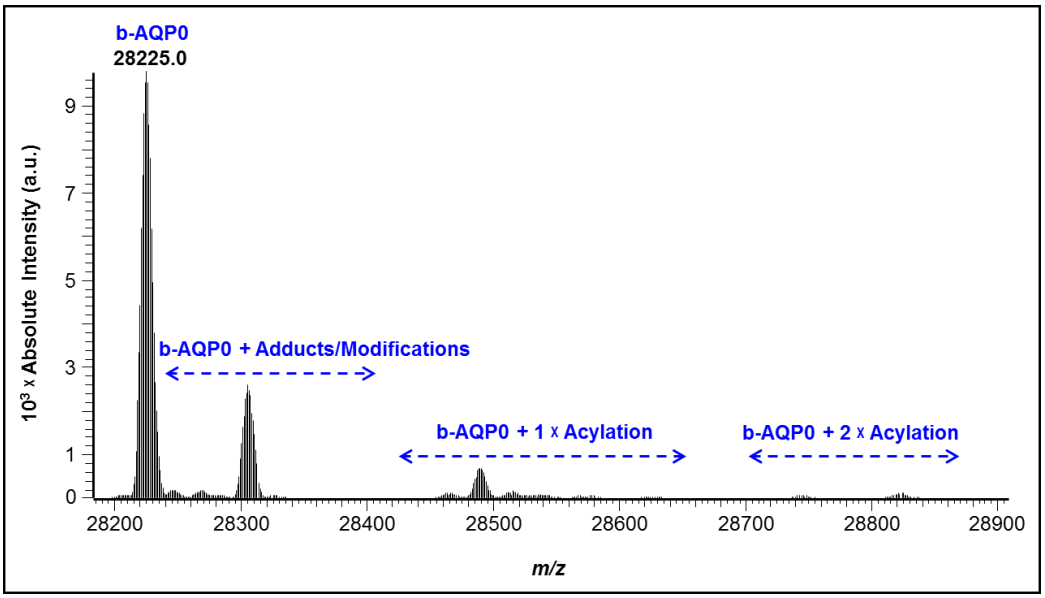

Figure 4.6. **Deconvoluted mass spectrum at 9.7-10.9 min of the LC gradient for the protonated species $[M + H]^+$ in the inner cortex (IC) fraction, modeled as a Gaussian distribution. Details provided in Table 4.2.**

Table 4.2. **The identified modified proteins in deconvolved spectra of b-AQP0-IC.**

Entry	*m/z* Meas‡	Mass Shift*	Assignment of Identified Modifications
1	28246.8	21.8	Na
2	28266.9	41.9	Acetyl
3	28282.8	57.8	Acetyl + O
4	28304.9	79.9	P
5	28326.9	101.9	Na + P
6	28463.2	238.2	Palmitoyl (C16:0)
7	28489.2	264.2	Oleoyl (C18:1)
8	28491.3	266.3	Stearoyl (C18:0)
9	28513.0	288.0	Dihomo-γ-linolenoyl (C20:3)
10	28514.9	289.9	Eicosadienoyl (C20:2)
11	28529.1	304.1	Dihomo-γ-linolenoyl (C20:3) + O
12	28535.2	310.2	Docosahexaenoyl (C22:6)
13	28537.0	312.0	Docosapentaenoyl (C22:5)
14	28543.2	318.2	Docosadienoyl (C22:2)
15	28569.0	344.0	Oleoyl (C18:1) + P
16	28571.1	346.1	Tetracosadienoyl (C24:2) or Stearoyl (C18:0) + P
17	28623.0	398.0	Palmitoyl (C16:0) + 2 × P
18	28743.3	518.3	Palmitoyl (C16:0) + Oleoyl (C18:1) + O
19	28771.3	546.3	Oleoyl (C18:1) + Stearoyl (C18:0) + O
20	28795.9	570.9	Oleoyl (C18:1) + Eicosadienoyl (C20:2) + O
21	28807.0	582.0	Palmitoyl (C16:0) + Oleoyl (C18:1) + P
22	28823.2	598.2	Palmitoyl (C16:0) + Oleoyl (C18:1) + P + O
23	28825.1	600.1	Palmitoyl (C16:0) + Stearoyl (C18:0) + P + O

‡Meas: measured most abundant isotope, obtained from deconvolution spectrum $[M + H]^+$ (see Figures 4.6 and 4.7).

*Mass shifts calculated from the most abundant b-AQP0 at *m/z* 28225.0 (see Figure 4.6) and thus all modifications matches contain double deamidation.

Similarly, single acylated and double acylated b-AQP0 are still visible in this fraction of b-AQP0-IC (Figure 4.7 and Table 4.2). This illustrates the lens composition similarity in both outer and inner fractions of the lens cortex. It is visible that more oxidation found with acylated b-AQP0-IC than b-AQP0-OC, suggesting increasing the level of oxidation in the lens with age. Increasing the level of protein oxidation with increasing lens age is documented in different studies.[16-18] Interestingly, higher level of protein oxidation (oxidative damage) has also shown to be directly related with the lens cataract.[16-18]

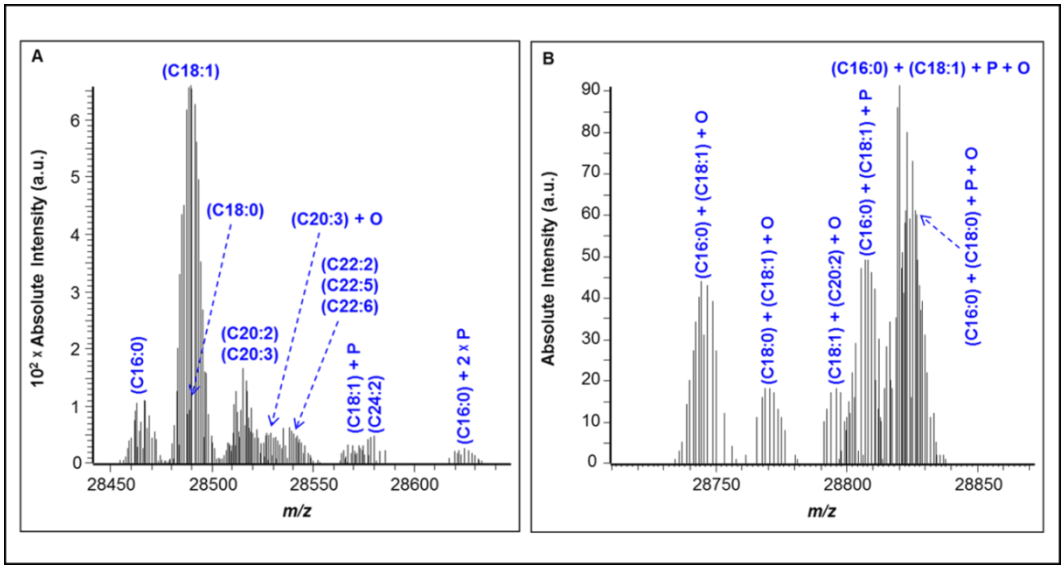

Figure 4.7. **Magnified regions of b-AQP0-IC single acylation and double acylation (see Figure 4.6) from deconvoluted mass spectrum for $[M + H]^+$. (A) b-AQP0-IC single acylation at *m/z* 28450-28650; (B) b-AQP0-IC double acylation at *m/z* 28700-28850. Details provided in Table 4.2.**

The older lens fraction, b-AQP0-ON, with a range of modified species were recorded, as shown in Figure 4.8 and Table 4.3.

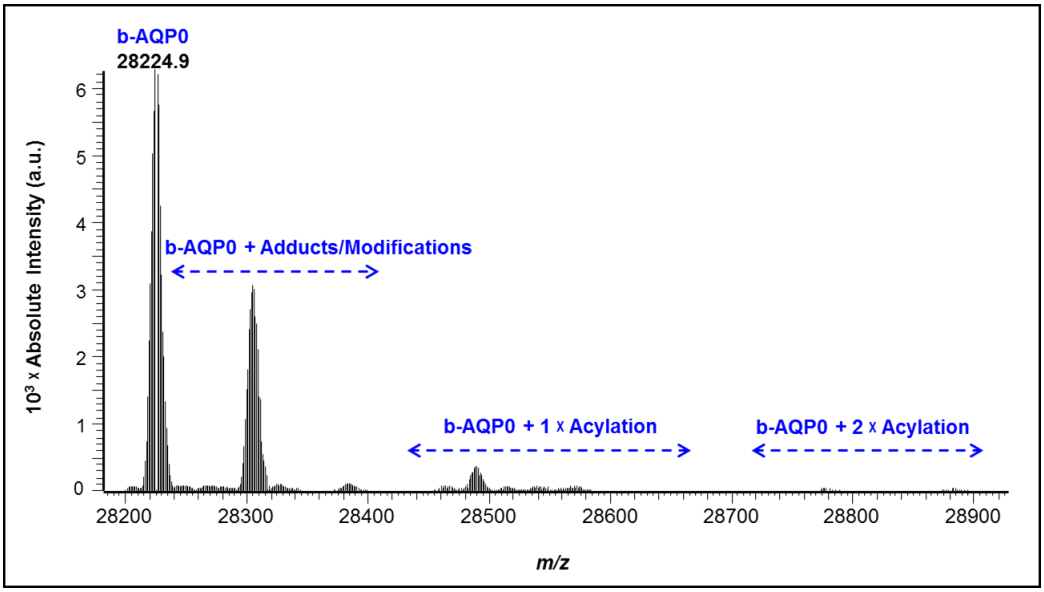

Figure 4.8. **Deconvoluted mass spectrum at 9.7-10.9 min of the LC gradient for the protonated species $[M + H]^+$ in the outer nucleus (ON) fraction, modeled as a Gaussian distribution. Details provided in Table 4.3.**

Table 4.3. **The identified modified proteins in deconvolved spectra of b-AQP0-ON.**

Entry	*m/z* Meas‡	Mass Shift*	Assignment of Identified Modifications
1	28246.9	22.0	Na
2	28266.9	42.0	Acetyl
3	28278.9	54.0	Na + 2 × O
4	28282.9	58.0	Acetyl + O
5	28304.8	79.9	P
6	28326.9	102.0	Na + P
7	28384.8	159.9	2 × P
8	28463.4	238.5	Palmitoyl (C16:0)
9	28489.1	264.2	Oleoyl (C18:1)
10	28491.2	266.3	Stearoyl (C18:0)
11	28513.2	288.3	Dihomo-γ-linolenoyl (C20:3)
12	28515.0	290.1	Eicosadienoyl (C20:2)
13	28529.0	304.1	Dihomo-γ-linolenoyl (C20:3) + O
14	28535.2	310.3	Docosahexaenoyl (C22:6)
15	28539.1	314.2	Docosatetraenoyl (C22:4)

16	28543.0	318.1	Docosadienoyl (C22:2)
17	28569.1	344.2	Oleoyl (C18:1) + P
18	28571.1	346.2	Tetracosadienoyl (C24:2) or Stearoyl (C18:0) + P
19	28807.1	582.2	Palmitoyl (C16:0) + Oleoyl (C18:1) + P
20	28825.4	600.5	Palmitoyl (C16:0) + Stearoyl (C18:0) + P + O

‡Meas: measured most abundant isotope, obtained from deconvolution spectrum $[M + H]^+$ (see Figures 4.8 and 4.9).

*Mass shifts calculated from the most abundant b-AQP0 at *m/z* 28224.9 (see Figure 4.8) and thus all modifications matches contain double deamidation.

All single acylation modifications in this fraction (Figure 4.9 A) are consistent with the previous recorded acylations in the cortex fractions (see Tables 4.1 and 4.2) except docosatetraenoyl (C22:4), Table 4.3, entry 15. Interestingly, fewer double acylation modifications were observed in this fraction, as shown in Figure 4.9B.

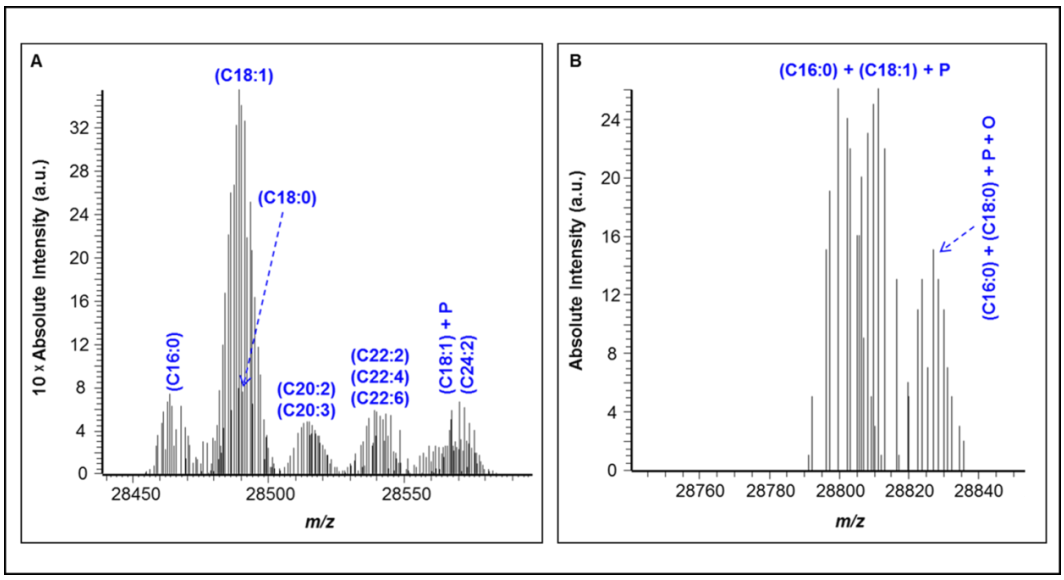

Figure 4.9. **Magnified regions of b-AQP0-ON single acylation and double acylation (see Figure 4.8) from deconvoluted mass spectrum for $[M + H]^+$. (A) b-AQP0-ON single acylation at *m/z* 28450-28650; (B) b-AQP0-ON double acylation at *m/z* 28700-28850. Details provided in Table 4.3.**

The oldest section of the lens, b-AQP0-IN, with all identified modifications are shown in Figure 4.10 and Table 4.4. The number of observed single and double acylated b-AQP0 in this fraction is much less than the identified acylations in the other fractions (see Figures 4.5, 4.7 and 4.9), as shown in Figure 4.11. It is interesting to see that triple and quadruple oxidation products is only observed in this fraction (Table 4.4, entries 14 and 15), this is additionally suggest higher level of oxidation in older lens fractions.

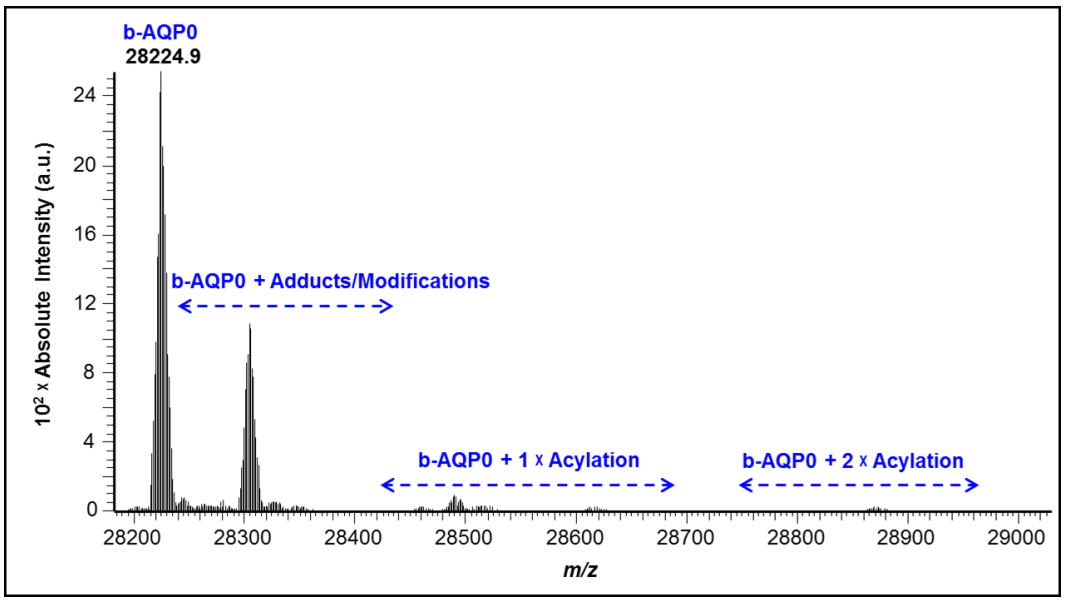

Figure 4.10. **Deconvoluted mass spectrum at 9.7-10.9 min of the LC gradient for the protonated species $[M + H]^+$ in the inner nucleus (IN) fraction, modeled as a Gaussian distribution. Details provided in Table 4.4.**

Table 4.4. **The identified modified proteins in deconvolved spectra of b-AQP0-IN.**

Entry	*m/z* Meas‡	Mass Shift*	Assignment of Identified Modifications
1	28246.7	21.8	Na
2	28266.7	41.8	Acetyl
3	28282.9	58.0	Acetyl + O
4	28304.8	79.9	P
5	28326.9	102.0	Na + P
6	28347.3	122.4	Acetyl + P
7	28358.8	133.9	Na + P + 2 × O
8	28384.8	159.9	2 × P
9	28463.2	238.3	Palmitoyl (C16:0)
10	28489.5	264.6	Oleoyl (C18:1)
11	28491.2	266.3	Stearoyl (C18:0)
12	28513.0	288.1	Dihomo-γ-linolenoyl (C20:3)
13	28515.1	290.2	Eicosadienoyl (C20:2)
14	28616.3	391.4	Oleoyl (C18:1) + P + 3 × O
15	28871.4	646.5	Palmitoyl (C16:0) + Oleoyl (C18:1) + P + 4 × O

‡Meas: measured most abundant isotope, obtained from deconvolution spectrum $[M + H]^+$ (see Figures 4.10 and 4.11).

*Mass shifts calculated from the most abundant b-AQP0 at *m/z* 28224.9 (see Figure 4.10) and thus all modifications matches contain double deamidation.

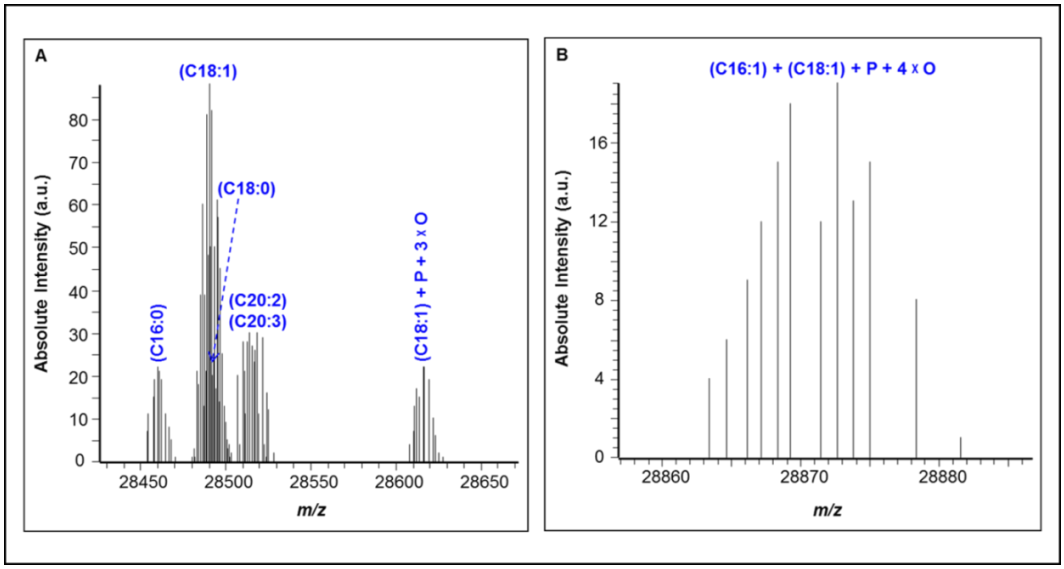

Figure 4.11. **Magnified regions of b-AQP0-IN single acylation and double acylation (see Figure 4.10) from deconvoluted mass spectrum for $[M + H]^+$. (A) b-AQP0-IN single acylation at *m/z* 28450-28650; (B) b-AQP0-IN double acylation at *m/z* 28700-28900. Details provided in Table 4.4.**

Moreover, for the set of samples processed and analysed in one batch, a distinct difference can be seen in the abundance of b-AQP0 in moving from the cortex (younger) to the nucleus (older) fractions of the lens, as shown in Figure 4.12. This is in agreement with the reduction in the signal intensity of the intact AQP0 as a result of increasing protein truncation and other PTMs in the nucleus fraction of the lens.[6,7] Consequently, a heterogeneous population of AQP0 species is introduced.[7] Interestingly, a relative ratio between non-acylated b-AQP0 and acylated b-AQP0 for the most abundant oleoyl product (see Figures 4.2, 4.6, 4.8 and 4.10) has shown a comparable amount of oleoylation in the three fractions of OC, IC and ON, but with the lowest amount in IN. Therefore, it is proposed that increasing protein homogeneity causes ion suppression and resulting in decreasing sensitivity to detect low abundance species. However, the relation between acylated b-AQP0 and lens age can be further characterised through quantitative analysis of digested samples, this can be found in later sections in this chapter (see section 4.2).

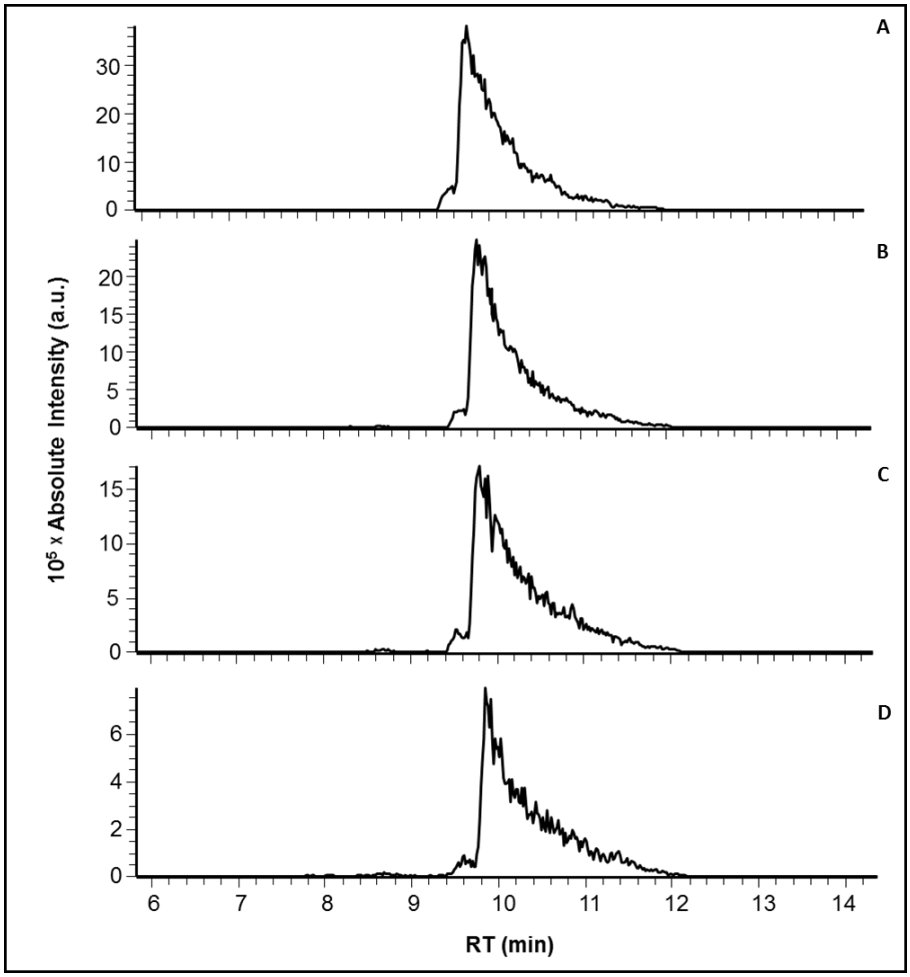

Figure 4.12. **Combined extracted ion chromatogram (EIC) for intact b-AQP0 at *m/z* 831.2 (*z*=34), 911.5 (*z*=31), 1046.4 (*z*=27), 1086.6 (*z*=26), 1177.0 (*z*=24) and 1345.0 (*z*=21) for all the four different bovine lens fractions including (A) OC; (B) IC; (C) ON; (D) IN. Analysed on LTQFT using LC-MS Method-I (see section 8.1.2.1.1).**

4.1.2. The identification of truncated proteins by ESI-LC-MS

C-terminal truncation of b-AQP0 is observed at different sites (Figure 4.13 and Table 4.5), in agreement with the previous recorded truncations.[13,19] Interestingly, AQP0 truncations at K238 (Table 4.5, entries 1 and 2) and E244 (Table 4.5, entry 3) are observed herein for the first time. The most abundant truncation site at T260 (Table 4.5, entry 7) is consistent with the previous study.[13] This truncated protein (1-260) is also found to be phosphorylated (Table 4.5, entries 8 and 9) or oleoylated (Table 4.5, entry10). The results also show that the number of observed truncated proteins decrease in moving from the older section of the lens (Figure 4.13 A and B) to the cortex

fraction (Figure 4.13 C), consistent with reports for age dependent truncation in bovine[13,19] and human lenses[6,7,20,21].

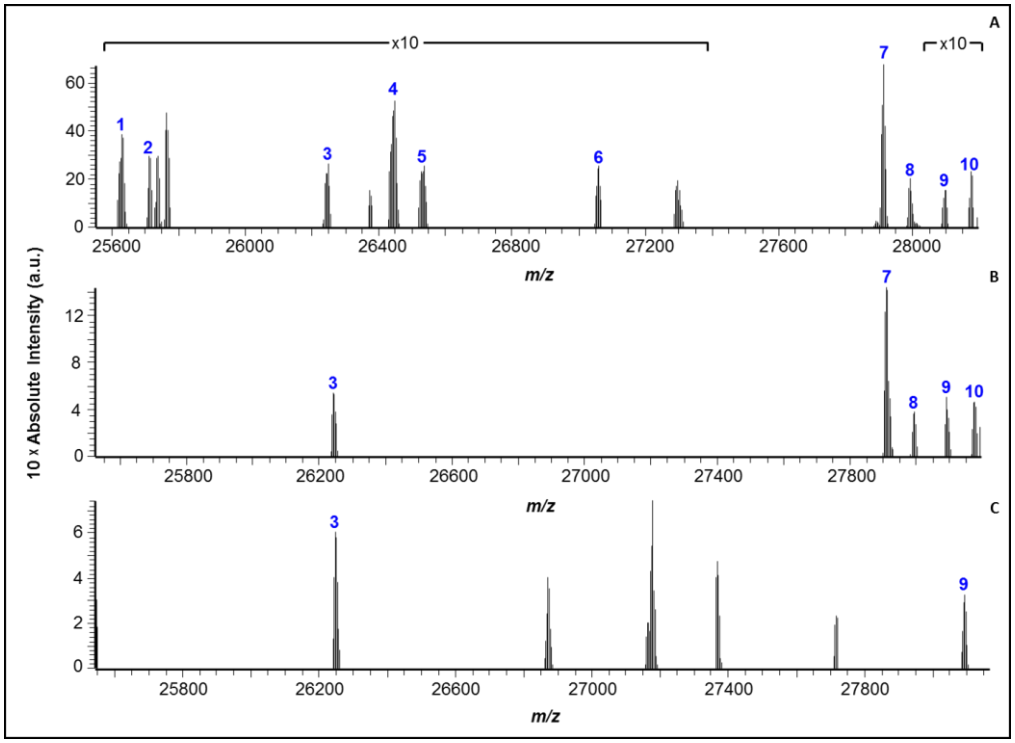

Figure 4.13. **Deconvoluted mass spectra at 9.7-10.9 min of the LC gradient for the protonated species $[M + H]^+$ in the fractions (A) IN, (B) ON and (C) IC, modeled as a Gaussian distribution. Details provided in Table 4.5.**

Table 4.5. **The identified truncated proteins in deconvolved spectra of b-AQP0-IN.**

Entry	*m/z* Meas*	C-terminal Truncation Site	Assignment of Identified Truncation Proteins
1	25630.5	K238	(1-238) + Deamidation
2	25711.5	K238	(1-238) + P + 2 × Deamidation
3	26244.9	E244	(1-244) + 2 × Deamidation
4	26447.0	E246	(1-246) + 2 × Deamidation
5	26526.9	E246	(1-246) + P + 2 × Deamidation
6	27058.4	T252	(1-252) + 2 × Deamidation
7	27911.8	T260	(1-260) + 2 × Deamidation
8	27992.6	T260	(1-260) + P + 2 × Deamidation
9	28094.7	T260	(1-260) + 2 x P + Na + 2 × Deamidation
10	28176.6	T260	(1-260) + Oleoyl (C18:1) + 2 × Deamidation

*Meas: measured most abundant isotope, obtained from deconvolution spectrum $[M + H]^+$, (see Figure 4.13).

4.1.3. The identification of neutral lipid classes in bovine lens by ESI-LC-MS

The inner leaflet of mammalian cytoplasmic membranes is rich with phosphatidylethanolamine (PE), phosphatidylserine (PS) and phosphatidylinositol (PI), while the outer (exoplasmic) leaflet is rich with sphingomyelin (SM) and phosphatidylcholine (PC) which reflects the asymmetric nature of the membrane.[22] LC-MS analysis of b-AQP0 directly after isolation from lens samples by decapsulation and aqua–dissection showed the presence of a range of neutral PLs (PC, PE and SM) and as well as LPLs (LPE and LPCs) through ESI+ MS (Table 4.6), while negatively charged PLs (PI and PS) have not been included in this study of lipids. This is because the nature of the analysis focused around ESI+ MS to facilitate the detection of the protein-based compounds. Moreover, the identified PLs here (PC, PE and SM), Table 4.6, were also reported to be the major eye lens membrane lipids.[14,23-28]

In addition, the presence of 19 plasmalogen PE (Table 4.6, entries 47, 50-52, 54, 57-60, 65-72, and 75-76) relative to 11 PE (Table 4.6, entries 48, 49, 53, 55, 56, 61-64, 73 and 74) suggest the abundance of PE that exists as plasmalogen (PEpl) lipid. This is supported in previous studies by reporting the presence of major PE lipids in the form of PEpl.[23,24,29] Plasmalogen PE lipids are biosynthesized in peroxisomes.[30,31] Mutations in the enzymes that are responsible for their synthesis changes their cellular level. Consequently, their deficiency causes several disease related to brain, lens and bone development.[30,31] The results here also show SM association with palmitoyl (C16:0) and nervonoyl (C24:1), Table 4.6, entries 15, 18 and 20-23, in good agreement with reports of SM rich with these identified fatty acyl chains[14,24,25,27,32].

Table 4.6. **Free neutral PLs and LPLs identified in the four fractions of bovine lens extracts. LPLs and PLs eluted at 6-10 min and 11-14 min of the chromatogram respectively (see Figure 4.2).**

Entry	Lipid Class	Theor* *m/z* $[M + H]^+$	Meas *m/z* $[M + H]^+$	Error (ppm)
1	LPC (14:0)	468.3085	468.3087	0.4
2	LPC (16:1)	494.3241	494.3244	0.6
3	LPC (16:0)	496.3398	496.3399	0.2
4	LPC (18:1)	522.3554	522.3557	0.6
5	LPC (18:0)	524.3711	524.3714	0.6
6	LPE (16:1)	452.2772	452.2774	0.4
7	LPE (16:0)	454.2928	454.2931	0.7
8	LPE (17:1)	466.2928	466.293	0.4
9	LPE (17:0)	468.3085	468.3087	0.4
10	LPE (18:1)	480.3085	480.3086	0.2
11	LPE (18:0)	482.3241	482.3243	0.4
12	LPE (19:1)	494.3241	494.3244	0.6
13	LPE (19:0)	496.3398	496.3399	0.2
14	LPE (22:6)	526.2928	526.2933	0.95
15	SM (34:1)	703.5748	703.5754	0.85
16	SM (36:1)	731.6061	731.6066	0.7
17	SM (38:2)	757.6218	757.6229	1.45
18	SM (40:2)	785.6531	785.6541	1.3
19	SM (40:1)	787.6687	787.6688	0.1
20	SM (41:2)	799.6687	799.6692	0.6
21	SM (42:3)	811.6687	811.6696	1.1
22	SM (42:2)	813.6844	813.6856	1.5
23	SM (43:2)	827.7000	827.7029	3.5
24	SM (44:2)	841.7157	841.7180	2.7
25	PC (28:0)	678.5068	678.5075	1.0
26	PC (29:1)	690.5068	690.5072	0.6
27	PC (30:0)	706.5381	706.5386	0.7
28	PC (32:1)†	716.5589	716.5595	0.8
29	PC (31:1)	718.5381	718.5391	1.4
30	PC (31:0)	720.5538	720.5548	1.4
31	PC (32:0)‡	720.5902	720.5910	1.1
32	PC (32:3)	728.5225	728.5209	2.2
33	PC (32:2)	730.5381	730.5388	0.95
34	PC (34:1)†	730.5745	730.5752	0.95
35	PC (32:1)	732.5538	732.5543	0.7
36	PC (32:0)	734.5694	734.5701	0.95
37	PC (34:1)†	744.5902	744.5911	1.2
38	PC (34:0)†	746.6058	746.6067	1.2
39	PC (34:3)	756.5538	756.5522	-2.1
40	PC (34:2)	758.5694	758.5713	2.5
41	PC (36:1)	758.6058	758.6086	3.7

42	PC (34:1)	760.5851	760.5858	0.9
43	PC (34:0)	762.6007	762.6015	1.05
44	PC (35:4)	768.5538	768.5521	-2.2
45	PC (36:4)	782.5694	782.5682	-1.5
46	PC (36:3)	784.5851	784.5837	-1.8
47	PE (33:1)†	688.5276	688.5322	6.7
48	PE (32:1)	690.5069	690.5421	-1.6
49	PE (33:0)	690.5432	690.5072	0.43
50	PE (34:2)†	700.5276	700.5283	1.0
51	PE (34:1)†	702.5432	702.5438	0.85
52	PE (35:2)†	714.5432	714.5415	-2.4
53	PE (34:2)	716.5225	716.5225	0.0
54	PE (35:1)†	716.5589	716.5595	0.8
55	PE (34:1)	718.5382	718.5391	1.25
56	PE (34:0)	720.5538	720.5548	1.4
57	PE (36:4)†	724.5276	724.526	-2.2
58	PE (36:3)†	726.5432	726.5417	-2.1
59	PE (36:2)†	728.5589	728.5596	1.0
60	PE (36:1)†	730.5745	730.5748	0.4
61	PE (36:0)	732.5902	732.5924	3.0
62	PE (36:4)	740.5225	740.5208	-2.3
63	PE (36:3)	742.5382	742.5377	-0.7
64	PE (36:2)	744.5538	744.5546	1.1
65	PE (37:1)†	744.5902	744.5953	6.8
66	PE (37:0)†	746.6058	746.6067	1.2
67	PE (38:6)†	748.5276	748.5266	-1.3
68	PE (38:5)†	750.5432	750.5442	1.3
69	PE (38:4)†	752.5589	752.5598	1.2
70	PE (38:3)†	754.5745	754.5759	1.85
71	PE (38:2)†	756.5902	756.5924	2.9
72	PE (38:1)†	758.6058	758.6086	3.7
73	PE (38:5)	766.5382	766.5364	-2.3
74	PE (38:4)	768.5538	768.5538	0.0
75	PE (40:7)†	774.5432	774.5439	0.9
76	PE (40:6)†	776.5589	776.5598	1.1

*Theoretical (Theor) *m/z* of lipids $[M + H]^+$ obtained from lipidomics gateway (http://www.lipidmaps.org/data/structure/LMSDSearch.php).

†The presence of alkenyl ether (plasmalogen) substituent.

‡The presence of alkyl ether substituent.

Association of lens lipids with AQP0 showed that lipids are tightly integrated into the protein's architecture where they can affect the function, structure, quaternary assembly, and the stability of the membrane protein.[33] The observation of intact AQP0 lipidation with different acyl chains herein

assumed to be reflecting this tight lipid-protein interaction *in vivo*. To avoid protein acylation by the detected lipids *in vitro*, the extraction of lipids were performed by using monophasic methanol[34] or cold acetone was used to precipitate AQP0 protein and thus separated from insoluble PLs in acetone[35]. Both methods were successfully applied to remove PEs, PCs and SMs but not LPCs and LPEs. This is most likely related with LPLs higher dispersion in aqueous solution and thus remains attached with the protein in aqueous layer.

Further, the relationship between lens membrane lipids and b-AQP0 acylation profile has been followed by the major fatty acyl compositions found with bovine major lens PLs. Interestingly, the most abundant acylated b-AQP0 in all of the four different age fractions is oleoylated b-AQP0 (Figures 4.5, 4.7, 4.9 and 4.11 (panel A in all)), which predicted to reflect the major oleoyl composition associated with PE in mammals[14,24,29,36]. In addition, PE and PC were also found to be rich with palmitoyl (C16:0) and stearoyl (C18:0) alongside longer fatty acyl chains, reflect natural abundance[24,29,32,36]. Although SM is rich with palmitoyl (C16:0) and nervonoyl (C24:1),[24] the contribution of SM fatty acyl chains in lipidation is not described herein. This is because unlike the ester-linked fatty acyl chain in PC/PE, the amide-linked fatty acyl chain in SM is unable to perform aminolysis reaction with proteins without a catalyst[37]. The recorded fatty acyl composition in weight% for bovine lens PE and PC lipids[24] are given in Table 4.7.

Table 4.7. **Weight% of fatty acyl groups in bovine lens PE and PC lipids obtained by GC-MS/TLC analysis.[24]**

Acyl Group	Weight% in PE	Weight% in PC
C16:0	12.9	64.0
C16:1	3.3	3.0
C18:0	9.5	4.3
C18:1	63.8	19.1
C20:0	Trace	0.4
C20:1	1.9	0.3
C20:3	2.4[§]	Trace

§This value represents the combination between C20:3 and C22:0 (these were not separated).

4.1.4. Analysis of the intact b-AQP0 by MALDI-MS

Performing further MS analysis on the same batch of samples (intact b-AQP0), as was shown in section 4.1.1, with MALDI-ToF-MS instrument showed a consistent result as was obtained on ESI-FTICR-MS by monitoring the intact b-AQP0 as the most abundant species in all four different age fractions of the lens, as shown in Figure 4.14. The measured mass of $[M + H]^+$ is detected at around 28220 Da for full-length (1-263), which is a broad and tail peak. This is most likely related with the presence of a number of expected modified species with b-AQP0. This is not surprising that biological samples on MALDI analysis in the absence of LC separation can experience difficulties in the detection of poor signals such as lipidation modifications, as there are a large number of components competing in ionisation thus suppressing the efficiency to detect low abundance and higher mass species. The lower detection efficiency on MALDI for larger proteins is already well documented.[38,39] This is shown to be related with the instrument issue and/or chemical behaviour of the ions in the gas-phase or solution-phase.[38] In addition of singly protonated b-AQP0, doubly protonated was also detected at around *m/z* 14100. The abundance of intact b-AQP0 protein decreases by moving from cortex fraction to core fraction of the lens (Figure 4.14), yet again demonstrating increasing protein homogeneity in the older fractions of the lens,[6,7] and consistent with the analysis performed using ESI-FTICR-MS (see section 4.1.1).

Interestingly, a number of different noticeable outcomes have been observed between cortex and core sections of the lens. A labelled band with b-AQP0 (1-246) is around *m/z* 26400 for $[M + H]^+$, which is an indication of C-terminal protein truncation, confirming the previous results (Table 4.5, entry 4). The truncated product of b-AQP0 (1-246) is hard to resolve from the noisy signal in b-AQP0-OC (Figure 4.14 A) but its peak intensity increases for the older sections of the lens and reaches its maximum amount in both b-AQP0-ON and b-AQP0-IN (Figure 4.14 C and D). This indicates an increasing amount of protein truncation with increasing the age of the lens, consistent with the previous results (see Figure 4.13). The other outstanding difference between the young and old lens fractions is the presence of two overlapped

peaks with apices at *m/z* 19800 and 19900 Da, only observed in b-AQP0-OC fraction (Figure 4.14 A). The split peak is proposed to be α-crystallin protein,[19,40] which is another abundant protein in lens fibre cell and found as αA-crystallin (1-173) and αB-crystallin (1-175) at 19790 and 20037 Da respectively (theoretical neutral average mass). This protein has shown to function as a molecular chaperone.[41] Moreover, looking to the magnified region of α-crystallin (Figure 4.14, panel Ai) shows peak tailing. This is proposed to account for modifications (phosphorylation) on α-crystallin, as both of AQP0 and α-crystallin proteins in lens have shown to undergo a number of different modifications with age. In addition, the formation of different salt adducts and matrix adducts in MALDI-MS have also the influence on peak tailing and broadening of the peak.

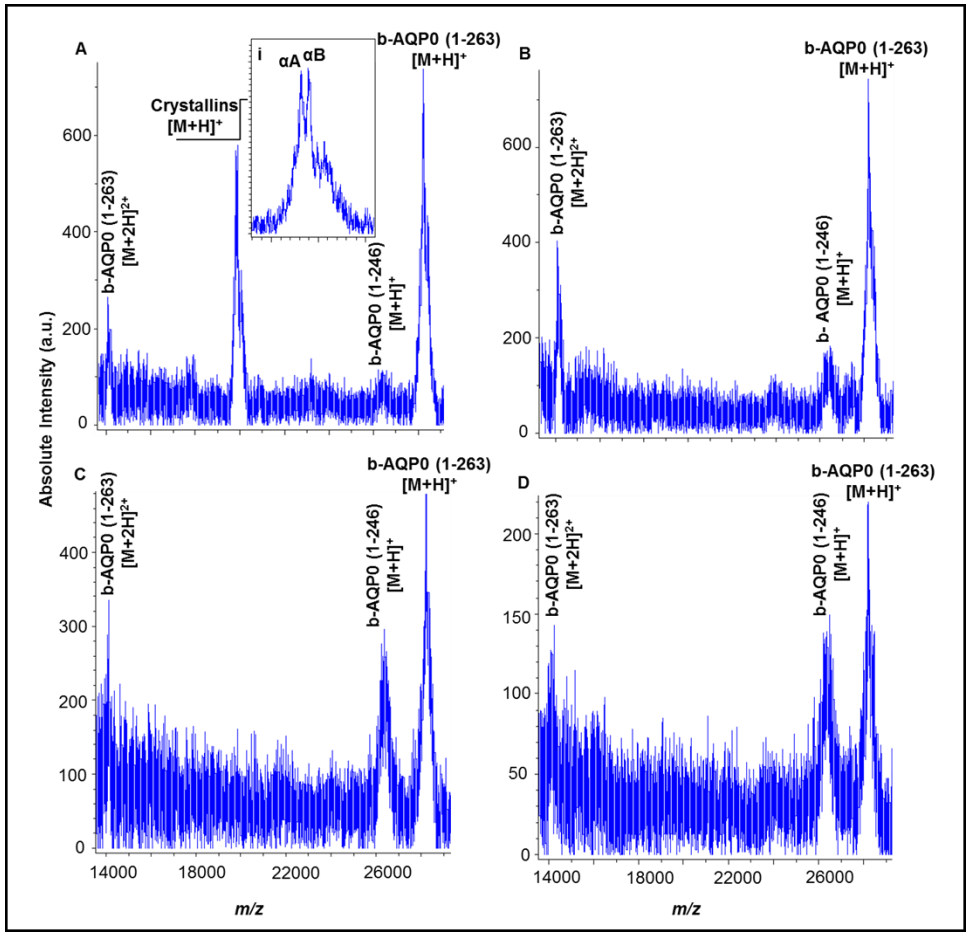

Figure 4.14. **MALDI mass spectra for b-AQ0-OC (A), b-AQ0-IC (B), b-AQ0-ON (C) and b-AQ0-IN (D). The insert spectrum (i) represents a magnified region around *m/z* 20 kDa of the spectrum, which is α-crystallin protein.**

4.2. Exploring the modifications on AQP0 by LC-MS analysis

4.2.1. Analytical approach in proteolytic analysis of bovine AQP0 (b-AQP0)

The intact protein analysis provides key information about the presence of various modifications on b-AQP0 but without assigning the site of modifications. However, treating b-AQP0-OC with dithiothreitol (DTT) reducing agent and followed by tryptic digestion has recorded a range of eluted peaks around 1-12.5 min of the chromatogram by LC-MS (Figure 4.15). This can be split into three main regions; the first region contain the common non-acylated peptides at 1-7.5 min of the chromatogram, and the second region is the most interesting region where the lipidated peptide [234-259] (Figure 4.15, Region A) and lipidated peptide [1-5] (Figure 4.15, Region B) were eluted over 7.3-8.0 min and 10.0-11.0 min respectively. In addition, the third region with the late elution time contain LPLs over 9.3-12.5 min of the chromatogram.

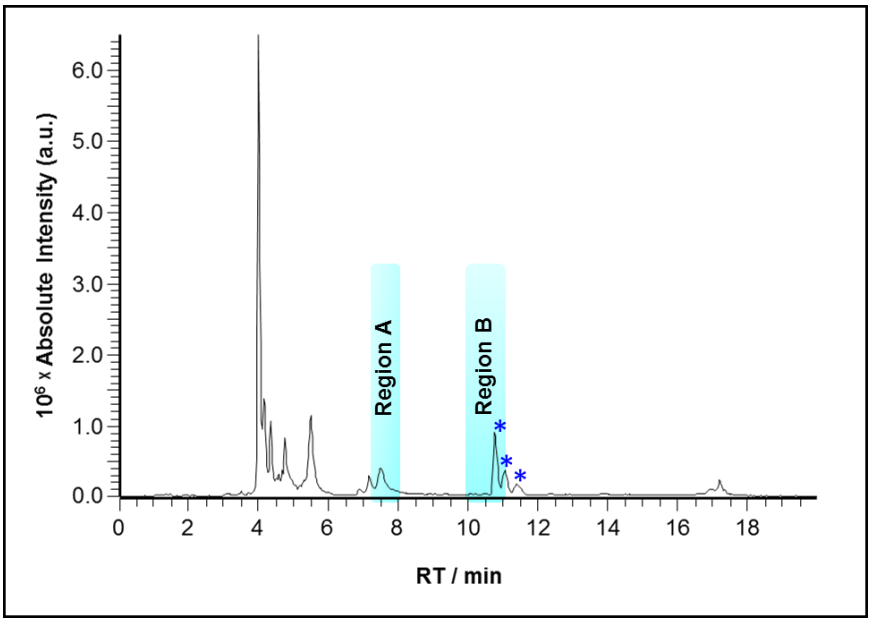

Figure 4.15. **TIC from trypsin digestion of b-AQP0-OC, analysed on LTQFT using LC-MS Method-I (see section 8.1.2.1.1) and digestion protocol Method-A (see Table 8.1 and section 8.2.2.1.2). The two highlighted regions (Region A) and (Region B) represent the regions that contain lipidated peptide [234-259] and lipidated peptide [1-5] respectively. The most abundant peaks highlighted with asterisk around Region B represent LPLs.**

The protein cleavage sites at C-terminus of lysine (K) and Arginine (R) amino acid residues by trypsin were achieved to confirm about 70% of the protein sequence coverage (183 of 263 amino acid (AA) residues), as shown in Figure 4.16. Deamidation modification were identified on peptide [153-187], peptide [234-259], peptide [239-259] and peptide [239-263]. The three later deamidation residues are in agreement with the previous findings[1,5,11,42] for non-enzymatic[43,44] conversion of N246 to aspartic acid (D246), while, it is interesting to see that deamidated peptide [153-187] is not within the recorded C-terminus deamidation sites of b-AQP0. This suggests that deamidation does occur to the residue close to N-terminus and thus suggesting deamidation on either N154 or N184. In addition, phosphorylation and oxidation modifications were also recorded herein, covering the same amino acid residues reported for serine (S) phosphorylation[5,10-13] and tryptophan (W) oxidation[5]. The results also support similar modifications found on intact b-AQP0 (see section 4.1.1).

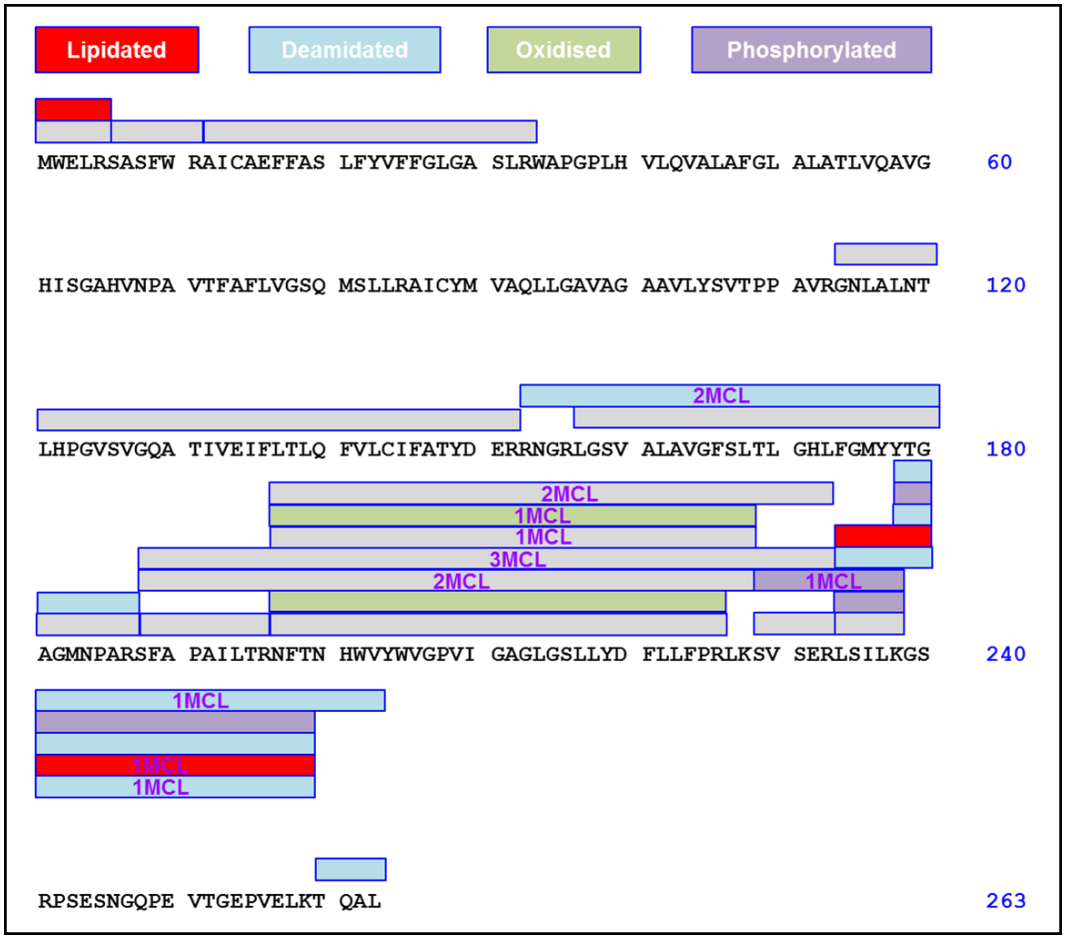

Figure 4.16. **The highlighted regions of the protein represent the confirmed peptides from b-AQP0-OC tryptic digestion, using digestion protocol Method-A (see Table 8.1 and section 8.2.2.1.2) and LC-MS Method-I (see section 8.1.2.1.1). Peptide residues with the observed modifications illustrated in bright colours; peptide residues with more than one missed cleavages (MCL) presented on each specific sequence. Details tabulated in Appendix C Table 9.31.**

The missing portion of the protein (30% for peptide [34-85] and peptide [86-113]) is quite a significant portion. These two missing peptides are among six transmembrane domains, which are known for their spanning in the lipid-bilayer and are rich with neutral and non-polar amino acid residues (Figure 4.17)[5]. Consequently, their more hydrophobic nature and position in the membrane could be account for preventing identifying them in the digestion mixture.

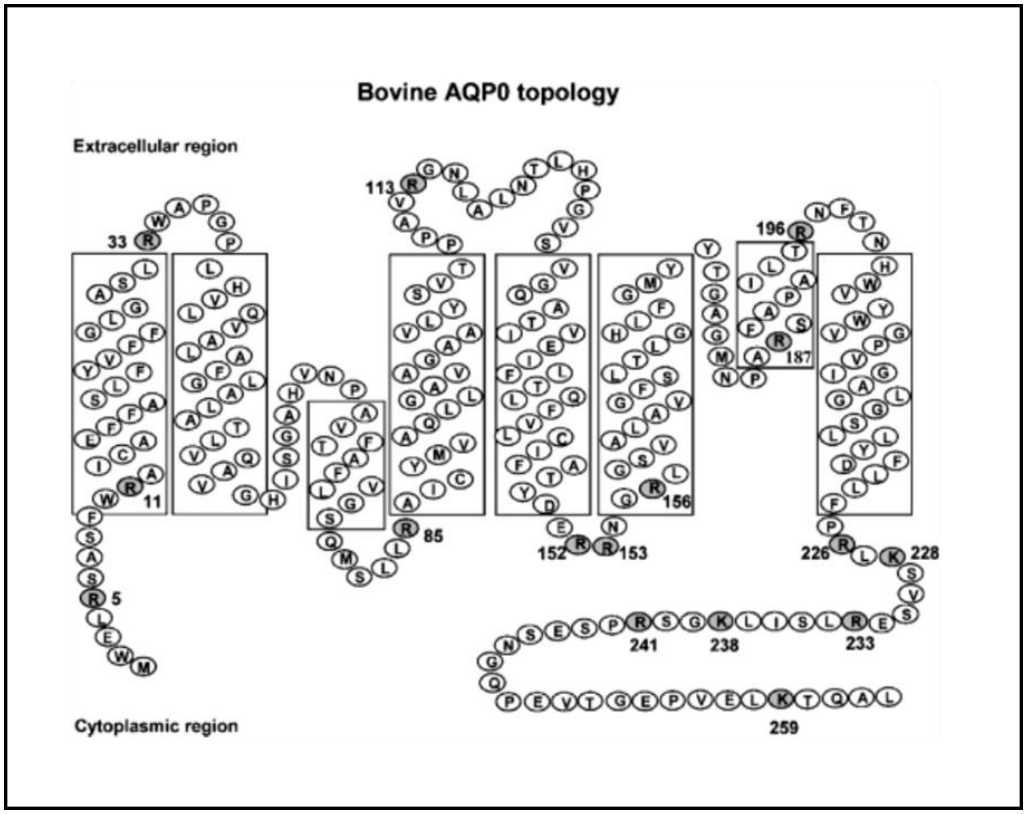

Figure 4.17. **"Topology of b-AQP0 with six transmembrane domains spanning the lens lipid-bilayer. The predicted tryptic cleavage sites of the protein highlighted in grey". Reprinted with permission from, Jun Han and Kevin L. Schey, Journal of Proteome Research, 3, 807-812. Copyright (2004) American Chemical Society.**

The two lipidated peptides, peptide [1-5] and peptide [234-259], were assigned herein with palmitoyl (C16:0), oleoyl (C18:1) and novel stearoyl (C18:0) acyl chains, as shown in Figure 4.18 and Table 4.8). The two former acylations were also reported previously,[1,7,15] while stearoylation is not documented before. This is also reassures the observed lipidation species in the intact protein analysis. Further, the elution times for the lipidation profile increase in the order of palmitoyl < oleoyl < stearoyl for both peptide sets. This is consistent with the RT increasing by increasing the length of acyl chain and decreasing the number of unsaturation,[45] also shown in previous work[46,47].

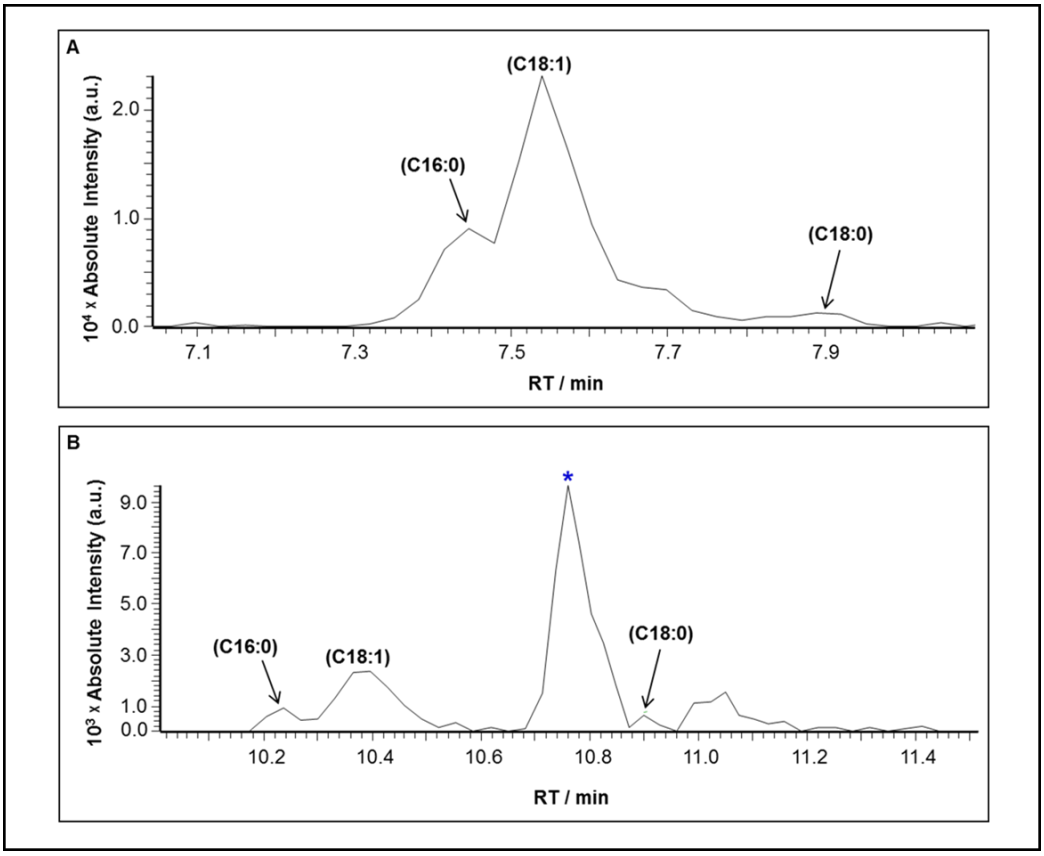

Figure 4.18. **Combined EIC for (A) peptide [234-259] at *m/z* 997.5610 palmitoyl (C16:0), *m/z* 1006.2328 oleoyl (C18:1) and *m/z* 1006.9034 stearoyl (C18:0); (B) peptide [1-5] at *m/z* 972.5945 palmitoyl (C16:0), *m/z* 998.6106 oleoyl (C18:1) and *m/z* 1000.6292 stearoyl (C18:0), using digestion protocol Method-A (see Table 8.1 and section 8.2.2.1.2) and LC-MS Method-I (see section 8.1.2.1.1). The asterisk represents the LPL elution peak at the indicated RT. Details provided in Table 4.8.**

Table 4.8. **The identified acylated peptides followed trypsin digestion of b-AQP0-OC.**

Theor *m/z*‡	Meas *m/z*‡	*z*	RT (min)	Error (ppm)	Assignment
^{234}LSILKGSRPSESNGQPEVTGEPVELK^{259}					
997.5602	997.5610	3	7.41	0.8	Peptide [234-259] + (C16:0) + 1 × Deamidation/Palmitoyl
1006.2321	1006.2328	3	7.54	0.7	Peptide [234-259] + (C18:1) + 1 × Deamidation/Oleoyl
1006.9039	1006.9034	3	7.80	-0.5	Peptide [234-259] + (C18:0) + 1 × Deamidation/Stearoyl
^{1}MWELR^{5}					
972.5951	972.5945	1	10.24	0	Peptide [1-5] + (C16:0)/Palmitoyl
998.6107	998.6106	1	10.40	-0.1	Peptide [1-5] + (C18:1)/Oleoyl
1000.6264	1000.6292	1	10.90	2.8	Peptide [1-5] + (C18:0)/Stearoyl

‡Both theoretical (Theor) and measured (Meas) *m/z* are for the monoisotopic peak. Theoretical mass obtained from mMass software.

Moreover, the digestion mixture is missing lipidated peptides with longer acyl chains (C20, C22 and C24) that are recorded in the intact form of the protein. This is assumed to be related with their lower biological abundance and therefore lower ionisation efficiency. In addition, they are more hydrophobic nature so late RT and co-elution with LPLs (see Figure 4.15 and 4.18 B) accounts for suppressing them. In summary, modified peptides with deamidation, phosphorylation, oxidation and acylation are consistent with the modifications on the intact b-AQP0. The two new recorded modifications here are N154 or N184 deamidation and also stearoylation modification on each of peptide [1-5] and peptide [234-259].

4.2.1.1. Method development: improving the LC separation and the proteolytic digestion

4.2.1.1.1. Optimising the LC-MS

In attempt to separate co-eluting species and search for any extra products, the chromatography was optimised, within the limits of the instrumentation available. The difference between the two chromatographic methods is shown in Figure 4.19.

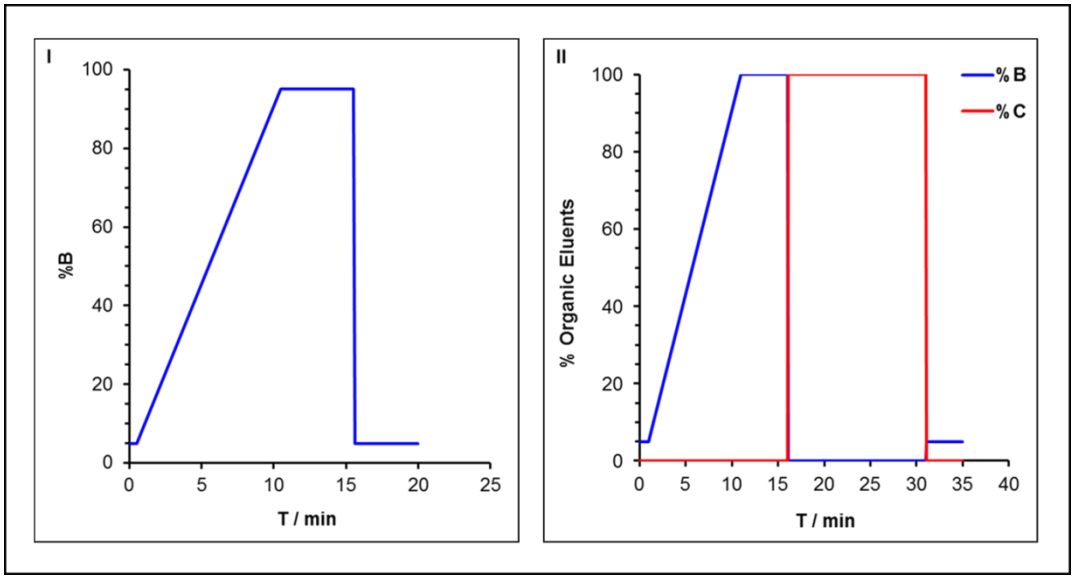

Figure 4.19. **The two LC methods over (I) 20 min and (II) 35 min used for separating tryptic digestion mixture of b-AQP0 on the LTQFT. These methods described as (I) LC-MS Method-I and (II) LC-MS Method-II in the experimental chapter (see sections 8.1.2.1.1). The LC eluents labelled as B for 0.1% formic acid in acetonitrile and C for 0.1% formic acid in methanol.**

The improved LC method (Figure 4.19 (II)) evident that LPLs are now eluted between 11-15 min of the chromatogram and thus no longer overlapped with acylated peptides which are now over 7.5-10.8 min (Figure 4.20). Consequently, this new LC method enabled a wider range of acylated peptides to be detected, many of which have not been previously reported. Newly identified peptides are given in Figure 4.20 and further listed in detail in Appendix C Table 9.32.

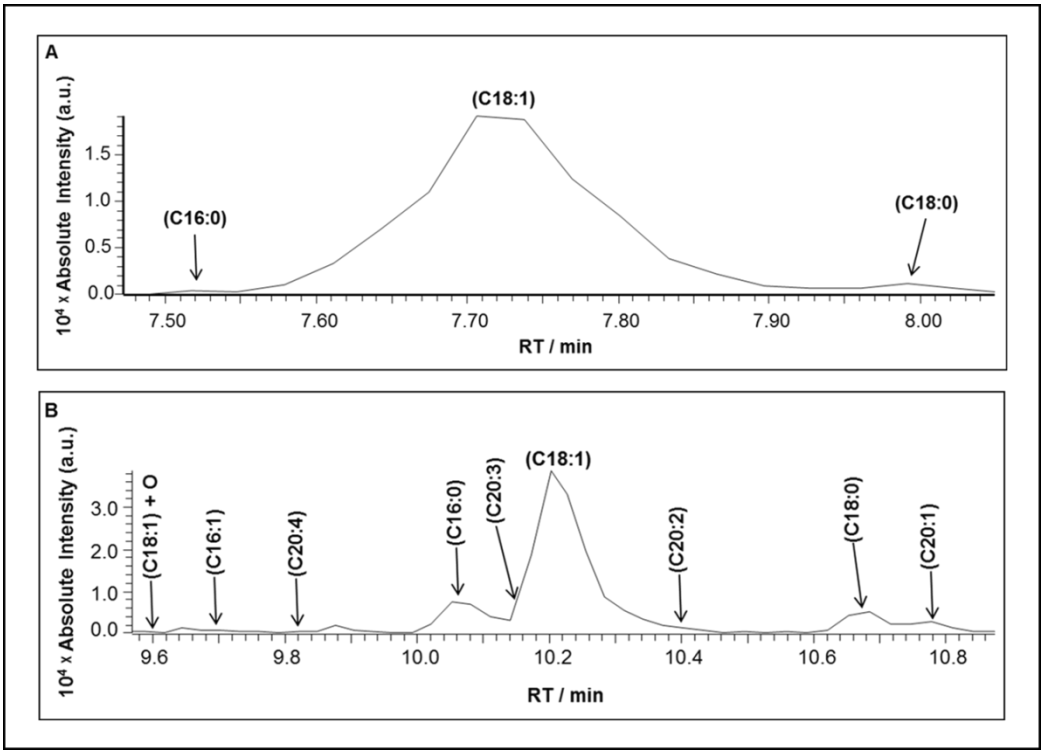

Figure 4.20. **Combined EIC for (A) peptide [234-259] at *m/z* 997.5615 palmitoyl (C16:0), *m/z* 1006.2326 oleoyl (C18:1) and *m/z* 1006.9040 stearoyl (C18:0); (B) peptide [1-5] at *m/z* 1014.6039 oleoyl (C18:1) + O, *m/z* 970.5791 palmitoleoyl (C16:1), *m/z* 1020.5957 arachidonoyl (C20:4), *m/z* 972.5951 palmitoyl (C16:0), *m/z* 1022.6125 dihomo-γ-linolenoyl (C20:3), *m/z* 998.6116 oleoyl (C18:1), *m/z* 1024.6285 eicosadienoyl (C20:2), *m/z* 1000.6272 stearoyl (C18:0) and *m/z* 1026.6427 eicosenoyl (C20:1). Using digestion protocol Method-A (see Table 8.1 and section 8.2.2.1.2) and LC-MS Method-II (see section 8.1.2.1.1). Details provided in Appendix C Table 9.32.**

The consistency between the abundance of b-AQP0 lipidation profile (Figure 4.21) and the fatty acyl composition for bovine lens PE lipid (see Table 4.7) is visible on both lipidated peptides. In addition, the abundance of lipidation profile on peptide [1-5] is much stronger than that on peptide [234-259] although each peptide set has different ionisation efficiency. This is also account for missing C20 fatty acyl lipids on peptide [234-259]. On the other hand, protein modifications with acyl groups longer than C20, specifically C22 and C24 observed for the intact b-AQP0 (see Figure 4.5 and Table 4.1), were not observed as tryptic peptides. The absence of C24 is more likely related with its lower abundance, as observed from the lowest abundance of the equivalent acylated intact protein, combined with increased

hydrophobicity and reduced ionisation efficiency. However, although C22 acyl chains, (C22:2) and (C22:5), have strong abundance with intact form of AQP0 but still cannot be revealed by digestion. Overall, optimising LC conditions showed a significant improvement in detecting different novel acylation profile and inspired further optimisation to identify any extra modifications within the digestion mixture.

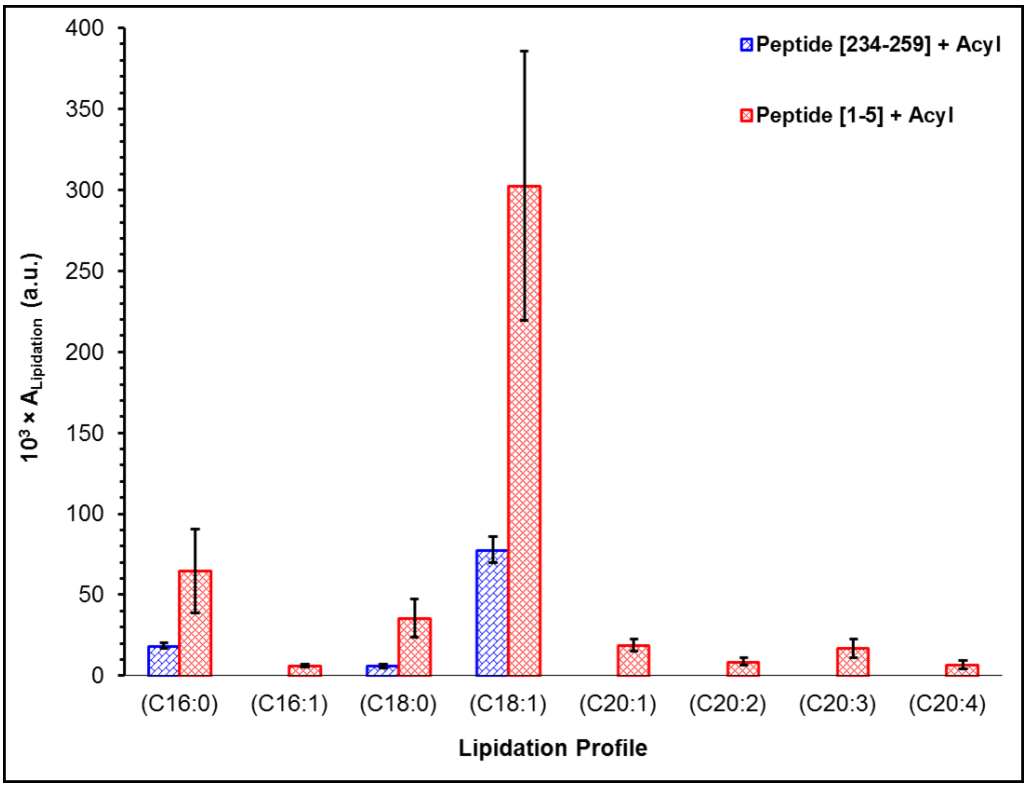

Figure 4.21. **The abundance of identified lipidated peptides described in Figure 4.20 for both lipidated sites of peptide [1-5] and peptide [234-29]. The peak area (A) for each species has summed over all observed charge states, (*z*=1-2) for peptide [1-5]; (*z*=2-4) for peptide [234-259]. All acylated species of peptide [234-259] matches contain one deamidation. The abundance of peptide [1-5] oleoylation include the summation of peak area for peptide $[1\text{-}5]_{ole}$ and peptide $[1\text{-}5]_{ole}$ + O, while the other acylation products include just their individual peak area. Errors reported as the standard error of the mean (SEM) of peak area when n=2. Details are tabulated in Appendix C Table 9.32.**

4.2.1.1.2. Optimising the proteolytic digestion

Different tryptic digestion conditions were tested with a view to exploring the more hydrophobic part of the membrane protein b-AQP0, the results are summarised in Table 4.9. Many of which were also applied in different studies to explore peptide mapping of hydrophobic peptides.

Table 4.9. **Results obtained from different digestion protocols/LC-MS methods used for b-AQP0-OC. *Note: details for each digestion protocol (see sections 8.2.2.1.2, and 8.2.2.2.1) or LC-MS (see sections 8.1.2.1.1 and 8.2.2.2.1) is provided in the experimental chapter.**

Entry	Digestion Protocol*	LC-MS Method*	Reagents Included	%Protein Sequence Coverage	Lipidation Products	
		LTQFT			Peptide [1-5]	Peptide [234-259]
1	Method-A	LC-MS Method-I	DTT	70	3	3
		LC-MS Method-II	DTT	89	8	3
2	Method-B	LC-MS Method-II	DTT + Urea	11	0	0
3	Method-C	LC-MS Method-II	DTT + PFOA	70	8	1
		Synapt G2-s				
4	Method-A	LC-MS Method-IIII	DTT	54	0	0
5	Method-C	LC-MS Method-IIII	DTT + PFOA	41	0	0
6	Method-D	LC-MS Method-IIII	DTT + SDS	100	10	6

The detailed results for b-AQP0 digestion by using **Method-A** is already discussed in earlier section (see section 4.2.1). Further, urea is one of the common protein denaturant[48,49] prior proteolytic digestion which has been also examined in this study, however one of its disadvantage is the effective role of urea to denature the protein only when it presents at very high concentration which must be diluted to a low level that is still keep the enzyme activity[48]. This massive dilution is evident in getting just 11% sequence coverage (Table 4.9, entry 2). On the other hand, protein solubilisation is another important step to increase the protein sequence coverage in the proteolytic digestion. The advantage of the surfactant PFOA for solubilising b-AQP0 as its intact form is already shown herein for the first time (see section 4.1.1) whilst being compatible with LC-MS. Using this

surfactant in combination with DTT reducing agent has shown good sequence coverage with a number of lipidation products (Table 4.9, entry 3). However, the absence of PFOA has shown to advantage in both protein sequence coverage and/or the number of lipidation peptides (Table 4.9, entry 1 (**LC-MS Method-II**) and entry 4). Interestingly, major improvement is achieved by using ionic surfactant/detergent SDS (sodium dodecyl sulfate), which reported its compatibility with LC-MS for solubilising and denaturing integral membrane proteins[50] (Table 4.9, entry 6). Overall, different digestion protocols (reagents) provide different outcomes for both protein sequence coverage and the number of lipidation products with regarding SDS as the optimum digestion condition for b-AQP0.

4.2.2. Biological approach in proteolytic analysis of b-AQP0

The advantage of SDS in protein digestion is clearly visible in achieving 100% protein sequence coverage with a range of modified peptides, as shown in Figure 4.22.

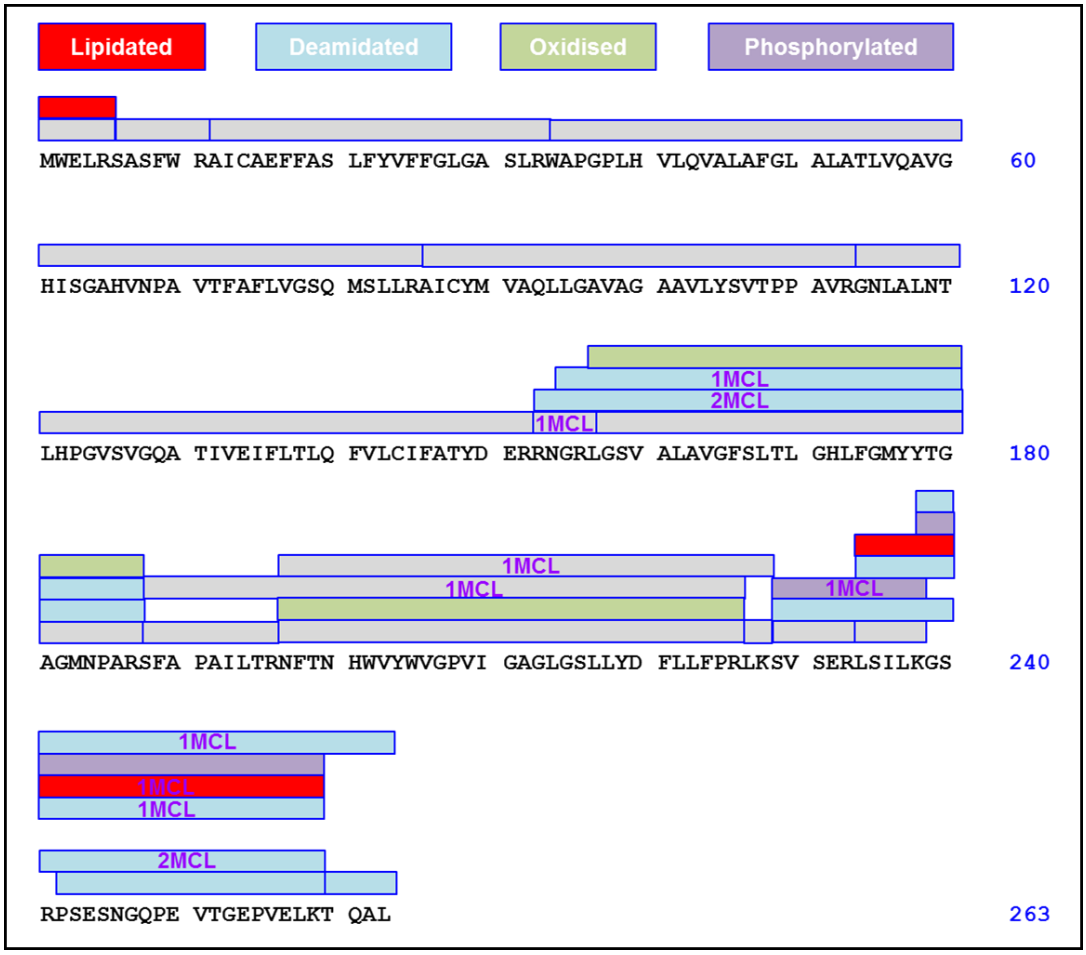

Figure 4.22. **The highlighted regions of the protein represent the confirmed peptides from b-AQP0-OC tryptic digestion, using digestion protocol Method-D and LC-MS Method-IIII (see section 8.2.2.2.1). Peptide residues with the observed modifications illustrated in bright colours; peptide residues with more than one missed cleavages (MCL) presented on each specific sequence. Details tabulated in Appendix C Table 9.33.**

Moreover, Protein digestion with SDS is also shown to enhance the detection of more hydrophobic acyl chains (C22:2 and C22:5) together with the other shorter acyl chains, as shown in Figures 4.23 and 4.24.

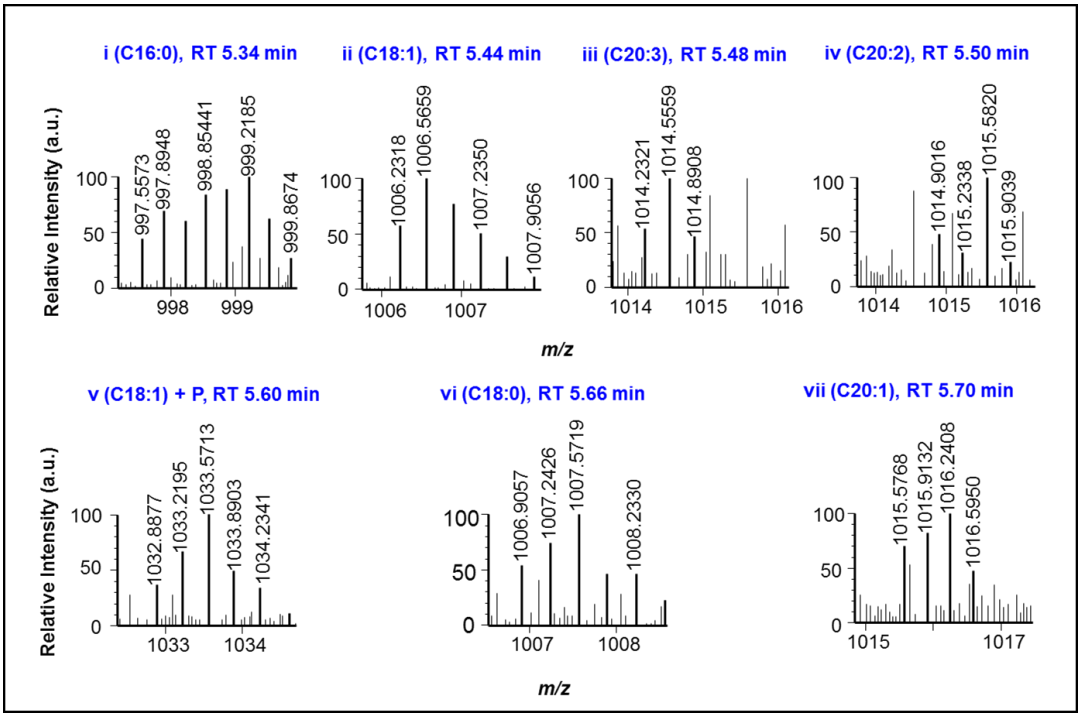

Figure 4.23. **Mass spectra for the range of acylated products for peptide [234-259] from trypsin digestion of b-AQP0-OC, using digestion protocol Method-D and LC-MS Method-IIII (see section 8.2.2.2.1). Each spectrum labelled with the acyl group identity, see Appendix C Table 9.34 for detailed information about the acyl groups added to the peptide [234-259]. The lines were made thicker just to stand out the peaks of interest.**

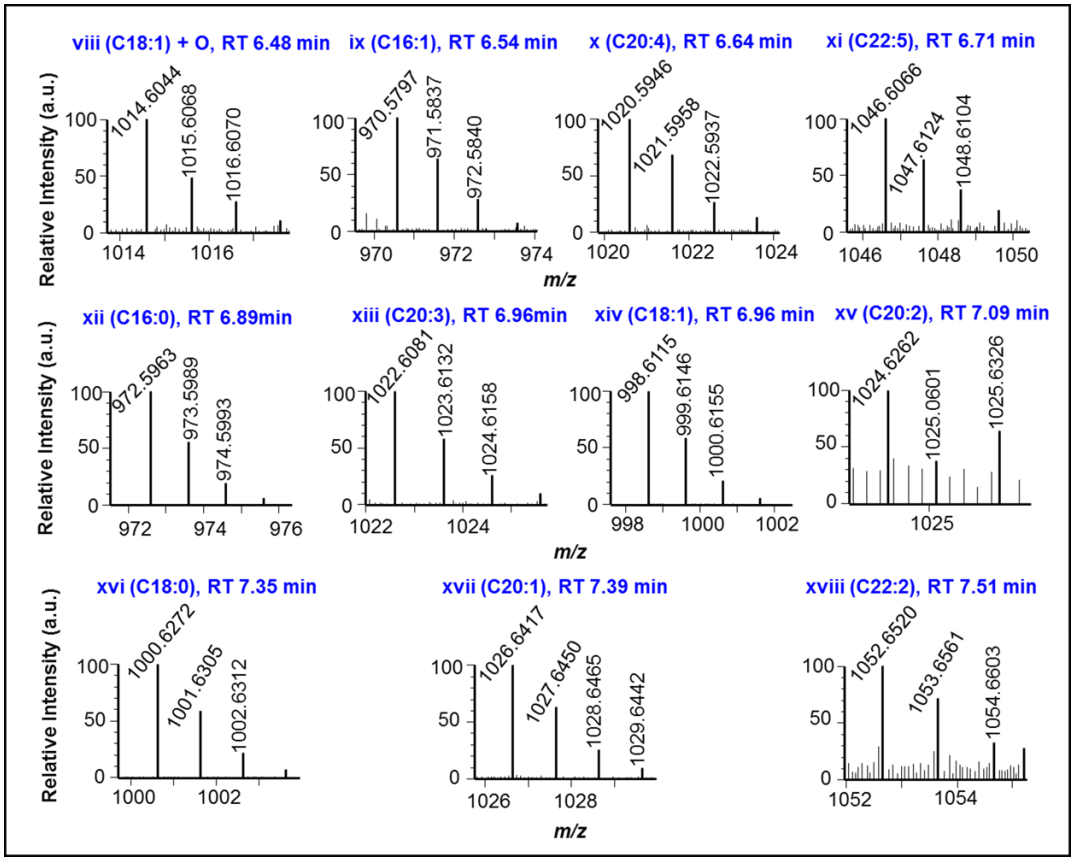

Figure 4.24. **Mass spectra for the range of acylated products for peptide [1-5] from trypsin digestion of b-AQP0-OC, using digestion protocol Method-D and LC-MS Method-IIII (see section 8.2.2.2.1). Each spectrum labelled with the acyl group identity, see Appendix C Table 9.34 for detailed information about the acyl groups added to the peptide [1-5].**

It is interesting to see the consistency between the lipidation profile on both peptide sets of peptide [1-5] and peptide [234-259], Figure 4.25, that are both embedded in the cytoplasmic leaflet of lens lipid-bilayer (see Figure 4.17). This cytoplasmic leaflet in bovine lens is known to be rich with PE lipid,[22] which has fatty acid composition (see Table 4.7) that matches the observed lipidated profile herein. Consequently, one can strongly predict *in vivo* lipid transfer from membrane lipids to membrane protein.

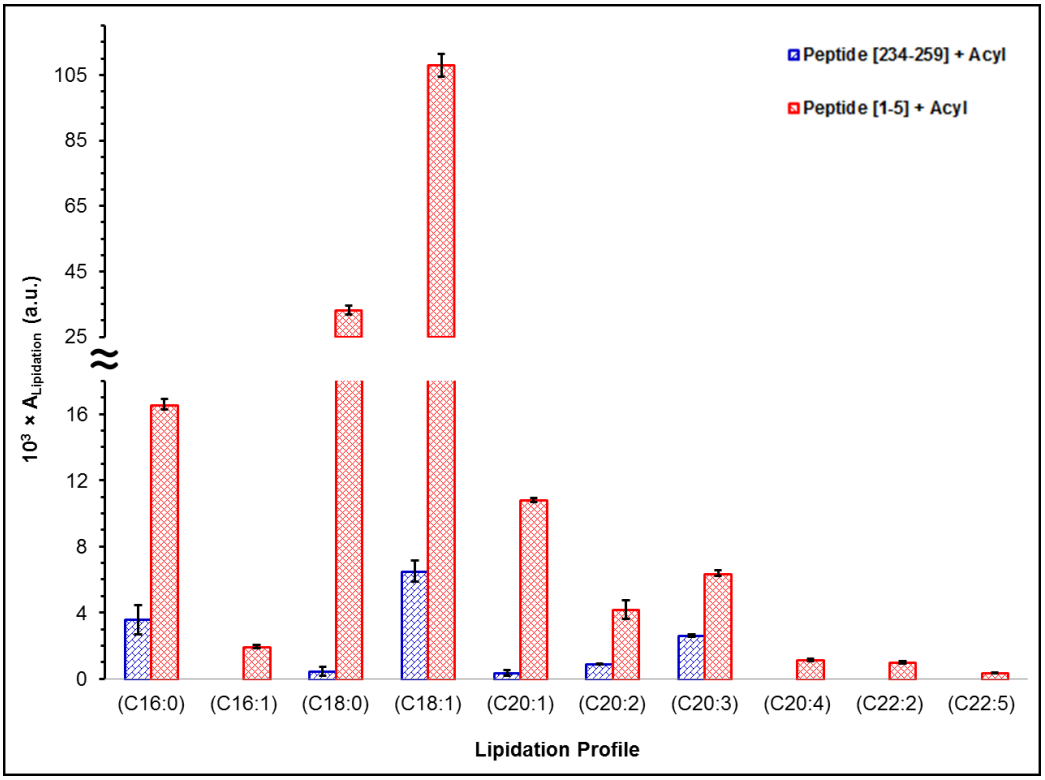

Figure 4.25. **The abundance of identified lipidated peptides described in Figures 4.23 and 4.24 for both lipidated sites of peptide [234-259] and peptide [1-5] respectively. The peak area (A) represents the summation of peak area over all observed charge states for each acylated peptide, (*z*=1-2) for peptide [1-5]; (*z*=2-4) for peptide [234-259]. All acylated species of peptide [234-259] matches contain one deamidation. The abundance of peptide [1-5] oleoylation include the summation of peak area for peptide $[1\text{-}5]_{ole}$ and peptide $[1\text{-}5]_{ole}$ + O; the abundance of peptide [234-259] oleoylation include the summation of peak area for peptide $[234\text{-}259]_{ole}$ and peptide $[234\text{-}259]_{ole}$ + P, while the other acylation products include just their individual peak area. Errors reported as the standard error of the mean (SEM) of peak area when n=2. Details are tabulated in Appendix C Table 9.34.**

In addition, the presence of four truncation sites towards C-terminus of the protein has been confirmed, as shown in Table 4.10. These truncation sites were also identified in the intact form of the protein (see Table 4.5). Interestingly, all truncated peptides are assigned with lipidation modification but this is not surprising as all truncated peptides are residing K238 AA which is reported to be lipidated[1]. Consequently, both lipidation and truncation process are not mutually exclusive events.

Table 4.10. **The deconvoluted truncated peptides identified from b-AQP0-OC tryptic digestion, using digestion protocol Method-D and LC-MS Method-IIII (see section 8.2.2.2.1).**

Truncation Site	AA Residue	Sequence + Modifications	Theor *m/z* ‡ $[M + H]^+$	Meas *m/z*‡ $[M + H]^+$	RT (min)	10^2 × Total $A_{Lipidation}$ § (a.u.)	Error (ppm)
K238	[229-238]	SVSERLSILK [1×Oleoyl]	1395.9191	1395.9211	5.7	1 ± 0.7	1.4
E244	[234-244]	LSILKGSRPSE	1186.6796	1186.6784	3.57	203.5 ± 21	-1
	[234-244]	LSILKGSRPSE [1×P]	1266.6459	1266.6442	2.97	137 ± 14	-1.3
	[234-244]	LSILKGSRPSE [1×Palmitoyl]	1424.9092	1424.9054	5.7	0.6 ± 0.02	-2.7
	[234-244]	LSILKGSRPSE [1×Stearoyll]	1452.9406	1452.9422	5.89	1.5 ± 0.3	1.1
	[234-244]	LSILKGSRPSE [1×Oleoyl]	1450.9249	1450.926	5.77	2 ± 0.1	0.8
	[234-244]	LSILKGSRPSE [Eicosenoyl]	1478.9562	1478.9562	6.25	0.3 ± 0.07	3.1
	[234-244]	LSILKGSRPSE [1×Eicosadienoyl]	1476.9406	1476.935	5.89	0.6 ± 0.03	-3.8
	[234-244]	LSILKGSRPSE [1× Dihomo-γ-linolenoyl]	1474.9249	1474.9254	5.7	0.6 ± 0.06	0.3
N246	[229-246]	SVSERLSILKGSRP SESN [1×Deamidation; 1×P]	2026.9811	2026.9861	3.53	38 ± 7	2.5
	[229-246]	SVSERLSILKGSRP SESN [1×Deamidation; 1×Oleoyl]	2211.26	2211.2566	5.41	31 ± 9	-1.5
	[234-246]	LSILKGSRPSESN [1×Deamidation]	1388.7385	1388.7382	3.53	178 ± 24	-0.2
	[234-246]	LSILKGSRPSESN [1×Deamidation; 1×P]	1468.7048	1468.7038	3	114 ± 16	-0.7

	[234-246]	LSILKGSRPSESN [1×Deamidation; 1×Palmitoyl]	1626.9681	1626.9812	5.67	0.7 ± 0.08	8.1
	[234-246]	LSILKGSRPSESN [1×Deamidation; 1×Oleoyl]	1652.9839	1652.9758	5.73	1 ± 0.07	-4.9
	[239-246]	GSRPSESN [1×Deamidation]	834.3594	834.3596	2.13	21 ± 19	0.2
	[239-246]	GSRPSESN [1×Deamidation; 1×P]	914.3257	914.3272	0.87	2.5 ± 0.2	1.6
T260	[234-260]	LSILKGSRPSESNG QPEVTGEPVELKT [1×Deamidation]	2853.4848	2853.4814	3.82	95 ± 7	-1.1
	[239-260]	GSRPSESNGQPEV TGEPVELKT [1×Deamidation]	2299.1055	2299.1065	3.29	61 ± 0.8	0.4
	[239-260]	GSRPSESNGQPEV TGEPVELKT [1×Deamidation; 1×P]	2379.0718	2379.0794	2.68	8 ± 0.8	3.2

‡Both theoretical (Theor) and measured (Meas) *m/z* are for the monoisotopic peak. Theoretical mass obtained from MassLynx software (V4.1).

§ The peak area (A) represents the summation of peak area over all observed charge states for each identified peptide. Errors reported as SEM (n=2).

4.2.2.1. The localisation of acylation modifications on b-AQP0 by LC-MS^2

Performing LC-MS^2 experiment on digested b-AQP0 yielded a profile of product ions for the different peptide species. The most intense oleoyl-modified b-AQP0 is confirmed by isolating the precursor ion at *m/z* 998.61 (*z*=1) and 1006.23 (*z*=3) for each peptide [1-5] (Figure 4.26 A and Table 4.11) and peptide [234-259] (Figure 4.26 B and Table 4.12). The confirmed sites of oleoylation (M1 and K238) are consistent with the results in previous study[1]. This is also in agreement with the nucleophilic character of the N-terminal amino group and the ε-amino group of the K238 on the protein in the aminolysis reaction.[46,47,51] However, although both K238 and K259 are nucleophile candidates in the peptide [234-259], but K238 is the only acylation candidate within this peptide sequence because if K259 is acylated then this site will be blocked and no longer available for trypsin cleavage.

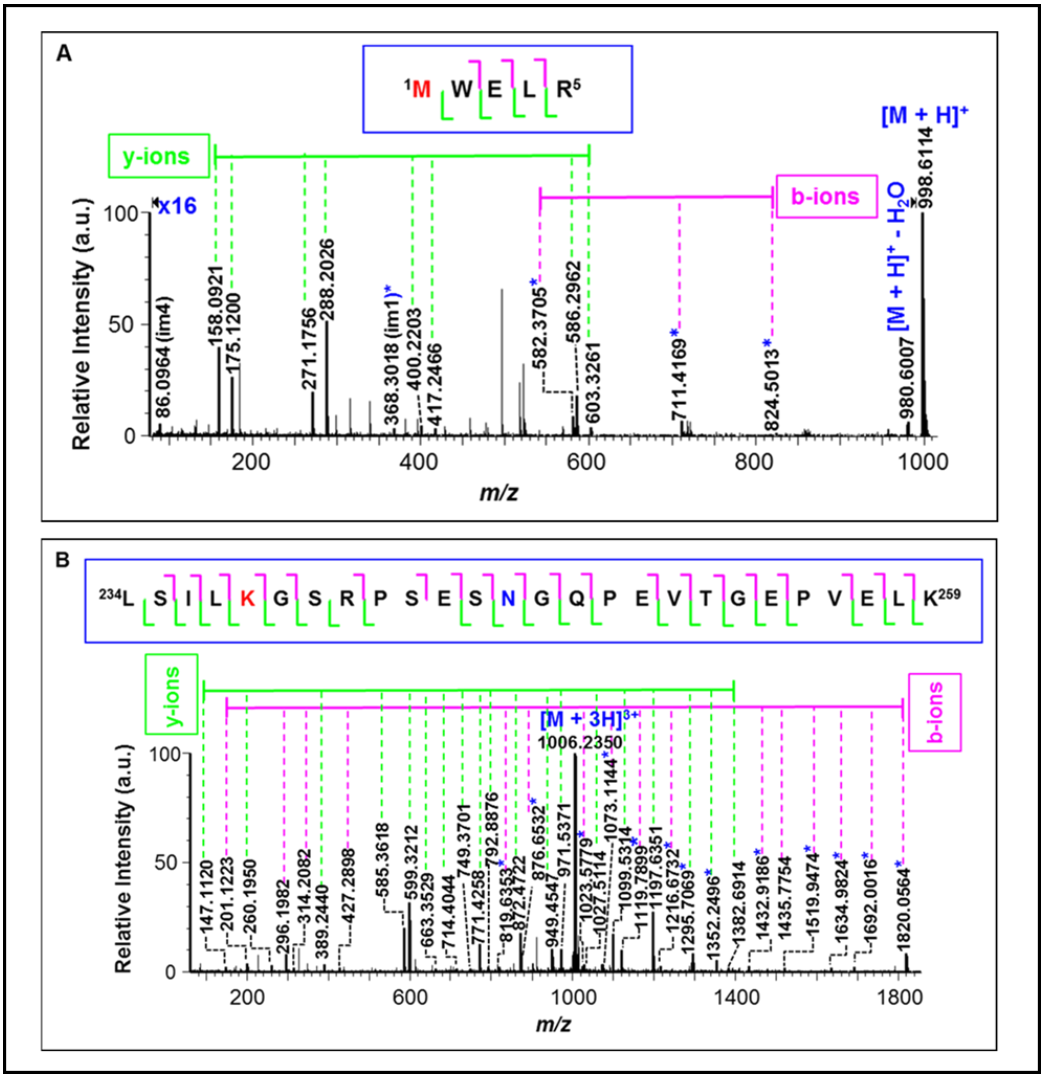

Figure 4.26. **MS^2 spectra of (A) peptide [1-5] + oleoyl (C18:1) for [M + H]$^+$ and (B) peptide [234-259] + oleoyl (C18:1) for [M + 3H]$^{3+}$, using Synapt G2-s (see section 8.2.2.2.2). Peptide fragments containing oleoyl acyl chain are marked with an asterisk. The b- and y-ion series are clearly labelled and correlate to the sequences given above each corresponding spectrum. Oleoylated residues are labelled in red and the deamidation site for peptide [234-259]$_{ole}$ is given in blue. For more details, see Tables 4.11 and 4.12.**

Table 4.11. **Product ions identified following the isolation and fragmentation of the [M + H]$^+$ precursor ion N-oleoylated peptide [1-5] at *m/z* 998.61. The amino acid residue highlighted in red indicates the site of oleoylation.**

Ion	AA Residues	Meas *m/z*	*z*	Sequence Ladder	Error (ppm)
[M + H]$^+$	[1-5]	998.6114	1	MWELR	0.1
[M + H]$^+$ - H_2O	[1-5]	980.6007	1	MWELR	0
b2	[1-2]	582.3705	1	MW	-4.1
b3	[1-3]	711.4169	1	MWE	2.0
b4	[1-4]	824.5013	1	MWEL	2.1
y1	[5-5]	175.12	1	R	2.9
y2	[4-5]	288.2026	1	LR	-3.5
y3	[3-5]	417.2466	1	ELR	1.0
y4	[2-5]	603.3261	1	WELR	1.0
y1-NH_3	[5-5]	158.0921	1	R	-5.7
y2-NH_3	[4-5]	271.1756	1	LR	-5.2
y3-NH_3	[3-5]	400.2203	1	ELR	1.7
y4-NH_3	[4-5]	586.2962	1	WELR	-4.8
im1	[1-1]	368.3018	1	M	8.4
im4	[4-4]	86.0973	1	L	3.5

Table 4.12. **Product ions identified following the isolation and fragmentation of the [M + 3H]$^{3+}$ precursor ion K238-oleoylated peptide [234-259] at *m/z* 1006.23. The amino acid residue highlighted in red indicates the site of oleoylation and the deamidation site marked in blue.**

Ion	AA Residues	Meas *m/z*	*z*	Sequence Ladder	Error (ppm)
[M + 3H]$^{3+}$	[1-26]	1006.2350	3	LSILKGHSRPSESNGQPEVTGEPVELK	2.4
b2	[1-2]	201.1223	1	LS	-8.0
b3	[1-3]	314.2082	1	LSI	0.6
b3-H_2O	[1-3]	296.1982	1	LSI	2.7
b4	[1-4]	427.2898	1	LSIL	-5.4
b5	[1-5]	819.6353	1	LSILK	3.7
b6	[1-6]	876.6532	1	LSILKG	-0.7
b8	[1-8]	1119.7899	1	LSILKGSR	2.6
b11	[1-11]	1432.9186	1	LSILKGSRPSE	3.0
b12	[1-12]	1519.9474	1	LSILKGSRPSES	0.7
b13	[1-13]	1634.9824	1	LSILKGSRPSESN	5.6
b14	[1-14]	1692.0016	1	LSILKGSRPSESNG	4.0
b15	[1-15]	1820.0564	1	LSILKGSRPSESNGQ	1.7
b17	[1-17]	1023.5779	2	LSILKGSRPSESNGQPE	-0.3
b18	[1-18]	1073.1144	2	LSILKGSRPSESNGQPEV	1.9
b20	[1-20]	1152.1464	2	LSILKGSRPSESNGQPEVTG	-0.5
b21	[1-21]	1216.6732	2	LSILKGSRPSESNGQPEVTGE	4.0

b24	[1-24]	1379.2488	2	LSILKGSRPSESNGQPEVTGEPVE	-1.0
b25	[1-25]	1435.7754	2	LSILKGSRPSESNGQPEVTGEPVEL	-11.7
y1	[26-26]	147.1120	1	K	-9.5
y2	[25-26]	260.1950	1	LK	-9.2
y3	[24-26]	389.2440	1	ELK	10.3
y5	[22-26]	585.3618	1	PVELK	1.0
y6	[21-26]	714.4044	1	EPVELK	0.8
y7	[20-26]	771.4258	1	GEPVELK	0.8
y8	[19-26]	872.4722	1	TGEPVELK	-0.8
y9	[18-26]	971.5371	1	VTGEPVELK	-4.3
y11	[16-26]	1197.6351	1	PEVTGEPVELK	-1.3
y11	[16-26]	599.3212	2	PEVTGEPVELK	-1.8
y12	[15-26]	663.3529	2	QPEVTGEPVELK	2.0
y13	[14-26]	1382.6914	1	GQPEVTGEPVELK	-18.2
y14	[13-26]	749.3701	2	NGQPEVTGEPVELK	-7.5
y15	[12-26]	792.8876	2	SNGQPEVTGEPVELK	-5.3
y18	[9-26]	949.4547	2	PSESNGQPEVTGEPVELK	-0.7
y19	[8-26]	1027.5114	2	RPSESNGQPEVTGEPVELK	5.3
y20	[7-26]	1071.0187	2	SRPSESNGQPEVTGEPVELK	-3.1
y21	[6-26]	1099.5314	2	GHSRPSESNGQPEVTGEPVELK	-1.2
y22	[5-26]	1295.7069	2	KGHSRPSESNGQPEVTGEPVELK	3.1
y23	[4-26]	1352.2496	2	LKGHSRPSESNGQPEVTGEPVELK	3.5
y24	[3-26]	1408.7911	2	ILKGHSRPSESNGQPEVTGEPVELK	2.9
y25	[2-26]	1452.2937	2	SILKGHSRPSESNGQPEVTGEPVELK	-6.4

Stearoylation and palmitoylation modifications are also confirmed at M1 and K238 sites of the protein by LC-MS^2, as shown in Figures 4.27 and 4.28.

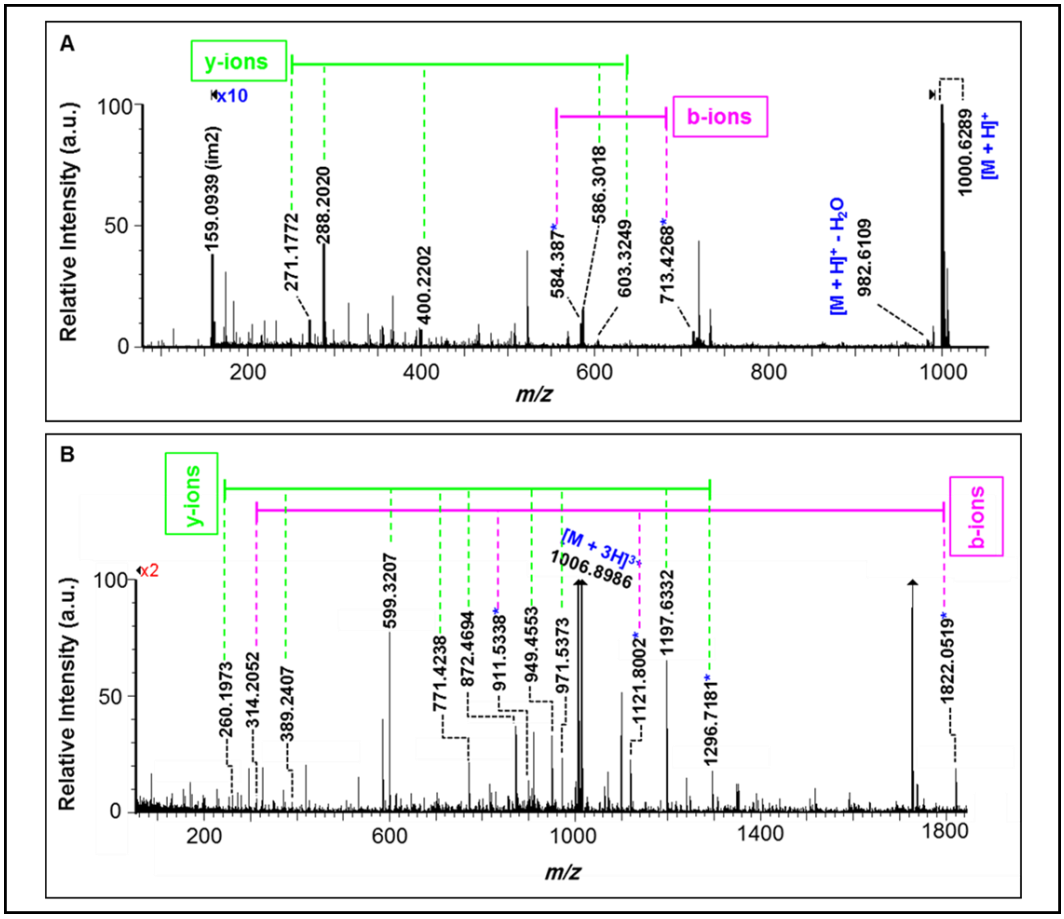

Figure 4.27. **MS^2 spectra of (A) peptide [1-5] + stearoyl (C18:0) [M + H]$^+$ and (B) peptide [234-259] + stearoyl (C18:0) [M + 3H]$^{3+}$, using Synapt G2-s (see section 8.2.2.2.2). Peptide fragments containing stearoyl acyl chain are marked with an asterisk. The b- and y-ion series are clearly labelled and correlate to the peaks that correspond to peptide fragments. For details, see appendix chapter (see Appendix C Tables 9.35 and 9.36).**

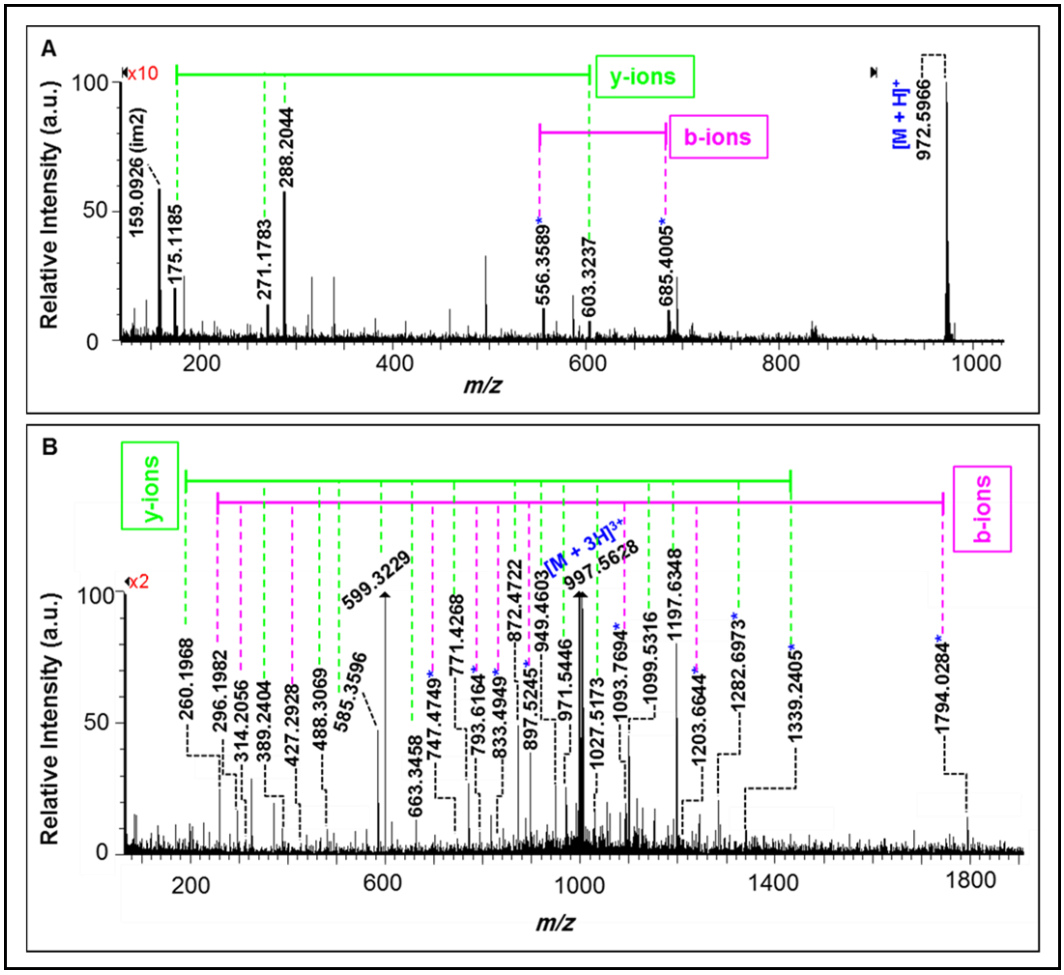

Figure 4.28. **MS^2 spectra of (A) peptide [1-5] + palmitoyl (C16:0) [M + H]$^+$ and (B) peptide [234-259] + palmitoyl (C16:0) [M + 3H]$^{3+}$, using Synapt G2-s (see section 8.2.2.2.2). Peptide fragments containing palmitoyl acyl chain are marked with an asterisk. The b- and y-ion series are clearly labelled and correlate to the peaks that correspond to peptide fragments. For details, see appendix chapter (see Appendix C Tables 9.37 and 9.38).**

Further MS^2 analysis enables localising M1 acylation by (C16:1) and C20 acyl chains (Figures 4.29 and 4.30), while unfortunately their resident on K238 could not be confirmed. This was due to their low signal-to-noise (S/N) ratio and thus there are not enough ions to produce a meaningful MS^2 spectrum.

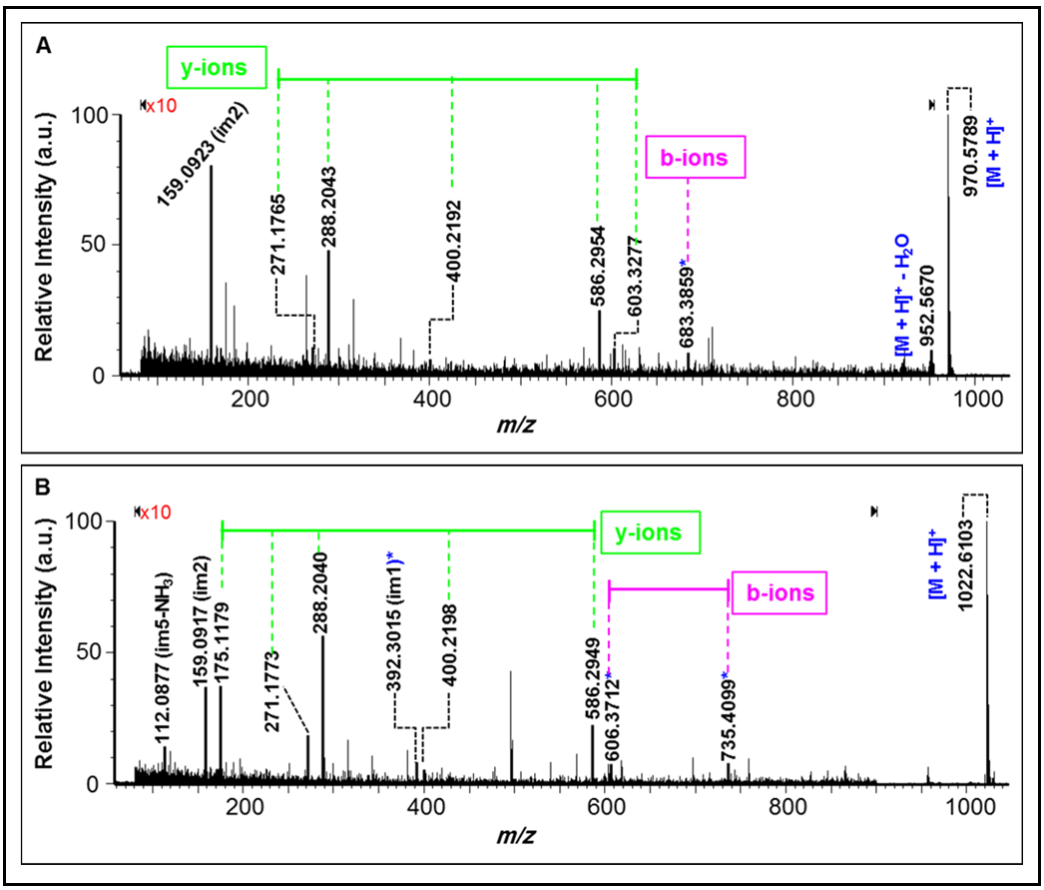

Figure 4.29. **MS^2 spectra of (A) peptide [1-5] + palmitoleoyl (C16:1) $[M + H]^+$ and (B) peptide [1-5] + dihomo-γ-linolenoyl (C20:3) $[M + H]^+$, using Synapt G2-s (see section 8.2.2.2.2). Peptide fragments containing palmitoleoyl or dihomo-γ-linolenoyl acyl chains are marked with an asterisk. The b- and y-ion series are clearly labelled and correlate to the peaks that correspond to peptide fragments. For details, see appendix chapter (see Appendix C Tables 9.39 and 9.40).**

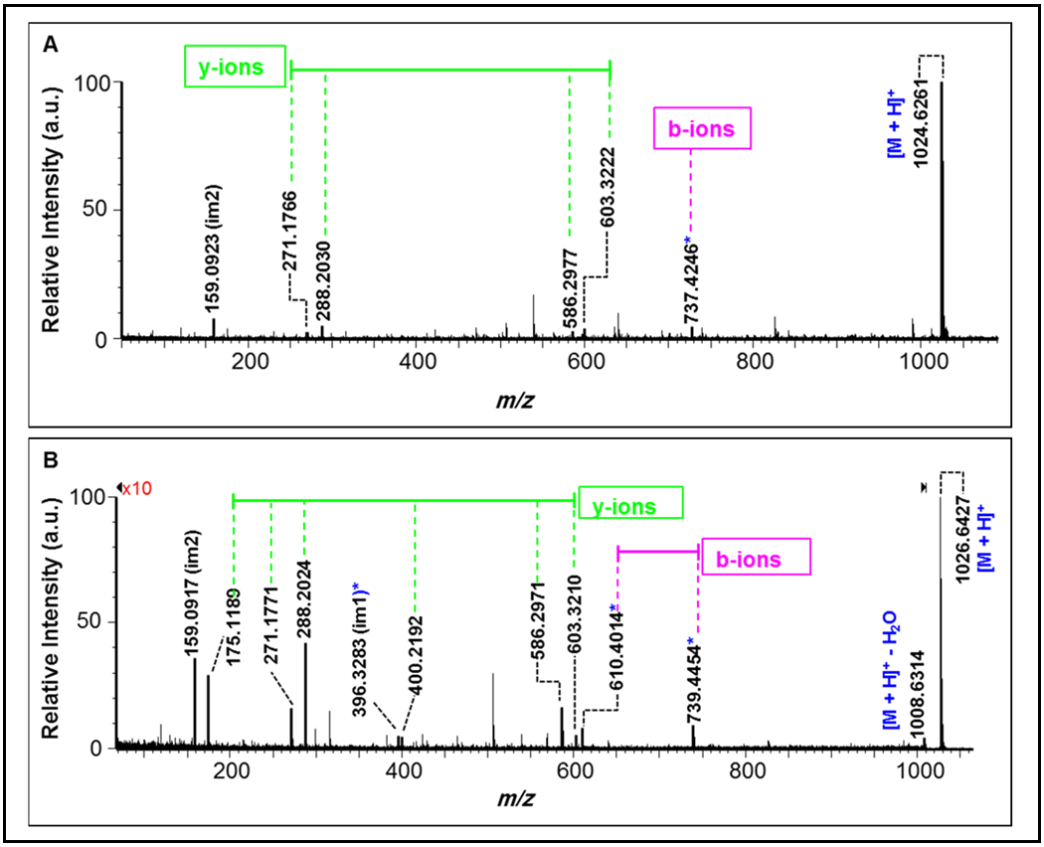

Figure 4.30. **MS^2 spectra of (A) peptide [1-5] + eicosadienoyl (C20:2) [M + H]$^+$ and (B) peptide [1-5] + eicosenoyl (C20:1) [M + H]$^+$, using Synapt G2-s (see section 8.2.2.2.2 Peptide fragments containing eicosadienoyl or eicosenoyl acyl chains are marked with an asterisk. The b- and y-ion series are clearly labelled and correlate to the peaks that correspond to peptide fragments. For details, see appendix chapter (see Appendix C Tables 9.41and 9.42).**

4.2.2.2. The effect of lens aging on the peptide modifications in b-AQP0

The relationship between lens age and the amount of protein modification has been followed herein by using the optimised conditions as described in Table 4.9 (entry 6). It is interesting to see that the level of N-terminus lipidation does not show a significant change by increasing the age of the lens except for ON fraction, which shows the lowest level of lipidation, as shown in Figure 4.31.

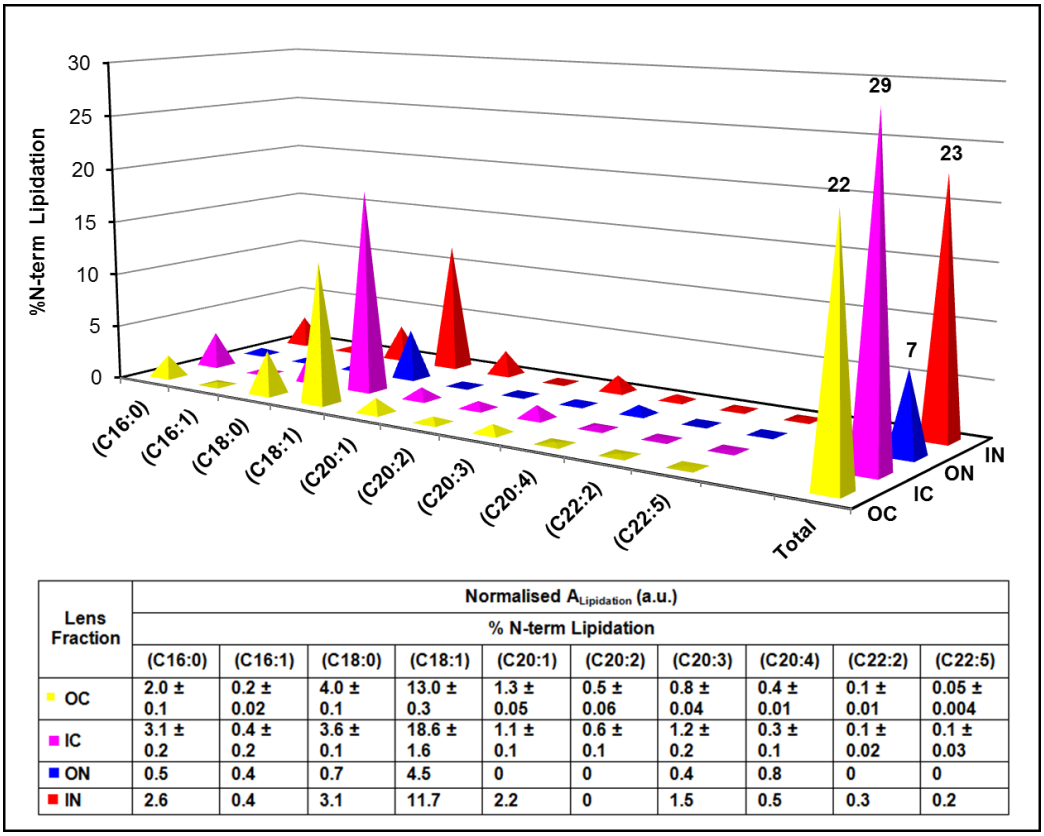

Lens Fraction	Normalised $A_{Lipidation}$ (a.u.) % N-term Lipidation									
	(C16:0)	(C16:1)	(C18:0)	(C18:1)	(C20:1)	(C20:2)	(C20:3)	(C20:4)	(C22:2)	(C22:5)
OC	2.0 ± 0.1	0.2 ± 0.02	4.0 ± 0.1	13.0 ± 0.3	1.3 ± 0.05	0.5 ± 0.06	0.8 ± 0.04	0.4 ± 0.01	0.1 ± 0.01	0.05 ± 0.004
IC	3.1 ± 0.2	0.4 ± 0.2	3.6 ± 0.1	18.6 ± 1.6	1.1 ± 0.1	0.6 ± 0.1	1.2 ± 0.2	0.3 ± 0.1	0.1 ± 0.02	0.1 ± 0.03
ON	0.5	0.4	0.7	4.5	0	0	0.4	0.8	0	0
IN	2.6	0.4	3.1	11.7	2.2	0	1.5	0.5	0.3	0.2

Figure 4.31. **The relative percentage of each single lipidation and total lipidation modification on N-terminus site of b-AQP0, using digestion protocol Method-D and LC-MS Method-IIII (see section 8.2.2.2.1). The normalisation of each acylation ratio on peptide [1-5] is performed relative to the equivalent non-acylated peptide residue (reference peptide) although both acylated and non-acylated peptide residues presumed to be very different in their ionisation efficiency. The ratio of peptide $[1\text{-}5]_{pal}$ = peak area peptide $[1\text{-}5]_{pal}$ / summed peak area (total of all lipidation on peptide [1-5] + reference peptide [1-5]); the ratio of peptide $[1\text{-}5]_{ole}$ = peak area peptide $[1\text{-}5]_{ole}$/summed peak area (total of all lipidation on peptide [1-5] + reference peptide [1-5]) and etc. Errors represent SEM, when n=2.**

On the other hand, K238 shows a higher level of lipidation in the older fractions of the lens, consistent with the increasing of lipidation from the membrane with time (Figure 4.32 and Appendix C Figure 9.1). This is also in agreement with the increasing of the other protein PTMs such as truncation, deamidation and phosphorylation with age.[13,20,21,40] The exact reason behind this difference in N-terminus *vs* K238 lipidation proportion with lens age is not known exactly, as both lipidated sites are located in the cytoplasmic leaflet of the lens. However, this could be suggested in relation with the highest degree of PTMs (truncation, deamidation, oxidation and phosphorylation) towards C-terminus of the protein.[5,10-13,20,21,40] Consequently, it can be concluded that each lipidation site has independent reactivity towards membrane lipids. Overall, N-terminus lipidation is more abundance than K238 lipidation but throughout one lens fraction the relative ratio of N-terminus:K238 total lipidation in the young and old lens fractions showed different outcomes. The lipidation ratio of N-terminus:K238 is nearly comparable in each of ON (7:5) or IN (23:7) relative to a significant difference in the lipidation ratio of N-terminus:K238 for OC (22:1) or IC (29:4). Consequently, it can be concluded that K238 is highly conserved in the youngest fraction of the lens (OC).

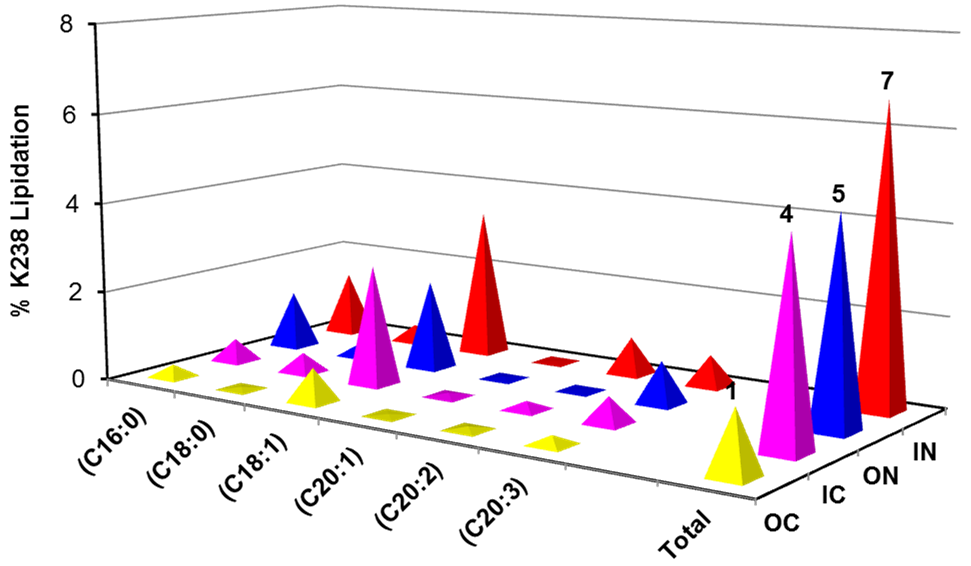

Lens Fraction	Normalised $A_{Lipidation}$ (a.u.) % K238 Lipidation					
	(C16:0)	(C18:0)	(C18:1)	(C20:1)	(C20:2)	(C20:3)
OC	0.3 ± 0.1	0.05 ± 0.02	0.75 ± 0.1	0.03 ± 0.01	0.1 ± 0.01	0.2 ± 0.01
IC	0.5 ± 0.02	0.4 ± 0.1	2.7 ± 0.1	0.1 ± 0.02	0.2 ± 0.03	0.6 ± 0.02
ON	1.3	0.3	2.0	0.04	0.03	1.0
IN	1.4	0.4	3.3	0.02	0.8	0.7

Figure 4.32. **The relative percentage of each single lipidation species and total lipidation on K238 AA site, using digestion protocol Method-D and LC-MS Method-IIII (see section 8.2.2.2.1). This lipidation site was assigned on different peptides including truncated peptides ([229-238], [234-244], [229-246] and [234-246], see Table 4.10) and as well as non-truncated peptide [234-259]. K238 lipidation for each acylation modification represents the summation of peak area for acylation on both truncated and non-truncated peptides. The normalisation of each acylation ratio is performed relative to the reference non-acylated peptide [234-259], as described in Figure 4.31. Errors represent SEM, when n=2.**

Increasing protein truncation has been well described for intact protein analysis (see sections 4.1.2 and 4.1.4), and consistent with earlier results.[6,7,13,19-21] This is also evident in the digestion mixture during monitoring lipidation ratio *vs* truncation ratio for truncated peptides (Figure 4.33). This is when truncated peptides with K238 site of acylation were normalised relative to a reference non-acylated peptide with non-truncation site of peptide [234-259], as shown in Figure 4.33, trend B. On the other

hand, increasing the amount of protein truncation with lens age has shown to be reflected in decreasing the amount of protein lipidation during normalisation relative to a reference non-acylated peptide with truncation site. This trend is confirmed by using three different truncated peptides such as peptide [229-246] (Figure 4.33, trend Ai), peptide [234-244] (Figure 4.33, trend Aii) and peptide [234-246] (Figure 4.33, trend Aiii).

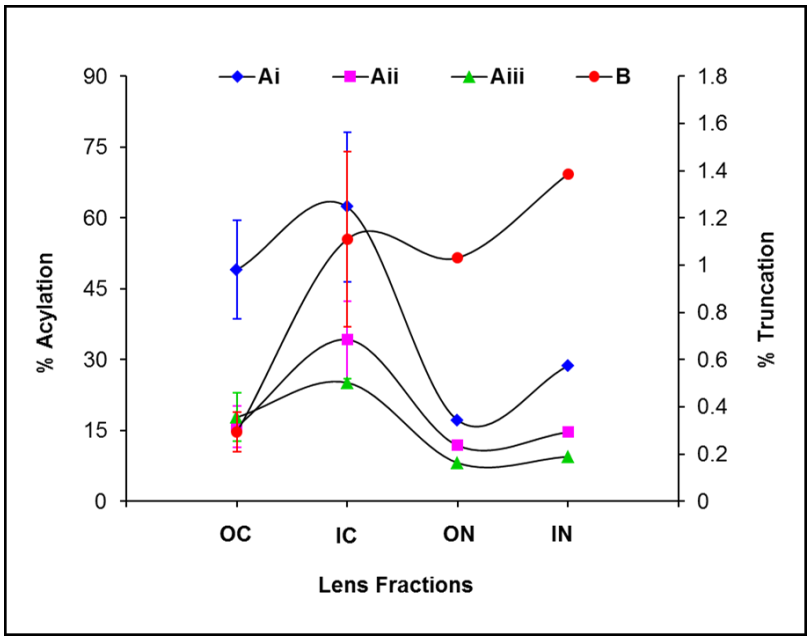

Figure 4.33. **The relative ratio of K238 lipidation on truncated peptides (trends Ai-Aiii) *vs* the relative ratio of truncation (trend B) in the four different bovine lens fractions, using digestion protocol Method-D and LC-MS Method-IIII (see section 8.2.2.2.1). The summation of all observed lipidation products on different truncated peptides were added together and the peak area was normalised relative to non-acylated peptide with the truncation site such as peptide [229-246] (trend Ai), peptide [234-244] (trend Aii) and peptide [234-246] (trend Aiii) as follows: %lipidation on truncated peptide = peak area total lipidation on truncated peptide/summed peak area (total lipidation on truncated peptide + reference peptide [229-246]) × 100. Peptide [234-244] and peptide [234-246] will follow the same. The relative ratio of truncation were calculated by normalisation of total lipidation products on truncated peptides relative to non-acylated peptide with non-truncation site such as peptide [234-259] as follows: %truncation = peak area total lipidated truncated peptide/summed peak area (total lipidated truncated peptide + reference peptide [234-259]) × 100. Errors represent SEM, when n=2.**

Moreover, the relation between lens age and AQP0 modification (deamidation, phosphorylation and truncation) is well documented in previous studies,[13,20,21,40] whilst AQP0 oxidation dependent on lens age has not been described in earlier researches. The two identified peptides with oxidation modification, peptide [157-187] and peptide [197-226], herein were followed to monitor the level of protein oxidation in different lens fractions. Interestingly, oxidised peptide [157-187] shows a slight increase in the level of oxidation by increasing lens age, while the level of oxidation on peptide [197-226] is significantly different between the older and younger fractions of the lens. This finding agrees with the age effect on increasing protein oxidation[16-18] (see section 4.1.1), however *in vitro* protein oxidation during sample preparation should be also take into account.

Table 4.13. **The proportion of oxidation level in the four different lens age fractions, using digestion protocol Method-D and LC-MS Method-IIII (see section 8.2.2.2.1). The data presented represent normalised peak area (A) for oxidised peptides to the summation of oxidised plus non-oxidised equivalent peptides. Errors represent SEM, when n=2.**

Lens Fractions	%Oxidation	
	Peptide [157-187] + 1 × O	Peptide [197-226] + 2 × O
OC	32 ± 3	6 ± 0.2
IC	32 ± 0.2	4.5 ± 1
ON	35	25
IN	40	14

4.2.2.3. Bovine lens PE/PEpl correlation with acylated b-AQP0

Correlating the relative proportions of naturally occurring transferrable fatty acyl composition of the major abundant PE/PEpl lipids in bovine lens[23,24,28] (Table 4.14) and the abundance of acylated b-AQP0 shows a strong correlation for both N-terminus and K238 lipidation sites, as shown in

Figure 4.34 and Appendix C Figure 9.2. Consequently, this strong correlation is supporting the concept of lipid transfer from host membrane to the protein.

Table 4.14. **Bovine lens transferrable fatty acid composition by lipid type created with data obtained by MS methods (Deeley *et al.*)[28]. Note: Error propagations are SEM.**

Acyl Group	PE nmol/g*	PEpl† nmol/g	Total PE (PE + PEpl) nmol/g
C14:0	0	0	0
C15:0	0	0	0
C16:0	42.9 ± 4.0	0	42.9 ± 4.0
C16:1	13.5 ± 0.4	0	13.59 ± 0.4
C18:0	20.5 ± 1.5	6.9 ± 0.5	27.4 ± 1.6
C18:1	239.5 ± 14.3	88.1 ± 2.2	327.6 ± 14.4
C18:2	3.9 ± 0.2	0	3.9 ± 0.2
C20:1	5.3 ± 0.6	0	5.3 ± 0.6
C20:2	0	0	0
C20:3	4.0 ±0.6	4.0 ± 0.3	8.0 ± 0.7
C20:4	5.2 ± 0.5	7.7 ± 1.1	12.9 ± 1.2
C22:2	0	0	0
C22:4	0	0	0
C22:5	0	0	0

†Lipid classes suffixed with “pl” refer to plasmalogen lipids which combine totals for both alkyl and alkenyl ether plasmalogens. There is a contribution of one mole of ester-linked fatty acyl chain per PEpl lipid.

*There is a contribution of two moles of ester-linked fatty acyl chain per PE lipid.

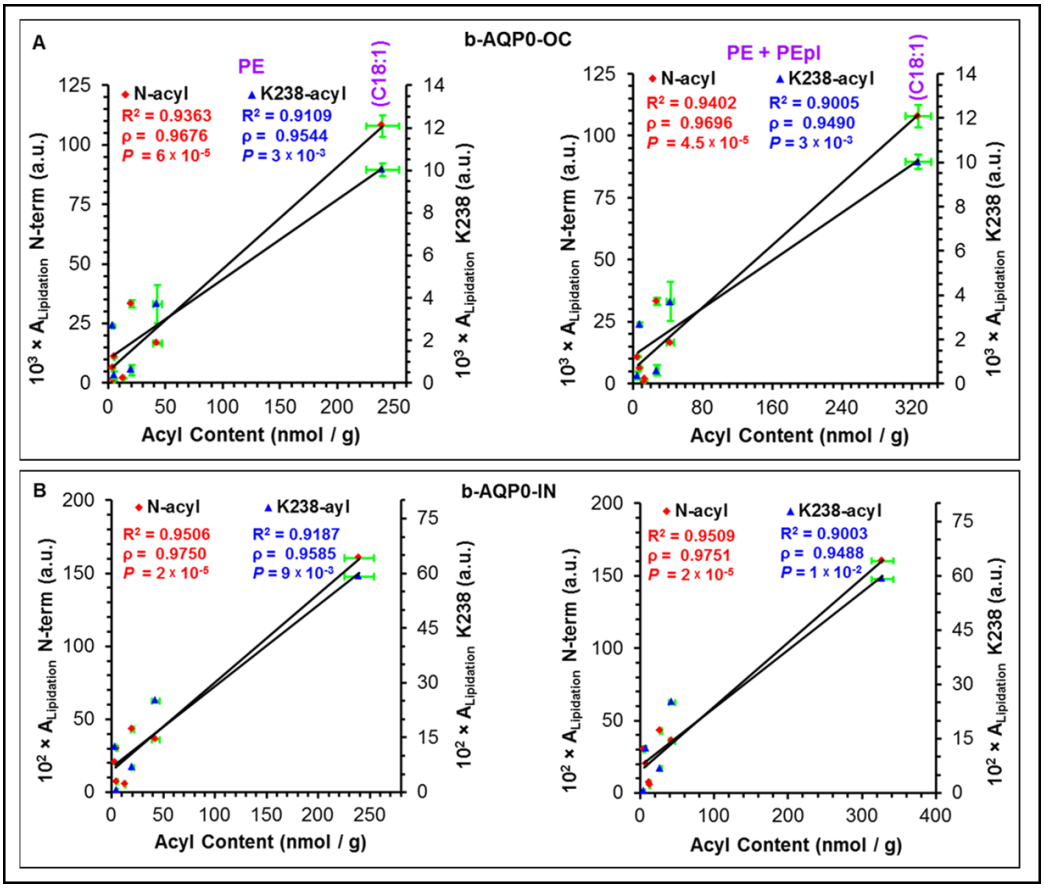

Figure 4.34. **Correlations between the amount of ester-linked transferrable fatty acyl content of bovine lens lipids and the peak area for lipidated peptides ($A_{Lipidation}$) of (A) b-AQP0-OC and (B) b-AQP0-IN, using digestion protocol Method-D and LC-MS Method-IIII (see section 8.2.2.2.1). Lipid data obtained from lipidomics MS analysis[28] (see Table 4.14). Peak areas for N-terminus acylation were calculated from EIC of each acylation on peptide [1-5], while peak areas for K238 acylation were calculated from EIC of each acylation on non-truncated peptide [234-259] and truncated peptides ([229-238], [234-244], [229-246] and [234-246]). Errors plotted as *X-axis* SEM (fatty acyl content, n=4) and *Y-axis* SEM (peak area for lipidated peptides, n=2). The line and the R^2 statistic are from linear regression analysis. The ρ-value represents the Pearson correlation coefficient (r) and the *p*-value represents the t-test of the correlation coefficient.**

Skewed distribution of the data is clearly visible in Figure 4.34. This is because the abundance of oleoyl (C18:1) in both protein lipidation and fatty acyl content data is an order of magnitude greater than that of the other fatty acyl profile. This reflects in generating much weaker correlation for the other data points by eliminating (C18:1) point, as shown in Figure 4.35.

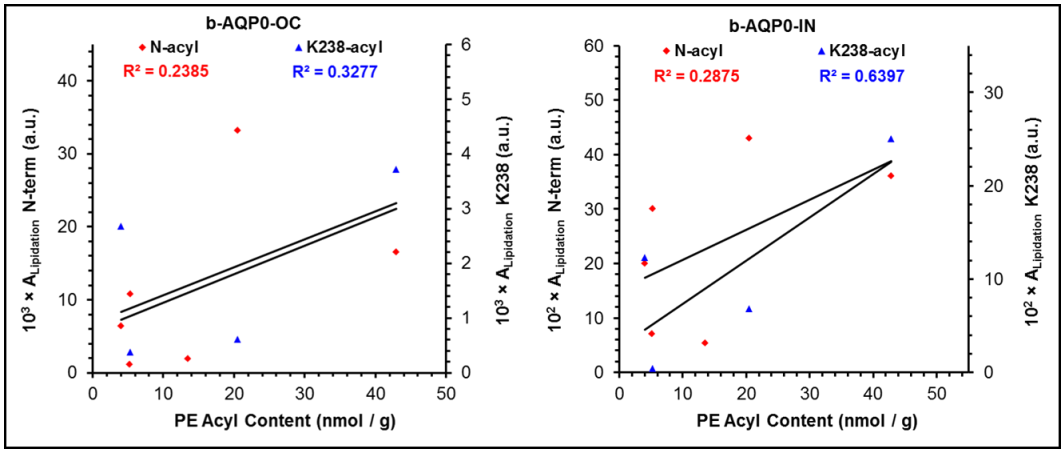

Figure 4.35. **Correlations between the amount of PE ester-linked transferrable fatty acyl content of bovine lens lipids and the peak areas for lipidated peptides of b-AQP0. These graphs were created by using the exact data as in Figure 4.34 A (PE acyl content) but by excluding the most abundant oleoylated data. The line and the R^2 statistic are from linear regression analysis.**

4.2.3. Biological approach in proteolytic analysis of h-AQP0

Different human lenses were obtained from male donors ages 22 (M22), 56 (M56), and 80 (M80) and female donors ages 56 (F56) and 76 (F76) have been decapsulated and dissected to the two major age fractions of the cortex (h-AQP0-C, younger fraction) and nucleus (h-AQP0-N, older fraction). The two main eye lens fraction is shown in Figure 4.36.

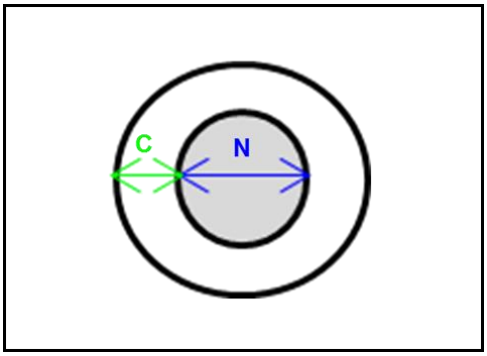

Figure 4.36. **Schematic diagram for human eye lens fractions. Different lens age fractions include C = cortex fraction/the youngest (4 mm) and N = nucleus fraction/the oldest (8 mm).**

The amino acid sequence of h-AQP0 is shown in Figure 4.37 with the illustration of protein spanning the lens membrane lipid-bilayer. Theoretical average neutral mass of h-AQP0 is 28121.5 Da, calculated from the provided AA sequence from Uniprot entry P30301 (http://www.uniprot.org/uniprot/P30301).

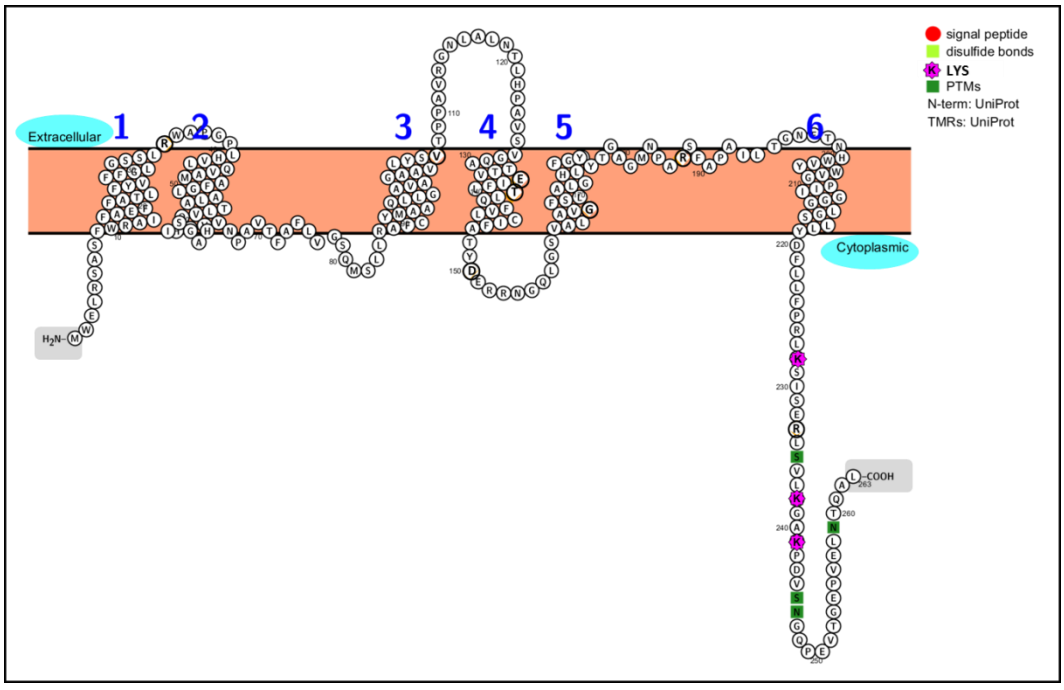

Figure 4.37. **Characteristic representation of h-AQP0 amino acid sequence, created from Protter open source software package (http://wlab.ethz.ch/protter/start/). Both terminus stand out in cytoplasmic region of the cell and all six transmembranes are also highlighted.**

Extracted and purified h-AQP0 from each individual human donor was subjected to trypsin digestion as per **Method-D** (see experimental section 8.2.2.2.1). Following completion, the mixture was analysed using **LC-MS Method-IIII**. Full protein sequence coverage is shown in Figure 4.38 for male donor age 22 (M22) as an example typical of the five individual samples. Protein PTM including deamidation, phosphorylation and oxidation have been observed and recorded in this study with h-AQP0 as previously documented[1,5,13,52].

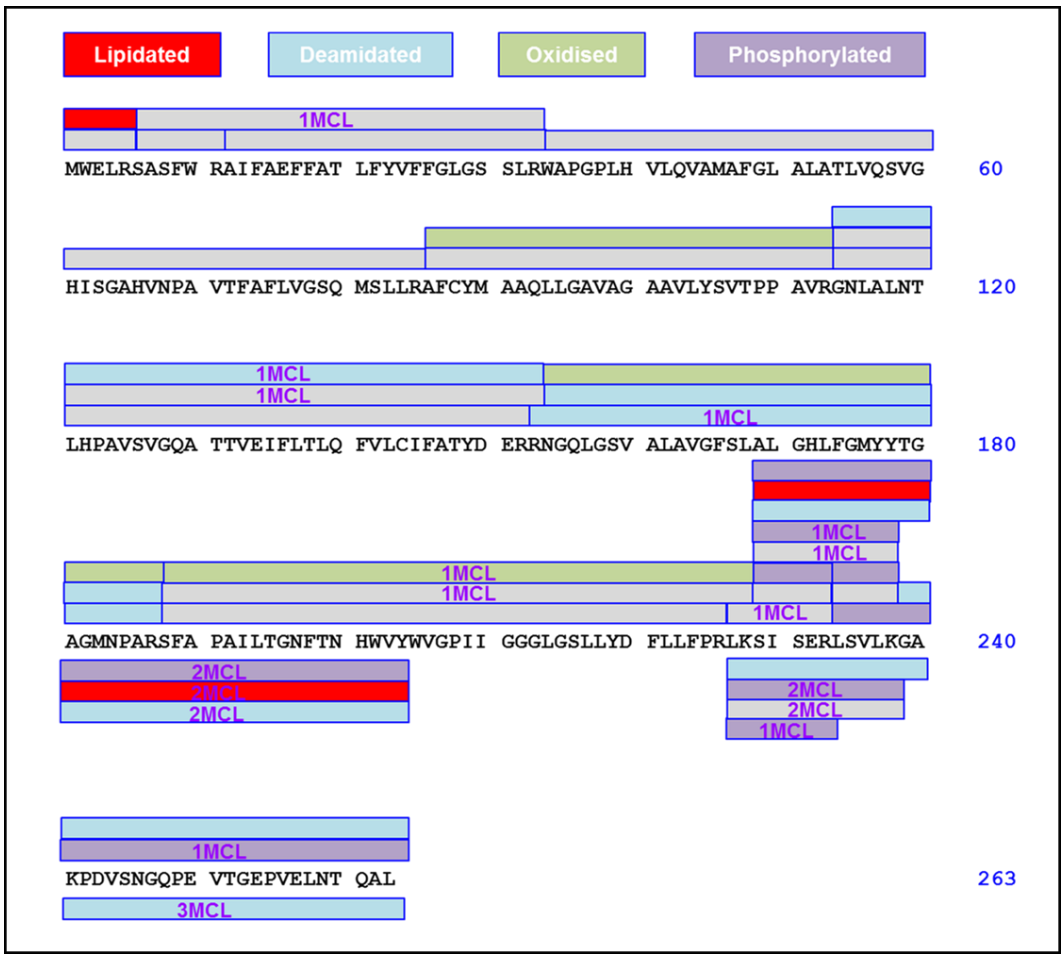

Figure 4.38. **The highlighted regions of the protein represent the confirmed peptides from h-AQP0-N male donor age 22 (M22) tryptic digestion, using digestion protocol Method-D and LC-MS Method-IIII (see section 8.2.2.2.1). Peptide residues with the observed modifications illustrated in bright colours; peptide residues with more than one missed cleavages presented on each specific sequence. Details tabulated in Appendix C Table 9.43.**

Evidence for lipidated peptides were seen over 5.0-5.6 and 6.4-7.4 min RT ranges of the chromatogram corresponding to peptide [227-263] and/or peptide [229-263] (Figure 4.39) and peptide [1-5] (Figure 4.40) respectively. This corroborates the work by Schey *et al.*[1] and Wenke *et al.*[7], who showed modification by oleoyl (C18:1) and palmitoyl (C16:0). Work herein now shows these two modifications together with a range of newly observed acyl chains including pentadecenoylation (C15:1), palmitoleoylation (C16:1), stearoylation (C18:0), eicosenoylation (C20:1), dihomo-ɣ-linolenoylation (C20:3), arachidonoylation (C20:4) and docosahexaenoylation (C22:6).

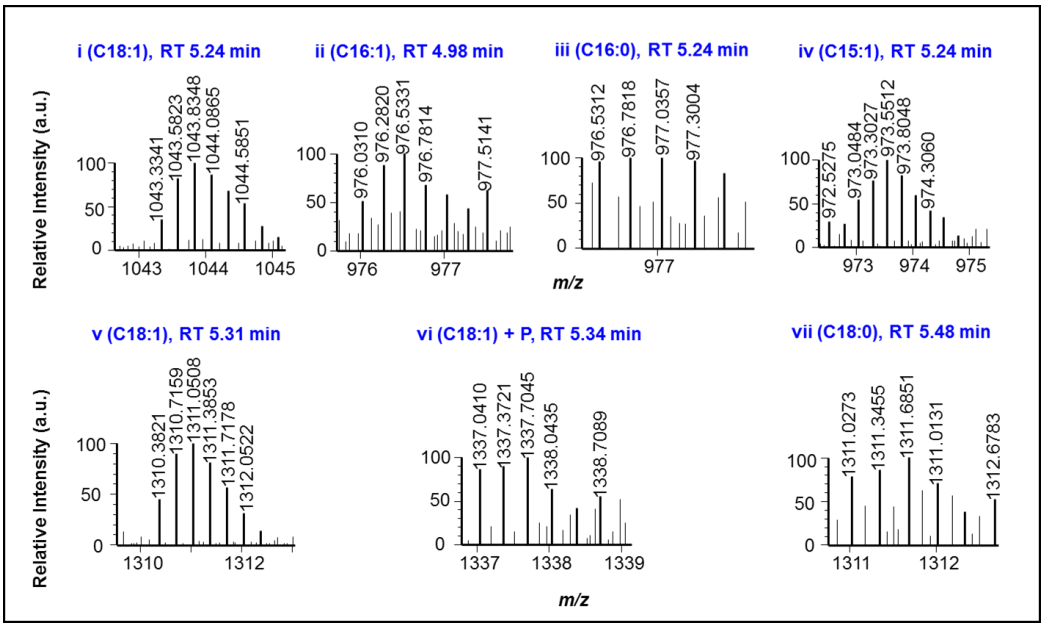

Figure 4.39. **Mass spectra for the range of acylated products for (i) peptide [227-263] and (ii-vii) peptide [229-263], from trypsin digestion of h-AQP0-N male donor age 22 (M22), using digestion protocol Method-D and LC-MS Method-IIII (see section 8.2.2.2.1). Each spectrum labelled with the acyl group identity, see Appendix C Table 9.44 for detailed information about the acyl groups added to the provided peptides.**

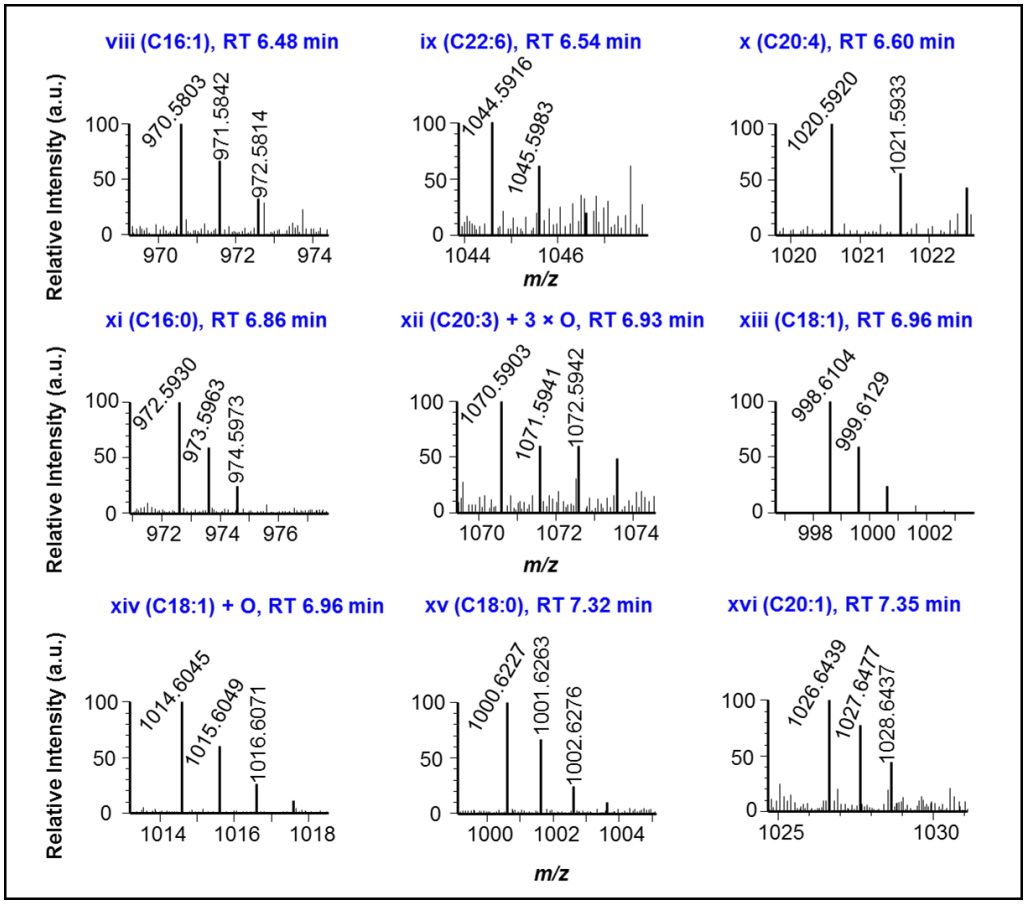

Figure 4.40. **Mass spectra for the range of acylated products for peptide [1-5] from trypsin digestion of h-AQP0-N male donor age 22 (M22), using digestion protocol Method-D and LC-MS Method-IIII (see section 8.2.2.2.1). Each spectrum labelled with the acyl group identity, see Appendix C Table 9.44 for detailed information about the acyl groups added to the peptide [1-5].**

As shown in Figures 4.39 and 4.40, protein modification by (C15:1) and (C22:6) were just recorded for h-AQP0 and were not seen for b-AQP0 (see Figures 4.23 and 4.24). The presence of poly unsaturated omega-3 fatty acyl chain (C22:6) with h-AQP0 is an additional supporting evidence for membrane lipid association in protein lipidation *in vivo*, as this fatty acyl species was found by Deeley *et al.*[28] just with human lens and not found with bovine lens. On the other hand, although C15 fatty acyl chain was recorded for both human and bovine lenses at low abundance by Deeley *et al.*,[28] its presence within the h-AQP0 lipidation profile herein and the absence with b-AQP0 is proposed to be related with the food intake by the human. Interestingly, Liao *et al.*[53] has already reported the change in PTMs of plasma

proteins when purple sweet potato, a root vegetable, was incorporated into the daily diet. This was followed by detecting the largest percentage of protein methylation using MS-based approach.[53]

In addition, the localization of M1- (N-terminus) and K238-oleoylation were confirmed in the product ion spectra for h-AQP0-N (M22), as shown in Figure 4.41. This is consistent with the characterized lipidation sites in b-AQP0 (see section 4.2.2.1) and as it is reported in previous study[1].

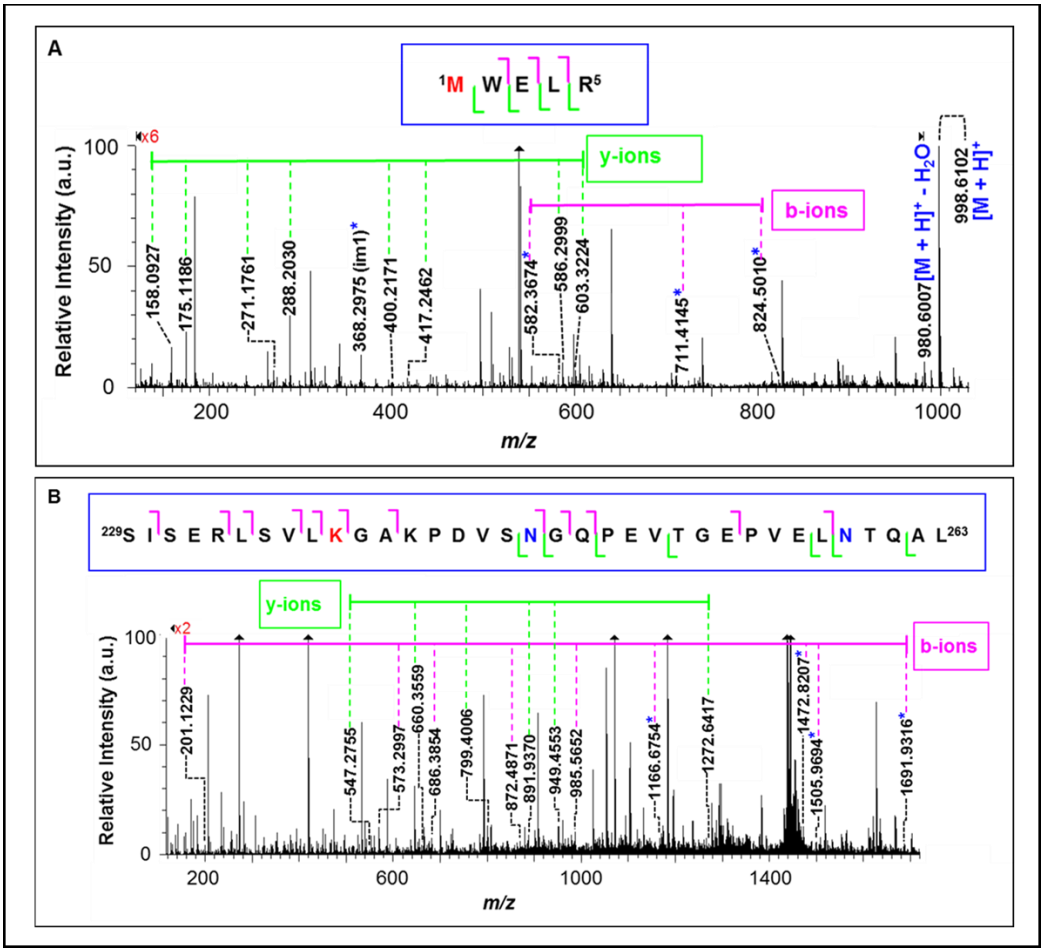

Figure 4.41. **MS^E spectra of (A) peptide [1-5]$_{ole}$ (C18:1) and (B) peptide [229-263]$_{ole}$ (C18:1). Using digestion protocol Method-D and LC-MS Method-IIII (see section 8.2.2.2.1). Peptide fragments containing oleoyl acyl chain are marked with an asterisk. The b- and y-ion series are clearly labelled and correlate to the sequences given above each corresponding spectrum. Oleoylated residues are labelled in red and the deamidation sites (N246 and N259) for peptide [229-263]$_{ole}$ are given in blue. For details, see appendix chapter (see Appendix C Tables 9.45 and 9.46 for more details).**

As summarized in Table 4.15, truncation in h-AQP0 is observed towards the C-terminus of the protein (D243, N246 and N259) similar to b-AQP0 (see Table 4.10). This non-enzymatic process[6,52] is well-documented in the literature[6,7,20,21,52] by presenting h-AQP0 truncation as an early age process and increasing the amount of truncation with age. It is interesting to see that most truncated peptides are also acylated with the two most abundant lipidation species herein (palmitoylation and oleoylation). This is consistent with K238 residency within the truncated peptide sequences and its high reactivity towards lens lipids. Although there is no direct evidence in this study to specify whether truncation or lipidation are happening first *in vivo*, the presence of protein lipidation in a 4-month human lens and the absence of protein truncation in this young age as reported by Wenke *et al.* in a MALDI imaging MS[7] suggests the protein lipidation is a faster process than truncation.

Table 4.15. **The deconvoluted truncated peptides identified from h-AQP0-N male donor age 22 (M22) tryptic digestion, using digestion protocol Method-D and LC-MS Method-IIII (see section 8.2.2.2.1)**

Truncation Site	AA Residue	Sequence + Modifications	Theor *m/z*‡ $[M + H]^+$	Meas *m/z*‡ $[M + H]^+$	RT (min)	10^2 × Total $A_{Lipidation}$§ (a.u.)	Error (ppm)
243	[227-243]	LKSISERLSVLKGAKPD [1×Palmitoyl]	2079.3157	2079.3046	5.31	1.6	-5.3
	[227-243]	LKSISERLSVLKGAKPD [1×Oleoyl]	2105.3313	2105.3209	5.38	3.6	-4.9
	[229-243]	SISERLSVLKGAKPD	1599.907	1599.9064	3.72	190.1	-0.4
	[229-243]	SISERLSVLKGAKPD [1×Oleoyl]	1864.1523	1864.1485	5.51	23.4	-2.0

246	[229-246]	SISERLSVLKGAKPDVSN [1×Deamidation]	1901.0344	1901.0342	3.72	124.3	-0.1
	[229-246]	SISERLSVLKGAKPDVSN [1×Deamidation; 1×Palmitoyl]	2139.2642	2139.2641	5.37	3.7	0.05
	[229-246]	SISERLSVLKGAKPDVSN [1×Deamidation; 1×Oleoyl]	2165.2798	2165.2756	5.48	26.5	-1.9
	[234-246]	LSVLKGAKPDVSN [1×Deamidation]	1328.7426	1328.7379	3.36	187.1	-3.5
	[234-246]	LSVLKGAKPDVSN [1×Deamidation; Palmitoyl]	1566.9722	1566.9708	5.67	0.4	-0.9
	[234-246]	LSVLKGAKPDVSN [1×Deamidation; Oleoyl]	1592.9879	1592.9802	5.73	1.1	-4.8
	[239-246]	k.GAKPDVSN.g [1×Deamidation]	788.3790	788.3776	2.32	38.8	-1.8
259	[229-259]	SISERLSVLKGAKPDVSNGQPEVTGEPVELN [1×Deamidation]	3250.6807	3250.6814	3.69	23.8	0.2
	[234-259]	LSVLKGAKPDVSNGQPEVTGEPVELN [1×Deamidation]	2678.3889	2678.3851	3.40	100.0	-1.4
	[239-259]	GAKPDVSNGQPEVTGEPVELN [1×Deamidation]	2138.0254	2138.0258	2.75	125.4	0.2

‡Both theoretical (Theor) and measured (Meas) *m/z* are for the monoisotopic peak. Theoretical mass obtained from MassLynx software (V4.1).

§ The peak area (A) represents the summation of peak area over all observed charge states for each identified peptide.

Moreover, the abundance of lipidation profile on N-terminus *vs* K238 of h-AQP0-N is shown in Figure 4.42. It is clearly visible that the acylation species with the same acyl chain on both lipidation sites are comparable in their abundance.

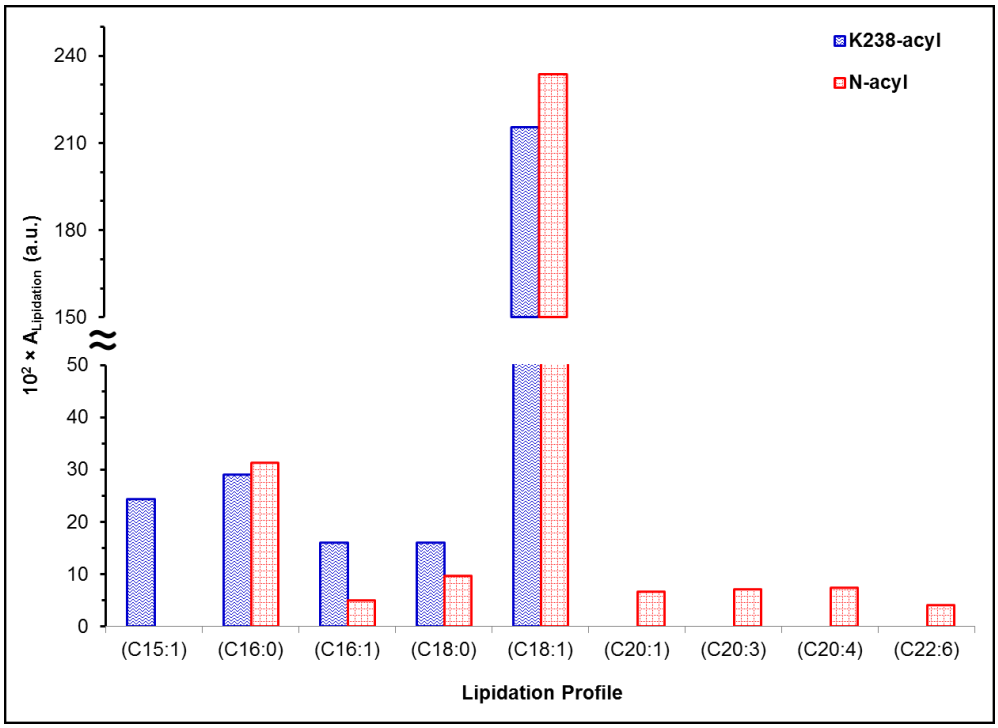

Figure 4.42. **The abundance of each identified lipidation modification on K238 and N-terminus site of h-AQP0-N male donor age 22 (M22), using digestion protocol Method-D and LC-MS Method-IIII (see section 8.2.2.2.1). The peak area (A) represents the summation of peak area over all observed charge states for each acylated peptide, (*z*=1-2) for peptide [1-5]; (*z*=3-5) for peptide [227-263] and peptide [229-263]. All acylated species on peptide [227-263] and peptide [229-263] matches contain two deamidated sites. The abundance of N-terminus acylation were calculated for each individual acyl chain of peptide [1-5] except N-oleoylation which include the summation of peptide $[1\text{-}5]_{ole}$ and peptide $[1\text{-}5]_{ole}$ + O; The abundance of K238 acylation were calculated for each individual acyl chain of peptide [229-263] except K238-palmitoylation and K238-oleoylation. K238-palmitoylation include the summation of peak area calculated for palmitoylated non-truncated peptide [229-263] and truncated peptides (peptide [227-243], peptide [229-246] and peptide [234-246]); K238-oleoylation include the summation of peak area calculated for oleoylated non-truncated peptides (peptide [229-263] and peptide [227-263]) plus truncated peptides (peptide [227-243], peptide [229-243], peptide [229-246] and peptide [234-246]).**

4.2.3.1. The effect of lens aging on h-AQP0 modifications

In order to illustrate the relation between protein lipidation and the lens age, total lipidation ratios were calculated in each of the five different human candidates, as shown in Figure 4.43. It is interesting to see that all the five candidates share two distinct results: **first**, %K238 lipidation is more abundant than %N-terminus lipidation; **second**, %N-terminus and %K238 lipidation is increasing by increasing the lens age (cortex to nucleus) with regarding that this change is more profound for N-terminus lipidation than K238. In addition, generally each of male and female sample sets were shown to exhibit an increase in %K238 and %N-terminus lipidation by increasing human age, although this trend is difficult to be shown for all.

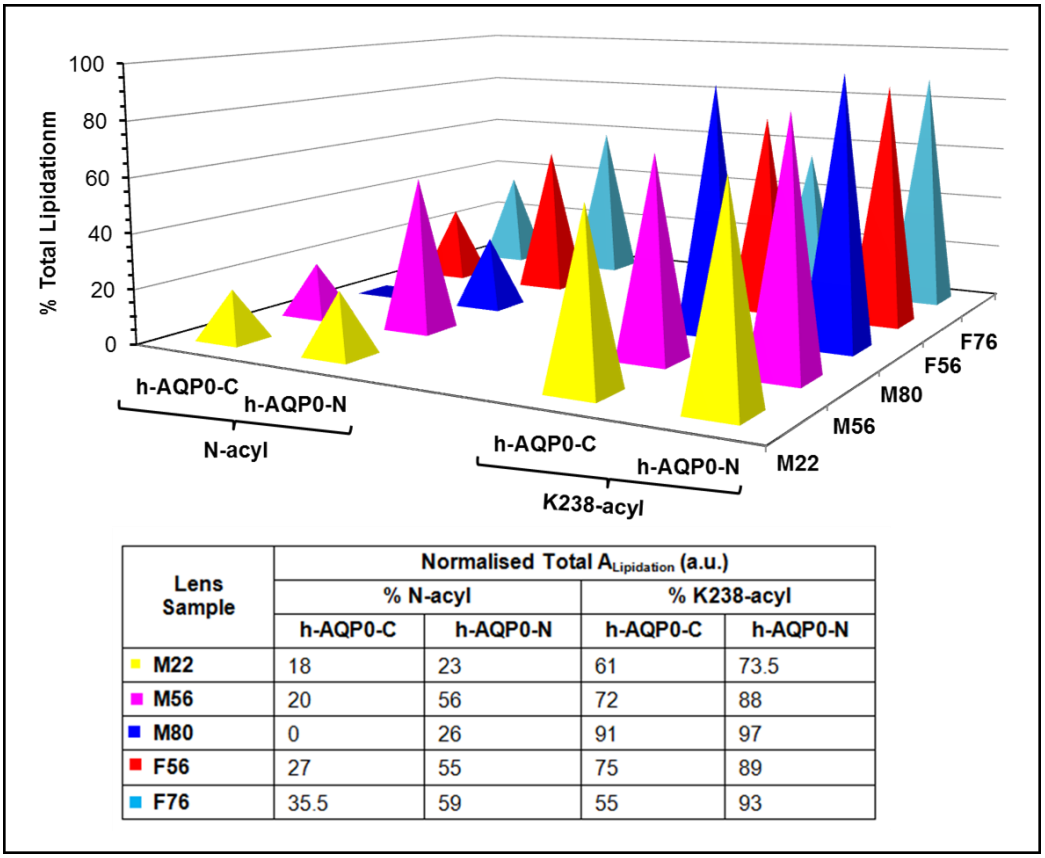

Lens Sample	Normalised Total $A_{Lipidation}$ (a.u.)			
	% N-acyl		% K238-acyl	
	h-AQP0-C	h-AQP0-N	h-AQP0-C	h-AQP0-N
M22	18	23	61	73.5
M56	20	56	72	88
M80	0	26	91	97
F56	27	55	75	89
F76	35.5	59	55	93

Figure 4.43. **The relative ratio of total lipidation modification on N-terminus and K238 sites of h-AQP0 in 5 different human candidates. Total lipidation includes the summation of all observed lipidation on each of N-terminus or K238 of the protein. The normalisation of each acylation ratio on N-terminus is performed relative to the reference non-acylated peptide [1-5], see Figure 4.31; normalisation of each acylation ratio on K238 is performed relative to the reference non-acylated peptide [229-263] after summing the peak area of K238 lipidation on truncated peptides (peptide [227-243], peptide [229-243], peptide [229-246] and peptide [234-246]) and non-truncated peptides (peptide [227-246] and peptide [229-246]), see Figure 4.32.**

Increasing protein truncation with age is still visible for human lenses (Figure 4.44, trend Y) as was described for bovine lenses (see Figure 4.33). However, this truncation trend is shown to be in a linear correlation with increasing K238 lipidation for truncated peptides, as shown in Figure 4.44, trends Xi-Xiii. This has been confirmed by using three different truncated peptides for normalisation process, including peptide [229-243], peptide [229-246] and peptide [234-246].

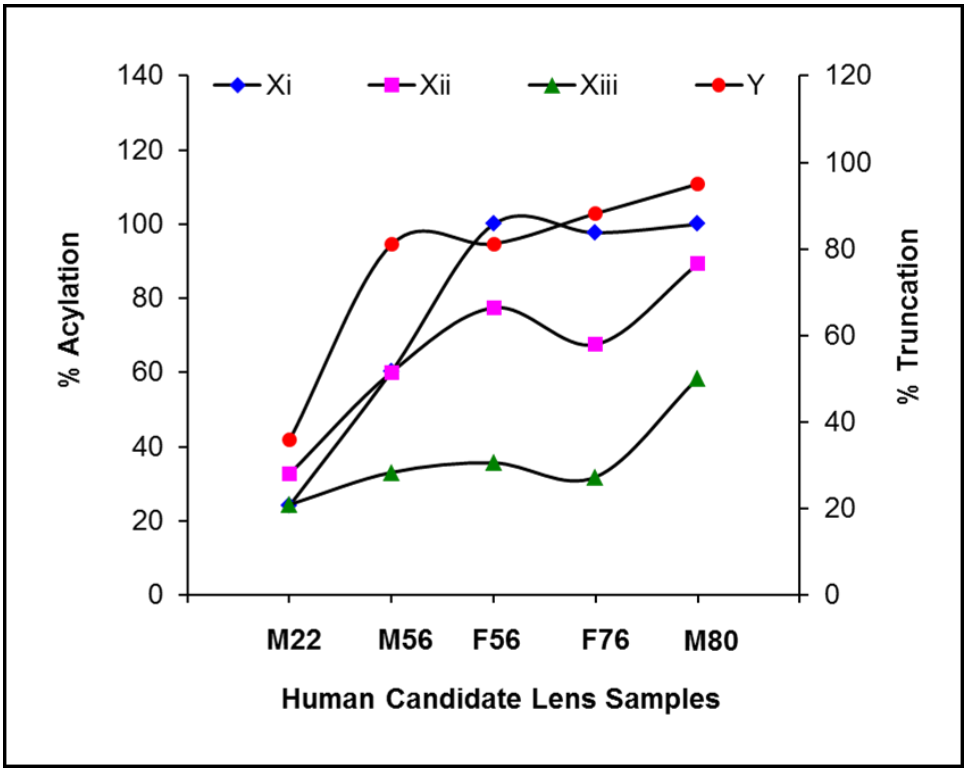

Figure 4.44. **The relative ratio of K238 lipidation on truncated peptides (trends Xi-Xiii) *vs* the relative ratio of truncation (trend Y) for five different human lens candidates (nucleus fraction), using digestion protocol Method-D and LC-MS Method-IIII (see section 8.2.2.2.1). The summation of all observed lipidation products on different truncated peptides were added together and the peak area was normalised relative to non-acylated peptide with the truncation site such as peptide [229-243] (trend Xi), peptide [229-246] (trend Xii) and peptide [234-246] (trend Xiii) as follows: %lipidation on truncated peptide = (peak area total lipidation on truncated peptide)/summed peak area (total lipidation on truncated peptide + reference peptide [229-243]) × 100. Peptide [229-246] and peptide [234-246] will follow the same calculation. The relative ratio of truncation were calculated by normalisation of total lipidation products on truncated peptides relative to non-acylated peptide with non-truncation site such as peptide [229-263] as follows: %truncation = (peak area total lipidated truncated peptide)/summed peak area (total lipidated truncated peptide + reference peptide [229-263]) × 100.**

Moreover, calculating the level of oxidation on two different peptide sets, including peptide [154-187] and peptide [188-228] showed an interesting finding of elevated amount of protein oxidation in the cortex fraction relative to nucleus fraction of the lens (Table 4.16). However, this is shown to be unexpected and different from what has been observed for b-AQP0, as there was being more oxidation in the nucleus fraction than cortex

fraction of the eye lens (see Table 4.13). In addition, there is not a significant change in the level of protein oxidation with increasing human age in this study.

Table 4.16. **The level of h-AQP0 oxidation in the five different human eye lens candidates, including male donor age 22 (M22), male donor age 56 (M56), male donor age 80 (M80), female donor age 56 (F56) and female donor age 76 (F76). Using digestion protocol Method-D and LC-MS Method-IIII (see section 8.2.2.2.1). The data presented represent normalised peak area (A) for oxidised peptides to the summation of oxidised plus non-oxidised equivalent peptides in both cortex and nucleus fractions of the lens.**

Human Lens Samples	%Oxidation			
	Cortex Fraction		Nucleus Fraction	
	Peptide [154-187] + 1 × O	Peptide [188-228] + 2 × O	Peptide [154-187] + 1 × O	Peptide [188-228] + 2 × O
M22	48	39	39	21
M56	53	46	36	16
M80	45	56	28	14
F56	44	43	29	13
F76	41	36	27	14

4.2.3.2. Human lens lipid correlation with acylated h-AQP0

Ester-linked fatty acyl composition with the major PE lipid and the minor PS and PI lipids in human lens is shown in Table 4.17. Owing to know that both lipidated sites, N-terminus (M1) and K238, are located in the cytoplasmic leaflet of the membrane, a correlation was drawn between lipidated peptides in h-AQP0 (M22) and transferrable fatty acyl content of cytoplasmic lipid composition, as shown in Figure 4.45. Stronger correlations are found between lipidation profile and (PE + PEpl)/total (PE/PS/PI) lipid composition, while poorer correlation is produced with PE lipid. This indicates that a mixed system of fatty acyl lipid transfer from cytoplasmic lipid

composition as a whole is more appropriate than a single lipid component. Similar correlations were also recorded for other human samples (M56, M80, F56 and F76), see Appendix C Figures 9.3-9.6.

Table 4.17. **Human lens transferrable fatty acid composition by lipid type created with data obtained by MS methods (Deeley *et al.*)[28]. Note: Error propagations are SEM.**

Acyl Group	PE nmol/g	PEpl† nmol/g	Total PE (PE + PEpl)† nmol/g	Total PS (PS + PSpl)† nmol/g	PI nmol/g	Total All (PE + PS + PI) nmol/g
C14:0	0	0	0	0	0	0
C15:0	0	0	0	0	0	0
C16:0	24.8 ± 2	0	24.8 ± 2	11.7 ± 1.2	0	36.5 ± 2.3
C16:1	5.3 ± 0.8	0	5.3 ± 0.8	0	0	5.3 ± 0.8
C18:0	38.2 ± 1.8	12.3 ± 1.8	50.5 ± 9.3	40.2 ± 3.3	16.2 ±2.6	106.9 ± 10.2
C18:1	85.1 ± 2.85	295.7±15.4	380.8±15.7	265.65 ± 10.5	1.5 ± 0.9	647.95 ± 18.9
C20:1	0	0	0	3.6 ± 0.2	0	3.6 ± 0.2
C20:3	0	0	0	0	2.5 ± 0.3	2.5 ± 0.3
C20:4	48.4 ± 9.4	40.2 ± 3.5	88.6 ± 10	13.1 ± 2.2	15.2 ± 2.8	116.9 ± 10.6
C22:3	0	13.9 ± 2.1	13.9 ± 2.1	0	0	13.9 ± 2.1
C22:4	0	11.3 ± 3.4	11.3 ± 3.4	0	0	11.3 ± 3.4
C22:5	0	8.9 ± 1	8.9 ± 1	0	0	8.9 ± 1
C22:6	0	9.4 ± 0.7	9.4 ± 0.7	3.6 ± 0.7	0	13 ± 1

†Lipid classes suffixed with “pl” refer to plasmalogen lipids which combine totals for both alkyl and alkenyl ether plasmalogens.

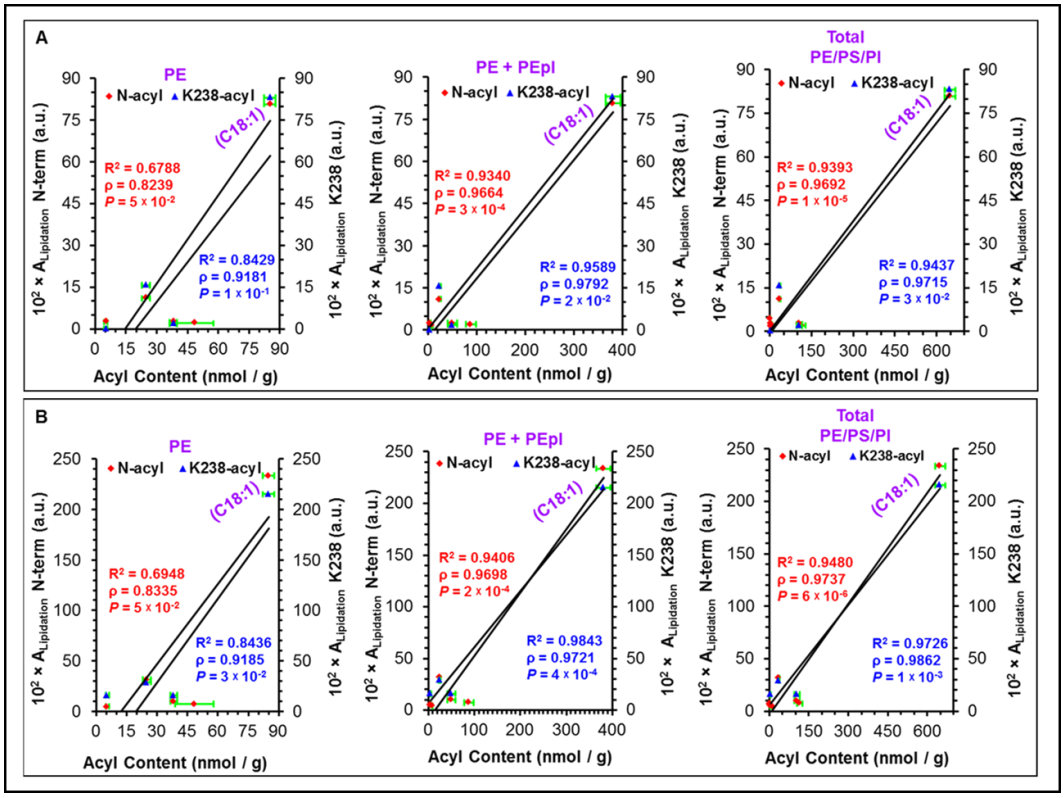

Figure 4.45. **Correlations between the amount of ester-linked transferrable fatty acyl content of human lens lipids and the peak areas for lipidated peptides of (A) h-AQP0-C male donor age 22 (M22) and (B) h-AQP0-N male donor age 22 (M22), using digestion protocol Method-D and LC-MS Method-IIII (see section 8.2.2.2.1). Lipid data obtained from lipidomics MS analysis[28] (see Table 4.17). Peak areas for N-terminus acylation were calculated from EIC of each acylation on peptide [1-5], while peak areas for K238 acylation were calculated by summing peak area from EIC of each acylation on non-truncated peptides (peptide [227-263] and peptide [229-263]) and truncated peptides (peptide [227-243], peptide [229-243], peptide [229-246] and peptide [234-246]). Errors plotted as *X-axis* SEM (fatty acyl content, n=4). The line and the R^2 statistic are from linear regression analysis. The ρ-value represents the Pearson correlation coefficient (r) and the *p*-value represents the t-test of the correlation coefficient.**

4.3. The lipid-binding amphipathic helix in AQP0

Crystallographic study on AQP0 crystal[54] showed different interactions between the N-terminus and C-terminus amino acid residues, which influences the conformation structure of this protein. Based on the results in this study, it is also true to conclude that both lipidation sites of AQP0, the N-terminus (M1) and C-terminus (K238) are adjacent to the cytoplasmic leaflet

of the plasma membrane, as shown in Figure 4.46. This suggests the presence of direct relation between lipidation profile on these two lipidated sites and the membrane lipid content of the cytoplasmic leaflet.

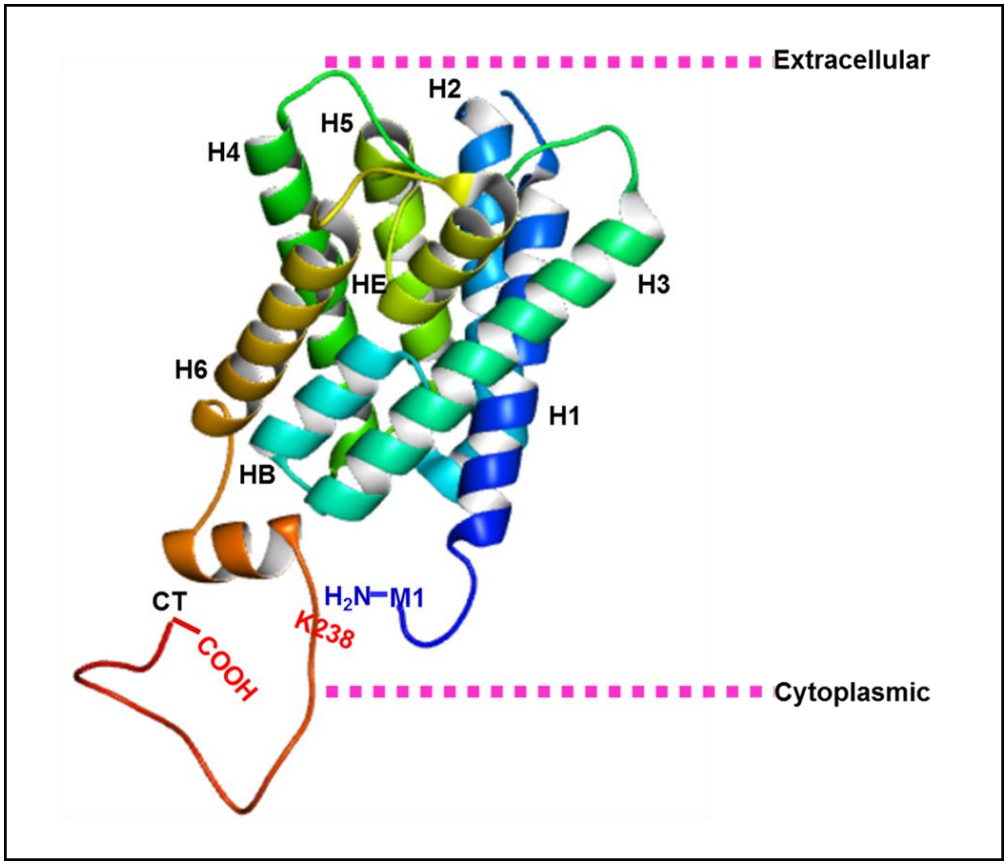

Figure 4.46. **X-ray structure for cattle AQP0 monomer obtained from protein Data Bank (PDB) 2b6p code.[54] The six helices spanning the lipid membrane are shown as H1-H6; the two loops are HB and HE; the C-terminal cytoplasmic tail is CT. Both lipidation sites are labelled as M1 and K238.**

By calculating the helical wheel conformation of [214-263] sequence of b-AQP0 and h-AQP0 by using 18-AA analysis window, this is the HELIQUEST software and available at (http://heliquest.ipmc.cnrs.fr),[55] it is possible to predict that this sequence forms a lipid-binding amphipathic helix. This has been enabled by using a factor called discrimination factor (D). Helices with discrimination factor greater than 0.68 are shown to have a high propensity for lipid-binding.[56,57] Consequently, the calculated helices (8-15) in

the provided sequence have a high lipid-binding region (Figure 4.47). Interestingly, all of these lipid-binding regions of the protein have K238 AA residue in their sequence.

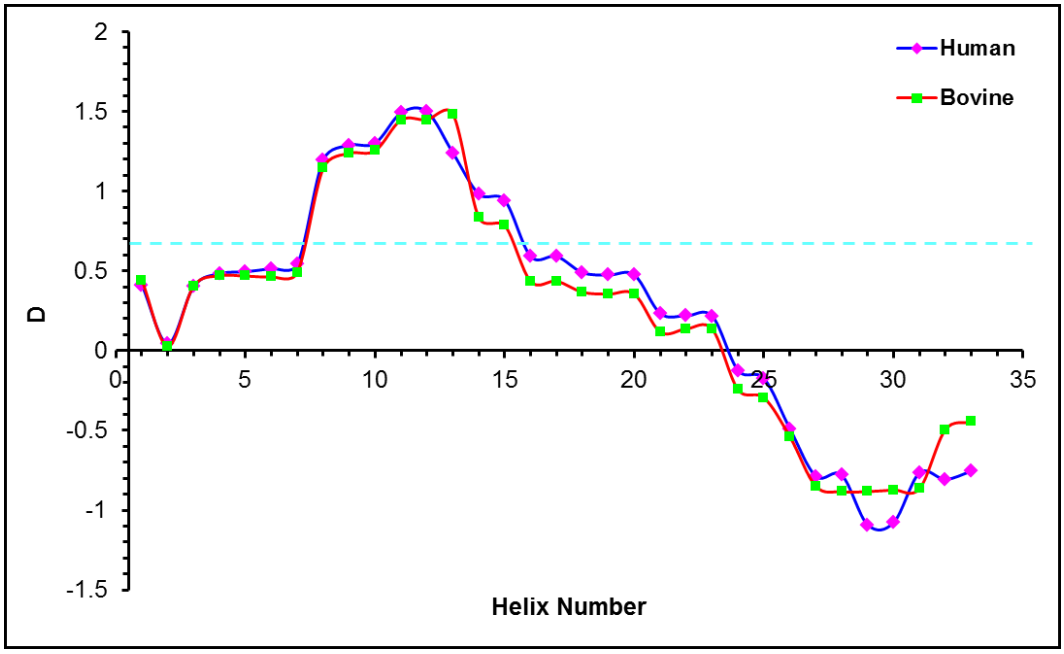

Figure 4.47. **Variation in discrimination factor (D) according to human and bovine helix number. Discrimination factor (D) calculated using the equation D = 0.944 (<μH>) + 0.33 (*z*).[56,57] Eight helices (8-15) with D > 0.68 located above the highlighted blue horizontal line. Detailed data are given in Appendix C Tables 9.47 and 9.48.**

Helices (10-12) with the highest discrimination factor are shown in Figure 4.48. Interestingly, lipidation site (K238) lies at the boundary of the predicted hydrophobic face of the helix, a feature that is known to promote acyl transfer from lipids to peptides that localise interfacially[47].

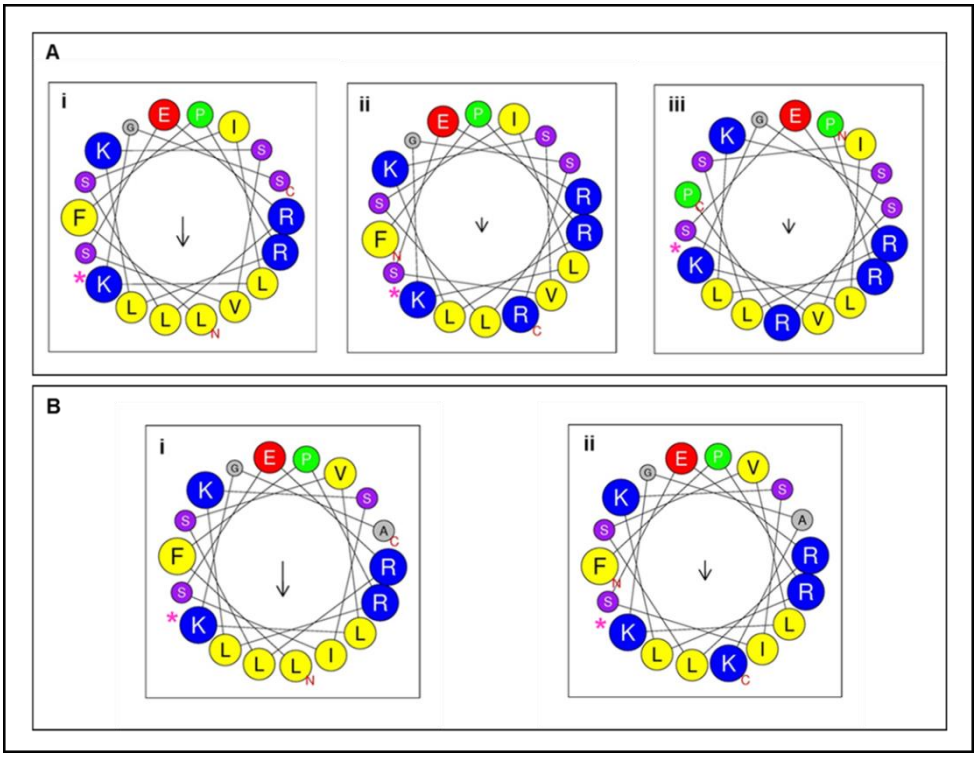

Figure 4.48. **Application of 18-AA analysis window from HELIQUEST[54] to examine [214-263] region of (A) b-AQP0 and (B) h-AQP0. The sequence in this region is ^{214}LGSLLYDFLLFPRLKSVSERLSILKGSRPSESNGQPEVTGEPVELKTQAL^{263} and ^{214}LGSLLYDFLLFPRLKSISERLSVLKGAKPDVSNGQPEVTGEPVELNTQAL^{263} for b-AQP0 and h-AQP0 respectively. Helix 10 (i) corresponds to amino acid [10-27] of this sequence (equivalent to [223-240] of b-AQP0 and h-AQP0); helix 11 (ii) corresponds to [11-28] (equivalent to [224-241] of b-AQP0 and h-AQP0); helix 12 (iii) corresponds to [12-29] (equivalent to [225-242] of b-AQP0). K238 amino acid residue is indicated by an asterisk.**

4.4. Conclusion

AQP0 is an interesting protein to study age related PTMs, as this protein is subjected to different modifications with lens age. This is particularly important because there is no protein turnover in mature fibre cell of the lens.[6,7,20,58] Among different modifications observed on AQP0 in this research such as deamidation, phosphorylation, oxidation, truncation, acetylation, and lipidation, a focus will be given to lipidated AQP0. The lipidation of AQP0 by membrane lipids has shown herein through observing a broad lipidation profile on two lipidated sites of N-terminus and K238 site of the protein. The presence of protein reactive sites, amino group, proximal to

lipid fatty acyl chains is a principle step for acyl transfer in protein:lipid system.[46,47] For AQP0, the location of both lipidated sites sufficiently close to the cytoplasmic leaflet of lipid membrane has shown by Gonen *et al.*[54] through X-ray structure. Additionally, 18-AA analysis window from HELIQUEST supports this by showing a lipid-binding ability for peptide helices with K238 site at the boundary of the helix. This direct interaction between lipid membrane and AQP0 is reflected herein by drawing a linear correlation between lipidated sites of AQP0 and the amount of transferrable fatty acyl composition from the most abundant PE/PEpl lipid in the cytoplasmic leaflet of the membrane.

Further, according to the results discussed for observing a broad lipidation profile on AQP0 and their moderate overall extent of modification, if AQP0 is lipidated enzymatically *in vivo* then an enzyme is required that shows two distinct features: first, relatively low efficiency in acyl transfer; second, poor selectivity towards acyl groups but also favours oleoyl transfer. Such an enzyme has not yet been observed. Consequently, it is more likely that acyl group transfer occurs via chemical-based ester aminolysis mechanism, as this method accounts both for the low efficiency of transfer and the differences observed between human and bovine lipidation profile. In addition, increasing protein modification as a function of lens age is suggested to reflect non-enzymatic process *in vivo*.[6,7,21,52] This is also proposed for AQP0 lipidation herein, as both b-AQP0 and h-AQP0 evident an accumulated amount of protein lipidation by moving from cortex fraction to the nucleus fraction of the lens.

Increasing protein aggregation with age[16] is an important factor causing the lens to lose its transparency and becomes more rigid,[18] therefor the formation of lens cataract.[16-19] Similar to AQP0, crystallins have also shown to undergo a number of age-related modifications.[17,19] This has reflected in their aggregation with age and thus lens cataract.[14,16,18] However, fatty acylated crystallin has not yet been observed and thus their effect on protein aggregation is not known. Therefore, further study is required to determine the effect of age-related lipidation on protein aggregation or structure and their outcomes on health and disease.

4.5. References

1 Schey, Kevin L., Danielle B. Gutierrez, Zhen Wang, Junhua Wei, and Angus C. Grey. "Novel fatty acid acylation of lens integral membrane protein aquaporin-0." *Biochemistry*, 49 (**2010**): 9858-9865.

2 Ismail, Vian S., Jackie A. Mosely, Antal Tapodi, Roy A. Quinlan, and John M. Sanderson. "The lipidation profile of aquaporin-0 correlates with the acyl composition of phosphoethanolamine lipids in lens membranes." *Biochimica et Biophysica Acta (BBA)-Biomembranes*, 1858 (**2016**): 2763-2768.

3 Wu, Christine C., and John R. Yates. "The application of mass spectrometry to membrane proteomics." *Nature Biotechnology*, 21 (**2003**): 262-267.

4 Speers, Anna E., and Christine C. Wu. "Proteomics of integral membrane proteins theory and application." *Chemical Reviews*, 107 (**2007**): 3687-3714.

5 Han, Jun, and Kevin L. Schey. "Proteolysis and mass spectrometric analysis of an integral membrane: aquaporin 0." *Journal of Proteome Research*, 3 (**2004**): 807-812.

6 Gutierrez, Danielle B., Donita Garland, and Kevin L. Schey. "Spatial analysis of human lens aquaporin-0 post-translational modifications by MALDI mass spectrometry tissue profiling." *Experimental Eye Research*, 93 (**2011**): 912-920.

7 Wenke, Jamie L., Kristie L. Rose, Jeffrey M. Spraggins, and Kevin L. Schey. "MALDI imaging mass spectrometry spatially maps age-related deamidation and truncation of human lens aquaporin-0." *Investigative Ophthalmology & Visual Science*, 56 (**2015**): 7398-7405.

8 Kadiyala, Chandra Sekhar Rao, Sara E. Tomechko, and Masaru Miyagi. "Perfluorooctanoic acid for shotgun proteomics." *Public Library of Science One*, 5 (**2010**): e15332.

9 Sweeney, Alison M., David L. Des Marais, Yih-En Andrew Ban, and Sönke Johnsen. "Evolution of graded refractive index in squid lenses." *Journal of the Royal Society Interface,* 4 (**2007**): 685-698.

10 Lampe, Paul D., and Ross G. Johnson. "Amino acid sequence of in vivo phosphorylation sites in the main intrinsic protein (MIP) of lens membranes." *The FEBS Journal*, 194 (**1990**): 541-547.

11 Schey, Kevin L., John G. Fowler, Jae C. Schwartz, Mark Busman, James Dillon, and Rosalie K. Crouch. "Complete map and identification of the phosphorylation site of bovine lens major intrinsic protein." *Investigative Ophthalmology & Visual Science*, 38 (**1997**): 2508-2515.

12 Wang, Zhen, Jun Han, and Kevin L. Schey. "Spatial differences in an integral membrane proteome detected in laser capture microdissected samples." *Journal of Proteome Research*, 7 (**2008**): 2696-2702.

13 Schey, Kevin L., Angus C. Grey, and Joshua J. Nicklay. "Mass spectrometry of membrane proteins: a focus on aquaporins." *Biochemistry*, 52 (**2013**): 3807-3817.

14 Borchman, Douglas, and Marta C. Yappert. "Lipids and the ocular lens." *Journal of Lipid Research*, 51 (**2010**): 2473-2488.

15 Manenti, Stéphane, Irène Dunia, and E. Lucio Benedetti. "Fatty acid acylation of lens fiber plasma membrane proteins." *FEBS Letters*, 262 (**1990**): 356-358.

16 Boscia, Francesco, Ignazio Grattagliano, Gianluigi Vendemiale, Tommaso Micelli-Ferrari, and Emanuele Altomare. "Protein oxidation and lens opacity in humans." *Investigative Ophthalmology & Visual Science,* 41 (**2000**): 2461-2465.

17 Beebe, David C., Nancy M. Holekamp, and Ying-Bo Shui. "Oxidative damage and the prevention of age-related cataracts." *Ophthalmic Research,* 44, **(2010**): 155-165.

18 Michael, R., and A. J. Bron. "The ageing lens and cataract: a model of normal and pathological ageing." *Philosophical Transactions of the Royal Society of London B: Biological Sciences,* 366 **(2011**): 1278-1292.

19 Grey, Angus C., Pierre Chaurand, Richard M. Caprioli, and Kevin L. Schey. "MALDI imaging mass spectrometry of integral membrane proteins from ocular lens and retinal tissue." *Journal of Proteome Research*, 8 (**2009**): 3278-3283.

20 Ball, Lauren E., Donita L. Garland, Rosalie K. Crouch, and Kevin L. Schey. "Post-translational modifications of aquaporin 0 (AQP0) in the normal human lens: spatial and temporal occurrence." *Biochemistry*, 43 (**2004**): 9856-9865.

21 Korlimbinis, Anastasia, Yoke Berry, Danielle Thibault, Kevin L. Schey, and Roger JW Truscott. "Protein aging: truncation of aquaporin 0 in human lens regions is a continuous age-dependent process." *Experimental Eye Research*, 88 (**2009**): 966-973.

22 Eeman, Marc, and Magali Deleu. "From biological membranes to biomimetic model membranes." *Biotechnology, Agronomy, Society and Environment*, 14 (**2010**): 719-736.

23 Broekhuyse, R. M. "Phospholipids in tissues of the eye I. Isolation, characterization and quantitative analysis by two-dimensional thin-layer chromatography of diacyl and vinyl-ether phospholipids." *Biochimica et Biophysica Acta (BBA)-Lipids and Lipid Metabolism*, 152 (**1968**): 307-315.

24 Anderson, Robert E., Maureen B. Maude, and Gerald L. Feldman. "Lipids of ocular tissues: I. The phospholipids of mature rabbit and bovine lens." *Biochimica et Biophysica Acta (BBA)-Lipids and Lipid Metabolism*, 187 (**1969**): 345-353.

25 Estrada, Rosendo, and M. Cecilia Yappert. "Regional phospholipid analysis of porcine lens membranes by matrix-assisted laser desorption/ionization time-of-flight mass spectrometry." *Journal of Mass Spectrometry,* 39 (**2004**): 1531-1540.

26 Borchman, Douglas, Marta C. Yappert, and Muhammad Afzal. "Lens lipids and maximum lifespan." *Experimental Eye Research*, 79 (**2004**): 761-768.

27 Rujoi, Madalina, Rosendo Estrada, and M. Cecilia Yappert. "In situ MALDI-TOF MS regional analysis of neutral phospholipids in lens tissue." *Analytical Chemistry*, 76 (**2004**): 1657-1663.

28 Deeley, Jane M., Todd W. Mitchell, Xiaojia Wei, John Korth, Jessica R. Nealon, Stephen J. Blanksby, and Roger JW Truscott. "Human lens lipids differ markedly from those of commonly used experimental animals." *Biochimica et Biophysica Acta (BBA)-Molecular and Cell Biology of Lipids*, 1781 (**2008**): 288-298.

29 Bartley, W., Ruth Van Heyningen, Brenda M. Notton, and A. Renshaw. "Fatty acid composition of lipids present in different parts of the ox eye." *Biochemical Journal*, 85 (**1962**): 332-335.

30 Gorgas, Karin, Andre Teigler, Dorde Komljenovic, and Wilhelm W. Just. "The ether lipid-deficient mouse: tracking down plasmalogen functions." *Biochimica et Biophysica Acta (BBA)-Molecular Cell Research*, 1763 (**2006**): 1511-1526.

31 Braverman, Nancy E., and Ann B. Moser. "Functions of plasmalogen lipids in health and disease." *Biochimica et Biophysica Acta (BBA)-Molecular Basis of Disease,* 1822 **(2012**): 1442-1452.

32 Li, Lu-Ku, Lydia So, and Abraham Spector. "Membrane cholesterol and phospholipid in consecutive concentric sections of human lenses." *Journal of Lipid Research*, 26 (**1985**): 600-609.

33 Reichow, Steve L., and Tamir Gonen. "Lipid–protein interactions probed by electron crystallography." *Current Opinion in Structural Biology*, 19 (**2009**): 560-565.

34 Byrdwell, William C., Hidetoshi Sato, Arne K. Schwarz, Douglas Borchman, M. C. Yappert, and Daxin Tang. "^{31}P NMR quantification and monophasic solvent purification of human and bovine lens phospholipids." *Lipids*, 37 (**2002**): 1087-1092.

35 Hajkova, Dagmar, Yoshikazu Imanishi, Vikram Palamalai, K. C. Sekhar Rao, Chao Yuan, Quanhu Sheng, Haixu Tang et al. "Proteomic changes in the photoreceptor outer segment upon intense light exposure." *Journal of Proteome Research*, 9 (**2010**): 1173-1181.

36 Feldman, Gerald L., W. Thomas, Lutrell S. Feldman, Charles K. Grantham, and Haldor T. Jonsson. "Phospholipids of the bovine, rabbit, and human lens." *Investigative Ophthalmology & Visual Science*, 3 (**1964**): 194-197.

37 Jencks, William P., D. G. Oakenfull, and Karin Salvesen. "Mechanism of general acid catalysis of the aminolysis of an amide." *Journal of the American Chemical Society*, 92 (**1970**): 3201-3202.

38 Chen, Xiaoyu, Michael S. Westphall, and Lloyd M. Smith. "Mass spectrometric analysis of DNA mixtures: instrumental effects responsible for decreased sensitivity with increasing mass." *Analytical Chemistry*, 75 (**2003**): 5944-5952.

39 Zhang, Xu, Mark Scalf, Travis W. Berggren, Michael S. Westphall, and Lloyd M. Smith. "Identification of mammalian cell lines using MALDI-TOF and LC-ESI-MS/MS mass spectrometry." *Journal of the American Society for Mass Spectrometry*, 17 (**2006**): 490-499.

40 Thibault, Danielle B., Christopher J. Gillam, Angus C. Grey, Jun Han, and Kevin L. Schey. "MALDI tissue profiling of integral membrane proteins from ocular tissues." *Journal of the American Society for Mass Spectrometry*, 19 (**2008**): 814-822.

41 Horwitz, Joseph. "α-crystallin can function as a molecular chaperone." *Proceedings of the National Academy of Sciences*, 89 (**1992**): 10449-10453.

42 Takemoto, L., and T. Emmons. "Age-dependent deamidation of the major intrinsic polypeptide from lens membranes." *Current Eye Research*, 10 (**1991**): 865-869.

43 Robinson, A., and Colette J. Rudd. "Deamidation of glutaminyl and asparaginyl residues." *Current Topics in Cellular Regulation*, 8 (**1974**): 247-295.

44 Tonie Wright, H., and Dan W. Urry. "Nonenzymatic deamidation of asparaginyl and glutaminyl residues in protein." *Critical Reviews in Biochemistry and Molecular Biology*, 26 (**1991**): 1-52.

45 Aveldano, M. I., M. VanRollins, and L. A. Horrocks. "Separation and quantitation of free fatty acids and fatty acid methyl esters by reverse phase high pressure liquid chromatography." *Journal of Lipid Research*, 24 (**1983**): 83-93.

46 Dods, Robert H., Jackie A. Mosely, and John M. Sanderson. "The innate reactivity of a membrane associated peptide towards lipids: acyl transfer to melittin without enzyme catalysis." *Organic & Biomolecular Chemistry*, 10 (**2012**): 5371-5378.

47 Dods, Robert H., Burkhard Bechinger, Jackie A. Mosely, and John M. Sanderson. "Acyl transfer from membrane lipids to peptides is a generic process." *Journal of Molecular Biology*, 425 (**2013**): 4379-4387.

48 Rajagopalan, K. V., Irwin Fridovich, and Philip Handler. "Competitive inhibition of enzyme activity by urea." *Journal of Biological Chemistry*, 236 (**1961**): 1059-1065.

49 Zhang, Xi. "Less is More: Membrane Protein Digestion Beyond Urea–Trypsin Solution for Next-level Proteomics." *Molecular & Cellular Proteomics*, 14 (**2015**): 2441-2453.

50 Hixson, Kim K., Nestor Rodriguez, David G. Camp, Eric F. Strittmatter, Mary S. Lipton, and Richard D. Smith. "Evaluation of enzymatic digestion and liquid chromatography-mass spectrometry peptide mapping of the integral membrane protein bacteriorhodopsin." *Electrophoresis,* 23 (**2002**): 3224-3232.

51 Pridmore, Catherine J., Jackie A. Mosely, Alison Rodger, and John M. Sanderson. "Acyl transfer from phosphocholine lipids to melittin." *Chemical Communications,* 47 (**2011**): 1422-1424.

52 Schey, Kevin L., Mark Little, John G. Fowler, and Rosalie K. Crouch. "Characterization of human lens major intrinsic protein structure." Investigative Ophthalmology & Visual Science, 41 (**2000**): 175-182.

53 Liao, Chen-Chung, Yen-Wei Chen, Toong-Long Jeng, Chien-Ru Li, and Chia-Feng Kuo. "Consumption of purple sweet potato affects post-translational modification of plasma proteins in hamsters." *Journal of Agricultural and Food Chemistry,* 61 (**2013**): 12450-12458.

54 Gonen, Tamir, Yifan Cheng, Piotr Sliz, Yoko Hiroaki, Yoshinori Fujiyoshi, Stephen C. Harrison, and Thomas Walz. "Lipid–protein interactions in double-layered two-dimensional AQP0 crystals." *Nature*, 438 (**2005**): 633-638.

55 Gautier, Romain, Dominique Douguet, Bruno Antonny, and Guillaume Drin. "HELIQUEST: a web server to screen sequences with specific α-helical properties." *Bioinformatics*, 24 (**2008**): 2101-2102.

56 Keller, Rob CA. "The prediction of novel multiple lipid-binding regions in protein translocation motor proteins: a possible general feature." *Cellular & Molecular Biology Letters*, 16 (**2010**): 40-54.

57 Keller, Rob CA. "New user-friendly approach to obtain an Eisenberg plot and its use as a practical tool in protein sequence analysis." *International Journal of Molecular Sciences,* 12 (**2011**): 5577-5591.

58 Stewart, Daniel N., Jozsef Lango, Krishnan P. Nambiar, Miranda JS Falso, Paul G. FitzGerald, David M. Rocke, Bruce D. Hammock, and Bruce A. Buchholz. "Carbon turnover in the water-soluble protein of the adult human lens." *Molecular Vision,* 19 (**2013**): 463-475.

Chapter five: Application of ion mobility separation-mass spectrometry (IMS-MS) to the analysis of phosphatidylcholine and synthetic lipidated melittin analogues

To study isomeric/isobaric structure of biomolecule classes such as lipids and peptides, a technique is required that has the potential to resolve different structures with the same *m/z*. This can be achieved to some degree using liquid chromatography coupled with mass spectrometry (LC-MS) or tandem MS (LC-MS^2).[1-8] The resolution can be improved by using ion mobility separation (IMS), and particularly powerful during its coupling with MS and/or LC-MS.[8] Herein, traveling wave ion mobility spectrometry (TWIMS) was used to correlate ions structure and/or conformation with drift time. The arrival time distributions (ATDs) are related to the physical size and number of charge states on the peptide. Acylated melittin with lower charge states, triply and quadruply, are found to be interesting candidate ions in the mobility cell and to be studied herein by TWIMS as a benchmark to begin distinguish between acylated melittin isomers. Triply and quadruply ions are also found to have more conformational changes and slower mobility. Partial resolution between N-M_{pal} *vs* K23-M_{pal} and N-M_{ole} *vs* K23-M_{ole} were suggested by transfer collision fragmentation approach coupled with TWIMS through time-aligned product ions with their corresponding precursor ions. In addition, although no difference in ATDs were observed for isomer mixtures of DOPC *vs* SLPC or POPC *vs* OPPC, partial resolution was observed between PPC and OPC or DOPC and DPPC.

5.1. Analysis of phosphatidylcholine by ion mobility separation-mass spectrometry (IMS-MS)

5.1.1. IMS-MS analysis of lysophosphatidylcholine (LPC)

Lysophosphatidylcholine (LPC) is a sub-class of phosphatidylcholines but with a single acyl chain at the *sn*-1 position. The two LPCs used in this study are 1-oleoyl-phosphatidylcholine (OPC) and 1-palmitoyl-phosphatidylcholine (PPC) with a distinct difference in the length of the acyl chain for palmitoyl (C16:0) and oleoyl (C18:1). Herein, the aim was to separate overlapped peaks obtained from liquid chromatography for PPC:OPC mixture and also the two in-solution positional isomers of 1-acyl-LPC and 2-acyl-LPC for each species (see chapter three, Figure 3.15) using the advantages in the analytical tool of ion mobility separation coupled with mass spectrometry (IMS-MS). For that, traveling wave ion mobility spectrometry (TWIMS) was used based on the principle of recording an ion's drift time (t_d) in the mobility cell in a relevance time. However, results for direct infusing of individual LPC solutions into ESI-IMS-MS showed a single broad peak in the mobilogram for each of PPC (Figure 5.1) and OPC (Figure 5.2) with the closeness in their arrival time or t_d. This illustrates that the arrival time distributions (ATDs) for both LPCs will be overlapped in a mixture of both species. In addition, the two isomeric LPC forms for each species are suggested to have the same t_d and hard to be resolved under these conditions, although, this separation has partially achieved previously using LC-MS (see chapter three, Figure 3.15).

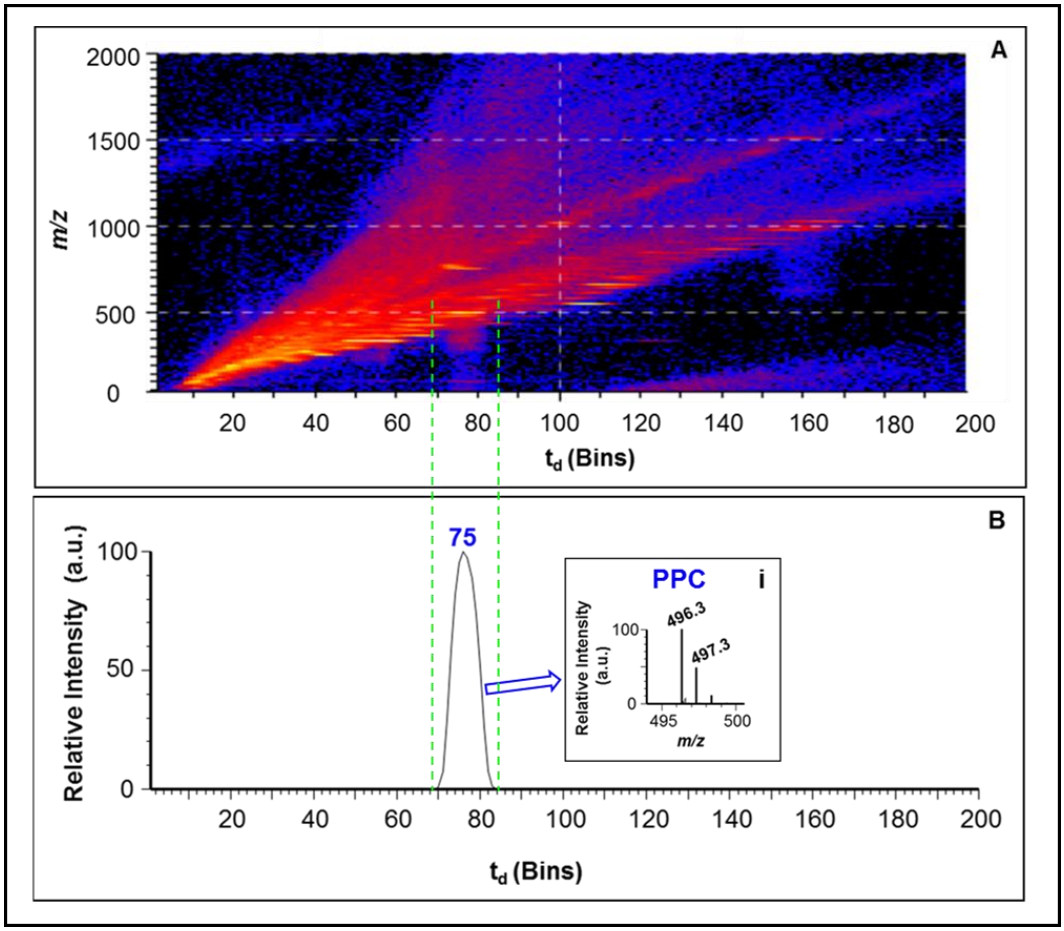

Figure 5.1. **(A) Mobilogram display for individual PPC, analysed on the Synapt G2-s through direct infusion IMS-MS (TWIMS). (B) Arrival time distribution (ATD) display from extracted ion mobilogram (EIM) for PPC at *m/z* 496.3. The insert panel (i) is the mass spectrum for PPC.**

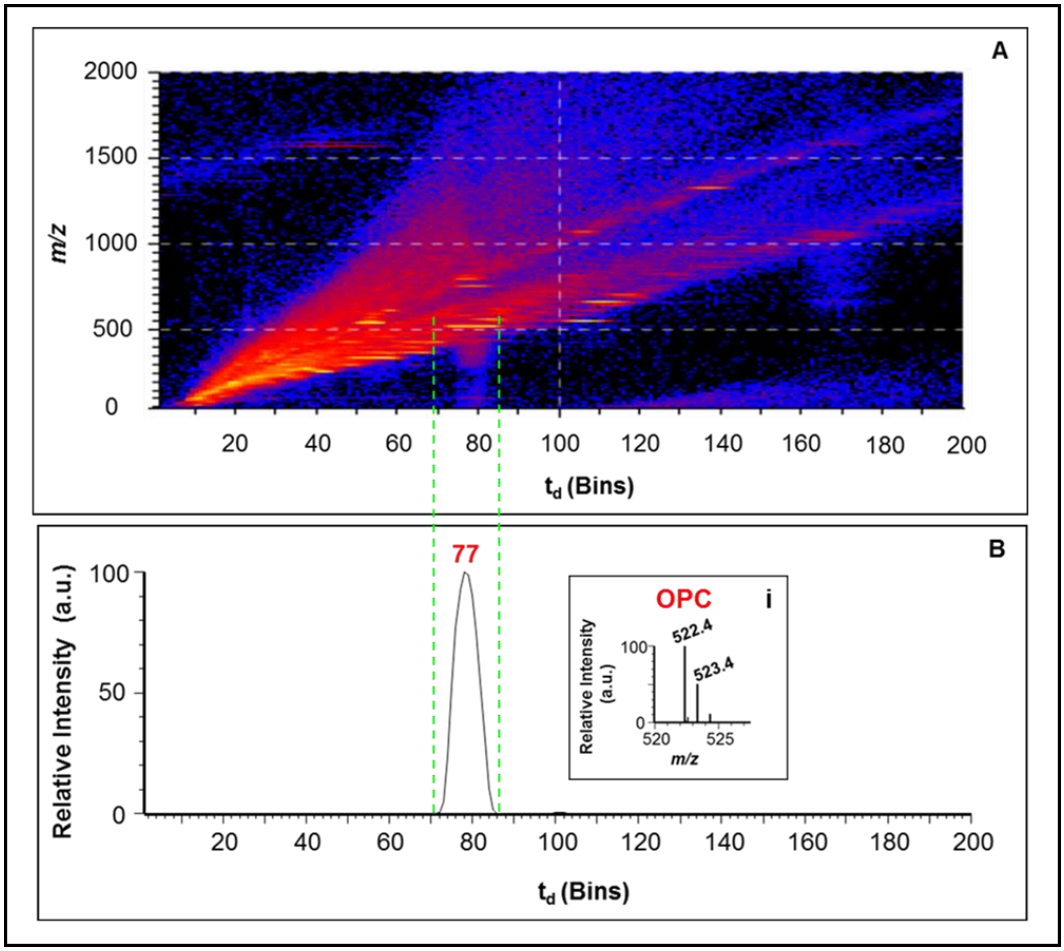

Figure 5.2. **(A) Mobilogram display for individual OPC, analysed on the Synapt G2-s through direct infusion IMS-MS (TWIMS). (B) ATD display from EIM for OPC at *m/z* 522.4. The insert panel (i) is the mass spectrum for OPC.**

Performing the experiments at the same time and under the same instrument conditions, a mixture of 50:50 PPC:OPC (Figure 5.3) showed comparable results as was described for each individual species (see Figures 5.1 and 5.2) and also see Table 5.1. A relatively longer ATD for OPC than PPC (Figure 5.3 and Table 5.1) is suggested to be reflected by higher number of -CH_2- group in oleoyl, as reported by Zhang *et al*.[9] Consequently, OPC will experience more interactions or collisions with the buffer gas and as a result it travels slower in the mobility cell. However, at the same time, the presence of one carbon-carbon double bond in OPC bent the molecule and decrease the conformational space occupied by two hydrogen atoms.[9] Therefore some reduction in OPC's ATD and thus overlapped with PPC's

ATD. The influence of the presence of double bond in the acyl chain on reducing the t_d is well documented in earlier reports.[8-13]

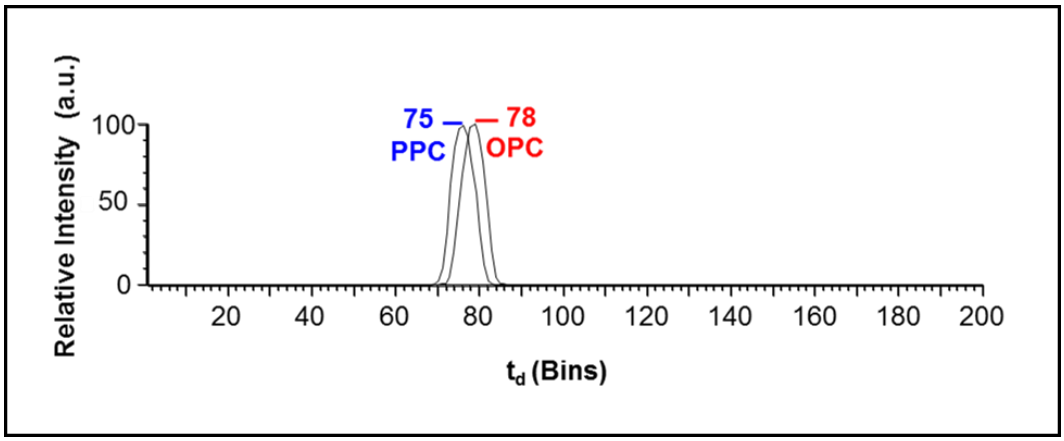

Figure 5.3. **ATD display from comparison EIMs for PPC at *m/z* 496.3 and OPC at m/z 522.4 taken from 50:50 OPC:PPC mixture and analysed on the Synapt G2-s through direct infusion IMS-MS (TWIMS).**

Table 5.1. **ATDs obtained from the mobilogram for each of PPC and OPC individually and from a mixture of 50:50 PPC:OPC, analysed on the Synapt G2-s through direct infusion IMS-MS (TWIMS).**

Sample		Meas‡ *m/z*	ATD
			t_d (Bins)
PPC		496.3	75
OPC		522.4	77
PPC:OPC	PPC	496.3	75
	OPC	522.4	78

‡Meas: measured m/z for [M + H]+.

5.1.2. IMS-MS analysis of diacylphosphatidylcholine (PC)

Examining a number of PCs with various acyl chain length, including 1,2-dimyrstoyl-PC (DMPC), 1,2-dipalmitoyl-PC (DPPC), 1-oleoyl-2-palmitoyl-PC (OPPC), 1-palmitoyl-2-oleoyl-PC (POPC), 1-stearoyl-2-linoleoyl-PC (SLPC) and 1,2-dioleoyl-PC (DOPC), Table 5.2, has shown six distinct peaks in the ATD display for the six individual lipid species each with its

corresponding t_d, as shown in Figure 5.4 and Table 5.3. While only four peaks were observed for the equimolar mixture of all the six analysed PCs (Figure 5.5 and Table 5.3). This is because the two regioisomers POPC *vs* OPPC and isobaric species of DOPC *vs* SLPC with exactly the same *m/z* could not be resolved herein by TWIMS and shown as a single broad peak for each pair of PC isomers (Figure 5.5). This is not surprising, as Castro-Perez *et al.* showed that the position of the fatty acyl chain in *sn*-1 and *sn*-2 position of POPC *vs* OPPC could only be achieved by using collision-induced dissociation (CID) coupled with TWIMS.[14] By showing that *sn*-2 position of PC precursor ion fragments preferentially over *sn*-1 position due to the tertiary α-hydrogen atom that forms hydrogen bond with the carbonyl oxygen of the *sn*-1 that hinders the fragmentation at this position.[14] Further, Kyle *et al.* showed that when both PC acyl chains with different length in a pair of positional PC isomers are saturated or have the same number and orientation of double bonds could be separated by IMS-MS because the lipid is more elongated when longer acyl chain is in the *sn*-1 position.[8] However, this is not applied herein, as POPC *vs* OPPC being mixed-chain between saturated and unsaturated PCs, while DOPC *vs* SLPC are a pair of PCs with the same number of -CH_2- group, but different number of double bonds.

Table 5.2. **Different diacylphosphatidylcholine lipids with their chemical formula, fatty acyl chains and theoretical masses.**

Phospholipids Nomenclature	Molecular Formula	Fatty Acyl Chain	Theor *m/z* ‡ $[M + H]^+$
1,2-dimyristoyl-PC (DMPC)	$C_{36}H_{72}NO_8P$	(C14:0/C14:0)	678.5074
1,2-dipalmitoyl-PC (DPPC)	$C_{40}H_{80}NO_8P$	(C16:0/C16:0)	734.5700
1-palmitoyl-2-oleoyl-PC (POPC)	$C_{42}H_{82}NO_8P$	(C16:0/C18:1)	760.5856
1-oleoyl-2-palmitoyl-PC (OPPC)	$C_{42}H_{82}NO_8P$	(C18:1/C16:0)	760.5856
1-stearoyl-2-linoleoyl-PC (SLPC)	$C_{44}H_{84}NO_8P$	(C18:0/C18:2)	786.6013
1,2-dioleoyl-PC (DOPC)	$C_{44}H_{84}NO_8P$	(C18:1/C18:1)	786.6013

‡Theoretical (Theor) *m/z* is obtained from MassLynx software (V4.1).

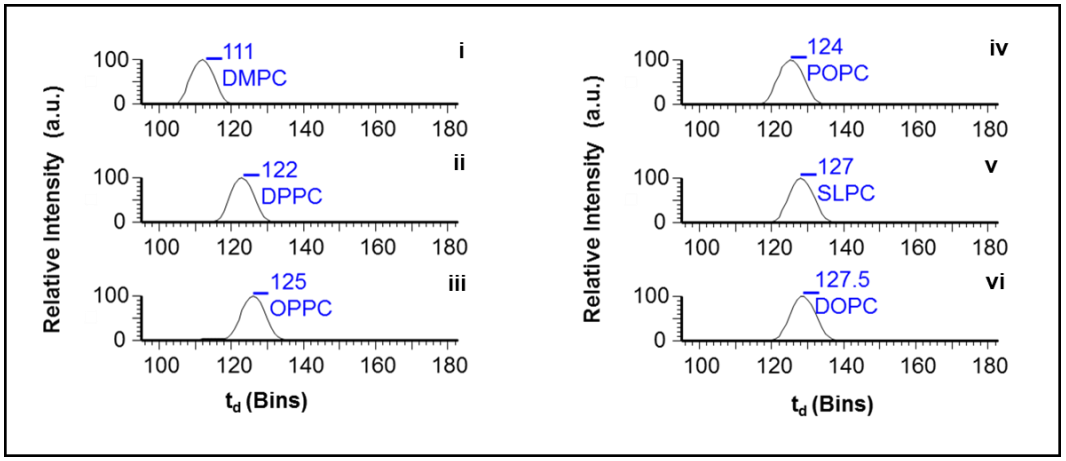

Figure 5.4. **ATD display from EIM for six individual PCs including, DMPC, DPPC, POPC, OPPC, SLPC and DOPC and analysed on the Synapt G2-s through direct infusion IMS-MS (TWIMS). ATDs were displayed from EIM for (i) DMPC at *m/z* 678.5; (ii) DPPC at *m/z* 734.6; (iii) OPPC at *m/z* 760.6; (iv) POPC at *m/z* 760.6; (v) SLPC at *m/z* 786.6; (vi) DOPC at *m/z* 786.6.**

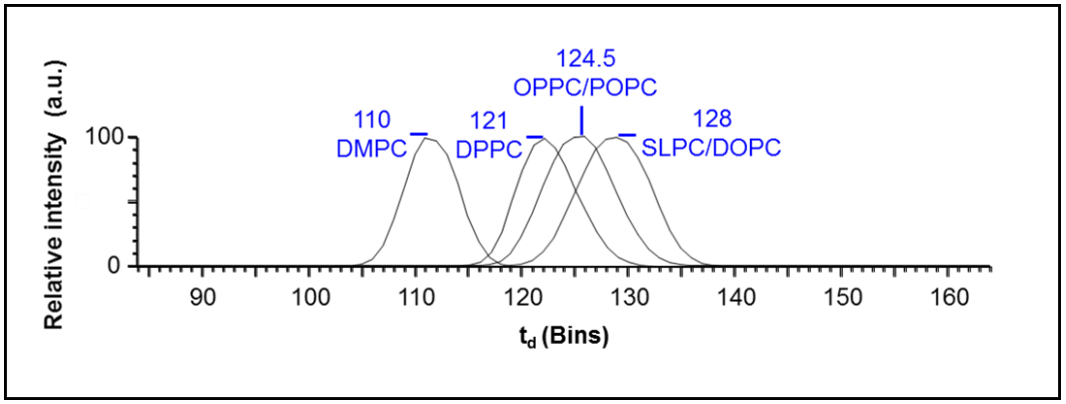

Figure 5.5. **ATD display from EIM for equimolar mixture of six PCs including, DMPC: DPPC:POPC:OPPC:SLPC:DOPC and analysed on the Synapt G2-s through direct infusion IMS-MS (TWIMS). ATDs were displayed from EIM for DMPC at *m/z* 678.5; DPPC at *m/z* 734.6; OPPC/POPC at *m/z* 760.6; SLPC/DOPC at *m/z* 786.6.**

Table 5.3. **ATDs obtained from the mobilogram for each of individual PC lipids including, DMPC, DPPC, POPC, OPPC, SLPC and DOPC and equal mole ratio for a mixture of all the subjected PCs herein. Sample solutions were analysed on the Synapt G2-s through direct infusion IMS-MS (TWIMS).**

Sample	Meas‡ *m/z*	ATD
Individual PCs		t_d **(Bins)**
DMPC	678.5	111
DPPC	734.6	122
POPC	760.6	125
OPPC	760.6	124
SLPC	786.6	127
DOPC	786.6	127.5
Mixture of PCs (DMPC : DPPC : POPC : OPPC : SLPC : DOPC)		
DMPC	678.5	110
DPPC	734.6	121
POPC/OPPC	760.6	124.5
SLPC/DOPC	786.6	128

‡Meas: measured *m/z* for [M + H]+.

Results also show that DMPC with the shortest acyl chains or lowest number of -CH_2- group (Table 5.3) has the highest mobility and thus lowest ATD, which is far enough from all the other PCs to expect a complete resolution by TWIMS. However, all the other PCs have close ATDs and therefore could not be fully resolved by TWIMS. Once more, increasing the number of -CH_2- groups of the fatty acyl chain has shown to be directly correlate with increasing ATD. This is consistent with the results described for PPC/OPC (see section 5.1.1), and also as reported earlier[8-11].

Interestingly, lipid isomers that could not be resolved by TWIMS or DTIMS could be resolved by field-asymmetric ion mobility spectrometry (FAIMS) a type of differential ion mobility spectrometry (DMS).[6,15-17] Maccarone *et al.*[15] showed that POPC could be resolved from OPPC regioisomer by DMS through cation adduct formation between silver ion (Ag^+)

and carbon-carbon double bond of the oleoyl fatty acyl chain. The main reason that FAIMS is so powerful for lipid separation is due to a strong orthogonality between FAIMS and MS, while this orthogonality is found to be poor between TWIMS/DTIMS and MS.[6,17,18] This is because in FAIMS there is a weaker correlation between ion's *m/z* from MS with the difference of the mobility (∆K) but this correlation is stronger with the absolute mobility (K) in TWIMS or DTIMS.[6,17,18] Consequently, a single trend line occupied by lipid ions with similar charge state (predominantly *z*=1) in the IMS-MS space is reported to be separated better with FAIMS than that with TWIMS or DTIMS.[6,17,18]

5.2. Analysis of synthetic lipidated melittin analogues by ion mobility separation-mass spectrometry (IMS-MS)

Synthesized lipidated melittin analogues with individual acyl chains, including palmitoyl (M_{pal}) and oleoyl (M_{ole}) at the two most reactive lipidation sites,[19,20] N-terminus and K23, (see chapter three, section 3.2.3) were directly infused to IMS-MS. Intact ions of M_{pal} (Figure 5.6) and M_{ole} (Figure 5.7) were observed at three different charge states together with some in-source product ions. The results clearly show that different charge states are moving at different speeds in the drift tube under the influence of electrical field. Quintuply charge states have shown to travel faster (shorter ATD), while triply charged ions travel slower (longer ATD). This illustrates that although quintuply charged ions are less folded than triply charged ions because Coulomb repulsion overcomes attractive intramolecular interactions by increasing peptide/protein charge state, as reported by Clemmer *et al.*[21] and Wu *et al.*[22], quintuply charged ions are still arrived first. This is because peptides/proteins with higher charge states are attracted more and thus travel faster under the influence of the electric field.

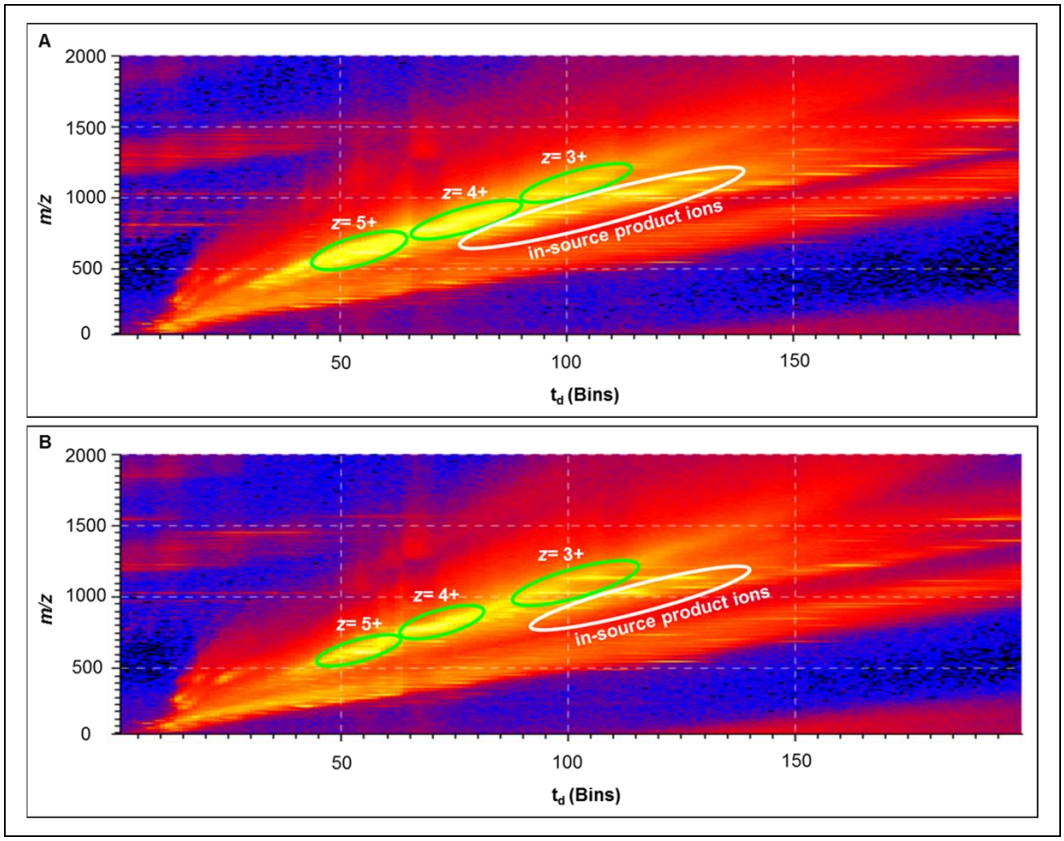

Figure 5.6. **Mobilogram display for (A) N-M_{pal} and (B) K23-M_{pal}, analysed on the Synapt G2-s through direct infusion IMS-MS (TWIMS).**

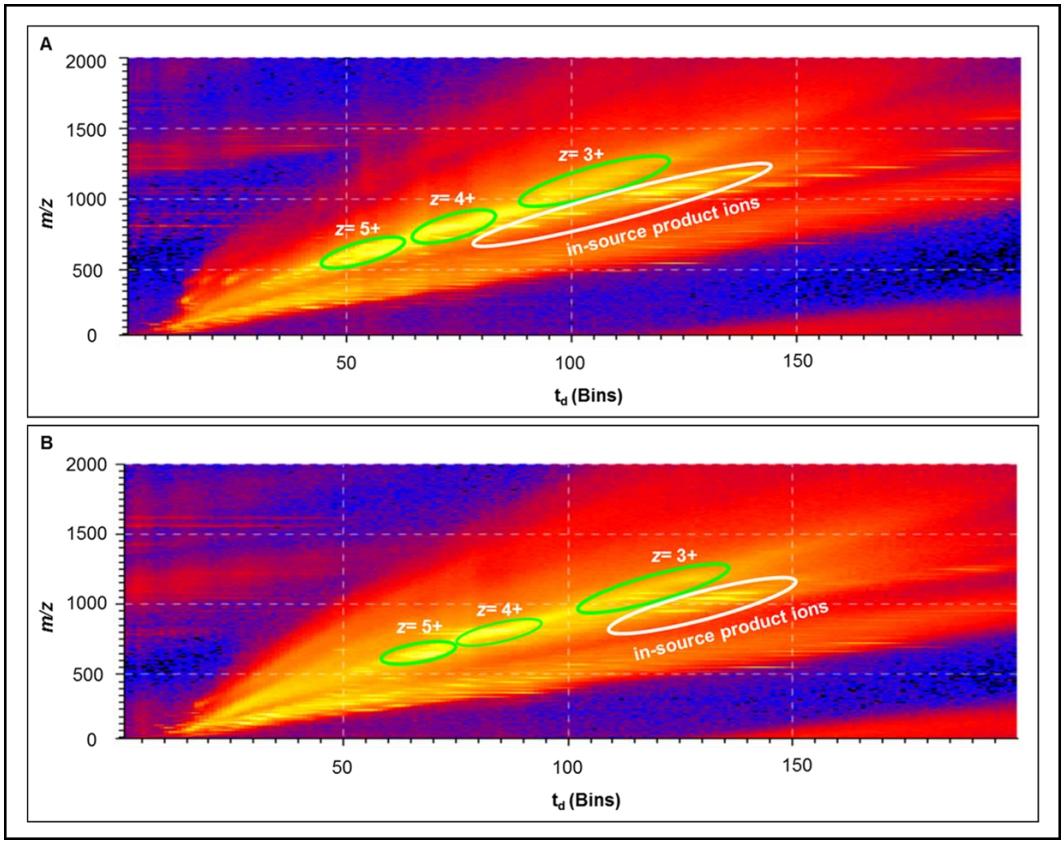

Figure 5.7. **Mobilogram display for (A) N-M_{ole} and (B) K23-M_{ole}, analysed on the Synapt G2-s through direct infusion IMS-MS (TWIMS).**

Further, ions with lower charge state have also shown to experience more conformational changes than higher charge state, as shown in Figures 5.8 and 5.9. The ATDs for N-M_{pal} $[M + 3H]^{3+}$ (Figure 5.8 (i) and (iv)) and K23-M_{pal} $[M + 3H]^{3+}$ (Figure 5.9 (i) and (iv)) showed only two peaks, while this has zoomed in mobilogram display and showed three conformations (Figures 5.8 (iv) and 5.9 (iv)) instead of two conformations (Figures 5.8 (i) and 5.9 (i)). The middle peak is therefore not resolved from the first peak. Increasing ions conformational changes by decreasing the number of charge states on the peptide can be concluded by more proton mobility on the free available basic amino acid residues on the peptide backbone, as melittin has 6 basic sites (see chapter one, section 1.7). Consequently, based on the location of the proton the peptide can exhibit different conformations. Interestingly, for triply charged ions the two conformations with lower ATD and therefore the more compact conformation are very similar for N-M_{pal} at ATD = 95 and 102 (Figure 5.8 (iv)) and K23-M_{pal} at ATD = 95 and 100 (Figure 5.9 (iv)) and therefor they

could not be expected to be resolved by TWIMS. However, the more elongated conformation with the highest ATD shows a difference in ATD between N-M_{pal} at ATD = 113 (Figure 5.8 (iv)) and K23-M_{pal} at ATD = 108 (Figure 5.9 (iv)) and therefore could expect some degree of resolution in such case. In addition, N-M_{pal} $[M + 4H]^{4+}$ shows two conformations (Figure 5.8 (ii) and (v)) but only the conformation with the lowest ATD (t_d = 68 bins) were seen for K23-M_{pal} $[M + 4H]^{4+}$ (Figure 5.9 (ii) and (v)). This could be concluded by more constrained palmitoyl acyl chain on K23 site than N-terminus of the peptide. The highest charge state for N-M_{pal} $[M + 5H]^{5+}$ (Figure 5.8 (iii) and (vi)) and K23-M_{pal} $[M + 5H]^{5+}$ (Figure 5.9 (iii) and (vi)) showed only one peak for each isomer with identical ATD. Consequently, no isomer resolution could be expected at this charge state. Fewer conformational structures for M_{pla} at higher charge states is suggested to be related with the existence of less free basic sites for the proton to move on the peptide backbone.

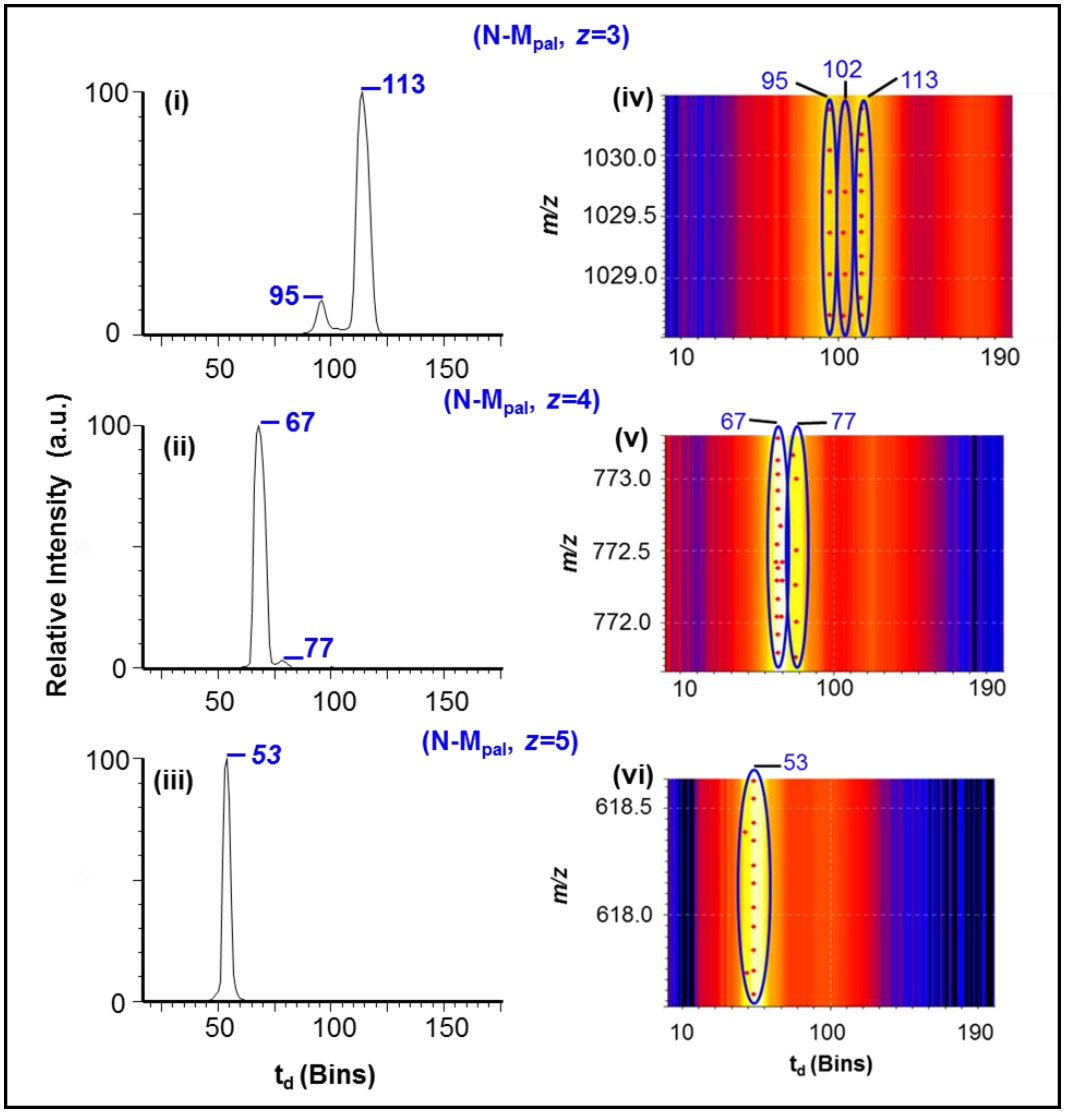

Figure 5.8. **ATD display from EIM for N-M_{pal} at (i) *m/z* 1028.7 $[N\text{-}M_{pal} + 3H]^{3+}$; (ii) *m/z* 771.8 $[N\text{-}M_{pal} + 4H]^{4+}$; (iii) *m/z* 617.6 $[N\text{-}M_{pal} + 5H]^{5+}$. Zoomed in sections of the mobilogram display for N-M_{pal} at (iv) *m/z* 1028.7; (v) *m/z* 771.8; (vi) *m/z* 617.6. Analysed on the Synapt G2-s through direct infusion IMS-MS (TWIMS).**

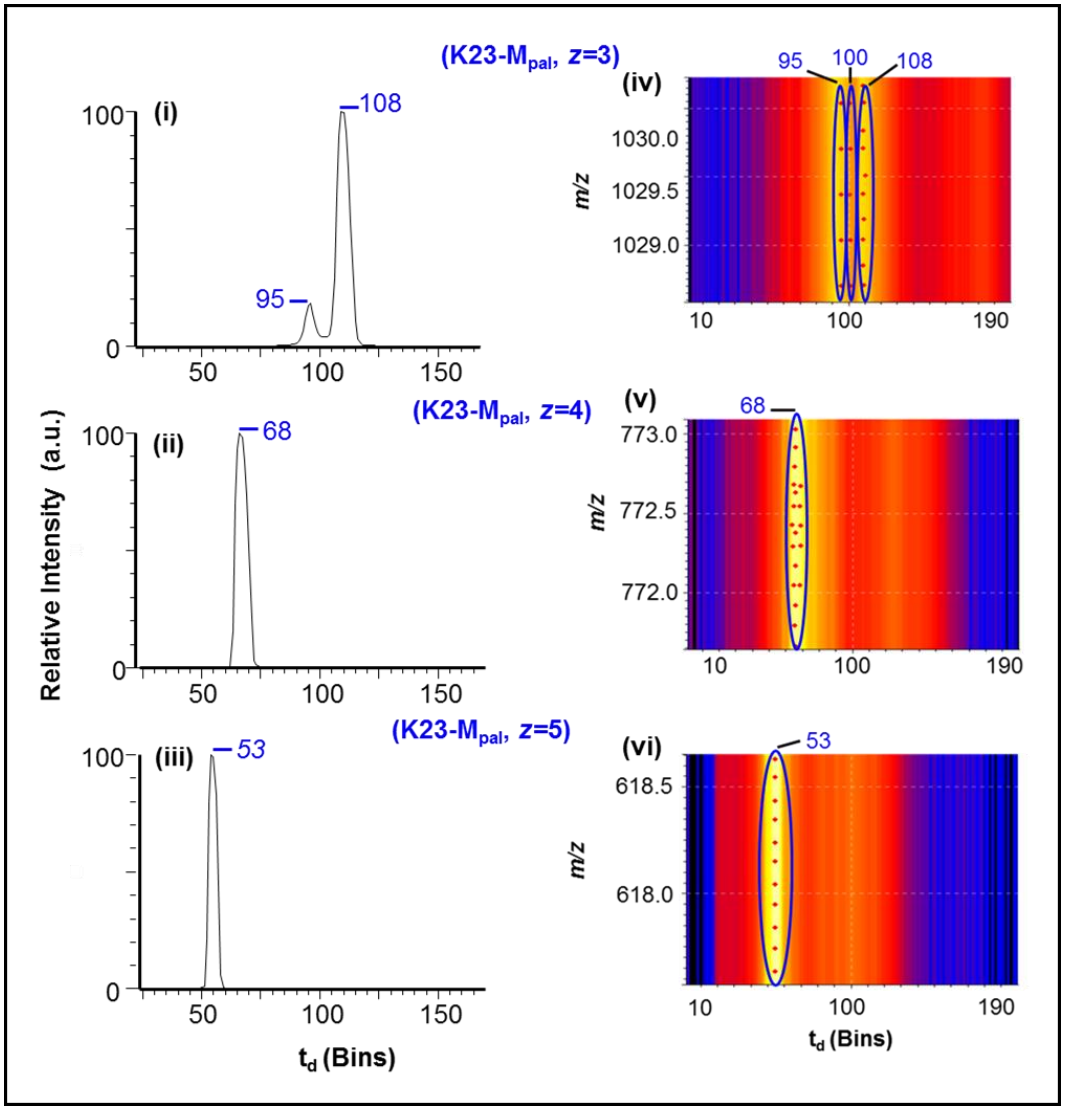

Figure 5.9. **ATD display from EIM for K23-M$_{pal}$ at (i) *m/z* 1028.7 [K23-M$_{pal}$ + 3H]$^{3+}$; (ii) *m/z* 771.8 [K23-M$_{pal}$ + 4H]$^{4+}$; (iii) *m/z* 617.6 [K23-M$_{pal}$ + 5H]$^{5+}$. Zoomed in sections of the mobilogram display for K23-M$_{pal}$ at (iv) *m/z* 1028.7; (v) *m/z* 771.8; (vi) *m/z* 617.6. Analysed on the Synapt G2-s through direct infusion IMS-MS (TWIMS).**

Similarly, more conformational changes for lower charge states is evident for N-M$_{ole}$ [M + 3H]$^{3+}$ (Figure 5.10 (i) and (iv)) and K23-M$_{ole}$ [M + 3H]$^{3+}$ (Figure 5.11 (i) and (iv)) but this conformational changes reduced by increasing the peptide charge states to quadruply and quintuply charged ions for each of N-M$_{ole}$ (Figure 5.10 (ii-vi)) and K23-M$_{ole}$ (Figure 5.11 (ii-vi)). It is interesting to see that when oleoyl acyl chain is bound to the peptide a greater difference in ADTs is evident between N-M$_{ole}$ and K23-M$_{ole}$ for all the

three charge states. It is then proposing a promising resolution between both lipidated sites when they will come together in a mixture.

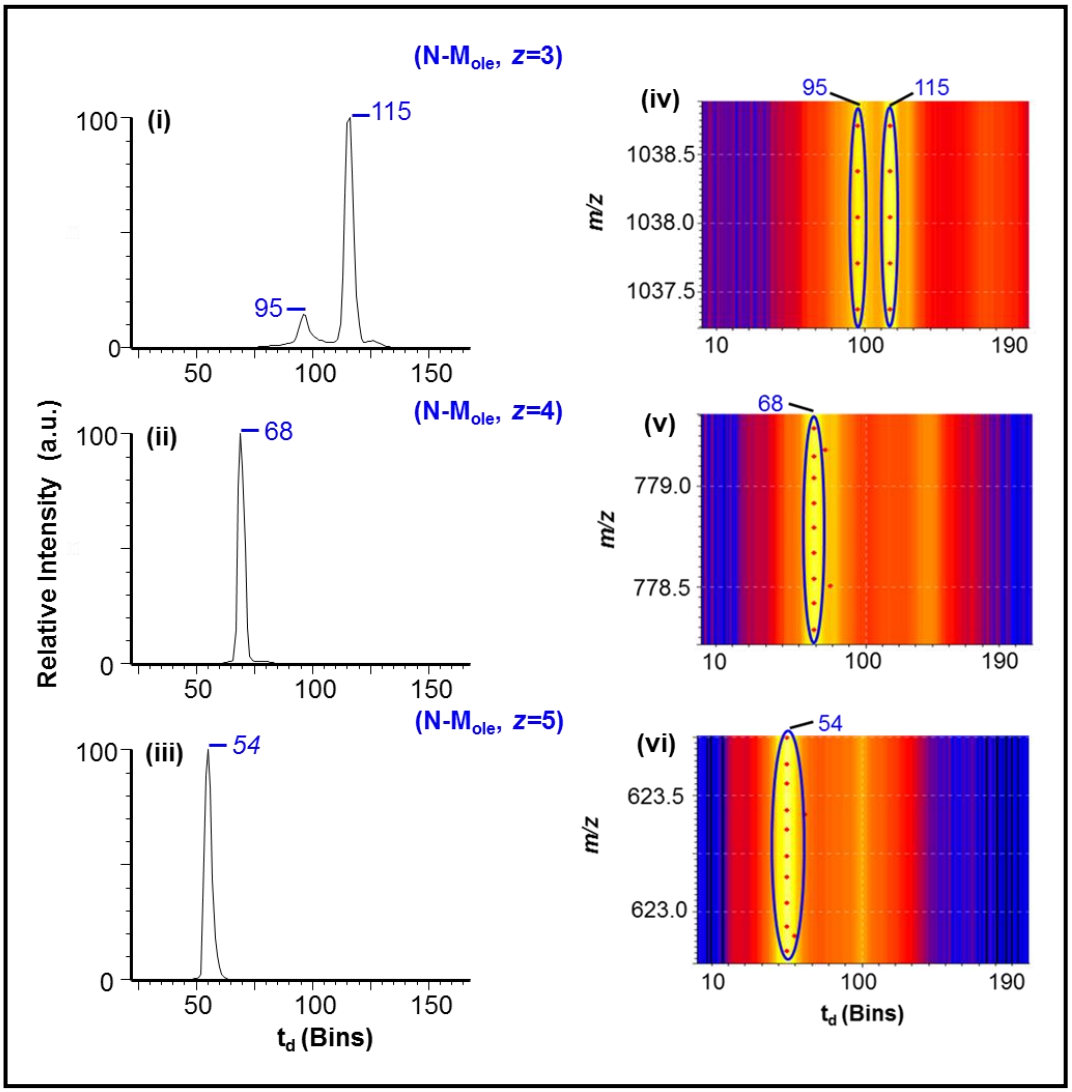

Figure 5.10. **ATD display from EIM for N-M_{ole} at (i) *m/z* 1037.4 $[N\text{-}M_{ole} + 3H]^{3+}$; (ii) *m/z* 778.3 $[N\text{-}M_{ole} + 4H]^{4+}$; (iii) *m/z* 622.8 $[N\text{-}M_{ole} + 5H]^{5+}$. Zoomed in sections of the mobilogram display for N-M_{ole} at (iv) *m/z* 1037.4; (v) *m/z* 778.3; (vi) *m/z* 622.8. Analysed on the Synapt G2-s through direct infusion IMS-MS (TWIMS).**

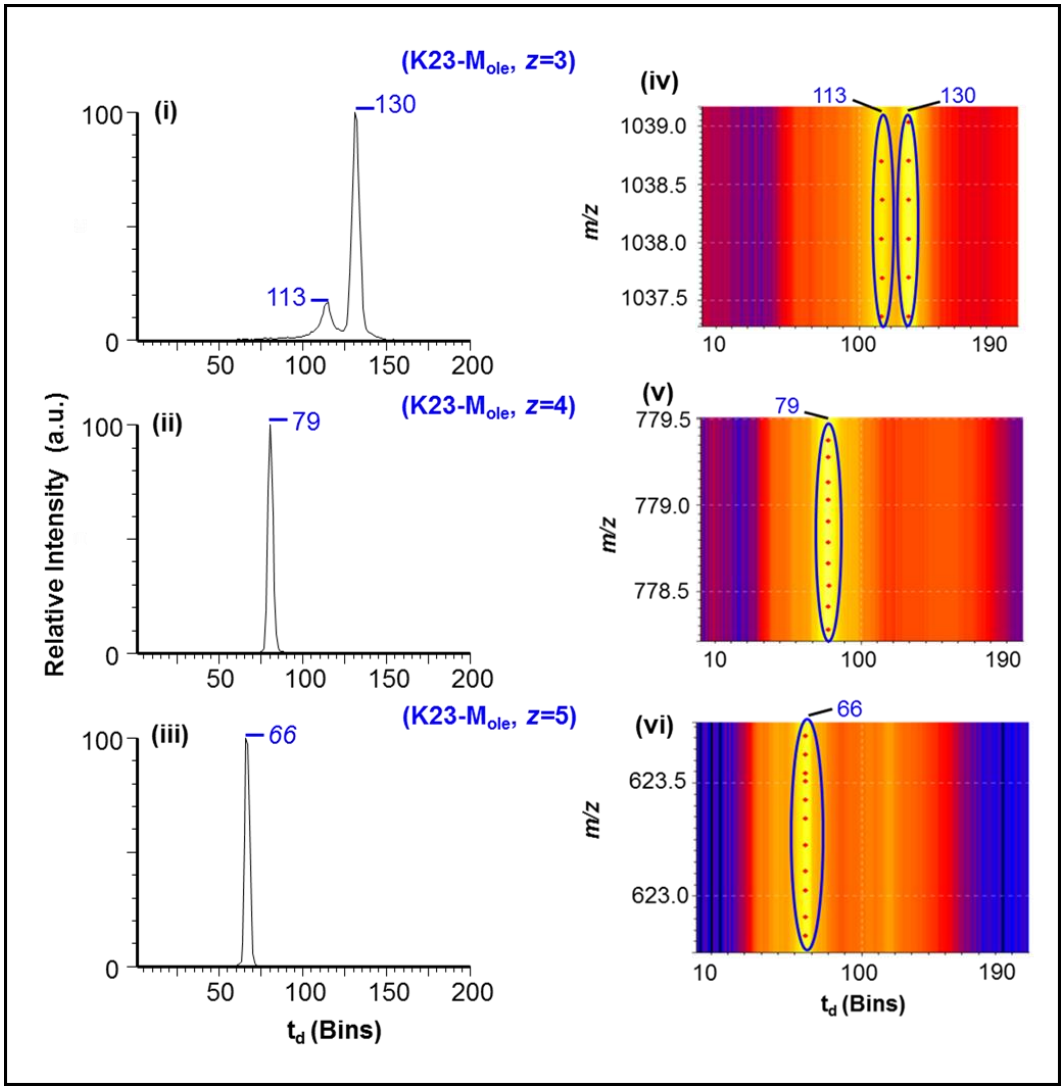

Figure 5.11. **ATD display from EIM for K23-M$_{ole}$ at (i) *m/z* 1037.4 [K23-M$_{ole}$ + 3H]$^{3+}$; (ii) *m/z* 778.3 [K23-M$_{ole}$ + 4H]$^{4+}$; (iii) *m/z* 622.8 [K23-M$_{ole}$ + 5H]$^{5+}$. Zoomed in sections of the mobilogram display for K23-M$_{ole}$ at (iv) *m/z* 1037.4; (v) *m/z* 778.3; (vi) *m/z* 622.8. Analysed on the Synapt G2-s through direct infusion IMS-MS (TWIMS).**

Results by comparing ATDs for M_{pal} and M_{ole} (Table 5.4) showed that both palmitoylated isomers of N-M_{pal} and K23-M_{pal} are overlapped with N-M_{ole} and therefore it suggests a struggle in resolving between these three species in a mixture, while the ATD for K23-M_{ole} is far from the other species and thus proposing to be distinguished from the other acylated species. Non-acylated melittin (M) was also examined herein by TWIMS as a control experiment (Figure 5.12). Lower ATD for non-acylated species relative to acylated species is consistent with the smaller size of M and thus travels faster in the mobility cell. Once more greater conformation structure for triply charged ions (Figure 5.12 (i) and (iv)) is evident relative to fewer conformation structure for quadruply (Figure 5.12 (ii) and (v)) and quintuply charged ions (Figure 5.12 (iii) and (vi)).

Table 5.4. **ATDs obtained from the mobilogram for each individual species of non-acylated melittin (M), N-M_{pal}, K23-M_{pal}, N-M_{ole} and K23-M_{ole} and equimolar mixture of (M:N-M_{pal}:K23-M_{pal}:N-M_{ole}:K23-M_{ole}).**

Sample	Meas‡ *m/z*	*z*	ATD
Individual species			**t_d (Bins)**
M	949.3	3	85
			99
	712.2	4	59
	570.0	5	50
N-M_{pal}	1028.7	3	95
			102
			113
	771.8	4	67
			77
	617.6	5	53
K23-M_{pal}	1028.7	3	95
			100
			108
	771.8	4	68
	617.6	5	53
N-M_{ole}	1037.4	3	95
			115
	778.3	4	68
	622.8	5	54
K23-M_{ole}	1037.4	3	113
			130
	778.3	4	79
	622.8	5	66
Mixture			
M	949.3	3	86
			99
	712.2	4	59
	570.0	5	48
N-M_{pal}/K23-M_{pal}	1028.7	3	95
			100
			113
	771.8	4	66
			76
	617.6	5	47
			53
N-M_{ole}/K23-M_{ole}	1037.4	3	94
			102
			110
			115
	778.3	4	67
			69
			78
	622.8	5	48
			53
			58

‡Measured (Meas) *m/z* is for the monoisotopic peak.

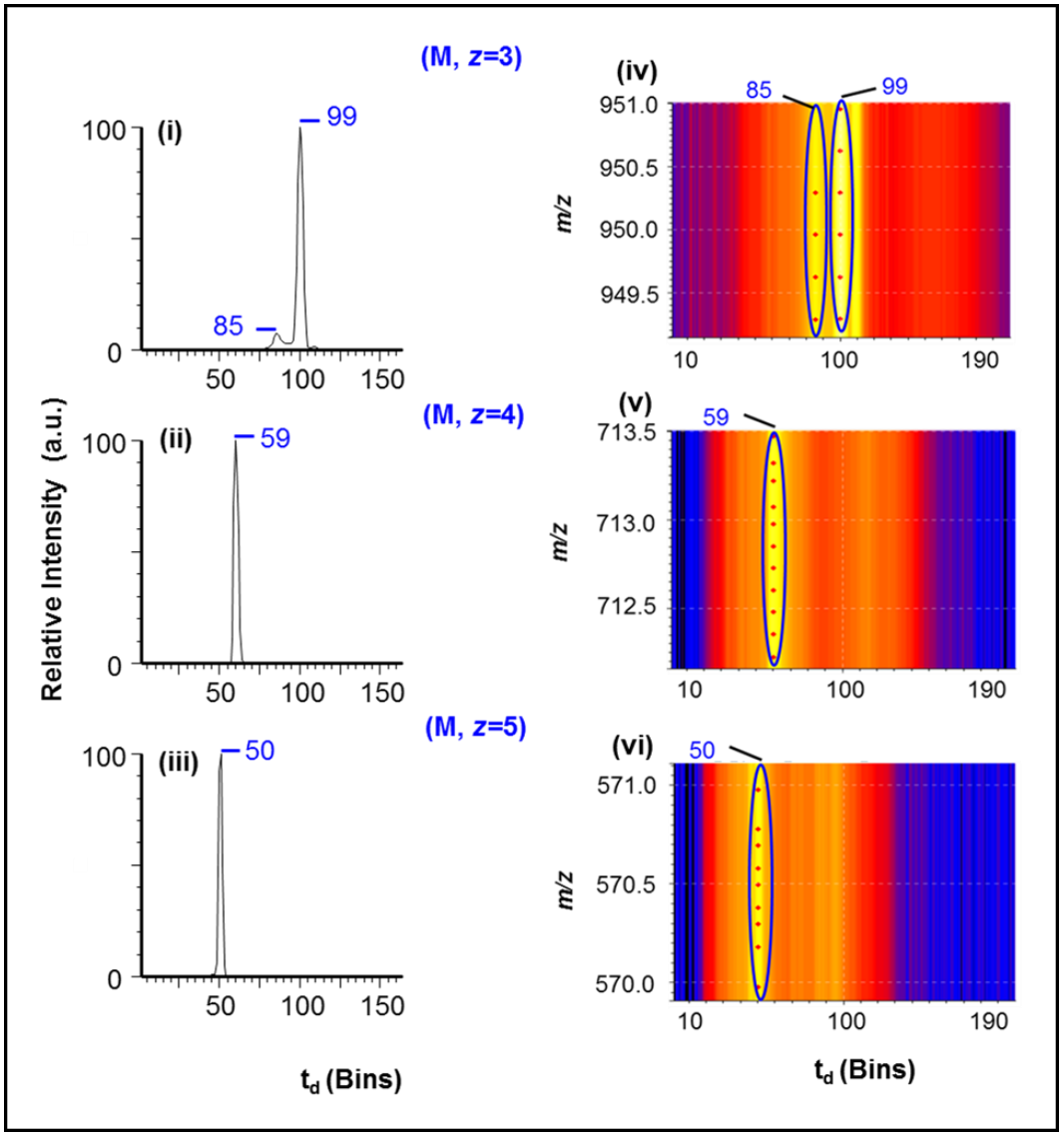

Figure 5.12. **ATD display from EIM for non-acylated melittin (M) at (i) *m/z* 949.3 $[M + 3H]^{3+}$; (ii) *m/z* 712.2 $[M + 4H]^{4+}$; (iii) *m/z* 570.0 $[M + 5H]^{5+}$. Zoomed in sections of the mobilogram display is for (iv) *m/z* 949.3; (v) *m/z* 712.2; (vi) *m/z* 570.0. Analysed on the Synapt G2-s through direct infusion IMS-MS (TWIMS).**

Analyses for individual species suggested that, at least for the triply charged ion, the isomers could be separated so in an effort to see if the four species could be resolved from one mixture an equimolar ratio of all the peptide species were directly infused and analysed by TWIMS. Figure 5.13 (i) shows three unresolved peaks for M_{ole} but the zoomed in region from the mobilogram confirms four conformations (see Table 5.4). Similar results was also found with the other charge states (Figure 5.13 (ii-vi) and see Table 5.4). The higher number of peptide conformations for each species and at each

charge state in the mixture relative to fewer conformations when individual species were analysed (see Table 5.4) clearly suggests that all the four acylated species N-M_{ole} *vs* K23-M_{ole} isomers and N-M_{pal} *vs* K23-M_{pal} isomers were detected in the mixture but hardly to be resolved clearly under these conditions. The resolution between a pair of isomers is more promising for lower charge states with broader peak shapes (when *z*=3 and 4), Figure 5.13 (i), (ii), (iv) and (v), than higher charge state with sharper peak shape (Figure 5.13 (iii) and (vi). This is further supported in the results obtained from the analysis of non-acylated melittin by TWIMS (see Table 5.4). Because during travelling non-acylated melittin through the mobility cell as its individual form or during its mixing with the other acylated species, preserved its conformation structure at all the three different charge states and thus with identical ATDs in both analyses (see Table 5.4). On the other hand, acylated melittin isomers show a change in their conformation structure and also their ATDs upon their mixing (see Table 5.4). This clearly suggests the effect of bounded fatty acyl chains on the conformation of melittin in the gas phase.

In addition, comparing the same charge states for M_{pal} *vs* M_{ole} (Figure 5.13), results show that M_{pal} is slightly shifted towards shorter ATDs than higher ATDs for M_{ole}, this is when there is 26 Da mass difference between M_{pal} (C16:0) and M_{olel} (C18:1). Consequently, M_{pal} is suggested to be partially resolved from M_{ole} by using their different in *m/z* to extract the ion and then comparing their ATDs.

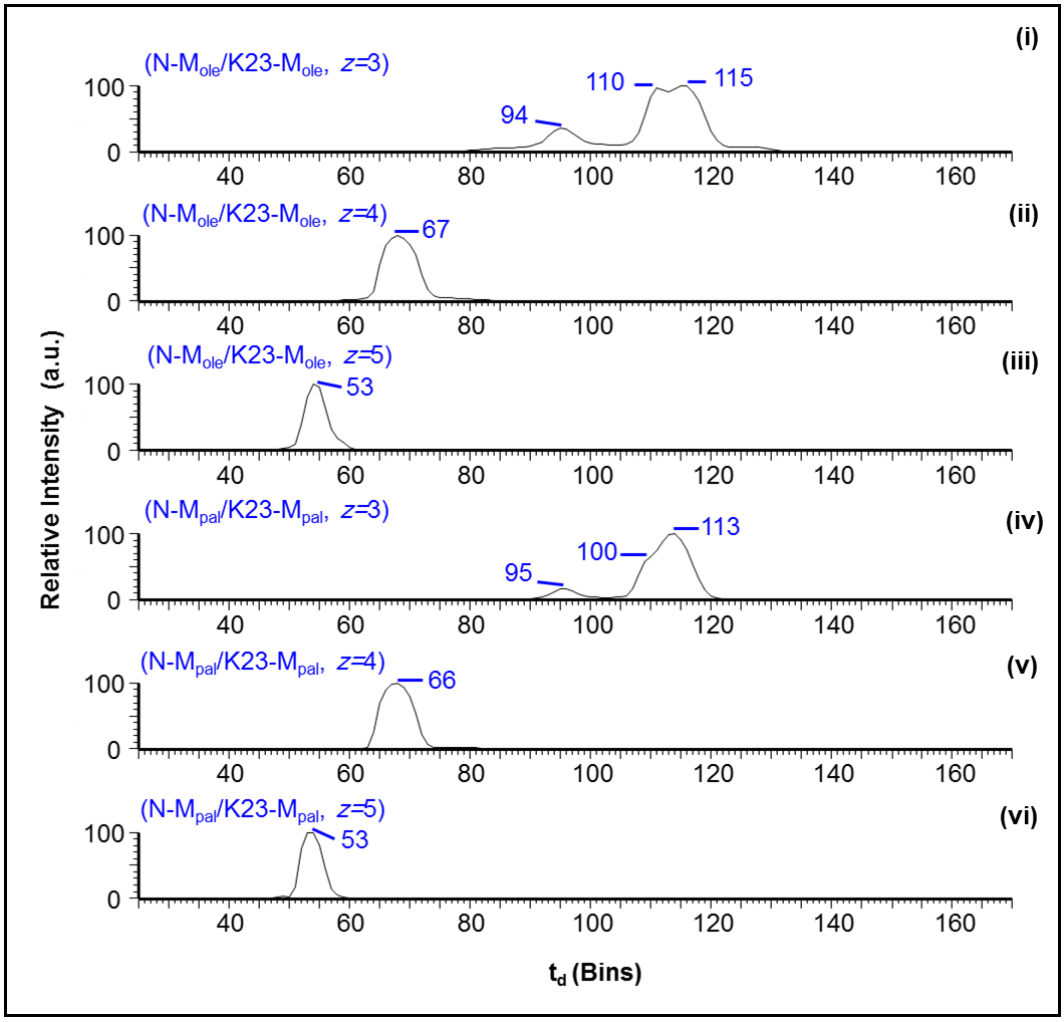

Figure 5.13. **ATD display from comparison of EIMs for (i) N-M_{ole}/K23-M_{ole} at *m/z* 1037.4 $[M + 3H]^{3+}$; (ii) N-M_{ole}/K23-M_{ole} at *m/z* 778.3 $[M + 4H]^{4+}$; (iii) N-M_{ole}/K23-M_{ole} at *m/z* 622.8 $[M + 5H]^{5+}$; (iv) N-M_{pal}/K23-M_{pal} at *m/z* 1028.7 $[M + 3H]^{3+}$; (v) N-M_{pal}/K23-M_{pal} at *m/z* 771.8 $[M + 4H]^{4+}$; (vi) N-M_{pal}/K23-M_{pal} at *m/z* 617.6 $[M + 5H]^{5+}$obtained from an equimolar mixture of N-M_{ole}:K23-M_{ole}:N-M_{pal}:K23-M_{pal}, and analysed on the Synapt G2-s through direct infusion IMS-MS (TWIMS). For details, see Table 5.4.**

5.3. Ion mobility separation and transfer cell CID fragmentation (IMS-MS^2) for synthetic lipidated melittin

Further IMS analysis was carried out on the different isomeric structures of synthesized lipidated melittin in order to localize the site of lipidation and study the ability of IMS to improve the analysis. CID of the precursor ions for individual M_{pal} at *m/z* 772 $[M_{pal} + 4H]^{4+}$ and M_{ole} at *m/z* 778 $[M_{ole} + 4H]^{4+}$ were performed in the transfer cell of TWIMS. Accumulated product ions were found to be time-aligned with their corresponding precursor ions, as shown in Figures 5.14 and 5.15. The results clearly show a broad peak for each isomer but with a slight shift of ATDs for K23 lipidation species towards shorter t_d. This is evident for each of K23-M_{pal} (Figure 5.14 A, 95 ATD) *vs* N-M_{pal} (Figure 5.14 B, 96 ATD) and K23-M_{ole} (Figure 5.15 A, 96 ATD) *vs* N-M_{ole} (Figure 5.15 B, 99 ATD).

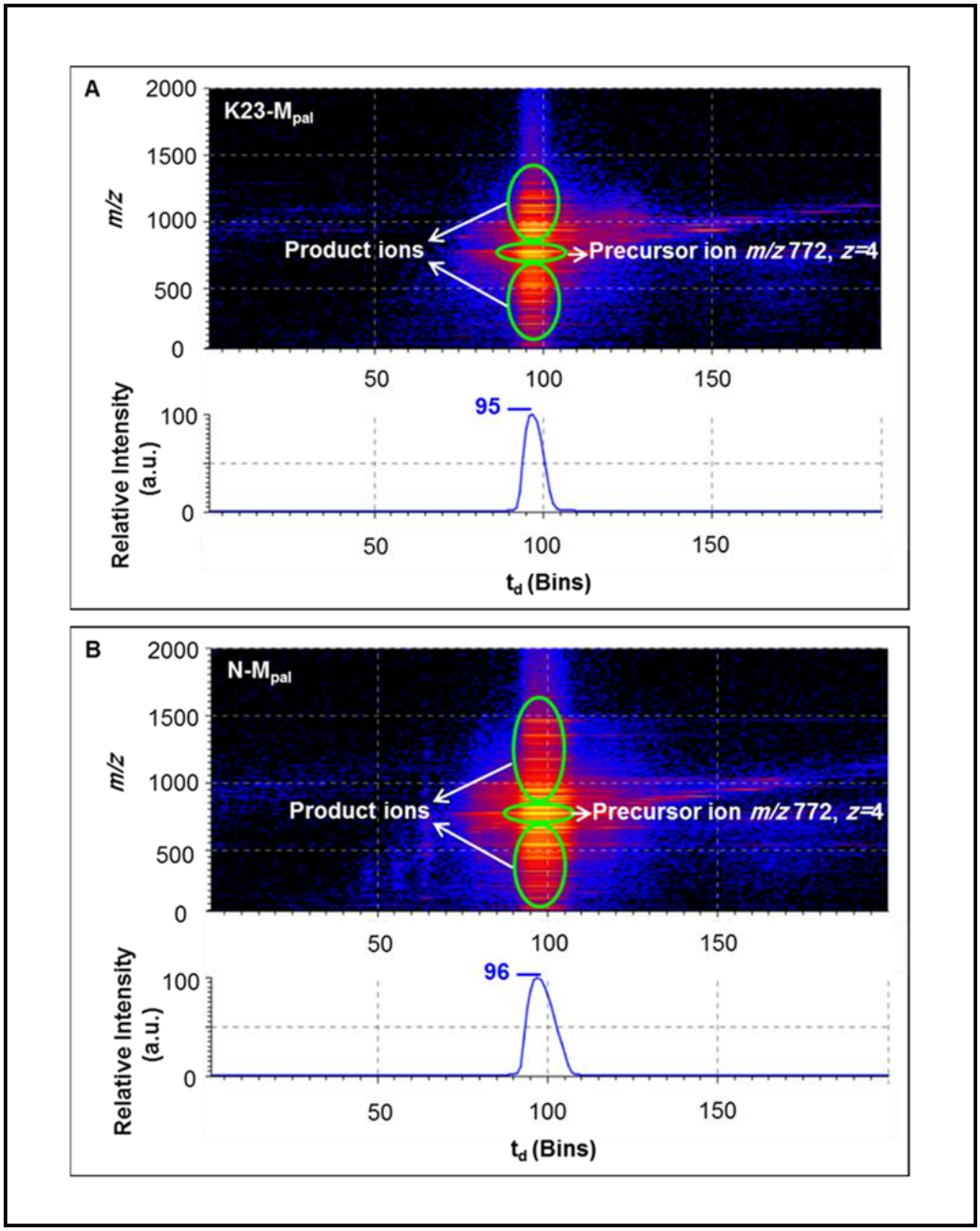

Figure 5.14. **Mobilogram display for product ions obtained through collision fragmentation of precursor ion $[M_{pal} + 4H]^{4+}$ at *m/z* 771.8 for each individual species of (A) K23-M_{pal} and (B) N-M_{pal} through the transfer cell on Synapt G2-s by direct infusion IMS-MS (TWIMS).**

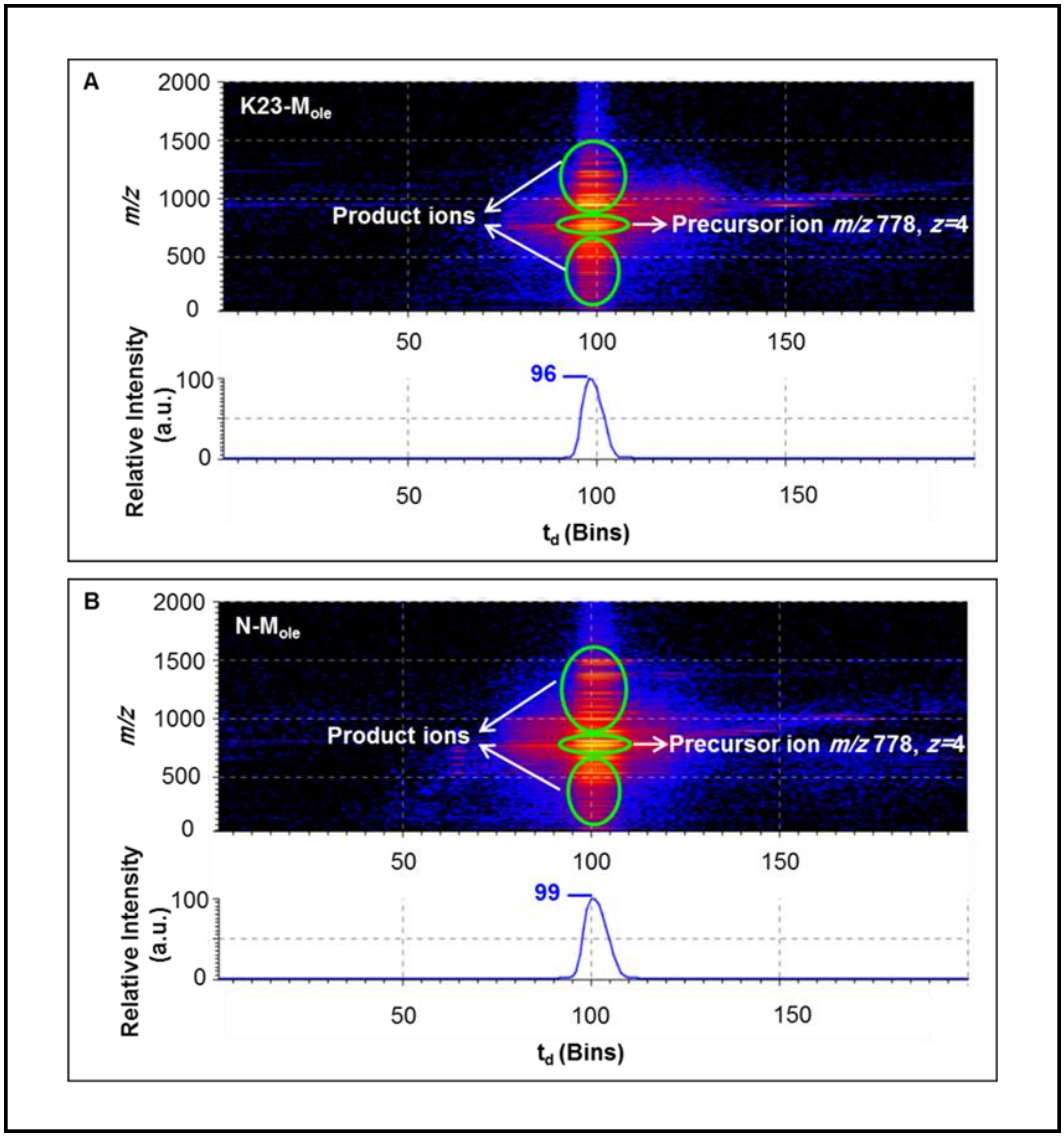

Figure 5.15. **Mobilogram display for product ions obtained through collision fragmentation of precursor ion $[M_{ole} + 4H]^{4+}$ at *m/z* 778.3 for each individual species of (A) K23-M_{ole} and (B) N-M_{ole} through the transfer cell on Synapt G2-s by direct infusion IMS-MS (TWIMS).**

To illustrate whether fragmentation approach in transfer cell allows further resolution of lipidated melittin isomers, a mixture of K23-M_{pal} *vs* N-M_{pal} and K23-M_{ole} *vs* N-M_{ole} were directly infused to ESI-IMS-MS and followed by collision fragmentation of M_{pal} and M_{ole} precursor ions at *m/z* 772 and 778 for $[M_{pal} + 4H]^{4+}$ and $[M_{ole} + 4H]^{4+}$ respectively. Figure 5.16 (A) shows just a hint of two peaks, but not clearly resolved. However, extracting the most abundant diagnostic product ion of y13 for N-M_{pal} at *m/z* 812 $[y13 + 2H]^{2+}$ (Figure 5.16 B) and $y13_{pal}$ for K23-M_{pal} at *m/z* 931 $[y13_{pal} + 2H]^{2+}$ (Figure 5.16

C) it is again evident that K23-M_{pal} shifts towards lower ATD (Figure 5.16 C, 90 ATD) and N-M_{pal} towards higher ATD (Figure 5.16 B, 105 ATD). Consequently, a broad peak from the total ion mobilogram contains more than one species and can be split into three main regions, including front region (i), middle region (ii) and tail region (iii). The product ion spectrum of b- and y-ions from (i) (Figure 5.16 D) confirms the presence of palmitoyl modification just on K23 amino acid residue, while b- and y-ions obtained from mass spectrum of (iii) (Figure 5.16 E) confirms N-terminus site of palmitoylation. This illustrates that time-aligned product ions of K23-M_{pal} is resolved from those of N-M_{pal} by controlling the time where each isomer travels in the drift cell. The middle region (ii) is the overlap region for both isomeric species and enriched with their corresponding product ions (Figure 5.16 A, 100 ATD).

Similarly, time-aligned product ions obtained from isomeric oleoylated mixture of K23-M_{ole} shifts towards lower ATD (Figure 5.17 C, 93 ATD) relative to N-M_{ole} towards higher ATD (Figure 5.17 B, 108 ATD) by extracting $y13_{ole}$ at *m/z* 944 $[y13_{ole}+ 2H]^{2+}$ and y13 at *m/z* 812 $[y13 + 2H]^{2+}$ respectively. The corresponding spectrum for each isomer species is shown in Figure 5.17 D and E. The results also evident some improvement in the resolution between M_{pal} (Figure 5.16 A) and M_{ole} (Figure 5.17 A) because their corresponding time-aligned product ions in IMS-MS^2 (Figures 5.16 and 5.17) show a greater difference in ATDs relative to much closer ATDs for intact ions in IMS-MS (Table 5.4). The application of TWIMS was also reported by Santos *et al.*[23] for separating peptide isomers modified with peptide cross-linking agent at different sites of the peptide.

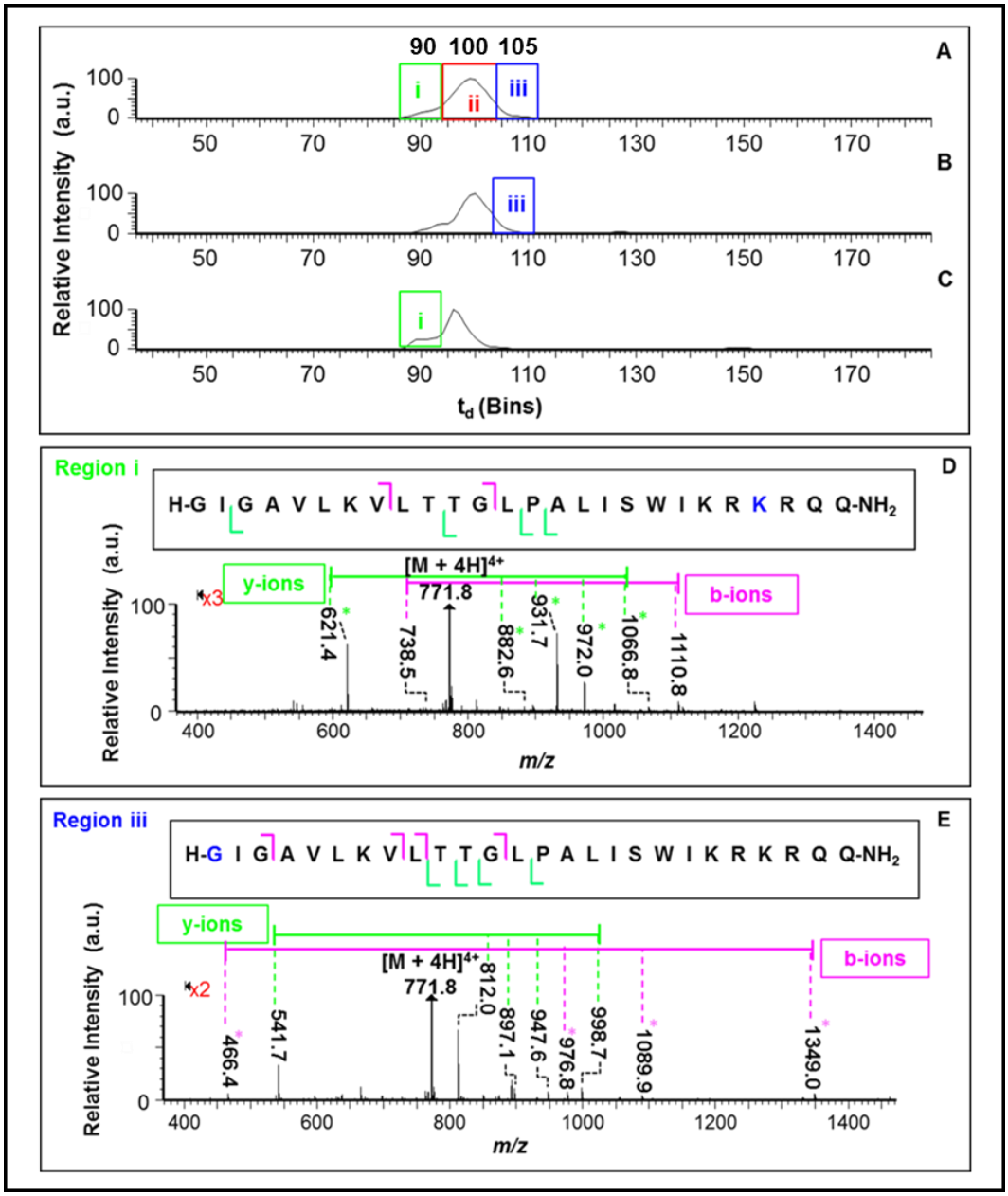

Figure 5.16. **(A) Total ATD for $[M_{pal} + 4H]^{4+}$ upon CID in the transfer cell on Synapt G2-s by direct infusion IMS-MS^2 (TWIMS). (B) ATD from EIM at *m/z* 812.0 for y13 ion (N-M_{pal}). (C) ATD from EIM at *m/z* 931.2 for $y13_{pal}$ ion (K23-M_{pal}). (D) Product ion spectrum corresponding to (C) at region (i), and labelled y-ions with the asterisk represent modified sites with palmitoyl towards K23 amino acid residue. (E) Product ion spectrum corresponding to (B) at region (iii), and labelled b-ions with the asterisk represent modified sites with palmitoyl towards N-terminus. All b-ions are singly protonated, while y-ions are doubly and/ or triply protonated.**

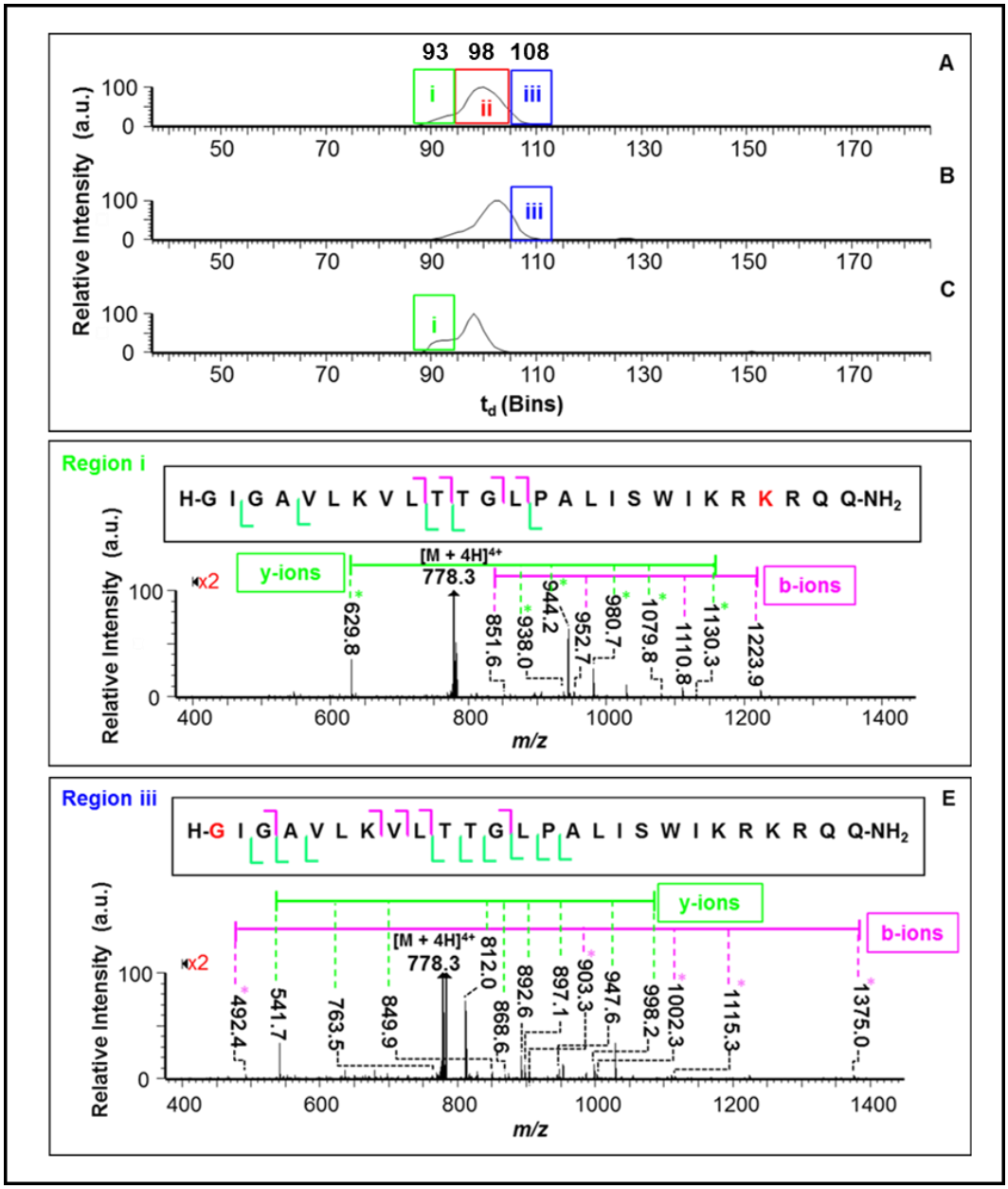

Figure 5.17. **(A) Total ATD for $[M_{ole} + 4H]^{4+}$ upon CID in the transfer cell on Synapt G2-s by direct infusion IMS-MS^2 (TWIMS). (B) ATD from EIM at *m/z* 812.0 for y13 ion (N-M_{ole}). (C) ATD from EIM at *m/z* 944.2 for $y13_{ole}$ ion (K23-M_{ole}). (D) Product ion spectrum corresponding to (C) at region (i), and labelled y-ions with the asterisk represent modified sites with oleoyl towards K23 amino acid residue. (E) Product ion spectrum corresponding to (B) at region (iii), and labelled b-ions with the asterisk represent modified sites with oleoyl towards N-terminus. All b-ions are singly protonated, while y-ions are doubly and/ or triply protonated.**

5.4. Conclusion

Since isomeric modified peptides or more precisely altering the position of post-translational modification (PTM) on peptides/proteins can have a critical influence on biological activity and functions,[23-25] different strategies of analyses were performed herein. The two LPCs with palmitoyl (PPC) and oleoyl (OPC), also known to modify melittin readily, were shown to have different ATDs but that different is not sufficient to fully resolve them by TWIMS. This was also evident in DPPC *vs* DOPC, but DMPC with the smallest size is proposed to be fully resolved from the other PCs. The resolution is even harder for PC isomers POPC *vs* OPPC and DOPC *vs* SLPC, as they could not be resolved under the conditions described herein. This is not surprising, as PCs/LPCs with one charge state (*z*=1) and thus one trend line is very hard to be resolved by TWIMS as their intact form or without any further structural modification.

Unlike PCs with a single trend line, multiple trend lines corresponding to multiple charge states for acylated melittin suggested there is a potential to distinguish between M_{pal} from M_{ole} or their isomers including acylation on N-terminus *vs* K23, and particularly evident for triply and quadruply ions. The presence of fatty acyl chains covalently bound to melittin is suggested to have an influence on changing peptide conformation in the gas phase. The location of the fatty acyl chain towards N-terminus and K23 of the peptide was also found to provide interesting results, as it is believed that fatty acyl chains on N-terminus of the peptide might be more flexible, while on K23 it can be either stick up or lie along the peptide backbone. Particularly was evident for N-M_{ole} *vs* K23-M_{ole} when *z*=3 and 4. This suggested to be related with the kink by carbon-carbon double bond in oleoyl acyl chain. The position of the acyl chain could also be suggested to reflect in shifting of time-aligned product ions corresponds to K23 acylation precursor ion towards shorter ATD than time-aligned product ions corresponds to N-terminus acylation precursor ion through collision transfer fragmentation approach coupled with TWIMS. The complexity reflected by being both lipid and peptide molecules attached to each other has been studied herein by TWIMS for the first time. However, results show that further analytical and as well as instrumental approaches

are required in order to overcome this complexity and to obtain a complete resolution between lipidated peptide isomers.

5.5. References

1 Wasburn, M. P., D. Wolters, and J. R. Yates. "Large-scale analysis of the yeast proteome by multidimensional protein identification technology." *Nature Biotechnology*, 19 (**2001**): 242-247.

2 Aalberg, Laura, C. Randall Clark, and Jack DeRuiter. "Chromatographic and mass spectral studies on isobaric and isomeric substances related to 3,4-methylenedioxymethamphetamine." *Journal of Chromatographic Science*, 42 (**2004**): 464-469.

3 Momchilova, Svetlana, Yutaka Itabashi, Boryana Nikolova-Damyanova, and Arnis Kuksis. "Regioselective separation of isomeric triacylglycerols by reversed-phase high-performance liquid chromatography: Stationary phase and mobile phase effects." *Journal of Separation Science*, 29 (**2006**): 2578-2583.

4 Winter, Dominic, Rüdiger Pipkorn, and Wolf D. Lehmann. "Separation of peptide isomers and conformers by ultra performance liquid chromatography." *Journal of Separation Science*, 32 (**2009**): 1111-1119.

5 Nie, Hongang, Ranran Liu, Youyou Yang, Yu Bai, Yafeng Guan, Daqing Qian, Tao Wang, and Huwei Liu. "Lipid profiling of rat peritoneal surface layer by an online NP/RP 2D LC-QToF-MS system." *Journal of Lipid Research*, 51 (**2010**): 2833-2844.

6 Shvartsburg, Alexandre A., Giorgis Isaac, Nathalie Leveque, Richard D. Smith, and Thomas O. Metz. "Separation and classification of lipids using differential ion mobility spectrometry." *Journal of the American Society for Mass Spectrometry*, 22 (**2011**): 1146-1155.

7 Fujii, Norihiko, Hiroaki Sakaue, Hiroshi Sasaki, and Noriko Fujii. "A rapid, comprehensive liquid chromatography-mass spectrometry (LC-MS)-based survey of the Asp isomers in crystallins from human cataract lenses." *Journal of Biological Chemistry*, 287 (**2012**): 39992-40002.

8 Kyle, Jennifer E., Xing Zhang, Karl K. Weitz, Matthew E. Monroe, Yehia M. Ibrahim, Ronald J. Moore, Jeeyeon Cha et al. "Uncovering biologically significant lipid isomers with liquid chromatography, ion mobility spectrometry and mass spectrometry." *Analyst*, 141 (**2016**): 1649-1659.

9 Zhang, Fang, Su Guo, Manyu Zhang, Zhixu Zhang, and Yinlong Guo. "Characterizing ion mobility and collision cross section of fatty acids using electrospray ion mobility mass spectrometry." *Journal of Mass Spectrometry*, 50 (**2015**): 906-913.

10 Fasciotti, Maíra, Priscila M. Lalli, Gabriel Heerdt, Rafael A. Steffen, Yuri E. Corilo, Gilberto F. de Sá, Romeu J. Daroda et al. "Structure-drift time relationships in ion mobility mass spectrometry." *International Journal for Ion Mobility Spectrometry*, 16 (**2013**): 117-132.

11 Jackson, Shelley N., Damon Barbacci, Thomas Egan, Ernest K. Lewis, J. Albert Schultz, and Amina S. Woods. "MALDI-ion mobility mass spectrometry of lipids in negative ion mode." *Analytical Methods*, 6 (**2014**): 5001-5007.

12 Jackson, Shelley N., Michael Ugarov, Jeremy D. Post, Thomas Egan, Denis Langlais, J. Albert Schultz, and Amina S. Woods. "A study of phospholipids by ion mobility TOFMS." *Journal of the American Society for Mass Spectrometry*, 19 (**2008**): 1655-1662.

13 Kim, Hugh I., Hyungjun Kim, Eric S. Pang, Ernest K. Ryu, Luther W. Beegle, Joseph A. Loo, William A. Goddard, and Isik Kanik. "Structural characterization of unsaturated phosphatidylcholines using traveling wave ion mobility spectrometry." *Analytical Chemistry*, 81 (**2009**): 8289-8297.

14 Castro-Perez, Jose, Thomas P. Roddy, Nico MM Nibbering, Vinit Shah, David G. McLaren, Stephen Previs, Athula B. Attygalle et al. "Localization of fatty acyl and double bond positions in phosphatidylcholines using a dual stage CID fragmentation coupled with ion mobility mass spectrometry." *Journal of the American Society for Mass Spectrometry*, 22 (**2011**): 1552-1567.

15 Maccarone, Alan T., Jackson Duldig, Todd W. Mitchell, Stephen J. Blanksby, Eva Duchoslav, and J. Larry Campbell. "Characterization of acyl chain position in unsaturated phosphatidylcholines using differential mobility-mass spectrometry." *Journal of Lipid Research*, 55 (**2014**): 1668-1677.

16 Lintonen, Tuulia PI, Paul RS Baker, Matti Suoniemi, Baljit K. Ubhi, Kaisa M. Koistinen, Eva Duchoslav, J. Larry Campbell, and Kim Ekroos. "Differential mobility spectrometry-driven shotgun lipidomics." *Analytical Chemistry*, 86 (**2014**): 9662-9669.

17 Bowman, Andrew P., Rinat R. Abzalimov, and Alexandre A. Shvartsburg. "Broad separation of isomeric lipids by high-resolution differential ion mobility spectrometry with tandem mass spectrometry." *Journal of the American Society for Mass Spectrometry*, 28 (**2017**): 1552-1561.

18 Shvartsburg, Alexandre A. "*Differential Ion Mobility Spectrometry: Nonlinear Ion Transport and Fundamentals of FAIMS*." CRC Press**, 2008**.

19 Dods, Robert H., Jackie A. Mosely, and John M. Sanderson. "The innate reactivity of a membrane associated peptide towards lipids: acyl transfer to melittin without enzyme catalysis." *Organic & Biomolecular Chemistry*, 10 (**2012**): 5371-5378.

20 Dods, Robert H., Burkhard Bechinger, Jackie A. Mosely, and John M. Sanderson. "Acyl transfer from membrane lipids to peptides is a generic process." *Journal of Molecular Biology*, 425 (**2013**): 4379-4387.

21 Clemmer, David E., and Martin F. Jarrold. "Ion mobility measurements and their applications to clusters and biomolecules." *Journal of Mass Spectrometry*, 32 (**1997**): 577-592.

22 Wu, Ching, Jörg Klasmeier, and Herbert H. Hill. "Atmospheric pressure ion mobility spectrometry of protonated and sodiated peptides." *Rapid Communications in Mass Spectrometry*, 13 (**1999**): 1138-1142.

23 Santos, Luiz FA, Amadeu H. Iglesias, Eduardo J. Pilau, Alexandre F. Gomes, and Fabio C. Gozzo. "Traveling-wave ion mobility mass spectrometry analysis of isomeric modified peptides arising from chemical cross-linking." *Journal of the American Society for Mass Spectrometry*, 21 (**2010**): 2062-2069.

24 Sweet, Steve MM, Faraz K. Mardakheh, Kevin JP Ryan, Amy J. Langton, John K. Heath, and Helen J. Cooper. "Targeted online liquid chromatography electron capture dissociation mass spectrometry for the localization of sites of in vivo phosphorylation in human Sprouty2." *Analytical Chemistry*, 80 (**2008**): 6650-6657.

25 Mosammaparast, Nima, and Yang Shi. "Reversal of histone methylation: biochemical and molecular mechanisms of histone demethylases." *Annual Review of Biochemistry*, 79 (**2010**): 155-179.

Chapter six: Conclusion

6.1. Conclusion

The research in this thesis has shown that two of the most abundant biomolecules, lipid and peptides/proteins that are known to exist in close proximity to each other, or interact with each other, are not as chemically inert as previously thought.

In the absence of an enzyme and in physiological conditions, the lipids that form cell membranes can react with and modify melittin via aminolysis reaction in as a little as three hours. This provides lipidated products (PTMs) with increased hydrophobicity and is therefore likely to be missed by standard (LC-based) analytical approaches. Consequently, further steps are required to improve LC-based methods in order to detect more hydrophobic species. These hydrophobic species are proposed to have higher affinity to the hydrophobic part (fatty acyl chain) of membrane lipids and thus sit within the cell membrane. Further, studies of synthetic lipidated peptides have shown that increasing hydrophobicity via lipidation can modulate biological activity, biophysical properties and secondary structure.[1,2] These changes have shown to be highly implicated by the chemical structure of the attached fatty acyl chains and the site of acylation. This implies that lipidated peptide can find an application in drug design/pharmacology through binding to target receptors, as was proposed for synthetic lipidated peptides[1,2].

Although the level of LPL is generally low in natural cells,[3,4] the amount is proposed to increase during fatty acyl transfer from PLs to peptides thus leaving free LPL, as well as LPL production via enzymatic hydrolysis (phospholipase) of PLs. Therefore, lipidation does not just produce modified peptides with modified structure and function but also LPLs which have recently gained more attention. This is because despite LPL's role in phospholipid metabolism, they have been recently shown to exhibit a broad range of biological activities. They have used for developing drugs and targeting diseases and they also play important roles in the development, activation and regulation of the immune system.[5,6] However, the results presented in this thesis also shows acyl transfer in LPL:melittin system even at a faster acylation rate than that for PL:melittin system. Consequently, lipidation can be proposed between lipids with ester-linked fatty acyl chain

and the amino groups of membrane active peptides/proteins. As melittin is recorded to be the most reactive peptide to perform non-enzymatic lipidation[7] and is the major component of honey bee venom,[8,9] elucidating the role of lipidated melittin on its activity in the venom when a mammal has been sting could facilitate targeted therapies or intervention for the allergic reactions caused by bee sting. This is because melittin is reported to be basically responsible for pain and allergens in bee, wasp and ant.[8,9]

Study of non-enzymatic acyl transfer for melittin:lipid system *in vitro* provides the basics to start understanding lipidated proteins *in vivo*. AQP0 has become the focus of special attention because it undergoes many types of PTMs with age, thus increasing protein heterogeneity. Generally, these PTMs of proteins alter their conformation and function.[10-12] Frequently recorded phosphorylation on C-terminal AQP0 was recorded to reduce binding affinity of calmodulin and thus regulating water permeability of AQP0.[13,14] C-terminal truncated AQP0 encourages the protein to from cell-cell junction by removing protein-protein binding region,[14-16] while reported deamidation and isomerization of AQP0 were not fully characterised.[14,17,18] Modified AQP0 with fatty acylation (palmitoylation and oleoylation) may target the protein to lipid raft regions of the plasma membrane.[14,19,20] Consequently, all of these protein modifications are contributing in their localization and functioning *in vivo*. The detection of a broad range of lipidated AQP0 in this research, including palmitoyl (C16:0), palmitoleoyl (C16:1), stearoyl (C18:0), oleoyl (C18:1), eicosenoyl (C20:1), dihomo-γ-linolenoyl (C20:3) and arachidonoyl (C20:4) for both human and bovine eye lens candidates; eicosadienoyl (C20:2), docosadienoyl (C22:2) and docosapentaenoyl (C22:5) only for bovine eye lenses; pentadecenoyl (C15:1) and docosahexaenoyl (C22:6) only for human eye lenses, illustrates that protein fatty acylation is not just restricted to the two major observed protein fatty acylation *in vivo,* including myristoylation and palmitoylation[12,21,22] and recently oleoylation[14,19,20]. These newly observed lipidated species of AQP0 suggest non-enzymatic based acyl transfer because a specific enzyme that is responsible to perform fatty acyl transfer to lysine site of the protein has not yet been identified, as also suggested by Marilyn Resh[12] and Wenke *et al.*[14]. The observation of lipidated AQP0 products that mirror fatty acyl composition

of PE lipid composition of cytoplasmic leaflet of the membrane proximal to lipidated sites additionally suggests chemical lipidation reaction rather than enzymatic acyl transfer.

Finding a range of fatty acylation modification on AQP0, a long-lived protein in the lens, suggests similar lipidation pattern for other long-lived proteins in the lens or other tissues. Therefore, characterizing and understanding the mechanism/activity of these newly recorded lipidated products provide a new insight to understand the role of these lipidation on health and disease. This is because there is the awareness of the relation between long-lived proteins and the resultant protein PTMs with aging and age-related diseases, however, details of this remain to be elucidated.[23-25]

Greater hydrophobicity is also found for the heterogeneous mixture of possible acylation products, particularly evident when more than one acyl chain is transferred to membrane active peptide, melittin, and the integral membrane protein, AQP0. This means both factors, heterogeneity and hydrophobicity, will cause the MS signal for each species will be low and further increase the challenges during their analysis. This is a challenge for understanding the real biological processes within a biological system. Further analysis by ion mobility separation coupled with mass spectrometry (IMS-MS) suggests that covalently bound fatty acyl chains wrap around the peptide and therefore performing less structural changes in the gas-phase by changing the composition or the position of the fatty acyl chain.

6.2. References

1 Zhang, L., and G. Bulaj. "Converting peptides into drug leads by lipidation." *Current Medicinal Chemistry,* 19 (**2012**): 1602-1618.

2 Ward, Brian P., Nickki L. Ottaway, Diego Perez-Tilve, Dejian Ma, Vasily M. Gelfanov, Matthias H. Tschöp, and Richard D. DiMarchi. "Peptide lipidation stabilizes structure to enhance biological function." *Molecular Metabolism,* 2 (**2013**): 468-479.

3 Ansell, G. B., J. M. Hawthorne, and R. M. C. Dawson. "*In Form and Function of Phospholipids*." Elsevier, Amsterdam, **1973**.

4 Stafford, Richard E., Tahsin Fanni, and Edward A. Dennis. "Interfacial properties and critical micelle concentration of lysophospholipids." *Biochemistry,* 28 (**1989**): 5113-5120.

5 D'Arrigo, Paola, and Stefano Servi. "Synthesis of lysophospholipids." *Molecules,* 15 (**2010**): 1354-1377.

6 D'Arrigo, Paola, and Massimo Scotti. "Lysophospholipids: synthesis and biological aspects." *Current Organic Chemistry,* 17 (**2013**): 812-830.

7 Dods, Robert H., Burkhard Bechinger, Jackie A. Mosely, and John M. Sanderson. "Acyl transfer from membrane lipids to peptides is a generic process." *Journal of Molecular Biology,* 425 (**2013**): 4379-4387.

8 Ali, M. A. A. S. M. "Studies on bee venom and its medical uses." *International Journal of Advancements in Research & Technology,* 1 (**2012**): 69-83.

9 Choi, Ji Hae, A. Yeung Jang, Shunmei Lin, Sangyong Lim, Dongho Kim, Kyungho Park, Sang-Mi Han, Joo-Hong Yeo, and Ho Seong Seo. "Melittin, a honeybee venom-derived antimicrobial peptide, may target methicillin-resistant Staphylococcus aureus." *Molecular Medicine Reports,* 12 (**2015**): 6483-6490.

10 Jensen, Ole Nørregaard. "Modification-specific proteomics: characterization of post-translational modifications by mass spectrometry." *Current Opinion in Chemical Biology,* 8 (**2004**): 33-41.

11 Triola, Gemma, Herbert Waldmann, and Christian Hedberg. "Chemical biology of lipidated proteins." *ACS Chemical Biology,* 7 (**2012**): 87-99.

12 Resh, Marilyn D. "Fatty acylation of proteins: The long and the short of it." *Progress in Lipid Research,* 63 (**2016**): 120-131.

13 Lindsey Rose, K. M., Z. Wang, G. N. Magrath, E. S. Hazard, J. D. Hildebrandt, and K. L. Schey. "Aquaporin 0−calmodulin interaction and the effect of aquaporin 0 phosphorylation." *Biochemistry,* 47 (**2008**): 339-347.

14 Wenke, Jamie L., Kristie L. Rose, Jeffrey M. Spraggins, and Kevin L. Schey. "MALDI imaging mass spectrometry spatially maps age-related deamidation and truncation of human lens aquaporin-0 MALDI imaging mass spectrometry." *Investigative Ophthalmology & Visual Science,* 56 **(2015**): 7398-7405.

15 Korlimbinis, Anastasia, Yoke Berry, Danielle Thibault, Kevin L. Schey, and Roger JW Truscott. "Protein aging: truncation of aquaporin 0 in human lens regions is a continuous age-dependent process." *Experimental Eye Research*, 88 (**2009**): 966-973.

16 Schey, Kevin L., Angus C. Grey, and Joshua J. Nicklay. "Mass spectrometry of membrane proteins: a focus on aquaporins." *Biochemistry*, 52 (**2013**): 3807-3817.

17 Schey, Kevin L., Mark Little, John G. Fowler, and Rosalie K. Crouch. "Characterization of human lens major intrinsic protein structure." Investigative Ophthalmology & Visual Science, 41 (**2000**): 175-182.

18 Ball, Lauren E., Donita L. Garland, Rosalie K. Crouch, and Kevin L. Schey. "Post-translational modifications of aquaporin 0 (AQP0) in the normal human lens: spatial and temporal occurrence." *Biochemistry*, 43 (**2004**): 9856-9865.

19 Schey, Kevin L., Danielle B. Gutierrez, Zhen Wang, Junhua Wei, and Angus C. Grey. "Novel fatty acid acylation of lens integral membrane protein aquaporin-0." *Biochemistry*, 49 (**2010**): 9858-9865.

20 Gutierrez, Danielle B., Donita Garland, and Kevin L. Schey. "Spatial analysis of human lens aquaporin-0 post-translational modifications by MALDI mass spectrometry tissue profiling." *Experimental Eye Research*, 93 (**2011**): 912-920.

21 Magee, Tony, and Miguel C. Seabra. "Fatty acylation and prenylation of proteins: what's hot in fat." *Current Opinion in Cell Biology,* 17 (**2005**): 190-196.

22 Triola, G. "The protein lipidation and its analysis." *Journal of Glycomics & Lipidomics*, S2:001 (**2011**): 1-14.

23 Lyons, Brian, Ann H. Kwan, Joanne Jamie, and Roger JW Truscott. "Age-dependent modification of proteins: N-terminal racemization." *The FEBS Journal*, 280 (**2013**): 1980-1990.

24 Liddy, Kiersten A., Melanie Y. White, and Stuart J. Cordwell. "Functional decorations: post-translational modifications and heart disease delineated by targeted proteomics." *Genome Medicine,* 5 (**2013**): 1-12.

25 Santos, Ana L., and Ariel B. Lindner. "Protein posttranslational modifications: roles in aging and age-related disease." *Oxidative Medicine and Cellular Longevity,* 2017 (**2017**): 1-19.

Chapter seven: Future work

7.1. Future work

The aminolysis reaction between melittin/AQP0 and ester-linked fatty acyl chains of lipids that form cell membrane have been characterised in this research. Although melittin acylation has been extensively studied herein, other membrane active peptides such as magainin II, PGLa, LAK1, LAK3 and penetratin are also reported.[1] However, investigating this non-enzymatic acyl transfer is further required to include a comparison study between membrane active peptides and other peptides that do no exhibit membrane binding and permeation due to missing the threshold hydrophobicity and are called non-membrane active peptides. This is also important to study the biological activity of lipidated peptides. In addition, although lipidated proteins are known to regulate protein structure and function,[2-4] lipidated AQP0 with a broad range of saturated and unsaturated fatty acyl chains with their consequences on AQP0 function/structure in the lens is not studied herein. Following the activity of lipidated AQP0 *in vivo* would be particularly important in evaluating the relationship between lipidated AQP0 and cataract of eye lens and thus proposing a cure without a need for operation. Therefore including non-MS based analytical approach is important to investigate non-acylated *vs* acylated peptide/protein structures such as using circular dichroism (CD), solid-state NMR, and X-ray crystallography. These methods of analysis could also provide an insight into investigating differences between melittin:PC *vs* melittin:LPC binding structure and the outcomes of the difference in lipidation reactivity between the two systems that have been reported in this research. In addition, the application of recent improvements in computational studies or called molecular modelling[5] will provide valuable information on the peptide/protein-membrane interactions.

Further analysis is also required to take cells and incubate with melittin and analyse the possible products. The challenge here would be to detect such a low amount of hydrophobic products. Improving liquid chromatography (LC) and mass spectrometry (MS) instrument parameters could also have a great impact on observing previously undetected low abundance modified peptides/proteins. One approach could be the application of nanospray MS in attempt to increase the sensitivity. Using long

gradient chromatography is also essential, as was found in enhancing protein identification from biological complex mixture or whole cell extracts.[6,7] Further improvement will be to deal with dynamic range problem[8] due to the incredibly low abundance of modify peptides in the presence of highly abundant unmodified peptide. If a successful extraction of acylated peptides will be achieved and followed by their study alone then there will be a potential to optimise the chromatography separation for these species.

Collision induced dissociation (CID) was exclusively used as a fragmentation technique throughout this research to characterise/localise lipidation sites. However, using other fragmentation techniques such as electron capture dissociation (ECD) and electron transfer dissociation (ETD) may further characterise lipidation products and produce complementary tandem mass spectra. Because theses electron-based techniques are known to be more favourable towards labile modification, cleaving the backbone bonds and preserving the modified side chain.[9-11]

More challenges were found in resolving overlapped peaks in chromatography. Even with single acylation products in one of the four abundant places of acylation on melittin we could barely resolve chromatographically different acyl modifications on the same amino acid residue. Consequently, this is a challenge for quantification approach for lipidated products and thus a lack in fully understanding the kinetics of lipidated peptides/proteins. This research shows that for acylated peptides with lower charge state the different isomers have conformations sufficiently different to begin to separate by ion mobility separation (IMS) coupled with MS or MS^2, but there is still much here that can be improved. One approach could be to use other ion mobility gases other than N_2 that has been used in this study, such as Ar, CO_2, He or mixtures of these regarding their difference in polarizabilities, sizes, and shapes.[12] Kaszycki *et al*.[13] showed that adding light gases such as He to heavier gases such as N_2 tremendously improves the separation of isomeric species of peptide, protein and lipids. Using He-rich gases in IMS is also suggested by Shvartsburg *et al*.[14] to improve the resolution of lipid isomers.

In addition, investigating experimental parameters surrounding sample preparation can also explore further details. Such that include optimizing enzymatic digestion, pH control and adding/removing salts. Adding salt cations[12,15] such as Li or Na to change peptide/lipid ions from protonated species to cation may make the cation to sit in a different place on the acylated product. This may affect charge state distribution, ionisation and collision cross-section (CCS or Ω). This would also help electron-based tandem MS. Wu *et al*.[15] showed that replacing a proton by sodium for peptide ions cause a decrease in CCS. This is because Na ion strongly coordinates with functional groups on the peptide backbone and stabilizes gas phase conformation.

7.2. References

1 Dods, Robert H., Burkhard Bechinger, Jackie A. Mosely, and John M. Sanderson. "Acyl transfer from membrane lipids to peptides is a generic process." *Journal of Molecular Biology,* 425 (**2013**): 4379-4387.

2 Jensen, Ole Nørregaard. "Modification-specific proteomics: characterization of post-translational modifications by mass spectrometry." *Current Opinion in Chemical Biology,* 8 (**2004**): 33-41.

3 Triola, Gemma, Herbert Waldmann, and Christian Hedberg. "Chemical biology of lipidated proteins." *ACS Chemical Biology,* 7 (**2012**): 87-99.

4 Resh, Marilyn D. "Fatty acylation of proteins: The long and the short of it." *Progress in Lipid Research,* 63 (**2016**): 120-131.

5 Li, Zhen-lu, Hong-ming Ding, and Yu-qiang Ma. "Interaction of peptides with cell membranes: insights from molecular modeling." *Journal of Physics: Condensed Matter,* 28 (**2016**): 1-17.

6 Köcher, Thomas, Peter Pichler, Remco Swart, and Karl Mechtler. "Analysis of protein mixtures from whole-cell extracts by single-run nanoLC-MS/MS using ultralong gradients." *Nature Protocols,* 7 (**2012**): 882-890.

7 Wang, Hong, Yanling Yang, Yuxin Li, Bing Bai, Xusheng Wang, Haiyan Tan, Tao Liu, Thomas G. Beach, Junmin Peng, and Zhiping Wu. "Systematic optimization of long gradient chromatography mass spectrometry for deep analysis of brain proteome." *Journal of Proteome Research,* 14 (**2014**): 829-838.

8 Hortin, Glen L., and Denis Sviridov. "The dynamic range problem in the analysis of the plasma proteome." *Journal of Proteomics,* 73 (**2010**): 629-636.

9 Srikanth, R., Jonathan Wilson, Juma D. Bridgewater, Jason R. Numbers, Jihyeon Lim, Mark R. Olbris, Ali Kettani, and Richard W. Vachet. "Improved sequencing of oxidized cysteine and methionine containing peptides using electron transfer dissociation." *Journal of the American Society for Mass Spectrometry*, 18 (**2007**): 1499-1506.

10 Creese, Andrew J., and Helen J. Cooper. "Liquid chromatography electron capture dissociation tandem mass spectrometry (LC-ECD-MS/MS) versus liquid chromatography collision-induced dissociation tandem mass spectrometry (LC-CID-MS/MS) for the identification of proteins." *Journal of the American Society for Mass Spectrometry,* 18 (**2007**): 891-897.

11 Breuker, Kathrin, Mi Jin, Xuemei Han, Honghai Jiang, and Fred W. McLafferty. "Top-down identification and characterization of biomolecules by mass spectrometry." *Journal of the American Society for Mass Spectrometry,* 19 (**2008**): 1045-1053.

12 Kim, Hugh I., Hyungjun Kim, Eric S. Pang, Ernest K. Ryu, Luther W. Beegle, Joseph A. Loo, William A. Goddard, and Isik Kanik. "Structural characterization of unsaturated phosphatidylcholines using traveling wave ion mobility spectrometry." *Analytical Chemistry,* 81 (**2009**): 8289-8297.

13 Kaszycki, Julia L., Andrew P. Bowman, and Alexandre A. Shvartsburg. "Ion mobility separation of peptide isotopomers." *Journal of the American Society for Mass Spectrometry,* 27 (**2016**): 795-799.

14 Shvartsburg, Alexandre A., Giorgis Isaac, Nathalie Leveque, Richard D. Smith, and Thomas O. Metz. "Separation and classification of lipids using differential ion mobility spectrometry." *Journal of the American Society for Mass Spectrometry*, 22 (**2011**): 1146-1155.

15 Wu, Ching, Jörg Klasmeier, and Herbert H. Hill. "Atmospheric pressure ion mobility spectrometry of protonated and sodiated peptides." *Rapid Communications in Mass Spectrometry*, 13 (**1999**): 1138-1142.

Chapter eight: Materials and methods

8.1. Sample preparation and instrument parameters for chapter three - Understanding the role of lysophosphatidylcholine (LPC) and diacylphosphatidylcholine (PC) in the lipidation of melittin

8.1.1. Chemicals and sample preparation

8.1.1.1. Liposome and lysophospholipid preparation

All diacylphospholipids (PLs) 1,2-dioleoyl-*sn*-glycero-3-phosphatidylcholine (DOPC), 1,2-dipalmitoyl-*sn*-glycero-3-phosphatidylcholine (DPPC), 1-palmitoyl-2-oleoyl-*sn*-glycero-3-phosphatidylcholine (POPC), 1-oleoyl-2-palmitoyl-*sn*-glycero-3-phosphatidylcholine (OPPC), and 1,2-dimyristoyl-*sn*-glycero-3-phosphatidylcholine (DMPC) were purchased from Sigma-Aldrich, UK while 1-stearoyl-2-linoleoyl-*sn*-glycero-3-phosphatidylcholine (SLPC) and 1-stearoyl-2-linoleoyl-*sn*-glycero-3-phosphatidylserine (SLPS) were purchased from Avanti Polar Lipids, USA. Lysophospholipids (LPLs) 1-oleoyl-2-hydroxy-*sn*-glycero-3-phosphatidylcholine (OPC), 1-palmitoyl-2-hydroxy-*sn*-glycero-3-phosphatidylcholine (PPC), 1-oleoyl-2-hydroxy-*sn*-glycero-3-phosphatidylserine (OPS), 1-oleoyl-2-hydroxy-*sn*-glycero-3-phosphatidylethanolamine (OPE), and 1-oleoyl-2-hydroxy-*sn*-glycero-3-phosphatidylglycerol (OPG) were purchased from Avanti Polar Lipids, USA. Stock solutions of PLs were prepared in $CHCl_3$ at 1 mg/mL. Chloroform was purchased from Fisher Scientific, UK. These solutions were then used to produce individual PC liposomes and/or a binary lipid system of 4:1 molar ratio for PC:PS. A volume of dissolved PC was transferred to a highly cleaned 5 mL round bottom flask. After mixing well (vortex-mixer), the organic solvent was removed *in vacuo* to leave a thin film of lipid on the side of the flask. The lipid film was then left overnight under vacuum to remove any residual organic solvent. The concentration of lipid was made to 1 mg/mL in aqueous buffer solution: 10 mM sodium bicarbonate ($NaHCO_3$) and 90 mM sodium chloride (NaCl), pH 7.4. The lipid dispersion in 1 mL aqueous buffer solution was then subjected to five freeze-thaw cycles (from liquid nitrogen temperature to 55 °C) and extruded 10 times through a track-etched 100 nm

polycarbonate membrane (Whatman), using a thermobarrel extruder (Northern Lipids Inc., Burnaby, Canada) under a stream of N_2 to give a 100 nm diameter of unilamellar liposomes. The extruder was warmed first at 50 °C, which is a temperature above phase transition temperature for all prepared lipids. LPL solutions were prepared by dilution in the aqueous buffer solution (10:90 $NaHCO_3$:NaCl, pH 7.4) to a final concentration of 1.3 mM.

8.1.1.2. Melittin acylation preparation

Synthetic melittin (SynM, ≥ 97% by HPLC, UK) and extracted melittin from bee venom (BVM, 85% by HPLC, UK) were purchased from Sigma-Aldrich, and a stock solution was prepared at approximately 1 mg/mL in water. Water was purified using Milli-Q Direct Q system from Millipore (Millipore (UK) Ltd) with resistivity approximately 18.2 MΩ cm. The actual concentration was determined using absorbance measurement on UV spectrophotometer (VARIAN Carry 50 Bio) at wavelength (λ = 280 nm) with molar absorption coefficient 5500 $M^{-1}cm^{-1}$ for the tryptophan amino acid residue.[1] The dispersed LPLs and PC liposomes were then combined at molar ratios: 100:0, 75:25, 50:50, 25:75 and 0:100 in addition of 50:50 a pair of LPLs with different acyl chains. Prepared lipid solutions then mixed with SynM and/or BVM so as to give the molar ratio 1:13 of peptide:total lipid ratio (**peptide:lipid**), giving a final concentration of 50 µM of peptide and 0.65 mM of lipid. The final **peptide:lipid** mixture incubated at 37 °C for 0, 3, 24, 48, 96, and 168 h respectively, diluted by a factor of 5 in water and analysed by reverse phase LC-MS.

8.1.2. LC-MS and instrument parameters

8.1.2.1. LC-MS on LTQFT instrument

8.1.2.1.1. LC-FTICR-MS

The positive ion mass spectra were recorded over *m/z* 200-2000 using an LTQFT mass spectrometer equipped with a 7 Tesla magnet

(ThermoFinnigan Corporation, Bremen, Germany). Electrospray ionisation (ESI) was used to generate positive ions from the following conditions: source voltage 4.0 kV, capillary voltage 30.0 V, capillary temperature 350.0 °C and tube lens 100.0 V. The auxiliary gas flow and sweep gas flow were set at 5.0 arbitrary units; nitrogen sheath gas flow at 15.0 arbitrary units. Separation was achieved by reverse phase LC (Surveyor HPLC from ThermoFisher Scientific Inc.) using an Xbridge C18 column: 3.5 µm particle size and 2.1 mm internal diameter, 100 mm length (Waters UK, Manchester, UK) by injecting 5 µL sample volumes into a solvent flow rate of 200 µL/min. LC separation used the following eluents: aqueous phase (A) was 0.1% (v/v) formic acid in water; organic phase (B) consisted of 0.1% (v/v) formic acid in acetonitrile; organic phase (C) consisted of 0.1% (v/v) formic acid in methanol. The organic solvents for the LC mobile phases were purchased from Scientific Fisher, UK.

- **LC-MS Method-I** used a total run time of 20 min with the reverse phase gradient composed of 95% A: 5% B to 5% A: 95% B over 10 min, followed by 5 mins washing at 5% A: 95% B, then 5 min re-equilibration at 95%A: 5% B.
- **LC-MS Method-II** used a 35 min LC run with the reverse phase gradient of 95% A: 5% B to 5% A: 95% B over 10 min, followed by 5 min at 100% B and 15 min at 100% C, with 5 min re-equilibration at 95%:A5% B.

Xcalibur software version 2.0.7 was used for data acquisition and processing used the embedded program Qual Browser (ThermoFisher Scientific Inc.). The spectral deconvolution was also performed with Qual Browser (ThermoFisher Scientific Inc.). The charge state distribution was deconvoluted to $[M + H]^+$ in each case. R Statistical Environment[2] in the XCMS package[3] was also applied for further data processing.

8.1.2.1.2. LC-LTQ-MS^2

For tandem MS experiments (MS^2), the precursor ion was isolated with a fixed isolation window of 4 *m/z* in the LTQ mass analyser and

activated through collisions with helium gas with normalised collision energy at 25%. Product ions resulting from the collision induced dissociation (CID) were measured in the linear ion trap (LTQ) The same mass spectrometer settings and LC conditions were used as described earlier (see section 8.1.2.1.1).

8.1.2.2. LC-MS on Synapt G2-s instrument

8.1.2.2.1. LC-QToF-MS

The Synapt G2-s (Waters corp.) was operated using ESI to generate positive ions. The source settings were optimized at 1.0 kV of capillary voltage, 20.0 V sample cone, and a source offset at 40.0 V. The source and desolvation temperature were set at 150.0 and 300.0 °C respectively with using cone gas and desolvation gas flow at 60.0 and 450.0 L/h respectively. The samples were separated on Xbridge C18 column, the same column that used and described earlier (see section 8.1.2.1.1), by injecting 1 µL sample volume at a solvent flow rate of 600 µL/min using Acquity UPLC^{TM} I class.

- **LC-MS Method-III** a 6 min LC separation used the following reverse phase gradient: 80% A: 20% B to 40% A: 60% B followed by 30% A: 70% B and then 5% A: 95% B over 4 min, followed by 1.4 min at 5% A: 95% B and 0.6 min re-equilibration at 80% A: 20% B.

A full scan ToF-MS over the mass range of 50-2000 *m/z* was recorded in the resolution mode. The data was acquired in centroid format and fully processed using MassLynx software version 4.1 SCN924.

8.2. Sample preparation and instrument parameters for chapter four - New insight to integral membrane protein (AQP0) lipidation by membrane lipids

8.2.1. Chemicals and sample preparation

8.2.1.1. Chemicals

Bovine eye lenses from calves (age 6–12 months) were obtained from Linden Burradon Food Supply (FSA Approval No.2056). Human lenses from different candidates were obtained: male donors ages 22 (M22), 56 (M56), and 80 (M80) and female donors ages 56 (F56) and 76 (F76) from the Bristol Eye Bank with national research ethics committee approval and were used as recommended by the Declaration of Helsinki and following the procedures recommended under the Human Tissue Authority license to the University of Durham. All the required chemicals to make various buffers for the bovine/human lens membrane washing and extraction were purchased from VWR. Proteomics grade trypsin from porcine pancreas, dithiothreitol (DTT) and sodium dodecyl sulfate (SDS) were purchased from Sigma-Aldrich, UK. Pentafluorooctanoic acid (PFOA) was purchased from Analytical grade. Purified water was used for all the preparations.

8.2.1.2. Lens membrane extraction

Integral membrane proteins were purified by designing a sequential extraction method,[4] this then adapted to purify human/bovine lens membranes rich in AQP0 protein[5,6]. The sequential extraction method was as follows: **buffer 1** contains 10 mM sodium phosphate (pH 7.4), 100 mM NaCl and 5 mM EDTA; **buffer 2** contains 10 mM sodium phosphate (pH 7.4), 1.5 M NaCl and 5 mM EDTA; **buffer 3** contains 10 mM ammonium bicarbonate containing 1 mM EDTA pH 8.0; **buffer 4** contains 10 mM sodium phosphate (pH 7.4), 8 M urea and 5 mM EDTA; **buffer 5** composed of a highly basic solution of 0.1 M NaOH. All buffers were kept at 4 °C. A ratio of 2:1 buffer:lens was maintained throughout the procedure. The bovine eye lenses were decapsulated and the lenses aqua-dissected by stirring in **buffer 1** to remove sequentially the youngest (cortical) fibre cells through to the oldest

(nuclear) fibre cells. Lens fibre cell extracts were first Dounce homogenized and then centrifuged (rav = 30,000 x g 20 minutes, 4 °C; Beckman JA-20 rotor) to separate the membrane and cytosol fractions. Membrane fractions were defined by the diameter of the residual lens membranes in the remaining pellet, generating four different b-AQP0 age fractions as follows; b-AQP0-outer cortex 15 mm (b-AQP0-OC, the youngest), b-AQP0-inner cortex 10 mm (b-AQP0-IC), b-AQP0-outer nucleus 8 mm (b-AQP0-ON) and the oldest part of b-AQP0-inner nucleus 4 mm (b-AQP0-IN, the oldest). Membrane pellets from the four different lens regions were re-suspended in the appropriate buffer in the sequence above, Dounce homogenized, stirred for 20 min and then re-centrifuged. Membranes were always washed once with **buffer 1** when transitioning to a new extraction buffer. At the conclusion of the extraction procedure, membrane pellets were stored in **buffer 3** containing 0.02% sodium azide (w/v) as a preservative and kept at 4 °C until analysis. Human lens samples were initially prepared similarly as described[7], and stored at −20 °C, before completing the extraction protocol with **buffers 3-5** as described above. The two main fractions obtained from human lens pellet were h-AQP0-cortex 4 mm (b-AQP0-C, the youngest) and h-AQP0-nucleus 8 mm (h-AQP0-N, the oldest).

8.2.2. LC-MS and instrument parameters

The applied LC-MS methods and digestion protocols is provided in Table 8.1. The digestion protocols; **Method-A, Method-B, Method-C and Method-D** will be discussed and explained in the following sections 8.2.2.1.2 and 8.2.2.2.1. LC-MS methods, **Method-I** and **Method-II**, were discussed in section 8.1.2.1.1, While **Method-IIII** will be discussed in section 8.2.2.2.1.

Table 8.1. **Different digestion protocols and LC-MS methods used in AQP0 analysis.**

Digestion Protocol	Reagent	Method Description	LC-MS method
Method-A	DTT (protein reducing agent)	10 µL DTT (100 mM)	**Method-I and Method-II**
Method-B	DTT + Urea (protein denaturant)	10 µL DTT (100 mM) + 7 M Urea, followed by dilution so as to give less than 1 M urea	**Method-II**
Method-C	DTT + PFOA (surfactant)	10 µL DTT (100 mM) + 0.8% (w/v) PFOA	**Method-II**
Method-D	DTT + SDS (surfactant/detergent)	10 µL DTT (100 mM) + 100 µL (0.1% (w/v)) SDS	**Method-IIII**

8.2.2.1. LC-MS on LTQFT instrument

8.2.2.1.1. Analysis of intact protein by LC-FTICR-MS

An aliquot of suspended b-AQP0 in **buffer 3** plus 0.02% sodium azide was solubilized in 0.8% PFOA (w/v) and centrifuged using a mini centrifuge for 1 minute. The supernatant was analysed using a reverse phase LC using an Xbridge BEH300 C4 column: 3.5 µm particle size and 2.1 mm internal diameter, 150 mm length (Waters Ltd., USA) by injecting 5 µL sample volumes into a solvent flow rate of 200 µL/min. The same LC and MS conditions that described in section 8.1.2.1.1 (**LC-MS Method-I**) were also applied for intact b-AQP0 analysis. Data were acquired and processed using Xcalibur software.

8.2.2.1.2. Analysis of protein digestion by LC-FTICR-MS

An aliquot of 100 µL re-suspended b-AQP0 in **buffer 3** plus 0.02% sodium azide was combined with the reagents represented in Table 8.1, **Methods A-C**. This followed by adding 10 µL of trypsin (0.2 mg/mL in a 50 mM acetic acid) in each described method, and the solution then incubated for 24 h at 37 °C. The supernatant solution after 1 min centrifugation was run

on LC-FTICR-MS using **Method-I** and/or **Method-II** through Xbridge C18 column and the same conditions described in section 8.1.2.1.1.

8.2.2.2. LC-MS on Synapt G2-s instrument

8.2.2.2.1. Analysis of protein digestion by LC-QToF-MS

An aliquot of 100 µL re-suspended AQP0 in **buffer 3** plus 0.02% sodium azide digested using the following digestion protocol: **Method-D** (see Table 8.1) 10 min sample sonication at 37 °C (Ultrawave Ltd., Cardiff, UK), followed by centrifuging the sample for 2 min at 13000 rpm and then the supernatant was discarded and 100 µL of 0.1% (w/v) SDS was added, followed by adding 10 µL of each DTT (100 mM) and trypsin (0.2 mg/mL in a 50 mM acetic acid). After gentle mixing, the mixture was incubated at 37 °C for 24 h and centrifuged for 2 min at 13000 rpm. The supernatant was analysed by LC-QToF-MS. Reverse phase LC was performed by injecting 5 µL digested sample at a flow rate 400 µL/min. MassLynx was used for full data processing (se section 8.1.2.2.1).

- **LC-MS Method-IIII** A 12 min LC run used the following reverse phase gradient: 95% A: 5% B to 5% A: 95% B over 8 minute followed by 5% A: 95% B for 2 minute and then 95% A: 5% B over 2 minute for column re-equilibration by using the same Xbridge C18 column and the A and B eluent compositions as described in section 8.1.2.1.1. Details for MS conditions are given in section 8.1.2.2.1.

8.2.2.2.2. Analysis of protein digestion by LC-QToF-MS^2 and LC-QToF-MS^E

Using the same LC conditions (see section 8.2.2.2.1, **LC-MS Method-IIII**) and MS conditions (see section 8.1.2.2.1), tandem MS spectra were obtained by collision induced dissociation (CID) in the trap cell of the Triwave. This is performed by using helium as a collision gas. MS^2 of an isolated precursor ion or MS^E for all ions were acquired with a trap collision energy ramp set at 30–50 eV.

8.2.3. Analysis of intact protein by MALDI-ToF-MS (Autoflex II instrument)

MALDI-MS analysis was performed on intact b-AQP0 samples by calibrating the instrument first for a mixture of standard proteins. The standard calibrant made of myoglobin, cytochrome c, and ubiquitin mixture and they were mixed with sinapinic acid (SA) matrix which made in 30:70 acetonitrile:water with 0.1% trifluoroacetic acid (TFA) at a ratio of 1:9. Prior spotting 2 x 0.5 µL aliquots of this pre-prepared matrix:protein calibration solution on top of each other, spot 0.5 µL of SA matrix made in ethanol and allow it to air dry. The same preparation and spotting conditions were also applied on the biological sample of b-AQP0 after extracting from bovine lenses. The data were acquired on Autoflex II MALDI-ToF spectrometer with 337 nm nitrogen laser (Bruker Daltonics Ltd., Coventry, UK) in positive linear mode by using 200 shots for each 45 laser pulses. Methanol and acetone were used for cleaning a ground steel target plate before using. Data were processed using Flex Analysis version from 3.0 Bruker Daltonics Ltd. (Coventry, UK).

8.2.4. Prediction of potential lipid binding regions

Sections in the C-terminal region of AQP0 with the potential for lipid binding were identified using HELIQUEST[8] and the Discrimination Factor, *D*, calculated using the equation $D = 0.944 (\langle \mu H \rangle) + 0.33 (z)$.[9] When this discrimination factor is above 0.68, the corresponding sequence can be considered to be a (potential) lipid-binding region[9,10].

8.3. Sample preparation and instrument parameters for chapter five - Application of ion mobility separation-mass spectrometry (IMS-MS) to the analysis of phosphatidylcholine and synthetic lipidated melittin analogues

8.3.1. Chemicals and sample preparation

The purchase details and the preparation of stock solutions for PCs (DOPC, DMPC, DPPC, SLPC, POPC and OPPC) and LPCs (PPC and OPC) were described earlier in section 8.1.1.1. Sample solutions of PC and LPC were diluted from stock solution (1 mg/mL) to 0.5 µg/mL with 1:1 water:acetonitrile with 0.1% (v/v) formic acid. Synthetic lipidated melittin analogous, including N-palmitoyl melittin (N-M_{pal}), K23-palmitoyl melittin (K23-M_{pal}), N-oleoyl melittin (N-M_{ole}) and K23-oleoyl melittin (K23-M_{ole}) were synthesized by ALMAC (Elvingston Science Centre by Gladsmuir, East Lothian, Scotland, UK) and were prepared as stock solution in water at concentration 1 mg/mL. This then diluted to 1 µg/mL with 1:1 water:acetonitrile with 0.1% (v/v) formic acid. All solutions were directly infused into ESI-IMS-MS at a flow rate of 5 µL/min using a syringe pump (Harvard Apparatus, Holliston, MA, U.S.).

8.3.2. IMS-MS/MS^2 and instrument parameters on Synapt G2-s instrument

8.3.2.1. IMS-MS analysis for phosphatidylcholine

For ion mobility separation by using traveling wave ion mobility spectrometry (TWIMS), N_2 drift gas was used at a flow rate of 70 mL/min. An optimised T-wave velocity of 1000 m/s and T-wave height of 40 V was used. The source settings (ESI+) were optimized at 1.5 kV of capillary voltage, 50.0 V sample cone, and a source offset at 30.0 V. The source and desolvation temperature were set at 150.0 and 500.0 °C respectively with using cone gas and desolvation gas flow at 60.0 and 500.0 L/h respectively. A full scan ToF-MS over the mass range of 50-2000 *m/z* was recorded in the resolution mode. Data were acquired in continuum format for 1 min and at 1 second

scan time. The data was processed using MassLynx software version 4.1 SCN924 and DriftScope version 2.7.

8.3.2.2. IMS-MS/MS^2 analysis for synthetic lipidated melittin analogues

TWIMS by using N_2 drift gas was optimised at T-wave velocity of 800 m/s and T-wave height of 40.0 V for both IMS-MS and IMS-MS^2. The source settings (ESI+) were optimized at 3.0 kV of capillary voltage, 70.0 V sample cone, and a source offset at 50.0 V. The source and desolvation temperature were set at 150.0 and 350.0 °C respectively with using cone gas and desolvation gas flow at 60.0 and 600.0 L/h respectively. Data were acquired for 3 min and at 1 second scan time. For IMS-MS^2 a precursor ion was selected at the resolving quadruplole and followed by ion mobility separation. Collision energy (CID) in the transfer cell of Triwave (TWIMS) was used to fragment isolated precursor ion with a ramp Transfer collision energy at 20-35 eV by using helium as a collision gas, while trap collision energy set at fixed collision energy of 4 eV. MassLynx was used for data processing (see section 8.3.2.1).

8.4. Reference

1 Edelhoch, Harold. "Spectroscopic determination of tryptophan and tyrosine in proteins." *Biochemistry*, 6 (**1967**): 1948-1954.

2 R Development Core Team R "a language and environment for statistical computing, R Foundation for Statistical Computing." Vienna, Austria (**2008**). (*ISBN 3-900051-07-0, URL http://www.R-project.org*).

3 Benton, H. Paul, Dawn M. Wong, Sunia A. Trauger, and Gary Siuzdak. "XCMS2: processing tandem mass spectrometry data for metabolite identification and structural characterization." *Analytical Chemistry*, 80 (**2008**): 6382-6389.

4 Milks, Linda C., Nalin M. Kumar, Richard Houghten, Nigel Unwin, and Norton B. Gilula. "Topology of the 32-kd liver gap junction protein determined by site-directed antibody localizations." *The European Molecular Biology Organization Journal*, 7 (**1988**): 2967-2975.

5 Der Perng, Ming, Aileen Sandilands, Jer Kuszak, Ralf Dahm, Alfred Wegener, Alan R. Prescott, and Roy A. Quinlan. "The intermediate filament systems in the eye lens." *Methods in Cell Biology*, 78 (**2004**): 597-624.

6 Schey, Kevin L., Danielle B. Gutierrez, Zhen Wang, Junhua Wei, and Angus C. Grey. "Novel fatty acid acylation of lens integral membrane protein aquaporin-0." *Biochemistry*, 49 (**2010**): 9858-9865.

7 Quinlan, Roy A., Jane M. Carter, Aileen M. Hutcheson, and David G. Campbell. "The 53 kDa polypeptide component of the bovine fibre cell cytoskeleton is derived from the 115 kDa beaded filament protein: evidence for a fibre cell specific intermediate filament protein." *Current Eye Research*, 11 (**1992**): 909-921.

8 Gautier, Romain, Dominique Douguet, Bruno Antonny, and Guillaume Drin. "HELIQUEST: a web server to screen sequences with specific α-helical properties." *Bioinformatics*, 24 (**2008**): 2101-2102.

9 Keller, Rob CA. "New user-friendly approach to obtain an Eisenberg plot and its use as a practical tool in protein sequence analysis." *International Journal of Molecular Sciences*, 12 (**2011**): 5577-5591.

10 Keller, Rob CA. "The prediction of novel multiple lipid-binding regions in protein translocation motor proteins: a possible general feature." *Cellular & Molecular Biology Letters*, 16 (**2010**): 40-54.

Chapter nine: Appendices

9.1. Appendix A

Table 9.1. **Amino acid residues with their abbreviation and molecular mass.**

AA Molecular Formula	3-Letter Code	1-Letter Code	Mass (Da)	AA Molecular Formula	3-Letter Code	1-Letter Code	Mass (Da)
Glycine (C_2H_3NO)	Gly	G	57	**Aspartic acid ($C_4H_5NO_3$)**	Asp	D	115
Alanine (C_3H_5NO)	Ala	A	71	**Glutamine ($C_5H_8N_2O_2$)**	Gin	Q	128
Serine ($C_3H_5NO_2$)	Ser	S	87	**Lysine ($C_6H_{12}N_2O$)**	Lys	K	128
Proline (C_5H_7NO)	Pro	P	97	**Glutamic acid ($C_5H_7NO_3$)**	Glu	E	129
Valine (C_5H_9NO)	Val	V	99	**Methionine (C_5H_9NOS)**	Met	M	131
Threonine ($C_4H_7NO_2$)	Thr	T	101	**Histidine ($C_6H_7N_3O$)**	His	H	137
Cysteine (C_3H_5NOS)	Cys	C	103	**Phenylalanine (C_9H_9NO)**	Phe	F	147
Isoleucine ($C_6H_{11}NO$)	lie	I	113	**Arginin ($C_6H_{12}N_4O$)**	Arg	R	156
Leucine ($C_6H_{11}NO$)	Leu	L	113	**Tyrosine ($C_9H_9NO_2$)**	Tyr	Y	163
Aspargine ($C_4H_6N_2O_2$)	Asn	N	114	**Tryptophan ($C_{11}H_{10}N_2O$)**	Trp	W	186

Table 9.2. **The structure and nomenclature for common phospholipids used in this research.**

Phospholipids Nomenclature	Phospholipids Structure
1,2-dioleoyl-*sn*-glycero-3-phosphatidylcholine (DOPC)	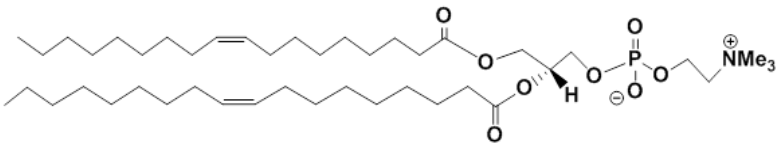
1,2-dipalmitoyl-*sn*-glycero-3-phosphatidylcholine (DPPC)	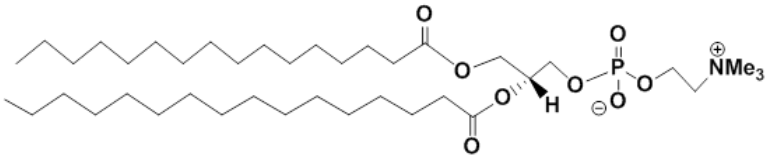
1,2-dimyristoyl-*sn*-glycero-3-phosphatidylcholine (DMPC)	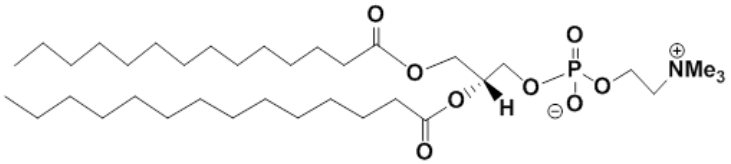
1-stearoyl-2-linoleoyl-*sn*-glycero-3-phosphatidylcholine (SLPC)	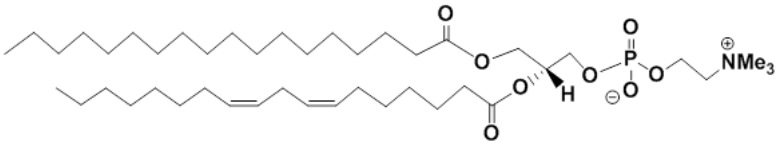
1-palmitoyl-2-oleoyl-*sn*-glycero-3-phosphatidylcholine (POPC)	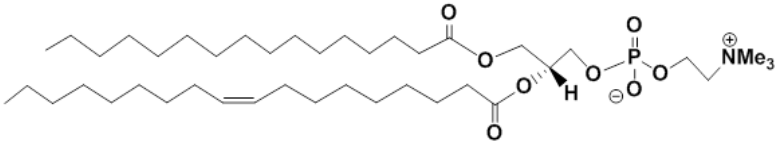
1-oleoyl-2-palmitoyl-*sn*-glycero-3-phosphatidylcholine (OPPC)	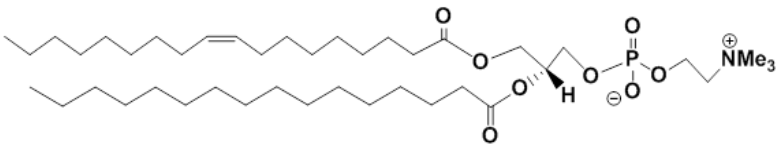

1-stearoyl-2-linoleoyl-*sn*-glycero-3-phosphatidylserine (SLPS)	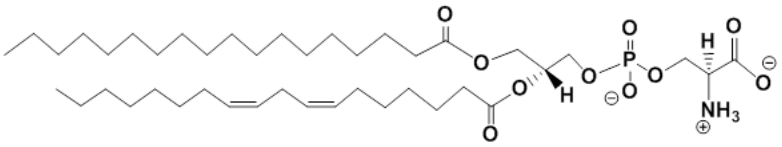
1-oleoyl-2-hydroxy-*sn*-glycero-3-phosphatidylcholine (OPC)	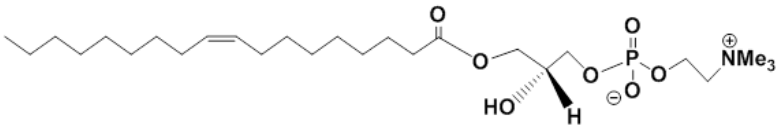
1-palmitoyl-2-hydroxy-*sn*-glycero-3-phosphatidylcholine (PPC)	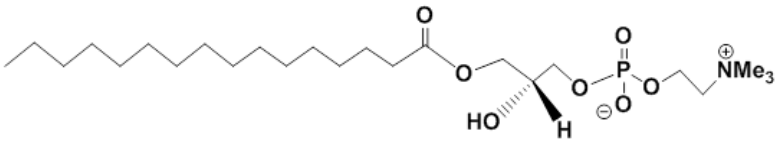
1-oleoyl-2-hydroxy-*sn*-glycero-3-phosphatidylserine (OPS)	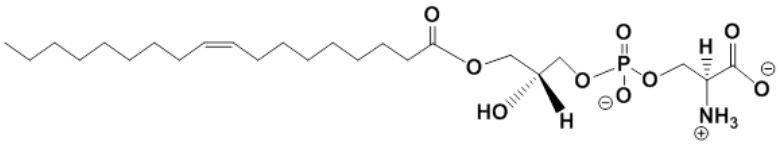
1-oleoyl-2-hydroxy-*sn*-glycero-3-phosphatidylethanolamine (OPE)	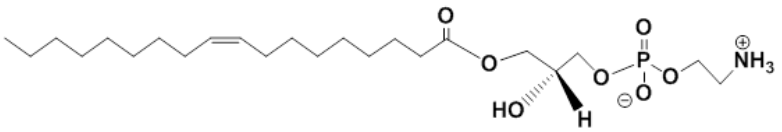
1-oleoyl-2-hydroxy-*sn*-glycero-3-phosphatidylglycerol (OPG)	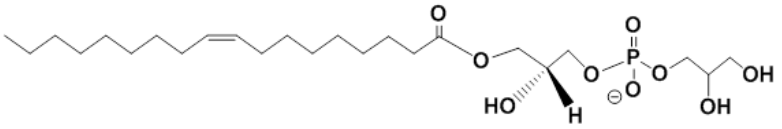

9.2. Appendix B: Supplementary information for Chapter three - Understanding the role of lysophosphatidylcholine (LPC) and diacylphosphatidylcholine (PC) in the lipidation of melittin

Table 9.3. **The range of single and multiple acylation ions observed from SynM/50:50 PPC:DOPC incubation at 37 °C for 168 h.**

^{1}H-GIGAVLKVLTTGLPALISWIKRKRQQ-NH_2 ^{26}					
***m/z* Theor‡**	***m/z* Meas‡**	***z***	**Error (ppm)**	**RT (min)**	**Assignment**
1037.3404	1037.3423	3	1.83	8.9	$SynM_{ole}$/single oleoylation
778.2572	778.2580	4	1.03		
622.8072	622.8076	5	0.64		
1028.6686	1028.6689	3	0.29	8.5	$SynM_{pal}$/single palmitoylation
771.7532	771.7532	4	0.00		
617.6040	617.6048	5	1.30		
1125.4222	1125.4205	3	-1.51	11.0	$SynM_{2ole}$/double oleoylation
844.3185	844.3196	4	1.30		
675.6562	675.6562	5	0.00		
1108.0784	1108.0811	3	2.44	11.0	$SynM_{2pal}$/double palmitoylation
831.3107	831.3117	4	1.20		
665.2500	665.2509	5	1.35		
1116.7503	1116.7489	3	-1.25	11.0	$SynM_{pal+ole}$ / single palmitoylation + single oleoylation
837.8146	837.8157	4	1.31		
670.4531	670.4540	5	1.34		
1125.4222	1125.4242	3	1.78	17.8	$SynM_{3ole}$/labile triple oleoylation
844.3185	844.3190	4	0.59		
1108.0784	1108.0554	3	-20.76	17.7	$SynM_{3pal}$/labile triple palmitoylation
831.3107	831.3108	4	0.12		
1116.7503	1116.7476	3	-2.42	17.7	$SynM_{2pal+ole}$ or $SynM_{2ole+pal}$/labile (double palmitoylation + single oleoylation) or (double oleoylation + single palmitoylation)
837.8146	837.8159	4	1.55		
670.4531	670.4553	5	3.28		
1213.5040	1213.5038	3	-0.16	18.1	$SynM_{3ole}$/triple oleoylation
910.3798	910.3758	4	-4.39		
1187.4883	1187.4899	3	1.35	18.2	$SynM_{3pal}$/triple palmitoylation
890.8681	890.8683	4	0.22		
1204.8321	1204.8300	3	-1.74	18.1	$SynM_{2ole+pal}$/double oleoylation + single palmitoylation
903.8759	903.8759	4	0.00		
1196.1602	1196.1633	3	2.59	18.2	$SynM_{2pal+ole}$/double palmitoylation + single oleoylation
897.3720	897.3736	4	1.78		

‡Both theoretical (Theor) and measured (Meas) *m/z* values are for the monoisotopic peak. Theoretical mass obtained from mMass software (V5.5).

Table 9.4. **The range of single and multiple acylation ions observed from SynM/50:50 OPC:DPPC incubation at 37 °C for 168.**

^{1}H-GIGAVLKVLTTGLPALISWIKRKRQQ-NH_2 [26]					
***m/z* Theor‡**	***m/z* Meas‡**	***z***	**Error (ppm)**	**RT (min)**	**Assignment**
1037.3404	1037.3405	3	0.09	8.6	$SynM_{ole}$/single oleoylation
778.2572	778.2585	4	1.67		
622.8072	622.8077	5	0.80		
1028.6686	1028.6687	3	0.10	8.5	$SynM_{pal}$/ single palmitoylation
771.7532	771.7542	4	1.30		
617.6040	617.6046	5	0.97		
1125.4222	1125.4232	3	0.89	11.0	$SynM_{2ole}$/double oleoylation
844.3185	844.3193	4	0.95		
675.6562	675.6549	5	-1.92		
1108.0784	1108.0789	3	0.45	11.0	$SynM_{2pal}$/double palmitoylation
831.3107	831.3115	4	0.96		
665.2500	665.2499	5	-0.15		
1116.7503	1116.7505	3	0.18	11.0	$SynM_{pal+ole}$/single palmitoylation + single oleoylation
837.8146	837.8159	4	1.55		
670.4531	670.4542	5	1.64		
1125.4222	1125.4195	3	-2.40	17.7	$SynM_{3ole}$/labile triple oleoylation
844.3185	844.3195	4	1.18		
831.3107	831.3134	4	3.25	17.7	$SynM_{3pal}$/labile triple palmitoylation
1116.7503	1116.7491	3	-1.07	17.8	$SynM_{2pal+ole}$ or $SynM_{2ole+pal}$/labile (double palmitoylation + single oleoylation) or (double oleoylation + single palmitoylation)
837.8146	837.8154	4	0.95		
670.4531	670.4537	5	0.89		
1213.504	1213.5011	3	-2.39	18.2	$SynM_{3ole}$/triple oleoylation
910.3798	910.3813	4	1.65		
1187.4883	1187.4921	3	3.20	18.1	$SynM_{3pal}$/triple palmitoylation
890.8681	890.8680	4	-0.11		
1204.8321	1204.8315	3	-0.50	18.2	$SynM_{2ole+pal}$/double oleoylation + single palmitoylation
903.8759	903.8751	4	-0.89		
1196.1602	1196.1632	3	2.51	18.2	$SynM_{2pal+ole}$/double palmitoylation + single oleoylation
897.3720	897.3710	4	-1.11		

‡Both theoretical (Theor) and measured (Meas) *m/z* values are monoisotopic. Theoretical mass obtained from mMass software (V5.5).

Table 9.5. **Ions produced by fragmenting SynM$_{2pal}$ at *m/z* 832 (*z*=4) over 9.1 min of the EIC (see Figure 3.27, SynM/50:50 PPC:DOPC). Product ions correspond to S18/K21 double palmitoylation (see Figure 3.29 A).**

b-Ions	*m/z*	*z*	Sequence Ladder*	y-Ions	*m/z*	*z*	Sequence Ladder*
b4	299.1	1	H-GIGA	y24	1051.3	3	GAVLKVLTTGLPALI**S**WI**K**RKRQQ-NH_2
b5	398.1	1	H-GIGAV	y24	789.0	4	GAVLKVLTTGLPALI**S**WI**K**RKRQQ-NH_2
b6	511.4	1	H-GIGAVL	y22	1008.8	3	VLKVLTTGLPALI**S**WI**K**RKRQQ-NH_2
b8	738.4	1	H-GIGAVLKV	y21	976.0	3	LKVLTTGLPALI**S**WI**K**RKRQQ-NH_2
b9	851.5	1	H-GIGAVLKVL	y20	938.1	3	KVLTTGLPALI**S**WI**K**RKRQQ-NH_2
b10	953.0	1	H-GIGAVLKVLT	y19	1342.5	2	VLTTGLPALI**S**WI**K**RKRQQ-NH_2
b12	1110.6	1	H-GIGAVLKVLTTG	y18	1293.2	2	LTTGLPALI**S**WI**K**RKRQQ-NH_2
b13	1223.7	1	H-GIGAVLKVLTTGL	y17	1236.7	2	TTGLPALI**S**WI**K**RKRQQ-NH_2
				y16	1186.1	2	TGLPALI**S**WI**K**RKRQQ-NH_2
				y15	1135.5	2	GLPALI**S**WI**K**RKRQQ-NH_2
				y14	1107.1	2	LPALI**S**WI**K**RKRQQ-NH_2
				y13	1050.5	2	PALI**S**WI**K**RKRQQ-NH_2
				y13	700.7	3	PALI**S**WI**K**RKRQQ-NH_2
				y12	1002.1	2	ALI**S**WI**K**RKRQQ-NH_2
				y10	910.3	2	I**S**WI**K**RKRQQ-NH_2
				y9	853.6	2	**S**WI**K**RKRQQ-NH_2
				y7	598.1	2	I**K**RKRQQ-NH_2
				y6	541.0	2	**K**RKRQQ-NH_2
				y5	357.7	2	RKRQQ-NH_2

*Palmitoylation sites are highlighted in blue within the amino acid sequence of the peptide.

Table 9.6. **Ions produced by fragmenting $SynM_{2pal}$ at *m/z* 832 (*z*=4) over 9.4 min of the EIC (see Figure 3.27, SynM/50:50 PPC:DOPC). Product ions correspond to K21/K23 double palmitoylation (see Figure 3.29 B).**

b-Ions	*m/z*	*z*	Sequence Ladder*	y-Ions	*m/z*	*z*	Sequence Ladder*
b4	299.3	1	H-GIGA	y24	1052.1	3	GAVLKVLTTGLPALISWI**K**R**K**RQQ-NH_2
b5	398.2	1	H-GIGAV	y24	789.0	4	i.GAVLKVLTTGLPALISWI**K**R**K**RQQ-NH_2
b6	511.3	1	H-GIGAVL	y22	1009.0	3	VLKVLTTGLPALISWI**K**R**K**RQQ-NH_2
b8	738.6	1	H-GIGAVLKV	y21	976.0	3	LKVLTTGLPALISWI**K**R**K**RQQ-NH_2
b9	851.6	1	H-GIGAVLKVL	y20	938.3	3	KVLTTGLPALISWI**K**R**K**RQQ-NH_2
b10	952.9	1	H-GIGAVLKVLT	y19	1342.9	2	VLTTGLPALISWI**K**R**K**RQQ-NH_2
b12	1110.7	1	H-GIGAVLKVLTTG	y18	1293.1	2	LTTGLPALISWI**K**R**K**RQQ-NH_2
b13	1223.6	1	H-GIGAVLKVLTTGL	y17	1236.7	2	TTGLPALISWI**K**R**K**RQQ-NH_2
				y16	1186.1	2	TGLPALISWI**K**R**K**RQQ-NH_2
				y15	1135.5	2	GLPALISWI**K**R**K**RQQ-NH_2
				y14	1106.8	2	LPALISWI**K**R**K**RQQ-NH_2
				y13	1050.2	2	PALISWI**K**R**K**RQQ-NH_2
				y13	700.9	3	PALISWI**K**R**K**RQQ-NH_2
				y12	1001.8	2	ALISWI**K**R**K**RQQ-NH_2
				y11	966.2	2	LISWI**K**R**K**RQQ-NH_2
				y10	910.0	2	ISWI**K**R**K**RQQ-NH_2
				y9	853.6	2	SWI**K**R**K**RQQ-NH_2
				y8	809.5	2	WI**K**R**K**RQQ-NH_2
				y6	659.4	2	**K**R**K**RQQ-NH_2

*Palmitoylation sites are highlighted in blue within the amino acid sequence of the peptide.

Table 9.7. **Ions produced by fragmenting $SynM_{2pal}$ at *m/z* 832 (*z*=4) over 9.4 min of the EIC (see Figure 3.27, SynM/50:50 PPC:DOPC). Product ions correspond to N-terminus/K21 double palmitoylation (see Figure 3.29 C).**

b-Ions	*m/z*	*z*	Sequence Ladder*	y-Ions	*m/z*	*z*	Sequence Ladder*
b3	466.2	1	H-**G**IG	y24	972.5	3	GAVLKVLTTGLPALISWI**K**RKRQQ-NH_2
b4	537.3	1	H-**G**IGA	y21	896.7	3	LKVLTTGLPALISWI**K**RKRQQ-NH_2
b5	636.2	1	H-**G**IGAV	y19	1223.6	2	VLTTGLPALISWI**K**RKRQQ-NH_2
b6	749.2	1	H-**G**IGAVL	y18	1174.0	2	LTTGLPALISWI**K**RKRQQ-NH_2
b7	877.4	1	H-**G**IGAVLK	y17	1117.5	2	TTGLPALISWI**K**RKRQQ-NH_2
b8	976.1	1	H-**G**IGAVLKV	y16	1066.9	2	TGLPALISWI**K**RKRQQ-NH_2
b9	1089.6	1	H-**G**IGAVLKVL	y15	1016.1	2	GLPALISWI**K**RKRQQ-NH_2
b10	1190.9	1	H-**G**IGAVLKVLT	y14	987.8	2	LPALISWI**K**RKRQQ-NH_2
b12	1348.6	1	H-**G**IGAVLKVLTTG	y13	931.1	2	PALISWI**K**RKRQQ-NH_2
b12 - H_2O	1330.7	1	H-**G**IGAVLKVLTTG	y13	621.4	3	PALISWI**K**RKRQQ-NH_2
b12 - H_2O	666.0	2	H-**G**IGAVLKVLTTG	y12	883.0	2	ALISWI**K**RKRQQ-NH_2
b13	1461.5	1	H-**G**IGAVLKVLTTGL	y11	847.3	2	LISWI**K**RKRQQ-NH_2
b13 - H_2O	1443.7	1	H-**G**IGAVLKVLTTGL	y10	790.6	2	ISWI**K**RKRQQ-NH_2
b15	816.1	2	H-**G**IGAVLKVLTTGLPA	y9	734.1	2	SWI**K**RKRQQ-NH_2
				y6	1080.1	1	**K**RKRQQ-NH_2
				y4	558.3	1	KRQQ-NH_2
				y4 – NH_3	541.8	1	KRQQ-NH_2

*Palmitoylation sites are highlighted in blue within the amino acid sequence of the peptide.

Table 9.8. **Ions produced by fragmenting $SynM_{2pal}$ at *m/z* 832 (*z*=4) over 10.9 min of the EIC (see Figure 3.27, SynM/50:50 PPC:DOPC). Product ions correspond to N-terminus/R22 double palmitoylation (see Figure 3.30 A).**

b-Ions	*m/z*	*z*	Sequence Ladder*	y-Ions	*m/z*	*z*	Sequence Ladder*
b3	466.2	1	H-**G**IG	y24	972.4	3	GAVLKVLTTGLPALISWIK**R**KRQQ-NH_2
b4	537.2	1	H-**G**IGA	y22	929.5	3	VLKVLTTGLPALISWIK**R**KRQQ-NH_2
b5	636.3	1	H-**G**IGAV	y21	896.6	3	LKVLTTGLPALISWIK**R**KRQQ-NH_2
b6	749.4	1	H-**G**IGAVL	y20	859.0	3	KVLTTGLPALISWIK**R**KRQQ-NH_2
b7	877.5	1	H-**G**IGAVLK	y19	1223.7	2	VLTTGLPALISWIK**R**KRQQ-NH_2
b7	439.7	2	H-**G**IGAVLK	y18	1173.8	2	LTTGLPALISWIK**R**KRQQ-NH_2
b8	976.6	1	H-**G**IGAVLKV	y17	1117.5	2	TTGLPALISWIK**R**KRQQ-NH_2
b9	1089.6	1	H-**G**IGAVLKVL	y16	1067.1	2	TGLPALISWIK**R**KRQQ-NH_2
b10	1190.4	1	H-**G**IGAVLKVLT	y15	1016.5	2	GLPALISWIK**R**KRQQ-NH_2
b12	1348.7	1	H-**G**IGAVLKVLTTG	y14	987.9	2	LPALISWIK**R**KRQQ-NH_2
b12 - H_2O	1330.7	1	H-**G**IGAVLKVLTTG	y13	931.5	2	PALISWIK**R**KRQQ-NH_2
b12 - H_2O	665.9	2	H-**G**IGAVLKVLTTG	y13	621.5	3	PALISWIK**R**KRQQ-NH_2
b13	1461.8	1	H-**G**IGAVLKVLTTGL	y12	882.9	2	ALISWIK**R**KRQQ-NH_2
b13 - H_2O	1443.8	1	H-**G**IGAVLKVLTTGL	y11	847.4	2	LISWIK**R**KRQQ-NH_2
b15	815.9	2	H-**G**IGAVLKVLTTGLPA	y10	790.8	2	ISWIK**R**KRQQ-NH_2
				y9	734.0	2	SWIK**R**KRQQ-NH_2
				y5	477.1	2	**R**KRQQ-NH_2

*Palmitoylation sites are highlighted in blue within the amino acid sequence of the peptide.

Table 9.9. **Ions produced by fragmenting $SynM_{2pal}$ at *m/z* 832 (*z*=4) over 11.2 min of the EIC (see Figure 3.27, SynM/50:50 PPC:DOPC). Product ions correspond to N-terminus/R24 double palmitoylation (see Figure 3.30 B).**

b-Ions	*m/z*	*z*	Sequence Ladder*	y-Ions	*m/z*	*z*	Sequence Ladder*
b3	466.2	1	H-**G**IG	y24	972.2	3	GAVLKVLTTGLPALISWIKRK **R**QQ-NH_2
b4	537.1	1	H-**G**IGA	y22	929.5	3	VLKVLTTGLPALISWIKRK**R**QQ-NH_2
b5	636.3	1	H-**G**IGAV	y21	896.6	3	LKVLTTGLPALISWIKRK**R**QQ-NH_2
b6	749.4	1	H-**G**IGAVL	y20	859.1	3	KVLTTGLPALISWIKRK**R**QQ-NH_2
b7	877.6	1	H-**G**IGAVLK	y19	1223.4	2	VLTTGLPALISWIKRK**R**QQ-NH_2
b7	439.4	2	H-**G**IGAVLK	y18	1173.8	2	LTTGLPALISWIKRK**R**QQ-NH_2
b8	976.6	1	H-**G**IGAVLKV	y17	1117.4	2	TTGLPALISWIKRK**R**QQ-NH_2
b9	1089.7	1	H-**G**IGAVLKVL	y16	1067.4	2	TGLPALISWIKRK**R**QQ-NH_2
b10	1190.7	1	H-**G**IGAVLKVLT	y15	1016.5	2	GLPALISWIKRK**R**QQ-NH_2
b12	1348.7	1	H-**G**IGAVLKVLTTG	y14	987.9	2	LPALISWIKRK**R**QQ-NH_2
b12 - H_2O	1330.8	1	H-**G**IGAVLKVLTTG	y13	931.5	2	PALISWIKRK**R**QQ-NH_2
b12 - H_2O	665.9	2	H-**G**IGAVLKVLTTG	y13	621.5	3	PALISWIKRK**R**QQ-NH_2
b13	1461.8	1	H-**G**IGAVLKVLTTGL	y12	882.7	2	ALISWIKRK**R**QQ-NH_2
b13 - H_2O	1443.8	1	H-**G**IGAVLKVLTTGL	y11	847.5	2	LISWIKRK**R**QQ-NH_2
b15	816.3	2	H-**G**IGAVLKVLTTGLPA	y10	790.3	2	ISWIKRK**R**QQ-NH_2
				y9	733.3	2	SWIKRK**R**QQ-NH_2
				y8 - NH_3	681.4	2	WIK**R**QQ-NH_2
				y5	477.1	2	RK**R**QQ-NH_2
				y5 - NH_3	468.5	2	RK**R**QQ-NH_2
				y4 - NH_3	390.5	2	K**R**QQ-NH_2

*Palmitoylation sites are highlighted in blue within the amino acid sequence of the peptide.

Table 9.10. **Ions produced by fragmenting $SynM_{2ole}$ at *m/z* 845 (*z*=4) over 9.2 min of the EIC (see Figure 3.31, SynM/50:50 PPC:DOPC). Product ions correspond to S18/K21 double oleoylation (see Figure 3.32 A).**

b-Ions	*m/z*	*z*	Sequence Ladder*	y-Ions	*m/z*	*z*	Sequence Ladder*
b4	299.1	1	H-GIGA	y24	1069.1	3	GAVLKVLTTGLPALI**S**WI**K**RKRQQ-NH_2
b5	398.2	1	H-GIGAV	y22	1026.3	3	VLKVLTTGLPALI**S**WI**K**RKRQQ-NH_2
b6	511.3	1	H-GIGAVL	y21	993.4	3	LKVLTTGLPALI**S**WI**K**RKRQQ-NH_2
b12	1348.7	1	H-GIGAVLKVLTTG	y20	955.7	3	KVLTTGLPALI**S**WI**K**RKRQQ-NH_2
b13	1461.8	1	H-GIGAVLKVLTTGL	y19	1368.6	2	VLTTGLPALI**S**WI**K**RKRQQ-NH_2
				y18	1318.6	2	LTTGLPALI**S**WI**K**RKRQQ-NH_2
				y17	1262.6	2	TTGLPALI**S**WI**K**RKRQQ-NH_2
				y16	1211.8	2	TGLPALI**S**WI**K**RKRQQ-NH_2
				y15	1161.6	2	GLPALI**S**WI**K**RKRQQ-NH_2
				y14	1132.0	2	LPALI**S**WI**K**RKRQQ-NH_2
				y13	1076.1	2	PALI**S**WI**K**RKRQQ-NH_2
				y13 - H_2O	1066.9	2	PALI**S**WI**K**RKRQQ-NH_2
				y13	718.3	3	PALI**S**WI**K**RKRQQ-NH_2
				y12	1027.6	2	ALI**S**WI**K**RKRQQ-NH_2
				y11	992.1	2	LI**S**WI**K**RKRQQ-NH_2
				y10	935.6	2	I**S**WI**K**RKRQQ-NH_2
				y7	610.3	2	I**K**RKRQQ-NH_2
				y6	554.2	2	**K**RKRQQ-NH_2
				y5	714.4	1	RKRQQ-NH_2

*Oleoylation sites are highlighted in red within the amino acid sequence of the peptide.

Table 9.11. **Ions produced by fragmenting $SynM_{2ole}$ at *m/z* 845 (*z*=4) over 9.6 min of the EIC (see Figure 3.31, SynM/50:50 PPC:DOPC). Product ions correspond to K21/K23 double oleoylation (see Figure 3.32 B).**

b-Ions	*m/z*	*z*	Sequence Ladder*	y-Ions	*m/z*	*z*	Sequence Ladder*
b4	299.1	1	H-GIGA	y24	1069.2	3	GAVLKVLTTGLPALISWI**K**R**K**RQQ -NH_2
b5	398.2	1	H-GIGAV	y22	1026.4	3	VLKVLTTGLPALISWI**K**R**K**RQQ-NH_2
b6	511.3	1	H-GIGAVL	y19	1368.7	2	VLTTGLPALISWI**K**R**K**RQQ-NH_2
b10	952.5	1	H-GIGAVLKVLT	y18	1318.9	2	LTTGLPALISWI**K**R**K**RQQ-NH2
b12	1110.6	1	H-GIGAVLKVLTTG	y17	1262.7	2	TTGLPALISWI**K**R**K**RQQ-NH_2
b13	1223.6	1	H-GIGAVLKVLTTGL	y16	1211.9	2	TGLPALISWI**K**R**K**RQQ-NH_2
				y15	1161.5	2	GLPALISWI**K**R**K**RQQ-NH_2
				y14	1132.8	2	LPALISWI**K**R**K**RQQ-NH_2
				y13	1076.6	2	PALISWI**K**R**K**RQQ-NH_2
				y13-H_2O	1067.6	2	PALISWI**K**R**K**RQQ-NH_2
				y13	718.3	3	PALISWI**K**R**K**RQQ-NH_2
				y12	1028.3	2	ALISWI**K**R**K**RQQ-NH_2
				y11	992.8	2	LISWI**K**R**K**RQQ-NH_2
				y10	935.9	2	ISWI**K**R**K**RQQ-NH_2
				y8	835.8	2	WI**K**R**K**RQQ-NH_2
				y7	742.2	2	I**K**R**K**RQQ-NH_2
				y5	490.3	2	R**K**RQQ-NH_2

*Oleoylation sites are highlighted in red within the amino acid sequence of the peptide.

Table 9.12. **Ions produced by fragmenting $SynM_{2ole}$ at *m/z* 845 (*z*=4) over 9.6 min of the EIC (see Figure 3.31, SynM/50:50 PPC:DOPC). Product ions correspond to N-terminus/K21 double oleoylation (see Figure 3.32 C).**

b-Ions	*m/z*	*z*	Sequence Ladder*	y-Ions	*m/z*	*z*	Sequence Ladder*
b3	492.3	1	H-**G**IG	y24	981.0	3	GAVLKVLTTGLPALISWI**K**RKRQQ-NH_2
b4	563.2	1	H-**G**IGA	y21	1356.6	2	LKVLTTGLPALISWI**K**RKRQQ-NH_2
b5	662.3	1	H-**G**IGAV	y19	1236.4	2	VLTTGLPALISWI**K**RKRQQ-NH_2
b6	775.3	1	H-**G**IGAVL	y18	1187.0	2	LTTGLPALISWI**K**RKRQQ-NH_2
b7	903.4	1	H-**G**IGAVLK	y17	1130.5	2	TTGLPALISWI**K**RKRQQ-NH_2
b8	1002.6	1	H-**G**IGAVLKV	y16	1079.8	2	TGLPALISWI**K**RKRQQ-NH_2
b9	1115.6	1	H-**G**IGAVLKVL	y15	1029.4	2	GLPALISWI**K**RKRQQ-NH_2
b10	1216.7	1	H-**G**IGAVLKVLT	y14	1001.0	2	LPALISWI**K**RKRQQ-NH_2
b12	1374.7	1	H-**G**IGAVLKVLTTG	y13	944.4	2	PALISWI**K**RKRQQ-NH_2
b13	1487.8	1	H-**G**IGAVLKVLTTGL	y13	630.1	3	PALISWI**K**RKRQQ-NH_2
				y12	895.2	2	ALISWI**K**RKRQQ-NH_2
				y11	860.4	2	LISWI**K**RKRQQ-NH_2
				y10	803.3	2	ISWI**K**RKRQQ-NH_2
				y9	746.9	2	SWI**K**RKRQQ-NH_2
				y8	703.7	2	WI**K**RKRQQ-NH_2
				y7	609.2	2	I**K**RKRQQ-NH_2
				y5	714.5	1	RKRQQ-NH_2
				y4	558.5	1	KRQQ-NH_2

*Oleoylation sites are highlighted in red within the amino acid sequence of the peptide.

Table 9.13. **Ions produced by fragmenting $SynM_{2ole}$ at *m/z* 845 (*z*=4) over 10.2 min of the EIC (see Figure 3.31, SynM/50:50 PPC:DOPC). Product ions correspond to K7/K21 double oleoylation (see Figure 3.33 A).**

b-Ions	*m/z*	*z*	Sequence Ladder*	y-Ions	*m/z*	*z*	Sequence Ladder*
b4	299.1	1	H-GIGA	y24	1069.1	3	GAVL**K**VLTTGLPALISWI**K**RKRQQ-NH_2
b5	398.2	1	H-GIGAV	y24	801.8	4	GAVL**K**VLTTGLPALISWI**K**RKRQQ-NH_2
b6	511.3	1	H-GIGAVL	y22	1026.0	3	VL**K**VLTTGLPALISWI**K**RKRQQ-NH_2
b7	903.5	1	H-GIGAVL**K**	y21	993.9	3	L**K**VLTTGLPALISWI**K**RKRQQ-NH_2
b8	1002.6	1	H-GIGAVL**K**V	y20	1432.5	2	**K**VLTTGLPALISWI**K**RKRQQ-NH_2
b9	1115.7	1	H-GIGAVL**K**VL	y19	1236.7	2	VLTTGLPALISWI**K**RKRQQ-NH_2
b10	1216.6	1	H-GIGAVL**K**VLT	y18	1187.0	2	LTTGLPALISWI**K**RKRQQ-NH_2
b11	1317.8	1	H-GIGAVL**K**VLTT	y17	1130.5	2	TTGLPALISWI**K**RKRQQ-NH_2
b12	1374.7	1	H-GIGAVL**K**VLTTG	y17	754.3	3	TTGLPALISWI**K**RKRQQ-NH_2
b13	1487.8	1	H-GIGAVL**K**VLTTGL	y16	1079.6	2	TGLPALISWI**K**RKRQQ-NH_2
				y15	1029.2	2	GLPALISWI**K**RKRQQ-NH_2
				y14	1000.7	2	LPALISWI**K**RKRQQ-NH_2
				y13	944.4	2	PALISWI**K**RKRQQ-NH_2
				y13	630.1	3	PALISWI**K**RKRQQ-NH_2
				y12	895.8	2	ALISWI**K**RKRQQ-NH_2
				y11	860.4	2	LISWI**K**RKRQQ-NH_2
				y10	803.4	2	ISWI**K**RKRQQ-NH_2
				y9	747.6	2	SWI**K**RKRQQ-NH_2
				y8	703.8	2	WI**K**RKRQQ-NH_2
				y7	609.2	2	I**K**RKRQQ-NH_2
				y6	553.5	2	**K**RKRQQ-NH_2
				y4 - NH_3	271.2	2	KRQQ-NH_2

*Oleoylation sites are highlighted in red within the amino acid sequence of the peptide.

Table 9.14. **Ions produced by fragmenting $SynM_{2ole}$ at *m/z* 845 (*z*=4) over 10.6 min of the EIC (see Figure 3.31, SynM/50:50 PPC:DOPC). Product ions correspond to N-terminus/K23 double oleoylation (see Figure 3.33B).**

b-Ions	*m/z*	*z*	Sequence Ladder*	y-Ions	*m/z*	*z*	Sequence Ladder*
b3	492.3	1	H-**G**IG	y24	980.9	3	GAVLKVLTTGLPALISWIKR**K**RQQ-NH_2
b4	563.3	1	H-**G**IGA	y24	736.0	4	GAVLKVLTTGLPALISWIKR**K**RQQ-NH_2
b5	662.3	1	H-**G**IGAV	y22	938.4	3	VLKVLTTGLPALISWIKR**K**RQQ-NH_2
b6	775.3	1	H-**G**IGAVL	y21	1356.7	2	LKVLTTGLPALISWIKR**K**RQQ-NH_2
b7	903.6	1	H-**G**IGAVLK	y21	905.5	3	LKVLTTGLPALISWIKR**K**RQQ-NH_2
b8	1002.5	1	H-**G**IGAVLKV	y21	678.9	4	LKVLTTGLPALISWIKR**K**RQQ-NH_2
b9	1115.6	1	H-**G**IGAVLKVL	y20	868.0	3	KVLTTGLPALISWI**K**RKRQQ-NH_2
b10	1216.7	1	H-**G**IGAVLKVLT	y19	1236.4	2	VLTTGLPALISWIKR**K**RQQ-NH_2
b12	1374.7	1	H-**G**IGAVLKVLTTG	y18	1187.0	2	LTTGLPALISWIKR**K**RQQ-NH_2
b13	1488.0	1	H-**G**IGAVLKVLTTGL	y17	1130.2	2	TTGLPALISWIKR**K**RQQ-NH_2
				y17	754.3	3	TTGLPALISWIKR**K**RQQ-NH_2
				y16	1079.7	2	TGLPALISWIKR**K**RQQ-NH_2
				y15	1029.4	2	GLPALISWIKR**K**RQQ-NH_2
				y14	1000.9	2	LPALISWIKR**K**RQQ-NH_2
				y13	944.5	2	PALISWIKR**K**RQQ-NH_2
				y13	630.1	3	PALISWIKR**K**RQQ-NH_2
				y12	895.8	2	ALISWIKR**K**RQQ-NH_2
				y11	860.4	2	LISWIKR**K**RQQ-NH_2
				y10	803.7	2	ISWIKR**K**RQQ-NH_2
				y9	747.1	2	SWIKR**K**RQQ-NH_2
				y8	703.8	2	WIKR**K**RQQ-NH_2
				y7	609.1	2	IKR**K**RQQ-NH_2
				y5	490.0	2	R**K**RQQ-NH_2
				y4	822.9	1	**K**RQQ-NH_2
				y4 - NH_3	806.1	1	**K**RQQ-NH_2

*Oleoylation sites are highlighted in within the amino acid sequence of the peptide.

Table 9.15. **Ions produced by fragmenting $SynM_{2ole}$ at *m/z* 845 (*z*=4) over 10.9 min of the EIC (see Figure 3.31, SynM/50:50 PPC:DOPC). Product ions correspond to N-terminus/R22 double oleoylation (see Figure 3.34 A).**

b-Ions	*m/z*	*z*	Sequence Ladder*	y-Ions	*m/z*	*z*	Sequence Ladder*
b3	492.3	1	H-**G**IG	y24	981.4	3	GAVLKVLTTGLPALISWIK**R**KRQQ-NH_2
b4	563.2	1	H-**G**IGA	y24	735.9	4	GAVLKVLTTGLPALISWIK**R**KRQQ-NH_2
b5	662.3	1	H-**G**IGAV	y22	938.3	3	VLKVLTTGLPALISWIK**R**KRQQ-NH_2
b6	775.2	1	H-**G**IGAVL	y21	1356.7	2	LKVLTTGLPALISWIK**R**KRQQ-NH_2
b7	903.4	1	H-**G**IGAVLK	y21	905.5	3	LKVLTTGLPALISWIK**R**KRQQ-NH_2
b8	1002.7	1	H-**G**IGAVLKV	y21	678.9	4	LKVLTTGLPALISWIK**R**KRQQ-NH_2
b9	1115.6	1	H-**G**IGAVLKVL	y20	867.7	3	KVLTTGLPALISWIK**R**KRQQ-NH_2
b10	1216.7	1	H-**G**IGAVLKVLT	y20	650.5	4	KVLTTGLPALISWIK**R**KRQQ-NH_2
b12	1374.7	1	H-**G**IGAVLKVLTTG	y19	1236.5	2	VLTTGLPALISWIK**R**KRQQ-NH_2
b13	1487.9	1	H-**G**IGAVLKVLTTGL	y18	1187.5	2	LTTGLPALISWIK**R**KRQQ-NH_2
				y17	1130.6	2	TTGLPALISWIK**R**KRQQ-NH_2
				y17	754.2	3	TTGLPALISWIK**R**KRQQ-NH_2
				y16	1080.2	2	TGLPALISWIK**R**KRQQ-NH_2
				y15	1029.6	2	GLPALISWIK**R**KRQQ-NH_2
				y14	1001.0	2	LPALISWIK**R**KRQQ-NH_2
				y13	944.4	2	PALISWIK**R**KRQQ-NH_2
				y13	630.2	3	PALISWIK**R**KRQQ-NH_2
				y12	895.6	2	ALISWIK**R**KRQQ-NH_2
				y11	860.0	2	LISWIK**R**KRQQ-NH_2
				y10	803.8	2	ISWIK**R**KRQQ-NH_2
				y9	747.5	2	SWIK**R**KRQQ-NH_2
				y8	703.7	2	WIK**R**KRQQ-NH_2
				y7	609.1	2	IK**R**KRQQ-NH_2
				y5	490.1	2	**R**KRQQ-NH_2
				y4	558.5	1	KRQQ-NH_2

*Oleoylation sites are highlighted in red within the amino acid sequence of the peptide.

Table 9.16. **Ions produced by fragmenting $SynM_{2ole}$ at *m/z* 845 (*z*=4) over 11.2 min of the EIC (see Figure 3.31, SynM/50:50 PPC:DOPC). Product ions correspond to N-terminus/R24 double oleoylation (see Figure 3.34 B).**

b-Ions	*m/z*	*z*	Sequence Ladder*	y-Ions	*m/z*	*z*	Sequence Ladder*
b3	492.3	1	H-**G**IG	y24	981.1	3	GAVLKVLTTGLPALISWIKRK**R**QQ-NH_2
b4	563.1	1	H-**G**IGA	y24	736.3	4	GAVLKVLTTGLPALISWIKRK**R**QQ-NH_2
b5	662.3	1	H-**G**IGAV	y22	938.3	3	VLKVLTTGLPALISWIKRK**R**QQ-NH_2
b6	775.4	1	H-**G**IGAVL	y21	1356.9	2	LKVLTTGLPALISWIKRK**R**QQ-NH_2
b7	903.5	1	H-**G**IGAVLK	y21	905.4	3	LKVLTTGLPALISWIKRK**R**QQ-NH_2
b8	1002.6	1	H-**G**IGAVLKV	y21	679.0	4	LKVLTTGLPALISWIKRK**R**QQ-NH_2
b9	1115.7	1	H-**G**IGAVLKVL	y20	867.7	3	KVLTTGLPALISWIKRK**R**QQ-NH_2
b10	1216.8	1	H-**G**IGAVLKVLT	y20	650.6	4	KVLTTGLPALISWIKRK**R**QQ-NH_2
b12	1374.7	1	H-**G**IGAVLKVLTTG	y19	1236.1	2	VLTTGLPALISWIKRK**R**QQ-NH_2
b13	1487.9	1	H-**G**IGAVLKVLTTGL	y18	1187.0	2	LTTGLPALISWIKRK**R**QQ-NH_2
				y17	1130.4	2	TTGLPALISWIKRK**R**QQ-NH_2
				y17	754.2	3	TTGLPALISWIKRK**R**QQ-NH_2
				y16	1079.7	2	TGLPALISWIKRK**R**QQ-NH_2
				y15	1029.1	2	GLPALISWIKRK**R**QQ-NH_2
				y14	1001.1	2	LPALISWIKRK**R**QQ-NH_2
				y13	944.4	2	PALISWIKRK**R**QQ-NH_2
				y13	630.1	3	PALISWIKRK**R**QQ-NH_2
				y12	895.7	2	ALISWIKRK**R**QQ-NH_2
				y11	860.5	2	LISWIKRK**R**QQ-NH_2
				y10	803.8	2	ISWIKRK**R**QQ-NH_2
				y9	747.3	2	SWIKRK**R**QQ-NH_2
				y8	703.7	2	WIKRK**R**QQ-NH_2
				y7	609.1	2	IKRK**R**QQ-NH_2
				y5	490.4	2	RK**R**QQ-NH_2
				y4	822.8	1	K**R**QQ-NH_2

*Oleoylation sites are highlighted in red within the amino acid sequence of the peptide.

Table 9.17. **Ions produced by fragmenting $SynM_{pal+ole}$ at *m/z* 838 (*z*=4) over 9.1 min of the EIC (see Figure 3.35, SynM/50:50 PPC:DOPC). Product ions correspond to S18 oleoylation and K21 palmitoylation (see Figure 3.36 A).**

b-Ions	*m/z*	*z*	Sequence Ladder*	y-Ions	*m/z*	*z*	Sequence Ladder*
b4	299.2	1	H-GIGA	y24	1060.9	3	GAVLKVLTTGLPALI**S**WI **K**RKRQQ-NH_2
b5	398.2	1	H-GIGAV	y24	795.4	4	GAVLKVLTTGLPALI**S**WI **K**RKRQQ-NH_2
b6	511.3	1	H-GIGAVL	y22	1017.5	3	VLKVLTTGLPALI**S**WI**K**R KRQQ-NH_2
b8	738.8	1	H-GIGAVLKV	y20	1419.9	2	KVLTTGLPALI**S**WI**K**RKR QQ-NH_2
b9	851.6	1	H-GIGAVLKVL	y20	946.7	3	KVLTTGLPALI**S**WI**K**RKR QQ-NH_2
b12	1110.8	1	H-GIGAVLKVLTTG	y19	1355.7	2	VLTTGLPALI**S**WI**K**RKRQ Q-NH_2
b13	1223.7	1	H-GIGAVLKVLTTGL	y18	1306.5	2	LTTGLPALI**S**WI**K**RKRQQ -NH_2
b15 – NH_3	1374.6	1	H-GIGAVLKVLTTGLPA	y17	1249.5	2	TTGLPALI**S**WI**K**RKRQQ-NH_2
b16	753.7	2	H-GIGAVLKVLTTGLPAL	y16	1199.0	2	TGLPALI**S**WI**K**RKRQQ-NH_2
b17	809.8	2	H-GIGAVLKVLTTGLPALI	y15	1148.7	2	GLPALI**S**WI**K**RKRQQ-NH_2
b18	985.0	2	H-GIGAVLKVLTTGLPALI**S**	y14	1119.2	2	LPALI**S**WI**K**RKRQQ-NH_2
				y13	1063.5	2	PALI**S**WI**K**RKRQQ-NH_2
				y13	709.7	4	PALI**S**WI**K**RKRQQ-NH_2
				y10	922.8	2	I**S**WI**K**RKRQQ-NH_2
				y9	866.3	2	**S**WI**K**RKRQQ-NH_2

*Oleoylation and palmitoylation sites are highlighted in red and blue respectively within the amino acid sequence of the peptide.

Table 9.18. **Ions produced by fragmenting $SynM_{pal+ole}$ at *m/z* 838 (*z*=4) over 9.1 min of the EIC (see Figure 3.35, SynM/50:50 PPC:DOPC). Product ions correspond to S18 palmitoylation and K21 oleoylation (see Figure 3.36 B).**

b-Ions	*m/z*	*z*	Sequence Ladder*	y-Ions	*m/z*	*z*	Sequence Ladder*
b4	299.2	1	H-GIGA	y24	1060.9	3	GAVLKVLTTGLPALI**S**WI**K** RKRQQ-NH_2
b5	398.2	1	H-GIGAV	y24	795.4	4	GAVLKVLTTGLPALI**S**WI**K** RKRQQ-NH_2
b6	511.3	1	H-GIGAVL	y22	1017.5	3	VLKVLTTGLPALI**S**WI**K**RK RQQ-NH_2
b8	738.8	1	H-GIGAVLKV	y20	1419.9	2	KVLTTGLPALI**S**WI**K**RKR QQ-NH_2
b9	851.6	1	H-GIGAVLKVL	y20	946.7	3	KVLTTGLPALI**S**WI**K**RKR QQ-NH_2
b12	1110.8	1	H-GIGAVLKVLTTG	y19	1355.7	2	VLTTGLPALI**S**WI**K**RKRQ Q-NH_2
b13	1223.7	1	H-GIGAVLKVLTTGL	y18	1306.5	2	LTTGLPALI**S**WI**K**RKRQQ-NH_2
b15 – NH_3	1374.6	1	H-GIGAVLKVLTTGLPA	y17	1249.5	2	TTGLPALI**S**WI**K**RKRQQ-NH_2
b16	753.7	2	H-GIGAVLKVLTTGLPAL	y16	1199.0	2	TGLPALI**S**WI**K**RKRQQ-NH_2
b17	809.8	2	H-GIGAVLKVLTTGLPALI	y15	1148.7	2	GLPALI**S**WI**K**RKRQQ-NH_2
b18	971.9	2	H-GIGAVLKVLTTGLPALI**S**	y14	1119.2	2	LPALI**S**WI**K**RKRQQ-NH_2
				y13	1063.5	2	PALI**S**WI**K**RKRQQ-NH_2
				y13	709.7	3	PALI**S**WI**K**RKRQQ-NH_2
				y10	922.8	2	I**S**WI**K**RKRQQ-NH_2
				y9	866.3	2	**S**WI**K**RKRQQ-NH_2

*Oleoylation and palmitoylation sites are highlighted in red and blue respectively within the amino acid sequence of the peptide.

Table 9.19. **Ions produced by fragmenting $SynM_{pal+ole}$ at *m/z* 838 (*z*=4) over 9.5 min of the EIC (see Figure 3.35, SynM/50:50 PPC:DOPC). Product ions correspond to K21 oleoylation and K23 palmitoylation (see Figure 3.37 A).**

b-Ions	*m/z*	*z*	Sequence Ladder*	y-Ions	*m/z*	*z*	Sequence Ladder*
b4	299.1	1	H-GIGA	y24	1060.7	3	GAVLKVLTTGLPALISW IKRKRQQ-NH_2
b5	398.2	1	H-GIGAV	y24	795.6	4	GAVLKVLTTGLPALISW IKRKRQQ-NH_2
b6	511.4	1	H-GIGAVL	y22	1017.4	3	VLKVLTTGLPALISWIK RKRQQ-NH_2
b8	738.6	1	H-GIGAVLKV	y20	1419.5	2	KVLTTGLPALISWIKRK RQQ-NH_2
b9	851.5	1	H-GIGAVLKVL	y19	1355.8	2	VLTTGLPALISWIKRKR QQ-NH_2
b12	1110.8	1	H-GIGAVLKVLTTG	y18	1306.5	2	LTTGLPALISWIKRKRQ Q-NH_2
b13	1223.6	1	H-GIGAVLKVLTTGL	y17	1249.4	2	TTGLPALISWIKRKRQ Q-NH_2
b15 – NH_3	1374.6	1	H-GIGAVLKVLTTGLPA	y16	1199.1	2	TGLPALISWIKRKRQQ-NH_2
b19	946.3	2	H-GIGAVLKVLTTGLPALISW	y15	1148.4	2	GLPALISWIKRKRQQ-NH_2
b20	1002.7	2	H-GIGAVLKVLTTGLPALISWI	y14	1119.2	2	LPALISWIKRKRQQ-NH_2
				y13	1063.5	2	PALISWIKRKRQQ-NH_2
				y13	709.5	3	PALISWIKRKRQQ-NH_2
				y10	923.3	2	ISWIKRKRQQ-NH_2
				y9	866.1	2	SWIKRKRQQ-NH_2
				y8	822.5	2	WIKRKRQQ-NH_2
				y7	729.4	2	IKRKRQQ-NH_2
				y5	476.7	2	RKRQQ-NH_2

*Oleoylation and palmitoylation sites are highlighted in red and blue respectively within the amino acid sequence of the peptide.

Table 9.20. **Ions produced by fragmenting $SynM_{pal+ole}$ at *m/z* 838 (*z*=4) over 9.5 min of the EIC (see Figure 3.35, SynM/50:50 PPC:DOPC). Product ions correspond to K21 palmitoylation and K23 oleoylation (see Figure 3.37 B).**

b-Ions	*m/z*	*z*	Sequence Ladder*	y-Ions	*m/z*	*z*	Sequence Ladder*
b4	299.2	1	H-GIGA	y24	1060.7	3	GAVLKVLTTGLPALISWI KRKRQQ-NH_2
b5	398.2	1	H-GIGAV	y24	795.6	4	GAVLKVLTTGLPALISWI KRKRQQ-NH_2
b6	511.4	1	H-GIGAVL	y22	1017.4	3	VLKVLTTGLPALISWIKR KRQQ-NH_2
b8	738.6	1	H-GIGAVLKV	y20	1419.9	2	KVLTTGLPALISWIKRKR QQ-NH_2
b9	851.5	1	H-GIGAVLKVL	y19	1355.8	2	VLTTGLPALISWIKRKRQ Q-NH_2
b12	1110.8	1	H-GIGAVLKVLTTG	y18	1306.5	2	LTTGLPALISWIKRKRQ Q-NH_2
b13	1223.6	1	H-GIGAVLKVLTTGL	y17	1249.4	2	TTGLPALISWIKRKRQQ-NH_2
b15 – NH_3	1374.6	1	H-GIGAVLKVLTTGLPA	y16	1199.0	2	TGLPALISWIKRKRQQ-NH_2
b19	946.3	2	H-GIGAVLKVLTTGLPALISW	y15	1148.4	2	GLPALISWIKRKRQQ-NH_2
b20	1002.7	2	H-GIGAVLKVLTTGLPALISWI	y14	1119.2	2	LPALISWIKRKRQQ-NH_2
				y13	1063.5	2	PALISWIKRKRQQ-NH_2
				y13	709.5	3	PALISWIKRKRQQ-NH_2
				y10	923.3	2	ISWIKRKRQQ-NH_2
				y9	866.1	2	SWIKRKRQQ-NH_2
				y8	822.5	2	WIKRKRQQ-NH_2
				y7	729.4	2	IKRKRQQ-NH_2
				y5	490.4	2	RKRQQ-NH_2
				y4	412.3	1	KRQQ-NH_2

*Oleoylation and palmitoylation sites are highlighted in red and blue respectively within the amino acid sequence of the peptide.

Table 9.21. **Ions produced by fragmenting $SynM_{pal+ole}$ at *m/z* 838 (*z*=4) over 9.5 min of the EIC (see Figure 3.35, SynM/50:50 PPC:DOPC). Product ions correspond to N-terminus oleoylation and K21 palmitoylation (see Figure 3.38 A).**

b-Ions	*m/z*	*z*	Sequence Ladder*	y-Ions	*m/z*	*z*	Sequence Ladder*
b3	492.3	1	H-**G**IG	y24	972.3	3	GAVLKVLTTGLPALISWI**K**RKRQQ-NH_2
b4	563.3	1	H-**G**IGA	y21	896.7	3	LKVLTTGLPALISWI**K**RKRQQ-NH_2
b5	662.3	1	H-**G**IGAV	y20	859.1	3	KVLTTGLPALISWI**K**RKRQQ-NH_2
b6	775.3	1	H-**G**IGAVL	y19	1223.6	2	VLTTGLPALISWI**K**RKRQQ-NH_2
b8	1002.7	1	H-**G**IGAVLKV	y18	1174.2	2	LTTGLPALISWI**K**RKRQQ-NH_2
b9	1115.6	1	H-**G**IGAVLKVL	y17	1117.7	2	TTGLPALISWI**K**RKRQQ-NH_2
b10	1216.8	1	H-**G**IGAVLKVLT	y16	1066.6	2	TGLPALISWI**K**RKRQQ-NH_2
b12	1374.7	1	H-**G**IGAVLKVLTTG	y15	1016.5	2	GLPALISWI**K**RKRQQ-NH_2
b13	1487.8	1	H-**G**IGAVLKVLTTGL	y14	987.9	2	LPALISWI**K**RKRQQ-NH_2
b13 - H_2O	1469.7	1	H-**G**IGAVLKVLTTGL	y13	931.2	2	PALISWI**K**RKRQQ-NH_2
				y13	621.5	3	PALISWI**K**RKRQQ-NH_2
				y12	882.9	2	ALISWI**K**RKRQQ-NH_2
				y11	847.2	2	LISWI**K**RKRQQ-NH_2
				y10	790.6	2	ISWI**K**RKRQQ-NH_2
				y9	733.7	2	SWI**K**RKRQQ-NH_2
				y7	597.1	2	I**K**RKRQQ-NH_2
				y6	1080.1	1	**K**RKRQQ-NH_2
				y4	558.4	1	KRQQ-NH_2
				y4 - NH_3	541.9	1	KRQQ-NH_2

*Oleoylation and palmitoylation sites are highlighted in red and blue respectively within the amino acid sequence of the peptide.

Table 9.22. **Ions produced by fragmenting $SynM_{pal+ole}$ at *m/z* 838 (*z*=4) over 9.5 min of the EIC (see Figure 3.35, SynM/50:50 PPC:DOPC). Product ions correspond to N-terminus palmitoylation and K21 oleoylation (see Figure 3.38 B).**

b-Ions	*m/z*	*z*	Sequence Ladder*	y-Ions	*m/z*	*z*	Sequence Ladder*
b3	466.3	1	H-**G**IG	y24	980.8	3	GAVLKVLTTGLPALISWI **K**RKRQQ-NH_2
b4	537.1	1	H-**G**IGA	y21	1356.8	2	LKVLTTGLPALISWI**K**RK RQQ-NH_2
b5	636.5	1	H-**G**IGAV	y21	904.8	3	LKVLTTGLPALISWI**K**RK RQQ-NH_2
b6	749.2	1	H-**G**IGAVL	y21	679.1	4	LKVLTTGLPALISWI**K**RK RQQ-NH_2
b8	976.6	1	H-**G**IGAVLKV	y20	1299.9	2	KVLTTGLPALISWI**K**RKR QQ-NH_2
b9	1089.6	1	H-**G**IGAVLKVL	y20	650.7	4	KVLTTGLPALISWI**K**RKR QQ-NH_2
b10	1190.8	1	H-**G**IGAVLKVLT	y19	1236.7	2	VLTTGLPALISWI**K**RKRQ Q-NH_2
b12	1348.8	1	H-**G**IGAVLKVLTTG	y18	1187.5	2	LTTGLPALISWI**K**RKRQQ -NH_2
b12 - H_2O	1330.8	1	H-**G**IGAVLKVLTTG	y17	1130.5	2	TTGLPALISWI**K**RKRQQ-NH_2
b12 - H_2O	666.2	2	H-**G**IGAVLKVLTTG	y16	1080.1	2	TGLPALISWI**K**RKRQQ-NH_2
b13	1461.7	1	H-**G**IGAVLKVLTTGL	y15	1029.1	2	GLPALISWI**K**RKRQQ-NH_2
b13 - H_2O	1443.8	1	H-**G**IGAVLKVLTTGL	y14	1000.9	2	LPALISWI**K**RKRQQ-NH_2
b18	972.3	2	H-**G**IGAVLKVLTTGLPALIS	y13	944.4	2	PALISWI**K**RKRQQ-NH_2
				y13	630.1	3	PALISWI**K**RKRQQ-NH_2
				y12	896.7	2	ALISWI**K**RKRQQ-NH_2
				y10	803.2	2	ISWI**K**RKRQQ-NH_2
				y9	747.2	2	SWI**K**RKRQQ-NH_2
				y8	703.8	2	WI**K**RKRQQ-NH_2
				y7	609.1	1	I**K**RKRQQ-NH_2
				y4	558.4	1	KRQQ-NH_2
				y4 – NH_3	541.9	1	KRQQ-NH_2

*Oleoylation and palmitoylation sites are highlighted in red and blue respectively within the amino acid sequence of the peptide.

Table 9.23. **Ions produced by fragmenting $SynM_{pal+ole}$ at *m/z* 838 (*z*=4) over 10.2 min of the EIC (see Figure 3.35, SynM/50:50 PPC:DOPC). Product ions correspond to K7 oleoylation and K21 palmitoylation (see Figure 3.39 A).**

b-Ions	*m/z*	*z*	Sequence Ladder*	y-Ions	*m/z*	*z*	Sequence Ladder*
b4	299.1	1	H-GIGA	y24	1060.6	3	GAVL**K**VLTTGLPALISW I**K**RKRQQ-NH_2
b5	398.2	1	H-GIGAV	y24	795.4	4	GAVL**K**VLTTGLPALISW I**K**RKRQQ-NH_2
b6	511.3	1	H-GIGAVL	y22	1017.7	3	VL**K**VLTTGLPALISWI**K** RKRQQ-NH_2
b7	903.6	1	H-GIGAVL**K**	y22	763.8	4	VL**K**VLTTGLPALISWI**K** RKRQQ-NH_2
b8	1002.6	1	H-GIGAVL**K**V	y21	1476.2	2	L**K**VLTTGLPALISWI**K**R KRQQ-NH_2
b9	1115.7	1	H-GIGAVL**K**VL	y20	1419.9	2	**K**VLTTGLPALISWI**K**RK RQQ-NH_2
b10	1216.7	1	H-GIGAVL**K**VLT	y19	1223.6	2	VLTTGLPALISWI**K**RKR QQ-NH_2
b10 - H_2O	1198.9	1	H-GIGAVL**K**VLT	y18	1174.0	2	LTTGLPALISWI**K**RKRQ Q-NH_2
b11	1317.7	1	H-GIGAVL**K**VLTT	y17	1117.4	2	TTGLPALISWI**K**RKRQQ -NH2
b12	1374.7	1	H-GIGAVL**K**VLTTG	y16	1067.3	2	TGLPALISWI**K**RKRQQ-NH_2
b12 - H_2O	1356.6	1	H-GIGAVL**K**VLTTG	y15	1016.4	2	GLPALISWI**K**RKRQQ-NH_2
b12 - H_2O	678.1	2	H-GIGAVL**K**VLTTG.l	y14	987.6	2	LPALISWI**K**RKRQQ-NH_2
b13	1488.0	1	H-GIGAVL**K**VLTTGL	y13	931.1	2	PALISWI**K**RKRQQ-NH_2
b13 - H_2O	1470.1	1	H-GIGAVL**K**VLTTGL	y13	621.5	3	PALISWI**K**RKRQQ-NH_2
b14 - H_2O	783.2	2	H-GIGAVL**K**VLTTGLP	y9	733.5	2	SWI**K**RKRQQ-NH_2
b18	985.1	2	H-GIGAVL**K**VLTTGLPALIS	y7	597.5	2	I**K**RKRQQ-NH_2
				y6	1080.5	1	**K**RKRQQ-NH_2
				y6	540.9	2	**K**RKRQQ-NH_2
				y6 - NH_3	1063.5	1	**K**RKRQQ-NH_2
				y4	558.3	1	KRQQ-NH_2

*Oleoylation and palmitoylation sites are highlighted in red and blue respectively within the amino acid sequence of the peptide.

Table 9.24. **Ions produced by fragmenting $SynM_{pal+ole}$ at *m/z* 838 (*z*=4) over 10.2 min of the EIC (see Figure 3.35, SynM/50:50 PPC:DOPC). Product ions correspond to K7 palmitoylation and K21 oleoylation (see Figure 3.39 B).**

b-Ions	*m/z*	*z*	Sequence Ladder*	y-Ions	*m/z*	*z*	Sequence Ladder*
b4	299.1	1	H-GIGA	y24	1060.6	3	GAVL**K**VLTTGLPALISW I**K**RKRQQ-NH_2
b5	398.2	1	H-GIGAV	y24	795.4	4	GAVL**K**VLTTGLPALISW I**K**RKRQQ-NH_2
b6	511.3	1	H-GIGAVL	y22	1017.7	3	VL**K**VLTTGLPALISWI**K** RKRQQ-NH_2
b7	877.5	1	H-GIGAVL**K**	y22	763.8	4	VL**K**VLTTGLPALISWI**K** RKRQQ-NH_2
b8	976.6	1	H-GIGAVL**K**V	y21	1476.2	2	L**K**VLTTGLPALISWI**K**R KRQQ-NH_2
b9	1089.6	1	H-GIGAVL**K**VL	y20	1419.9	2	**K**VLTTGLPALISWI**K**RK RQQ-NH_2
b10	1190.7	1	H-GIGAVL**K**VLT	y19	1236.6	2	VLTTGLPALISWI**K**RKR QQ-NH_2
b11	1291.7	1	H-GIGAVL**K**VLTT	y18	1187.2	2	v.LTTGLPALISWI**K**RKR QQ-NH_2
b11 - H_2O	1273.7	1	H-GIGAVL**K**VLTT	y17	1130.3	2	TTGLPALISWI**K**RKRQQ -NH_2
b12	1348.6	1	H-GIGAVL**K**VLTTG	y16	1080.0	2	TGLPALISWI**K**RKRQQ- NH_2
b12 - H_2O	1330.8	1	H-GIGAVL**K**VLTTG	y15	1030.1	2	GLPALISWI**K**RKRQQ- NH_2
b12 - H_2O	665.9	2	H-GIGAVL**K**VLTTG	y14	1000.7	2	LPALISWI**K**RKRQQ- NH_2
b13	1461.8	1	H-GIGAVL**K**VLTTGL	y13	944.3	2	PALISWI**K**RKRQQ-NH_2
b15	816.1	2	H-GIGAVL**K**VLTTGLPA	y13	630.1	3	PALISWI**K**RKRQQ-NH_2
b18	972.4	2	H-GIGAVL**K**VLTTGLPALIS	y12	896.4	2	ALISWI**K**RKRQQ-NH_2
				y11	860.0	2	LISWI**K**RKRQQ-NH_2
				y10	803.2	2	ISWI**K**RKRQQ-NH_2
				y9	745.9	2	SWI**K**RKRQQ-NH_2
				y8	703.5	2	WI**K**RKRQQ-NH_2
				y7	610.5	2	I**K**RKRQQ-NH_2
				y4	558.3	2	KRQQ-NH_2

*Oleoylation and palmitoylation sites are highlighted in red and blue respectively within the amino acid sequence of the peptide.

Table 9.25. **Ions produced by fragmenting $SynM_{pal+ole}$ at *m/z* 838 (*z*=4) over 10.6 min of the EIC (see Figure 3.35, SynM/50:50 PPC:DOPC). Product ions correspond to N-terminus oleoylation and K23 palmitoylation (see Figure 3.40 A).**

b-Ions	*m/z*	*z*	Sequence Ladder*	y-Ions	*m/z*	*z*	Sequence Ladder*
b3	492.3	1	H-GIG	y24	972.3	3	GAVLKVLTTGLPALISWIKRKRQQ-NH_2
b4	563.3	1	H-GIGA	y22	929.6	3	VLKVLTTGLPALISWIKRKRQQ-NH_2
b5	662.3	1	H-GIGAV	y21	896.6	3	LKVLTTGLPALISWIKRKRQQ-NH_2
b6	775.3	1	H-GIGAVL	y20	858.9	3	KVLTTGLPALISWIKRKRQQ-NH_2
b8	1002.6	1	H-GIGAVLKV	y19	1223.6	2	VLTTGLPALISWIKRKRQQ-NH_2
b9	1115.6	1	H-GIGAVLKVL	y18	1173.9	2	LTTGLPALISWIKRKRQQ-NH_2
b10	1216.8	1	H-GIGAVLKVLT	y17	1117.8	2	TTGLPALISWIKRKRQQ-NH_2
b12	1374.7	1	H-GIGAVLKVLTTG	y16	1067.0	2	TGLPALISWIKRKRQQ-NH_2
b13	1487.7	1	H-GIGAVLKVLTTGL	y15	1016.3	2	GLPALISWIKRKRQQ-NH_2
b13 - H_2O	1470.1	1	H-GIGAVLKVLTTGL	y14	988.0	2	LPALISWIKRKRQQ-NH_2
				y13	931.4	2	PALISWIKRKRQQ-NH_2
				y13	621.5	3	PALISWIKRKRQQ-NH_2
				y12	882.9	2	ALISWIKRKRQQ-NH_2
				y11	847.3	2	LISWIKRKRQQ-NH_2
				y10	790.5	2	ISWIKRKRQQ-NH_2
				y9	734.0	2	SWIKRKRQQ-NH_2
				y8	690.8	2	WIKRKRQQ-NH_2
				y7	598.6	2	IKRKRQQ-NH_2
				y6	1080.3	1	KRKRQQ-NH_2
				y5	952.9	1	RKRQQ-NH_2
				y5	476.9	2	RKRQQ-NH_2
				y4	796.4	1	KRQQ-NH_2
				y4 - NH_3	779.7	1	KRQQ-NH_2

*Oleoylation and palmitoylation sites are highlighted in red and blue respectively within the amino acid sequence of the peptide.

Table 9.26 **Ions produced by fragmenting $SynM_{pal+ole}$ at *m/z* 838 (*z*=4) over 10.6 min of the EIC (see Figure 3.35, SynM/50:50 PPC:DOPC). Product ions correspond to N-terminus palmitoylation and K23 oleoylation (see Figure 3.40 B).**

b-Ions	*m/z*	*z*	Sequence Ladder*	y-Ions	*m/z*	*z*	Sequence Ladder*
b3	466.3	1	H-**G**IG	y24	980.0	3	GAVLKVLTTGLPALISWIKR**K**RQQ-NH_2
b4	537.2	1	H-**G**IGA	y22	938.3	3	VLKVLTTGLPALISWIKR**K**RQQ-NH_2
b5	636.2	1	H-**G**IGAV	y21	1356.7	2	LKVLTTGLPALISWIKR**K**RQQ-NH_2
b6	749.1	1	H-**G**IGAVL	y21	905.3	3	LKVLTTGLPALISWIKR**K**RQQ-NH_2
b7	877.4	1	H-**G**IGAVLK	y20	1299.9	2	KVLTTGLPALISWIKR**K**RQQ-NH_2
b8	976.6	1	H-**G**IGAVLKV	y20	867.5	3	KVLTTGLPALISWIKR**K**RQQ-NH_2
b9	1089.7	1	H-**G**IGAVLKVL	y19	1236.5	2	k.VLTTGLPALISWIKR**K**RQQ-NH_2
b10	1190.2	1	H-**G**IGAVLKVLT	y18	1186.8	2	LTTGLPALISWIKR**K**RQQ-NH_2
b12	1348.6	1	H-**G**IGAVLKVLTTG	y17	1130.6	2	TTGLPALISWIKR**K**RQQ-NH_2
b12 - H_2O	1330.8	1	H-**G**IGAVLKVLTTG	y16	1080.1	2	TGLPALISWIKR**K**RQQ-NH_2
b12 - H_2O	666.1	2	H-**G**IGAVLKVLTTG	y15	1029.5	2	GLPALISWIKR**K**RQQ-NH_2
b13	1461.7	1	H-**G**IGAVLKVLTTGL	y14	1001.0	2	LPALISWIKR**K**RQQ-NH_2
b13 - H_2O	1443.7	1	H-**G**IGAVLKVLTTGL	y13	944.4	2	PALISWIKR**K**RQQ-NH_2
				y13	630.2	2	PALISWIKR**K**RQQ-NH_2
				y12	896.6	2	ALISWIKR**K**RQQ-NH_2
				y11	860.4	2	LISWIKR**K**RQQ-NH_2
				y10	803.7	2	ISWIKR**K**RQQ-NH_2
				y9	746.7	2	SWIKR**K**RQQ-NH_2
				y7	703.8	2	IKR**K**RQQ-NH_2
				y5	609.1	2	R**K**RQQ-NH_2
				y4	822.6	1	**K**RQQ-NH_2
				y4	411.4	2	**K**RQQ-NH_2

*Oleoylation and palmitoylation sites are highlighted in red and blue respectively within the amino acid sequence of the peptide.

Table 9.27. **Ions produced by fragmenting $SynM_{pal+ole}$ at *m/z* 838 (*z*=4) over 10.9 min of the EIC (see Figure 3.35, SynM/50:50 PPC:DOPC). Product ions correspond to N-terminus oleoylation and R22 palmitoylation (see Figure 3.41 A).**

b-Ions	*m/z*	*z*	Sequence Ladder*	y-Ions	*m/z*	*z*	Sequence Ladder*
b3	492.3	1	H-**G**IG	y24	972.2	3	GAVLKVLTTGLPALISWIK**R**KR QQ-NH_2
b4	563.2	1	H-**G**IGA	y22	929.8	3	VLKVLTTGLPALISWIK**R**KRQQ-NH_2
b5	662.3	1	H-**G**IGAV	y21	896.8	3	LKVLTTGLPALISWIK**R**KRQQ-NH_2
b6	775.3	1	H-**G**IGAVL	y20	859.0	3	KVLTTGLPALISWIK**R**KRQQ-NH_2
b8	1002.5	1	H-**G**IGAVLKV	y19	1223.6	2	VLTTGLPALISWIK**R**KRQQ-NH_2
b9	1115.7	1	H-**G**IGAVLKVL	y18	1173.8	2	LTTGLPALISWIK**R**KRQQ-NH_2
b10	1216.7	1	H-**G**IGAVLKVLT	y17	1117.9	2	TTGLPALISWIK**R**KRQQ-NH_2
b12	1374.7	1	H-**G**IGAVLKVLTTG	y16	1067.1	2	TGLPALISWIK**R**KRQQ-NH_2
b13	1487.7	1	H-**G**IGAVLKVLTTGL	y15	1016.5	2	GLPALISWIK**R**KRQQ-NH_2
b13 – H_2O	1470.2	1	H-**G**IGAVLKVLTTGL	y14	988.1	2	LPALISWIK**R**KRQQ-NH_2
				y13	931.4	2	PALISWIK**R**KRQQ-NH_2
				y13	621.6	2	PALISWIK**R**KRQQ-NH_2
				y12	882.8	2	ALISWIK**R**KRQQ-NH_2
				y11	847.3	2	LISWIK**R**KRQQ-NH_2
				y10	790.4	2	ISWIK**R**KRQQ-NH_2
				y9	734.1	2	SWIK**R**KRQQ-NH_2
				y8	690.7	2	WIK**R**KRQQ-NH_2
				y7	598.6	2	IK**R**KRQQ-NH_2
				y6	1080.1	1	K**R**KRQQ-NH_2
				y5	953.2	1	**R**KRQQ-NH_2
				y4	558.6	1	KRQQ-NH_2
				y4 - NH_3	541.3	1	KRQQ-NH_2

*Oleoylation and palmitoylation sites are highlighted in red and blue respectively within the amino acid sequence of the peptide.

Table 9.28. **Ions produced by fragmenting $SynM_{pal+ole}$ at *m/z* 838 (*z*=4) over 10.9 min of the EIC (see Figure 3.35, SynM/50:50 PPC:DOPC). Product ions correspond to N-terminus palmitoylation and R22 oleoylation (see Figure 3.41 B).**

b-Ions	*m/z*	*z*	Sequence Ladder*	y-Ions	*m/z*	*z*	Sequence Ladder*
b3	466.3	1	H-**G**IG	y24	980.0	3	GAVLKVLTTGLPALISWIK**R**KRQQ-NH_2
b4	537.2	1	H-**G**IGA	y22	938.4	3	VLKVLTTGLPALISWIK**R**KRQQ-NH_2
b5	636.2	1	H-**G**IGAV	y21	1356.7	2	LKVLTTGLPALISWIK**R**KRQQ-NH_2
b6	749.3	1	H-**G**IGAVL	y21	905.0	3	LKVLTTGLPALISWIK**R**KRQQ-NH_2
b7	877.4	1	H-**G**IGAVLK	y20	867.8	3	KVLTTGLPALISWIK**R**KRQQ-NH_2
b8	976.6	1	H-**G**IGAVLKV	y18	1186.9	2	LTTGLPALISWIK**R**KRQQ-NH_2
b9	1089.6	1	H-**G**IGAVLKVL	y17	1130.5	2	TTGLPALISWIK**R**KRQQ-NH_2
b12 - H_2O	1330.8	1	H-**G**IGAVLKVLTTG	y16	1080.1	2	TGLPALISWIK**R**KRQQ-NH_2
b12 - H_2O	666.0	2	H-**G**IGAVLKVLTTG.I	y15	1029.5	2	GLPALISWIK**R**KRQQ-NH_2
				y14	1000.8	2	LPALISWIK**R**KRQQ-NH_2
				y13	944.4	2	PALISWIK**R**KRQQ-NH_2
				y13	630.2	3	PALISWIK**R**KRQQ-NH_2
				y12	896.4	2	ALISWIK**R**KRQQ-NH_2
				y11	860.4	2	LISWIK**R**KRQQ-NH_2
				y10	803.7	2	ISWIK**R**KRQQ-NH_2
				y9	747.2	2	SWIK**R**KRQQ-NH_2
				y8	703.8	2	WIK**R**KRQQ-NH_2
				y7	609.1	2	IK**R**KRQQ-NH_2
				y5	978.8	1	**R**KRQQ-NH_2
				y5	489.9	1	**R**KRQQ-NH_2
				y4	558.3	1	KRQQ-NH_2
				y4 - NH_3	541.1	1	KRQQ-NH_2

*Oleoylation and palmitoylation sites are highlighted in red and blue respectively within the amino acid sequence of the peptide.

Table 9.29. **Ions produced by fragmenting $SynM_{pal+ole}$ at *m/z* 838 (*z*=4) over 11.2 min of the EIC (see Figure 3.35, SynM/50:50 PPC:DOPC). Product ions correspond to N-terminus oleoylation and R24 palmitoylation (see Figure 3.42 A).**

b-Ions	*m/z*	*z*	Sequence Ladder*	y-Ions	*m/z*	*z*	Sequence Ladder*
b3	492.2	1	H-**G**IG	y24	972.3	3	GAVLKVLTTGLPALISWIKRK**R**QQ-NH_2
b4	563.2	1	H-**G**IGA	y22	929.7	3	VLKVLTTGLPALISWIKRK**R**QQ-NH_2
b5	662.4	1	H-**G**IGAV	y21	896.3	3	LKVLTTGLPALISWIKRK**R**QQ-NH_2
b6	775.2	1	H-**G**IGAVL	y20	859.0	3	KVLTTGLPALISWIKRK**R**QQ-NH_2
b8	1002.6	1	H-**G**IGAVLKV	y19	1223.7	2	VLTTGLPALISWIKRK**R**QQ-NH_2
b9	1115.6	1	H-**G**IGAVLKVL	y18	1174.2	2	LTTGLPALISWIKRK**R**QQ-NH_2
b10	1216.7	1	H-**G**IGAVLKVLT	y17	1117.7	2	TTGLPALISWIKRK**R**QQ-NH_2
b12	1374.7	1	H-**G**IGAVLKVLTTG	y16	1066.9	2	TGLPALISWIKRK**R**QQ-NH_2
b13	1487.7	1	H-**G**IGAVLKVLTTGL	y15	1016.4	2	GLPALISWIKRK**R**QQ-NH_2
b13 – H_2O	1469.8	1	H-**G**IGAVLKVLTTGL	y14	988.0	2	LPALISWIKRK**R**QQ-NH_2
				y13	931.5	2	PALISWIKRK**R**QQ-NH_2
				y13	621.5	3	PALISWIKRK**R**QQ-NH_2
				y12	882.8	2	ALISWIKRK**R**QQ-NH_2
				y11	847.2	2	LISWIKRK**R**QQ-NH_2
				y10	790.8	2	ISWIKRK**R**QQ-NH_2
				y9	734.2	2	SWIKRK**R**QQ-NH_2
				y8	690.8	2	WIKRK**R**QQ-NH_2
				y7	598.0	2	IKRK**R**QQ-NH_2
				y6	1080.1	1	KRK**R**QQ-NH_2
				y5	953.2	1	RK**R**QQ-NH_2
				y4	796.1	1	K**R**QQ-NH_2
				y4 - NH_3	779.5	1	K**R**QQ-NH_2

*Oleoylation and palmitoylation sites are highlighted in red and blue respectively within the amino acid sequence of the peptide.

Table 9.30. **Ions produced by fragmenting $SynM_{pal+ole}$ at *m/z* 838 (*z*=4) over 11.2 min of the EIC (see Figure 3.35, SynM/50:50 PPC:DOPC). Product ions correspond to N-terminus palmitoylation and R24 oleoylation (see Figure 3.42 B).**

b-Ions	*m/z*	*z*	Sequence Ladder*	y-Ions	*m/z*	*z*	Sequence Ladder*
b3	466.3	1	H-**G**IG	y24	981.1	3	GAVLKVLTTGLPALISWIKRK**R**QQ-NH_2
b4	537.2	1	H-**G**IGA	y22	938.7	3	VLKVLTTGLPALISWIKRK**R**QQ-NH_2
b5	636.4	1	H-**G**IGAV	y21	1356.8	2	LKVLTTGLPALISWIKRK**R**QQ-NH_2
b6	749.8	1	H-**G**IGAVL	y21	905.3	3	LKVLTTGLPALISWIKRK**R**QQ-NH_2
b7	877.7	1	H-**G**IGAVLK	y20	867.5	3	KVLTTGLPALISWIKRK**R**QQ-NH_2
b8	976.6	1	H-**G**IGAVLKV	y19	1236.5	2	VLTTGLPALISWIKRK**R**QQ-NH_2
b9	1089.6	1	H-**G**IGAVLKVL	y18	1186.5	2	LTTGLPALISWIKRK**R**QQ-NH_2
b10	1190.1	1	H-**G**IGAVLKVLT	y17	1130.4	2	TTGLPALISWIKRK**R**QQ-NH_2
b12	1348.7	1	H-**G**IGAVLKVLTTG	y16	1079.7	2	TGLPALISWIKRK**R**QQ-NH_2
b12 - H_2O	1330.6	1	H-**G**IGAVLKVLTTG	y15	1029.1	2	GLPALISWIKRK**R**QQ-NH_2
b12 - H_2O	665.8	2	H-**G**IGAVLKVLTTG.I	y14	1000.7	2	LPALISWIKRK**R**QQ-NH_2
b13	1462.2	1	H-**G**IGAVLKVLTTGL	y13	944.5	2	PALISWIKRK**R**QQ-NH_2
b13 - H_2O	1443.9	1	H-**G**IGAVLKVLTTGL	y13	630.2	3	PALISWIKRK**R**QQ-NH_2
				y12	896.0	2	ALISWIKRK**R**QQ-NH_2
				y11	860.5	2	LISWIKRK**R**QQ-NH_2
				y10	803.9	2	ISWIKRK**R**QQ-NH_2
				y9	746.8	2	SWIKRK**R**QQ-NH_2
				y8	703.8	2	WIK**R**QQ-NH_2
				y5	489.9	2	RK**R**QQ-NH_2
				y4	822.6	1	K**R**QQ-NH_2

*Oleoylation and palmitoylation sites are highlighted in red and blue respectively within the amino acid sequence of the peptide.

9.3. Appendix C: Supplementary information for Chapter four - New insight to integral membrane protein (AQP0) lipidation by membrane lipids

Table 9.31. **The deconvoluted *m/z* for non-acylated peptides identified from b-AQP0-OC tryptic digestion (see Figure 4.16).**

AA Residues	MCL‡	Sequence + Modification	Theor *m/z*‡ $[M + H]^+$	Meas *m/z*‡ $[M + H]^+$	Error (ppm)
[1-5]	0	MWELR	734.3654	734.3658	0.5
[6-11]	0	SASFWR	753.3678	753.3687	1.2
[12-33]	0	AICAEFFASLFYVFFGLGASLR	2429.2362	2429.237	0.3
[114-152]	0	GNLALNTLHPGVSVGQATIVEIFLTLQFVLCIFATYDER	4263.2522	4263.2677	3.6
[153-187]	2	RNGRLGSVALAVGFSLTLGHLFGMYYTGAGMNPAR [1×Deamidation]	3655.8624	3655.8681	1.6
[157-187]	0	LGSVALAVGFSLTLGHLFGMYYTGAGMNPAR	3171.6118	3171.6151	1.0
[188-196]	0	SFAPAILTR	975.5622	975.5626	0.4
[188-228]	2	SFAPAILTRNFTNHWVYWVGPVIGAGLGSLLYDFLLFPRLK	4649.5224	4649.5286	1.3
[188-233]	3	SFAPAILTRNFTNHWVYWVGPVIGAGLGSLLYDFLLFPRLKSVSER	5207.7986	5207.7970	-0.3
[197-226]	0	NFTNHWVYWVGPVIGAGLGSLLYDFLLFPR	3451.799	3451.8018	0.8
[197-226]	0	NFTNHWVYWVGPVIGAGLGSLLYDFLLFPR [1×O]	3467.7939	3467.7932	-0.2
[197-228]	1	NFTNHWVYWVGPVIGAGLGSLLYDFLLFPRLK	3692.978	3692.9811	0.8
[197-228]	1	NFTNHWVYWVGPVIGAGLGSLLYDFLLFPRLK [2×O]	3724.9679	3724.9593	-2.3
[197-233]	2	NFTNHWVYWVGPVIGAGLGSLLYDFLLFPRLKSVSER	4251.2542	4251.2547	0.1
[229-233]	0	SVSER	577.294	577.2942	0.3
[229-238]	1	SVSERLSILK [1×P]	1211.6395	1211.6406	0.9
[234-238]	0	LSILK	573.397	573.3972	0.3
[234-238]	0	LSILK [1×P]	653.3634	653.364	0.9
[234-259]	1	LSILKGSRPSESNGQPEVTGEPVELK [1×Deamidation]	2752.4363	2752.4389	0.9
[239-259]	0	GSRPSESNGQPEVTGEPVELK [1×Deamidation]	2198.0571	2198.0585	0.6
[239-259]	0	GSRPSESNGQPEVTGEPVELK [1×Deamidation; 1×P]	2278.0235	2278.024	0.2
[239-263]	1	GSRPSESNGQPEVTGEPVELKTQAL [1×Deamidation]	2611.2846	2611.286	0.5
[260-263]	0	TQAL	432.2453	432.2454	0.2

‡Both theoretical (Theor) and measured (Meas) *m/z* are for the monoisotopic peak. Theoretical mass obtained from mMass software. (MCL) is number of missed cleavages.

Table 9.32. **The deconvoluted *m/z* for identified acylated peptides followed trypsin digestion of b-AQP0-OC.**

Theor *m/z*‡ $[M + H]^+$	Meas *m/z*‡ $[M + H]^+$	RT (min)	Error (ppm)	$10^3 \times A_{Lipidation}$ § (a.u.)	Assignment
^{234}LSILKGSRPSESNGQPEVTGEPVELK^{259}					
2990.6660	2990.6689	7.64	1.3	18.5 ± 2	Peptide [234-259] + (C16:0) + 1 × Deamidation/Palmitoylation
3016.6816	3016.6822	7.74	0.5	78 ± 8	Peptide [234-259] + (C18:1) + 1 × Deamidation/Oleoylation
3018.6973	3018.6964	7.99	0.03	6 ± 1	Peptide [234-259] + (C18:0) + 1 × Deamidation/Stearoylation
^{1}MWELR^{5}					
1014.6056	1014.6039	9.59	-1.7	46 ± 18	Peptide [1-5] + (C18:1) + O/ Oleoylation
970.5794	970.5791	9.64	-0.3	6 ± 1	Peptide [1-5] + (C16:1)/Palmitoleoylation
1020.5951	1020.5957	9.82	0.6	7 ± 2.5	Peptide [1-5] + (C20:4)/Arachidonoylation
972.5951	972.5951	10.05	0	65 ± 26	Peptide [1-5] + (C16:0) / Palmitoylation
1022.6107	1022.6125	10.17	1.8	17 ± 6	Peptide [1-5] + (C20:3)/Dihomo-γ-linolenoylation
998.6107	998.6116	10.20	0.9	256 ± 81	Peptide [1-5] + (C18:1)/Oleoylation
1024.6264	1024.6285	10.40	2.0	9 ± 2	Peptide [1-5] + (C20:2)/Eicosadienoylation
1000.6264	1000.6272	10.68	0.8	36 ± 12	Peptide [1-5] + (C18:0)/Stearoylation
1026.6420	1026.6427	10.78	0.7	19 ± 3.5	Peptide [1-5] + (C20:1)/Eicosenoylation

‡ Both theoretical (Theor) and measured (Meas) *m/z* are for the monoisotopic peak. Theoretical mass obtained from mMass software.

§ The peak area (A) represents the summation of peak area over all observed charge states for each acylated peptide, z=1-2 for peptide [1-5]; z=2-4 for peptide [234-259]. Errors reported as the standard error of the mean (SEM) of peak area when n=3.

Table 9.33. **The deconvoluted *m/z* for non-acylated peptides identified from b-AQP0-OC tryptic digestion, using digestion protocol Method-D and LC-MS Method-IIII on Synapt G2-s (see section 8.2.2.2.1).**

AA Residues	MCL‡	Sequence + Modification	Theor *m/z*‡ $[M + H]^+$	Meas *m/z*‡ $[M + H]^+$	Error (ppm)
[1-5]	0	MWELR	734.3660	734.3664	0.5
[6-11]	0	SASFWR	753.3684	753.3678	-0.8
[12-33]	0	AICAEFFASLFYVFFGLGASLR	2429.2368	2429.2370	0.1
[34-85]	0	WAPGPLHVLQVALAFGLALATLVQAVGHIS GAHVNPAVTFAFLVGSQMSLLR	5345.9507	5345.9558	1.0
[86-113]	0	AICYMVAQLLGAVAGAAVLYSVTPPAVR	2804.5208	2804.5249	1.5
[114-152]	0	GNLALNTLHPGVSVGQATIVEIFLTLQFVLCIFA TYDER	4263.2529	4263.2689	3.8
[153-156]	1	RNGR	502.2850	502.2906	11.1
[153-187]	2	RNGRLGSVALAVGFSLTLGHLFGMYYTGAGM NPAR [1×Deamidation]	3655.8630	3655.8628	-0.1
[154-187]	1	NGRLGSVALAVGFSLTLGHLFGMYYTGAGMN PAR [1×Deamidation]	3499.7620	3499.7622	0.1
[157-187]	0	LGSVALAVGFSLTLGHLFGMYYTGAGMNPAR	3171.6123	3171.6054	-2.2
[157-187]	0	LGSVALAVGFSLTLGHLFGMYYTGAGMNPAR [1×O]	3187.6072	3187.6102	0.9
[188-196]	0	SFAPAILTR	975.5627	975.5668	4.2
[188-226]	1	SFAPAILTRNFTNHWVYWVGPVIGAGLGSLLY DFLLFPR	4408.3438	4408.3466	0.6
[197-226]	0	NFTNHWVYWVGPVIGAGLGSLLYDFLLFPR	3451.7996	3451.8002	0.2
[197-226]	0	NFTNHWVYWVGPVIGAGLGSLLYDFLLFPR [2×O]	3483.7893	3451.8002	-1.3
[197-228]	1	NFTNHWVYWVGPVIGAGLGSLLYDFLLFPRLK	3692.9785	3692.9802	0.5
[227-228]	0	LK	260.1974	260.1971	-1.2
[229-233]	0	SVSER	577.2946	577.2943	-0.5
[229-238]	1	k.SVSERLSILK.g [1×Phospho]	1211.6401	1211.6392	-0.7
[229-259]	2	SVSERLSILKGSRPSESNGQPEVTGEPVELK [1×Deamidation]	3310.7131	3310.7133	0.1
[234-238]	0	LSILK	573.3976	573.3913	-11.0
[234-259]	1	LSILKGSRPSESNGQPEVTGEPVELK [1×Deamidation]	2752.4368	2752.4374	0.2
[239-259]	0	GSRPSESNGQPEVTGEPVELK [1×Deamidation; 1×P]	2278.0240	2278.0249	0.4
[239-263]	1	GSRPSESNGQPEVTGEPVELKTQAL [1×Deamidation]	2611.2852	2611.2883	1.2
[242-259]	0	PSESNGQPEVTGEPVELK [1×Deamidation]	1897.9031	1897.9034	0.2
[260-263]	0	TQAL	432.2458	432.2458	0

‡Both theoretical (Theor) and measured (Meas) *m/z* are for the monoisotopic peak. Theoretical mass obtained from MassLynx software (V4.1). (MCL) is number of missed cleavages.

Table 9.34. **The deconvoluted *m/z* for identified acylated peptides followed trypsin digestion of b-AQP0-OC.**

Entry	Theor *m/z*‡ $[M + H]^+$	Meas *m/z*‡ $[M + H]^+$	RT (min)	Error (ppm)	10^3 × Total $A_{Lipidation}$§ (a.u.)	Assignment
^{234}LSILKGSRPSESNGQPEVTGEPVELK^{259}						
i	2990.6665	2990.6563	5.34	-3.4	3.5 ± 1	Peptide [234-259] + (C16:0) + 1 × Deamidation/Palmitoylation
ii	3016.6821	3016.6798	5.44	-0.8	6 ± 1	Peptide [234-259] + (C18:1) + 1 × Deamidation/Oleoylation
iii	3040.6821	3040.6807	5.48	-0.5	3 ± 0.1	[Peptide 234-259] + (C20:3) + 1 × Deamidation/Dihomo-γ-linolenoylation
iv	3042.6978	3042.6892	5.50	-2.9	1 ± 0.1	Peptide [234-259] + (C20:2)/Eicosadienoylation
v	3096.6484	3096.6475	5.60	-0.5	0.4 ± 0.1	Peptide [234-259] + (C18:1) + P + 1 × Deamidation/Oleoylation
vi	3018.6978	3018.7015	5.66	1.2	0.5 ± 0.4	Peptide [234-259] + (C18:0) + 1 × Deamidation/Stearoylation
vii	3044.7134	3044.7148	5.70	0.5	0.3 ± 0.2	Peptide [234-259] + (C20:1) + 1 × Deamidation/Eicosenoylation
^{1}MWELR^{5}						
viii	1014.6062	1014.6044	6.48	-1.8	3 ± 2	Peptide [1-5] + (C18:1) + O /Oleoylation
ix	970.5800	970.5797	6.54	-0.3	2 ± 0.1	Peptide [1-5] + (C16:1)/Palmitoleoylation
x	1020.5956	1020.5946	6.64	-1.0	1 ± 0.1	Peptide [1-5] + (C20:4) / Arachidonoylation
xi	1046.6113	1046.6066	6.71	-4.5	0.4 ± 0.03	[Peptide 1-5] + (C22:5) / Docosapentaenoylation
xii	972.5956	972.5963	6.89	0.7	16.5 ± 0.5	Peptide [1-5] + (C16:0)/Palmitoylation
xiii	1022.6113	1022.6081	6.96	-3.1	6 ± 0.2	Peptide [1-5] + (C20:3)/Dihomo-γ-linolenoylation
xiv	998.6113	998.6115	6.96	0.2	105 ± 4.5	Peptide [1-5] + (C18:1)/Oleoylation
xv	1024.6269	1024.6262	7.09	-0.7	4 ± 1	Peptide [1-5] + (C20:2)/Eicosadienoylation
xvi	1000.6269	1000.6272	7.35	0.3	33 ± 2	Peptide [1-5] + (C18:0)/Stearoylation
xvii	1026.6426	1026.6417	7.39	-0.9	11 ± 0.2	Peptide [1-5] + (C20:1)/Eicosenoylation
xviii	1052.6582	1052.6520	7.51	-5.9	1 ± 0.1	Peptide [1-5] + (C22:2)/Docosadienoylation

‡ Both theoretical (Theor) and measured (Meas) *m/z* are for the monoisotopic peak. Theoretical mass obtained from MassLynx software (V4.1).

§ The peak area (A) represents the summation of peak area over all observed charge states for each acylated peptide, z=1-2 for peptide [1-5]; z=2-4 for peptide [234-259]. Errors reported as SEM (n=2).

Table 9.35. **Product ions identified following the isolation and fragmentation of the [M + H]$^+$ precursor ion N-stearoylated peptide [1-5] at *m/z* 1000.63. The amino acid residue highlighted in red indicates the site of stearoylation.**

Ion	AA Residues	Meas *m/z*	*z*	Sequence Ladder	Error (ppm)
[M + H]$^+$	[1-5]	1000.6289	1	**M**WELR	2.0
[M + H]$^+$ - H_2O	[1-5]	982.6109	1	**M**WELR	-5.5
b2	[1-2]	584.3873	1	**M**W	-2.2
b3	[1-3]	713.4268	1	**M**WE	-6.2
y2	[4-5]	288.2020	1	LR	-5.2
y4	[2-5]	603.3249	1	WELR	-0.8
y2-NH_3	[4-5]	271.1772	1	LR	0.7
y3-NH_3	[3-5]	400.2202	1	ELR	1.5
y4-NH_3	[4-5]	586.3018	1	WELR	5.0
im1	[1-1]	370.3099	1	**M**	-11.9
im2	[2-2]	159.0939	1	L	10.7

Table 9.36. **Product ions identified following the isolation and fragmentation of the [M + 3H]$^{3+}$ precursor ion K238-stearoylated peptide [234-259] at *m/z* 1006.91. The amino acid residue highlighted in red indicates the site of stearoylation and the deamidation site in blue.**

Ion	AA Residues	Meas *m/z*	*z*	Sequence Ladder	Error (ppm)
[M + 3H]$^{3+}$	[1-26]	1006.8986	3	LSIL**K**GHSRPSES**N**GQPEVTGEPVELK	-5.9
b3	[1-3]	314.2052	1	LSI	-8.9
b8	[1-8]	1121.8002	1	LSIL**K**GSR	-2.1
b15	[1-15]	1822.0519	1	LSIL**K**GSRPSES**N**GQ	-9.4
b15	[1-15]	911.5338	2	LSIL**K**GSRPSES**N**GQ	-5.0
y2	[25-26]	260.1973	1	LK	-0.4
y3	[24-26]	389.2407	1	ELK	8.7
y6	[21-26]	714.3996	1	EPVELK	-5.9
y7	[20-26]	771.4238	1	GEPVELK	-1.8
y8	[19-26]	872.4694	1	TGEPVELK	-4.0
y9	[18-26]	971.5373	1	VTGEPVELK	-4.1
y11	[16-26]	1197.6332	1	PEVTGEPVELK	-2.9
y11	[16-26]	599.3207	2	PEVTGEPVELK	-2.5
y14	[13-26]	749.3765	2	**N**GQPEVTGEPVELK	1.1
y15	[12-26]	792.8932	2	S**N**GQPEVTGEPVELK	1.9
y18	[9-26]	949.4553	2	PSES**N**GQPEVTGEPVELK	-0.1
y19	[8-26]	1027.5060	2	RPSES**N**GQPEVTGEPVELK	0.2
y22	[5-26]	1296.7181	2	**K**GHSRPSES**N**GQPEVTGEPVELK	5.7
y23	[4-26]	1339.2335	2	L**K**GHSRPSES**N**GQPEVTGEPVELK	-2.6

Table 9.37. **Product ions identified following the isolation and fragmentation of the [M + H]$^+$ precursor ion N-palmitoylated peptide [1-5] at *m/z* 972.59. The amino acid residue highlighted in red indicates the site of palmitoylation.**

Ion	AA Residues	Meas *m/z*	*z*	Sequence Ladder	Error (ppm)
[M + H]$^+$	[1-5]	972.5966	1	**M**WELR	1.0
b2	[1-2]	556.3589	1	**M**W	2.9
b3	[1-3]	685.4005	1	**M**WE	0.9
b4	[1-4]	798.4790	1	**M**WEL	-8.6
y1	[5-5]	175.1185	1	R	-5.7
y2	[4-5]	288.2044	1	LR	3.1
y4	[2-5]	603.3237	1	WELR	-2.8
y2-NH_3	[4-5]	271.1783	1	LR	-1.8
y3-NH_3	[3-5]	400.2203	1	ELR	1.7
im1	[1-1]	342.2855	1	**M**	7.3
im2	[2-2]	159.0926	1	L	2.5

Table 9.38. **Product ions identified following the isolation and fragmentation of the [M + 3H]$^{3+}$ precursor ion K238-palmitoylated peptide [234-259] at *m/z* 997.56. The amino acid residue highlighted in red indicates the site of palmitoylation and the deamidation site in blue.**

Ion	AA Residues	Meas *m/z*	*z*	Sequence Ladder	Error (ppm)
[M + 3H]$^{3+}$	[1-26]	997.5628	3	LSILKGHSRPSESNGQPEVTGEPVELK	2.1
b3	[1-3]	314.2056	1	LSI	-7.6
b3-H_2O	[1-3]	296.1982	1	LSI	2.7
b4	[1-4]	427.2928	1	LSIL	1.9
b5	[1-5]	793.6164	1	LSILK	-0.3
b6	[1-6]	850.6384	1	LSILKG	0.4
b8	[1-8]	1093.7694	1	LSILKGSR	-1.7
b11	[1-11]	1406.8931	1	LSILKGSRPSE	-3.9
b12	[1-12]	747.4749	2	LSILKGSRPSES	7.5
b13	[1-13]	1608.9670	1	LSILKGSRPSESN	5.8
b14	[1-14]	833.4949	2	LSILKGSRPSESNG	1.7
b15	[1-15]	1794.0284	1	LSILKGSRPSESNGQ	-5.2
b15	[1-15]	897.5245	2	LSILKGSRPSESNGQ	1.9
b21	[1-21]	1203.6644	2	LSILKGSRPSESNGQPEVTGE	2.8
y2	[25-26]	260.1968	1	LK	-2.3
y3	[24-26]	389.2404	1	ELK	1.0
y4	[23-26]	488.3069	1	VELK	-3.1
y5	[22-26]	585.3596	1	PVELK	-2.7
y7	[20-26]	771.4268	1	GEPVELK	2.1
y8	[19-26]	872.4722	1	TGEPVELK	-0.8
y9	[18-26]	971.5446	1	VTGEPVELK	3.4
y11	[16-26]	1197.6348	1	PEVTGEPVELK	-1.6
y11	[16-26]	599.3229	2	PEVTGEPVELK	1.2
y12	[15-26]	663.3458	2	QPEVTGEPVELK	-8.6
y13	[14-26]	1382.7062	1	GQPEVTGEPVELK	-7.6
y15	[12-26]	792.8846	2	SNGQPEVTGEPVELK	-8.9
y18	[9-26]	949.4603	2	PSESNGQPEVTGEPVELK	5.2
y19	[8-26]	1027.5173	2	RPSESNGQPEVTGEPVELK	11.2
y21	[6-26]	1099.5316	2	GHSRPSESNGQPEVTGEPVELK	-1.0
y22	[5-26]	1282.6973	2	KGHSRPSESNGQPEVTGEPVELK	1.8
y23	[4-26]	1339.2405	2	LKGHSRPSESNGQPEVTGEPVELK	2.6

Table 9.39. **Product ions identified following the isolation and fragmentation of the [M + H]$^+$ precursor ion N-palmitoleoylated peptide [1-5] at *m/z* 970.58. The amino acid residue highlighted in red indicates the site of palmitoleoylation.**

Ion	AA Residues	Meas *m/z*	*z*	Sequence Ladder	Error (ppm)
[M + H]$^+$	[1-5]	970.5789	1	**M**WELR	-1.1
[M + H]$^+$ - H_2O	[1-5]	952.5670	1	**M**WELR	-2.5
b2	[1-2]	554.3373	1	**M**W	-7.8
b3	[1-3]	683.3859	1	**M**WE	-2.5
b4	[1-4]	796.4628	1	WELR	-6.9
y2	[4-5]	288.2043	1	LR	2.8
y4	[2-5]	603.3277	1	WELR	3.8
y2-NH_3	[4-5]	271.1765	1	LR	-1.5
y3-NH_3	[3-5]	400.2192	1	ELR	-1.0
y4-NH_3	[4-5]	586.2954	1	WELR	-6.0
im1	[1-1]	340.2664	1	**M**	-2.9
im2	[2-2]	159.0921	1	L	-0.6
im5	[5-5]	129.1130	1	R	-7.7
im5-NH_3	[5-5]	112.0877	1	R	2.7

Table 9.40. **Product ions identified following the isolation and fragmentation of the [M + H]$^+$ precursor ion N-dihomo-γ-linolenoylated peptide [1-5] at *m/z* 1022.61. The amino acid residue highlighted in red indicates the site of dihomo-γ-linolenoylation.**

Ion	AA Residues	Meas *m/z*	*z*	Sequence Ladder	Error (ppm)
[M + H]$^+$	[1-5]	1022.6103	1	**M**WELR	-1.0
b2	[1-2]	606.3712	1	**M**W	-2.8
b3	[1-3]	735.4099	1	**M**WE	-7.6
y1	[5-5]	175.1179	1	R	-9.1
y2	[4-5]	288.2040	1	LR	-1.7
y3	[3-5]	417.2445	1	ELR	-3.8
y4	[2-5]	603.3189	1	WELR	-10.8
y2-NH_3	[4-5]	271.1773	1	LR	1.1
y3-NH_3	[3-5]	400.2198	1	ELR	0.5
y3-H_2O	[3-5]	399.2372	1	ELR	4.0
y4-NH_3	[4-5]	586.2949	1	WELR	-6.8
im1	[1-1]	392.3015	1	**M**	7.1
im2	[2-2]	159.0917	1	L	-3.1
im5-NH_3	[5-5]	112.0877	1	R	2.7

Table 9.41. **Product ions identified following the isolation and fragmentation of the [M + H]$^+$ precursor ion N-eicosadienoylated peptide [1-5] at *m/z* 1024.63. The amino acid residue highlighted in red indicates the site of eicosadienoylation.**

Ion	AA Residues	Meas *m/z*	*z*	Sequence Ladder	Error (ppm)
[M + H]$^+$	[1-5]	1024.6261	1	**M**WELR	-0.8
b2	[1-2]	608.3840	1	**M**W	-7.6
b3	[1-3]	737.4246	1	**M**WE	-8.9
y1	[5-5]	175.1199	1	R	2.3
y2	[4-5]	288.2030	1	LR	-1.7
y4	[2-5]	603.3222	1	WELR	-5.3
y2-NH_3	[4-5]	271.1766	1	LR	-1.5
y4-NH_3	[4-5]	586.2977	1	WELR	-2.0
im1	[1-1]	394.3110	1	**M**	-8.4
im2	[2-2]	159.0923	1	L	0.6

Table 9.42. **Product ions identified following the isolation and fragmentation of the [M + H]$^+$ precursor ion N-eicosenoylated peptide [1-5] at *m/z* 1026.64. The amino acid residue highlighted in red indicates the site of eicosenoylation.**

Ion	AA Residues	Meas *m/z*	*z*	Sequence Ladder	Error (ppm)
[M + H]$^+$	[1-5]	1026.6427	1	**M**WELR	0.1
[M + H]$^+$ - H_2O	[1-5]	1008.6314	1	**M**WELR	-0.6
b2	[1-2]	610.4014	1	**M**W	-4.6
b3	[1-3]	739.4454	1	**M**WE	-1.9
y1	[5-5]	175.1189	1	R	-3.4
y2	[4-5]	288.2024	1	LR	-3.8
y4	[2-5]	603.3210	1	WELR	-7.3
y1-NH_3	[5-5]	158.0940	1	R	6.9
y2-NH_3	[4-5]	271.1771	1	LR	0.4
y3-NH_3	[3-5]	400.2192	1	ELR	-1.0
y3-H_2O	[3-5]	399.2348	1	ELR	-2.0
y4-NH_3	[4-5]	586.2971	1	WELR	-3.1
im1	[1-1]	396.3283	1	**M**	-4.3
im2	[4-4]	159.0917	1	L	-3.1
im5-NH_3	[5-5]	112.0877	1	R	2.7

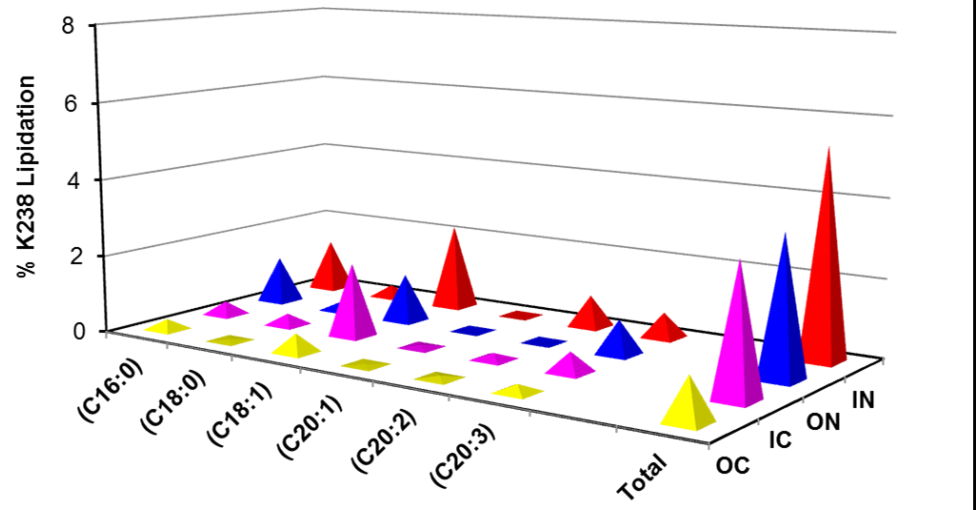

Lens Fraction	Normalised $A_{Lipidation}$ (a.u.) % K238 Lipidation					
	(C16:0)	(C18:0)	(C18:1)	(C20:1)	(C20:2)	(C20:3)
OC	0.3 ± 0.1	0.04 ± 0.02	0.5 ± 0.01	0.03 ± 0.01	0.1 ± 0.01	0.2 ± 0.01
IC	0.4 ± 0.1	0.3 ± 0.0	1.9 ± 0.1	0.1 ± 0.01	0.2 ± 0.01	0.5 ± 0.05
ON	1.2	0.2	1.2	0	0	0.9
IN	1.3	0.3	2.2	0	0.8	0.65

Figure 9.1. **The relative percentage of each single lipidation species and total lipidation on K238 AA site, using digestion protocol Method-D and LC-MS Method-IIII (see section 8.2.2.2.1). The normalisation of each acylation ratio is performed relative to the reference non-acylated peptide [234-259] as follows: the ratio of peptide [234-259]$_{pal}$ = peak area peptide [234-259]$_{pal}$/summed peak area (total of all lipidation on peptide [234-259] + reference peptide [234-259]); the ratio of peptide [234-259]$_{ole}$ = peak area peptide [234-259]$_{ole}$/summed peak area (total of all lipidation on peptide [23-259] + reference peptide [234-259]) and etc. Errors represent SEM, when n=2.**

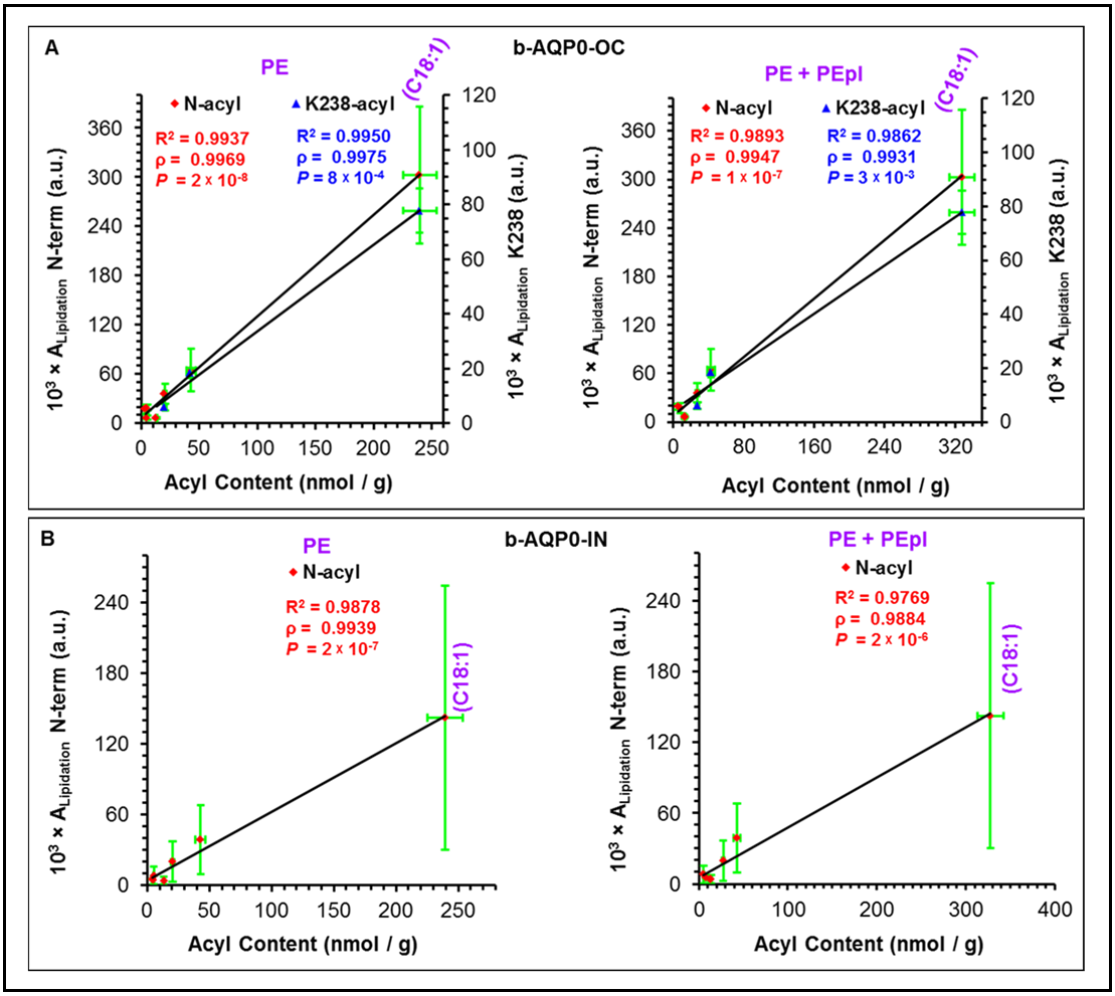

Figure 9.2. **Correlations between the amount of ester-linked transferrable fatty acyl content of bovine lens lipids and the peak areas for lipidated peptides ($A_{Lipidation}$) of (A) b-AQP0-OC and (B) b-AQP0-IN, using digestion protocol Method-A (see section 8.2.2.1.2) and LC-MS Method-II (see section 8.1.2.1.1). Lipid data obtained from lipidomics MS analysis[1] (see Table 4.14). Peak areas for N-terminus acylation were calculated from EIC of each acylation on peptide [1-5], while peak areas for K238 acylation were calculated from EIC of each acylation on non-truncated peptide [234-259]. Errors plotted as *X-axis* SEM (fatty acyl content, n=4) and *Y-axis* SEM (peak area for lipidated peptides, n=2). The line and the R^2 statistic are from linear regression analysis. The ρ-value represents the Pearson correlation coefficient (r) and the *p*-value represents the t-test of the correlation coefficient.**

Table 9.43. **The deconvoluted *m/z* for non-acylated peptides identified from h-AQP0-N male donor age 22 (M22) tryptic digestion, using Method-D and LC-MS Method-IIII on Synapt G2-s (see experimental section 8.2.2.2.1).**

AA Residues	MCL‡	Sequence + Modification	Theor *m/z*‡ $[M + H]^+$	Meas *m/z*‡ $[M + H]^+$	Error (ppm)
[1-5]	0	MWELR	734.3660	734.3642	-2.4
[6-11]	0	SASFWR	753.3684	753.3670	-1.9
[6-33]	1	SASFWRAIFAEFFATLFYVFFGLGSSLR	3237.6565	3237.6540	-0.8
[12-33]	0	AIFAEFFATLFYVFFGLGSSLR	2503.3066	2503.3051	-0.6
[34-85]	0	WAPGPLHVLQVAMAFGLALATLVQSVGHISGAHVNPAVTFAFLVGSQMSLLR	5379.9019	5379.8970	-0.9
[86-113]	0	AFCYMAAQLLGAVAGAAVLYSVTPPAVR	2810.4736	2810.4559	-6.3
[86-113]	0	AFCYMAAQLLGAVAGAAVLYSVTPPAVR [1×O]	2826.4688	2826.4594	-3.3
[114-152]	0	GNLALNTLHPAVSVGQATTVEIFLTLQFVLCIFATYDER	4265.2319	4265.2234	-2.0
[114-153]	1	GNLALNTLHPAVSVGQATTVEIFLTLQFVLCIFATYDERR	4421.3330	4421.3298	-0.7
[114-153]	1	GNLALNTLHPAVSVGQATTVEIFLTLQFVLCIFATYDERR [1×Deamidation]	4422.3174	4422.3076	-2.2
[153-187]	1	RNGQLGSVALAVGFSLALGHLFGMYYTGAGMNPAR [1×Deamidation]	3597.8098	3597.8078	-0.6
[154-187]	0	NGQLGSVALAVGFSLALGHLFGMYYTGAGMNPAR [1×Deamidation]	3441.7087	3441.7039	-1.4
[154-187]	0	NGQLGSVALAVGFSLALGHLFGMYYTGAGMNPAR [1×Deamidation; 1×O]	3457.7036	3457.6970	-1.9
[188-226]	0	SFAPAILTGNFTNHWVYWVGPIIGGGLGSLLYDFLLFPR	4309.2642	4309.2650	0.2
[188-228]	1	r.SFAPAILTGNFTNHWVYWVGPIIGGGLGSLLYDFLLFPRLK.s	4550.4434	4550.4294	-3.1
[188-228]	1	SFAPAILTGNFTNHWVYWVGPIIGGGLGSLLYDFLLFPRLK [2×O]	4582.4331	4582.4221	2.4
[227-233]	1	LKSISER	832.4893	832.4845	-5.8
[227-233]	1	LKSISER [1×P]	912.4556	912.4546	-1.1
[227-238]	2	LKSISERLSVLK	1372.8528	1372.8484	-3.2
[227-238]	2	LKSISERLSVLK [1×P]	1452.8191	1452.8146	-3.1
[227-263]	3	LKSISERLSVLKGAKPDVSNGQPEVTGEPVELNTQAL [2×Deamidation]	3906.0710	3906.0678	-0.8
[229-233]	0	SISER	591.3102	591.3093	-1.5
[229-233]	0	SISER [1×P]	671.2766	671.2742	-3.6
[229-238]	1	SISERLSVLK	1131.6737	1131.6704	-2.9
[229-238]	1	SISERLSVLK [1×P]	1211.6401	1211.6386	-1.2
[229-238]	1	SISERLSVLK [2×P]	1291.6064	1291.6008	-4.3
[229-263]	2	SISERLSVLKGAKPDVSNGQPEVTGEPVELNTQAL [2×Deamidation]	3664.8921	3664.8949	0.8
[229-263]	2	SISERLSVLKGAKPDVSNGQPEVTGEPVELNTQAL [2×Deamidation; 1×P]	3744.8584	3744.8542	-1.1
[234-238]	0	LSVLK	559.3819	559.3809	-1.8
[234-238]	0	LSVLK [1×P]	639.3483	639.3464	-3.0
[234-263]	1	LSVLKGAKPDVSNGQPEVTGEPVELNTQAL [2×Deamidation]	3092.6003	3092.5994	-0.3
[234-263]	1	LSVLKGAKPDVSNGQPEVTGEPVELNTQAL [2×Deamidation; 1×P]	317.5667	3172.5616	-1.6
[239-263]	0	GAKPDVSNGQPEVTGEPVELNTQAL [2×Deamidation]	2552.2368	2552.2342	-1.0

‡Both theoretical (Theor) and measured (Meas) *m/z* are for the monoisotopic peak. Theoretical mass obtained from MassLynx software (V4.1). (MCL) is number of missed cleavages.

Table 9.44. **The deconvoluted *m/z* for identified acylated peptides followed trypsin digestion of h-AQP0-N male donor age 22 (M22).**

Entry	Theor *m/z*‡ $[M + H]^+$	Meas *m/z*‡ $[M + H]^+$	RT (min)	Error (ppm)	10^3 × Total $A_{Lipidation}$§ (a.u.)	Assignment
^{227}LKSISERLSVLKGAKPDVSNGQPEVTGEPVELNTQAL^{263}						
i	4170.313	4170.3164	5.24	-0.8	4.3	Peptide [227-263] + (C18:1) + 2 × Deamidation/Oleoylation
^{229}SISERLSVLKGAKPDVSNGQPEVTGEPVELNTQAL^{263}						
ii	3901.1006	3901.1062	4.98	-1.4	1.6	Peptide [229-263] + (C16:1) + 2 × Deamidation/Palmitoleoylation
iii	3903.1014	3903.1218	5.24	-5.2	2.3	Peptide [229-263] + (C16:0) + 2 × Deamidation/Palmitoylation
iv	3887.0866	3887.0906	5.24	-1.0	2.4	Peptide [229-263] + (C15:1) + 2 × Deamidation/Pentadecenoylation
v	3929.1307	3929.1375	5.31	-1.7	9.2	Peptide [229-263] + (C18:1) + 2 × Deamidation/Oleoylation
vi	4009.1074	4009.1038	5.34	0.9	2.6	Peptide [229-263] + (C18:1) + P + 2 × Deamidation/Oleoylation
vii	3931.0663	3931.1531	5.48	-22.1	1.6	Peptide [229-263] + (C18:0) + 2 × Deamidation/Stearoylation
^{1}MWELR^{5}						
viii	970.5800	970.5803	6.48	0.3	0.5	Peptide [1-5] + (C16:1)/Palmitoleoylation
ix	1044.5956	1044.5916	6.54	-3.8	0.4	Peptide [1-5] + (C22:6)/Docosahexaenoylation
x	1020.5956	1020.5920	6.60	-3.5	0.7	Peptide [1-5] + (C20:4)/Arachidonoylation
xi	972.5956	972.5930	6.86	-2.7	3.1	Peptide [1-5] + (C16:0)/Palmitoylation
xii	1070.5961	1070.5903	6.93	-5.4	0.7	Peptide [1-5] + (C20:3) + 3 × O /Dihomo-γ-linolenoylation
xiii	998.6113	998.6104	6.96	-0.9	20.6	Peptide [1-5] + (C18:1)/Oleoylation
xiv	1014.6062	1014.6045	6.96	-1.7	2.7	Peptide [1-5] + (C18:1) + O /Oleoylation
xv	1000.6269	1000.6227	7.32	-4.2	1.0	Peptide [1-5] + (C18:0)/Stearoylation
xvi	1026.6426	1026.6439	7.35	1.3	0.6	Peptide [1-5] + (C20:1)/Eicosenoylation

‡ Both theoretical (Theor) and measured (Meas) *m/z* are for the monoisotopic peak. Theoretical mass obtained from MassLynx software (V4.1).

§ The peak area (A) represents the summation of peak area over all observed charge states for each acylated peptide, z=1-2 for peptide [1-5]; z=3-5 for peptide [227-263] and peptide [229-263].

Table 9.45. **Product ions identified for N-oleoyl (peptide [1-5]) h-AQP0-N male donor age 22 (M22), obtained from total ion chromatogram (TIC) at 6.94 min following MS^E experiment on Synapt G2-s. The amino acid residue highlighted in red indicates the site of oleoylation.**

Ion	AA Residues	Meas *m/z*	*z*	Sequence Ladder	Error (ppm)
$[M + H]^+$	[1-5]	998.6102	1	**M**WELR	-1.1
$[M + H]^+ - H_2O$	[1-5]	980.6007	1	**M**WELR	0
b2	[1-2]	582.3674	1	**M**W	-9.4
b3	[1-3]	711.4145	1	**M**WE	-1.4
b4	[1-4]	824.501	1	**M**WEL	1.7
y1	[5-5]	175.1186	1	R	-5.1
y2	[4-5]	288.203	1	LR	-1.7
y3	[3-5]	417.2462	1	ELR	0.2
y4	[2-5]	603.3224	1	WELR	-5.0
$y1-NH_3$	[5-5]	158.0927	1	R	-1.3
$y2-NH_3$	[4-5]	271.1761	1	LR	-3.3
$y3-NH_3$	[3-5]	400.2171	1	ELR	-6.2
$y4-NH_3$	[4-5]	586.2999	1	WELR	1.7
im1	[1-1]	368.2975	1	**M**	-3.25
im2	[2-2]	159.0923	1	W	0.6
im4	[4-4]	86.097	1	L	1.2

Table 9.46. **Product ions identified for K238-oleoyl (peptide [229-263]) h-AQP0-N male donor age 22 (M22), obtained from total ion chromatogram (TIC) at 5.3 min following MS^E experiment on Synapt G2-s. The amino acid residue highlighted in red indicates the site of oleoylation and the deamidation sites in highlighted blue.**

Ion	AA Residues	Meas *m/z*	*z*	Sequence Ladder	Error (ppm)
b2	[1-2]	201.1229	1	SI	-4.5
b5	[1-5]	573.2997	1	SISER	0.2
b6	[1-6]	686.3854	1	SISERL	2.5
b8	[1-8]	872.4871	1	SISERLSV	3.4
b9	[1-9]	985.5652	1	SISERLSVL	-3.0
b10	[1-10]	1377.908	1	SISERLSVL**K**	-0.4
b12	[1-12]	1505.9694	1	SISERLSVL**K**GA	1.5
b18	[1-18]	1074.1372	2	SISERLSVL**K**GAKPDVS**N**	-1.2
b19	[1-19]	1102.6251	2	SISERLSVL**K**GAKPDVS**N**G	-21.8
b20	[1-20]	1166.6754	2	SISERLSVL**K**GAKPDVS**N**GQ	-2.6
b26	[1-26]	1472.8207	2	SISERLSVL**K**GAKPDVS**N**GQPEVTGE	3.0
b30	[1-30]	1691.9316	2	SISERLSVL**K**GAKPDVS**N**GQPEVTGEPVEL	-5.1
y2	[34-35]	203.1382	1	AL	-6.4
y5	[31-35]	547.2755	1	**N**TQAL	5.1
y6	[30-35]	660.3559	1	L**N**TQAL	-1.4
y12	[24-35]	1272.6417	1	TGEPVEL**N**TQAL	7.4
y15	[21-35]	799.4006	2	PEVTGEPVEL**N**TQAL	-1.7
y17	[19-35]	891.937	2	GQPEVTGEPVEL**N**TQAL	-5.5
y18	[18-35]	949.4553	2	NGQPEVTGEPVEL**N**TQAL	-0.2

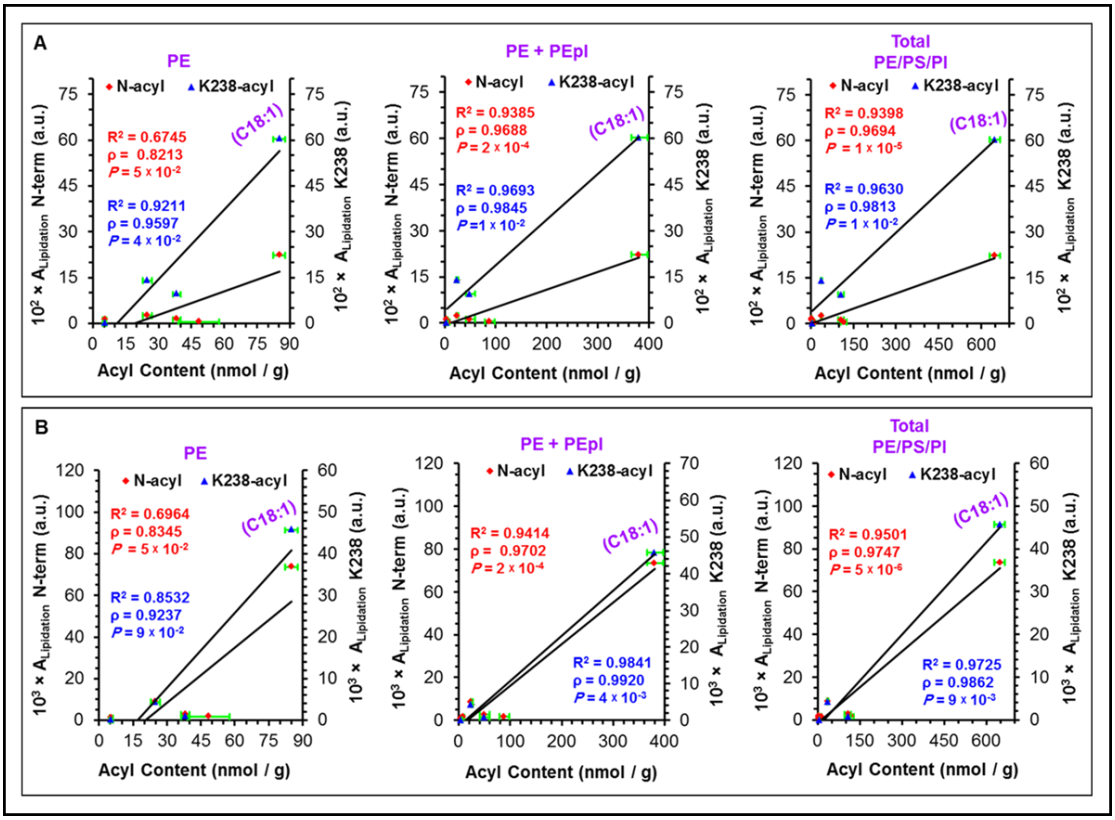

Figure 9.3. **Correlations between the amount of ester-linked transferrable fatty acyl content of human lens lipids and the peak areas for lipidated peptides of (A) h-AQP0-C male donor age 56 (M56) and (B) h-AQP0-N (M56). Lipid data obtained from lipidomics MS analysis[1] (see Table 4.17). Peak areas for N-terminus acylation were calculated from EIC of each acylation on peptide [1-5], while peak areas for K238 acylation were calculated from EIC of each acylation on non-truncated peptides (peptide [227-263] and peptide [229-263]) and truncated peptides (peptide [227-243], peptide [229-243], peptide [229-246] and peptide [234-246]). Errors plotted as *X-axis* SEM (fatty acyl content, n=4). The line and the R^2 statistic are from linear regression analysis. The ρ-value represents the Pearson correlation coefficient (r) and the *p*-value represents the t-test of the correlation coefficient.**

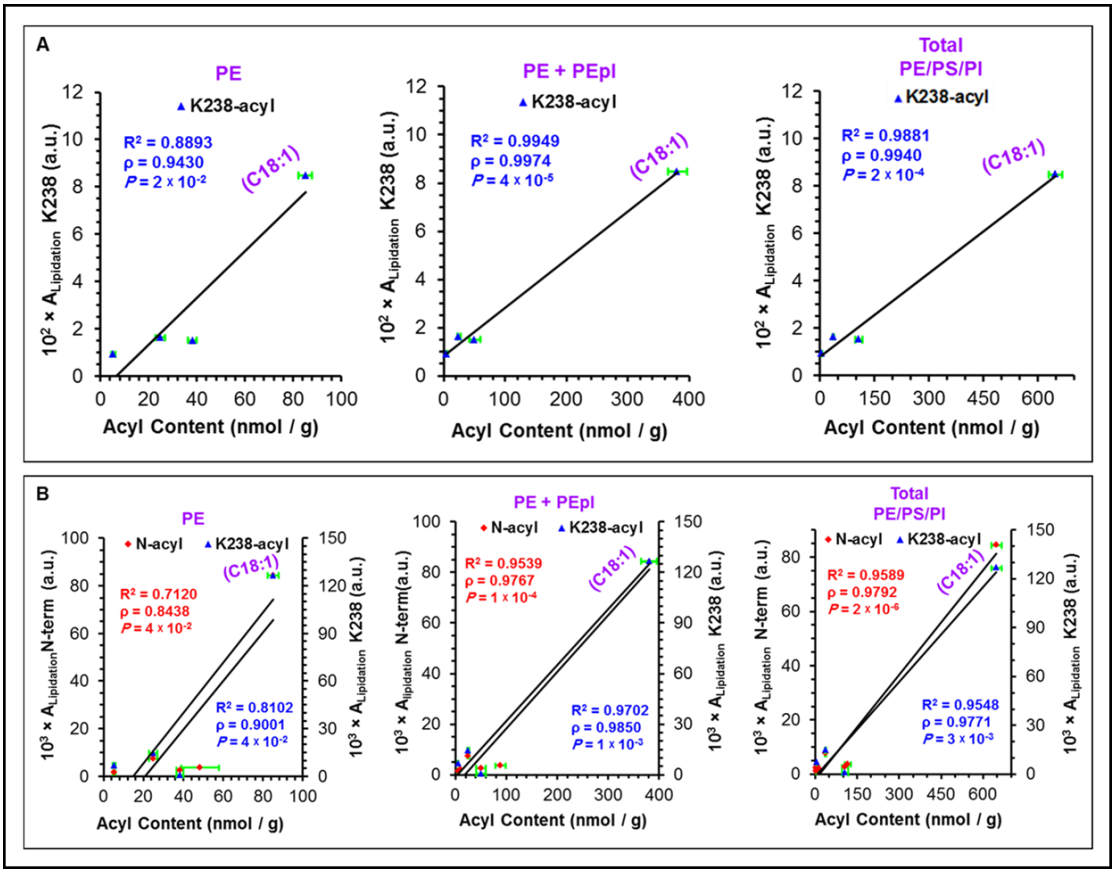

Figure 9.4. **Correlations between the amount of ester-linked transferrable fatty acyl content of human lens lipids and the peak areas for lipidated peptides of (A) h-AQP0-C male donor age 80 (M80) and (B) h-AQP0-N (M80). Lipid data obtained from lipidomics MS analysis[1] (see Table 4.17). Peak areas for N-terminus acylation were calculated from EIC of each acylation on peptide [1-5], while peak areas for K238 acylation were calculated from EIC of each acylation on non-truncated peptides (peptide [227-263] and peptide [229-263]) and truncated peptides (peptide [227-243], peptide [229-243], peptide [229-246] and peptide [234-246]). Errors plotted as *X-axis* SEM (fatty acyl content, n=4). The line and the R^2 statistic are from linear regression analysis. The ρ-value represents the Pearson correlation coefficient (r) and the *p*-value represents the t-test of the correlation coefficient.**

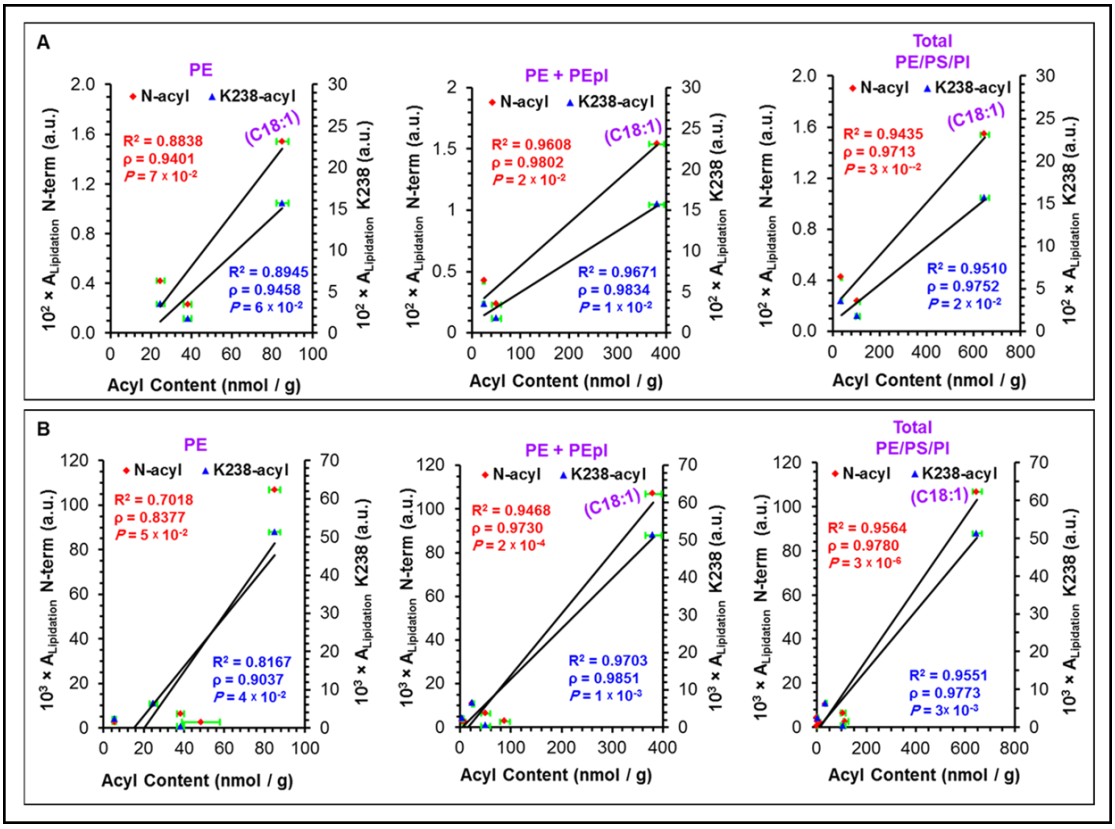

Figure 9.5. **Correlations between the amount of ester-linked transferrable fatty acyl content of human lens lipids and the peak areas for lipidated peptides of (A) h-AQP0-C female donor age 56 (F56) and (B) h-AQP0-N (F56). Lipid data obtained from lipidomics MS analysis[1] (see Table 4.17). Peak areas for N-terminus acylation were calculated from EIC of each acylation on peptide [1-5], while peak areas for K238 acylation were calculated from EIC of each acylation on non-truncated peptides (peptide [227-263] and peptide [229-263]) and truncated peptides (peptide [227-243], peptide [229-243], peptide [229-246] and peptide [234-246]). Errors plotted as *X-axis* SEM (fatty acyl content, n=4). The line and the R^2 statistic are from linear regression analysis. The ρ-value represents the Pearson correlation coefficient (r) and the *p*-value represents the t-test of the correlation coefficient.**

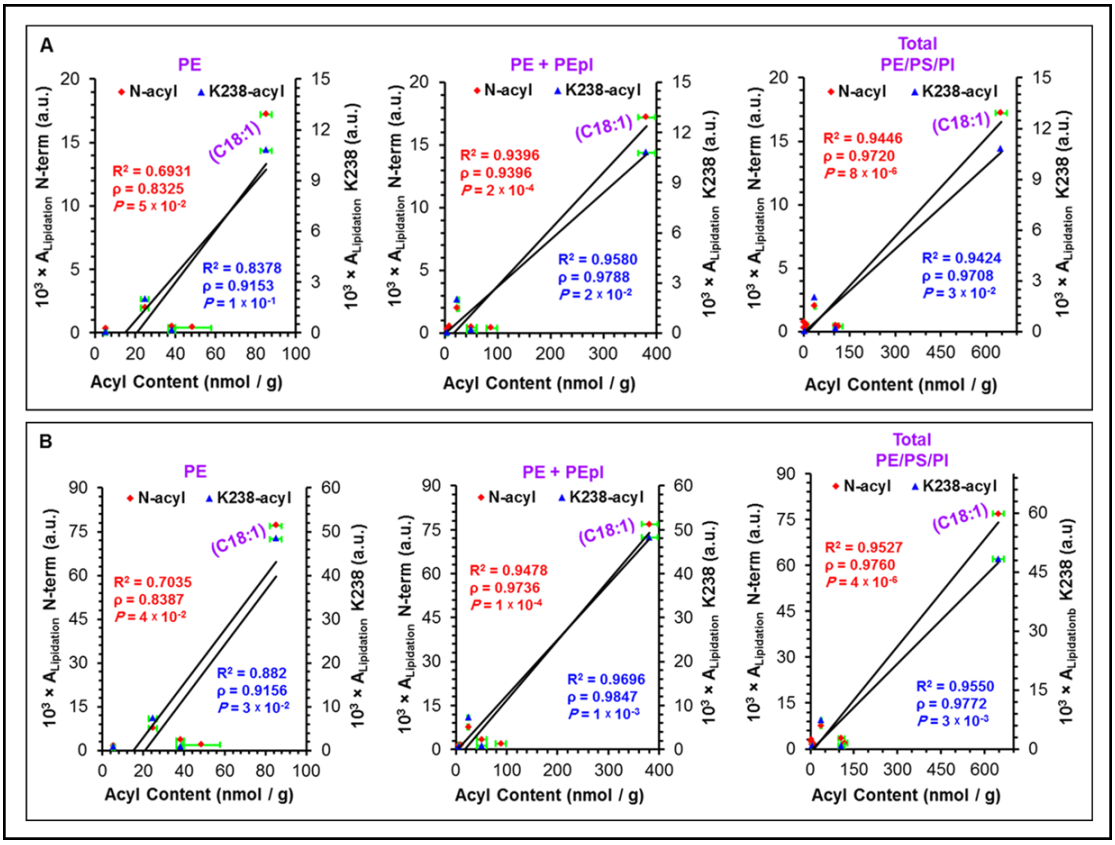

Figure 9.6. **Correlations between the amount of ester-linked transferrable fatty acyl content of human lens lipids and the peak areas for lipidated peptides of (A) h-AQP0-C female donor age 76 (F76) and (B) h-AQP0-N (F76). Lipid data obtained from lipidomics MS analysis[1] (see Table 4.17). Peak areas for N-terminus acylation were calculated from EIC of each acylation on peptide [1-5], while peak areas for K238 acylation were calculated from EIC of each acylation on non-truncated peptides (peptide [227-263] and peptide [229-263]) and truncated peptides (peptide [227-243], peptide [229-243], peptide [229-246] and peptide [234-246]). Errors plotted as *X-axis* SEM (fatty acyl content, n=4). The line and the R^2 statistic are from linear regression analysis. The ρ-value represents the Pearson correlation coefficient (r) and the *p*-value represents the t-test of the correlation coefficient.**

Table 9.47. **HELIQUEST[2] analysis of the [214-263] region of b-AQP0 and available at (http://heliquest.ipmc.cnrs.fr).**

Helix	Hydrophobicity	HMom*	*z*	Freq. Polar†	Freq. Non-polar†	D§
1	0.766	0.119	1	0.389	0.611	0.4423
2	0.636	0.028	0	0.444	0.556	0.0264
3	0.580	0.080	1	0.444	0.556	0.4055
4	0.677	0.148	1	0.389	0.611	0.4697
5	0.580	0.146	1	0.444	0.556	0.4678
6	0.586	0.141	1	0.444	0.556	0.4631
7	0.627	0.171	1	0.444	0.556	0.4914
8	0.614	0.165	3	0.444	0.556	1.1458
9	0.515	0.262	3	0.500	0.500	1.2373
10	0.418	0.279	3	0.500	0.500	1.2534
11	0.268	0.134	4	0.611	0.389	1.4465
12	0.208	0.135	4	0.611	0.389	1.4474
13	0.166	0.174	4	0.667	0.333	1.4843
14	0.187	0.185	2	0.667	0.333	0.8346
15	0.090	0.133	2	0.722	0.278	0.7855
16	0.112	0.111	1	0.722	0.278	0.4348
17	0.114	0.112	1	0.722	0.278	0.4357
18	0.034	0.039	1	0.778	0.222	0.3668
19	0.076	0.026	1	0.722	0.278	0.3545
20	0.076	0.026	1	0.722	0.278	0.3545
21	0.200	0.124	0	0.667	0.333	0.1171
22	0.120	0.145	0	0.722	0.278	0.1369
23	0.122	0.144	0	0.722	0.278	0.1359
24	-0.013	0.091	-1	0.778	0.222	-0.2441
25	-0.068	0.037	-1	0.778	0.222	-0.2951
26	0.055	0.128	-2	0.722	0.278	-0.5392
27	0.019	0.148	-3	0.722	0.278	-0.8503
28	0.116	0.112	-3	0.667	0.333	-0.8843
29	0.117	0.113	-3	0.667	0.333	-0.8833
30	0.092	0.124	-3	0.722	0.278	-0.8729
31	0.082	0.132	-3	0.722	0.278	-0.8654
32	0.134	0.175	-2	0.667	0.333	-0.4948
33	0.231	0.227	-2	0.611	0.389	-0.4457

*Hydrophobic moment (<μH>).

†Frequency of polar and non-polar residues in the segment.

§Discrimination factor calculated using the equation D = 0.944 (<μH>) + 0.33 (z).[3,4]

Table 9.48. **HELIQUEST[2] analysis of the [214-263] region of h-AQP0 and available at (http://heliquest.ipmc.cnrs.fr).**

Helix	Hydrophobicity	HMom*	*z*	Freq. Polar†	Freq. Non-polar†	D§
1	0.798	0.087	1	0.389	0.611	0.4121
2	0.668	0.046	0	0.444	0.556	0.0434
3	0.612	0.077	1	0.444	0.556	0.4027
4	0.709	0.162	1	0.389	0.611	0.4829
5	0.612	0.175	1	0.444	0.556	0.4952
6	0.586	0.197	1	0.444	0.556	0.5160
7	0.627	0.226	1	0.444	0.556	0.5433
8	0.614	0.219	3	0.444	0.556	1.1967
9	0.515	0.315	3	0.500	0.500	1.2874
10	0.438	0.329	3	0.500	0.500	1.3006
11	0.288	0.181	4	0.556	0.444	1.4909
12	0.229	0.188	4	0.556	0.444	1.4975
13	0.146	0.265	3	0.611	0.389	1.2402
14	0.270	0.341	2	0.556	0.444	0.9819
15	0.173	0.299	2	0.611	0.389	0.9423
16	0.195	0.277	1	0.611	0.389	0.5915
17	0.197	0.277	1	0.611	0.389	0.5915
18	0.085	0.169	1	0.667	0.333	0.4895
19	0.127	0.153	1	0.611	0.389	0.4744
20	0.127	0.153	1	0.611	0.389	0.4744
21	0.251	0.247	0	0.556	0.444	0.2332
22	0.171	0.232	0	0.611	0.389	0.2190
23	0.173	0.230	0	0.611	0.389	0.2171
24	0.070	0.219	-1	0.667	0.333	-0.1233
25	0.016	0.165	-1	0.667	0.333	-0.1742
26	0.138	0.181	-2	0.611	0.389	-0.4891
27	0.103	0.215	-3	0.611	0.389	-0.7870
28	0.180	0.222	-3	0.611	0.389	-0.7804
29	0.202	0.242	-4	0.611	0.389	-1.0915
30	0.176	0.257	-4	0.667	0.333	-1.0774
31	0.207	0.238	-3	0.667	0.333	-0.7653
32	0.156	0.194	-3	0.667	0.333	-0.8069
33	0.253	0.249	-3	0.611	0.389	-0.7549

*Hydrophobic moment (<μH>).

†Frequency of polar and non-polar residues in the segment.

§Discrimination factor calculated using the equation D = 0.944 (<μH>) + 0.33 (z).[3,4]

9.4. Reference

1 Deeley, Jane M., Todd W. Mitchell, Xiaojia Wei, John Korth, Jessica R. Nealon, Stephen J. Blanksby, and Roger JW Truscott. "Human lens lipids differ markedly from those of commonly used experimental animals." *Biochimica et Biophysica Acta (BBA)-Molecular and Cell Biology of Lipids*, 1781 (**2008**): 288-298.

2 Gautier, Romain, Dominique Douguet, Bruno Antonny, and Guillaume Drin. "HELIQUEST: a web server to screen sequences with specific α-helical properties." *Bioinformatics*, 24 (**2008**): 2101-2102.

3 Keller, Rob CA. "The prediction of novel multiple lipid-binding regions in protein translocation motor proteins: a possible general feature." *Cellular & Molecular Biology Letters*, 16 (**2011**): 40-54.

4 Keller, Rob CA. "New user-friendly approach to obtain an Eisenberg plot and its use as a practical tool in protein sequence analysis." *International Journal of Molecular Sciences*, 12 (**2011**): 5577-5591.